Physics of Atomic Nuclei, Vol. 66, No. 5, 2003, pp. 787–797. Translated from Yadernaya Fizika, Vol. 66, No. 5, 2003, pp. 819–829.

NUCLEI
Experiment

Production of Neutral and Charged Pions in the Reaction $^{12}C(\gamma, \pi p)$ in the Second Resonance Region

I. V. Glavanakov*

Institute of Nuclear Physics, Tomsk Polytechnic University, Tomsk, 634004 Russia

Received July 18, 2001; in final form, May 13, 2002

Abstract—The results are presented that were obtained by investigating the production of pion–proton pairs in the reaction $^{12}C(\gamma, \pi p)$. The experiment in question was performed in the second resonance region of photon energy. The results of this measurement are analyzed on the basis of a model that takes into account the processes of single and double quasifree pion photoproduction. © *2003 MAIK "Nauka/Interperiodica".*

1. INTRODUCTION

Pion photoproduction on nuclei in $(\gamma, \pi N)$ reactions accompanied by nucleon emission has attracted the attention of researchers for quite a long time. The first studies devoted to this subject were performed as far back as the early 1970s [1, 2], and interest in these reactions has only grown since that time. The latest experimental results in these realms were obtained at four research centers: at the Tomsk synchrotron in Russia [3, 4], at the MIT-Bates accelerator in the United States [5], at the MAMI electron microtron in Germany [6, 7], and at the BNL-LEGS in the United States by using a linearly polarized photon beam [8]. In all of the aforementioned studies, the measurements were performed in a kinematical region that includes the quasifree-pion-production domain, which is close in kinematics to that of two-particle (γ, π) processes on free nucleons.

Keen interest in quasifree pion photoproduction on nuclei at intermediate energies is motivated predominantly by the fact that, with a high probability, all nonstrange nucleon resonances decay into a pion and a nucleon; therefore, reactions of the $A(\gamma, \pi N)$ type provide a convenient tool for studying the properties of nucleon resonances emerging in nuclei or existing there prior to interaction.

Resonance nucleon states clearly manifest themselves in pion scattering on protons in the reaction $\pi p \to \pi p$. Eight resonance states of this type are known in the mass region extending up to 1700 MeV. Three of these, $\Delta(1232)P_{33}$, $N(1520)D_{13}$, and $N(1680)F_{15}$, are observed as resolved peaks in the energy dependence of the total cross section for the hadronic absorption of photons on a proton [9].

The production of nucleon resonances in a nucleus via electromagnetic excitation offers a promising method for studying their properties. Experiments were performed in which the total cross sections for hadronic photoabsorption were measured in the resonance region for a wide range of nuclei from extremely light (H, D, He [10, 11]) through light (Be, C [12, 13]) to heavy (Pb, U [14–16]) ones. The observation that the $N(1520)D_{13}$ and $N(1680)F_{15}$ resonances, whose excitation is clearly seen in the interaction of photons with free nucleons, do not manifest themselves in the interaction of photons with nuclei is the most surprising result of those experiments, which has not yet been explained satisfactorily.

A direct way to solve the problem of the photoexcitation of higher resonances in nuclei consists in performing a detailed analysis of individual reactions leading to photon absorption. At the photon-energy value corresponding, in photoabsorption on a proton, to the cross-section maximum associated with the excitation of the $N(1520)$ resonance, two processes that have approximately identical cross sections are dominant—these are single and double pion production. It can be expected that processes of single and double quasifree pion photoproduction will be dominant in the interaction of photons with a nucleus. It seems unlikely that the exclusive cross sections for $A(\gamma, \pi N)$ reactions—and the more so for $A(\gamma, \pi\pi N)$ reactions—will be measured in the near future over the entire phase space. In all probability, it would be optimal to compare data on the process of photoabsorption on nuclei with the results obtained by measuring inclusive and semiexclusive cross sections for pion production. In order to test the assumption that the width of the $N(1520)$ resonance changes in nuclei, the semi-inclusive cross

*e-mail: glavanak@npi.tpu.ru

1063-7788/03/6605-0787$24.00

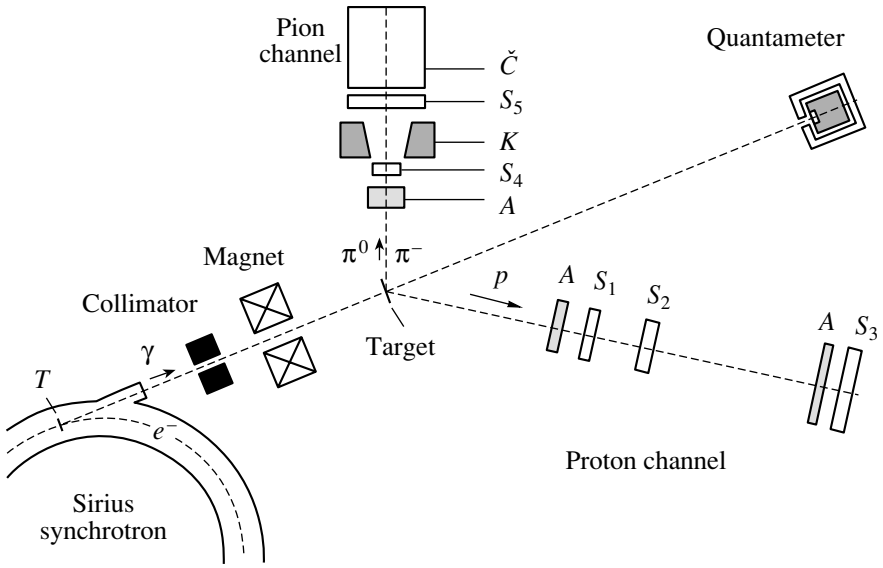

Fig. 1. Layout of the experimental facility: (T) internal target of the synchrotron, ($S_{1,2,3,4,5}$) scintillation counters, ($\check{C}$) total-absorption Cherenkov counter, (K) aperture collimator of the γ spectrometer, and (A) absorbers.

sections for neutral-pion photoproduction on a number of nuclei were recently measured in the second resonance region by using the TAPS detector at the MAMI microtron [17]. With the aim of obtaining information about quasifree pion production in the same energy region, a semiexclusive experiment devoted to studying the photoproduction of pion–proton pairs on Li, C, and Al nuclei was performed at the Tomsk synchrotron.

The present article reports on the results of an experiment performed to study the production of pion–proton pairs on carbon nuclei and the single and double production of pions on hydrogen nuclei. The ensuing exposition is organized as follows. An account of the experimental facility and procedure used is given in Section 2. The results obtained by measuring the cross section for pion production on hydrogen are reported in Section 3, and data for a carbon target are presented in Section 4. The experimental results are analyzed on the basis of a model that takes into account processes of single and double pion photoproduction.

2. EXPERIMENTAL PROCEDURE

The experiment was performed in a beam of bremsstrahlung photons from the Tomsk synchrotron. The layout of the experimental facility used is depicted in Fig. 1. The bremsstrahlung photons were produced as the result of moderating 900-MeV electrons on an internal tantalum target T of the accelerator, the target thickness being 0.07 radiation units. The duration of radiation pulses was 20 ms. The beam was formed by a collimator that ensured an angular divergence of 1 mrad, was purified from charged particles by a dipole magnet, and was transported to the experimental hall to hit the target under study arranged there. The total energy of the photon beam was measured by a Gauss quantameter [18] to a precision of 3%. Carbon of natural isotopic composition in the form of a plate having a thickness of $n_{\mathrm{C}} = 4.3 \times 10^{22}$ nucl./cm^2 was used for a target. The cross sections for pion production on a proton were measured in experiments with a carbon and a CH_2 target.

The experimental facility used had three detection channels. These were the proton channel and the channels for recording neutral and charged pions. The last two channels were arranged on the same axis. A major part of the measuring equipment of this facility was previously used in the experiment reported in [19]. The proton channel was formed by a scintillation time-of-flight spectrometer consisting of three counters (S_1, S_2, S_3) that recorded charged particles within a solid angle of 4.2 msr. The energy of the detected particle was determined from the time of flight over the base of 3.5 m between counters S_1 and S_3. The accuracy in measuring the proton kinetic energy (root-mean-square deviation) within the range 140–280 MeV was 13–40 MeV. The identification of protons in this energy range was performed with the aid of absorbers that removed the background from low-energy electrons and pions.

Figures 2*a* and 2*b* show, respectively, an example of the time-of-flight spectrum and the calculated time-of-flight (t) dependences of the pion and proton energy losses in the scitillation counter S_3 of the

proton channel. The position of relativistic electrons in the figure is indicated by the arrow. Data used to estimate the cross sections in question were taken from the range of proton times of flight that is bounded in the figure by two vertical dotted straight lines.

The proton channel was arranged at an angle of 41° with respect to the photon-beam axis. The precision in measuring the polar and azimuthal angles (θ_p and ϕ_p, respectively) depended on the detector dimensions and on multiple Coulomb scattering in the scintillators and absorbers used; for protons of energy in the range 140–280 MeV, the respective uncertainties are $\sigma_{\theta_p} = 1.8°–1.5°$ and $\sigma_{\phi_p} = 2.7°–2.3°$.

The pion channel was positioned at an angle of 61° with respect to the photon-beam axis. Neutral pions were recorded by one decay photon with the aid of a total-absorption Cherenkov γ spectrometer, which consisted of a total-absorption Cherenkov counter $\check{C}$ based on a TF-1 crystal, a lead aperture collimator K forming the solid angle of the γ spectrometer, and a thin scintillation counter S_5 suppressing the detection of charged particles. The solid angle of the γ spectrometer was 30 msr. The spectrometer recorded photons of energy in excess of about 80 MeV. In the pion-energy range being studied, the angular distribution of decay photons is sharply stretched in the pion-momentum direction. Therefore, a high-energy photon reproduces the spatial features of a neutral pion to a satisfactory precision. For the pion kinetic energies of $T_\pi = 200$, 400, and 600 MeV, Fig. 2*c* shows the efficiency of neutral-pion detection as a function of the polar emission angle θ_π. At these energy values, the uncertainties in determining the polar angle of neutral-pion emission are $\sigma_{\theta_\pi} = 10°$, 8°, and 6°, while those in determining the relevant azimuthal angle are $\sigma_{\phi_\pi} = 12°$, 9°, and 7°. Charged pions were detected by two scintillation counters (S_4, S_5) in a solid angle of 25 msr, the relevant uncertainties being $\sigma_{\theta_\pi} = 2.2°$ and $\sigma_{\phi_\pi} = 2.4°$.

The blocks of fast electronics that processed signals from the detectors of the facility selected events according to the logical schemes

$$S_1 \wedge S_2 \wedge S_3 \wedge \bar{S}_5 \wedge \check{C} \text{ and } S_1 \wedge S_2 \wedge S_3 \wedge S_4 \wedge S_5.$$

Events of the first logical scheme were identified as those in which a proton was detected in coincidence with a neutral pion ($\pi^0 p$ events), while events of the second scheme were identified as those in which a charged pion was detected together with a proton ($\pi^{ch} p$ events). A charge state of the recorded charged pion was not identified in this experiment. Here and below in the article, the symbol π^{ch} therefore stands for the sum of π^- and π^+. From theoretical estimates, it follows, however, that, in the kinematical region being considered, about 80% of the yield of $\pi^{ch} p$ pairs is due to the production of negative pions.

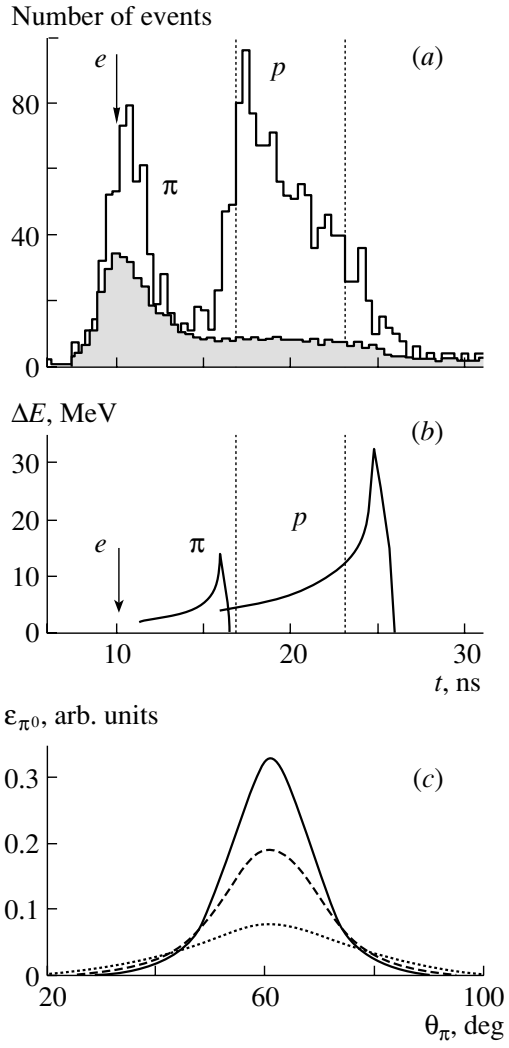

Fig. 2. (*a*) Time-of-flight spectrum of particles recorded by the proton channel of the experimental facility in coincidence with a pion. The spectral regions where relativistic electrons, charged pions, and protons are concentrated are labeled with *e*, π, and *p*, respectively. The shaded histogram represents the contribution of random coincidences. (*b*) Time-of-flight (t) dependences of the pion and proton energy losses ΔE in the scintillation counter S_3 of the proton channel. (*c*) Efficiency of neutral-pion detection, ε_{π^0}, as a function of the polar emission angle θ_π at three kinetic-energy values of $T_\pi =$ (dotted curve) 200 MeV, (dashed curve) 400 MeV, and (solid curve) 600 MeV.

Random coincidences of events recorded by the proton and pion channels are the main source of background events in the present experiment. The dependence of the intensity of random coincidences on the time of flight t reproduces, in the case at hand, the shape of the time-of-flight spectrum measured for the proton channel in an independent mode (the

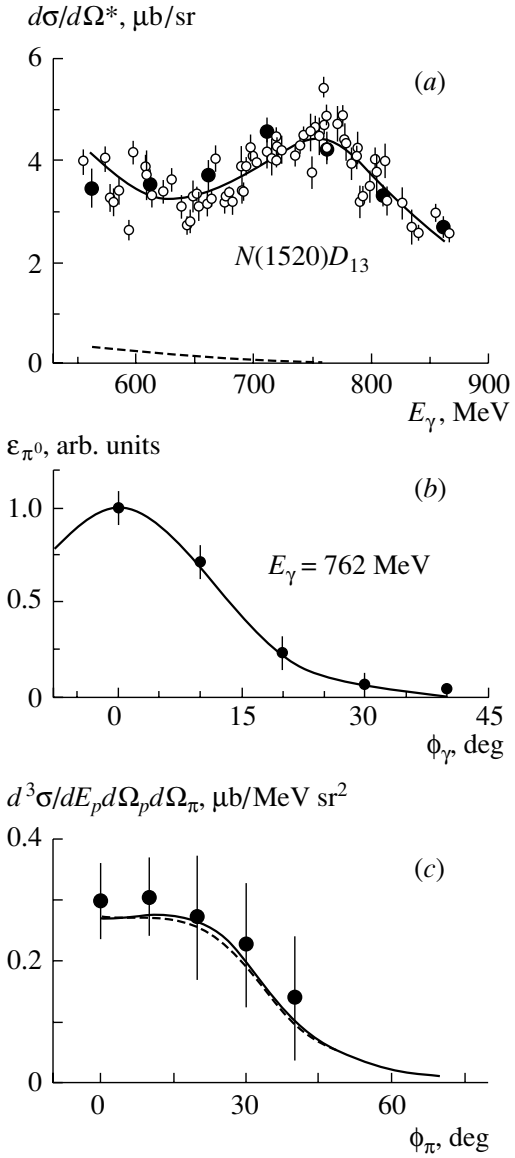

Fig. 3. Results of measurements with a hydrogen target: (*a*) differential cross section for the reaction $\gamma p \to p\pi^0$ as a function of the photon energy at $\theta_\pi^* = 90°$ {(open circles) data from the compilation of Menze *et al.* [20], (closed circles) data of the present experiment, (dashed curve) contribution of the double production of neutral pions, and (solid curve) data from [22]}; (*b*) dependence of the detection efficiency ε_{π^0} for neutral pions from the reaction $\gamma p \to p\pi^0$ on the azimuthal angle ϕ_γ of the γ spectrometer [(closed circles) results of the measurements and (curve) calculated detection efficiency]; (*c*) azimuthal dependence of the quantity obtained by averaging the differential cross section for the reaction $\gamma p \to p\pi^-\pi^+$ for protons of energy in the range $T_p = 140 \pm 20$ MeV over the bremsstrahlung-photon spectrum characterized by the mean energy of $\bar{E}_\gamma = 770$ MeV and the root-mean-square deviation of $\sigma_{E_\gamma} = 70$ MeV {(closed circles) data of the present experiment, (solid curve) theoretical cross section calculated on the basis of the isobar model [24], and (dashed curve) theoretical cross section calculated on the basis of the approximation specified by Eq. (13)}.

corresponding logical scheme is $S_1 \wedge S_2 \wedge S_3$). The level of random coincidences in the spectrum was determined from the number of events recorded in the unphysical time-of-flight region. The contribution of random coincidences in the spectrum of $\pi^{ch}p$ events in Fig. 2*a* is shown by a shaded histogram. In the time-of-flight spectra of $\pi^0 p$ events, the level of background events was severalfold lower.

The experiment resulted in determining the differential cross sections for the photoproduction of neutral and charged pions on ^{1}H nuclei and the differential yield for the production of $\pi^0 p$ and $\pi^{ch}p$ pairs in photon interaction with ^{12}C nuclei as a function of the proton energy T_p and the azimuthal pion-emission angle ϕ_π. The polar angles of proton and pion emission were 41° and 61°, respectively. The azimuthal angle of proton emission was equal to a constant values of π, while the azimuthal angle of pion emission changed between 0 and 50° with a step of 10°.

3. PION PHOTOPRODUCTION ON A PROTON

The present measurements with hydrogen target nuclei pursued two goals.

(i) The first was to obtain experimental data on the reaction

$$\gamma + p \to p + \pi^0 \qquad (1)$$

in order to validate, via a comparison with currently available cross sections, the calculation of various corrections associated with the measuring equipment that affect the detection efficiency in the experimental facility used.

(ii) The second was to deduce estimates of the cross section for pion-pair photoproduction on a proton in the reaction

$$\gamma + p \to p + \pi^- + \pi^+ \qquad (2)$$

over the kinematical region of interest; these data will be used in testing a model for reaction (2).

In the photon-energy range 760–900 MeV, quantities that are measured in the present experiment are sufficient for performing identification and a complete kinematical reconstruction of events of reaction (1). The experimental equipment used was deployed in such a way that, in the c.m. frame, the emission angle θ_π^* of the pion produced in reaction (1) in the $N(1520)$-resonance region was about 90°. The differential cross section $d\sigma/d\Omega^*$ measured in the present experiment for reaction (1) is displayed in Fig. 3*a*, along with the data borrowed from the compilation of Menze *et al.* [20]. This cross section is related

to the experimental event distribution $d^2N_{\pi^0}/dE_p d\Omega_p$ by the equation

$$\frac{d^2N_{\pi^0}}{dE_p d\Omega_p} = \frac{d\sigma}{d\Omega^*}\frac{\partial\Omega^*}{\partial\Omega_p}\frac{W_\gamma}{E_{\max}}f(E_\gamma)\frac{\partial E_\gamma}{\partial E_p}n_{\mathrm{H}}\varepsilon_{\pi^0}\varepsilon_p, \quad (3)$$

where E_γ and E_p are, respectively, the photon energy and the total proton energy; W_γ is the total energy of the photon beam; $E_{\max}$ is the endpoint energy of bremsstrahlung; n_{H} is the proton-target thickness (in nucl./cm^2 units); ε_{π^0} and ε_p are, respectively, the proton-detection and the neutral-pion-detection efficiency; and $f(E_\gamma)$ is the bremsstrahlung spectrum [21], which is normalized by the condition

$$\int_0^{E_{\max}} f(E_\gamma)E_\gamma dE_\gamma = E_{\max}.$$

The efficiency ε_{π^0} of neutral-pion detection by the γ spectrometer was calculated by the formula

$$\varepsilon_{\pi^0}(\mathbf{p}_\pi) = \frac{1}{2\pi}\int\limits_{\Delta\Omega_\gamma}\frac{m_\pi^2\varepsilon_\gamma}{(E_\pi - \dfrac{\mathbf{p}_\gamma\cdot\mathbf{p}_\pi}{E_\gamma})^2}d\Omega_\gamma, \quad (4)$$

where m_π, E_π, and $\mathbf{p}_\pi$ are the pion mass, energy, and momentum, respectively; $\mathbf{p}_\gamma$ is the photon momentum; and ε_γ is the photon-detection efficiency, which was calculated with allowance for the spectrometric features of the γ spectrometer and for the probability of pion absorption in the the target, absorber, and scintillation counters of the pion channel. Integration in (4) is performed over the solid angle of the γ spectrometer.

At a photon energy below 760 MeV, the cross section measured in the present experiment for reaction (1) features a small contribution of events of the reaction $\gamma p \to p\pi^0\pi^0$. In Fig. 3*a*, the estimate of this contribution is represented by the dashed curve.

Figure 3*b* shows the calculated efficiency of the detection of neutral pions produced in reaction (1), ε_{π^0}, and the corresponding detection efficiency measured in the experiment, the latter being coincident in shape with the dependence of the experimental event distribution (3) on the azimuthal angle of the γ spectrometer. The agreement of the measured cross section for reaction (1) with experimental data obtained previously and a faithful reproduction of the azimuthal dependence of the reaction yield indicate that the experimental facility operates quite satisfactorily and that the parameters of the measuring equipment were estimated correctly.

In order to determine the exclusive differential cross section for reaction (2), it is necessary to measure six kinematical quantities that characterize the state of the particles involved in this reaction. Only five quantities were measured in present experiment; therefore, the result of this measurement appears to be a cross section averaged over some range of photon energies. For protons of energy in the range $T_p = 140 \pm 20$ MeV, Fig. 3*c* displays the azimuthal dependence of the quantity obtained by averaging the sum $d^3\sigma/dE_p d\Omega_p d\Omega_\pi$ of the differential cross sections for the production of positive and negative pions on a proton over the bremsstrahlung-photon spectrum $f(E_\gamma)$ characterized by the average energy of $\bar{E}_\gamma = 770$ MeV and the root-mean-square deviation of $\sigma_{E_\gamma} = 70$ MeV.

The results of the present experiment will be analyzed within the distorted-wave impulse approximation (DWIA) by using the quasifree approximation, according to which the squared modulus of the amplitude for pion production on a nucleus is expressed in terms of the squared modulus of the amplitude for pion production on free nucleons. The amplitudes for the single and double production of pions on nucleons, $M_{\gamma N\to\pi p}$ and $M_{\gamma N\to\pi\pi p}$, are related to the corresponding differential cross sections for the reactions $N(\gamma,\pi)p$ and $N(\gamma,\pi_1\pi_2)p$ in the laboratory frame by the equations

$$\frac{d\sigma}{d\Omega_p} = \frac{1}{(2\pi)^2}\frac{p_p^3E_pE_\pi}{|E_\pi p_p^2 - E_p\mathbf{p}_\pi\cdot\mathbf{p}_p|}\overline{|M_{\gamma N\to\pi p}|^2}, \quad (5)$$

$$\frac{d^3\sigma(E_\gamma)}{dE_p d\Omega_p d\Omega_{\pi_1}} = \frac{1}{(2\pi)^5} \times \frac{p_p p_{\pi_1}^3 E_p E_{\pi_1} E_{\pi_2}}{|E_{\pi_2}p_{\pi_1}^2 - E_{\pi_1}\mathbf{p}_{\pi_1}\cdot\mathbf{p}_{\pi_2}|}\overline{|M_{\gamma N\to\pi\pi p}|^2}, \quad (6)$$

where the bar over $|M|^2$ denotes averaging over the initial states of interacting particles and summation over their final states.

Presently, the experimental differential cross sections for the photoproduction of single pions on nucleons are known to a high precision. We will make use of the data given in the compilation of Genzel *et al.* [22] and represented as expansions in powers of $\cos\theta_\pi^*$. For the kinematical region being studied, the energy dependence of the cross section for the reaction $\gamma p \to p\pi^0$ is represented by the solid curve in Fig. 3*a*. The situation around double pion production is totally different. The results obtained by measuring the total cross sections and the distributions of events with respect to the invariant mass of pion–nucleon pairs form the bulk of information about double pion photoproduction on nucleons (see, for example, [23]). In order to calculate the theoretical cross sections for the production of a pion pair on a nucleus, it is therefore necessary to have a model that would describe, in the kinematical region being studied, double pion production on free nucleons. A

few simple models of the reaction $\gamma N \to N\pi\pi$ that satisfactorily reproduce the single-particle differential cross sections $d^2\sigma/dpd\Omega$ for pion production on protons were analyzed in [24].[1)] In Fig. 3*c*, the azimuthal dependence of the sum $d^3\sigma/dE_p d\Omega_p d\Omega_\pi$ of the differential cross sections for the production of positive and negative pions in the reaction $\gamma p \to p\pi^-\pi^+$ is given according to calculations on the basis of the isobar model [24], where pion-pair production on a nucleon proceeds predominantly through the formation of an intermediate $\Delta(1232)$ isobar. In just the same way as the experimental cross section also given in this figure, the calculated cross section was averaged over the photon spectrum and proton energies. As can be seen, the agreement between the calculated cross section and the experimental data is quite good.

4. PRODUCTION OF PION–PROTON PAIRS ON CARBON NUCLEI

The differential yield $d^3Y/dE_p d\Omega_p d\Omega_\pi$ of pion–proton pairs is defined as

$$\frac{d^3Y}{dE_p d\Omega_p d\Omega_\pi} = \int dE_\gamma f(E_\gamma) \frac{d^3\sigma}{dE_p d\Omega_p d\Omega_\pi}. \quad (7)$$

The experimentally measured yield of $\pi^{\mathrm{ch}}p$ pairs is related to the number $N_{\pi^{\mathrm{ch}}p}$ of detected events and the parameters of the facility by the equation

$$\frac{d^3Y_{\pi^{\mathrm{ch}}}}{dE_p d\Omega_p d\Omega_\pi} = \frac{N_{\pi^{\mathrm{ch}}p} E_{\max}}{\Delta E_p \Delta\Omega_p \Delta\Omega_\pi n_{\mathrm{C}} \varepsilon_p \varepsilon_{\pi^{\mathrm{ch}}} W_\gamma},$$

where ΔE_p is the range of averaging of the experimental data over the proton energy; $\Delta\Omega_p$ and $\Delta\Omega_\pi$ are the solid angles of, respectively, the proton and the pion channel of the facility; and $\varepsilon_{\pi^{\mathrm{ch}}}$ is the charged-pion-detection efficiency.

In the case of neutral pions, the event distribution

$$\frac{d^2N_{\pi^0}}{dE_p d\Omega_p} = \frac{N_{\pi^0 p} E_{\max}}{\Delta E_p \Delta\Omega_p n_{\mathrm{C}} \varepsilon_p W_\gamma}$$

is related to the differential cross section for neutral-pion photoproduction by the equation

$$\frac{d^2N_{\pi^0}}{dE_p d\Omega_p} = \int dE_\gamma f(E_\gamma) \times \int d\Omega_\pi \frac{d^3\sigma_{\pi^0}}{dE_p d\Omega_p d\Omega_\pi} \varepsilon_{\pi^0}(\mathbf{p}_\pi).$$

As can be seen from Fig. 2*c*, the detection efficiency ε_{π^0} (4), which reflects the spatial distribution of decay photons, has a maximum at an angle of 61° in the γ-spectrometer direction $\mathbf{l}_\gamma$; therefore, we can write

$$\int d\Omega_\pi \frac{d^3\sigma_{\pi^0}}{dE_p d\Omega_p d\Omega_\pi} \varepsilon_{\pi^0}(\mathbf{p}_\pi) \simeq \frac{d^3\sigma_{\pi^0}}{dE_p d\Omega_p d\Omega_\pi}\bigg|_{\hat{\mathbf{p}}_\pi = \mathbf{l}_\gamma} \int d\Omega_\pi \varepsilon_{\pi^0}(\mathbf{p}_\pi).$$

Considering that

$$\int d\Omega_\pi \varepsilon_{\pi^0}(\mathbf{p}_\pi) = 2\overline{\varepsilon}_\gamma \Delta\Omega_\gamma,$$

we can represent the yield of neutral pions in the form

$$\frac{d^3Y_{\pi^0}}{dE_p d\Omega_p d\Omega_\pi} = \frac{N_{\pi^0 p} E_{\max}}{2\Delta E_p \Delta\Omega_p \Delta\Omega_\gamma n_{\mathrm{C}} \overline{\varepsilon}_\gamma \varepsilon_p W_\gamma}.$$

The experimental results for $d^3Y_{\pi^{\mathrm{ch}}}/dE_p d\Omega_p d\Omega_\pi$ and $d^3Y_{\pi^0}/dE_p d\Omega_p d\Omega_\pi$ are given in Tables 1 and 2, respectively. The quoted experimental errors are purely statistical. The systematic error in determining the reaction yields, which includes errors in measuring the total energy of the photon beam and the target thickness, uncertainties in estimating the detection efficiency for the proton and pion detection channels, and uncertainties in the calibration of the time-of-flight system, does not exceed 10%.

Models based on the impulse approximation are used here to analyze data obtained in this experiment. In the second resonance region of photon energies, the production of $\pi^{\mathrm{ch}}p$ and $\pi^0 p$ pairs on a ^{12}C nucleus may occur in the quasifree approximation via single pion production in the reactions

$$^{12}\mathrm{C}(\gamma,\pi^- p)^{11}\mathrm{C} \quad \text{and} \quad ^{12}\mathrm{C}(\gamma,\pi^0 p)^{11}\mathrm{B} \quad (8)$$

and via double photoproduction in the three reactions

$$^{12}\mathrm{C}(\gamma,\pi^-\pi^+ p)^{11}\mathrm{B}, \quad ^{12}\mathrm{C}(\gamma,\pi^0\pi^0 p)^{11}\mathrm{B}, \quad \text{and} \quad ^{12}\mathrm{C}(\gamma,\pi^-\pi^0 p)^{11}\mathrm{C}. \quad (9)$$

The last reaction contributes both to the yield of $\pi^{\mathrm{ch}}p$ pairs and to the yield of $\pi^0 p$ pairs.

The differential cross section for single pion production in the reaction $^{12}\mathrm{C}(\gamma,\pi p)$ in the laboratory frame is given by

$$\frac{d^3\sigma}{dE_p d\Omega_p d\Omega_\pi} = \frac{p_\pi^3 p_p E_\pi E_p E_r}{|E_r p_\pi^2 - E_\pi \mathbf{p}_\pi \cdot \mathbf{p}_r|} \frac{\overline{|M_\pi|^2}}{(2\pi)^5}, \quad (10)$$

where E_r and $\mathbf{p}_r$ are, respectively, the energy and the momentum of the residual nucleus.

The analogous expression for the exclusive cross section describing double pion production in $A(\gamma,\pi_1\pi_2 p)B$ reactions in the laboratory frame has the form

$$\frac{d^5\sigma(E_\gamma)}{dE_p d\Omega_p dE_{\pi_1} d\Omega_{\pi_1} d\Omega_{\pi_2}} \quad (11)$$

[1)] There is an error in Fig. 4 of [24] in the dimensionality of the cross section: μb should be replaced by nb.

$$= \frac{p_p p_{\pi_1} p_{\pi_2}^3 E_p E_{\pi_1} E_{\pi_2} E_r}{|E_r p_{\pi_2}^2 - E_{\pi_2} \mathbf{p}_{\pi_1} \cdot \mathbf{p}_r|} \frac{\overline{|M_{\pi\pi}|^2}}{(2\pi)^8}.$$

In the factorization approximation, the squared moduli of the amplitudes for the production of one pion and two pions on nuclei, $\overline{|M_\pi|^2}$ and $\overline{|M_{\pi\pi}|^2}$, respectively, are related to the amplitudes $M_{\gamma N\to\pi p}$ (5) and $M_{\gamma N\to\pi\pi p}$ (6) for pion production on a nucleon by the equations

$$\overline{|M_\pi|^2} = (2\pi)^3 \rho(\mathbf{p}_\gamma - \mathbf{p}_\pi - \mathbf{p}_p) \overline{|M_{\gamma N\to\pi p}|^2},$$

$$\overline{|M_{\pi\pi}|^2} = (2\pi)^3 \rho(\mathbf{p}_\gamma - \mathbf{p}_{\pi_1} - \mathbf{p}_{\pi_2} - \mathbf{p}_p) \overline{|M_{\gamma N\to\pi\pi p}|^2},$$

where $\rho(\mathbf{p})$ is the distorted momentum distribution of the nucleons of the ^{12}C nucleus.

In order to perform a comparison with experimental data, the differential cross sections in (10) and (11) were averaged, according to (7), over the bremsstrahlung photon spectrum $f(E_\gamma)$, while the cross section for the production of two pions in (11) was additionally integrated with respect to the energy and solid angle of the undetected pion. Over a major part of the photon-energy range, the bremsstrahlung spectrum $f(E_\gamma)$ (see Fig. 3*a*) can be approximated by the expression $0.9/E_\gamma$ to a satisfactory precision.

The momentum distribution $\rho(\mathbf{p})$ was calculated on the basis of the harmonic-oscillator model. The parameters of the proton wave functions were determined by using data on the ^{12}C charge radius, which was set to 2.45 fm [25]. The oscillator parameters of neutrons bound in the nucleus were taken to be equal to the corresponding proton parameters.

In the plane-wave approximation, the momentum distribution $\rho(\mathbf{p})$ was normalized to the number N_{lj} of nucleons in the corresponding charge state in the lj state of the nucleus; that is,

$$\int \rho(\mathbf{p}_r) d\mathbf{p}_r = N_{lj},$$

where $N_{s_{1/2}} = 2$ and $N_{p_{3/2}} = 4$. Thus, we have used the maximum possible values of the spectroscopic factors for the $s_{1/2}$ and $p_{3/2}$ states of nucleons.

Final-state interaction was taken into account on the basis of the optical model in the eikonal approximation; according to this model, a pion and a proton propagate in a complex pion–nucleus and a complex proton–nucleus optical potential. For the proton–nucleus optical potential, use was made of that which is presented in [26] and which is based on the phenomenological analysis of proton–nucleus scattering. The application of this optical potential made it possible to explain the effect of proton interaction with a residual nucleus in the reaction $^{12}\mathrm{C}(\gamma, \pi^- p)$ in the $\Delta(1232)$-resonance region [27]. The pion wave function was distorted by the pion–nucleus optical potential derived in [28] according to [29]. The authors of [28] were able to obtain a satisfactory description of the inclusive spectra of charged pions produced on carbon and copper nuclei in the kinematical region of quasifree pion photoproduction [30, 31].

The calculated yields of $\pi^0 p$ and $\pi^{\mathrm{ch}} p$ pairs are displayed in Fig. 4, along with relevant data. The dashed curves represent the calculated yield of pion–proton pairs that is due to the single production of (Fig. 4*a*) neutral and (Fig. 4*b*) charged pions. The solid curves correspond to the total yield from the single- and double-pion-production reactions [(8) and (9), respectively]. In the region of moderately small azimuthal angles, which, according to calculations, is dominated by single-pion-production processes, the calculated yields satisfactorily reproduce the energy dependence of their experimental counterparts both in absolute value and in shape.

In the region of large azimuthal angles, where the contribution of double pion production is significant, the experimental yield of pion–proton pairs is systematically in excess of the theoretical estimates. The measured azimuthal dependence of the neutral-pion yield for protons of energy T_p in the range 140–180 MeV is presented in Fig. 5; also shown there is the reaction yield calculated (dotted curve) in the plane-wave and (solid curve) in the distorted-wave impulse approximation (PWIA and DWIA, respectively). As can be seen, final-state interaction reduces the reaction cross section considerably. In the region of $\Delta(1232)$ photoexcitation, such an effect of final-state interaction is described in the eikonal approximation to a satisfactory precision [27]. According to the results of the present study, a significant suppression of the reaction cross section due to final-state interaction within the model used here is of importance for quantitatively explaining experimental data in the second resonance region. The situation around the description of the reaction cross section in the region where it is minimal is different. In this case, variations do not reduce exclusively to the suppression of the cross section because of particle absorption: the reaction yield can change significantly—in particular, increase—owing to particle scattering on a residual nucleus. A systematic excess of the experimental reaction yield over the theoretical results at large pion emission angles may possibly be due to rescattering effects induced by final-state interaction, which are expected to be underestimated in the eikonal approximation.

The in-medium modification of the rho-meson features, which has been widely discussed in recent years (see, for example, [32, 33]), is yet another possible source of an enhanced yield of pion–proton

Table 1. Differential yield $d^3Y_{\pi^{\rm ch}}/dE_p d\Omega_p d\Omega_\pi$ [in 10^{-32} cm^2/(MeV sr)^2 units] of charged-pion photoproduction in the reaction ^{12}C$(\gamma, \pi p)$ versus the proton kinetic energy T_p and the azimuthal pion-emission angle ϕ_π

T_p, MeV	ϕ_π, deg					
	0	10	20	30	40	50
150	38.6 ± 4.2	34.4 ± 3.7	28.4 ± 3.8	15.0 ± 3.6	11.6 ± 2.5	9.0 ± 2.3
170	26.7 ± 3.2	27.7 ± 3.5	18.6 ± 3.1	18.7 ± 3.9	7.7 ± 2.0	4.2 ± 1.7
190	28.2 ± 2.7	33.3 ± 4.6	20.3 ± 3.2	12.2 ± 3.2	7.5 ± 1.9	6.2 ± 1.9
210	23.6 ± 2.4	23.6 ± 3.5	11.1 ± 2.4	13.7 ± 3.3	1.4 ± 1.9	6.9 ± 1.9
230	20.2 ± 2.2	16.4 ± 2.6	11.1 ± 2.3	6.5 ± 2.4	4.6 ± 1.5	3.4 ± 1.4
250	15.8 ± 2.2	17.4 ± 2.6	7.1 ± 1.9	2.1 ± 1.5	4.0 ± 1.5	5.9 ± 1.8
270	14.5 ± 2.1	8.9 ± 2.4	6.5 ± 1.8	4.6 ± 2.0	2.5 ± 1.5	1.8 ± 1.4

Table 2. Differential yield $d^3Y_{\pi^0}/dE_p d\Omega_p d\Omega_\pi$ [in 10^{-32} cm^2/(MeV sr)^2 units] of neutral-pion photoproduction in the reaction ^{12}C$(\gamma, \pi p)$ versus the proton kinetic energy T_p and the azimuthal pion-emission angle ϕ_π

T_p, MeV	ϕ_π, deg					
	0	10	20	30	40	50
150	20.9 ± 2.2	19.4 ± 2.8	15.5 ± 2.8	9.4 ± 2.8	6.5 ± 1.8	5.0 ± 1.6
170	23.4 ± 2.4	18.7 ± 2.7	13.1 ± 2.6	7.5 ± 2.5	7.4 ± 1.9	6.1 ± 1.8
190	14.5 ± 1.8	16.4 ± 2.6	17.8 ± 3.0	5.5 ± 2.1	1.9 ± 1.9	3.5 ± 1.4
210	11.8 ± 1.6	13.1 ± 2.5	11.0 ± 2.3	4.2 ± 1.9	6.0 ± 1.7	3.0 ± 1.3
230	9.8 ± 1.5	10.8 ± 2.0	7.2 ± 1.9	2.3 ± 1.4	3.1 ± 1.5	4.1 ± 1.5
250	9.5 ± 1.6	7.2 ± 1.7	6.3 ± 1.8	3.6 ± 1.7	2.3 ± 1.5	1.6 ± 1.5
270	7.0 ± 1.5	6.4 ± 1.7	4.4 ± 1.5	5.2 ± 2.5	1.3 ± 1.5	1.3 ± 1.5

pairs in the $N(1520)$-resonance region. The $N(1520)$ resonance has three dominant decay modes:

$$\begin{aligned} N(1520) &\to N\pi,\ \Gamma_{N^*\to N\pi} \sim 0.55\Gamma_{N^*};\\ &\to \Delta\pi,\ \Gamma_{N^*\to \Delta\pi} \sim 0.25\Gamma_{N^*}; \\ &\to N\rho,\ \Gamma_{N^*\to N\rho} \sim 0.20\Gamma_{N^*}. \end{aligned} \qquad (12)$$

The first mode of $N(1520)$ decay leads to the production of single pions, while the remaining two yield predominantly two pions. The last decay mode is of interest because this channel is energetically forbidden at the pole values of the particle masses. The $N(1520)$-resonance decay $N^* \to N\rho$ proceeds owing to a partial overlap of the tails of the resonance and rho-meson spectral functions. If the decay of the resonance occurs in a nuclear medium, changes in the particle states due to interaction with the medium with respect to their vacuum counterparts will be different for different states, with the result that the relationship between the branching ratios for the decay modes of interest will also change; of course, this will concern the branching ratios for the one- and two-pion modes, if any. The above is valid for any nucleon resonance, but, for $N(1520)$, the effect may be significant because of the specific properties of the rho-meson mode [33]. Thus, we can conclude that, in the second resonance region, a change in the relationship between the branching ratios for the production single- and two-pion final states in nuclear reactions induced by pions or photons may be an indication of in-medium modifications to the parameters of the $N(1520)$ resonance and of the rho meson.

According to the predictions obtained in [34] within QCD, the expected decrease in the mass of the rho meson in the carbon nucleus is about 80 MeV. Provided that the mass distributions of the $N(1520)$ resonance and the rho meson are described by a Breit–Wigner function and that all other conditions remain unchanged, this decrease in the rho-meson mass will lead to an increase in the phase space by

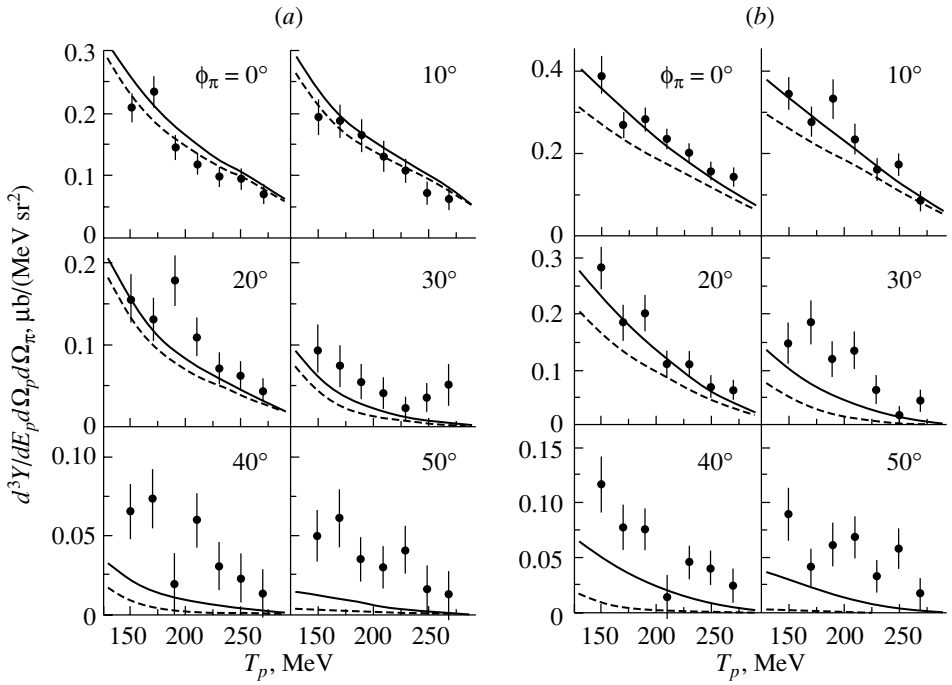

Fig. 4. Differential yield from the photoproduction of (a) neutral and (b) charged pions in the reaction $^{12}\mathrm{C}(\gamma, \pi p)$ versus the proton kinetic energy T_p at various values of the azimuthal angle ϕ_π of pion emission: (closed circles) data of the present study, (dashed curves) quasifree photoproduction of single pions, and (solid curves) sum of the contributions from single and double pion production.

a factor greater than 2. As a result, the probability of the rho-meson mode of $N(1520)$ decay will become greater, which will lead to an increase in the cross section for the production of two pions.

Let us estimate the effect of changes in the parameters of the rho meson in the $^{12}\mathrm{C}$ nucleus on the yield of pion–proton pairs. For this, we will use a somewhat extended version of the isobar model [24], isolating, in the expression for the squared modulus of the amplitude for the reaction $\gamma N \to \pi\pi p$, the term corresponding to the decay of the $N(1520)$ resonance into a final state involving a rho meson; that is,

$$\overline{|M_{\gamma N\to\pi\pi p}|^2} = \frac{(2\pi)^5}{8E_p E_{\pi_1} E_{\pi_2}} \times \left(\frac{\sigma_{\mathrm{tot}} - \sigma_{N^*\to p\rho}}{S_\Delta}\frac{B_\Delta(m_{\pi_2 p})}{2m_{\pi_2 p}} + \frac{\sigma_{N^*\to p\rho}}{S_\rho}\frac{B_\rho(m_{\pi_1\pi_2})}{2m_{\pi_1\pi_2}}\right), \quad (13)$$

where $\sigma_{N^*\to p\rho}$ is the contribution to the total cross section σ_{tot} for the photoproduction of two pions on a nucleon from the reaction mechanism corresponding to the decay scheme

$$\gamma + N \to N(1520) \to p + \rho; \quad \hookrightarrow \pi_1 + \pi_2$$

$m_{\pi_2 p}$ and $m_{\pi_1\pi_2}$ are the invariant masses of, respectively, the $\pi_2 p$ system and the system of two pions;

$$B_R(m) = \frac{1}{\pi}\frac{\Gamma_R/2}{(m_R - m)^2 + \Gamma_R^2/4}$$

is a Breit–Wigner function that describes the distribution of an R resonance of mass m_R and width Γ_R

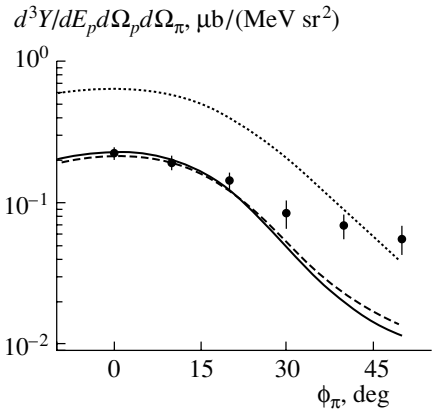

Fig. 5. Yield of neutral pions in the reaction $^{12}\mathrm{C}(\gamma, \pi^0 p)$ as a function of the azimuthal angle ϕ_π of pion emission at $T_p = 140$–180 MeV: (closed circles) data of the present study, (dotted curve) theoretical yields computed in the plane-wave impulse approximation, (solid curve) theoretical yields computed in the distorted-wave impulse approximation, and (dashed curve) results of the calculation on the basis of the extended isobar model [which is specified by Eqs. (13) and (14)].

with respect to the mass m; and

$$S_\Delta = \frac{2\pi^2}{m_0}\int\limits_{m_\pi+m_N}^{m_0-m_\pi} p^*_{\pi_1}p^{**}_{\pi_2}\frac{B_\Delta(m)}{2m}dm,$$

$$S_\rho = \frac{2\pi^2}{m_0}\int\limits_{2m_\pi}^{m_0-m_p} p^*_p p^{***}_\pi \frac{B_\rho(m)}{2m}dm.$$

Here, m_0 is the invariant mass of the γN system; $p^*_{\pi_1}$ and p^*_p are the momenta of, respectively, the first pion and the proton in the γN c.m. frame; and $p^{**}_{\pi_2}$ and p^{***}_π are the momenta of the second pion in, respectively, the $\pi_2 p$ c.m. frame and the c.m. frame of the two pions. The contributions of the $N(1520)$ resonance to the cross section for the production of a single pion and to the cross section for the production of two pions were determined on the basis of the results presented in [35].

The azimuthal dependence that was calculated for the differential cross section for the reaction $\gamma p \to p\pi^-\pi^+$ on the basis of the model specified by Eq. (13) and which is represented by the dashed curve in Fig. 3*c* differs only slightly from the results of the calculations within the isobar model used in [24].

The effect of a decrease in the mass of the rho meson in the ^{12}C nucleus can be evaluated under the assumption that $N(1520)$ decay into a final state containing a rho meson will be a dominant mode because of an increase in the corresponding phase space; that is,

$$\Gamma_{N^*\to N\rho} \simeq \Gamma_{N^*}. \qquad (14)$$

In Fig. 5, the azimuthal dependences calculated for the yields of $\pi^0 p$ pairs within the plane-wave impulse approximation and within the distorted-wave impulse approximation by using relations (12) for the branching ratios of the modes of $N(1520)$ decay in a vacuum are represented by the dotted and the solid curve, respectively. The dashed curve corresponds to the theoretical results obtained with the aid of relation (14). As can be seen, the assumption that the branching ratio for the rho-meson decay mode increases leads to an enhancement of the yield of $\pi^0 p$ pairs at large azimuthal angles of pion emission. In the region of small values of the angle ϕ_π, a decrease in the cross section for the production of single neutral pions because of the enhancement of the two-pion mode of $N(1520)$ decay is almost completely compensated by the increase in the cross section for the production of two pions. For charged pions, the use of the assumption specified by Eq. (14) improves the quantitative agreement between the theoretical and experimental results at large values of the angle ϕ_π, but this impairs somewhat the agreement at small values of this angle.

5. CONCLUSION

In the second resonance region of photon energies, the differential yield from the production of pion–proton pairs on ^{12}C nuclei has been measured as a function of the proton energy and the azimuthal angle of pion emission. The experiment was performed in a bremsstrahlung-photon beam, the endpoint energy of the bremsstrahlung spectrum being 900 MeV. The product protons were recorded in the energy range 150–270 MeV. The polar angles of pion and proton emission were 41° and 61°, respectively. The azimuthal angle of proton emission was fixed at π, while that for pions was varied with a step of 10° over the range 0°–50°. The results of the measurements have been analyzed in the distorted-wave impulse approximation on the basis of a model that takes into account processes leading to single and double pion production. The calculated yields of pion–proton pairs satisfactorily reproduce experimental data in the region of moderately small azimuthal angles of pion emission, this region being dominated by the quasifree production of single pions. At large azimuthal angles, pion–proton pairs are predominantly produced via the quasifree photoproduction of two pions. In this region, the experimental reaction yield exceeds systematically, both for neutral and for charged pions, that which is calculated within the distorted-wave impulse approximation. A slight enhancement of the yield of proton–pion pairs at large azimuthal angles has been obtained on the basis of a model that assumes an increase in the branching ratio for the rho-meson mode of $N(1520)D_{13}$-resonance decay because of the in-medium modification to the rho-meson mass, but by no means does this enhancement change the general relationship between the theoretical and experimental results.

ACKNOWLEDGMENTS

I am grateful to P.S. Anan'in and N.P. Fedorov for assistance in performing the measurements and to the personnel of the Tomsk synchrotron for ensuring the required mode of accelerator operation.

This work was supported by the Russian Foundation for Basic Research (project no. 97-02-17765).

REFERENCES

1. P. E. Argan, G. Audit, N. De Botton, *et al.*, Phys. Rev. Lett. **29**, 23 (1972).
2. P. S. Ananien, I. V. Glavanakov, V. N. Kryshkin, *et al.*, Lett. Nuovo Cimento **8**, 651 (1973).

3. P. S. Anan'in and I. V. Glavanakov, Yad. Fiz. **52**, 323 (1990) [Sov. J. Nucl. Phys. **52**, 205 (1990)].
4. I. V. Glavanakov, Yu. F. Krechetov, A. V. Moiseenko, and E. N. Shuvalov, Yad. Fiz. **61**, 2175 (1998) [Phys. At. Nucl. **61**, 2064 (1998)].
5. L. D. Pham, S. Høibråten, R. P. Redwine, *et al.*, Phys. Rev. C **46**, 621 (1992).
6. J. A. MacKenzie, D. Branford, J. Ahrens, *et al.*, Phys. Rev. C **54**, R6 (1996).
7. M. Liang, D. Branford, T. Davinson, *et al.*, Phys. Lett. B **411**, 244 (1997).
8. K. Hick, H. Baghaei, A. Caracappa, *et al.*, Phys. Rev. C **55**, R12 (1997).
9. A. Deppman, N. Bianchi, E. De Sanctis, *et al.*, nucl-th/9809085.
10. M. MacCormick *et al.*, Phys. Rev. C **53**, 41 (1996).
11. M. MacCormick *et al.*, Phys. Rev. C **55**, 1033 (1997).
12. M. Anghinolfi *et al.*, Phys. Rev. C **47**, 922 (1993).
13. N. Bianchi *et al.*, Phys. Lett. B **309**, 5 (1993).
14. M. Mirazita *et al.*, Phys. Lett. B **407**, 225 (1997).
15. T. Frommhold *et al.*, Phys. Lett. B **295**, 28 (1992).
16. N. Bianchi *et al.*, Phys. Lett. B **299**, 219 (1993).
17. B. Krusche, J. Ahrens, R. Beck, *et al.*, Phys. Rev. Lett. **86**, 4764 (2001).
18. A. P. Komar, S. P. Kruglov, and I. V. Lopatin, *Measurement of the Total Energy of Bremsstrahlung Beams from Electron Accelerators* (Nauka, Leningrad, 1972).
19. P. S. Anan'in, I. V. Glavanakov, and V. N. Stibunov, Pis'ma Zh. Éksp. Teor. Fiz. **23**, 298 (1976) [JETP Lett. **23**, 269 (1976)].
20. D. Menze, W. Pfeil, and R. Wilcke, *Physics Data. Compilation of Pion Photoproduction Data* (Bonn, 1977).
21. A. F. Khodyachikh, Preprint No. 087 VE-035, Institute of Physics and Technology, National Academy of Sciences of Ukraine (Kharkov, 1964).
22. H. Genzel, P. Joos, and W. Pfail, *Photoproduction of Elementary Particles* (Springer-Verlag, Berlin, 1973).
23. J. A. Gomes Tejedor and E. Oset, Nucl. Phys. A **571**, 667 (1994).
24. I. V. Glavanakov, Yad. Fiz. **63**, 2187 (2000) [Phys. At. Nucl. **63**, 2091 (2000)].
25. R. C. Barrett and D. F. Jackson, *Nuclear Sizes and Structure* (Clarendon, Oxford, 1977; Naukova Dumka, Kiev, 1981).
26. J. M. Laget, Nucl. Phys. A **194**, 81 (1972).
27. I. V. Glavanakov, Yad. Fiz. **31**, 342 (1980) [Sov. J. Nucl. Phys. **31**, 181 (1980)].
28. Y. Futami and J. Suzumura, Prog. Theor. Phys. **66**, 534 (1981).
29. R. M. Frank, J. L. Gammel, and K. M. Watson, Phys. Rev. **101**, 891 (1956).
30. K. Baba, I. Endo, M. Fujisaki, *et al.*, Nucl. Phys. A **306**, 292 (1978).
31. K. Baba, I. Endo, M. Fujisaki, *et al.*, Nucl. Phys. A **322**, 349 (1979).
32. L. A. Kondratyuk and Ye. S. Golubeva, Yad. Fiz. **61**, 951 (1998) [Phys. At. Nucl. **61**, 865 (1998)].
33. U. Mosel, nucl-th/9811065.
34. T. Hatsuda and S. Lee, Phys. Rev. C **46**, R34 (1992).
35. M. Effenberger, A. Hombach, S. Teis, and U. Mosel, Nucl. Phys. A **614**, 501 (1997).

Translated by A. Isaakyan

Physics of Atomic Nuclei, Vol. 66, No. 5, 2003, pp. 798–803. Translated from Yadernaya Fizika, Vol. 66, No. 5, 2003, pp. 830–836.

NUCLEI
Experiment

Investigation of Fragment Yields from ^{239}U Fission at Anomalously High Values of the Total Kinetic Energy

V. A. Khriatchkov*, M. V. Dunaev, I. V. Dunaeva, N. N. Semenova, and A. I. Sergachev

Institute of Physics and Power Engineering, pl. Bondarenko 1, Obninsk, Kaluga oblast, 249020 Russia

Received May 21, 2002; in final form, August 6, 2002

Abstract—The yields of fragments originating from ^{238}U fission induced by 5-MeV neutrons are investigated. Accumulated statistics—2.5×10^6 events of binary fission—make it possible to study fission-fragment yields at anomalously high values of the total kinetic energy. The spectra of the cold fragmentation of ^{239}U are obtained. Events characterized by the total kinetic energy that is equal to the total reaction energy are found for some fragment masses. Methods of digital signal processing permit a highly reliable identification of these rare events. An interpretation of this phenomenon on the basis of the liquid-drop model of the fission process is proposed. © *2003 MAIK "Nauka/Interperiodica".*

INTRODUCTION

The phenomenon that is referred to as cold fragmentation has been studied over the past decades. It carries information about the earliest stages of the evolution of a system undergoing fission. Investigation of cold fragmentation makes it possible to understand the regularities of the formation of mass and energy distributions of fission fragments and, hence, to explore in detail the structure of the potential-energy surface in a fissile nucleus. The spectra of cold fragmentation were comprehensively studied for nearly all of the nuclei whose cross sections for thermal-neutron-induced fission are large. Experiments devoted to investigating cold fragmentation in nuclear fission induced by fast neutrons have been performed at the Institute of Physics and Power Engineering (Obninsk, Russia) over the past decade. The range of nuclei subjected to examination was supplemented with ^{236}U, ^{237}Np, and ^{232}Th [1–3], which can undergo fission only upon irradiation with fast neutrons. In this article, we present results obtained by exploring the cold fragmentation of ^{238}U under the effect of 5-MeV neutrons.

DESCRIPTION OF THE EXPERIMENT

A double ionization chamber that was equipped with Frisch grids and which was combined with a device converting a pulse shape into a digital form (wave-shape digitizer) served as a detector of fission fragments. The ^{238}U target used had a diameter of 3 cm and a thickness of 100 μg/cm^2. It was manufactured by means of the vacuum sputtering of uranium fluoride onto a thin substrate (50 μg/cm^2) made from Al_2O_3. For the target to have a nonzero electric conductivity over the entire surface, it was additionally coated with gold (50 μg/cm^2). The layout of the experimental facility is shown in Fig. 1. With the aid of the wave-shape digitizer (LeCroy 2262), anode signals from each chamber were transformed, with a step of 12.5 ns, into a digital form and were saved on the hard disk of a computer. Two arrays of numbers, each having a length of 512 elements, corresponded to each event. Via a subsequent analysis of digital oscillograms with the aid of methods based on digital signal processing, a determination of the kinetic energy, the mass, and the emission angle [4] and an investigation of the behavior of specific ionization losses [5] could be performed for each of the complementary fragments simultaneously. The energies of fragments were corrected for the inefficiency of the Frisch grid [6], for the energy loss in the target [7], and for the amplitude defect [4]. In addition, each signal was subjected to a thorough test for the presence superpositions from alpha particles or scattered protons.

The measurements were performed in a beam from the KG-2.5 accelerator installed at the Institute of Physics and Power Engineering (Obninsk, Russia). The reaction $T(p,n)^3$He was used to obtain 5-MeV neutrons. The mean current at the target was 50 μA. Over a month of measurements, we were able to accumulate and analyze 2.5 million digital oscillograms corresponding to events of ^{238}U fission. In order to calibrate the detector used, we took data reported in [8], where one can find mass and energy distribu-

*e-mail: hva@ippe.obninsk.ru

1063-7788/03/6605-0798$24.00

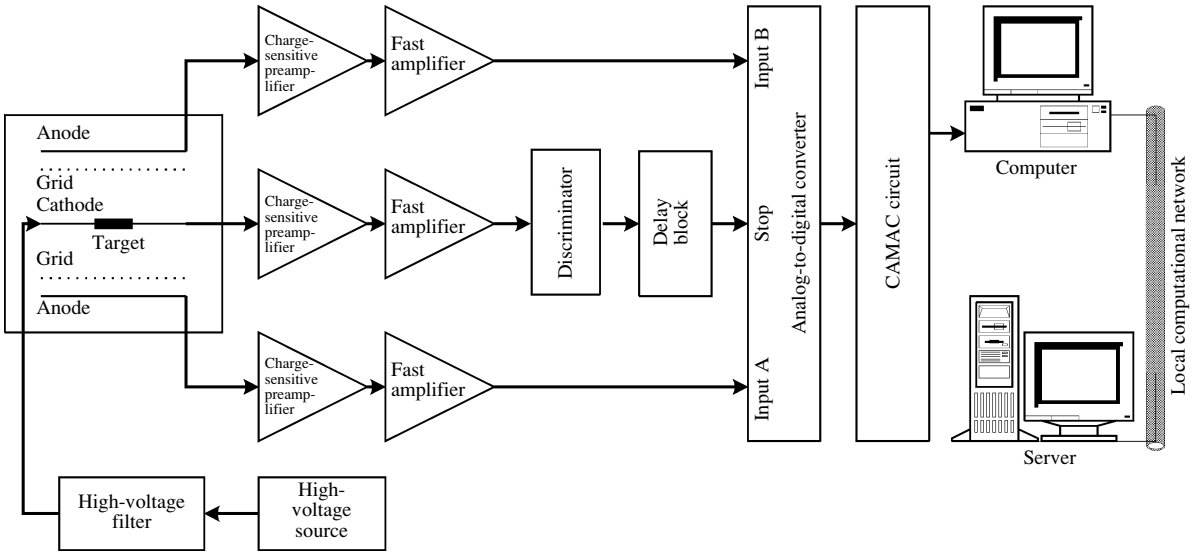

Fig. 1. Layout of spectrometer electronics.

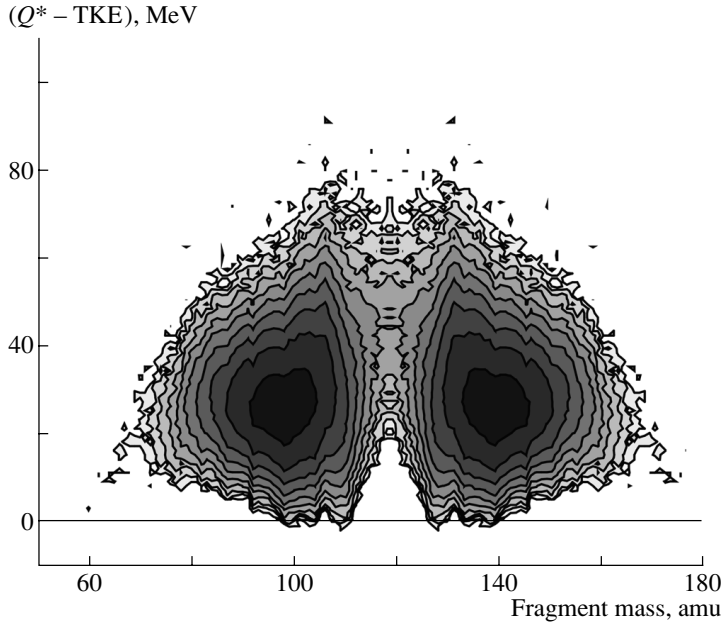

Fig. 2. Two-dimensional spectrum of fragment yields from ^{238}U fission induced by 5-MeV neutrons with respect to the fragment mass and the available energy (Q^* – TKE). The displayed yields are given on a logarithmic scale.

tions investigated, to a high precision, for ^{238}U over a wide range of excitation energies. Signals from the detector were processed in two steps. At the first step, the masses and energies were reconstructed with the aid of a standard iterative procedure including corrections for the amplitude defect and for the emission of prompt neutrons from fission fragments. The probabilities of neutron emission from fragments of different masses were borrowed from [8]. The resulting energy, mass, and angular distributions were found to be in good agreement with data presented in [8]. At this stage, we were also able to reconstruct the gross structure of the mass and energy distributions. The value of the mean total kinetic energy (mean TKE) was 169.8 MeV in the present study (170.05 MeV in [8]). It should be noted that, within the approach used here, the inclusion of neutron emission was performed with allowance for the dependence on the mass of nascent fragments and that the correction is independent here of the released-energy fraction expended in the excitation of fragments. This leads, in particular, to a distortion in the hard section of

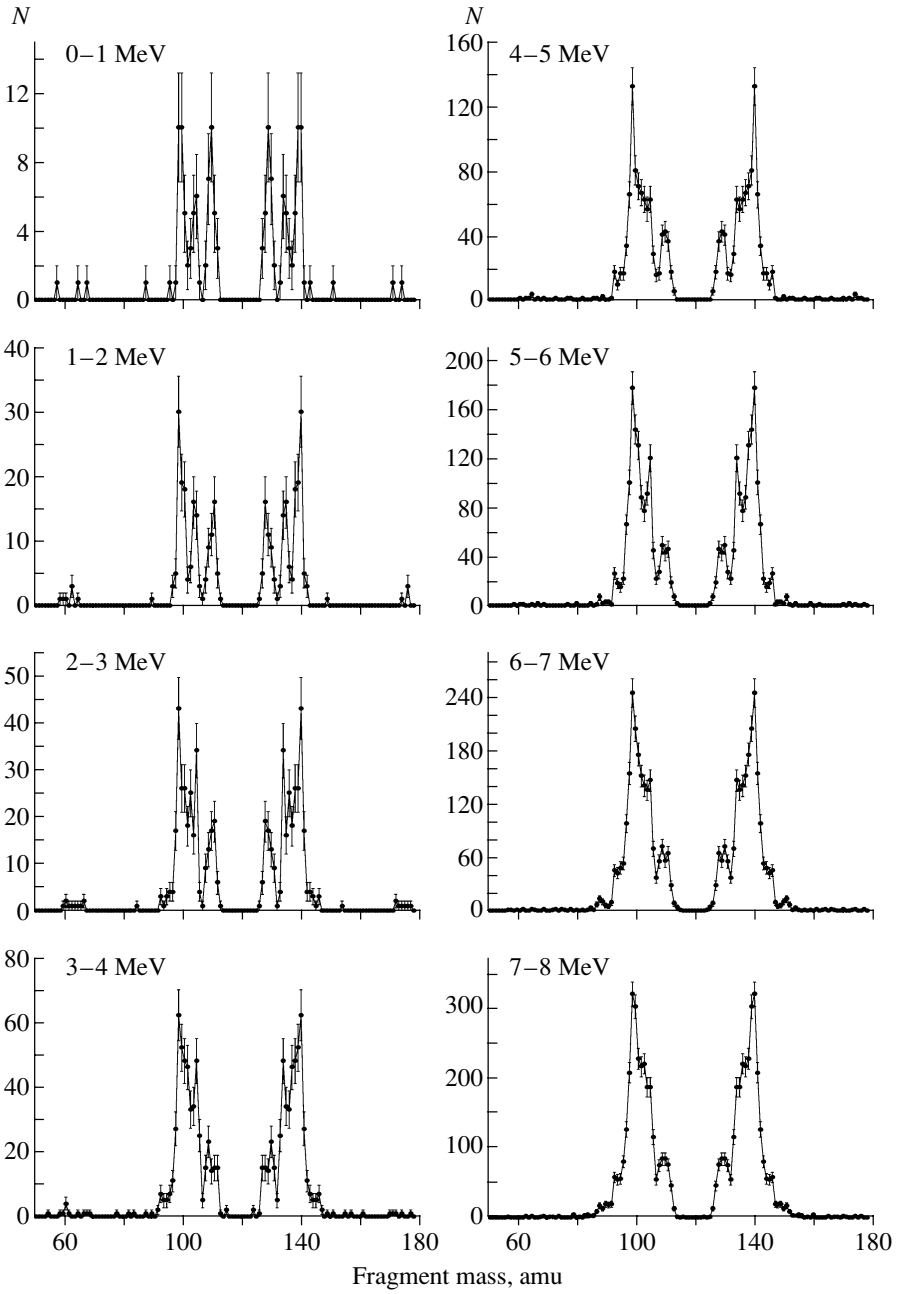

Fig. 3. Mass spectra of fragments originating from ^{238}U fission for various values of the available energy of a light fragment.

the spectrum of fragments, where neutron emission is energetically forbidden. In order to study this region, which is of greatest interest to us, it is necessary to perform a reanalysis of data by using the energy calibration obtained at the first step. The processing algorithm is similar to that employed at the first step, but the correction for neutron emission is excluded from the iterative process. Because of this, information about masses and energies appears to be distorted for the majority of the fragments, but there emerge correct values in the hard section of the spectrum, where neutron emission is impossible.

ANALYSIS OF THE RESULTS

In Fig. 2, the two-dimensional spectrum of the yields of fragments originating from ^{238}U fission induced by 5-MeV neutrons is shown in terms of the coordinates of the fragment mass and available energy. In order to determine the available energy for each realizable mass splitting, we have calculated the

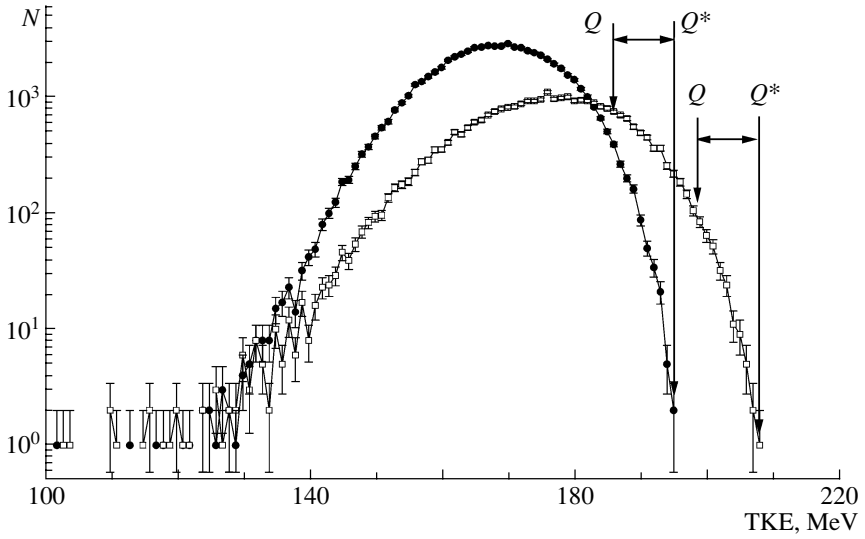

Fig. 4. Yields of (open boxes) 130- and (closed circles) 140-amu fission fragments versus the total kinetic energy. Arrows indicate the values of the total kinetic energy that correspond to the mass defect for the nonexcited nucleus ^{239}U (Q) and the mass defect with allowance for the excitation introduced by a 5-MeV neutron (Q^*).

total available energy Q^*,

$$Q^* = Q + B_n + T_n, \qquad (1)$$

where Q is the mass defect, B_n is the neutron binding energy, and T_n is the kinetic energy of the neutron involved. The mass defect was calculated by using the recommended values of nuclear masses [9]. For each mass value, we chose an isobar that ensured the maximum energy deposition. The available energy was determined as the difference of the total available energy Q^* and the total kinetic energy (TKE) of fragments (the sum of the energies of a light and the complementary heavy fragment). For various values of the available energy of a light fragment, the mass distributions for ^{238}U (sections of the two-dimensional distribution in Fig. 2) are shown in Fig. 3. At small values of the available energy, the mass spectrum has a pronounced structure. Groups where the heavy-fragment masses are 129, 134, 140, and 146 amu stand out in the spectra. This behavior of the fragment mass spectra is typical of the entire family of uranium isotopes. Our attention was captured by the fact that events in which the total kinetic energy is commensurate with the total available energy were observed for a number of mass values. Figure 4 displays the distributions of the total kinetic energy for fragments of mass 130 and 140 amu. For higher values of the total kinetic energy, the shape of the distribution differs significantly from a Gaussian shape and has a clear-cut boundary. By way of example, we indicate that, at the mass value of 140 amu, the maximum energy is realized for the $^{140}_{54}$Xe + $^{99}_{38}$Sr pair (Q = 185.69 MeV, Q^* = 195.49 MeV), while, for the mass value of 130 amu, it is realized for the $^{130}_{50}$Sn + $^{109}_{42}$Mo pair (Q = 198.06 MeV, Q^* = 207.86 MeV). In ^{232}Th fission induced by 5-MeV neutrons, a similar phenomenon was observed at the mass value of 134 amu [3]. The minimum available energy observed in the present experiment is given in Fig. 5 for various values of the mass splitting. It can be seen that the total kinetic energy amounts to the total reaction energy over the entire mass range between 134 and 140 amu and within the range 127–131 amu. It is advisable to address the question of whether the data that we obtained are reliable. We note that, for various masses of fragments whose yields reach limiting values, the total reaction energy changes within the range of width 15 MeV; therefore, the observed boundary cannot be explained by mechanical and electronic limitations arising in the spectrometer. The total kinetic energy is measured more reliably than the kinetic energies of fragments. In dealing with thick layers, the main contribution to the error in determining energy comes from the uncertainty in the distance that a fragment must travel within the target prior to reaching the sensitive volume of the chamber. Measurements of the position of the peak corresponding to the light group of fragments at different values of the emission angle made it possible to determine the scatter of the energy loss in the layer. For fragments emitted in the orthogonal direction, it is 1.6 MeV. The errors in determining the energies of complementary fragments are not independent. The total distance traveled by fragments in the fissile layer is a constant quantity that is equal to the layer thickness divided by the cosine of the fragment emission angle. An underestimation of the energy loss for one fragment automatically leads to the corresponding overestimation of the en-

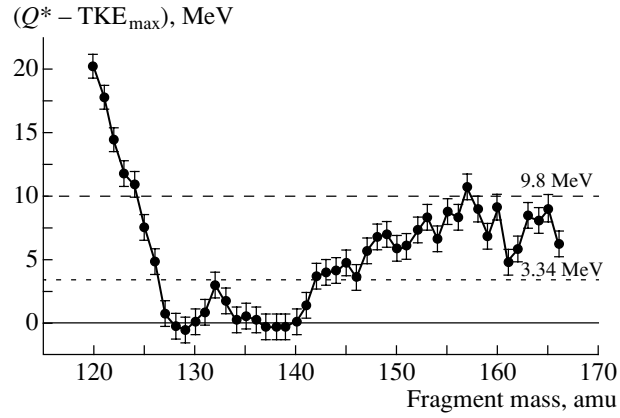

Fig. 5. Minimum excitation energy and fragment deformation ($Q^* - \mathrm{TKE}_{\max}$) versus the fragment mass. The line at 3.34 MeV shows the level that is accessible in the case where the excitation energy of the compound nucleus at the saddle point is transferred to fission fragments, while the line at 9.8 MeV corresponds to the level that is accessible in the case where the entire excitation energy of the compound nucleus is transferred to fission fragments.

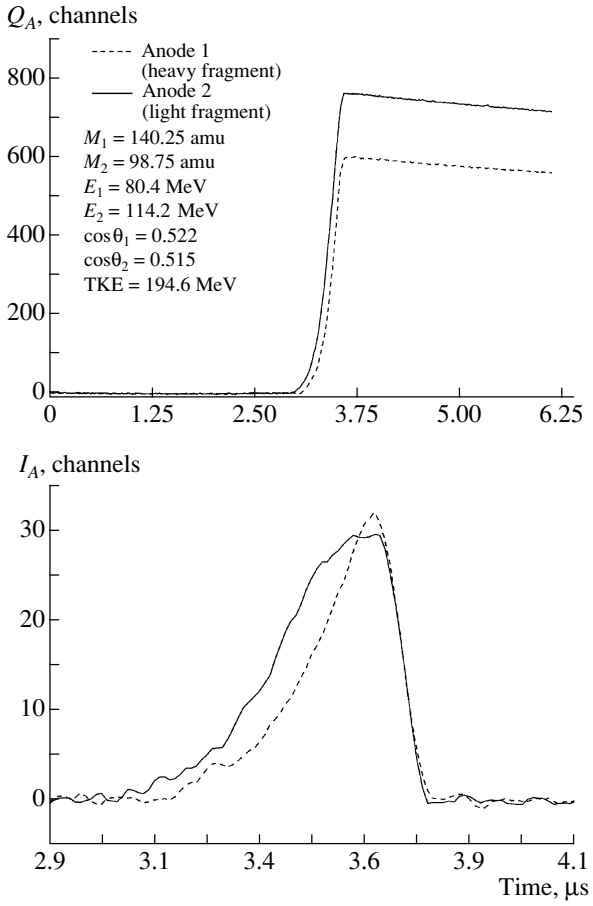

Fig. 6. Example of anode signals corresponding to the limiting values of the total kinetic energy in Fig. 4. The solid (dashed) curve is associated with a light (heavy) fragment. The upper panel shows signals upon the passage of the charge-sensitive preamplifier, while the lower panel shows the same signals upon channel-by-channel differentiation.

ergy loss for the complementary fragment. Therefore, the total kinetic energy of fragments is independent of the fragment-production depth in the layer. The errors in determining the energy of each fragment are canceled in computing the total kinetic energy. Estimations revealed that the total kinetic energy is determined to a precision of about 0.5 MeV. Although the limiting values of the total kinetic energy appear with a low probability, the digital method of recording makes it possible to identify oscillograms that correspond to fission events undistorted by outside factors. Figure 6 shows anode signals that are associated with one of the two events featuring the limiting kinetic energy for the mass of 140 amu that are given in Fig. 4. The signals depicted in the figure do not exhibit superpositions or sizable contributions from noises. The density of ionization losses (lower panel in Fig. 6) corresponds to a light and the complementary heavy fragment. The cosines of the emission angles ($\cos\theta$) as determined independently for each fragment agree to within 0.007. The method used to determine the cosine of the emission angle is based on an analysis of the shape of anode signals. Possible distortions of signals because of superimposed signals (for example, from a light third particle originating from fission) would inevitably distort the shape of one of the signals, with the result that the cosine values would differ from each other sizably.

Our result indicates that the primary excitation energy of the compound nucleus, 9.8 MeV, was converted into the kinetic energy of fragments. The resulting kinetic energy corresponds to the scission of the compound nucleus into two nonexcited fragments featuring the ground-state deformation. Attempts at discovering a similar nuclear decay in ^{233}U and ^{235}U fission induced by thermal neutrons [10, 11] revealed that total-kinetic-energy values corresponding to available energies of 2 to 3 MeV can be obtained only at relative yields below 10^{-7}. There then arises a situation that is paradoxical at first glance: in order to produce"cold" reaction products, it is necessary that the initial fissile system be hot. In order to explain the observed phenomenon qualitatively, one can make use of the Thomas diagram [12], which displays variations in the deformation, Coulomb, and total potential energies versus the position of the scission point (see Fig. 7). It can be seen from this figure that, in the cases where the total available energy is equal to the total reaction energy, there are two thermodynamic limits at the scission point. The limit at small deformations corresponds to the most

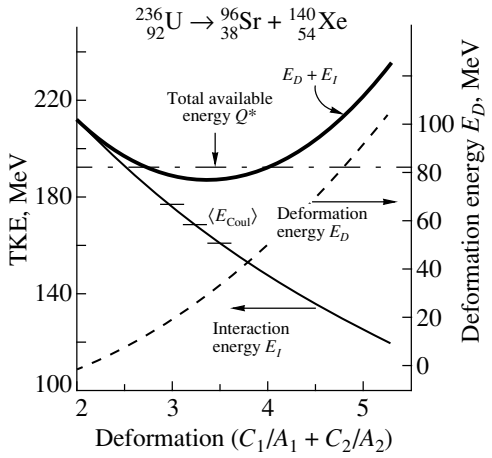

Fig. 7. Deformation energy, energy of Coulomb repulsion, and total potential energy at the scission point versus the deformation of the fissile system being considered [12]. Here, C/A is the ratio of the major and the minor axis of the ellipsoid that simulates the fragment shape.

compact scission configurations. If the fission process is induced by thermal neutrons, the system being considered does not have sufficient energy for forming the surface of two separated fragments immediately at the saddle point (the deformation parameter is about 2). According to data obtained for the case of thermal neutrons, the nucleus undergoing fission must descend along the potential-energy surface by 2 to 3 MeV, and only after that will the required energy be reached owing to Coulomb repulsion. In this case, however, fragments will not have the ground-state deformation at the scission point. An increase in the excitation energy of the compound nucleus corresponds to ascending the level of available energy. Concurrently, the limit at small deformations decreases, with the result that more compact scission configurations become accessible. In all probability, the additional excitation energy introduced in the compound nucleus (3.4 MeV at the barrier) is sufficient for the formation of the surface of two separated fragments even in the vicinity of the saddle point. Fragments originating from the decay of such a system will feature ground-state deformations, and their excitation energies will be low. It can be assumed that the additional energy will make it possible to overcome a different, higher, barrier that separates the so-called fusion valley, which is well known in heavy-ion physics. In the case of fission through the classical fission barrier, the compound system has to evolve over at least a minor stage of descent, with the result that nascent fragments appear to be elongated in relation to their ground-state deformation. In all probability, the situation inverse to that prevalent in the fusion of two heavy ions is realized in ^{238}U fission induced by 5-MeV neutrons.

That this phenomenon is not observed for all mass values may suggest that the effect in question is modulated by the yields of fragments (possibly, accumulated statistics are insufficient in the case of a symmetric and in the case of a strongly asymmetric mass splitting). Different penetrabilities of the barrier separating the saddle point and the fusion valley for different mass modes of fission may be another factor responsible for this.

Answers to many questions are expected from experiments where ^{238}U fission is induced by neutrons of different energies. The probability for the formation of fragments having limiting values of the total kinetic energy probably depends on excitation energy. Analysis of the yields will make it possible to obtain more realistic values of the height and penetrability of the barrier separating the saddle point and the fusion valley.

REFERENCES

1. V. A. Khryachkov, A. A. Goverdovskii, V. V. Ketlerov, *et al.*, Yad. Fiz. **57**, 1221 (1994) [Phys. At. Nucl. **57**, 1154 (1994)].
2. A. A. Goverdovski, V. A. Khryachkov, V. V. Ketlerov, *et al.*, Yad. Fiz. **62**, 965 (1999) [Phys. At. Nucl. **62**, 901 (1999)].
3. A. A. Goverdovskiĭ, V. A. Khryachkov, V. V. Ketlerov, *et al.*, Pis'ma Zh. Éksp. Teor. Fiz. **67**, 752 (1998) [JETP Lett. **67**, 793 (1998)].
4. C. Budtz-Jorgensen, H.-H. Knitter, Ch. Straede, *et al.*, Nucl. Instrum. Methods Phys. Res. A **258**, 209 (1987).
5. V. A. Khriatchkov, I. V. Gubareva, M. V. Dunaev, and N. N. Semenova, Preprint No. 2740, Inst. Phys. Power Eng. (Obninsk, 1998)
6. V. A. Khriatchkov, A. A. Goverdovski, V. V. Ketlerov, *et al.*, Nucl. Instrum. Methods Phys. Res. A **394**, 261 (1997).
7. M. V. Dunaev, I. V. Dunaeva, V. A. Khriatchkov, and N. N. Semenova, in *Proceedings of VIII Int. Seminar on Interaction of Neutrons with Nuclei, Dubna, 2000,* p. 363.
8. F. Vives, F.-J. Hambsch, S. Oberstedt, *et al.*, in *Proceedings of International Conference "Nuclear Fission and Fission-Product Spectroscopy", Seyssins, France, 1998,* p. 435.
9. G. Audi and A. H. Wapsta, Nucl. Phys. A **565**, 1 (1993).
10. U. Quade, K. Rudolph, S. Skorka, *et al.*, Nucl. Phys. A **487**, 1 (1988).
11. V. A. Khryachkov, A. A. Goverdovskiĭ, B. D. Kuz'minov, *et al.*, Yad. Fiz. **53**, 621 (1991) [Sov. J. Nucl. Phys. **53**, 387 (1991)].
12. T. D. Thomas, W. M. Gibson, and G. J. Safford, in *Proceedings of Symposium "Physics and Chemistry of Fission"* (IAEA, Vienna, 1966), Vol. 1, p. 467.

Translated by A. Isaakyan

Physics of Atomic Nuclei, Vol. 66, No. 5, 2003, pp. 804–811. From Yadernaya Fizika, Vol. 66, No. 5, 2003, pp. 837–844.

NUCLEI
Theory

The Analysis of the Densities of *s*-Wave Neutron Resonances Separated with Respect to Spin*

M. Kaczmarczyk**

Department of Nyclear Physics, University of Lodz, Poland

Received February 12, 2002

Abstract—The density ratio of s-wave neutron resonances $z = \rho(J_1)/\rho(J_2)$ was analyzed on the basis of the experimental data for 22 atomic nuclei and the Gilbert–Cameron formula for $\rho(J)$. Here, $J_1 = I_x - 1/2$ and $J_2 = I_x + 1/2$, where I_x denotes the spin of the target nucleus in the ground state. Our aim was to verify whether the factor $\eta(I_x)$, as a multiplier, can be applied in the expression describing $\rho(J_1)$, with the assumption that $\rho(J_2)$ values remain unchanged, or whether the factor $1/\eta(I_x)$ can be applied, as a multiplier with $\rho(J_2)$, while the $\rho(J_1)$ values remain unchanged. The final conclusions, e.g., the confirmation or the negation of the fact that it may be necessary to apply the $\eta(I_x)$ factor, depend on the values of "real" errors Δz of the z variable, which can be calculated if the optimal values of $\Delta\rho(J_1)$ and $\Delta\rho(J_2)$ are known. © *2003 MAIK "Nauka/Interperiodica".*

1. INTRODUCTION

The resonance levels originating as a result of interactions of s-wave neutrons with target nuclei with spin $I_x \neq 0$ are characterized by angular momenta $J_1 = I_x - 1/2$ and $J_2 = I_x + 1/2$. On the basis of experimental data available at present [1–7], it was possible to calculate the densities of neutron resonances separately for J_1 and J_2 and take up an analysis of the values $\rho(J_1)$ and $\rho(J_2)$.

The analysis made in the present paper was based on the theoretical description given by formula (1) from the paper by Gilbert and Cameron [8]. This formula is widely known and commonly used when describing the spin dependence of ρ:

$$\rho(J)_{\text{theor}} = \frac{2J+1}{24\sqrt{2}\sigma^3 a^{1/4}U^{5/4}} \times \exp\left[-\frac{(J+1/2)^2}{2\sigma^2}\right]\exp\left(2\sqrt{aU}\right). \quad (1)$$

The main purpose of the present research was to make an attempt to answer the question of whether formula (1) gives the correct description of the dependence of the resonance level density on spin.

Our papers on the resonance level density (see, e.g., [9, 10]) were based on the assumption that Eq. (1) is valid, and so were the papers of other authors (see [11, 12]), where the correctness of formula (1) was also taken for granted.

2. THE SYSTEMATICS OF THE EXPERIMENTAL VALUES OF s-WAVE NEUTRON RESONANCES

Table 1 presents the experimental values of $\rho(J_1)$ and $\rho(J_2)$ calculated with the data taken from [1–7], where the energies E of s-wave neutron resonances were given for both values J_1 and J_2 of spin. The values of $\rho(J_1)$ and $\rho(J_2)$ for the resonances of the nucleus were calculated to be equal to the respective gradients of the straight-line relation between the serial number of the resonance and its energy. The whole range of nuclei with $25 < A < 250$ has been analyzed in this way. The resonance energies E together with J_1 and J_2 values were found only for 77 nuclides. From all these available data, only those resonance data were chosen for which the number of s-wave resonances with fixed J was at least equal to 20. Within this limitation, it turned out that the intended analysis can be carried out for only 22 nuclides in the whole range of mass numbers A, with the obvious exclusion of even–even target nuclei. Among these 22 nuclides, there are two of them, ^{155}Gd and ^{163}Dy, for which the authors [6] give the recommended values of $\rho(J_1)$ and $\rho(J_2)$ but there is no information about the number of resonances $n(J_1)$ and $n(J_2)$.

In the preliminary investigations (see Subsection 4.1), the errors $\Delta\rho(J_1)$ and $\Delta\rho(J_2)$ were calculated with the assumption that the Wigner distribution gives a correct description of the neutron resonance level spacing distribution of the neighboring resonances with fixed J values [13].

*This article was submitted by the author in English.

** e-mail: marykacz@uni.lodz.pl

Table 1. The experimental values of neutron resonance level density $\rho(J_1 = I_x - 1/2)$ and $\rho(J_2 = I_x + 1/2)$ and number of resonances $n(J_1)$ and $n(J_2)$ for excitation energy $U = S_n - P(N) - P(Z)$ [the numbers in parentheses (fourth and sixth columns) are for the power of ten factor]

Nuclide	I_x	$n(J_1)$	$\rho(J_1)$, MeV^{-1}	$n(J_2)$	$\rho(J_2)$, MeV^{-1}	$z = \rho(J_1)/\rho(J_2)$	R	References
$^{45}Sc_{24}$	7/2	43	4.343(2)	20	3.824(2)	1.140	0.991	[1]
$^{51}V_{28}$	7/2	24	1.149(2)	24	1.200(2)	0.957	0.992	[3]
$^{55}Mn_{30}$	5/2	32	2.466(2)	23	2.125(2)	1.160	0.843	[2]
$^{59}Co_{32}$	7/2	36	4.367(2)	33	3.745(2)	1.170	0.952	[3]
$^{63}Cu_{34}$	3/2	52	3.704(2)	36	2.500(2)	1.480	0.661	[4]
$^{65}Cu_{36}$	3/2	39	2.703(2)	29	2.000(2)	1.350	0.662	[4]
$^{67}Zn_{37}$	5/2	197	1.171(3)	52	1.259(3)	0.930	0.813	[1]
$^{89}Y_{50}$	1/2	46	6.060(1)	90	1.600(2)	0.379	0.347	[5]
$^{147}Sm_{85}$	7/2	30	7.207(4)	29	6.988(4)	1.030	0.844	[1]
$^{149}Sm_{87}$	7/2	22	1.780(5)	40	2.436(5)	0.731	0.840	[1]
$^{155}Gd_{91}$	3/2	–	2.012(5)	–	3.236(5)	0.622	0.622	[6]
$^{157}Gd_{93}$	3/2	21	6.213(4)	32	9.208(4)	0.675	0.624	[1]
$^{159}Tb_{94}$	3/2	28	9.578(4)	20	1.634(5)	0.586	0.623	[7]
$^{163}Dy_{97}$	5/2	–	4.525(4)	–	7.519(4)	0.602	0.756	[6]
$^{165}Ho_{98}$	7/2	27	6.862(4)	27	1.275(5)	0.538	0.837	[1]
$^{167}Er_{99}$	7/2	25	8.705(4)	27	1.333(5)	0.653	0.836	[1]
$^{177}Hf_{105}$	7/2	34	1.822(5)	23	2.292(5)	0.795	0.832	[1]
$^{179}Hf_{107}$	9/2	22	1.114(5)	20	9.263(4)	1.200	0.892	[2]
$^{197}Au_{118}$	3/2	21	2.328(4)	62	3.527(4)	0.660	0.621	[1]
$^{235}U_{143}$	7/2	104	8.862(5)	108	1.089(6)	0.814	0.820	[1]
$^{237}Np_{144}$	5/2	125	7.860(5)	141	9.367(5)	0.839	0.743	[1]
$^{239}Pu_{145}$	1/2	29	1.309(5)	42	2.677(5)	0.489	0.338	[1]

Table 1 also gives the values of

$$z = (\rho(J_1)/\rho(J_2))_{\exp},$$

which are the subject of analysis in this paper. The errors Δz were calculated with the use of the expression for the standard deviation of a random variable as given in the Wigner distribution. The neighboring resonance level spacings with fixed spin are considered as random variables described by the Wigner distribution.

The way in which Δz values were calculated is modified in a further part of this elaboration (see Subsection 4.2).

3. THE COMPARISON OF $z = (\rho(J_1)/\rho(J_2))_{\exp}$ WITH THE THEORETICALLY PREDICTED VALUES OF THE R RATIO

Formula (1), as written for J_1 and J_2, makes it possible to establish the theoretical value of the ratio

$$R = (\rho(J_1)/\rho(J_2))_{\text{theor}},$$

which leads to

$$R = \frac{I_x}{(I_x+1)} \exp\left(\frac{2I_x+1}{2\sigma^2}\right). \qquad (2)$$

Equation (2) (with an additional assumption that $z = R$) was used in [11] as a basis for the calculation of the experimental values of the parameter σ^2; it may

Table 2. The set of the coefficient values of the polynomial (the numbers with signs in parentheses are for the power of ten factor)

Degree of the polynomial	a_0	a_1	a_2	a_3
3	944.569(−3)	904.142(−3)	−520.667(−3)	75.601(-3)
2	155.987(−2)	−231.319(−3)	243.819(−4)	−
1	145.174(−2)	−115.040(−3)	−	−
Constant function	$\eta(I_x) = 1.18505$			

be concluded then that the authors were convinced as to the correctness of formula (1).

In the present paper, the following expression was adopted for σ^2, according to [8]:

$$\sigma^2 = 0.145A^{2/3}\,(aU)^{1/2} \qquad (3)$$

for $U = S_n - P(Z) - P(N)$, where S_n is neutron separation energy for a composite nucleus, while $P(Z)$ and $P(N)$ are the neutron and proton pairing energies, respectively.

In the calculations of R values, which were made according to Eqs. (2) and (3), we applied the values of the level density parameter a obtained with the use of the method of fitting expression (1) to the experimental densities $\rho_{\rm tot} = \rho(J_1) + \rho(J_2)$. This means that we made an assumption that parameter a does not depend on the spins of neutron resonances and, what is more, that $\sigma(J_1) = \sigma(J_2)$.

Table 1 also presents the values of R that were obtained according to (2) for the 22 investigated nuclides.

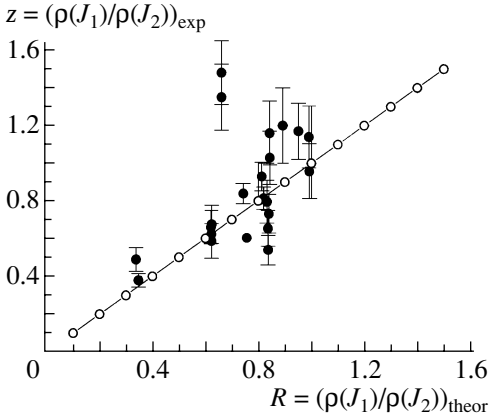

Fig. 1. The dependence of the experimental values of the $z = \rho(J_1)/\rho(J_2)$ ratio on the respective theoretical values R. The line that links the open circles represents the equation $z = R$. The errors of the points were calculated under the assumption that the spacing between the neighboring resonances is a variable as given in the Wigner distribution.

In Fig. 1, a set of points, together with the marked errors Δy, as calculated under the assumption (A) that the neighboring resonances level spacings with fixed J can be described by the Wigner distribution, is presented in the plane with the coordinates $x = R$ and $y = z$.[1)] The χ^2 variable was calculated for the theoretical dependence $z = R$ (open circles in Fig. 1) and found to be equal to 81.8, whereas $\chi^2_{\rm theor}(\alpha = 0.05, k = 19) = 30.144$ (see the data set below in Table 3).

The dependence $z/R = f(A)$ (where A is a mass number of a nucleus) is presented in Fig. 2 for the investigated nuclei, while in Fig. 3 the dependence $z/R = f(I_x)$ is shown, where I_x denotes the spin of the target nucleus in the ground state.

Owing to the analysis of these graphs, it was possible to formulate the following conclusions:

(i) In the region of R values not greater than 0.62, there is a pretty good correlation between the theoretical (R) and experimental (z) values of the $\rho(J_1)/\rho(J_2)$ ratio. However, for $R > 0.62$, the experimental values $\rho(J_1)$ greater than $\rho(J_2)$ occur predominantly. With regard to the character of Fig. 1, it can also be noted that the values $\rho(J_2)_{\rm theor}$ are overestimated with regard to the values $\rho(J_1)_{\rm theor}$, if only the experimental values $\rho(J_1)$ and $\rho(J_2)$ are believed to be correct.

(ii) It can be seen from Fig. 2 that, for nuclei with mass numbers $150 < A < 200$, the values of $\eta = z/R$

[1)] In Fig. 1, the errors of R are not marked. The calculations of ΔR have been carried out for the case when the errors of the density parameter a, Δa, were obtained using the uncertainty $\Delta\rho_{\rm tot}$, which, in turn, was obtained on the basis of the Wigner distribution dispersion for the resonances with spin J_1 and J_2. These calculations showed that, in the set of 22 analyzed points, the greatest relative error $\Delta R/R$ was not greater than 0.13%. In the case when the errors ΔR were calculated with the use of the values of $\Delta\rho_{\rm tot}$ (see Subsection 4.2), which were obtained under the assumption that the fluctuations of the number of resonances can be described by the Poisson distribution, it can be observed that the greatest relative error $\Delta R/R$ does not exceed 0.25% for the set of 22 analyzed points.

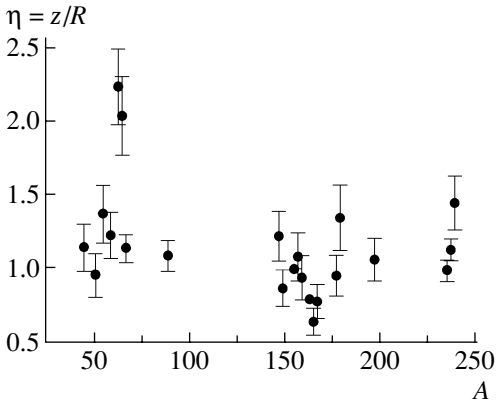

Fig. 2. The dependence of the coefficient $\eta = z/R$ on the mass number A. The errors of the points were calculated under the assumption that the spacing between the neighboring resonances is a variable as given in the Wigner distribution.

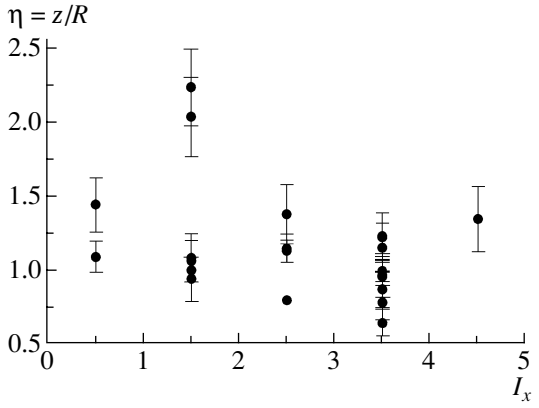

Fig. 3. The dependence of the correction factor $\eta(I_x)$ on the spin I_x of the target nucleus. The errors of the points were calculated under the assumption that the spacings between neutron resonances are the variables as given in the Wigner distribution.

spread around unity quite symmetrically in the interval from about 0.6 up to slightly above 1.3.

(iii) Dispersion of the points in Fig. 3 is so significant that it makes it difficult to find an unmistakable description of the η dependence on spin I_x. It can be noted, however, that most of the points in this figure decidedly appear mainly in the region $\eta > 1$.

4. THE SPIN CORRECTION TERM IN THE GILBERT–CAMERON FORMULA

4.1. Preliminary Description of the Correction Factor $\eta(I_x)$

The analysis presented in Section 3 indicates that there is the need for introducing a correction factor in formula (1) for $\rho\,(J_1)$. The aim is to make it possible to describe the set of points in Fig. 1 with a straight line (i.e., a line joining the open circles in Fig. 1), which makes the situation quantitatively advantageous. It can be easily shown that the correction factor should have a character of the coefficient $\eta = z/R$.

Then, the dependence of the factor η on A (mass number), Z (atomic number), N (number of neutrons), U (effective excitation energy), and I_x was examined. However, as was pointed out in the above consideration, it was somewhat doubtful whether Eq. (1) represents the dependence of ρ on the spin correctly. It was proposed then to insert the correction factor η into the function $\rho(J_1)_{\rm theor}$ in Eq. (1) in a form that is dependent on the target nucleus spin I_x, i.e.,

$$\rho^*(J_1) = \rho(J_1)_{\rm theor}\,\eta(I_x), \qquad (4)$$

with the unchanged theoretical description for $\rho(J_2)$ according to (1) or the factor $1/\eta(I_x)$ for $\rho(J_2)_{\rm theor}$, i.e.,

$$\rho^*(J_2) = \rho(J_2)_{\rm theor}/\eta(I_x), \qquad (5)$$

with the unchanged description for $\rho(J_1)$ according to (1).

It was suggested that such a functional description for $\eta(I_x)$ may be given in the form of a first, second, and third degree polynomial, respectively, or as a constant function. The expansion coefficients for the respective solutions are given in Table 2.

In order to fulfill the requirements necessary for carrying out the χ^2 test, the errors $\Delta\eta = \Delta z/R$ were calculated here with the use of Δz values. Those values were derived based on the expression that describes the dispersion of the Wigner distribution for spacings of the neighboring resonances with a fixed J value.

The χ^2 test, performed for each of the four functions, provided undesirable results. It is worth noting, however, that, for the third degree polynomial, the obtained value of the variable χ^2 is the smallest of all the values obtained in the χ^2 test for the four investigated functions.

4.2. The Reasons for Introducing the Proposed Correction Function $\eta(I_x)$

The results presented in Subsection 4.1, provided that the aforementioned assumptions were made, show that none of the investigated functions $\eta\,(I_x)$ (with coefficients from Table 2) can be approved of and proposed as a correction factor to the Gilbert–Cameron formula.

The contradictory results of the χ^2 test for each of the above functions $\eta(I_x)$ could have been obtained as a consequence of the following reasons:

(i) The values of $\Delta\eta = \Delta z/R$ could have been lowered while calculated under the assumption that

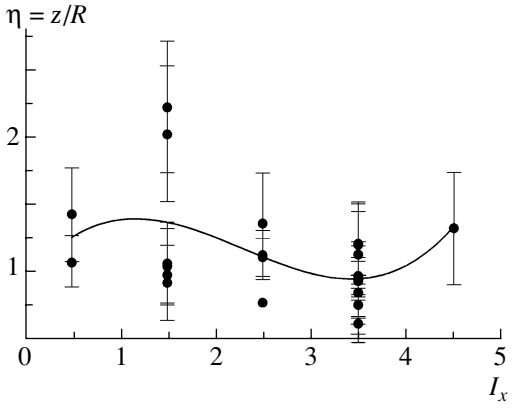

Fig. 4. The dependence of the correction factor $\eta(I_x)$ on the spin I_x of the target nucleus. The solid curve represents the polynomial of the third order. The errors of the points were calculated under assumption that the number of resonances with a fixed spin J is treated as a variable whose fluctuations are described by the Poisson distribution.

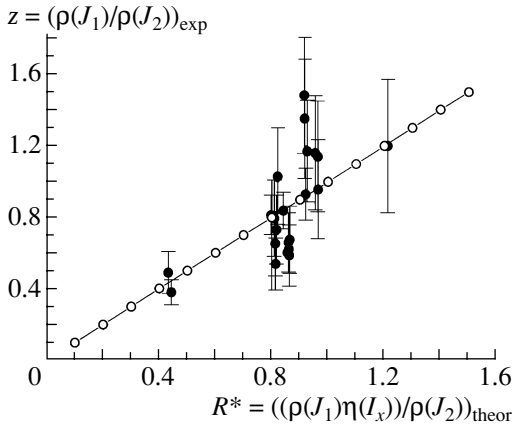

Fig. 5. The influence of the correction factor $\eta(I_x)$ on the z dependence on R. The line, which links the open circles, represents the equation $z = R^*$ and was confirmed by the χ^2 test for the Δz values, calculated under the assumption that the fluctuations of the number of resonances with fixed J are described by the Poisson distribution.

the Wigner function correctly describes the spacing distribution of the neighboring resonance levels with a fixed J value.

(ii) Too small a number of nuclides were taken into account in the analysis (22 points in the figures and 20 in χ^2 test calculations).

(iii) Formula (3) was used for the description of σ^2.

Although the requirement that the number of neutron resonances with a fixed J (for a definite nuclide) should be not lower than 20, as was adopted in the present paper, seems to be reasonable, then, with the view to carrying out the χ^2 test, the remark made in point 2 is less significant than the remark in point 1.

It was pointed out in [14] that the relative error of the average value of the resonance level spacings ($\Delta\langle D(J)\rangle$) with a fixed J is greater than the statistical error only, as expressed by the dispersion of the Wigner distribution. On this ground, it should be expected that also the relative error of the density $\Delta\rho(J)/\rho(J)$, as estimated from the Wigner distribution, gives only a lower limit of the possible error values.

As the values $\Delta\rho(J_1)$ and $\Delta\rho(J_2)$ define both Δz and $\Delta\eta$, such a variant of calculations as described in Subsection 4.1, which is based on the lowered error values, could have led to the unsatisfactory results.

Another suggestion (B) as to the calculation of $\Delta\eta$ will then be made in the following part of the paper. It will be suggested that the number of resonances with a fixed J value should be treated as a variable whose fluctuations are described by a Poisson distribution. In order to examine the correctness of such a suggestion, the following resonances, as the most numerous, were chosen for the analysis: (i) 125 resonances ^{237}Np with spin $J_1 = 2$, (ii) 141 resonances ^{237}Np with spin $J_2 = 3$, and (iii) 197 resonances ^{67}Zn with spin $J = 2$. For two of those three distributions of the resonance number [e.g., for events (i) and (iii)], an agreement with the Poisson distribution was obtained at the significance level $\alpha = 0.05$. It can be concluded then that the adopted assumption may be considered as a reasonable one and that it can become a basis for the quantitative analysis, e.g., for the calculations of the errors $\Delta\eta$ and then calculations of the values of the variable χ^2_{cal} for the four functions $\eta(I_x)$ with the expansion coefficients from Table 2. It should also be noted that the errors $\Delta\eta$ calculated in such a way are relatively greater than the respective values obtained when calculated from the dispersion of the Wigner distribution.

The results of the calculations show that, if the errors $\Delta\eta$ of the points (see Fig. 4) are calculated under the assumption that the number of resonances with a fixed spin J is treated as a variable whose fluctuations are described by the Poisson distribution, then the smallest value of χ^2_{cal} can be obtained for such a function $\eta(I_x)$ given in the form of a polynomial of the third degree (the curve in Fig. 4). The polynomial coefficients are listed in Table 2. What is more, at the significance level $\alpha = 0.05$ and for the number of degrees of freedom $k = 16$, there is $\chi^2_{cal} < \chi^2_{theor}$, so it can be assumed that in this case the third degree polynomial is a sought function and that it represents a dependence of correction coefficient η in formula (1) on the spin I_x of the target nucleus as follows:

$$\eta(I_x) = a_0 + a_1 I_x + a_2 I_x^2 + a_3 I_x^3. \qquad (6)$$

Table 3. The set of values of the χ^2 variables that resulted from the testing of the linear relations $z = R$ and $z = R^*$ for two variants of the error Δz calculations

Type of relation	A	B
$z = R$	81.8 (see Fig. 1)	23
$z = R^*$	62.3	17.6 (see Fig. 5)
$\chi^2_{\text{theor}}(\alpha = 0.05, k = 19) = 30.144$		

Note: A—Δz is calculated according to Wigner dispersion; B—Δz is calculated under assumption that the Poisson distribution describes fluctuations of the resonance number.

The dependence $z = f(R^*)$, where $R^* = R\eta(I_x)$ is a corrected value of the ratio $\rho^*(J_1)/\rho(J_2)$, is presented in Fig. 5, $\rho^*(J_1)$ being described by (4). This figure, as compared with Fig. 1, allows for the conclusion that the agreement between z and R^* values becomes more advantageous in this case.

For the linear dependence $z = R^*$ presented in Fig. 5 (the line linking the open circles), the variable χ^2_{cal} is equal to $\chi^2_{\text{cal}} = 17.6 < \chi^2_{\text{theor}} = 30.144$, at the significance level $\alpha = 0.05$ and $k = 19$ (for a detailed presentation, see Table 3). The calculation of the errors Δz in this case was carried out with the use of the dispersion of the Poisson distribution for the number of resonances.

5. FINAL CONCLUSIONS

The problem undertaken in this paper to examine the correctness of the use of Eq. (1) from [8] in order to describe the neutron resonance densities is still receiving consideration at present. For example, the authors of [15] have noted that the values $\rho(J)$ derived from the so-called Bethe formula are overestimated in the range of large J values at fixed excitation energy. In addition, the graphs presented in [15] also show that, in the region of $J < 10\hbar$, the line representing the function $\rho(U, J)$ calculated according to the Bethe formula lies slightly above the line which corresponds to the calculations of the authors of [15]. The function $\rho(J)$ as given by the Bethe formula depends on the J in the same way as in the formula from [8]. The fact that, in the course of the calculation based on the Bethe formula, the values of $\rho(J)$ were overestimated, especially in the region of large J values, was commented on by the authors of [15] by their statement: "The Bethe formula is based on a spin cutoff (or Gaussian) approximation which ignores the effect of Pauli's exclusion principle." It is such a pity that the research in [15] dealt merely with the excited levels of one (^{110}Sn) nucleus.

The s-wave resonance data make it possible to carry out an analysis in the region $J = 0$–5 (for the nuclei from Table 1), whereas the research in [15] comprised a much wider range of variability of J for ^{110}Sn. Yet, the theoretical description of $\rho(J)$ as given by Eq. (1) seems not to be fully correct when it comes to neutron resonances, which is consequently bespoken by Fig. 1.

Table 3 presents the values of χ^2 for the linear relations $z = R$ and $z = R^*$ as obtained in the two cases: (A) when Δz were calculated with the use of the expression that gives the dispersion of the Wigner distribution for the spacings of neighboring resonances, and (B) when Δz values were calculated under the assumption that fluctuations of the resonance number are described by the Poisson distribution.

A detailed inspection of Table 3 has led us to interpretation of the results in terms of considering the possibility of describing both relations $z = f(R)$ and $z = f(R^*)$ with linear functions. In the calculation variant A, the χ^2 test excludes such a possibility, while in variant B both dependences can be considered as linear, even though the variable χ^2_{cal} for the $z = R^*$ dependence is evidently lower than the one representing the dependence $z = R$. So we can say that, if the errors Δz of the z variable are calculated under the assumption B, then the χ^2 test makes it possible to decide that the following two descriptions of the experimental values of the ratio $z = \rho(J_1)/\rho(J_2)$ are correct: that which is based on the R expression resulting from the Gilbert–Cameron formula and multiplied by the $\eta(I_x)$ function and that which is based on the R formula but without that $\eta(I_x)$ multiplier.

On the basis of the set of the data given in Table 3, it can be said that, if "real" values of the errors Δz fall within the interval limited by the two analyzed values, which correspond to the extreme cases A and B, then and only then does it seem to be reasonable

to introduce a correction factor $\eta(I_x)$, as given by formula (6), in Eq. (4) or a factor $1/\eta(I_x)$ in Eq. (5).[2)]

6. SUMMARY

In the present paper, it has been pointed out that there is a requirement for further experimental investigations on the estimation of spins of the neutron resonance levels for nuclei in the whole range of mass numbers A, so that the already existing data can be enriched.

In the problem under consideration, it was also expected, on a well-grounded basis, that another theoretical description of the σ^2 parameter should be found as a possible alternative on the way which leads to corrected $\rho^*(J_1)$ or $\rho^*(J_2)$ values being obtained. In the present work, Eq. (3) from [8] was assumed in the calculations of σ^2. However, it is not the only formula describing σ^2. In [17], for example, the authors presented the calculations of σ^2 according to microscopic theory. However, their results were obtained only for energy $E = 7$ MeV, while the values of the effective excitation energies for neutron resonances of the investigated nuclei (as given in Table 1) vary quite a lot and fall within the interval 5.36–8.70 MeV. The observed wide range of the effective excitation energy values makes it impossible to apply the results on σ^2 [17] to the analysis that was carried out in this work. The author of [18] also suggests that there is possibility of calculating σ^2 on the basis of the microscopic variant of the MSFM model [19]. However, the results on σ^2 obtained by the author of [18] were not calculated for a wide range of mass numbers and were presented only as a graph, which makes them unsuitable for calculation in such a problem dealt with in the present paper. On the other hand, the σ^2 values [20] could not have been used in calculations in the present paper because they correspond to excitation energies that were lower than the resonance energies.

To sum up, it can be said that the meaning of this paper lies in the fact that we examine the legitimacy of inserting the correction factor $\eta(I_x)$ into the Gilbert and Cameron formula, for, e.g., the densities $\rho(J_1)$ of s-wave neutron resonances. Moreover, this analysis makes it possible to define the way of obtaining this factor.

However, it seems that, as the set of data on resonances of many nuclei (by means of experimental investigations) is extended and as the development of theoretical models describing the σ^2 parameter for a wide range of nuclei follows, the undertaken task will require reconsideration in the future with precisely specified calculations. At present, although attempts were made to discuss the problem with the authors of [17, 18] specific to this topic, they did not result in extending the analysis, e.g., in the part concerning the description of the variable $R = (\rho(J_1)/\rho(J_2))_{\text{theor}}$ with other functions defining the σ^2 parameter.

It should be mentioned here that it is the present state of the experimental database on energy (E) and spin (J), available in the bibliography [1–7], which is responsible for the fact that the author has not been able to express final conclusions in a radical way in disfavor of formula (1). The published values of E and J of neutron resonances come from the experimental research of different scientific groups, which means that they were obtained with different resolution and also with the use of different techniques and methods of measurement.

At present, there are too few known resonances whose spins are defined. That fact, together with difficulties in evaluating the errors of experimental data, makes estimation of the number of the so-called "lost resonances" much less possible. The way of prescribing the spin may alone, in some cases and especially for weak resonances, raise doubts. Such a situation leads to the fact that the results obtained in the present paper cannot be fully trusted, particularly those which concern the variable $z = \rho(J_1)/\rho(J_2)$ and consequently the relation between this variable z and the R values as calculated from the Gilbert–Cameron formula.

It seems reasonable then to conclude that there are no reasons, at present, to reject the dependence of neutron resonance densities on spin as postulated by formula (1).

ACKNOWLEDGMENTS

The author wishes to thank Prof. M. Przytuła and Dr. L. Łasoń for many fruitful discussions concerning this subject.

[2)] The conclusions resulting from the present paper [i.e., confirmation or negation of the fact that the correction factor $\eta(I_x)$ should be inserted into Eq. (1)] depend to a great extent on the correctness of the estimation as to the values of the errors $\Delta\rho(J_1)$ and $\Delta\rho(J_2)$ (in both cases A and B) and on the type of their relation with the optimal values of the errors $\Delta\rho(J_1)$ and $\Delta\rho(J_2)$. The computational data $\Delta\rho(J_1)$, $\Delta\rho(J_2)$ (or the errors of average level spacings: $\Delta\langle D(J_1)\rangle$ and $\Delta\langle D(J_2)\rangle$) are not available in the present systematics of the neutron resonance parameters for a wide range of nuclei. Even in [11], where the Gilbert and Cameron formula [8] was used to define $\rho(J)$ and the experimental data on $\rho(J_1)$ and $\rho(J_2)$ were involved in the calculation of σ^2, the values of $\rho(J_1) \pm \Delta\rho(J_1)$ and $\rho(J_2) \pm \Delta\rho(J_2)$ were not published. The review of the systematics of the average values of distances $\langle D\rangle \pm \Delta\langle D\rangle$ for s-wave resonances, as described in [16], demonstrates that those data are related to the resonances without any differentiation due to spin J.

REFERENCES

1. S. F. Mughabghab, M. Divadeenam, and N. E. Holden, *Neutron Cross Section* (BNL, New York, 1981), Vol. 1, Part A; S. F. Mughabghab, *Neutron Cross Section* (BNL, New York, 1984), Vol. 1, Part B.
2. *Neutron Cross Section* (BNL-325, 1973).
3. J. B. Garg, Nucl. Sci. Eng. **65**, 76 (1978).
4. M. S. Pandey, J. B. Garg, and J. A. Harvey, Phys. Rev. C **15**, 600 (1977).
5. H. M. Agrawal, J. B. Garg, and J. A. Harvey, Nucl. Phys. A **501**, 18 (1989).
6. B. V. Efimov *et al.*, in *Neutronics* (Moscow, 1988), Vol. 2, p. 214 (in Russian).
7. V. P. Alfimienkov *et al.*, Yad. Fiz. **25**, 930 (1977) [Sov. J. Nucl. Phys. **25**, 495 (1977)].
8. A. Gilbert and A. G. W. Cameron, Can. J. Phys. **43**, 1446 (1965).
9. M. Kaczmarczyk and M. Przytuła, Yad. Fiz. **63**, 828 (2000) [Phys. At. Nucl. **63**, 758 (2000)].
10. M. Kaczmarczyk, J. Phys. G **26**, 253 (2000).
11. S. F. Mughabghab and C. L. Dunford, Phys. Rev. Lett. **81**, 4083 (1998).
12. S. F. Mughabghab and C. L. Dunford, in *Proceedings of the Int. Conf. on the Physics of Nuclear Science and Technology, Islandia Marriott Long Island Hauppauge, New York, 1998* (American Nuclear Society, La Grange Park, 1998), Vol. 1, p. 784.
13. A. V. Ignatiuk, *Statistical Properties of Excited Nuclei* (Energoatomizdat, Moscow, 1983), p. 96 (in Russian).
14. H. Vonach, M. Uhl, and B. Strohmaier, Phys. Rev. C **38**, 2541 (1988).
15. B. K. Agraval and A. Ansari, Nucl. Phys. A **640**, 362 (1998).
16. Data obtained by courtesy of G. Rohr.
17. A. N. Behkami and Z. Kargar, J. Phys. G **18**, 1023 (1992).
18. O. T. Grudzevich, Yad. Fiz. **58**, 1758 (1995) [Phys. At. Nucl. **58**, 1658 (1995)].
19. V. G. Soloviev, *Theory of Complex Nuclei* (Nauka, Moscow, 1971; Pergamon, Oxford, 1976).
20. O. T. Grudzevich, private communications.

Physics of Atomic Nuclei, Vol. 66, No. 5, 2003, pp. 812–823. Translated from Yadernaya Fizika, Vol. 66, No. 5, 2003, pp. 845–855.

NUCLEI
Theory

Elastic Deuteron–Deuteron Scattering and Relevant Reaction Involving the Flip of Deuteron Spins and Isospins into a Singlet versus the Predictions of the Supermultiplet Potential Model for Cluster Interaction

B. G. Struzhko[1)], V. M. Lebedev, and V. G. Neudatchin

Institute of Nuclear Physics, Moscow State University, Vorob'evy gory, Moscow, 119899 Russia

Received January 28, 2002; in final form, May 6, 2002

Abstract—A brief survey of experimental results on elastic deuteron–deuteron scattering is given. Data from an experiment performed at the Institute for Nuclear Research (National Academy of Sciences of Ukraine, Kiev) at $E_{\text{c.m.}} = 23.4$ and 25.0 MeV and data from the literature at $E_{\text{c.m.}} = 11.6$ MeV are used to analyze the reaction involving the flip of the spins and isospins of two dinucleons into a singlet, $d + d \to d_s + d_s$ or $(pp)_s + (nn)_s$. Two-dimensional coincidence spectra of protons from the reaction $d + d \to p + p + n + n$ are simulated with allowance for dominant quasibinary processes, including quasifree proton scattering and final-state nucleon–nucleon interaction. It is concluded that this reaction is dominated by the mechanism involving double spin–isospin flip. The differential cross sections $d\sigma/d\Omega$ for the reaction ${}^2H(d, d_s)d_s$ at $E_{\text{c.m.}} = 23.4$ MeV and the reaction ${}^2\text{H}(d, (pp)_s)(nn)_s$ at $E_{\text{c.m.}} = 11.6$ MeV are determined. The elastic-scattering cross sections and the cross sections for spin-flip reactions leading to the formation of a singlet ground state are compared with the results produced by the supermultiplet potential model where the interaction between clusters A and B is described by a potential $V^{[f]}(R)$ ($[f]$ is an orbital Young diagram). The theory faithfully reproduces experimental results, but data on the flip of the spins and isospins of two deuterons are scanty (it is desirable to supplement them). © *2003 MAIK "Nauka/Interperiodica".*

1. INTRODUCTION

The three- and the four-body breakup of extremely light nuclei through the reactions

$$d + p \to p + p + n, \tag{1}$$

$$d + t \to p + n + t, n + n + h, \tag{2}$$

$$d + d \to p + p + n + n \tag{3}$$

have been studied experimentally for a long time at several laboratories worldwide {see [1] for references concerning reactions (1) and (2) and [2–7] for references concerning reaction (3)}. A wide series of studies were performed at the Institute for Nuclear Research (National Academy of Sciences of Ukraine, Kiev, Ukraine) [8–12].

Even the first experimental studies devoted to reactions (1)–(3) revealed an interesting effect—the reaction cross section receives a considerable contribution from the mechanism involving the production of a nucleon pair in the singlet state. While, in reactions (1) and (2), this effect manifested itself predominantly under specific kinematical conditions, in reaction (3), it proved to be significant even in the case where the geometry of an experiment was chosen in such a way as to correspond to the quasifree-scattering process.

Theoretical investigations into reactions (1)–(3) were initiated by the well-known articles of Migdal and Watson [13–15], who introduced final-state nucleon–nucleon interaction, which is of crucial importance here.

Later on, reaction (1) was used, along with elastic pd scattering, as an important testing ground for Faddeev–Yakubovsky equations [16, 17]. Issues being treated in this connection included off-shell interactions [16] and three-body nuclear forces [16, 17]. At a microscopic level, no theoretical investigation of reaction (3) has been performed so far, since this would involve cumbersome calculations.

In the early 1990s, the permutation symmetry of the system in orbital space, as symbolized by the Young diagram $[f]$, was introduced as a new element in theoretical analyses of the processes in question [18]. This symmetry enters into the supermultiplet potential model of cluster interaction [18], where use is made of the quantum numbers $[f]LSJT$. By

[1)]Institute for Nuclear Research, National Academy of Sciences of Ukraine, pr. Nauki 47, Kiev, 03680 Ukraine.

way of example, we indicate that, for the $d+t$ system, this approach makes it possible to obtain a good description of the totality of data on elastic scattering, the radiative-capture reaction $d+t \to {}^3\mathrm{He}+\gamma$, and the scattering process involving the flip of the deuteron spin and isospin into a singlet [18] (for an analysis of the processes occurring in the $t+p$ system, the interested reader is referred to [19]). Within this model, elastic dd scattering in the $S=1$ (odd L) and $S=2$ (even L) channels corresponds to the well-known problem of potential scattering of the $t+h$ type [20], since only one Young diagram is possible in each case ($[f]=[31]$ for $S=1$ and $[f]=[22]$ for $S=2$). At the same time, two amplitudes, the $[f]=[4]$ and the $[f]=[22]$ one, interfere in the $S=0$ channel, the relevant potentials differing in strength by a factor of 3 [18]! Therefore, these channels of elastic dd scattering are nonpotential and nonunitary. In this case, the probabilities of the d_s+d_s and $(nn)_s+(pp)_s$ channels [here, d_s is the singlet state of a deuteron, while $(nn)_s$ and $(pp)_s$ are the singlet states of, respectively, a neutron–neutron and a proton–proton pair], which involve double spin–isospin flip, significantly increase. Here and below, we imply situations where $E_{\mathrm{c.m.}} \gg \Delta E_d(t \to s) \simeq 2.2$ MeV, with $\Delta E_d(t \to s)$ being the energy required for exciting a deuteron into the singlet state.

The formulas that describe, within the supermultiplet potential model, the differential cross sections for reactions involving the flip of the spin and isospin of a deuteron or of two deuterons simultaneously [$d+t \to d_s+t((nn)_s+h)$, $d+d \to d_s+d_s((nn)_s+(pp)_s)$, etc.] possess a high predictive power and, at the same time, are very convenient in what is concerned with a numerical realization; moreover, they make it possible to cover a wide range of experimental results under various kinematical conditions quite straightforwardly. In this respect, they are much more profitable than fully microscopic approaches [16, 17]. Here, the basis is provided by polarization data on elastic scattering, where amplitudes corresponding to different values of the total spin S are separated. It is precisely these data that make it possible to predict, within the supermultiplet potential model, the cross section for the reaction involving the flip of the spins and isospins of deuterons.

In connection with these possibilities, which appeared for the first time, there arises the natural question of systematizing (summarizing) all experimental results obtained worldwide for reactions (1)–(3) over the relevant kinematical domain. The nontrivial problem of isolating, in a three-nucleon (four-nucleon) continuum, the contribution of the aforementioned singlet deuteron states on the basis of Migdal–Watson theory is of prime importance here. Making use of rich experience accumulated for such problems at the Kiev Institute for Nuclear Research, we were able, in our previous article [1], to perform, along with an analysis of elastic scattering, such a systematization for the reactions $d+t \to d_s+t$ $[(nn)_s+h]$ and $d+h \to d_s+h$, which result in transitions to a singlet state, as well as for the analogous reactions in the $d+p$ system. A comparison of relevant experimental data with the predictions of the supermultiplet potential model made it possible to arrive at an interesting conclusion that calls for a preliminary explanation.

In both systems, $d+t$ and $d+p$, a transition to a singlet state occurs in the $S=1/2$ channels (this value of the total spin is minimal under such conditions), where two scattering amplitudes interfere, the relevant Young diagrams being $[f]=[41]$ and $[f]=[32]$ for the former and $[f]=[3]$ and $[f]=[21]$ for the latter system. Within the supermultiplet potential model, the cross section for deuteron transition to a singlet state is determined by the phase-shift differences $(\delta_L^{[f_1]}-\delta_L^{[f_2]})$ [18]. These differences are small for the $d+p$ system, and so is the cross section in question, because the potentials $V^{[3]}$ and $V^{[21]}$ differ in strength only by 20% [18]. As a result, the model describes experimental data only qualitatively since the contributions of reaction mechanisms that are disregarded in the supermultiplet potential model are superimposed on the small calculated cross sections. But for the $d+t$ system, the potential $V^{[41]}$, which corresponds to the most symmetric Young diagram $[f]=[41]$, is stronger than the potential $V^{[32]}$ by 50%, with the result that the relevant cross section proves to be much larger, in which case the supermultiplet potential model is able to describe experimental data even at a quantitative level [1, 18].

The present article reports on the next step, covering both elastic dd scattering and transitions of two-nucleon systems to a singlet state through the reactions $dd \to d_s+d_s$ and $d+d \to (nn)_s+(pp)_s$. Because of the aforementioned large distinction in strength between the deuteron–deuteron potentials for the Young diagrams $[f]=[4]$ and $[f]=[22]$—this distinction is explained below at the quantitative level—the results produced by the supermultiplet potential model are expected to be especially reliable here. In order to verify its predictions, one needs detailed measurements of the cross sections for the transition of both deuterons into a singlet state, but such data are very scanty. In this connection, an experiment that was performed at the Kiev Institute for Nuclear Research—its result are given in the present article below—proved to be of paramount importance.

A feature peculiar to the reaction in which two deuterons undergo a transition to a singlet state

is that, at comparatively modest beam energies ($E_{\text{c.m.}} \sim 10$–20 MeV), global soft rescattering occurs in the final state (four-fermion continuum), in which case it is necessary to pay special attention to methodological issues in extracting the required cross sections from experimental data. These issues are also discussed below.

The ensuing exposition is organized as follows. A survey of available experimental data on the reaction $d + d \to p + p + n + n$ is given in Section 2. The procedure used in the experiment at the Kiev Institute for Nuclear Research is briefly described in Section 3. A simulation of experimental spectra and a method for isolating the cross section for double spin–isospin flip into a singlet state are discussed in Sections 4 and 5, respectively. A brief account of the formalism of the supermultiplet potential model is given in Section 6. In the last section (Section 7), data obtained previously for elastic *dd* scattering and supplemented with those from the experiment described here, which are required to be extended, however, are compared with the relevant theoretical results based on the application of the supermultiplet potential model, and good agreement between these experimental and theoretical results is found. Thus, the use of supermultiplet symmetry enables one to describe, within a unified conceptual framework, a broad range of nuclear reactions occurring in the systems of extremely light nuclei [such as the $d + d$, $d + t$, and $p + t(h)$ systems]—these include elastic scattering, the flip of the spin–isospin of a deuteron (two deuterons) into a singlet state, the charge-exchange reaction $p + t(h) \to n + h$, and photonuclear reactions—and to make relevant predictions.

2. ANALYSIS OF AVAILABLE DATA ON THE REACTION $d + d \to p + p + n + n$

The four-body reaction (3) is the simplest process that can be used to study neutron scattering on charged-particle beams. Quasibinary mechanisms, such as final-state interaction and quasifree nucleon scattering, are the most promising for a program of this type. An attempt at implementing the first possibility was described in [2]. The experiment reported there measured the two-dimensional proton-coincidence spectra $N(E_1, E_2)$ at the laboratory deuteron-beam energy of $\mathrm{E_0} = 23.15$ MeV ($E_{\text{c.m.}} = 11.6$ MeV). The particle emission angles θ_1 (θ_2) were chosen to be 18° (36°) and 25° (43°) in the $\varphi_1 = 0$ and $\varphi_2 = 0$ planes, respectively. This geometry corresponds to the realization of the kinematical situation of final-state interaction both in the proton–proton and in the neutron–neutron pair simultaneously—that is, of the conditions of the quasibinary reaction $^2\mathrm{H}(d, pp)nn$.

In the calculations performed in the Migdal–Watson approximation [13, 15], the authors were able to reproduce the shape of experimental distributions, but the resulting values of the neutron scattering length a_{nn} proved to be different under different geometric conditions [about -15 fm for angles of $\theta_1 = 18°$ and $\theta_2 = 36°$ and about -50 fm for $\theta_1 = 25°$ and $\theta_2 = 43°$]. The absolute values of the differential cross sections $d^2\sigma/d\Omega_1\Omega_2$ integrated with respect to the particle energies from the detection threshold of 3 MeV (or above) proved to be 0.84 ± 0.04 and 0.63 ± 0.03 mb/sr^2, respectively.

In the presence of final-state neutron–proton interaction in reaction (3), two versions of this reaction are possible. The first proceeds via the formation of two singlet deuterons that is followed by their decay:

$$d + d \to d_s + d_s \to p + n + p + n. \qquad (4)$$

The first experimental data suggesting a high probability of the process in which the spins and isospins of two deuterons are flipped into singlet states were obtained in the late 1970s and the early 1980s [2–4]. Later on, this effect was corroborated on the basis of the supermultiplet potential model [18], where it is naturally explained as the result of action of Majorana exchange forces. In reaction (4), the final-state interaction in the neutron–proton pair was observed, for example, in [8] at the deuteron-beam energy of $E_0 = 50$ MeV and in the kinematically complete experiment reported in [5] and performed at $E_0 = 15.7$ MeV; however, the absolute cross-section values were not obtained there. By and large, the shape of the experimental spectra is consistent with that of the distributions within the Migdal–Watson model.

The second process is the formation of two triplet neutron–proton pairs. It cannot be disregarded a priori, and the relationship between the branching fractions of the two processes in question must be the subject of a dedicated investigation.

It should be emphasized that the formation of one singlet pair in the $d + d$ reaction is forbidden by selection rules in isospin, provided that this is an exact quantum number. Available experimental data indicate that violations of these selection rules, if any, are insignificant [9].

The quasifree scattering of nucleons, where two nucleons (one from the beam deuteron and the other from the target deuteron) do not change their primary momenta, is yet another significant quasibinary mechanism of reaction (3). Since effects associated with the possible violations of the charge symmetry of nuclear forces are quite small, it is natural to begin studying the regularities of such a reaction by exploring the quasifree scattering of protons, which is simpler for experimentalists.

A reliable identification of the quasifree-scattering mechanism is possible in a kinematically complete experiment, where it is necessary to record the spectra of coincidence of three products of reaction (3) in the final state—that is, of the spectator neutron emitted at zero angle and two scattered protons. In the cases of recording only the spectra of double proton–proton coincidences (kinematically incomplete experiment), the interpretation of the results is complicated by the competition of reactions featuring final-state interaction, and it is rather difficult to distinguish between these mechanisms.

A kinematically incomplete experiment at the deuteron-beam energy of $E_0 = 80$ MeV [3] was among the first measurements of this type. For the reaction $^2\mathrm{H}(d, pp)nn$, the spectra of proton–proton coincidences were measured in symmetric coplanar geometry for a few pairs of angles in the interval 34°–52°. Reasonably good agreement was attained in an attempt at describing the experimental differential cross sections $d^4\sigma(E_1, E_2)/d\Omega_1 d\Omega_2 dE_1 dE_2$ on the basis of calculations in the Born approximation with plane waves.

In analyzing the data from [3], it was proposed in [4] to take into account only final-state interaction in the neutron–proton pair; that is; the possible contribution from the quasifree scattering of protons was disregarded in that treatment. In the Migdal–Watson approximation for the triplet and singlet amplitudes, a reasonably good description of the spectra was obtained for all angles with two free parameters that determine the weights of these amplitudes. In the spectra for angles of 36.5° and 43°, the contributions of the singlet states were, respectively, 33 and 56% of the total cross section, these values being much greater than the statistical weight (10%) of the $^1S_0$ state in the mixture of all spin states.

The reaction $^2\mathrm{H}(d, pp)nn$ was also studied at symmetric angles of $\theta = 34.8°$ at a beam energy of $E_d = 34.7$ MeV in [6] (the experimental spectra were not presented there). The results may be treated as a piece of indirect evidence in favor of the occurrence of effects that are associated with final-state interaction in the neutron–proton pair under the kinematical conditions being considered.

A comparison of the cross sections for the reactions $^2\mathrm{H}(d, pp)nn$ and $^2\mathrm{H}(d, pn)pn$ may provide additional arguments in favor of one reaction mechanism or another. It is obvious that, in the processes involving final-state interaction, the yield of events of proton–proton coincidences must be identical to that for proton–neutron coincidences, while the cross sections for quasifree neutron–proton scattering may

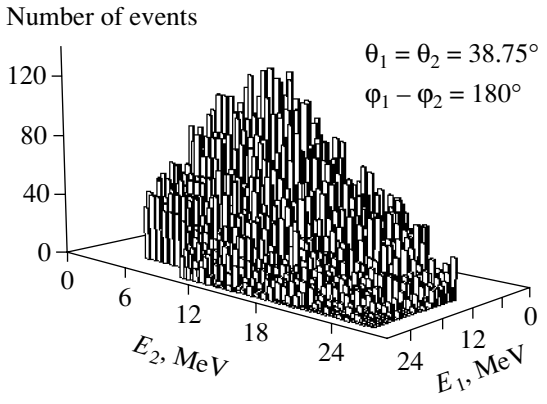

Fig. 1. Experimental two-dimensional spectrum of coincidences of two protons from the reaction $^2\mathrm{H}(d, pp)nn$ at an energy of $E_0 = 46.7$ MeV. Indicated in the figure are the proton-detection angles.

be larger than those for quasifree proton–proton scattering because of the difference in spin statistics between the two cases, in just the same way as this occurs for the analogous processes in the $p + d$ reactions [21]. A comparison of this type was performed in [7], where the spectra of proton–neutron coincides were measured at angles that differed from the angles of detection of proton–proton coincidences. In view of this, it would be illegitimate to perform a direct comparison there, but, by and large, the yield of the former was somewhat greater (by a factor of 1.5 according to the opinion of the authors of that study), which may be treated as indirect evidence in favor of the quasifree-scattering mechanism.

So far, only one attempt has been made to measure the cross sections for quasifree proton scattering in a kinematically complete experiment [10]. There, the spectra of double proton–proton coincidences and the spectra of triple proton–proton–neutron coincidences were measured at a deuteron-beam energy of 46.7 MeV, and this made it possible to identify the mechanism of quasifree proton scattering in the reaction $^2\mathrm{H}(d, pp)nn$. In the present study, the experimental data obtained in [10] are analyzed with allowance for both quasifree proton scattering and final-state neutron–proton interaction. We were able to simulate, to a fairly high degree of precision, the experimental two-dimensional spectrum of proton–proton coincidences and to determine the cross section for each process individually—in particular, the cross section for the reaction of double spin–isospin flip. The cross section for this process is then compared with the theoretical values computed on the basis of the supermultiplet potential model [18].

3. BRIEF DESCRIPTION OF THE EXPERIMENT

The spectra of double proton–proton and triple proton–proton–neutron coincidences were measured upon irradiating a deuterium–titanium target with deuterons accelerated at the U240 cyclotron installed at the Kiev Institute for Nuclear Research, the deuteron energy at the target center being 46.7 MeV. The charged products of the nuclear reaction in question were recorded by two telescopes formed by ΔE–E detectors and arranged symmetrically with respect to the beam axes. The recorded-particle emission angles of 38.75° corresponded to the kinematics of quasifree proton scattering in reaction (3). The detector solid angles were determined by diaphragms that had rectangular apertures of dimension 18×5 mm^2 and which were positioned immediately in front of the ΔE detectors at a distance of 80 mm from the target. Neutrons emitted along the beam axis (that is, at an angle of 0°) were recorded by a plastic scintillator having the shape of a parallelepiped of dimension $10 \times 10 \times 20$ cm^3. The distance from the target to the front face of the detector was 1.3 m.

A general shape of the resulting experimental two-dimensional spectrum of double proton–proton coincidences is depicted in Fig. 1. Upon the subtraction of the background of random coincidences and of events of the reaction $^1\mathrm{H}(d,pp)n$ occurring on the admixture of light (ordinary) hydrogen in the target, there remained more than 30 000 events in the resulting spectrum (N_{pp}). Concurrently, more than 100 triple-coincidence events (N_{ppn}) were recorded in a kinematically complete experiment. The experimental yield ratio N_{ppn}/N_{pp} was found to be 0.0061 ± 0.0007. A more detailed account of the experimental procedure used was given in [9, 10].

It is obvious that, in order to obtain the differential cross section for the reaction $^2\mathrm{H}(d,d_s)d_s$, it is necessary to perform a simulation of the resulting spectra and to integrate the simulated spectra for the reaction being considered. The corresponding procedure for experimental-data processing is described in the next two sections.

4. SIMULATION OF EXPERIMENTAL SPECTRA

Let us write the energy- and momentum-conservation laws for the four-body reaction (3) in the form

$$E_0 + Q = E_1 + E_2 + E_3 + E_4, \tag{5}$$

$$\mathbf{p}_0 = \mathbf{p}_1 + \mathbf{p}_2 + \mathbf{p}_3 + \mathbf{p}_4, \tag{6}$$

where E_0 and $\mathbf{p}_0$ are, respectively, the kinetic energy and the momentum of a beam particle in the laboratory frame; $Q = -4.449$ MeV is the reaction energy; E_1 and E_2 ($\mathbf{p}_1$ and $\mathbf{p}_2$) are the proton energies (momenta); and E_3 and E_4 ($\mathbf{p}_3$ and $\mathbf{p}_4$) are the neutron energies (momenta). The differential cross section $d\sigma$ for reaction (3) leading to the transition to the preset phase-space region can then be represented as [14]

$$d\sigma = \frac{(2\pi)^4}{v_0}\delta^3\left(\mathbf{p} - \sum_{i=1}^{4}\mathbf{p}_i\right) \times \delta\left(E - \sum_{i=1}^{4}E_i\right)|F|^2\prod_{i=1}^{4}d\mathbf{p}_i, \tag{7}$$

where $v_0 = (E_0/m)^{1/2}$ is the relative velocity of the particles in the entrance channel, m is the nucleon mass, and $|F|^2$ is the matrix element for the transition being considered. Upon a subsequent integration with respect to momenta that are not determined in the experiment, the cross section for double proton–proton or triple proton–proton–neutron coincidences in the laboratory frame can be recast into the form

$$d\sigma(\theta_1,\varphi_1,\theta_2,\varphi_2,E_1,E_2)/d\Omega_1 d\Omega_2 dE_1 dE_2 = \frac{(2\pi)^4}{v_0}\int \rho|F|^2\sin\theta d\theta d\varphi. \tag{8}$$

Here, θ_1, φ_1, θ_2, and φ_2 are the emission angles of the detected protons; ρ is the phase-space factor [22]

$$\rho = m^{9/2}(E_1E_2\epsilon_{nn})^{1/2};$$

$$\epsilon_{nn} = E_0 + Q - E_1 - E_2 - |\mathbf{p}_0 - \mathbf{p}_1 - \mathbf{p}_2|^2/(4m);$$

and integration is performed with respect to the angles θ and φ, which determine the orientation of the relative momentum of the neutrons, $\mathbf{q}_{nn} = (\mathbf{p}_3 - \mathbf{p}_4)/2$. In calculating the double-coincidence spectrum $N_{pp}(E_1,E_2)$, the region of integration covers all possible orientations of the vector $\mathbf{q}_{nn}$ (within a solid angle of 4π), while, for the triple-coincidence spectrum $N_{ppn}(E_1,E_2)$, the analogous region is determined by the solid angle of the neutron detector. We will approximate the squared transition-matrix element $|F|^2$ by the incoherent sum

$$|F|^2 = c_1|F_{\mathrm{QF}}|^2 + c_2|F_{1s}|^2|F_{2s}|^2 + c_3|F_{1t}|^2|F_{2t}|^2, \tag{9}$$

where c_i are free constants; F_{QF} is the amplitude of quasifree proton scattering; F_{1s} and F_{2s} are the amplitudes for final-state interaction in singlet neutron–proton pairs emitted, respectively, to the left and to the right of the beam axis; and F_{1t} and F_{2t} are the analogous amplitudes for final-state interaction in triplet neutron–proton pairs.

In order to simulate the quasifree-scattering spectra, we use the version of the plane-wave impulse

approximation in the form proposed in [6]. In this case, we have

$$|F_{\mathrm{QF}}|^2 = |\Psi(\mathbf{p}_{pp}/2 - \mathbf{q}_{nn})|^2 \times |\Psi(\mathbf{q}_{nn} - \mathbf{p}_{nn}/2)|^2 d\sigma_{pp}(q_{pp})/d\Omega, \quad (10)$$

where

$$\mathbf{q}_{pp} = (\mathbf{p}_1 - \mathbf{p}_2)/2, \quad (11)$$
$$\mathbf{q}_{nn} = (\mathbf{p}_3 - \mathbf{p}_4)/2,$$
$$\mathbf{p}_{pp} = \mathbf{p}_1 + \mathbf{p}_2,$$
$$\mathbf{p}_{nn} = \mathbf{p}_0 - \mathbf{p}_{pp},$$
$$q_{nn} = (m\epsilon_{nn})^{1/2},$$
$$\Psi(\mathbf{q}) = (2\pi)^{-3/2} \int \Psi(\mathbf{r}) \exp(-i\mathbf{q}\cdot\mathbf{r}) d\mathbf{r}.$$

For the deuteron wave function, we choose the Hulthén wave function [6]

$$\Psi(r) = [\alpha\beta(\alpha+\beta)/2\pi]^{1/2}(\alpha-\beta)^{-1} \times [\exp(-\alpha r) - \exp(-\beta r)]/r \quad (12)$$

with $\alpha^2 = mE_\alpha$, where $E_\alpha = 2.2245$ MeV is the deuteron binding energy, and $\beta^2 = mE_\beta$, where $E_\beta = 59.8$ MeV. In the impulse approximation, we then have

$$|\Psi(\mathbf{q})|^2 = \alpha\beta(\alpha+\beta)^3/[\pi^2(\alpha^2+q^2)^2(\beta^2+q^2)^2].$$

Thus, we see that, in expression (8), it only remains to specify the quantity $d\sigma_{pp}(q_{pp})/d\Omega$, which appears in the transition amplitude F. Considering that values of the momentum q_{pp} are sufficiently moderate for retaining only the S-wave interaction of the protons and for employing the effective-range approximation to be reasonable, but that they are, at the same time, sufficiently high for disregarding of Coulomb corrections to be legitimate, we can write the cross section for elastic proton–proton scattering in the form [23]

$$d\sigma_{pp}(q_{pp})/d\Omega = [q_{pp}^2 + (-a^{-1} + rq_{pp}^2)^2]^{-1},$$

where a is the scattering length, $a = -7.813$ fm, and r is the effective range, $r = 2.78$ fm [24].

The amplitudes of final-state neutron–proton interaction were calculated in the Migdal–Watson approximation; that is,

$$F_{1s(t)}(q_{13}) = [r(q_{13}^2 + \eta^2)]/[2(-1/a + rq_{13}^2/2 - iq_{13})], \quad (13a)$$

$$F_{2s(t)}(q_{24}) = [r(q_{24}^2 + \eta^2)]/[2(-1/a + rq_{24}^2/2 - iq_{24})], \quad (13b)$$

$$\eta = (1/r)[1 + (1 - 2r/a)^{1/2}],$$

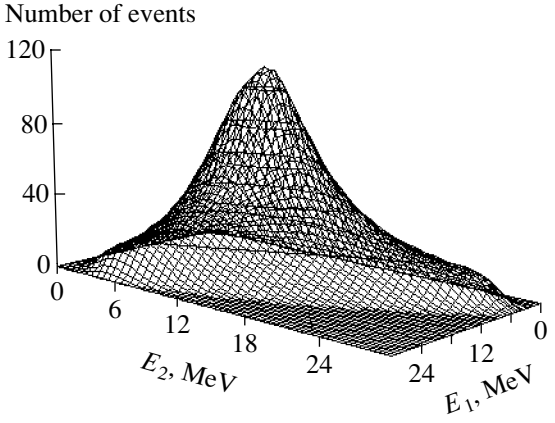

Fig. 2. Simulated spectrum of proton–proton coincidences for the reaction $^2\mathrm{H}(d, pp)nn$ at an energy of $E_0 = 46.7$ MeV and proton-detection angles of $\theta_1 = \theta_2 = 38.75^\circ$, $\varphi_1 - \varphi_2 = 180^\circ$. Here, we have taken into account quasifree proton–proton scattering and the amplitudes of final-state neutron–proton interaction.

where q_{13} and q_{24} are the momenta of relative motion in the corresponding neutron–proton subsystems. The np scattering length a and the effective range r assume the values of, respectively, -23.748 and 2.75 fm for the singlet state of the neutron–proton pair and of, respectively, 5.424 and 1.759 fm for its triplet state [24]. Integration in expression (7) was performed by the Monte Carlo method, the coordinates of points in the target and detectors and the angles θ and φ, which determine the orientation of the momentum $\mathbf{q}_{nn}$ of relative motion in the dineutron, being taken here for random variables.

The use of the plane-wave approximation at beam energies of about 50 MeV is open to criticism, since multiple-scattering effects are expected to come into play at such energies; however, the empirical fact that the model nevertheless reproduces the relative distributions of the cross sections with respect to momentum transfers to the spectator [6] (the normalized theoretical curves are in satisfactory agreement with the points of the experimental distributions) can be employed in the case being considered. Therefore, one can also have some degree of confidence in the ratio of the numbers of triple and double coincidences, N_{ppn}/N_{pp}, that was calculated in the plane-wave approximation and then assess that fraction of N_{pp} which can be associated with quasifree scattering.

The approximation specified by Eq. (9) can also meet an objection in view of the disregard of the interference between the amplitudes, but, with allowance for the fact that the angular and energy distributions of neutrons are different in the quasifree-scattering and final-state-interaction processes (in quasifree scattering, one neutron is emitted with an

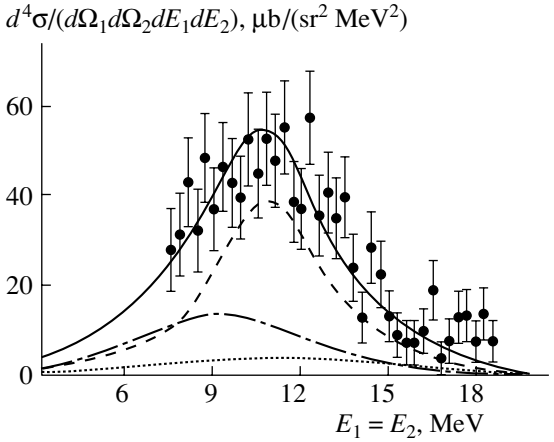

Fig. 3. Section of the surfaces in Figs. 1 and 2 along the diagonal $E_1 = E_2$. Errors indicated on the experimental points are purely statistical. The dash-dotted, the dashed, and the dotted curve correspond to the calculations for, respectively, quasifree proton–proton scattering, singlet final-state neutron–proton interaction, and triplet final-state neutron–proton interaction. The solid curve represents the sum of the contributions from these processes.

energy of about 24 MeV in a narrow cone around the beam axis and the other travels at a low energy, while, in the case of final-state interaction, the momenta of both neutrons are close to the momenta of the corresponding protons), its role appears to be negligible in the phase space being considered.

It is convenient to use the total number of events in the experimental spectrum of triple proton–proton–neutron coincidences to estimate the contribution of the quasifree-scattering mechanism to the spectrum of double proton–proton coincidences. For this purpose, the spectra of double and triple coincidences were simulated in the impulse approximation and with allowance for only the first term in the sum on the right-hand side of (9). Upon taking into account the neutron-detection efficiency k, the calculation of the ratio kN_{ppn}/N_{pp} for quasifree scattering by using these spectra yielded 0.026, which is approximately four times as great as the corresponding experimental value of 0.0061 ± 0.0007. This result can be understood under the assumption that the contribution of quasifree proton scattering to the experimental spectrum of double proton–proton coincidences is only one-fourth of the total number the events.

In the same approximation, we further simulated (see Fig. 2) the spectrum with allowance for all three terms in the sum on the right-hand side of (9). A fit was constructed by using a data array formed by 2694 elements of the experimental matrix. The region of fitting in the E_1–E_2 plane was bounded by the thresholds $E_1, E_2 = 7.8$ MeV. The contributions of individual terms in the sum on the right-hand side of (9) were in the proportion $(0.20 \pm 0.04) : (0.65 \pm 0.07) : (0.15 \pm 0.03)$. Upon rescaling these results over the entire kinematically allowed region, these contributions appear to be in the ratio $(0.24 \pm 0.04) : (0.61 \pm 0.05) : (0.15 \pm 0.03)$. The calculated differential cross sections, along with experimental data at $E_1 = E_2$ are given in Fig. 3. The curves in this figure represent the contributions of quasifree scattering, the singlet final-state-interaction component, and the triplet final-state-interaction component.

Thus, we see that an analysis of double-coincidence spectra measured in a kinematically incomplete experiment also makes it possible to identify reaction mechanisms, provided that the experimental data used are sufficiently accurate. The definitive conclusion that the flip of the spins and isospins of two deuterons is a dominant mechanism of reaction (3) is the most important result of this analysis. Its contribution to the cross section for the reaction $^2\mathrm{H}(d, pp)nn$ is about two-thirds even under the kinematical conditions of quasifree proton scattering. The quasifree-scattering contribution (about 20%) determined in fitting the two-dimensional spectrum of proton–proton coincidences agrees with the results of a kinematically complete experiment.

5. INTEGRATION OF THE DIFFERENTIAL CROSS SECTIONS FOR THE PROCESS INVOLVING DOUBLE SPIN–ISOSPIN FLIP

In order to compare the experimental data with the predictions of the supermultiplet potential model, it is necessary to rescale the experimental differential cross section for double spin–isospin flip to the c.m. frame and represent it in the form of the cross section $d\sigma/d\Omega$ for the binary reaction $^2\mathrm{H}(d, d_s)d_s$. It is more convenient to do this upon recasting the conservation laws (5) and (6) in the c.m. frame as

$$E_{13} + e_{13} + E_{24} + e_{24} = E_{0C} + Q,$$
$$\mathbf{p}_{13} + \mathbf{p}_{24} = 0,$$

where $E_{0C} = E_0/2$ is the kinetic energy of the deuterons in the entrance channel; E_{13} (E_{24}) and $\mathbf{p}_{13}$ ($\mathbf{p}_{24}$) are, respectively, the energy and the momentum of the center of mass of the np subsystem formed by particles 1 and 3 (2 and 4); and e_{13} (e_{24}) is the kinetic energy of the relative motion of the nucleons in the corresponding subsystem. Expression (7) for the differential cross section in the c.m. frame takes the form

$$d\sigma = [(2\pi)^4/v_0]d\mathbf{p}_{13}d\mathbf{p}_{24}d\mathbf{q}_{13}d\mathbf{q}_{24}|F|^2 \quad (14)$$
$$\times \delta(E_{0C} + Q - E_{13} - e_{13} - E_{24} - e_{24})$$
$$\times \delta(-\mathbf{p}_{13} - \mathbf{p}_{24}),$$

where

$$q_{13} = (me_{13})^{1/2}, \quad q_{24} = (me_{24})^{1/2},$$
$$|F|^2 = c_2|F_{1s}(q_{13})|^2|F_{2s}(q_{24})|^2.$$

The amplitudes F_{1s} and F_{2s} have the form (13), and the factor c_2 was determined from a fit to the experimental two-dimensional spectrum of proton coincidences by using expressions (8) and (9). Further, we integrate the cross section (14) with respect to all variables, with the exception of the emission angles of one of the singlet deuterons—for example, Ω_{13}—whereupon we obtain

$$d\sigma/d\Omega_{13} = [(2\pi)^6/v_0]m^{9/2} \qquad (15)$$
$$\times\, 2^{1/2}\int_0^{e_{13}^{\max}} c_2|F_{1s}(q_{13})|^2 e_{13}de_{13}\int_0^{e_{24}^{\max}}[e_{24}(E_{0C}+Q$$
$$-e_{13}-e_{24})]^{1/2}|F_{2s}(q_{24})|^2de_{24}.$$

If we integrate with respect to all kinematically allowed relative energies e_{13} and e_{24}, then $e_{13}^{\max} = E_{0C}+Q$ and $e_{24}^{\max} = E_{0C}+Q-e_{13}$.

For the reaction $^2\mathrm{H}(d,d_s)d_s$ at $E_0 = 46.7$ MeV, a numerical integration between these limits yielded the differential-cross-section value of $d\sigma(90^0)/d\Omega = 1.1 \pm 0.1$ mb/sr. Here, only the statistical error is presented; it was determined in fitting the experimental spectrum of double proton–proton coincidences. The error in the scale of the differential cross sections (about 25%) [10] must be added to the above statistical error. If the relative energies are bounded by e_m, we obtain $e_{13}^{\max} = \min(E_{0C}+Q; e_m)$ and $e_{24}^{\max} = \min(E_{0C}+Q-e_{13}; e_m)$.

6. FORMALISM OF THE SUPERMULTIPLET POTENTIAL MODEL

The quantity obtained upon averaging, over the initial orientations of the spins σ_A and σ_B, the cross section for A + B scattering accompanied by the flip of the deuteron spin and isospin and summing the result over final σ'_A and σ'_B (the scattering of unpolarized particles is considered here) has the form [18]

$$\frac{d\sigma}{d\Omega}(\theta) = \frac{1}{(2S_A+1)(2S_B+1)} \qquad (16)$$
$$\times \sum_{\sigma_A,\sigma_B,\sigma'_A,\sigma'_B}|f(\theta)|^2 = \frac{1}{4p_0^2}\frac{(2S'_A+1)(2S'_B+1)}{(2S_A+1)(2S_B+1)}$$
$$\times (t'_A\tau'_A, t'_B\tau'_B|t\tau)^2\left|\sum_L(2L+1)P_L(\cos\theta)\right.$$
$$\times\left\{\langle[\widetilde{f}_A]S_At_A,[\widetilde{f}_B]S_Bt_B|[\widetilde{f}_1]St\rangle\right.$$
$$\times\langle[\widetilde{f}'_A]S'_At'_A,[\widetilde{f}'_B]S'_Bt'_B|[\widetilde{f}_1]St\rangle T_L^{[f_1]}$$
$$+\langle[\widetilde{f}_A]S_At_A,[\widetilde{f}_B]S_Bt_B|[\widetilde{f}_2]St\rangle$$
$$\left.\left.\times\langle[\widetilde{f}'_A]S'_At'_A,[\widetilde{f}'_B]S'_Bt'_B|[\widetilde{f}_2]St\rangle T_L^{[f_2]}\right\}\right|^2,$$

where p_0 is the momentum of the relative motion of particles A and B in the c.m. frame; S, t, and $[\widetilde{f}]$ are, respectively, the spin, the isospin, and the spin–isospin Young diagram of the A + B system; σ and τ are the spin and isospin projections, respectively; $\langle[\widetilde{f}_A]S_At_A,[\widetilde{f}_B]S_Bt_B|[\widetilde{f}]St\rangle$ are the isoscalar factors of the Clebsch–Gordan coefficients of the $SU(4)$ group (spin–isospin fractional-parentage coefficients) [20, 25]; $T_L^{[f]}$ are the partial-wave amplitudes that are invariant under the transformations of the $SU(4)$ group; and $[f]$ is the orbital Young diagram for the $A+B$ system (in the present case, it can take two values, $[f_1]$ and $[f_2]$).

For the $d+d$ system, we have $S_B = 1$, $S'_B = 0$, $t_B = 0$, $t'_B = 1$, $[\widetilde{f}_B] = [\widetilde{f}'_B] = [\widetilde{2}]$, $S_A = 1$, $S'_A = 0$, $t_A = 0$, $t'_A = 1$, $[\widetilde{f}_A] = [\widetilde{f}'_A] = [\widetilde{2}]$, $t = 0$, $\tau = 0$, and $S = 0$. For the same system, $\tau'_A = \tau'_B = 0$ if the deuteron spin and isospin are flipped without charge exchange; in the case of charge exchange, $\tau'_A = 1$ and $\tau'_B = -1$.

Upon substituting into (16) the above quantum numbers and the specific values of the spin–isospin Clebsch–Gordan and fractional-parentage coefficients [20, 25], we obtain an expression that describes the cross section for the scattering process involving the flip of the spins and isospins of two deuterons and which has the form

$$\frac{d\sigma}{d\Omega}(\theta) = \frac{1}{432p_0^2} \qquad (17)$$
$$\times\left|\sum_L(2L+1)P_L(\cos\theta)\left[T_L^{[4]} - T_L^{[22]}\right]\right|^2.$$

In the case of the charge-exchange process $d+d\to nn+pp$, the expression for the cross section fully coincides with (17), since different values of the isospin projection τ'_B for a deuteron, on one hand, and a proton–proton and a neutron–neutron pair, on the other hand, lead to identical (in absolute value) Clebsch–Gordan coefficients $(t'_A\tau'_A, t'_B\tau'_B|t\tau)$.

For elastic dd scattering, we accordingly obtain

$$\frac{d\sigma}{d\Omega}(\theta) = \frac{1}{4p_0^2} \qquad (18)$$
$$\times\left\{\left|\sum_L(2L+1)P_L(\cos\theta)\left[\frac{1}{2}T_L^{[4]} + \frac{1}{2}T_L^{[22]}\right]\right|^2\right.$$

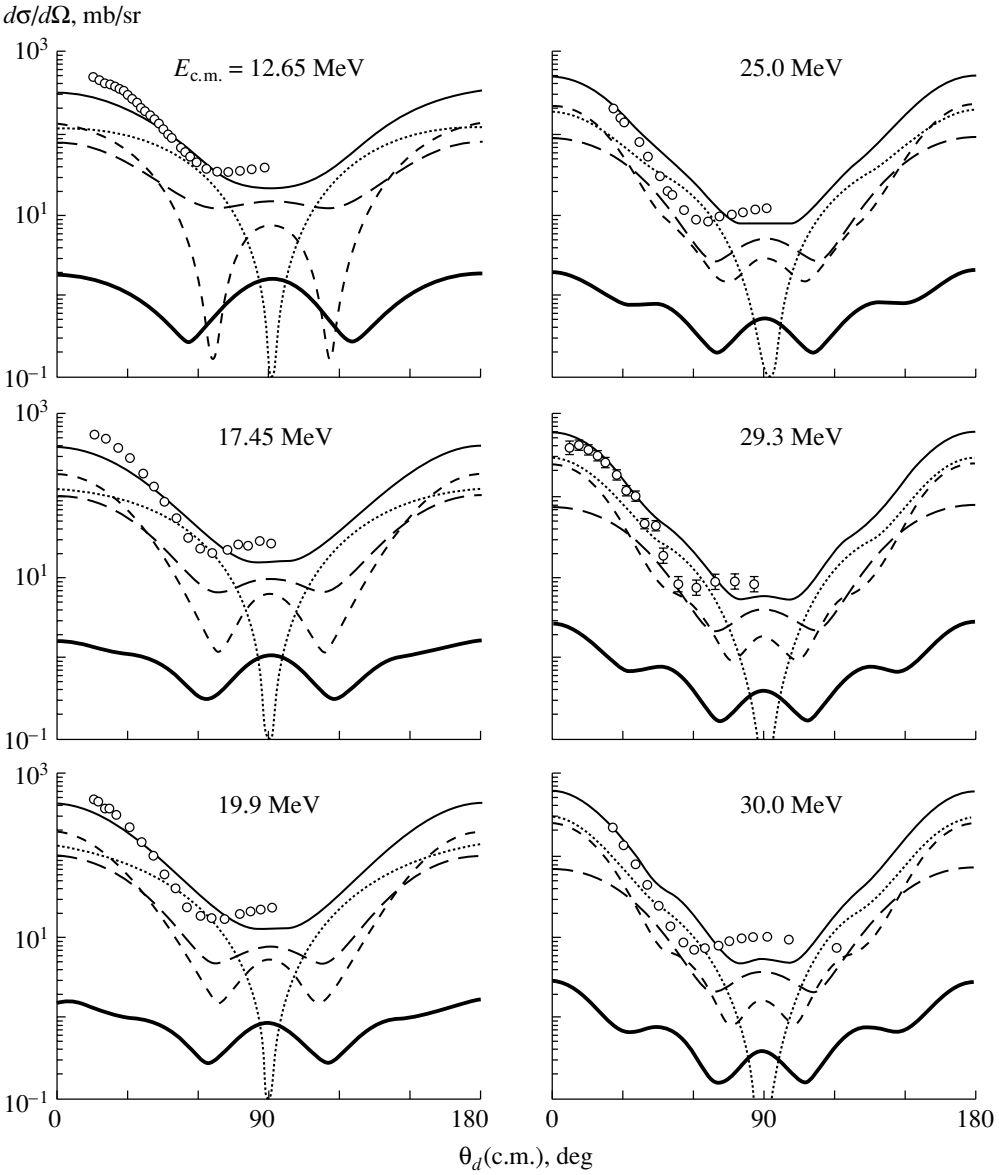

Fig. 4. (○) Experimental angular dependences of the differential cross sections for elastic dd scattering and (curves) their counterparts calculated within the supermultiplet potential model. The short-dashed, dotted, and long-dashed curves correspond to the cross sections obtained for the cases where the total spin of the system is $S = 0$, 1, and 2, respectively. The thin solid curve represents the sum of these three contributions. Also shown in this figure for the sake of comparison are (thick solid curve) the calculated cross sections for the reaction $^2\mathrm{H}(d, d_s)d_s$ producing neutron–proton pairs in the singlet state. References to the respective experimental studies can be found in the main body of the text. The energies are given in the c.m. frame.

$$+\left|\sum_L (2L+1)P_L(\cos\theta)T_L^{[31]}\right|^2$$
$$+\left|\sum_L (2L+1)P_L(\cos\theta)T_L^{[22]}\right|^2\Bigg\}.$$

We note that the three sums in (18) correspond to the values of $S = 0$, 1, and 2 for the total spin of the system.

In the supermultiplet potential model, the amplitude $T_L^{[f]}$ is represented as the potential-scattering amplitude

$$T_L^{[f]} = \exp(2i\delta_L^{[f]}) - 1, \qquad (19)$$

where the phase shift $\delta_L^{[f]}$ characterizes the potential $V_{AB}^{[f]}(R)$ describing interactions in the $A + B$ system, this potential being strongly dependent on the signature $[f]$.

A method for reconstructing potentials that corre-

spond to various allowed space permutation symmetries $[f]$ was described in [18]. For the $d + d$ system, they are constructed in the standard Woods–Saxon form on the basis of available data on phase shifts, the known allowed and forbidden states of the system in question being taken into account in this method. For the symmetries in which we are interested, the following values of the potential parameters were obtained in [18]:

$$[f] = [22], \quad V_0 = -41.5 \text{ MeV}, \quad R_0 = 1.45 \text{ fm}, \quad a = 0.81 \text{ fm};$$

$$[f] = [31], \quad V_0 = -31.8 \text{ MeV}, \quad R_0 = 2.33 \text{ fm}, \quad a = 0.76 \text{ fm};$$

$$[f] = [4], \quad V_0 = -70.0 \text{ MeV}, \quad R_0 = 1.92 \text{ fm}, \quad a = 0.95 \text{ fm}.$$

Estimating the potentials in strength as specified by the quantity $V_0 R_0^2$, we can see that, for the $[f] = [22]$ and $[f] = [4]$ space symmetries, they differ approximately by a factor of 3, which in turn leads to a significant distinction between the corresponding scattering amplitudes. Within the supermultiplet potential model, the cross section for the reaction involving the flip of the deuteron spins and isospins [see expression (17)] is determined precisely by the difference of the amplitudes $T_L^{[4]}$ and $T_L^{[22]}$; therefore, this model predicts a large contribution of the formation of two singlet deuterons in dd scattering. For the sake of comparison, we recall that, in the case of dp scattering, the distinction between the strengths of the main potential components corresponding to the $[f] = [3]$ and $[f] = [21]$ symmetries was as small as 20% [18], with the result that the description of experimental data within the supermultiplet potential model was only qualitative [1].

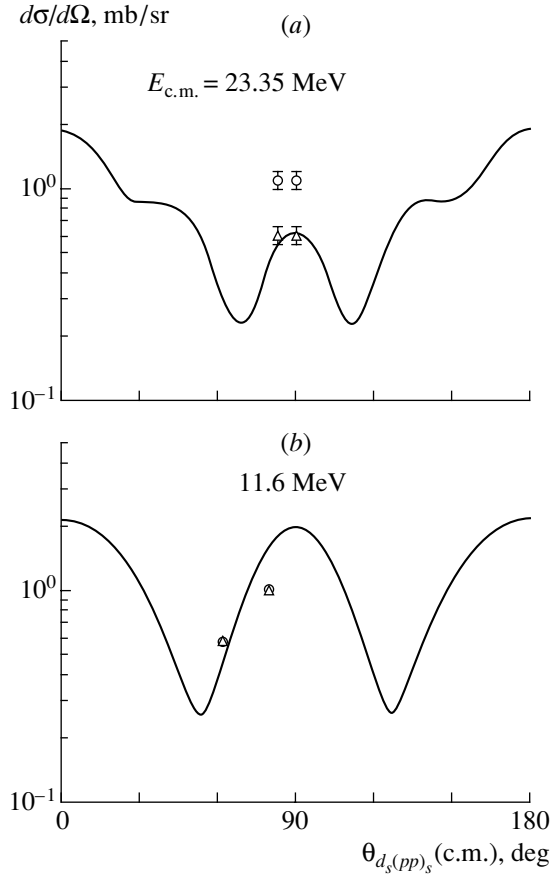

Fig. 5. Experimental angular distributions of singlet dinucleons from (a) the reaction $^2\mathrm{H}(d, d_s)d_s$ at the energy of $E_{c.m.} = 23.35$ MeV and (b) the reaction $^2\mathrm{H}(d, (pp)_s)(nn)_s$ at the energy of $E_{c.m.} = 11.6$ MeV (points) along with their counterparts calculated within the supermultiplet potential model (curves). References to the respective experimental studies are given in the main body of the text. Statistical errors are shown only in the cases where they exceed the dimensions of the points. The experimental points correspond to different upper limits in the integration of the spectra: (○) $e_m = e_{13}^{\max} = E_{0C} + Q$ and (△) $e_m = 7$ MeV.

7. DISCUSSION OF THE RESULTS OF THE CALCULATIONS BASED ON THE SUPERMULTIPLET POTENTIAL MODEL AND CONCLUSION

We begin discussing the results by considering experimental data on elastic dd scattering. These data are given in Fig. 4, along with the results of the calculations on the basis of the supermultiplet potential model [formula (18)]. The displayed experimental points were borrowed from [26–29] ($E_{c.m.} =$ 12.65 MeV [26], 17.45 and 19.9 MeV [27], 25.0 and 30.0 MeV [28], and 29.3 MeV [29]).

By and large, the experimental angular dependences $d\sigma(\theta)/d\Omega$ are in fairly good agreement with their experimental counterparts, albeit there are moderate discrepancies in some angular regions. It is noteworthy that the differential cross section allowing for all possible values of S is determined primarily by the $S = 0$ and $S = 1$ components in the region of small angles and by the $S = 2$ component in the region of medium angles. As a rule, the cross-section part associated with the $S = 0$ component is quite large and deviates from the calculated total elastic-scattering cross section (which receives contributions from the $S = 0$, 1, and 2 components) by not more than one order of magnitude. We would also like to indicate that, with increasing energy E_d, the theoretical angular distributions of the $S = 0$ component of the elastic-scattering cross section become ever more similar in shape to the analogous angular dependences for the reaction $d + d \to d_s + d_s$.

We now proceed to compare the experimental and

theoretical differential cross sections for the reaction $d + d \to d_s + d_s[(nn)_s + (pp)_s]$, which leads to the formation of two singlet dinucleons. In Fig. 5*a*, the experimental point that we obtained above ($\theta_{\text{c.m.}} = 90°$, $d\sigma/d\Omega = 1.1$ mb) is supplemented, by means of a relative normalization, with a point from [12] at $\theta_{\text{c.m.}} = 83.3°$. In Fig. 5*b*, we employed the aforementioned experimental data from [2] at $E_{\text{c.m.}} = 11.6$ MeV. We have compared the integrated cross sections presented in that article (in mb/sr^2 units) with those that were calculated according to the procedure described in Sections 4 and 5 (Coulomb corrections being additionally taken into account here) and obtained the normalization factors required for calculating the double-charge-exchange cross sections in the c.m. frame. As a result, we found the cross-section values of 0.57 and 1.01 mb/sr for the angles of $\theta_{\text{c.m.}} = 62.5°$ and 79.7°, respectively.

On the whole, we can see that scanty data available from the literature were confirmed and supplemented by means of measurements whose results are reported here. This makes it possible to determine, on the basis of a comparison with the results produced by the supermultiplet potential model, the phenomenological parameter e_m, which is the limiting value of the relative energy e_{13} in integrating the experimental spectra with the aim of deriving the cross section for the reaction $d + d \to d_s + d_s$ according to the procedure outlined above. As can be seen from the data in Figs. 5*a* and 5*b*, the value of the parameter e_m proves to be approximately equal to 7 MeV (at $E_{\text{c.m.}} = 11.6$ MeV, $e_m \approx e_{13}^{\max}$; therefore, the points in Fig. 5*b* coincide). It should be recalled that, for the reaction $d + t \to d_s + t$, it is 1 MeV [1]. So great a distinction reflects, in all probability, a large effect of "soft rescatterings" in the four-fermion continuum and is an interesting subject of investigation in terms of Faddeev–Yakubovsky equations (even with separable nucleon–nucleon potentials). The methodological recipes used in the present study to single out the cross section for the process $d + d \to d_s + d_s$ are, at a large value of $e_m \cong 7$ MeV, only the first step (the simplest one) toward solving the problem at hand. Nonetheless, available experimental data fully confirm the prediction of the supermultiplet potential model that the mechanism of double spin–isopspin flip makes a large contribution to the reaction being studied.

In future investigations, it would be of importance to explore in detail the angular dependence of the cross sections in question in order to assess more accurately the applicability limits of the supermultiplet potential model, which is quite simple from the point of view of numerical calculations. At the moment, this model exhibits, by and large, a high efficiency not only in exploring the issues considered here but also in analyzing the photonuclear reactions $^4\text{He} + \gamma \to t + p$, $^4\text{He} + \gamma \to d + d$, and $d + t \to {}^5\text{He} + \gamma$ [18, 19] and the charge-exchange reaction $t + p \to h + n$ [19]. It may also prove to be very useful in studying three-cluster systems whose binding energy is close to their decay threshold [30]. In view of all of the aforesaid, it is advisable not only to employ the equations of the resonating-group method in the supermultiplet form [31] but also to develop the Faddeev–Yakubovsky equations in the same form and to apply them.

REFERENCES

1. V. M. Lebedev, V. G. Neudatchin, and B. G. Struzhko, Yad. Fiz. **65**, 489 (2002) [Phys. At. Nucl. **65**, 462 (2002)].
2. R. E. Warner, S. B. Di Cenzo, G. G. Ball, *et al.*, Nucl. Phys. A **243**, 189 (1975).
3. B. Th. Leeman, H. G. Pugh, N. S. Chant, and C. C. Chang, Phys. Rev. C **17**, 410 (1978).
4. R. E. Warner, Phys. Rev. C **24**, 2759 (1981).
5. Ying-Ji Zhang, Jian-hua He, Jin-qing Yang, and Jie Zhang, Phys. Rev. C **47**, 468 (1993).
6. R. G. Allas, L. A. Beach, R. O. Bondelid, *et al.*, Nucl. Phys. A **304**, 461 (1978).
7. N. Koori, T. Ohsawa, S. Seki, *et al.*, Phys. Rev. C **31**, 246 (1985).
8. L. A. Golovach, V. V. Zerkin, B. G. Struzhko, *et al.*, Izv. Akad. Nauk SSSR, Ser. Fiz. **51**, 166 (1987).
9. V. I. Konfederatenko, B. G. Struzhko, G. Gurach, *et al.*, Ukr. Fiz. Zh. **42**, 274 (1997).
10. V. I. Konfederatenko, O. M. Povoroznik, B. G. Struzhko, *et al.*, Ukr. Fiz. Zh. **42**, 1175 (1997).
11. B. Struzhko, J. Phys. Stud. **3**, 431 (1999); Acta Phys. Pol. B **30**, 1487 (1999).
12. B. G. Struzhko, Ukr. Fiz. Zh. **44**, 305 (1999).
13. K. M. Watson, Phys. Rev. **88**, 1163 (1952).
14. M. Goldberger and K. Watson, *Collision Theory* (New York, 1964; Mir, Moscow, 1967).
15. A. B. Migdal, Zh. Éksp. Teor. Fiz. **28**, 3 (1955) [Sov. Phys. JETP **1**, 2 (1955)].
16. W. Glöckle, H. Witala, H. Kamada, *et al.*, Nucl. Phys. A **684**, 184c (2000).
17. W. Tornow, Nucl. Phys. A **684**, 193c (2000); R. Bieber, K. Bodek, K. Ermisch, *et al.*, Nucl. Phys. A **684**, 536c (2000); J. L. Friar, Nucl. Phys. A **684**, 200c (2000); W. Tachikawa, C. Yagita, M. Kondo, *et al.*, Nucl. Phys. A **684**, 583c (2000).
18. V. G. Neudatchin, V. I. Kukulin, V. N. Pomerantsev, and A. A. Sakharuk, Phys. Rev. C **45**, 1512 (1992); V. G. Neudachin, A. A. Sakharuk, and Yu. F. Smirnov, Fiz. Élem. Chastits At. Yadra **23**, 479 (1992) [Sov. J. Part. Nucl. **23**, 210 (1992)].
19. V. G. Neudatchin, A. A. Sakharuk, and S. B. Dubovitchenko, Few-Body Syst. **18**, 159 (1995).

20. V. I. Kukulin, V. G. Neudatchin, and Yu. F. Smirnov, Nucl. Phys. A **245**, 429 (1975); V. I. Kukulin, V. G. Neudatchin, and Yu. F. Smirnov, Fiz. Élem. Chastits At. Yadra **10**, 1236 (1979) [Sov. J. Part. Nucl. **10**, 492 (1979)]; O. F. Nemets, V. G. Neudatchin, A. A. Rudchik, *et al.*, *Nucleon Clustering in Nuclei and Multinucleon-Transfer Reactions* (Naukova Dumka, Kiev, 1988).
21. D. L. Durand, J. Arvieux, A. Fiore, *et al.*, Phys. Rev. C **6**, 393 (1972).
22. M. Furii and H. H. Forster, Nucl. Instrum. Methods **98**, 301 (1972).
23. W. Kluge, Fortschr. Phys. **22**, 691 (1974).
24. R. Machleidt, Adv. Nucl. Phys. **19**, 189 (1989).
25. V. G. Neudachin, I. T. Obukhovskiĭ, and Yu. F. Smirnov, Fiz. Élem. Chastits At. Yadra **15**, 1165 (1984) [Sov. J. Part. Nucl. **15**, 519 (1984)].
26. W. T. H. Van Oers, H. Arnold, and K. W. Brockman, Jr., Nucl. Phys. **46**, 611 (1963).
27. F. S. Chwieroth, Y. C. Tang, and D. R. Thompson, Nucl. Phys. A **189**, 1 (1972).
28. C. Alderliesten, A. Djaloeis, J. Bojowald, *et al.*, Phys. Rev. C **18**, 2001 (1978).
29. J. E. A. Lys and L. Lyons, Nucl. Phys. **74**, 261 (1965).
30. V. M. Lebedev, V. G. Neudatchin, and A. A. Sakharuk, Yad. Fiz. **63**, 248 (2000) [Phys. At. Nucl. **63**, 195 (2000)].
31. V. Iskra, A. I. Mazur, V. G. Neudachin, and Yu. F. Smirnov, Yad. Fiz. **49**, 672 (1989) [Sov. J. Nucl. Phys. **49**, 416 (1989)].

Translated by A. Isaakyan

Physics of Atomic Nuclei, Vol. 66, No. 5, 2003, pp. 824–827. Translated from Yadernaya Fizika, Vol. 66, No. 5, 2003, pp. 856–859.

NUCLEI
Theory

Effective Probabilities in a New Approach to Analyzing Angular Distributions in Elastic Heavy-Ion Scattering

Yu. A. Pozdnyakov

Institute for Nuclear Research, National Academy of Sciences of Ukraine, Kiev, Ukraine

Received January 10, 2002; in final form, May 20, 2002

Abstract—A new approach proposed previously to analyze angular distributions in elastic heavy-ion scattering is generalized to cases where total partial probabilities (that is, those that are summed over all channels) of the enhancement of "fusion" (in general, complete and incomplete fusion, quasifission, and deep-inelastic collisions) are commensurate with the total partial probabilities of the suppression of "fusion." This could be done with the aid of effective total partial probabilities, each of these being defined as a linear combination of actual total partial probabilities. It is shown that the probabilities introduced in this way have a specific physical meaning. Indeed, the effective total partial probabilities make it possible to calculate the cross section for "fusion" through the entrance channel and some reference total cross sections for peripheral processes, and a conclusion on whether fusion and peripheral reactions are enhanced or suppressed can be drawn from a comparison of the calculated or measured results for, respectively, the fusion cross section and the total cross section for peripheral reactions with the above two cross sections. It is also found that the enhancement of fusion is accompanied by the suppression of peripheral reactions, and vice versa. © *2003 MAIK "Nauka/Interperiodica"*.

1. INTRODUCTION

A new approach to analyzing angular distributions in the elastic scattering of heavy ions was recently proposed in [1–3]. This approach made it possible to extend considerably the range of calculable quantities. For example, the method in question makes it possible to calculate not only quantities that are determined within the traditional optical model but also the "fusion" cross section (in general, the sum of the cross sections for complete and incomplete fusion, quasifission, and deep-inelastic collisions) σ_F and the total cross section σ_D for peripheral (or quasielastic) reactions, the corresponding distributions in partial waves, and quantitative features of the enhancement or suppression of fusion and peripheral reactions.

Two approximations were considered in [1–3]. Within one of these, which corresponds to collisions of strongly bound ions, it is assumed that, in the corresponding partial waves, the total partial-wave probabilities (that is, those that are summed over all channels) for the enhancement of fusion are much greater than their counterparts for the suppression of fusion. Within the second approximation, it is assumed, on the contrary, that the total partial-wave probabilities for the suppression of fusion are much greater than those for the enhancement of fusion, this corresponding to collisions where at least one of the ions involved is weakly bound.

These approximations are valid in many cases. However, there are situations where this is not so. For example, it may be expected that, in the elastic scattering of loosely bound ions by heavy nuclei at near-barrier energies, the total partial-wave probabilities for the enhancement and suppression of "fusion" are commensurate. Let us dwell on this point at some length. On one hand, the Coulomb breakup of the projectile ion is not the only possible disintegration process in such a system: there will also occur a breakup process caused by nuclear forces, which is accompanied by virtual excitations—that is, by the return of particles to the entrance channel owing to recombination (see, for example, [4]). As was shown in [1–3], virtual excitations lead to the suppression of "fusion." On the other hand, the breakup process (both nuclear and Coulomb breakup) initiates incomplete fusion, in which case one or a few breakup fragments merge with the target nucleus. Such processes lead to the enhancement of "fusion." An additional mechanism of the enhancement of "fusion" for loosely bound ions is associated with the Coulomb polarizability. The aforesaid is confirmed experimentally. For example, an analysis of the angular distributions for the elastic scattering of ^{9}Be by ^{209}Bi at near-barrier energies [5] revealed that, at the strong-absorption radius, the optical potential obtained by means of fitting is equal to or exceeds the double-folding-model potential [6]. At the same time, it is well known (see, for example, [6]) that the double-folding-model potential must be weakened in order to describe angu-

1063-7788/03/6605-0824$24.00

lar distributions for the elastic scattering of loosely bound particles.

It is obvious that the method proposed in [1–3] to analyze angular distributions for elastic heavy-ion scattering must be modified in such a way as to render it applicable to situations where the total partial-wave probability for the enhancement of "fusion" is commensurate with its counterpart for the suppression of "fusion." The present study is devoted to constructing a modification of precisely this type.

2. SOME DEFINITIONS AND CONVENTIONS

Below, we will discuss the probabilities and cross sections for various processes induced by collisions of heavy ions. Therefore, it is necessary to characterize these processes briefly. In [1–3], all reaction channels other than the elastic-scattering channel were broken down into two groups. The first (group D) includes all peripheral reactions, while the second (group F) contains all reactions that are excited under the conditions of a large overlap of the densities of colliding nuclei (to denote reactions of this group, the term "fusion" has been introduced above for the sake of brevity). The total partial-wave probabilities for these reactions are denoted by, respectively, $P_{l,D}$ and $P_{l,F}$ (l is the orbital angular momentum), while the respective cross sections are denoted by σ_D and σ_F. The probability $P_{l,F}$ involves two terms. The first, $P_{l,EF}$, is the total partial-wave probability for the excitation of reactions belonging to the group F through the entrance channel, while the second, $P_{l,DF}$, is the total partial-wave probability for the multistep excitation of reactions belonging to this group. If, in the system, there is a Coulomb polarizability of the projectile ion, it also contributes to $P_{l,DF}$. The corresponding cross sections are denoted by σ_{EF} and σ_{DF}. In the case of loosely bound ions, the virtual breakup of the projectile particle due to nuclear forces results in the suppression of reactions belonging to the group F, this suppression being characterized by the total partial-wave probability $P_{l,HF}$. The corresponding reduction of the cross section σ_F is denoted by σ_{HF}.

In addition to the total partial-wave probabilities for peripheral reactions, $P_{l,D}$, the partial wave probabilities for peripheral processes, $P_{l,ED}$, are also introduced, the latter differing from the former in that some reactions excited in the peripheral region end up, at the second stage, either in the return to the entrance channel (virtual excitations—in particular, virtual breakup) or in the excitation of reactions belonging to the group F (multistep reactions of the group F—in particular, multistep fusion).

The above probabilities are expressed in terms of the elastic-scattering S-matrix elements S_l, $\tilde{S}_l^{(0)}$, and $S_l^{(0)}$. All of them were calculated on the basis of the incoming-wave-boundary-condition model [7–10]; the matrix elements S_l were obtained from a fit of the theoretical differential cross section for elastic scattering to its experimental counterpart, while $\tilde{S}_l^{(0)}$ and $S_l^{(0)}$ were computed with the identically vanishing imaginary part of the optical potential by using, respectively, a renormalized and a nonrenormalized double-folding-model potential. Thus, the angular distributions for elastic scattering are necessary for deriving the S-matrix elements S_l and $\tilde{S}_l^{(0)}$. No experimental data, other than those that are necessary for calculating the double-folding-model potential, are required for determining the S-matrix elements $S_l^{(0)}$.

3. EFFECTIVE PROBABILITIES

The method proposed in [1–3] to analyze angular distributions for elastic heavy-ion scattering features six total partial-wave probabilities, which must be found. These are $P_{l,F}$, $P_{l,D}$, $P_{l,EF}$, $P_{l,DF}$, $P_{l,HF}$, and $P_{l,ED}$. Two of these, $P_{l,F}$ and $P_{l,D}$, can be determined independently of the remaining ones. They are given by

$$P_{l,F} = \frac{|S_l|^2}{\left|\tilde{S}_l^{(0)}\right|^2}\left(1 - \left|\tilde{S}_l^{(0)}\right|^2\right), \tag{1}$$

$$P_{l,D} = 1 - \frac{|S_l|^2}{\left|\tilde{S}_l^{(0)}\right|^2}. \tag{2}$$

The remaining probabilities satisfy the set of equations

$$\begin{cases} P_{l,EF} + P_{l,DF} = P_{l,F}, \\ P_{l,EF} = \left(1 - \left|S_l^{(0)}\right|^2\right)(1 - P_{l,ED}), \\ P_{l,DF} - P_{l,HF} = \left(1 - \dfrac{\left|\tilde{S}_l^{(0)}\right|^2}{\left|S_l^{(0)}\right|^2}\right)(1 - P_{l,D}). \end{cases} \tag{3}$$

As can be seen, there are in all three equations for determining four total partial-wave probabilities, $P_{l,EF}$, $P_{l,DF}$, $P_{l,HF}$, and $P_{l,ED}$. Therefore, the method developed in [1–3] gives no way to determine the probabilities $P_{l,DF}$ and $P_{l,HF}$ simultaneously. However, this problem can be sidestepped by introducing effective total partial-wave probabilities, which, as will be shown below, have a specific physical meaning.

Thus, we assume that, in some system, the enhancement of reactions belonging to the group

F (that is, "fusion" reactions) is more significant than suppression. We then introduce an effective total partial-wave probability for the enhancement of fusion as

$$\mathcal{P}_{l,DF} \equiv P_{l,DF} - P_{l,HF} = \frac{|S_l|^2}{\left|\tilde{S}_l^{(0)}\right|^2}\left(1 - \frac{\left|\tilde{S}_l^{(0)}\right|^2}{\left|S_l^{(0)}\right|^2}\right). \quad (4)$$

In the opposite case, we introduce an effective total partial-wave probability for the suppression of fusion as

$$\mathcal{P}_{l,HF} \equiv P_{l,HF} - P_{l,DF} = \frac{|S_l|^2}{\left|S_l^{(0)}\right|^2}\left(1 - \frac{\left|S_l^{(0)}\right|^2}{\left|\tilde{S}_l^{(0)}\right|^2}\right). \quad (5)$$

The right-hand sides of Eqs. (4) and (5) are obtained by substituting expression (2) for the probability $P_{l,D}$ into the third equation in the set of Eqs. (3). The physical meaning of the probabilities $\mathcal{P}_{l,DF}$ and $\mathcal{P}_{l,HF}$ is quite clear. They are the observed total partial-wave probabilities for, respectively, the enhancement and the suppression of "fusion"; that is, it is precisely these probabilities that are responsible for the distinction between the measured "fusion" cross sections and the cross sections for "fusion" through the entrance channel that are calculated by one method or another (for example, on the basis of the barrier-penetration model [11, 12]). It should be noted that one cannot rule out the situation where "fusion" reactions are enhanced in one group of waves, but they are suppressed in the other group. In calculations, this can be revealed, however, only if use is made of an l-dependent optical potential.

On the left-hand side of the first equation in the set of Eqs. (3), we now add and subtract the probability $P_{l,HF}$. If the enhancement of "fusion" is more significant than its suppression, the resulting equation assumes the form

$$\mathcal{P}_{l,EF} + \mathcal{P}_{l,DF} = P_{l,F}. \quad (6)$$

If, on the contrary, the suppression of "fusion" is more significant than its enhancement, we obtain the equation

$$\mathcal{P}_{l,EF} - \mathcal{P}_{l,HF} = P_{l,F}. \quad (7)$$

The probability $\mathcal{P}_{l,EF}$ appearing in Eqs. (6) and (7) is the effective total partial-wave probability for the excitation of reactions of the group F through the entrance channel. It is given by

$$\mathcal{P}_{l,EF} \equiv P_{l,EF} + P_{l,HF} = \frac{|S_l|^2}{\left|S_l^{(0)}\right|^2}\left(1 - \left|S_l^{(0)}\right|^2\right). \quad (8)$$

The right-hand side of Eq. (8) can be obtained either from (6) or from (7) by using expressions (1) and (4) or (5) for $P_{l,F}$ and $\mathcal{P}_{l,DF}$ or $\mathcal{P}_{l,HF}$, respectively.

According to (8), the probability $\mathcal{P}_{l,EF}$ exceeds the actual probability of fusion through the entrance channel, $P_{l,EF}$, by the quantity $P_{l,HF}$. However, a comparison of Eqs. (1) and (8) reveals that the probabilities $\mathcal{P}_{l,EF}$ coincide with the total partial-wave probabilities for "fusion" in the case where there is no enhancement or suppression in the system (from the analysis performed in [1–3], it follows that, in such a situation, it is not required to renormalize the folding-model potential in describing the angular distributions for elastic scattering; therefore, $\tilde{S}_l^{(0)} = S_l^{(0)}$). Hence, the result obtained by calculating, with the probabilities $\mathcal{P}_{l,EF}$, the cross section

$$\sigma_{EF} = \frac{\pi}{k^2}\sum_{l=0}^{\infty}(2l+1)\mathcal{P}_{l,EF}, \quad (9)$$

where k is the wave number in the elastic-scattering channel, is precisely the cross section with which one must compare the actual "fusion" cross section σ_F in order to establish the presence of the enhancement or suppression of reactions of the group F in the system. From Eq. (8), it also follows that the suppression of "fusion" is caused by the reduction of the actual total partial-wave probabilities for "fusion" through the entrance channel, $P_{l,EF}$, as was indicated in [1–3] in discussing the approximation $P_{l,DF} \equiv 0$.

In order to introduce the effective partial-wave probability for peripheral processes, $\mathcal{P}_{l,ED}$, we add the probability $P_{l,HF}$ to both sides of the second equation in the set of Eqs. (3). After some simple algebra, we then obtain the relation

$$\mathcal{P}_{l,EF} = \left(1 - \left|S_l^{(0)}\right|^2\right)(1 - \mathcal{P}_{l,ED}), \quad (10)$$

where

$$\mathcal{P}_{l,ED} \equiv P_{l,ED} - \frac{P_{l,HF}}{1 - \left|S_l^{(0)}\right|^2} = 1 - \frac{|S_l|^2}{\left|S_l^{(0)}\right|^2}. \quad (11)$$

The right-hand side of Eq. (11) can be evaluated by substituting expression (8) for $\mathcal{P}_{l,EF}$ into Eq. (10). From Eq. (11), it follows that the probability $\mathcal{P}_{l,ED}$ is less than the actual total partial-wave probability for peripheral processes, $P_{l,ED}$, by the quantity $P_{l,HF}/\left(1 - \left|S_l^{(0)}\right|^2\right)$. However, a comparison of Eqs. (2) and (11) reveals that the probabilities $\mathcal{P}_{l,ED}$ are the total partial-wave probabilities for peripheral reactions if there is no enhancement or suppression

of "fusion" in the system being considered. Therefore, the cross section

$$\sigma_{ED} = \frac{\pi}{k^2}\sum_{l=0}^{\infty}(2l+1)\,\mathcal{P}_{l,ED} \qquad (12)$$

calculated with the probabilities $\mathcal{P}_{l,ED}$ is precisely the cross section with which one must compare the total cross section for peripheral reactions, σ_D, in order to answer the question of whether there is the enhancement or suppression of peripheral reactions in the system. Since the right-hand side of Eq. (11) is fixed for each value of l, it can be deduced from this equation that the greater $P_{l,ED}$, the greater $P_{l,HF}$ and, hence, the higher the degree to which "fusion" is suppressed. Thus, the suppression of "fusion" is caused by enhanced values of the actual total partial-wave probabilities of peripheral processes, $P_{l,ED}$, for loosely bound ions. In [1–3], the same conclusion was drawn in the approximation $P_{l,DF} \equiv 0$.

On the basis of the formulas derived above, it can easily be proven that the enhancement of "fusion" [relation (6) holds in this case] is accompanied by the suppression of peripheral reactions to the same degree; that is,

$$\mathcal{P}_{l,ED} - \mathcal{P}_{l,DF} = P_{l,D}. \qquad (13)$$

At the same time, the suppression of "fusion" [relation (7) holds in this case] is accompanied by the enhancement of peripheral reactions to the same degree; that is,

$$\mathcal{P}_{l,ED} + \mathcal{P}_{l,HF} = P_{l,D}. \qquad (14)$$

Since the probabilities $P_{l,F}$ and $P_{l,D}$ satisfy the unitarity relation [1–3], it can be shown, by using Eqs. (6) and (13) or (7) and (14), that the unitarity relation holds for the effective total partial-wave probabilities $\mathcal{P}_{l,EF}$ and $\mathcal{P}_{l,ED}$ as well; that is,

$$\mathcal{P}_{l,EF} + \mathcal{P}_{l,ED} = 1 - |S_l|^2. \qquad (15)$$

Thus, the effective total partial-wave probabilities for various processes induced by collisions of two nuclei were introduced here in such a way that these probabilities have a specific physical meaning. All of them are expressed in terms of elastic-scattering S-matrix elements S_l, $\tilde{S}_l^{(0)}$, and $S_l^{(0)}$, which can be obtained from an analysis of the corresponding angular distributions for elastic scattering. Having the effective total partial-wave probabilities at our disposal, we can calculate all the required cross sections by formulas similar to those in (9) and (12).

To conclude this section, we note that, if $P_{l,DF} \equiv 0$ or $P_{l,HF} \equiv 0$ at all values of l, the above formulas reduce to the formulas obtained in [1–3].

4. CONCLUSION

A new approach to analyzing angular distributions for elastic heavy-ion scattering [1–3] has been generalized to the cases where total partial-wave probabilities for the enhancement of "fusion" (in general, complete and incomplete fusion, quasifission, and deep-inelastic collisions) are commensurate with those for its suppression. This has been done with the aid of effective total partial-wave probabilities, which have a specific physical meaning. Cross sections calculated with these probabilities make it possible to find out whether there occurs enhancement or suppression of "fusion" and peripheral reactions in the system.

REFERENCES

1. Yu. A. Pozdnyakov and K. O. Terenetskiĭ, Collected Scientific Works of Institute for Nuclear Research, National Akademy of Sciences of Ukraine (Kiev, 2001), No. 1(3), p. 31.
2. Yu. A. Pozdnyakov and K. O. Terenetskiĭ, Izv. Akad. Nauk, Ser. Fiz. **66**, 435 (2002).
3. Yu. A. Pozdnyakov, Yad. Fiz. **65**, 1877 (2002) [Phys. At. Nucl. **65**, 1827 (2002)].
4. Y. Sakuragi, Phys. Rev. C **35**, 2161 (1987).
5. C. Signorini, A. Andrighetto, M. Ruan, *et al.*, Phys. Rev. C **61**, 061603 (2000).
6. G. R. Satchler and W. G. Love, Phys. Rep. **55**, 183 (1979).
7. V. M. Strutinsky, Nucl. Phys. **68,** 221 (1965).
8. G. H. Rawitscher, Nucl. Phys. **85**, 337 (1966).
9. Y. Eisen and Z. Vager, Nucl. Phys. A **187**, 219 (1972).
10. V. P. Verbitskiĭ, A. P. Il'in, Yu. A. Pozdnyakov, and K. O. Terenetskiĭ, Izv. Akad. Nauk SSSR, Ser. Fiz. **49**, 945 (1985).
11. L. C. Vaz, J. M. Alexander, and G. R. Satchler, Phys. Rep. **69**, 373 (1981).
12. M. Beckerman, Phys. Rep. **129**, 145 (1985).

Translated by A. Isaakyan

Physics of Atomic Nuclei, Vol. 66, No. 5, 2003, pp. 828–835. Translated from Yadernaya Fizika, Vol. 66, No. 5, 2003, pp. 860–867.

ELEMENTARY PARTICLES AND FIELDS
Experiment

Resonances in the $K_SK_SK_L$ System Produced in Collisions of Negative Pions with a Carbon Target at a Momentum of 40 GeV

G. D. Tikhomirov*, I. A. Erofeev, O. N. Erofeeva, and V. N. Luzin

Institute of Theoretical and Experimental Physics,
Bol'shaya Cheremushkinskaya ul. 25, Moscow, 117259 Russia

Received April 27, 2002; in final form, September 11, 2002

Abstract—The experimental spectrum of the $K_SK_SK_L$ system from the reaction $\pi^-\mathrm{C} \to K_SK_SK_L + Y$ at a momentum of 40 GeV was obtained experimentally with the aim of studying resonance states featuring open strangeness and occurring in the high-mass region. The experiment was performed at the 6-m spectrometer installed at the Institute for High Energy Physics (IHEP, Protvino). The spectrum displays, along with well-known resonances [$K_1(1640)$, $K_2(1770)$, $K_2(1820)$, $K_2(1980)$], which fit in the quark–antiquark classification, the exotic resonances $K_2(2280)$ and $K_4(2500)$. The $K_2(2280)$ resonance exhibits the properties of a hybrid and has an exotic decay mode producing a triplet of known resonance states related to each other by quark–gluon mixing. The mechanism of the formation of the observed hybrid $K_2(2280)$ is dominated by the exchange of a natural spin–parity in the t channel of the reaction. The mode of decay into $f_0(980)K_L$ and the mode of decay into $f_2(1270)K_L$ are observed for the $K_2(1770)$ and the $K_2(1980)$ resonance, respectively. © *2003 MAIK "Nauka/Interperiodica".*

In the literature, there are virtually no data on the $K_SK_SK_L$ system because recording this system involves serious difficulties. At the same time, great interest in studying the $K_SK_SK_L$ system is motivated by the desire to advance into the region of high-mass resonances featuring open strangeness. Investigation of the $K_SK_SK_L$ system is advantageous in that the K_SK_S and K_SK_L combinations have different sets of quantum numbers (even and odd series), and this facilitates the identification of the quantum numbers of the entire system considerably.

The experimental data subjected to the present analysis were obtained in one of the runs that employed the 6-m spectrometer developed at the Institute of Theoretical and Experimental Physics (ITEP, Moscow), equipped with a gamma and a hadronic calorimeter, and installed in a beam from the U-70 accelerator of the Institute for High Energy Physics (IHEP, Protvino). A detailed description of the spectrometer was given elsewhere [1]. A feature peculiar to the run being discussed was that a gamma and a hadronic calorimeter [2] placed one after the other were arranged downstream of the tracking spectrometer at distances of, respectively, 11.2 and 12.0 m from the carbon target used, their thicknesses being $21\mathrm{X}_0$ and 0.6λ for the gamma calorimeter and 4.5λ for the hadronic calorimeter (here, X_0 is the radiation length, while λ is the interaction range). The number of beam particles that traversed the spectrometer was 3.5×10^{10}. The composition of the beam was the following: 97% π^- mesons, 2% K^- mesons, 0.5% μ^- mesons, and 0.3% antiprotons. Beam K^- and π^- mesons were recorded by a differential Cherenkov counter and a threshold Cherenkov counter, respectively. Since a multitrigger mode was chosen for a neutral trigger, the separation of the $K_SK_SK_L$ system studied here was soft at the trigger level.

The system formed by K_S, K_S, and K_L particles was studied on the basis of a data sample consisting of vee events recorded in the spectrometer and unambiguously identified as K_S mesons, the corresponding signal from these events in the hadronic calorimeter also being required. Events featuring the pair production of K_S mesons were selected according to the procedure used at the 6-m spectrometer [3, 4]. Upon fitting vee tracks to each of the γ, K, Λ, and $\bar{\Lambda}$ hypotheses and selecting a pair of K_S mesons according to the χ^2 criterion, it was additionally required for selected events that both K_S mesons originate from the interaction vertex in the carbon target. The precision to which the effective mass of the $\pi^+\pi^-$ pair from K_S-meson decay is measured in the spectrometer (Fig. 1*a*) is $2\sigma = 18$ MeV, where σ is a standard deviation. In all, we have found 11 208 events of the inclusive reaction

$$\pi^-\mathrm{C} \to K_SK_S + X. \qquad (1)$$

*e-mail: Gena.Tikhomirov@itep.ru

1063-7788/03/6605-0828$24.00

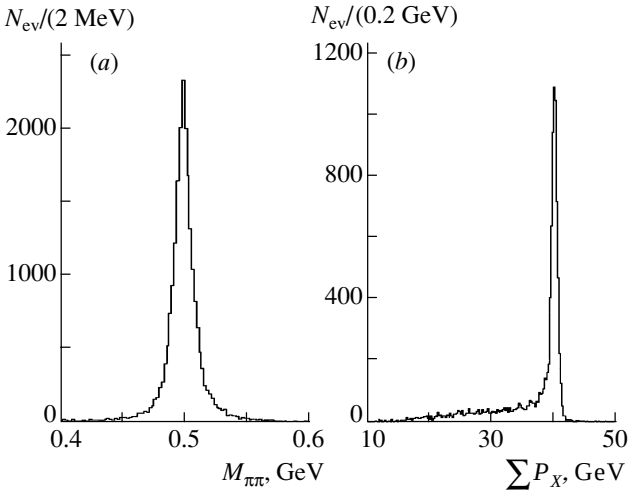

Fig. 1. Distribution of events with respect to (*a*) the effective mass of two pions from K_S-meson decay that are recorded by the spectrometer in the inclusive reaction $\pi^-\mathrm{C} \to K_SK_S + X$ and (*b*) the sum of the longitudinal components of the momenta ($\sum P_X$) of two K_S mesons.

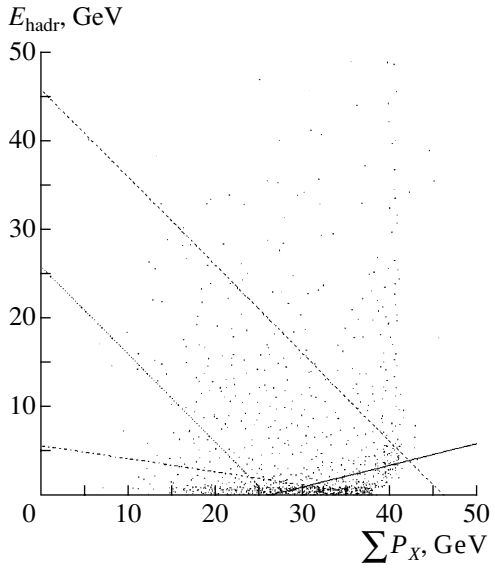

Fig. 2. Two-dimensional distribution of events with respect to $\sum P_X$ and E_{hadr}.

The distribution of these events with respect to the sum of the longitudinal components of the momenta ($\sum P_X$) of two K_S mesons is shown in Fig. 1*b*. The cross section for the production of K_S-meson pairs on a carbon target in the quasielastic reaction (1) was determined previously in [5]. The result was 2.0 ± 0.12 μb/nucleus, the systematic uncertainty being 20%. The quasielastic events of reaction (1) were rejected by discarding events where $\sum P_X > 38$ GeV, and the remaining events were tested for the presence of a signal in the hadronic calorimeter. The coordinates of a hadron were measured to a comparatively high precision, while the shower energy was determined to within 35%.

The quasielastic reaction

$$\pi^-\mathrm{C} \to K_SK_SK_L + Y \qquad (2)$$

was selected on the basis of the dependence $E_{\mathrm{hadr}} = f(\sum P_X)$ in Fig. 2 (here, E_{hadr} is the shower energy in the hadronic calorimeter), which displays all events of reaction (1), with the exception of those that fall within the region of the quasielastic production of a K_S-meson pair [$\sum P_X < (37.5\ \mathrm{GeV} + E_{\mathrm{hadr}})$]. For reaction (2), the total longitudinal momentum of three K mesons must be close to the momentum of the incident negative pion; that is, the events in question must be concentrated, on the graph, around the line specified by the condition $\sum P_X + E_{\mathrm{hadr}} = 40$ GeV. However, the points on the graph exhibit a large scatter because of an insufficiently high precision in determining the shower energy in the hadronic calorimeter. Under the selection conditions $E_{\mathrm{hadr}} > (5.7\ \mathrm{GeV} - 0.15 \sum P_X)$ and $\sum P_X < (26\ \mathrm{GeV} + 4E_{\mathrm{hadr}})$, the ensuing analysis included almost all events generating a response in the hadronic calorimeter with $E_{\mathrm{hadr}} > 2.5$ GeV, the boundary here lying well above the noises of the calorimeter. The subsequent selection of events characterized by $|P_{3K} - 36\ \mathrm{GeV}| < 10$ GeV removed the wings of the distribution constructed on the basis of the total energy deposition in reaction (2), $P_{3K} = \sum P_X + E_{\mathrm{hadr}}$.

For the selected region of reaction (2), the level of random coincidences of two correctly identified K_S mesons generating a response in the hadronic calorimeter can be estimated by taking events of the quasielastic production of a K_S-meson pair. In the band $38 < \sum P_X < 42$ GeV, the ratio of the number of events where $E_{\mathrm{hadr}} > 2.5$ GeV to the total number of events is 0.07, while, for the selected region, this ratio does not exceed 0.01.

The contribution of the background reaction

$$\pi^-\mathrm{C} \to K_SK_SK_L\pi^0 + X \qquad (3)$$

can be determined from the data on the neutral pion reconstructed in the electromagnetic calorimeter. Estimations reveal that the contribution of reaction (3), as well as that of the reaction $\pi^-\mathrm{C} \to K_SK_SK_LK_L + X$, is about 5 to 10%.

In order to improve the resolution in the mass spectrum of the $K_SK_SK_L$ system, we have used the conservation of the longitudinal component of the total momentum.

Figure 3 displays the distribution of events of reaction (2) with respect to the effective mass of the $K_SK_SK_L$ system; this distribution is fitted in terms of

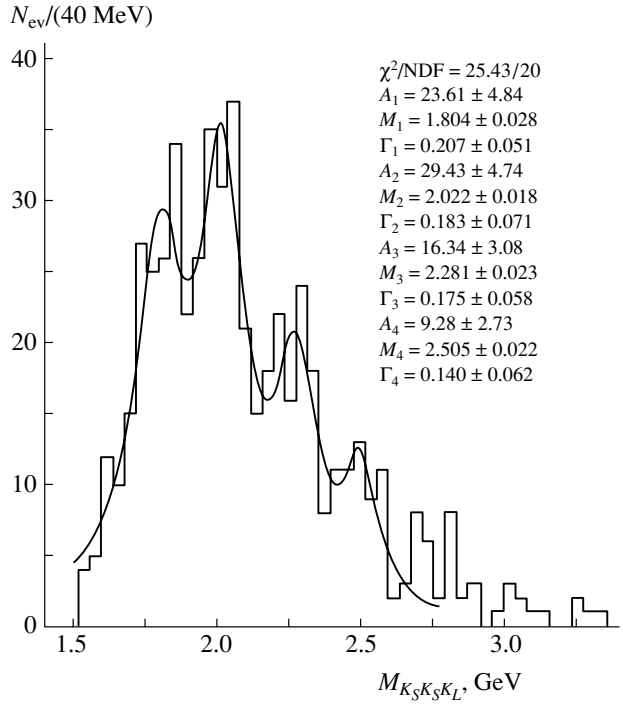

Fig. 3. Distribution of events with respect to the effective mass of the $K_SK_SK_L$ system (here and below, the values of M and Γ are given in GeV).

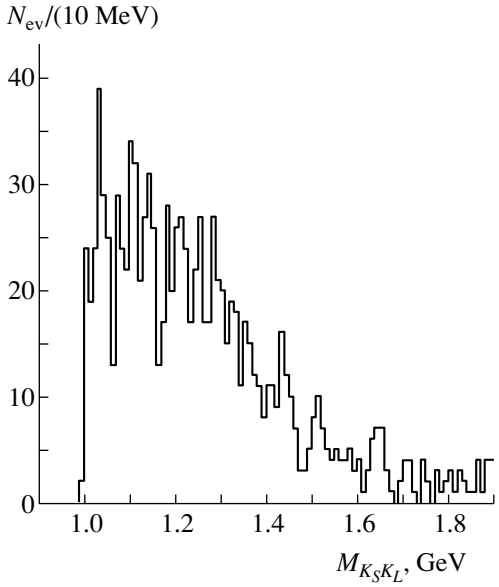

Fig. 4. Distribution of events with respect to the effective mass of the K_SK_L system.

four Breit–Wigner distributions with free parameters. The value of χ^2 per degree of freedom is 1.3, while the resulting values of the masses and widths of the observed resonance states are virtually coincident with those for already known resonances that are included in the systematics of the Particle Data Group [6]. It should also be noted that the description of the mass spectrum of the $K_SK_SK_L$ system in terms of a fourth-degree polynomial yields a χ^2 value per degree of freedom that is twice as great as that given above.

Since accumulated statistics (553 events) are not sufficient for performing a partial-wave analysis, we attempted to study the properties of these states on the basis of the angular distributions for their decays. For this purpose, the mass distribution was split into five bins: 1.50–1.70, 1.70–1.90, 1.90–2.14, 2.14–2.40, and 2.40–2.64 GeV; in each of these, the angular distributions for the decays in question were investigated in the Gottfried–Jackson frame—that is, in the rest frame of the $K_SK_SK_L$ system, with the z and the y axis being aligned with, respectively, the primary-beam axis and the normal to the production plane. In order to pinpoint the channels through which these states decay, we plotted, in Figs. 4 and 5, the effective-mass distributions of, respectively, the K_SK_L and the K_SK_S system and, in Fig. 6, the effective-mass distribution of the K_SK_S system for three regions lying above 1.9 GeV.

In the distribution of K_SK_L (Fig. 4), where both combinations are included for each event, there are no noticeable features, other than that which is associated with ϕ-meson production. For events where the mass of the K_SK_L system is less than 1.07 GeV, the effective-mass distribution of the $K_SK_SK_L$ system (see Fig. 7*a*) suggests that, at the beginning of the spectrum, there are two structures around 1.65 and 1.82 GeV. While, for the structure at 1.65 GeV, the K_SK_L system exhibits features peculiar to the ϕ meson (P_1 wave), for the structure at 1.82 GeV, the distribution with respect to the cosine of the decay angle for the K_SK_L system is isotropic. For the structure around 1.65 GeV, the preferred spin–parity values are $J^P = 1^+$.

In the K_SK_S spectrum (see Fig. 5), which has a maximum near the threshold, one can also clearly see maxima in the regions of the $f_2(1270)$, $f_0(1370)$, $f_2(1525)$, and $f_2(1710)$ resonances; in view of this, we described this spectrum in terms of five Breit–Wigner resonances with 15 parameters. The χ^2 value per degree of freedom was 0.7, and the resulting parameter values (masses and widths) were in agreement, within the errors, with the values known from [6, 7]. The maximum near the threshold has the properties of the $f_0(980)$ resonance, since the distributions with respect to $\cos\theta_{GJ}$ and ϕ_{TY} (that is, with respect to the polar and the azimuthal angle) exhibit a uniform character.

In the mass distribution of the $K_SK_SK_L$ system, events in the mass region $M_{K_SK_S} < 1.12$ GeV generate a distinct peak of mass $M = 1.743 \pm 0.015$ GeV and width $\Gamma = 0.147 \pm 0.07$ GeV (see Fig. 7*b*), its

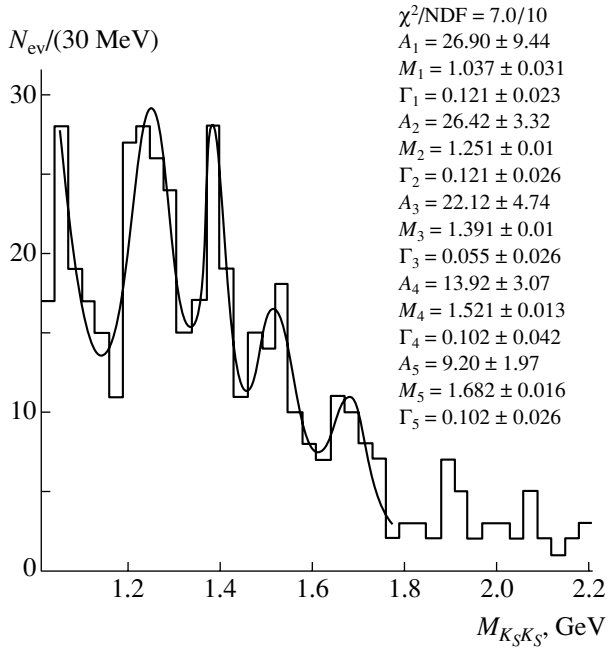

Fig. 5. Distribution of events with respect to the effective mass of the K_SK_S system (events involving a ϕ meson were discarded).

position and width being in agreement, within the errors, with those of the known $K_2(1770)$ resonance. The distributions with respect to $\cos\theta_{\mathrm{GJ}}$ and ϕ_{TY} in Fig. 8 are compatible with the D_1 wave at the χ^2 value of unity per degree of freedom, this corresponding to the spin–parity assignment of $J^P = 2^-$.

Events populating the interval 1.7–1.9 GeV of the $K_SK_SK_L$ mass may be associated with the decay of a 1.82-GeV resonance according to the scheme $K_2(1820) \to f_2(1270) + K_L$ and the formation of a $f_2(1270)$ resonance at the threshold. The angular distributions for the decay of the $f_2(1270)$ resonance are well described by the D_0 wave (see Fig. 9*a*), while the angular distributions for the decay of the $K_2(1820)$ resonance are isotropic, which makes it possible to assign the $K_2(1820)$ resonance the spin–parity of $J^P = 2^-$.

The feature in the mass range 1.90–2.14 GeV is observed predominantly in the decay channel $K_2(2020) \to f_2(1270) + K_L$ (see Fig. 6*a*), and the distribution with respect to $\cos\theta_{\mathrm{GJ}}$ (Fig. 9*b*) can be described in terms of the P_1 wave; in the set $J^P = 1^+, 2^+$, and 3^+, which is compatible with this, the spin–parity of $J^P = 2^+$ coincides with the corresponding quantum numbers of the $K_2(1980)$ resonance presented by the Particle Data Group, its decay producing the $K^*(890)\pi$ and $K\rho$ final states. The decay channel $K_2(2020) \to f_0(1370) + K_L$ can

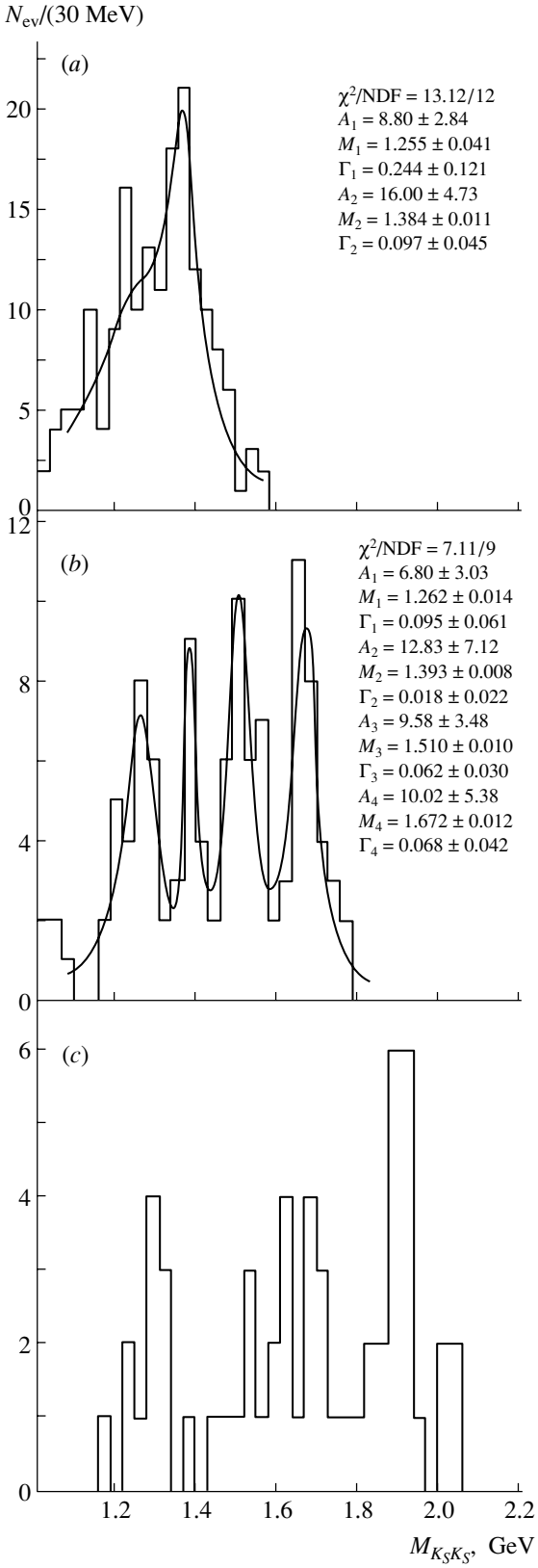

Fig. 6. Distribution of events with respect to the effective mass of the K_SK_S system for three regions of the $K_SK_SK_L$ spectrum: (*a*) 2.02 ± 0.12, (*b*) 2.27 ± 0.13, and (*c*) 2.52 ± 0.12 GeV.

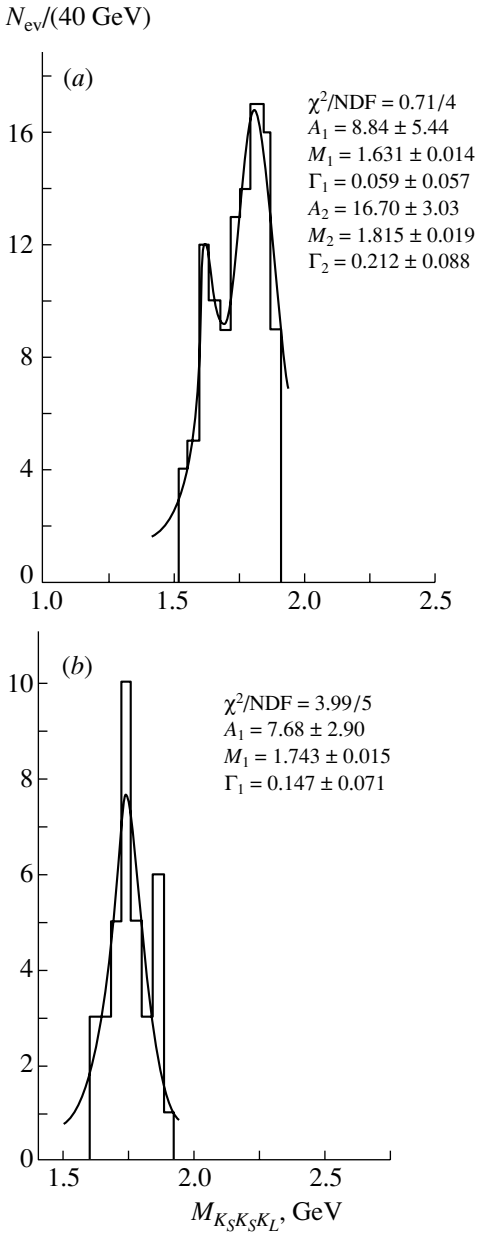

Fig. 7. Distribution of events with respect to the effective mass of the $K_SK_SK_L$ system for the following selection criteria: (*a*) $M_{K_SK_SK_L} < 1.92$ GeV, $M_{K_SK_L} < 1.07$ GeV and (*b*) $M_{K_SK_S} < 1.12$ GeV, $M_{K_SK_L} > 1.07$ GeV.

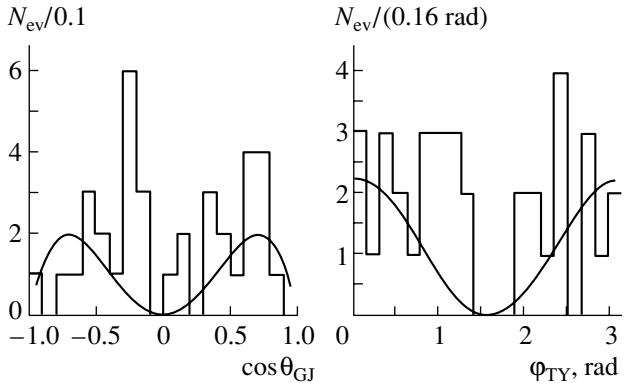

Fig. 8. Angular distributions for the decay of the $K_2(1740)$ resonance in the Gottfried–Jackson frame (θ_{GJ} and φ_{TY} are, respectively, the polar and the azimuthal angle).

also be realized,[1)] but, because of insufficient statistics, we were unable to give preference to one of the possible hypotheses, $J^P = 1^+$ or $J^P = 2^-$.

Of particular interest are the maxima around 2.28 and 2.50 GeV, for which the spectra of the K_SK_S system are given in Figs. 6*b* and 6*c*. A feature peculiar to the spectrum in Fig. 6*b* is that the relevant events are obviously concentrated around four known resonances, $f_2(1270)$, $f_0(1370)$, $f_2(1525)$, and $f_2(1710)$. The angular distributions for the decay of the structure at 2.28 GeV cannot be described in terms of a single specific partial wave. At the same time, the decay of the features at 2.28 and 2.50 GeV to a particular set of known resonance states may suggest that they are excited states. The properties of these excited states are in accord with the QCD predictions in [8] for hybrids, where the gluon degree of freedom is excited in the presence of a quark pair, the lightest of these hybrid states having mass values 1 GeV above those of their conventional $\overline{q}q$ counterparts. According to the color-tube model, the decay channels that play a dominant role for the lightest hybrids (the $J^P = 2^-$ hybrid in our case) are those that produce one meson in the ground ($^1S_0$ or $^3S_1$) state and the other meson in an orbitally excited ($^3P_2$ or $^3P_0$) state [9].

In [10], a neutral tensor meson involving a gluon component and participating in the mixing of the gluon component and the quark components in the $f_2(1270)$, $f_2(1525)$, and $f_2(1660)$ resonances is assumed to exist, which aids in explaining the branching fractions of their decays through various channels—in particular, the channel $f_2(1525) \to \gamma\gamma$.

Close and Kirk [7] presented pieces of evidence for the mixing of the gluon component and the quark components in the scalar resonances $f_0(1370)$, $f_0(1500)$, and $f_0(1710)$.

In Fig. 6*b*, it can clearly be seen that three resonances [$f_2(1270)$, $f_2(1525)$, $f_2(1660)$] correspond to

[1)] A Monte Carlo simulation performed later for the decay process $K_2(2270) \to f_0(1370) + K^*(890)$ revealed that the peak at a mass value of 1370 MeV in the K_SK_S spectra for two neighboring bins (1900–2014, 2014–2400 MeV) of the $K_SK_SK_L$ system may be associated with the same object, $K_2(2270)$, decaying into $f_0(1370)$ and $K^*(890)$. This is because we calculated the K_L-meson momentum from the law of conservation of the longitudinal momentum component in reaction (2).

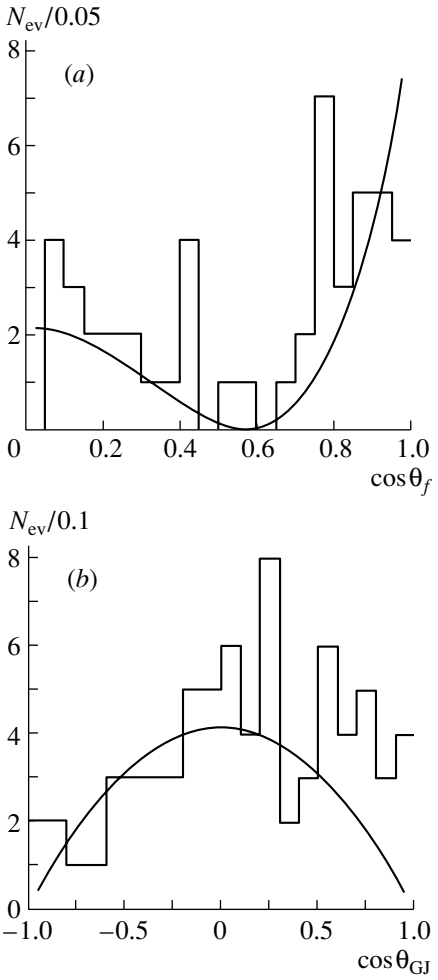

Fig. 9. Angular distributions in the Gottfried–Jackson frame for (a) the decay of the $f_2(1270)$ resonance (we selected events from the range 1.70–1.90 GeV of the $K_SK_SK_L$ spectrum, which are characterized by mass values in the region $M_{K_SK_S} > 1.12$ GeV, the index f indicating the decay of the K_SK_S system) and (b) the decay of the $K_2(1980)$ resonance through the channel $K_2(1980) \to f_2(1270) + K_L$ (we selected events from the range 1.90–2.14 GeV of the $K_SK_SK_L$ spectrum, which are characterized by mass values in the interval $1.12 < M_{K_SK_S} < 1.35$ GeV).

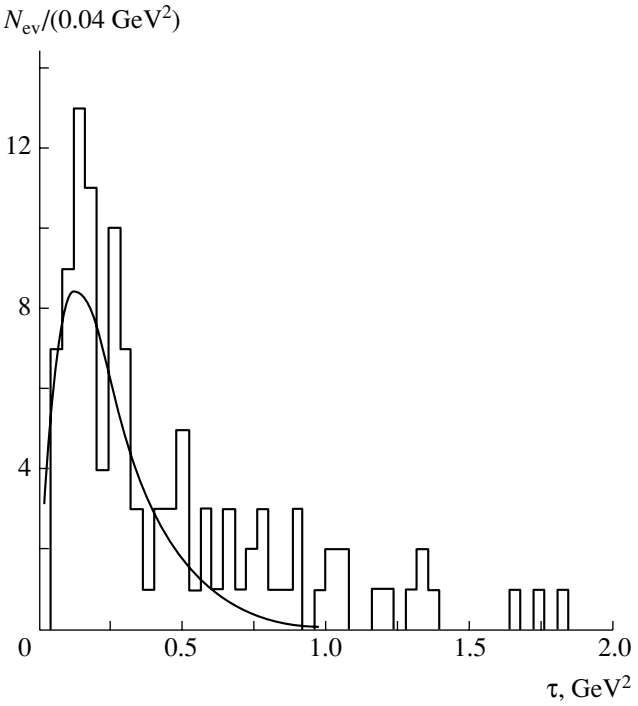

Fig. 10. Distribution of events with respect to the square of the transverse-momentum transfer to the $K_2(2280)$ hybrid.

the tensor triplet discussed in [10], both in position and in shape. We have attempted to consider the peak at 1390 MeV as a manifestation of a feature that is characterized by the same mass value and which is comparatively well produced in the $K_SK_SK_L$-spectrum section neighboring that value on the left. In attempting to move the boundary between the regions of the $K_2(1980)$ and $K_2(2280)$ resonances to the right, we revealed that the amplitudes of all four peaks decrease simultaneously, which may be indicative of an insufficient reliability of the hypothesis used. As a result, we have arrived at the conclusion that a scalar triplet is present in the decay of the $K_2(2280)$ resonance as well, and a peak that is seen at a mass value of 1390 MeV and which can be associated with the $f_0(1370)$ resonance is an obvious manifestation of this. An insufficient mass resolution in our experiment and paucity of statistics are the reasons why we were unable to distinguish between $f_0(1500)$ and $f_2(1525)$, as well as between $f_0(1710)$ and $f_2(1660)$.

Some of scalar mesons can go over to the region of low masses in the $K_SK_SK_L$ spectrum rather than fall within the interval 2.14–2.40 GeV. This is because scalar mesons must be produced in a pair with a meson in the $^3S_1$ state—that is, with the $K^*(890)$ resonance. In refining the K_L-meson momentum with the aid of the law of longitudinal-momentum-component conservation, we disregarded the neutral pion from $K^*(890)$ decay. If scalar mesons are produced in a pair with a $K^*(890)$ meson, then the $f_0(1500)$ and $f_0(1710)$ resonances occur beyond the threshold of their production in the decay of the $K_2(2280)$ feature. We can clearly see the $f_0(1370)$ resonance or some part of it, but it does not seem possible to prove, on the basis of our data, that this resonance is produced in a pair with the $K^*(890)$ resonance, since, in the mass range 2.14–2.40 GeV, the acceptance of the electromagnetic calorimeter recording neutral pions is one-fourth as great as the acceptance of the hadronic calorimeter recording K_L. Thus, we can assume that

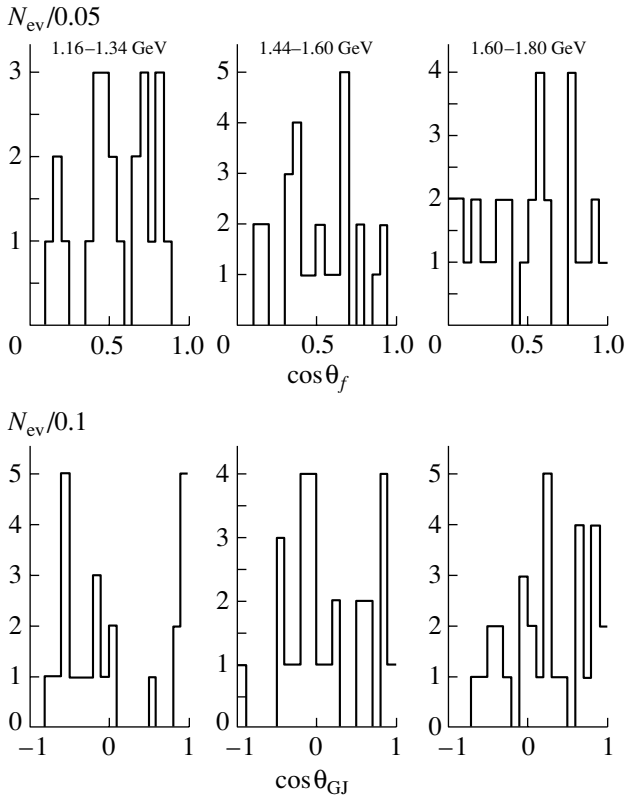

Fig. 11. Distribution of events in the cosine of the emission angles for various intervals of the mass of the K_SK_S system (1.16–1.34, 1.44–1.60, 1.60–1.80 GeV): (upper panels) distributions in $\cos\theta_f$ for the emission of a K_S meson with respect to the K_L meson in the rest frame of the two K_S mesons and (lower panels) distributions in $\cos\theta_{GJ}$ for the emission of the K_SK_S system with respect to the primary beam in the rest frame of the $K_2(2280)$ hybrid.

the decay of the $K_2(2280)$ feature involves a tensor and, most likely, a scalar triplet, which are coupled by the mixing of a gluon with a pair of quarkonia [11]. This gives reasons to believe that the feature in question is a hybrid.

The production of a $K_2(2280)$ hybrid is well described by a natural exchange, as can be seen in Fig. 10, where the distribution of events with respect to the square of the transverse-momentum transfer, τ, to the $K_2(2280)$ hybrid is well approximated by the function $d\sigma/d\tau = \alpha\tau\exp(-\beta\tau)$ at $\alpha = 183 \pm 53$ and $\beta = 8 \pm 1$.

The spin–parity of $J^P = 2^-$ for the $K_2(2280)$ hybrid can be predicted on the basis of its decay into f_2 and K_L with zero relative orbital angular momentum ($L = 0$). Despite an insufficient statistical significance of the experimental data, this conclusion can be confirmed by an analysis of the angular distributions for the decay of either the K_SK_S or the $K_SK_SK_L$ system (see Fig. 11). For the mass ranges

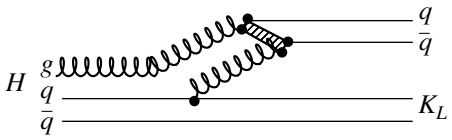

Fig. 12. Diagram for the decay of the H hybrid (the shaded box represents the place where a gluon pair undergoes color rearrangement and transitions to a quark–antiquark pair).

1.16–1.34 and 1.44–1.60 GeV in the K_SK_S spectrum, the distribution of events with respect to the cosine of the polar angle of the decay of the $K_SK_SK_L$ system can be considered to be isotropic, while the distribution with respect to the cosine of the polar angle of the decay of the K_SK_S system is compatible with the description in terms of the D_1 wave, but the assumption of isotropy is also admissible.

Figure 6*c* displays the spectrum of the K_SK_S system for the range 2.4–2.64 GeV, where the concentration of the relevant events in the regions of the $f_2(1270)$, $f_2(1710)$, and $f_2(1920)$ resonances is also indicative of a hybrid character of the $K_4(2500)$ maximum, but a reliable analysis of it is next to impossible because of insufficient statistics.

RESULTS AND DISCUSSION

We believe that, in reaction (2), the production of the $K_SK_SK_L$ system through resonance states with their subsequent cascade decay is energetically favorable, but that nonresonance events form a background (other reactions and random superpositions in reconstructing events), their estimation in various sections of the spectrum revealing that they do not exceed 10%.

The low-mass section of the $K_SK_SK_L$ spectrum (below 2 GeV) contains bound states formed by valence quark–antiquark pairs, but, with increasing mass, there emerge exotic mesons, the first of these being the $K_2(2280)$ resonance, whose observable properties are similar to those of a hybrid ($\bar{q}qg$ state). The mode of their decay into three tensor resonances $f_2(1270)$, $f_2(1525)$, and $f_2(1660)$ and, possibly, three scalar resonances $f_0(1370)$, $f_0(1500)$, and $f_0(1710)$ is also exotic. As to the content of the scalar mesons, we cannot draw definitive conclusions on the basis of our experimental data,[2)] but, as soon as statistics are enlarged and the geometry of recording the

[2)] In performing a further analysis of experimental data and in simulating the decay $K_2(2270) \to f_0(980) + K^*(890)$, we obtained a piece of evidence that, in the decay of K_2, there is also a threshold feature that can be identified with the production of the $f_0(980)$ resonance.

$K^*(890) + f_0$ states is improved, it will become possible to clarify the composition of the scalar nonet.

In the decay of the $K_2(2280)$ hybrid, the mechanism described by the diagram in Fig. 12, where the product gluon pair undergoing color rearrangement yields, at the final stage, a decomposition into the scalar and the tensor triplet, is likely to be operative.

The parameters of the $K_2(2280)$ resonance state are identical to those of the $K_2(2250)$ resonance [6], which was observed in the $\overline{p}\Lambda$ channel. If $J^P = 2^-$, it is quite possible to identify it with the quark–antiquark meson $2^3D_2/2^3D_1$, which is predicted in the same mass interval [12]. Observation of the $K\pi\pi$ decay mode, which is natural for quarkonium and which is strongly suppressed for a hybrid, would make it possible to distinguish between these two possibilities (a hybrid strange meson versus a quark–antiquark meson).

Let us briefly summarize the results of this study:

(i) For the $K_2(1770)$ resonance of mass $M = 1.743 \pm 0.015$ GeV, width $\Gamma = 0.147 \pm 0.07$ GeV, and spin–parity $J^P = 2^-$, we have obtained an indication of a new decay channel: $K_2(1770) \to f_0(980) + K_L$.

(ii) For the $K_2(1980)$ resonance of mass $M = 2.02 \pm 0.02$ GeV, width $\Gamma = 0.18 \pm 0.07$ GeV, and spin–parity $J^P = 2^+$, we have also obtained an indication of a new decay channel: $K_2(1980) \to f_2(1270) + K_L$.

(iii) For the first time, we have discovered an exotic decay channel for the $K_2(2280)$ resonance ($K_L + f_2$, $K^*(890) + f_0$); this is indicative of a hybrid nature of this object. Its features ($M = 2.28 \pm 0.02$ GeV, $\Gamma = 0.18 \pm 0.06$ GeV, $J^P = 2^-$) are identical to those of the $K_2(2250)$ resonance [6], which decays through the $K\pi\pi$ and $\overline{p}\Lambda$ channels.

ACKNOWLEDGMENTS

We are grateful to the personnel of the laboratory of the 6-m spectrometer at ITEP and to the staff of the U-70 accelerator at IHEP for help in implementing the run that produced the data set used in this study. Special thanks are due to V.V. Vladimirsky, A.B. Kaidalov, and Yu.S. Kalashnikova for stimulating discussions. We are also indebted to V.I. Lisin for kindly placing at our disposal processed data from the calorimeters.

REFERENCES

1. B. V. Bolonkin, O. N. Baloshin, *et al.*, Preprint No. 86, Inst. Theor. Exp. Phys. (Moscow, 1973); Preprint No. 154, Inst. Theor. Exp. Phys. (Moscow, 1981).
2. B. P. Barkov *et al.*, Preprint No. 93-15, Inst. High Energy Phys. (Protvino, 1993).
3. B. V. Bolonkin *et al.*, Preprint No. 62, Inst. Theor. Exp. Phys. (Moscow, 1981); Preprint No. 13, Inst. Theor. Exp. Phys. (Moscow, 1985).
4. V. N. Nozdrachev and V. V. Sokolovsky, Preprint No. 167, Inst. Theor. Exp. Phys. (Moscow, 1985).
5. O. N. Baloshin *et al.*, Yad. Fiz. **58**, 50 (1995) [Phys. At. Nucl. **58**, 46 (1995)].
6. Particle Data Group (D. E. Groom *et al.*), Eur. Phys. J. C **15**, 1 (2000).
7. F. Close and A. Kirk, Eur. Phys. J. C **21**, 531 (2001).
8. N. Isgur and J. Paton, Phys. Rev. D **31**, 2910 (1985).
9. L. G. Landsberg, Yad. Fiz. **57**, 47 (1994) [Phys. At. Nucl. **57**, 42 (1994)].
10. F. Caruso and E. Predazzi, Z. Phys. C **33**, 569 (1987).
11. F. Close, Preprint No. 95-045, RAL-TR (Chilton, 1995).
12. S. Godfrey and N. Isgur, Phys. Rev. D **32**, 189 (1985).

Translated by A. Isaakyan

Physics of Atomic Nuclei, Vol. 66, No. 5, 2003, pp. 836–846. Translated from Yadernaya Fizika, Vol. 66, No. 5, 2003, pp. 868–878.

ELEMENTARY PARTICLES AND FIELDS
Experiment

Features of pC Interactions at a Momentum of 4.2 GeV/c versus the Degree of Centrality of Collisions between Protons and Carbon Nuclei: Multiplicity of Secondary Particles

A. S. Galoyan[1)], E. N. Kladnitskaya[*], O. V. Rogachevski, R. Togoo[2)], and V. V. Uzhinskii[3)]

Joint Institute for Nuclear Research, Dubna, Moscow oblast, 141980 Russia

Received April 10, 2002; in final form, July 25, 2002

Abstract—New experimental data obtained for the multiplicities of charged pions and protons from the interaction of 4.2-GeV/c protons with a carbon nucleus by using the 2-m propane bubble chamber installed at the High Energy Laboratory (Joint Institute for Nuclear Research, Dubna) are presented versus the degree of collision centrality. The parameter Q defined for each individual event as the difference of the total multiplicities of positively and negatively charged particles without allowing for the multiplicity of evaporated protons whose momentum is less than 0.3 GeV/c is taken for a criterion of the degree of collision centrality. It is shown that, with increasing Q, the multiplicity of positively charged pions and the multiplicity of participant protons from the target nucleus grow considerably; concurrently, the multiplicity of negatively charged pions remains at nearly the same level, while the mean multiplicity of evaporated protons decreases sharply. Our experimental data are compared with the results of calculations based on the cascade–evaporation model and the modified FRITIOF model. Within the FRITIOF model, nonnucleon degrees of freedom in nuclei (Δ^+, Δ^0 isobars) are taken into account for the first time, and the resulting description of the features of secondary particles appears to be by and large satisfactory.

INTRODUCTION

The interaction of protons with carbon nuclei (pC interactions) at a momentum of 4.2 GeV/c under conditions of a 4π coverage was explored by many authors (see [1–8]). The authors of [1–3] presented inclusive features of secondaries from such interactions, while the authors of [4, 5] reported on an analysis of events resulting in a complete disintegration of a carbon nucleus. Some authors (see [6–8]) investigated the angular distributions of the invariant inclusive cross sections for the yield of pions and protons. In this study, we perform a detailed analysis of the features of secondaries at various values of the impact parameter of collisions between protons and carbon nuclei. First, we present the multiplicities of charged particles for six groups of pC interactions from peripheral to central ones and compare them with the predictions of various theoretical models. Investigation of these features of product particles is of paramount importance for reconstructing the spacetime pattern of pC interactions at various values of the impact parameter—in particular, of particle rescattering in a carbon nucleus—and for a further development of relevant theoretical concepts.

Among the existing theoretical models, the Glauber–Sitenko approximation [9], which makes it possible to calculate the total, elastic, and inelastic cross sections, is thought to be the most reliable. The treatment of this approximation within the Reggeon approach—this is sometimes referred to as the Glauber–Gribov approximation—makes it possible to evaluate cross sections for interactions involving various numbers of intranuclear nucleons. Therefore, a model that is employed to analyze experimental data must include the Glauber approximation. In addition, such a model must admit a broad variation in the presumed physics scenario of the interactions in question. The FRITIOF model [10, 11] satisfies these requirements.

The FRITIOF model includes the Glauber approximation [12]. Within the FRITIOF code version used in the present study, the Fermi motion of intranuclear nucleons [12] and special features of the two-body decays of excited nucleons [13] are taken correctly into account, which makes it possible to reduce the threshold of its applicability to 1–4 GeV

[1)]Joint Institute for Nuclear Research, Dubna, Moscow oblast, 141980 Russia; Yerevan Physics Institute, ul. Brat'ev Alikhanian 2, Yerevan, 375036 Armenia.
[2)]Institute for Physics and Technology, Ulan Bator, Mongolia.
[3)]Joint Institute for Nuclear Research, Dubna, Moscow oblast, 141980 Russia.
[*]e-mail: klad@sunhe.jinr.ru

per nucleon. In [14], elastic nucleon rescatterings were phenomenologically incorporated into the model in analyzing CC interactions. For hadron–nucleus interactions, this can be validated within the Glauber approximation [15]. The possibility of taking into account nonnucleon degrees of freedom in nuclei (specifically, Δ^+ and Δ^0 isobars) within the FRITIOF model is considered for the first time in the present study.

1. EXPERIMENTAL DATA

The experimental data used here were obtained on the basis of processing stereophotographs from the 2-m propane bubble chamber constructed at the High Energy Laboratory of the Joint Institute for Nuclear Research (JINR, Dubna), placed in a magnetic field of strength 1.5 T, and irradiated with a beam of protons accelerated to a momentum of 4.2 GeV/c at the JINR synchrophasotron.

In order to select events of inelastic pC interactions in the total set of proton interactions with propane (C_3H_8), we used criteria described in [1, 2, 16]. The procedure for isolating elastic pp and pC events, introducing corrections for the multiplicities of secondaries and their angular and momentum features, and specifying the weights of positively charged particles having momenta in excess of 0.5 GeV/c was described in detail elsewhere [16]. We recall that, under the conditions of the present experiment (which does not measure ionization induced by positively charged particles), positively charged pions and protons are reliably identified up to momenta of 0.5 GeV/c.

In the ensemble of pC interactions that is subjected to an analysis here, we selected charged pions, participant protons of momenta p in excess of 0.3 GeV/c, and evaporated protons ($0.15 < p < 0.3$ GeV/c).[4)] In addition, we have considered two groups of protons, those of momenta ranging between 0.3 and 0.75 GeV/c (these are predominantly participant protons from the target nucleus) and those of momenta $p > 0.75$ GeV/c. For the most part, the last group consisted of protons that interacted with a target nucleus and carbon-nucleus protons to which the momentum transfer in the interaction with a primary proton was high.

For the degree of centrality of a pC interaction, we have taken the quantity Q defined as $Q = n_+ - n_- - n_p^{\mathrm{evap}}$, where n_+ and n_- are the numbers of positively and negatively charged particles in an event, respectively, while n_p^{evap} is the number of evaporated protons. The quantity Q is equal to the total charge of particles in an event that participate in the interaction actively. It correlates with the impact parameter of colliding nuclei (see Fig. 1). The degree of interaction centrality increases with increasing Q.

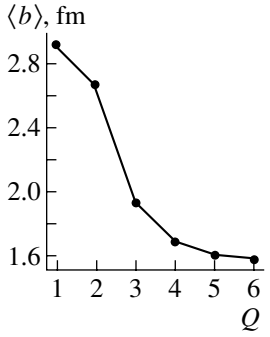

Fig. 1. Mean impact parameter $\langle b \rangle$ of pC interactions as a function of Q. Points represent the results of the calculations performed on the basis of the FRITIOF model with allowance for delta isobars (to guide the eye, the points are connected by a line).

2. MODIFIED FRITIOF MODEL

The FRITIOF model assumes a two-body kinematics of inelastic nucleon–nucleon interactions, $a + b \longrightarrow a' + b'$, where a' and b' are excited states of primary nucleons. An excited state is characterized by a mass. Within the modified FRITIOF model, the lower boundary of excited-nucleon masses, 1.1 GeV, and the mean square of the transverse momentum that colliding nuclei exchange, 0.15 (GeV/c)^2, were determined in fitting the features of np interactions over the momentum interval 1.25–5.1 GeV/c [13].

In the case of hadron–nucleus and nucleus–nucleus interactions, it is assumed that nucleons excited in primary collisions can interact both with one another and with other intranuclear nucleons and increase their mass. The probabilities of multiple collisions are calculated within the Glauber approach. In the present study, we have taken into account not only inelastic collisions of nucleons but also their elastic rescatterings by using a method that is similar to that in [14].

Excited hadrons are considered as QCD strings whose fragmentation yields hadrons.

In order to describe the disintegration of nuclei at the fast stage of interaction, the FRITIOF model was supplemented with the Reggeon model of nuclear disintegration [17]. At the first step, the number of nucleons that underwent inelastic interaction ("wounded"

[4)] Protons of momenta below 150 MeV/c are not recorded in the propane bubble chamber because of a short range (less than 2 mm). Their multiplicity was determined from the missing charge in an event.

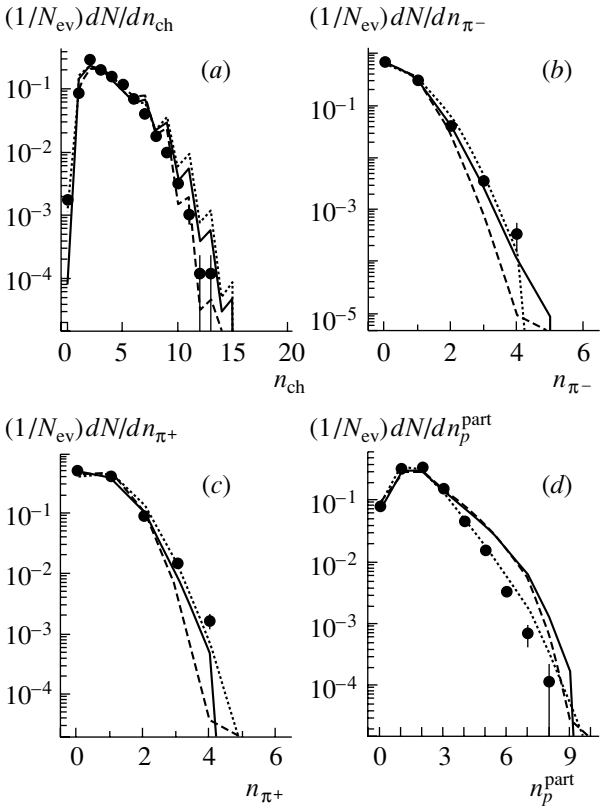

Fig. 2. Multiplicity distributions of (*a*) charged particles, (*b*) negatively charged pions, (*c*) positively charged pions, and (*d*) participant protons from *p*C interactions: (closed circles) experimental data; (solid and dashed curves) results of the calculations performed on the basis of the FRITIOF model, respectively, with and without allowance for Δ^+ and Δ^0 isobars; and (dotted curves) results of the calculations on the basis of the cascade–evaporation model.

ones) is determined within the Glauber approximation [18]. Noninteracted nucleons are considered at the second step. Such nucleons are involved in the Reggeon cascade with the probability

$$W = C_{nd}e^{-r^2/r_{nd}^2}, \quad C_{nd} = 1, \quad r_{nd} = 1.2 \text{ fm},$$

where r is the difference of the impact-parameter radius vectors of the nucleon initiating the interaction event being considered and a given involved nucleon. An involved nucleon can involve another spectator nucleon, and so on. It is assumed that all wounded and involved nucleons leave colliding nuclei. The relaxation of excited residual nuclei is simulated in terms of the evaporation model [19]. A more detailed description of the model used here can be found in [12, 14].

The model version described in [12, 14] yielded an underestimated multiplicity of negatively charged particles, especially in the region of target-nucleus fragmentation. In view of this, an attempt was made here to take into account nonnucleon degrees of freedom in nuclei.

There is no doubt that, in nuclei, nucleons can undergo virtual transitions of the $N \to N + \pi$ and $N + \pi \to N$ types. Upon suffering interaction with an incident hadron, virtual $N\pi$ pairs can approach the mass shell, becoming real. A calculation of the features of such processes, including their cross sections, would involve solving many problems in the theory of the nucleus; therefore, it cannot be fully performed at present. Moreover, it is necessary to consider the production of $N\pi$ pairs in the course of a Reggeon cascade. In order to obtain a qualitative insight into the processes in question, we therefore assumed that a wounded or an involved nucleon may become, with a probability of about 20%, a $N\pi$ pair. More specifically, we assumed that a proton or a neutron participating in the interaction may become, respectively, a Δ^+ or a Δ^0 isobar. From the point of view of the FRITIOF model, this is the simplest solution to the problem being discussed. It also removes the intricate question of the kinematical features of an $N\pi$ pair.[5)]

For the sake of completeness, a comparison of experimental data with the results of theoretical calculations was performed in terms of two versions of the modified FRITIOF model (with and without delta isobars) and in terms of the cascade–evaporation model [20].

3. MULTIPLICITY OF SECONDARIES FROM *p*C INTERACTIONS AT 4.2 GeV/*c*

Figure 2 gives an idea of the multiplicity distributions of various secondaries in *p*C interactions. The greatest number of charged particles recorded in *p*C interactions is 13; the greatest number of π^+ and π^- mesons is 4, while the greatest number of participant protons (with allowance for the charge-exchange processes $p \to n$ and $n \to p$) is 8. The number of *p*C events subjected to analysis and the mean multiplicities of secondaries for all *p*C interactions and for six groups of events characterized by specific values of the degree of centrality (as specified by the quantity Q) in each group are quoted in Table 1. One can see that peripheral interactions ($Q \leq 2$) constitute more than 70% of all inelastic *p*C interactions. The fraction of events that are characterized by the highest degree of centrality ($Q \geq 4$) is small (about a few percent). As a result, all *p*C interactions are characterized by a mean multiplicity of participant protons, $\left\langle n_p^{\text{part}} \right\rangle$, that is less than two. The mean multiplicity of positively

[5)] In the calculations, we disregarded the anisotropic decay of delta isobars.

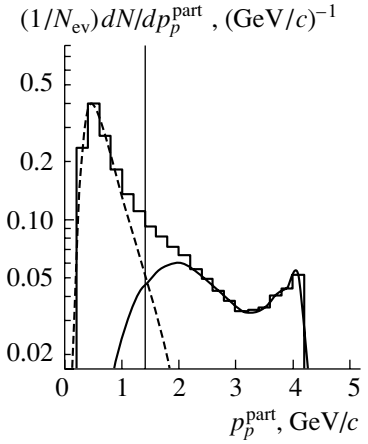

Fig. 3. Calculated momentum distributions of participant protons in pC interactions (histogram). The solid and the dashed curve represent, respectively, the contribution of surviving protons and the contribution of target protons. The vertical line indicates the optimum boundary between the spectra.

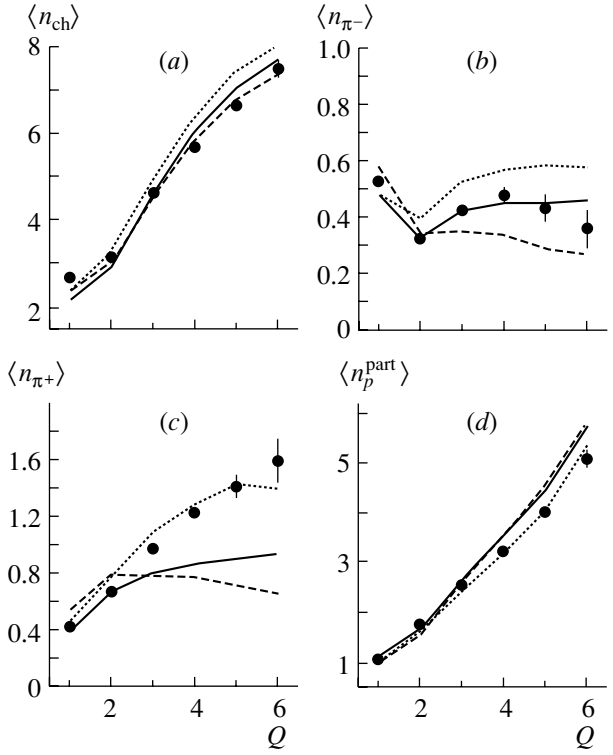

Fig. 4. Mean multiplicities of (*a*) charged particles, (*b*) negatively charged pions, (*c*) positively charged pions, and (*d*) participant protons versus Q. The notation for the points and curves is identical to that in Fig. 2.

charged pions, $\langle n_{\pi^+}\rangle$, considerably exceeds that of negatively charged pions, $\langle n_{\pi^-}\rangle$, and this is typical of proton interactions with symmetric nuclei [21].

As can be seen from Table 1, the mean multiplicities of positively and negatively charged pions in pC interactions exceed their counterparts in proton–nucleon collisions (in the case of a normalization to the total cross section for proton–nucleon interactions, σ_{pN}^{tot}, the relevant multiplicities in such collisions are $\langle n_{\pi^-}\rangle_{pN} = 0.31$ and $\langle n_{\pi^+}\rangle_{pN} = 0.51$) [22, 23]. A comparison of the mean multiplicities of pions in pC and pN collisions makes it possible to conclude that about 30% of negatively charged pions and about 40% of positively charged pions are formed in secondary interactions in the carbon nucleus involved.

The multiplicity of protons having momenta in excess of 1.4 GeV/c (see Table 1) is basically in agreement with the multiplicity of leading, most energetic, protons (primary protons after interaction). The choice of boundary between the momentum spectra of surviving and target protons was based on the FRITIOF model involving delta isobars. Within this model, we have determined the spectra of surviving protons and protons appearing as carbon-nucleus fragments. On the basis of these results, we have chosen the optimum boundary between the spectra at $p = 1.4$ GeV/c. For this choice, the mean multiplicity of leading protons that have momenta in the region $p < 1.4$ GeV/c and which are associated with the surviving projectile proton is $\langle n_p^{lead}\rangle_{p<1.4\ GeV/c} = 0.10$, while the multiplicity of leading protons that appear to be knock-on target protons is $\langle n_p^{tar}\rangle_{p>1.4\ GeV/c} = 0.09$. The momentum range between 0.3 and 1.0 GeV/c is populated predominantly by protons from the target nucleus. In the momentum range $1.0 < p < 1.8$ GeV/c, there is an overlap of target and surviving protons (see Fig. 3). Knowing the multiplicities and kinematical features of leading protons whose momenta take values in the region $p > 1.4$ GeV/c, one can in principle find the stopping power of carbon nuclei; we will address this problem in our next publication.

Let us now consider the mean multiplicities of secondaries versus the degree of centrality of pC collisions. The relevant dependences are illustrated in Table 1 and in Fig. 4. One can see that the mean multiplicities of all charged particles, positively charged pions, and participant protons increase considerably upon going over from peripheral to central interactions. At the same time, the mean multiplicity of negatively charged pions is only weakly sensitive to variations in Q. The greatest value of $\langle n_{\pi^-}\rangle$ is observed in $Q = 1$ events, while its smallest value is realized in $Q = 2$ events. This is because $Q = 1$ events are predominantly proton–neutron interactions ($\langle n_{\pi^-}\rangle_{pn} = 0.43$ [22]), while $Q = 2$ events are proton–proton in-

Table 1. Mean multiplicities of secondaries from pC interactions at 4.2 GeV/c versus the degree of collision centrality (the calculation based on the FRITIOF model was performed with allowance for delta isobars)

Q		N_{ev} (%)	$\langle n_{ch}\rangle$	$\langle n_{\pi^-}\rangle$	$\langle n_{\pi^+}\rangle$	$\langle n_p^{part}\rangle$	$\langle n_p^{part}\rangle$, $0.3 < p \le 0.75$ GeV/c	$\langle n_p^{part}\rangle$, $p > 1.4$ GeV/c	$\langle n_p^{evap}\rangle$, $0.15 < p \le 0.3$ GeV/c	$\langle n_p^{evap}\rangle$, $p < 0.15$ GeV/c
1	Expt.	2289 (27.3)	2.72 ± 0.08	0.522 ± 0.013	0.416 ± 0.010	1.054 ± 0.015	0.241 ± 0.009	0.588 ± 0.020	0.732 ± 0.020	5.32 ± 0.02
	FRITIOF	28457 (28.4)	2.152 ± 0.008	0.479 ± 0.004	0.379 ± 0.003	1.088 ± 0.005	0.114 ± 0.002	0.785 ± 0.006	0.206 ± 0.004	5.800 ± 0.003
2	Expt.	3814 (45.6)	3.15 ± 0.02	0.321 ± 0.007	0.660 ± 0.008	1.743 ± 0.010	0.584 ± 0.009	0.740 ± 0.018	0.425 ± 0.013	0.49 ± 0.01
	FRITIOF	37635 (37.6)	2.926 ± 0.007	0.321 ± 0.003	0.662 ± 0.004	1.658 ± 0.004	0.454 ± 0.003	0.794 ± 0.005	0.284 ± 0.004	4.716 ± 0.003
3	Expt.	1477 (17.6)	4.70 ± 0.04	0.423 ± 0.016	0.965 ± 0.020	2.526 ± 0.024	1.212 ± 0.024	0.664 ± 0.027	0.779 ± 0.026	3.15 ± 0.03
	FRITIOF	16675 (16.7)	4.594 ± 0.014	0.424 ± 0.005	0.787 ± 0.006	2.624 ± 0.007	1.219 ± 0.006	0.712 ± 0.007	0.759 ± 0.009	3.255 ± 0.009
4	Expt.	575 (6.9)	5.73 ± 0.07	0.476 ± 0.027	1.22 ± 0.04	3.22 ± 0.04	1.84 ± 0.05	0.57 ± 0.04	0.82 ± 0.04	2.22 ± 0.05
	FRITIOF	9551 (9.6)	6.00 ± 0.02	0.448 ± 0.006	0.857 ± 0.008	3.54 ± 0.01	2.03 ± 0.01	0.62 ± 0.01	1.15 ± 0.01	1.89 ± 0.01
5	Expt.	164 (2.0)	6.72 ± 0.12	0.43 ± 0.05	1.40 ± 0.08	4.02 ± 0.09	2.61 ± 0.10	0.47 ± 0.06	0.87 ± 0.03	1.15 ± 0.01
	FRITIOF	5166 (5.2)	6.96 ± 0.02	0.45 ± 0.01	0.89 ± 0.01	4.46 ± 0.02	2.89 ± 0.02	0.54 ± 0.01	1.16 ± 0.01	0.94 ± 0.01
6	Expt.	52 (0.6)	7.60 ± 0.20	0.36 ± 0.07	1.58 ± 0.16	5.10 ± 0.18	3.39 ± 0.21	0.56 ± 0.11	0.56 ± 0.08	0.11 ± 0.15
	FRITIOF	2516 (2.5)	7.71 ± 0.03	0.46 ± 0.01	0.93 ± 0.02	5.75 ± 0.03	4.17 ± 0.03	0.44 ± 0.01	0.57 ± 0.01	0.21 ± 0.01
All	Expt.	8371 (100)	3.61 ± 0.02	0.407 ± 0.006	0.706 ± 0.007	1.860 ± 0.010	0.747 ± 0.009	0.668 ± 0.010	0.640 ± 0.009	4.20 ± 0.02
events	FRITIOF	100 000 (100)	3.627 ± 0.007	0.406 ± 0.002	0.640 ± 0.002	2.085 ± 0.004	0.855 ± 0.004	0.739 ± 0.003	0.476 ± 0.003	4.204 ± 0.006

Table 2. Ratios $\langle n_\pi^\pm \rangle / \langle n_p^{\text{part}} \rangle$ in pC interactions at 4.2 GeV/c versus Q (the calculation based on the FRITIOF model was performed with allowance for delta isobars)

Q	$\langle n_{\pi^-} \rangle / \langle n_p^{\text{part}} \rangle$		$\langle n_{\pi^+} \rangle / \langle n_p^{\text{part}} \rangle$	
	expt.	FRITIOF	expt.	FRITIOF
1	0.495 ± 0.014	0.440 ± 0.005	0.395 ± 0.012	0.348 ± 0.004
2	0.184 ± 0.007	0.194 ± 0.002	0.379 ± 0.006	0.399 ± 0.003
3	0.167 ± 0.006	0.162 ± 0.002	0.382 ± 0.008	0.299 ± 0.003
4	0.148 ± 0.009	0.126 ± 0.002	0.378 ± 0.012	0.242 ± 0.003
5	0.108 ± 0.012	0.101 ± 0.003	0.349 ± 0.020	0.200 ± 0.003
6	0.070 ± 0.014	0.080 ± 0.002	0.310 ± 0.032	0.162 ± 0.004
All events	0.219 ± 0.004	0.195 ± 0.001	0.380 ± 0.004	0.307 ± 0.001

teractions ($\langle n_{\pi^-} \rangle_{pp} = 0.18$ [23]). This is suggested by peaks at odd values of n_{ch} in the multiplicity distributions of charged particles in $Q = 1$ events and, accordingly, peaks at even n_{ch} in the corresponding distributions for $Q = 2$ events (see Fig. 5). In $Q \geq 3$ events, the mean multiplicity of negatively charged pions is nearly invariable, while the mean multiplicity of positively charged pions continues growing and exceeds significantly that which is observed in peripheral interactions (see Table 1 and Fig. 4). The effect of the positive charge of a primary proton can be traced in all groups with respect to Q, with the exception of the $Q = 1$ group (only in this group do we have $\langle n_{\pi^+} \rangle < \langle n_{\pi^-} \rangle$). We note that, at 4 GeV/c, the cross section for the reaction $pp \to pn\pi^+$, σ_1, exceeds the cross section for the reaction $pn \to pp\pi^-$, σ_2, by a factor of 3 [23]. As the momentum of the primary proton decreases in the course of the interaction with the carbon nucleus, this excess becomes more pronounced (σ_1 increases significantly, while σ_2 decreases slowly [23]). In this way, one can explain the fact that the mean multiplicies $\langle n_{\pi^-} \rangle$ and $\langle n_{\pi^+} \rangle$ depend differently on Q.

Let us consider the effect of the degree of centrality of pC interactions on the mean multiplicities of slow protons appearing as target protons ($0.3 < p \leq 0.75$ GeV/c) and of fast protons ($p > 0.75$ GeV/c). The smallest value of $\langle n_p^{\text{part}} \rangle$ for momenta in the range $0.3 < p \leq 0.75$ GeV/c is observed in $Q = 1$ events (see Table 1), which, as was indicated above, result predominantly from the interaction of a primary proton with a carbon neutron. With increasing Q, the multiplicity of target protons grows—an ever greater number of carbon-nucleus nucleons is involved in the interaction process. Concurrently, the multiplicity of evaporated protons naturally decreases—in particular, the multiplicity of protons whose momenta do not exceed 150 MeV/c decreases to zero in $Q \geq 6$ events. The multiplicity of target protons with momenta in the region $p > 0.75$ GeV/c ($\langle n_p^{\text{part}} \rangle - \langle n_p^{\text{part}}(0.3 < p \leq 0.75 \text{ GeV}/c) \rangle - \langle n_p^{\text{lead}}(p > 1.4 \text{ GeV}/c) \rangle$) also grows with increasing Q. This occurs owing to an increase in the fraction of target protons to which the momentum transfer in a collision with an incident proton was high. Over the entire range of Q values, the mean multiplicity of leading protons takes values at a level of 0.6 to 0.7.

On the basis of data presented for $\langle n_{\pi^-} \rangle$, $\langle n_{\pi^+} \rangle$, and $\langle n_p^{\text{part}} \rangle$ at various values of Q, we have determined the ratios $\langle n_{\pi^\pm} \rangle / \langle n_p^{\text{part}} \rangle$ and obtained the dependences of these ratios on Q (see Table 2). As can be seen, the mean multiplicity of negatively charged pions per average participant proton from pC interactions at 4.2 GeV/c decreases considerably (by a factor of 7) upon going over from peripheral to central collisions. This suggests that, with increasing Q, the fraction of secondary interactions resulting in the production of negatively charged pions decreases. At the same time, the ratio $\langle n_{\pi^+} \rangle / \langle n_p^{\text{part}} \rangle$ proved to be less sensitive to variations in Q (see Table 2). A decrease in this ratio over the corresponding interval of Q is about 20%. This is quite clear since the mean multiplicity of positively charged pions increases with Q nearly in direct proportion to the increase in the mean multiplicity of participant protons with increasing Q, but this is not so for the mean multiplicity of negatively charged pions.

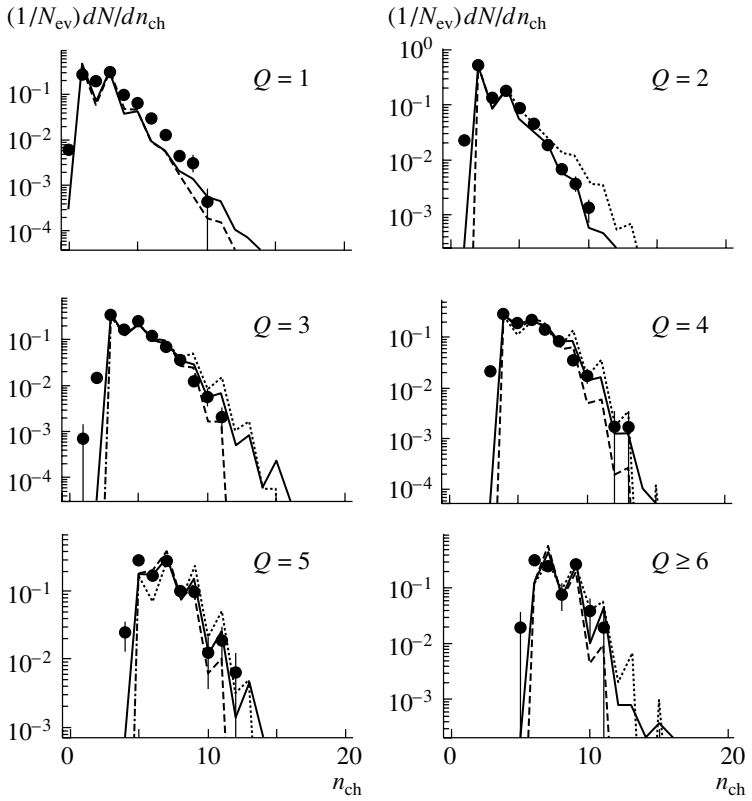

Fig. 5. Multiplicity distribution of charged particles from pC interactions at various values of Q. The notation for the points and curves is identical to that in Fig. 2.

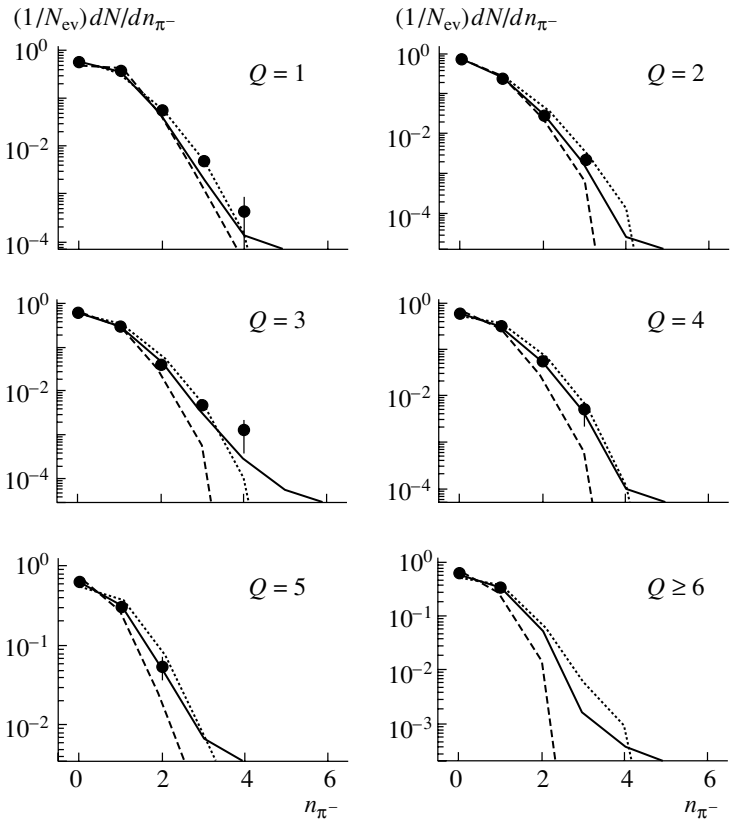

Fig. 6. Multiplicity distribution of negatively charged pions from pC interactions at various values of Q. The notation for the points and curves is identical to that in Fig. 2.

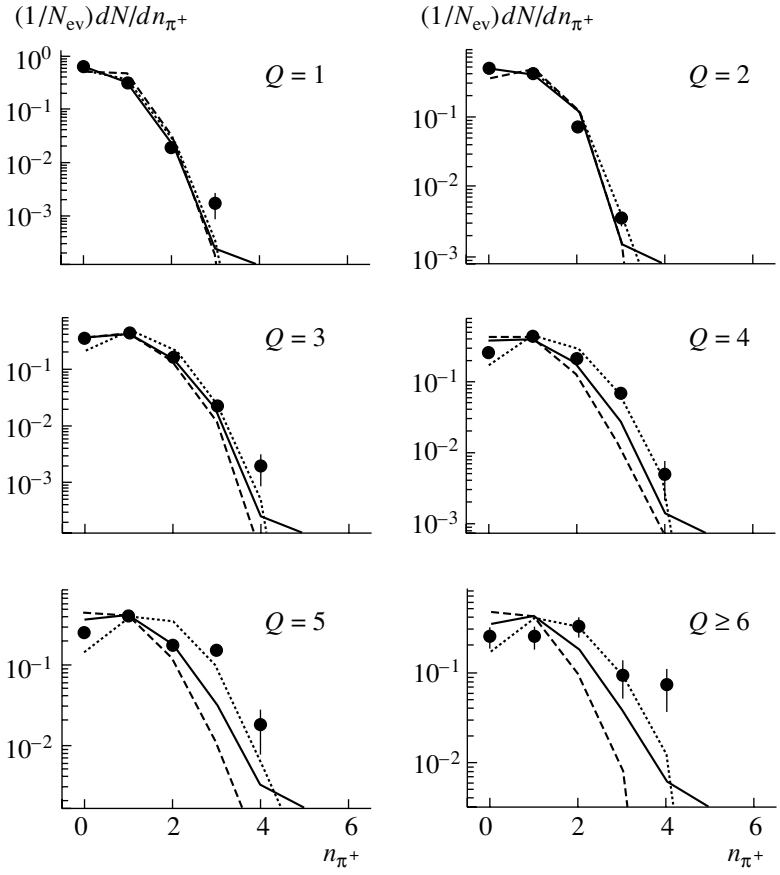

Fig. 7. Multiplicity distribution of positively charged pions from pC interactions at various values of Q. The notation for the points and curves is identical to that in Fig. 2.

The FRITIOF model taking into account Δ^+ and Δ^0 isobars satisfactorily reproduces experimental data on $\langle n_{\pi^-}\rangle/\langle n_p^{\text{part}}\rangle$. A comparison of experimental data on the mean multiplicities of secondaries with the results of the calculations based on the FRITIOF model revealed that the model is able to describe satisfactorily the mean multiplicities of all charged particles, negatively charged pions, and participant protons not only for the entire ensemble of pC interactions but also for their individual groups (see Table 1). The calculated values of $\langle n_{\pi^+}\rangle$ agree with their experimental counterparts only for peripheral interactions. The cascade model satisfactorily reproduces the Q dependences of $\langle n_{\pi^+}\rangle$ and $\langle n_p^{\text{part}}\rangle$, but it overestimates the multiplicity of negatively charged pions. If Δ^+ and Δ^0 isobars are not included in the FRITIOF model, it leads to underestimated values of $\langle n_{\pi^-}\rangle$ (see Fig. 4).

In addition to the Q dependences of the mean multiplicities of secondaries, we have also obtained the distributions of pC-interaction events with respect to the multiplicity n_{ch} of charged particles (Fig. 5), the multiplicities of negatively and positively charged pions (Figs. 6 and 7, respectively), the multiplicity n_p^{part} of participant protons (Fig. 8), and the multiplicity n_p^{evap} of evaporated protons (Fig. 9) for individual groups specified by Q values. Figures 5–9 give a clear idea of the effect that the degree of centrality of pC interactions exerts on the shapes of the distributions being studied. By way of example, we indicate that, with increasing Q, the maximum in the distributions with respect to n_{ch} is shifted toward greater values of n_{ch}, the distribution itself becoming narrower. The distributions with respect to n_{ch} proved to be unexpectedly broad for peripheral interactions ($Q = 1, 2$)—they feature multiprong events. An analysis of such events revealed that the increase in the number of particles in them is due to evaporated protons having momenta in the range 0.15–0.3 GeV/c and originating from the deexcitation of carbon-nucleus residues (see Fig. 9). It follows that, in some peripheral pC interactions, there occurs, in addition to proton–nucleon collisions producing pions (Figs. 6, 7), a significant excitation of the target nucleus. As Q becomes greater, the multiplicity of charged particles in pC events is determined to an ever greater extent by the number of target pro-

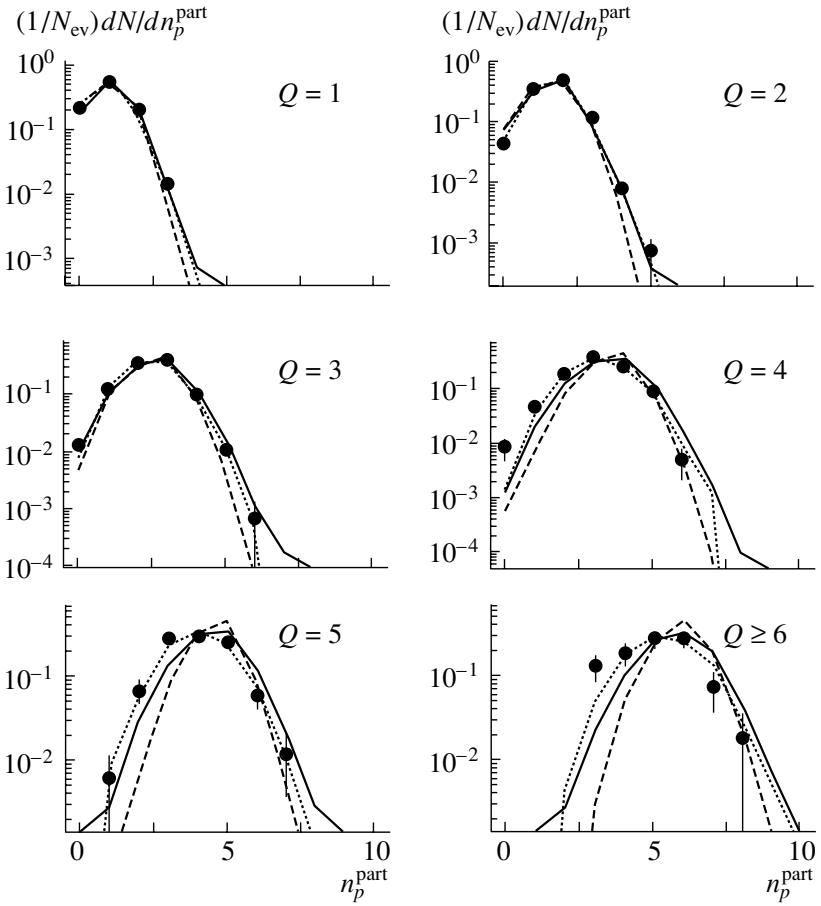

Fig. 8. Multiplicity distribution of participant protons from pC interactions at various values of Q. The notation for the points and curves is identical to that in Fig. 2.

tons involved in the interaction process. The excited carbon-nucleus residue survives until $Q \geq 6$ events occur (see Table 1 and Fig. 9). We note that the FRITIOF model (both versions) describes satisfactorily the distributions given in Fig. 5.

Figure 6 shows that a significant fraction (up to 70%) of pC events in all groups do not involve negatively charged pions. Along with this feature, the presence of two or three negatively charged pions for $Q \leq 4$ is worthy of note. Events characterized by maximum multiplicities of negatively and positively charged pions at a minimum multiplicity of participant protons also contribute to the number of events where the multiplicity of charged particles is high. With decreasing primary-proton momentum, the cross section for the reaction $pn \to pp\pi^-$ decreases (see above), which is manifested in the reduction of the number of $n_{\pi^-} \geq 2$ events (see Fig. 6 at $Q = 5$ and $Q \geq 6$).

The fraction of events featuring no positively charged pions is maximal among peripheral interactions. At greater values of Q, the set of pC interactions is enriched in events where the multiplicity of positively charged pions is not less than two (see Fig. 7). This is due to a sharp growth of the cross section for the reaction $pp \to pn\pi^+$ with decreasing momentum of the proton interacting with a target proton.

The distribution of pC-interaction events with respect to the multiplicity of negatively charged pions is well described by the FRITIOF model taking into account the production of Δ^+ and Δ^0 isobars in a carbon nucleus (see Fig. 6). The same applies to the description of the distributions of pC-interaction events with respect to the multiplicity of positively charged pions in the $Q \leq 3$ groups. More central interactions are better described by the cascade model [20].

A feature peculiar to the Q dependence of the distributions of pC-interaction events with respect to the multiplicity of participant protons is that the maximum in these distributions is shifted toward greater values of n_p^{part} with increasing Q (see Fig. 8). This phenomenon is due to an increase in the multiplicity of participant protons from the target as we go over

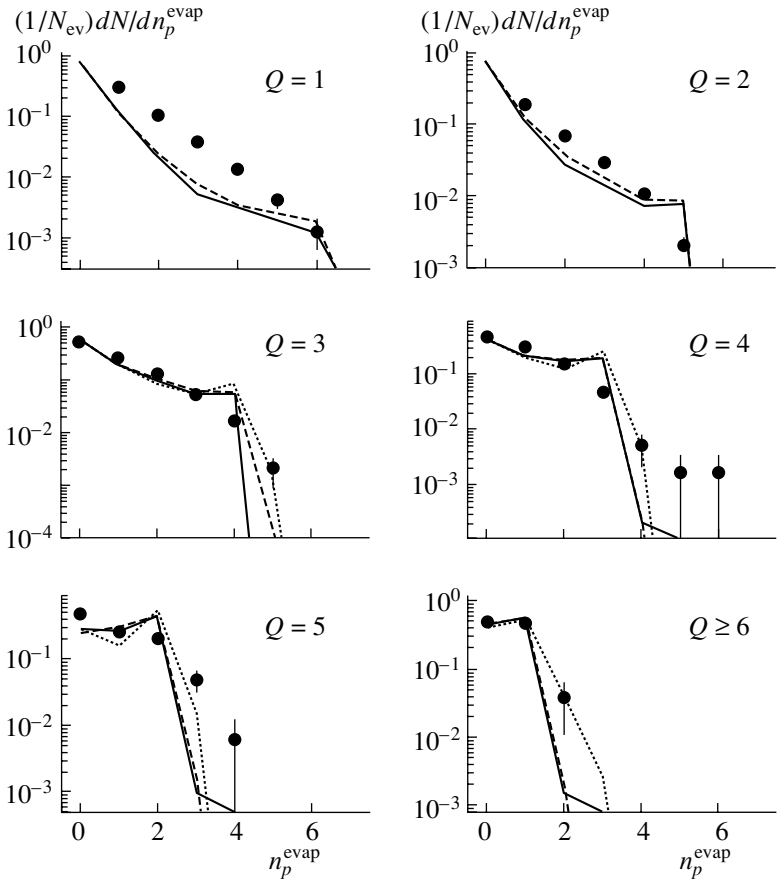

Fig. 9. Multiplicity distribution of evaporated protons from pC interactions at various values of Q. The notation for the points and curves is identical to that in Fig. 2.

from peripheral to central pC interactions. Both versions of the FRITIOF model and the cascade model describe satisfactorily the experimental distributions with respect to the multiplicity of participant protons.

It would be of interest to find out which mechanism of pC interaction is responsible for the disintegration of a carbon nucleus at the fast stage of the interaction. This may be a Reggeon cascade that was proposed in [17] and which develops through the involvement in it of nucleons that did not participate in the interaction at the first step of a collision between a proton and a carbon nucleus. The multiplicity of nucleons involved that was estimated on the basis of the FRITIOF model with allowance for delta isobars is about 30% of the mean multiplicity of protons having momenta in the range between 0.3 and 1.4 GeV/c. In $Q \geq 5$ events, $\langle n_p^{inv} \rangle$ may be as large as 50 to 60% of $\langle n_p^{tar} \rangle$. If the number of wounded nucleons is taken to be equal to the number of collisions between the primary proton and the target-nucleus nucleons, then we arrive at a reasonable idea of the spacetime picture of pC interactions.

4. CONCLUSIONS

(i) New experimental data on the multiplicities of charged pions and protons from the interactions of 4.2-GeV/c protons with carbon nuclei have been presented versus the parameter Q, which correlates with the impact parameter of colliding nuclei.

(ii) With increasing degree of the centrality of a collision between a proton and a carbon nucleus, the total multiplicity of charged particles grows significantly owing to an increase in the multiplicity of positively charged pions and participant protons from the target nucleus; concurrently, the multiplicity of negatively charged pions remains virtually unchanged, while the mean multiplicity of evaporated protons having momenta below 0.15 GeV/c decreases sharply (nearly down to zero).

(iii) In peripheral pC interactions ($Q = 1, 2$), there occurs target-nucleus excitation, which results in the emission of slow protons having momenta up to 0.3 GeV/c.

(iv) It has been shown that the cascade–evaporation model significantly overestimates the multiplicity

of negatively charged pions in multinucleon collisions in relation to experimental data and that the FRITIOF model underestimates it if no account is taken of nonnucleon degrees of freedom in nuclei.

(v) Upon taking into account Δ^+ and Δ^0 isobars, the experimental features of secondaries are satisfactorily described within the FRITIOF model.

ACKNOWLEDGMENTS

We are grateful to the technical staff for viewing relevant films and for measuring events and to the members of a collaboration involved in investigations at the 2-m propane bubble chamber for placing the required experimental data at our disposal.

This work was supported in part by the Russian Foundation for Basic Research (project nos. 00-01-00307, 01-02-16407, 01-02-16431) and by INTAS (grant no. 00-00366).

REFERENCES

1. G. N. Agakishiev *et al.*, Yad. Fiz. **40**, 1209 (1984) [Sov. J. Nucl. Phys. **40**, 767 (1984)]; Z. Phys. C **27**, 177 (1985).
2. D. Armutliĭskiĭ *et al.*, Yad. Fiz. **45**, 1047 (1987) [Sov. J. Nucl. Phys. **45**, 649 (1987)]; D. Armutliiski *et al.*, Z. Phys. A **328**, 455 (1987).
3. G. N. Agakishiev *et al.*, Yad. Fiz. **49**, 481 (1989) [Sov. J. Nucl. Phys. **49**, 300 (1989)].
4. A. I. Bondarenko, R. A. Bondarenko, and E. N. Kladnitskaya, Yad. Fiz. **60**, 2004 (1997) [Phys. At. Nucl. **60**, 1833 (1997)].
5. A. I. Bondarenko *et al.*, Yad. Fiz. **62**, 1612 (1999) [Phys. At. Nucl. **62**, 1513 (1999)].
6. S. Batskovich *et al.*, Yad. Fiz. **56** (4), 211 (1993) [Phys. At. Nucl. **56**, 540 (1993)].
7. G. N. Agakishiev *et al.*, Yad. Fiz. **56** (10), 170 (1993) [Phys. At. Nucl. **56**, 1397 (1993)].
8. G. N. Agakishiev *et al.*, Yad. Fiz. **51**, 1591 (1990) [Sov. J. Nucl. Phys. **51**, 1004 (1990)].
9. R. J. Glauber, *Lectures in Theoretical Physics*, Ed. by W. E. Brittin *et al.* (Interscience, New York, 1959), Vol. 1.
10. B. Andersson *et al.*, Nucl. Phys. B **281**, 289 (1987).
11. B. Nilsson-Almquist and E. Stenlund, Comput. Phys. Commun. **43**, 387 (1987).
12. EMU-01 Collab. (M. I. Adamovich *et al*), Z. Phys. A **358**, 337 (1997).
13. B. Gankhuyag and V. V. Uzhinskiĭ, Reports JINR Nos. R1-97-315, R2-97-397 (Dubna, 1997).
14. A. I. Bondarenko *et al.*, Reports JINR No. R1-2000-138 (Dubna, 2000); Yad. Fiz. **65**, 95 (2002) [Phys. At. Nucl. **65**, 90 (2002)].
15. O. Kofoed-Hansen, Nucl. Phys. B **39**, 42 (1972).
16. A. I. Bondarenko *et al.*, Reports JINR No. R1-98-292 (Dubna, 1998).
17. Kh. El-Waged and V. V. Uzhinskii, Yad. Fiz. **60**, 925 (1997) [Phys. At. Nucl. **60**, 828 (1997)].
18. S. Yu. Shmakov, V. V. Uzhinski, and A. M. Zadorojny, Comput. Phys. Commun. **54**, 125 (1989).
19. V. Weisskopf, Phys. Rev. **52**, 295 (1937).
20. V. S. Barashenkov, F. Zh. Zheregi, and Zh. Zh. Musul'manbekov, Preprint No. R2-83-117, JINR (Dubna, 1983).
21. T. Abbott *et al.*, Phys. Rev. Lett. **66**, 1567 (1991).
22. K. Beshliu *et al.*, Yad. Fiz. **43**, 888 (1986) [Sov. J. Nucl. Phys. **43**, 565 (1986)].
23. V. Flamino *et al.*, Preprint No. 79-03, CERN-HERA (Geneva, 1979).

Translated by A. Isaakyan

Physics of Atomic Nuclei, Vol. 66, No. 5, 2003, pp. 847–853. Translated from Yadernaya Fizika, Vol. 66, No. 5, 2003, pp. 879–885.

ELEMENTARY PARTICLES AND FIELDS
Experiment

Nuclear Composition of 1- to 20-PeV Primary Cosmic Rays According to Lateral Features of the Electron–Photon Component of All Extensive Air Showers and of Extensive Air Showers Accompanying High-Energy Gamma Rays and Hadrons in X-Ray Emulsion Chambers at the Tien Shan Level

N. M. Nesterova, V. P. Pavlyuchenko, A. P. Chubenko, and S. B. Shaulov

Lebedev Institute of Physics, Russian Academy of Sciences, Leninskii pr. 53, Moscow, 117924 Russia

Received January 29, 2002; in final form, June 10, 2002

Abstract—Data from the Tien Shan array Adron on the dependence of the lateral distributions of the electron–photon component (age parameter S) in extensive air showers of cosmic rays on the number of electrons, N_e, which is a quantity that characterizes the primary-nucleus energy E_0, are subjected to a comparative analysis. The distributions in question are given both for all showers and for showers accompanying high-energy gamma rays and hadrons in x-ray emulsion chambers. According to calculations, events associated with the latter are generated predominantly by primary protons, and this makes it possible to assess their role at various values of E_0. The distributions with respect to S suggest a significant fraction of light nuclei, predominantly protons, in the region after the knee in the spectrum for $N_e > 10^6$, at least up to $N_e = 5.6 \times 10^6$ ($E_0 \sim 10$ PeV). © *2003 MAIK "Nauka/Interperiodica".*

One of the main problems in the physics of cosmic rays at primary energies in the range 0.1–100 PeV is that of clarifying the reasons behind the change in the shape of the spectra of various components of extensive air showers—that is, the presence of the so-called knee in these spectra (a change in the exponent appearing in a power-law approximation of the spectra). A knee of this type was observed predominantly in the spectra of extensive air showers with respect to the number of electrons; it was recorded by many arrays, including those at the Moscow State University [1] and at Tien Shan [2]. The most comprehensive compilation of data on the knee and a detailed analysis of these data can be found in [3]. A knee is also obtained upon rescaling data to the energy of primary cosmic radiation on the basis of standard models—it occurs in the region around $E_0 \cong 3$ PeV. In a number of studies (see, for example, [4, 5]), the presence of a knee is explained in terms of a change in the nuclear composition of primary cosmic radiation according to the diffusion model, where it is stated that, as the energy of cosmic radiation becomes higher, its nuclear composition is depleted first in protons at an energy of a few PeV and then in other nuclear species at higher energies (in accordance with magnetic rigidity). This must lead to a considerable increase in the fraction of heavy nuclei at an energy of about 10 PeV. An analysis of experimental data on extensive air showers recorded by various arrays that was performed with the aim of revealing variations in the nuclear composition of primary cosmic radiation after the knee has not yet yielded a definitive result, albeit many authors of experimental studies devoted to extensive air showers believe that their data suggest that this nuclear composition becomes "heavier" after the knee. An alternative explanation of the change in the spectrum is based on the assumption that primary cosmic radiation receives an additional contribution from nuclei generated by a close cosmic source [3]. In [6], the presence of a knee is explained by a change in the character of the interaction between cosmic-ray radiation with nuclei of air atoms rather than by a change in the composition of primary cosmic radiation.

The lateral distribution of electrons at the observation level reflects the stage of the longitudinal development (age parameter S) of a shower, this stage being dependent on the charge number of the primary-cosmic-radiation nucleus and on the features of its interaction with nuclei of air atoms. Since the electron–photon components of extensive air showers initiated by light and by heavy nuclei develop differently in the atmosphere, their lateral distributions must also be different (under standard assumptions on the interaction). It should be recalled here that "young" extensive air showers (those that are characterized by smaller values of S) are generated predominantly by primary protons, albeit

1063-7788/03/6605-0847$24.00

Various features of S versus N_e

$N_e, 10^{-5}$	$\langle S\rangle$	$\sigma(S_{\text{expt}})$	$\sigma(S)$	$\sigma(S)/\langle S\rangle$
5.6–10	0.88	0.13	0.080	0.11
10–18	0.84	0.12	0.085	0.12
18–32	0.81	0.12	0.089	0.13
32–56	0.79	0.12	0.093	0.14
56–100	0.77	0.12	0.092	0.14
100–180	0.75	0.13	0.089	0.14
180–320	0.77	0.14	0.115	0.17

such showers have a rather broad distribution with respect to S because of significant fluctuations; at the same time, "old" extensive air showers (those that are characterized by greater values of S) are generated by heavy nuclei because of a faster development of the relevant cascade in the atmosphere. In a number of recent studies, this property, combined with various features of other components of extensive air showers, has been employed to estimate the composition of primary cosmic radiation. The total number of electrons, N_e, in an extensive air shower that was used to perform a classification of events is proportional to $E_0^{0.9}$, and this fact makes it possible to study changes in relevant processes with increasing energy of primary cosmic radiation.

At the Tien Shan multipurpose array Adron (690 g cm^{-2}) [2, 7], experimental data on the lateral distributions of the electron–photon component of extensive air showers and on its distributions with respect to S were obtained over a few intervals of the number N_e of electrons from 5.6×10^5 to 3.2×10^7 ($E_0 = 1$–50 PeV). The fluxes of the electron–photon component of extensive air showers were recorded at distances of 1 to 120 m from the axis with the aid of a multichannel system consisting of 130 scintillation detectors arranged in 46 groups at distances of up to 80 m from the array center (see Fig. 1). Each of 37 main groups contained three detectors of dimensions $0.5 \times 0.5 \times 0.05$ or $1.0 \times 1.0 \times 0.05$ m^3, and this made it possible to test the readings of individual detectors by comparing them with those of the neighboring ones. The parameters of the electron–photon component (the coordinates of the axis, x and y, and the zenith and azimuthal angles of its inclination, N_e and S) were determined by using the readings of the scintillation detectors [2]. The angles of inclination of the extensive-air-shower axis were found from the delay of signals in the scintillation detectors at a distance of 20 m from the array center with the aid of the Khronotron nanosecond system.

In order to observe high-energy gamma-ray and hadronic families, six rows of x-ray emulsion chambers interspersed with lead and carbon absorbers and four rows of ionization chambers were placed at the center of the array over an area of 160 m^2. For events in the x-ray emulsion chambers, their energies and coordinates were determined and then contrasted against the readings of the ionization chambers, whereupon they were associated with specific extensive air showers [8].

For various intervals in N_e for the energies of primary cosmic radiation in the range $E_0 = 1$–20 PeV, the distributions with respect to S were obtained both for all extensive air showers and for individual showers featuring high-energy gamma rays and hadrons recorded in the x-ray emulsion chambers. According to model calculations, showers of the latter type are generated predominantly by protons and light nuclei [9, 10]. Lateral distributions of electrons in extensive air showers are usually approximated by the calculated Nishimura–Kamata–Greisen (NKG) functions with various age parameters S depending on the steepness of their slump with increasing distance from the shower axis. In [11] and in some other studies, it was shown that, at various observation levels, lateral distributions obtained from experimental data correspond to S values that are less than those corresponding to calculations of the NKG type. The results of more recent calculations of lateral distributions approached experimental data (see, for example, [12]). In view of this, the NKG value of S was used here as a formal parameter in performing a comparison with other data in describing the lateral distributions of the electron–photon component of extensive air showers. For distances up to 120 m and zenith angles in the range 0°–30° with respect to the vertical direction ($\langle P\rangle = 720$ g cm^{-2}), where these lateral distributions were measured, they are well described by the NKG functions. It should be emphasized that, in processing data from the Adron experiment, the age parameter S was determined via approximating the lateral distributions obtained on the basis of scintillation-detector readings, S_{sc}, in each individual shower. In contrast to what was done in analyzing the previous data in [13], we did not eliminate here the photon contribution to scintillation-detector readings from the outset. In order to eliminate it, we later performed a calibration by using gas-discharge counters and thin scintillation detectors and compared the results being discussed with the readings of ionization chambers arranged under the central group of scintillation detectors. In order to extend the range of detection of the particle-flux density and to perform a calibration of extensive air showers characterized by N_e values up to 3×10^7, gas-discharge counters of small area were installed at various distances from the array center. According to the calculations performed in [12], the photon-detection efficiency becomes significantly lower as the scintillator thickness is reduced. In order to perform a

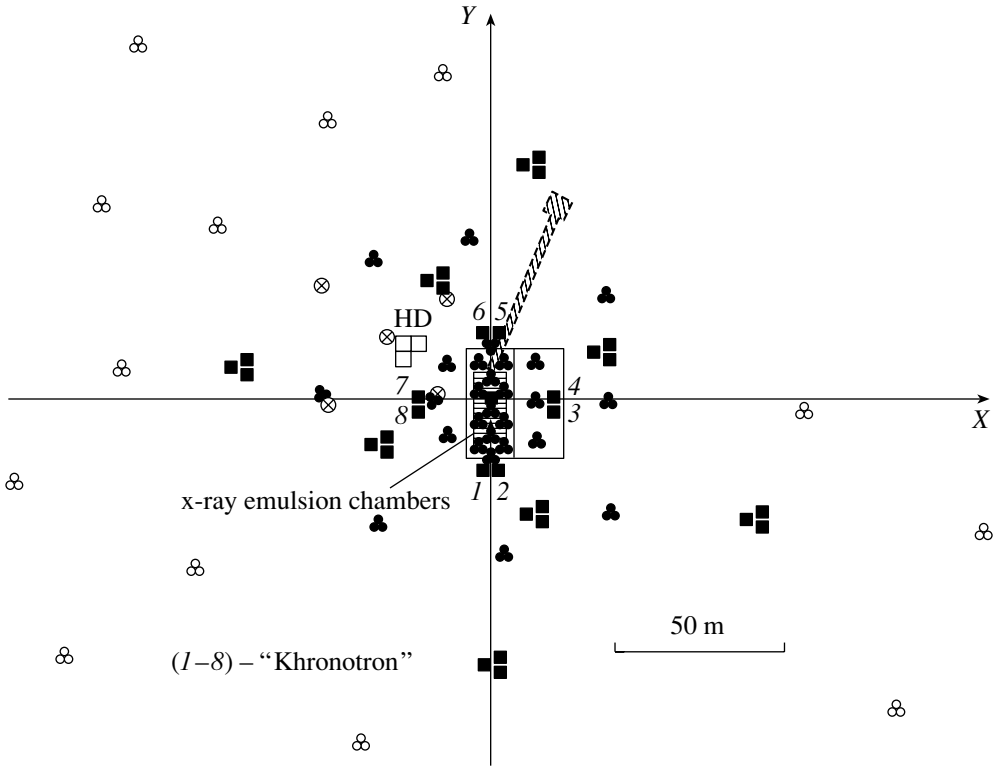

Fig. 1. Arrangement of detectors at the Tien Shan array Adron: (closed circles and boxes) scintillation detectors of area 0.25 and 1 m^2, respectively; (open circles) newly deployed scintillation detectors; (horizontal shading) x-ray emulsion chambers; (inclined shading) muon detector; (HD) neutron monitor (it will be used in future measurements); and (circumscribed inclined crosses) scintillation detectors for controlling HD.

calibration, scintillators of thickness 1.0 and 1.8 cm were therefore positioned near conventional scintillators of thickness 5.0 cm. On the basis of a comparison of the readings of all counters, we were able to establish, for a purely electron cascade (without a photon contribution), the S_{sc} dependence of S for our array. The results of experimental-data processing were obtained with the aid of the Space basic package [14] and were tested by using other codes—such as Q100 [15] and Nelde-Mid (A.P. Chubenko, O.M. Efimova)—that yielded close mean values of S_{sc} and close distributions with respect to S_{sc}, with somewhat different tails, however, the distributions at $S_{sc} = 0.5$–0.8 being shifted by $+0.05$. As a result, we found, taking calibration into account, that $S = S_{sc} + 0.15$ according to Space and that, to within ± 0.02, $S = S_{sc} + 0.10$ according to Q100.

The distributions with respect to S (S_{sc}) were obtained for all extensive air showers within various intervals of N_e (Fig. 2). Figure 2*a* shows such distributions for N_e values in the ranges $(5.6$–$10.0) \times 10^5$, $(10.0$–$17.8) \times 10^5$, and $(56$–$100) \times 10^5$, while Fig. 2*b* displays those for $(56$–$100) \times 10^5$ (this fragment of Fig. 2*a* is repeated for the sake of comparison), $(100$–$178) \times 10^5$, and $(178$–$316) \times 10^5$ (the errors given in Fig. 2 are purely statistical). From these figures, it can be seen that the fraction of extensive air showers characterized by small values of S (young extensive air showers) increases monotonically as N_e increases from 5.6×10^5 to 1.8×10^7. By way of example, we indicate that the contribution of $S < 0.75$ ($S_{sc} < 0.6$) extensive air showers increases from 15 to 43%, while the contribution of $S > 0.95$ ($S_{sc} > 0.8$) extensive air showers decreases from 29 to 7% over this range of N_e. The fraction of old extensive air showers characterized by $S > 1.2$ is very small.

We note that, at the old Tien Shan array, the corresponding reduction of S was observed for extensive air showers having smaller values of N_e (5×10^3–4.8×10^5) [6, 16]. With increasing N_e, the mean value $\langle S \rangle$ decreased monotonically, but this decrease became slower in the region $N_e > 5.6 \times 10^6$. Since the statistical accuracy is insufficient in the processed data sample for the interval $N_e = (1.8$–$3.2) \times 10^7$, we are unable to answer the question of whether this trend persists there.

However, a treatment of extensive air showers of ultrahigh energies [2] with $N_e > 3 \times 10^8$ according to different algorithms revealed that approximately

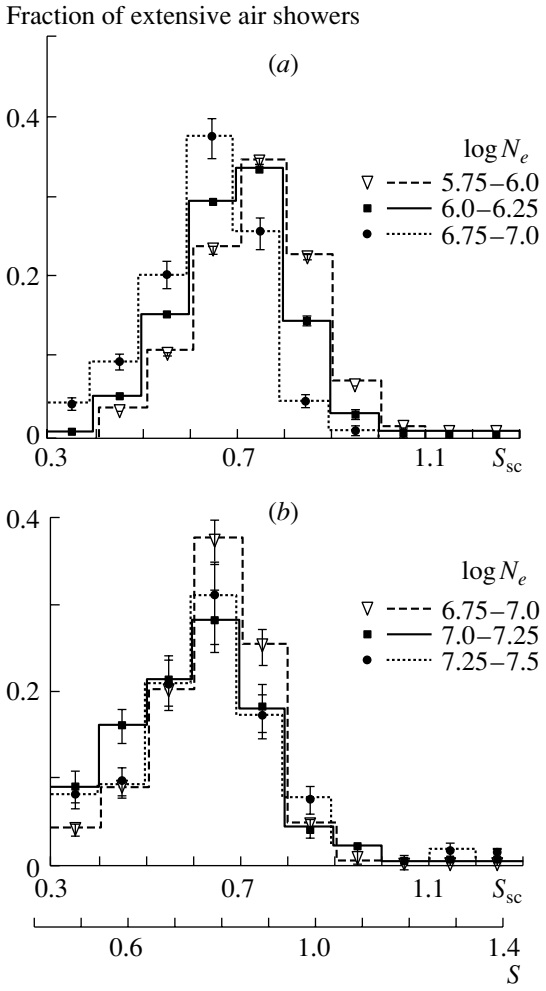

Fig. 2. Distributions with respect to the age parameter S and S_{sc} of extensive air showers for five intervals in the number of electrons, N_e, at a level of 720 g cm^{-2}.

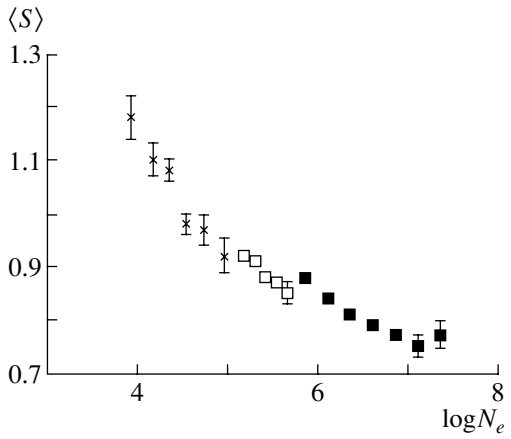

Fig. 3. Dependence of $\langle S \rangle$ on N_e according to data obtained in (closed boxes) the present study, (open boxes) [6], and (crosses) [16].

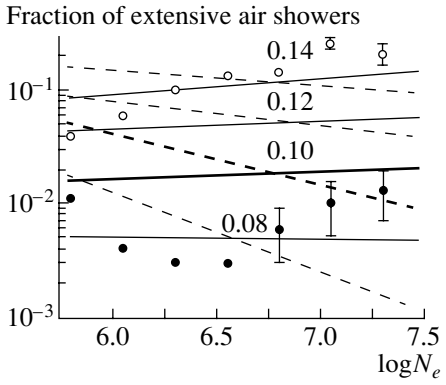

Fig. 4. Dependence of the ratio of the fraction of "young" ($S < 0.6$) and "old" ($S > 1.2$) extensive air showers to the fraction of middle-aged showers defined as those for which $S = 0.6$–0.8 on N_e for various values of the experimental error $\delta(S)$ (the values of δ are indicated on each line—for example, the thick lines correspond to $\delta = 0.1$). The lines depict the results of the calculations performed in [17], while the points represent our experimental data [($S < 0.6$) solid lines and open circles; ($S > 1.2$) dashed lines and closed circles]. The actual values of the experimental error lie in the region $\delta \leq 0.1$.

100% of such showers are characterized by $S_{sc} \leq 0.6$. Because of low statistics in [2] (in contrast to what was achieved in the present study), extensive air showers were considered over a wider region of zenith angles and distances from the array center.

The table presents the data of the present study, and Fig. 3 gives, in addition to them, data from [6, 16] on the mean value $\langle S \rangle$ as a function of N_e. The second column contains the values of $\langle S \rangle$. In the third column, we give the experimental values $\sigma(S_{expt})$ of the root-mean-square deviation in the distribution with respect to S. The fourth column presents the same results corrected for the measurement errors $\delta(S)$: $\sigma(S) = \sqrt{\sigma^2(S_{expt}) - \delta^2(S)}$. We obtained values of $\delta(S) \leq 0.1$ by sampling generated extensive air showers with allowance for actual experimental errors in measuring the particle flux through a scintillation detector and with the aid of the same codes for determining the parameters of extensive air showers.

The data in the fifth column on the relative half-width $\sigma(S)$, $\sigma(S)/\langle S \rangle$, demonstrate that the relative half-width of the distributions somewhat increases with increasing N_e, owing primarily to a growth of the fraction of young extensive air showers.

If the nuclear composition remains unchanged as the energy of primary cosmic radiation increases and if the character of the interaction changes according to currently used models, which are based on the extrapolation of accelerator data to the region of energies peculiar to extensive air showers, it can be expected that extensive air showers will become somewhat "younger" (the maximum of the development of

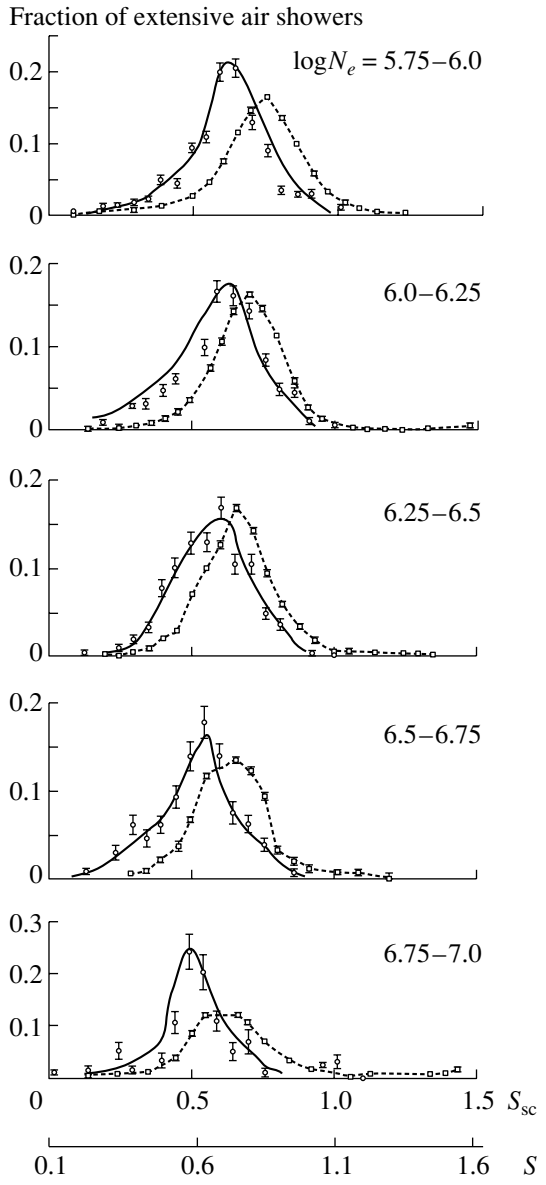

Fig. 5. Distributions with respect to S_{sc} or S for various intervals in N_e (according to the Q100 code) for (solid curves) extensive air showers featuring gamma rays and hadrons and (dashed curves) all extensive air showers.

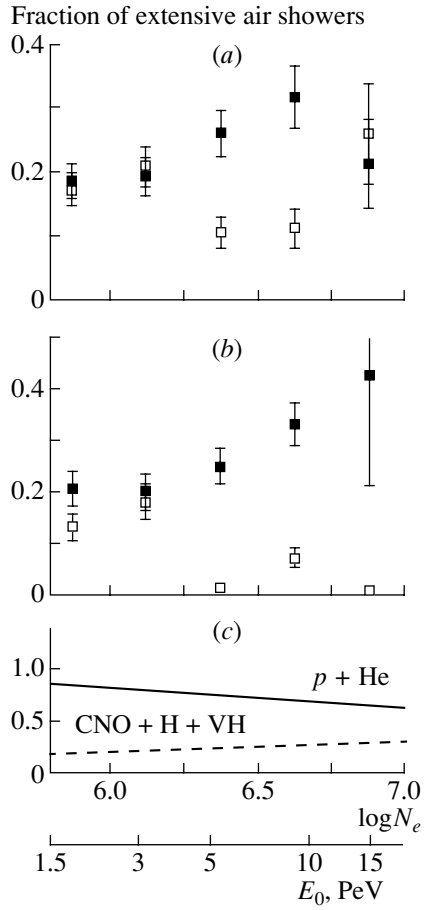

Fig. 6. Ratios of the numbers of (closed boxes) $S < 0.6$ and (open boxes) $S > 0.85$ extensive air showers involving (*a*) gamma rays and hadrons ($\sum E_\gamma > 10$ TeV, $\sum E_h^\gamma > 10$ TeV) to the total number of such extensive air showers (according to the Q100 code) and (*b*) gamma rays ($\sum E_\gamma > 16$ TeV) to the total number of such showers (according to the Space code) versus N_e and E_0; (*c*) results of the calculation performed within the MQ1 model for the N_e dependence of the fraction of extensive air showers involving gamma-ray families ($\sum E_\gamma > 16$ TeV) and originating from primary-cosmic-radiation nuclei [(p + He) solid line; (CNO + H + VH) dashed line].

extensive air showers will be shifted into the depth of the atmosphere). The evolution toward younger showers is enhanced if primary cosmic radiation is enriched in light nuclei and is moderated if it is enriched in heavy nuclei. Therefore, the change in S due to a change in the nuclear composition may be established on the basis of a comparison of experimental data with the results of model calculations, where it is considered that showers may become younger in response to a change in the features of interactions with increasing E_0.

We have compared our data with the results of the calculations performed in [17] on the basis of the QGSJET model and on the basis of the diffusion model of the propagation of primary cosmic radiation through the Milky Way Galaxy, where it is assumed that the nuclear composition changes, according to [4], from a "light" (about 65% of p + He and about 20% of H + VH) at an energy of a few PeV to a rather heavy (about 40% of p + He and about 40% of H + VH) one at a few tens of PeV. The results of this comparison are illustrated in Fig. 4, where our experimental results are superimposed on the graph from [17]. In just the same way as in [17], the graph displays a set of curves corresponding to different

assumptions on the values of the experimental error δ in determining the age parameter S for the fraction of extensive air showers having small and large values of S (less than 0.6 and greater than 1.2, respectively) with respect to the fraction of extensive air showers with average values of $\langle S\rangle = 0.6$–0.8 versus N_e at Tien Shan level. The experimental error obtained by simulating extensive air showers takes the value of $\delta \cong 0.1$ at $N_e = 5 \times 10^5$ and decreases somewhat with increasing N_e. The thick lines correspond to $\delta = 0.1$ (the solid and dashed lines represent the results for $S < 0.6$ and $S > 1.2$, respectively). In Fig. 4, open (closed) circles correspond to $S < 0.6$ ($S > 1.2$) experimental extensive air showers. As can be seen from Fig. 4, extensive air showers whose age parameter S exceeds 1.2 constitute not more than 1%.

It should be noted that, before the knee (at $N_e = 5.6 \times 10^5$), where a rather light nuclear composition is assumed in the calculations performed in [17], our experimental data are in good agreement with the results of the calculations performed on the basis of the QGSJET model. According to the results of the measurements, the fraction of young extensive air showers increases with increasing N_e, this increase exceeding considerably the possible errors of the measurements. As strong an increase in the fraction of H + VH nuclei at an energy of about 10 PeV as that which is assumed in [17] is at odds with our experimental data on the dependence of S on N_e. These data are indicative of a systematic growth of the steepness of the average lateral distribution of the electron–photon component of extensive air showers (decrease in S) as N_e changes from 5.6×10^5 to $(5.6$–$10) \times 10^6$ ($E_0 \cong 10$–20 PeV) and suggest that the fraction of light nuclei (including primarily protons) does not decrease—possibly, it even increases—in the energy region after the knee.

However, more justified conclusions can be drawn upon a comparison with the results of a simultaneous measurement of other components of extensive air showers. For this purpose, we have analyzed the distributions with respect to $S(N_e)$ in extensive air showers accompanying high-energy gamma rays and hadrons in the x-ray emulsion chambers. The efficiency of the formation of such events is moderately low at small N_e. The calculations performed in [10] revealed that, at $N_e = 10^5$, it is 0.003 of all extensive air showers for primary protons, is 10^{-4} of them for C, N, and O nuclei, and is negligible for heavy nuclei (for the formation of families where the total energy of gamma rays is in excess of 16 TeV). These events are generated by protons belonging to extensive air showers of small S and penetrating into the depth of the atmosphere. With increasing N_e, the efficiency of generation increases (at $N_e \sim 10^6$, it is about 0.1 for protons); accordingly, the values of S for showers in which such events are formed must also increase. Our measurements show that this does indeed occur up to $N_e = 10^6$. At greater values of N_e, however, where a knee is observed, the number of events corresponding to small S begins to grow. For the N_e intervals $(5.6$–$10.0) \times 10^5$, $(10$–$18) \times 10^5$, $(18$–$32) \times 10^5$, $(32$–$56) \times 10^5$, and $(56$–$100) \times 10^5$, the distributions with respect to S ($S_{\rm sc}$) that were obtained upon data processing according to the Q100 code are displayed in Fig. 5 for all extensive air showers (dashed curves) and for extensive air showers accompanying, in the x-ray emulsion chambers, gamma rays and hadrons associated with families of energy $\sum E_\gamma$ or $\sum E_h^\gamma > 10$ TeV at individual particle energies of E_γ or $E_h^\gamma > 2$ TeV for the case where their number in a family satisfies the condition $n > 1$ (solid lines). The errors displayed in Fig. 5 are purely statistical. From this figure, it can be seen that, as N_e increases from 5.6×10^5 to 5.6×10^6, the fraction of extensive air showers having small values of S (young extensive air showers) among extensive air showers generating events in x-ray emulsion chambers increases monotonically; the same is true for the fraction of young showers among all extensive air showers. In this range of N_e, the values of $\langle S\rangle$ for events in x-ray emulsion chambers are shifted toward smaller values by $\Delta S \sim 0.1$ in relation to the values of S for all extensive air showers. This might have been expected since, according to calculations, they are generated by light nuclei deep in the atmosphere. For a selection of extensive air showers involving gamma rays whose families containing more than one particle have total energies satisfying the condition $\sum E_\gamma > 16$ TeV and whose individual energies satisfy the condition $E_\gamma > 4$ TeV, similar distributions obtained according to the Space code yielded the same results [18].

For the N_e dependence of the fraction of events where extensive air showers generate, in the x-ray emulsion chambers, gamma rays and hadrons whose total energy satisfies the condition $\sum E_\gamma$ or $\sum E_h^\gamma > 10$ TeV, the results obtained by means of data processing on the basis of the Q100 code are displayed in Fig. 6*a*, where the open and closed boxes represent the relevant dependences for, respectively, young ($S < 0.6$) and somewhat older ($S > 0.85$) showers. For total gamma-ray-family energies satisfying the condition $\sum E_\gamma > 16$ TeV, similar data obtained on the basis of the Space code are shown in Fig. 6*b*. From Fig. 6, it can be seen that, in the range $N_e = (1.0$–$5.6) \times 10^6$ ($E_0 = 2$–10 PeV), the fraction of young extensive air showers grows with increasing N_e (E_0), while the fraction of older showers for which $S > 0.85$ decreases. At $N_e \sim 10^7$, this trend is possibly moderated (see Fig. 6*a*). Thus, the experimental

data on extensive air showers accompanying high-energy gamma rays and hadrons, as well as the data on all extensive air showers, indicate that the steepness of the lateral distribution of the electron–photon component of extensive air showers grows monotonically (accordingly, S decreases) as N_e changes from 10^6 to 5.6×10^6 ($E_0 = 2$–10 PeV).

For the case where simulated-data processing was based on the MQ1 model, the N_e dependence of the fraction of extensive air showers involving gamma-ray families whose total energy satisfies the condition $\sum E_\gamma > 16$ TeV that were generated by primary-cosmic-radiation nuclei is shown in Fig. 6*c* for (solid line) light (p + He) and (dashed line) medium-mass and heavy (CNO + H + VH) nuclei. As can be seen from Fig. 6*c*, extensive air showers accompanied by high-energy gamma rays are generated predominantly by primary protons and light nuclei.

Therefore, our data on the lateral distributions of the electron-photon component in such extensive air showers, as well as in all extensive air showers, suggest that, at Tien Shan level, the fraction of light nuclei does not decrease at primary-cosmic-radiation energies above the energy of the knee in the spectrum of extensive air showers with respect to the number of electrons (this being so at least up to primary-cosmic-radiation energies of about 10 PeV) or that the fraction of particles penetrating deep into the atmosphere increases in this region.

For primary cosmic radiation of energy up to 10 PeV, the same conclusion was drawn from an analysis of the energy spectra of gamma rays in the x-ray emulsion chambers for various intervals of N_e and from a comparison of the results of model calculations with the N_e spectra of extensive air showers accompanying such gamma rays. At energies of 10 to 20 PeV, these data are, however, indicative of the possible variations in the nuclear composition of primary cosmic radiation or in the character of its interactions.

ACKNOWLEDGMENTS

This work was supported by the Russian Foundation for Basic Research (project nos. 01-02-16725, 02-02-17047).

REFERENCES

1. Yu. A. Fomin, G. B. Khristiansen, G. V. Kulikov, *et al.*, in *Proceedings of the 22nd ICRC, Dublin, 1991*, Vol. 2, p. 85.
2. N. M. Nesterova, A. P. Chubenko, P. A. Djatlov, *et al.*, in *Proceedings of the 24th ICRC, Roma, 1995*, Vol. 2, p. 748.
3. A. D. Erlykin and A. W. Wolfendale, J. Phys. G **23**, 979 (1997).
4. S. Swordy, in *Proceedings of the 24th ICRC, Roma, 1994*, Vol. 2, p. 697.
5. Yu. A. Fomin, N. N. Kalmykov, G. B. Khristiansen, *et al.*, in *Proceedings of the 25th ICRC, Durban, 1997*, Vol. 4, p. 17.
6. S. I. Nikolsky and V. A. Romakhin, Yad. Fiz. **63**, 1888 (2000) [Phys. At. Nucl. **63**, 1799 (2000)].
7. S. F. Abdrashitov, D. S. Adamov, V. V. Arabkin, *et al.*, Izv. Akad. Nauk SSSR, Ser. Fiz. **50**, 2203 (1986).
8. S. B. Shaulov, Preprint No. 31, Lebedev Inst. Phys. (Moscow, 1987).
9. A. M. Dunaevsky *et al.*, AIP Conf. Proc. **276**, 136 (1995).
10. N. P. Krutikova and S. B. Shaulov, Preprint No. 7, Lebedev Inst. Phys. (Moscow, 1998).
11. J. N. Stamenov and S. Z. Ushev, in *Proceedings of the 15th ICRC, Plovdiv, 1977*, Vol. 8, p. 133.
12. A. I. Goncharov, A. K. Konoplenko, A. V. Plyashesh-nikov, *et al.*, Izv. Akad. Nauk SSSR, Ser. Fiz. **53**, 329 (1989).
13. V. S. Aseikin, A. G. Dubovy, N. V. Kabanova, *et al.*, in *Proceedings of the 15th ICRC, Plovdiv, 1977,* Vol. 8, p. 98.
14. V. S. Aseĭkin, N. M. Nikol'skaya, and V. P. Pavlyuchenko, Preprint No. 31, Lebedev Inst. Phys. (Moscow, 1987).
15. D. S. Adamov, V. V. Arabkin, S. P. Besshapov, *et al.*, Nuovo Cimento A **109**, 999 (1996).
16. V. S. Aseĭkin, N. G. Vil'danov, N. V. Kabanova, *et al.*, Preprint No. 178, Lebedev Inst. Phys. (Moscow, 1981).
17. N. N. Kalmykov, G. B. Khristiansen, S. S. Ostap-chenko, *et al.,* in *Proceedings of the 25th ICRC, Durban, 1997*, Vol. 6, p. 277.
18. S. B. Shaulov, Preprint No. 60, Lebedev Inst. Phys. (Moscow, 1996).

Translated by A. Isaakyan

Physics of Atomic Nuclei, Vol. 66, No. 5, 2003, pp. 854–863. Translated from Yadernaya Fizika, Vol. 66, No. 5, 2003, pp. 886–895.

ELEMENTARY PARTICLES AND FIELDS
Experiment

Ordered Structure of the Directions of Arrival of $E_0 \approx 5 \times 10^{17}$ eV Cosmic Rays According to Data from the Yakutsk Array for Recording Extensive Air Showers

A. V. Glushkov* **and M. I. Pravdin**

Institute for Cosmophysical Research and Aeronomy, Yakutsk Research Center, Siberian Division, Russian Academy of Sciences, Yakutsk, Russia

Received December 7, 2001; in final form, March 14, 2002

Abstract—Results are presented that were obtained by analyzing arrival directions for cosmic rays recorded by the Yakutsk array between 1974 and 2001 in the energy range $E_0 = 10^{17.6-17.9}$ eV for zenith angles in the region $\theta \leq 53°$. It is shown that their flux consists of two components—an isotropic (about 75%) and a cluster (about 25%) one—that are characterized by sharply different degrees of anisotropy. At $E_0 = 10^{17.7-17.8}$ eV, the observed showers are found to be strongly correlated with the Supergalaxy plane.

1. INTRODUCTION

There is the opinion that primary cosmic radiation of ultrahigh energy ($E_0 > 10^{17}$ eV) consists predominantly of charged particles, protons and nuclei of various chemical elements. They are strongly mixed by the magnetic field of the Milky Way Galaxy, with the result that their distribution over the celestial sphere is nearly isotropic. Under such conditions, it is very difficult to discover local sources of primary cosmic radiation.

In [1, 2] the AGASA (Akeno Giant Air Shower Array) group found, by the method of a harmonic analysis, a significant anisotropy at $E_0 \approx (8–20) \times 10^{17}$ eV, the amplitude of the first harmonic being about 4% according to its results. This anisotropy was due to an enhanced flux of primary cosmic radiation from a source occurring near the center of the Milky Way Galaxy. The AGASA result was then corroborated and refined by the Australian group SUGAR (Sydney University Giant Airshower Recorder) [3].

Unfortunately, the Yakutsk array does not see the center of the Milky Way Galaxy. Previously, it was reported in [4] that, in the directions of arrival of primary cosmic radiation of energy in the region $E_0 \geq 4 \times 10^{17}$ eV, a small-scale structure is observed, which may have some bearing on local sources. Some more pieces of evidence in favor of this point of view were obtained in [5, 6], where it was shown, among other things, that the contribution of primary cosmic radiation of extragalactic origin is quite sizable in the energy range $E_0 \approx (2–5) \times 10^{18}$ eV. Presented below are experimental data that shed some more light on the problem of the origin of ultrahigh-energy primary cosmic radiation.

2. FEATURES BEING INVESTIGATED AND DISCUSSION

In the present article, we consider extensive air showers recorded by the Yakutsk array between 1974 and 2001 at energies in the range $E_0 = (4–8) \times 10^{17}$ eV and zenith angles satisfying the condition $\cos\theta \geq 0.6$. We study a small-scale anisotropy—that is, local irregularities within about 5° to 10°. Our analysis included extensive air showers whose arrival directions were determined on the basis of data from four or more stations and whose axes traversed the central circle of the array with a radius of 1250 m (it was required that they never go beyond the perimeter of the array). Such events yield minimum errors in determining basic parameters of extensive air showers (such as the directions and coordinates of the axis and E_0). The primary-particle energy E_0 was determined from the relations

$$E_0 = (4.8 \pm 1.6) \times 10^{17} (\rho_{s,600}(0°))^{1.0\pm0.02} \text{ [eV]}, \quad (1)$$

$$\rho_{s,600}(0°) = \rho_{s,600}(\theta) \times \exp((\sec\theta - 1) \times 1020/\lambda_\rho) \text{ [m}^{-2}\text{]}, \quad (2)$$

$$\lambda_\rho = (450 \pm 44) + (32 \pm 15)\log(\rho_{s,600}(0°)) \text{ [g/cm}^2\text{]}, \quad (3)$$

*e-mail: a.v.glushkov@ikfia.ysn.ru

1063-7788/03/6605-0854$24.00

where $\rho_{s,600}(\theta)$ is the charged-particle density measured by scintillation detectors at the distance of $R = 600$ m from the shower axis.

We took three narrow energy intervals $E_0 = 10^{17.6-17.7}$, $10^{17.7-17.8}$, and $10^{17.8-17.9}$ eV and, in each of them, considered seven independent samples featuring approximately the same number of showers. These samples differed only in that their axes occurred in different annular areas (see Table 1), all other conditions being the same. Each of the 21 samples was explored individually for the presence in it of local groups of showers in the celestial sphere. This was done in the following way. Around the direction of arrival of any shower, we found all of its neighbors within three angular degrees ($d \leq 3^\circ$). If there were $n \geq 3$ showers in the circle, then we performed averaging over their coordinates and used, in the following, the result of this averaging as new points (we refer to them as nodes).

In this procedure, any isolated group of showers (that is, that which occurs at a distance in excess of d) is associated with the same node, while a chain of showers is preserved in the form of the same chain of nodes. In the following, nodes from different samples were considered from the point of view of coincidence of their celestial coordinates. If they intersected $m \geq 2$ times (under the condition that their centers were within the distance not larger than three angular degrees, $d \leq 3^\circ$), then we found a new, larger, node (cluster). It included all showers found at the preceding step.

The densest arrangement of nodes was observed in the vicinity of the North Pole of the Earth. The contribution of random events increased considerably there, since, in view of the geographic location of the Yakutsk array (61.7°N), this part of the sky has the largest exposure. In order to reduce the fraction of such events, it was therefore required that, in equatorial coordinates, the number of showers in nodes, n, gradually increase from 3 to 8 at latitudes in excess of 40°. An analysis revealed that this procedure is quite legitimate and that it made a major contribution to revealing true clusters.

For showers of energy in the range $E_0 = 10^{17.7-17.8}$ eV, the chart of the arrangement of nodes (points) and clusters in the developed celestial sphere is shown in Fig. 1 in terms of galactic coordinates. Clusters featuring $m = 2$ and $m \geq 3$ nodes are represented by crosses and closed circles, respectively. To give a clearer presentation of data, the equatorial coordinates are also shown in this chart. It is worthy of note that the majority of events are grouped into clusters and that the clusters themselves are often situated close to one another, forming chains.

A Monte Carlo simulation revealed that the positions of the clusters in Fig. 1 are not random. For the case of $d \leq 3^\circ$, $n \geq 3$, and $E_0 = 10^{17.7-17.8}$ eV, the distributions of 1812 showers at nodes with respect to arrival directions specified by the latitude of arrival (with a step of $\Delta b = 3^\circ$) are displayed in Figs. 2*a*–2*d* in terms of galactic (G) and supergalactic (SG) co-

Table 1. Radii of the circles for selecting extensive air showers according to location of their axes

Sample	R_1, m	R_2, m	Number of showers
$E_0 = 10^{17.6-17.7}$ eV			
1	0	280	1109
2	280	390	1091
3	390	480	1023
4	480	570	1040
5	570	660	1093
6	660	740	1076
7	740	822	1063
$E_0 = 10^{17.7-17.8}$ eV			
1	0	320	1087
2	320	450	1032
3	450	565	1076
4	565	665	1044
5	665	760	1058
6	760	853	1082
7	853	965	1061
$E_0 = 10^{17.8-17.9}$ eV			
1	0	380	1056
2	380	530	1034
3	530	660	1052
4	660	790	1097
5	790	910	1059
6	910	1050	1036
7	1050	1225	1044

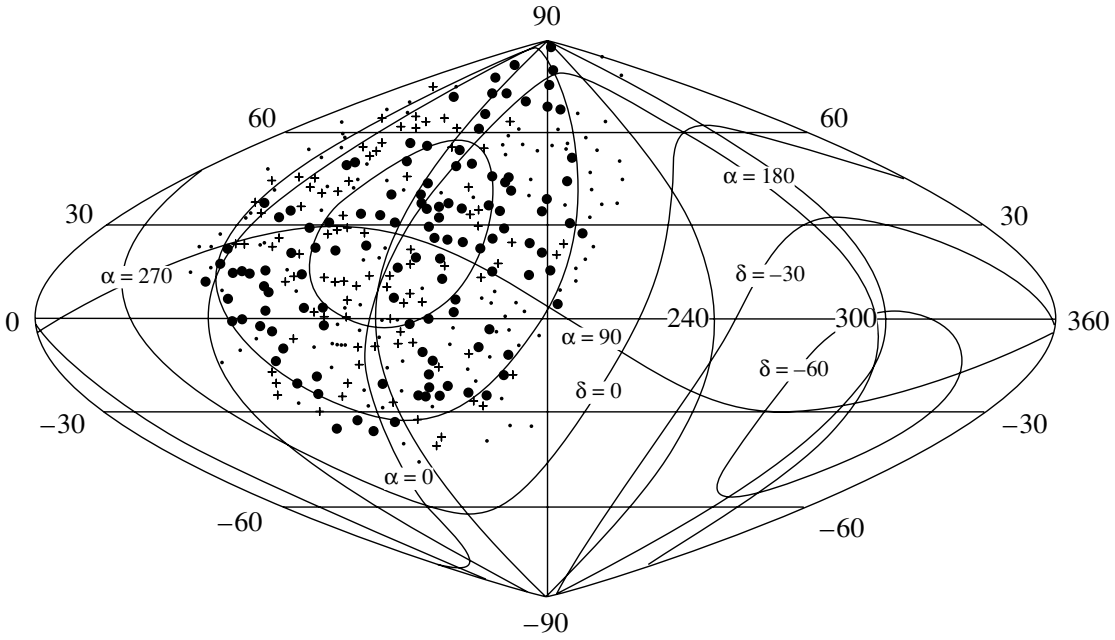

Fig. 1. Chart of the positions of nodes (points) and clusters from 1812 showers having energies of $E_0 = 10^{17.7-17.8}$ eV and arriving at zenith angles of $\theta \leq 53^\circ$ in terms of galactic coordinates according to data from the Yakutsk array for observing extensive air showers. The direct crosses and closed circles represent clusters consisting of, respectively, $m = 2$ and $m \geq 3$ nodes for $d \leq 3^\circ$.

ordinates. The North Pole of the Supergalaxy has the equatorial coordinates of $\alpha = 286.2^\circ$ and $\delta = 14.1^\circ$. Figures 2*a* and 2*b* show the observed (N_{expt}) and expected (N_{ran}) distributions, while Figs. 2*c* and 2*d* present the deviations of the number of measured events from the expected number in units of $\sigma = \sqrt{N_{\text{ran}}}$; here, $n_\sigma = (N_{\text{expt}} - N_{\text{ran}})/\sigma$. The smooth curves in Figs. 2*c* and 2*d* correspond to the averaged behavior of n_σ upon smoothing with the aid of a Fourier series involving five harmonics.

The values N_{ran} were obtained by simulating the explored number of showers distributed at random over the celestial sphere. This was done in the following way. For each measured shower, we determined 500 directions in terms of galactic coordinates by replacing the actual arrival time and azimuth (in the horizontal coordinate frame of the array) by random ones. The resulting distributions of random events were then normalized in absolute value to the actual ones.

In both coordinate frames, χ^2 takes here enormous values of $\chi^2 \approx 110$–150 for $k = 50$ degrees of freedom. The probability of such random events is estimated as $P < 10^{-5}$. A statistically significant (about 5σ) excess of events is quite pronounced in the Supergalaxy plane. On the contrary, the Galaxy plane manifests itself only as a modest dip (see Fig. 2*c*), which becomes more distinct against the background of the distribution segments adjacent to it on two sides. These results can be interpreted as an indication of an extragalactic origin of the primary-cosmic-radiation fraction contained in the clusters. In all probability, the Galaxy only absorbs this radiation, this absorption being more intense in its disk. Other significant peaks and dips in Figs. 2*a*–2*d* are likely to be indicative of a complex and nonuniform structure of the spatial region housing the sources of primary cosmic radiation that generate clusters.

Similar distributions for the remaining showers that did not enter into the aforementioned nodes (5614 events) are displayed in Fig. 2*a*′–2*d*′. It can be seen that the pattern here has changed abruptly. The measured distributions for random variables are close to the expected ones ($\chi^2 = 47$–59). This result suggests that the degree of isotropy in the primary-cosmic-radiation part singled out in this way is rather high. The fraction of these particles in the total flux is $5614/7426 \approx 0.75$.

Of particular interest in this connection are data in the energy regions adjacent to that which was considered above. Figures 3 and 4 display distributions that are similar to those in Fig. 2, but which were constructed for showers of energy in the ranges $E_0 = 10^{17.6-17.7}$ and $10^{17.8-17.9}$ eV, respectively. These distributions also exhibit multiple clusters. The distributions of showers in the clusters lead to values of $\chi^2 \approx 100$–120 not associated with random events ($P < 10^{-5}$). However, they do not feature noticeable

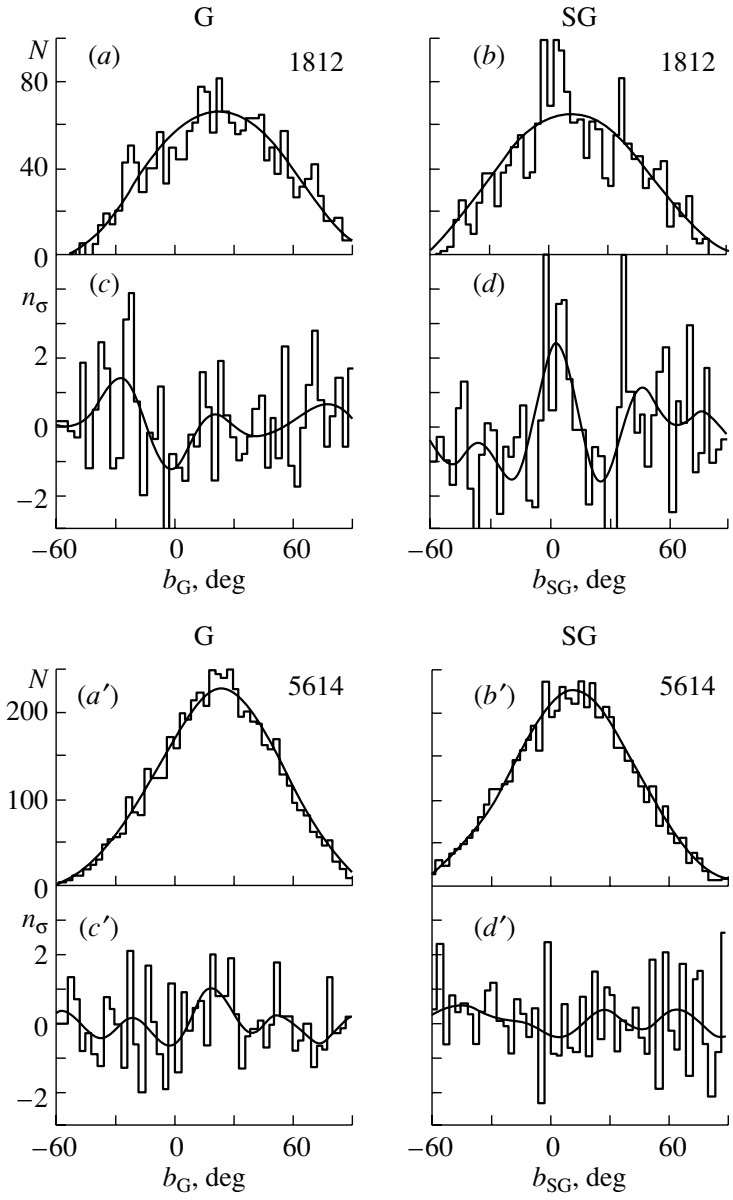

Fig. 2. Distributions of showers of energy in the range $E_0 = 10^{17.7-17.8}$ eV with respect to the latitude of their arrival in terms of the galactic (G) and supergalactic (SG) coordinates according to the results obtained for (a–d) nodes from seven samples featuring not less than three showers at $d \leq 3^\circ$ and (a'–d') for seven samples without nodes: (a, b; a', b') observed, N_{expt} (histograms), and expected, N_{ran} (curves), distributions; (c, d; c', d') deviations of the number of measured events from the expected number, $n_\sigma = (N_{\text{expt}} - N_{\text{ran}})/\sqrt{N_{\text{ran}}}$ (histograms), and averaged behavior of n_σ (curves). The numerals in the figure are the numbers of showers.

correlations with the Supergalaxy and Galaxy disks if we pay no attention to Fig. 4*d*, where there is yet some trend toward an excessive radiation from the Supergalaxy disk. As to showers that did not enter into the clusters, they still yield values of $\chi^2 = 46$–65, which are close to those peculiar to a random uniform distribution.

Figure 5*a* depicts a diagram illustrating the relative location of the Milky Way of the Galaxy (G) and the Milky Way of the Supergalaxy (SG), while Fig. 5*b* shows schematically the spiral structure of the Galaxy [7]. The shaded sectors represent regions that are visible to the Yakutsk array for studying extensive air showers. A nearly perpendicular orientation of the Galaxy plane with respect to the Supergalaxy plane in Fig. 5*a* makes it possible to refine some details in Fig. 2. For events induced by showers of energy in the range $E_0 = 10^{17.7-17.8}$ eV, the distributions of the directions of arrival of the showers in the nodes and clusters from the Galaxy and Supergalaxy disks

Table 2. Phases and amplitudes of the first harmonics

Energy, eV	Array	Total		Without nodes		Nodes	
		φ_1, deg	A_1, %	φ_1, deg	A_1, %	φ_1, deg	A_1, %
$10^{17.6-17.7}$	Yakutsk	317 ± 43	2.4	315 ± 37	5.8	296 ± 14	16.5
	AGASA	300 ± 5	2.0	–	–	–	–
$10^{17.7-17.8}$	Yakutsk	29 ± 115	0.2	211 ± 136	1.2	228 ± 95	1.3
	AGASA	292 ± 5	2.2	–	–	–	–
$10^{17.8-17.9}$	Yakutsk	15 ± 61	2.8	264 ± 124	1.6	56 ± 26	11.0
	AGASA	295 ± 5	3.0	–	–	–	–

($|b| \leq 2^\circ$) are shown in Figs. 6*a*–6*d* in terms of the longitude coordinates (with a step of $\Delta l = 3^\circ$). The longitude of the Supergalaxy was reckoned from the anticenter in the counterclockwise direction.

In the surveyed sectors of both disks ($l \approx 30^\circ$–210°), many peaks and dips are observed with a statistical significance not less than two standard deviations. Values of $\chi^2 \approx 93$–96 for $k = 50$ degrees of freedom correspond to probabilities of $P < 10^{-4}$ for such random events. In all probability, these spatial irregularities in the fluxes of primary cosmic radiation are associated with some small-scale structural features of the objects being considered. Here, we will dwell on only one point that supports the above assumption on an extragalactic origin of showers entering into the clusters. An intense peak (of statistical significance at a level of 5σ) in Fig. 6*c* in the direction $l_G \approx 137^\circ$, which coincides with the line of intersection of the Galaxy and Supergalaxy planes (*SO* in Fig. 5*a*), is a compelling piece of evidence in favor of this. As a matter of fact, this peak is a local section of data in Fig. 2*d*. It also manifests itself in Fig. 6*d* in the direction $l_{SG} \approx 94^\circ$.

Figures 6*a*′–6*d*′ display the distributions of showers not belonging to the nodes and clusters, having energies in the range $E_0 = 10^{17.7-17.8}$ eV, and originating from the regions of the Galaxy and Supergalaxy disks ($|b| \leq 2^\circ$). They were obtained by a method that is similar to that used to derive the distributions in Figs. 6*a*–6*d*. Here, the measured and the expected distributions for the isotropic flux of primary cosmic radiation are compatible ($\chi^2 = 54$–63).

Let us now consider the global anisotropy of primary cosmic radiation. For this, we will make use of the traditional harmonic-analysis method implemented in terms of equatorial coordinates. For groups of showers selected for the analysis, Table 2 presents the phases φ_1 and the amplitudes A_1 of the first harmonics of approximating functions:

$$N(a) = \langle N \rangle + A_1 \cos(\alpha - \varphi_1). \qquad (4)$$

Our data included only those events for which the arrival directions were determined by using not less than five stations and for which the shower axes traversed the central circle of the array with a radius of about 1000 m. Values quoted in the column under the heading "Total" correspond to samples subjected to no selections of clusters. The AGASA data were borrowed from [1].

Before proceeding to perform a comparative analysis of the results obtained to date, we note that they change significantly with the width of the energy intervals, since it is clear from the aforesaid that different regions of the sky have different primary-cosmic-radiation intensities depending on shower energy. For this reason, data from different arrays can hardly be subjected to a direct comparison. This can clearly be seen from Fig. 7, where the unshaded region around the North Pole of the Earth is the sky zone surveyed by the Yakutsk array at $\cos\theta \geq 0.6$, while the shaded region is the complementary part of the sky—it is seen from the AGASA array at $\cos\theta \geq 0.5$. The circles in Fig. 7 represent the magnetic fields in the Galaxy [8]: the open and closed ones correspond to the field orientation toward the observer and away from it. The dimensions of the circles are proportional to the field strength.

The dashed arrow *1* in Fig. 7 denotes the phase $\varphi_1 = 295^\circ$ according to the AGASA data (at $E_0 = 10^{17.6-17.7}$ eV) (Table 2); it points toward the outlet of the Orion arm at $l_G \approx 50^\circ$. The phase $\varphi_1 = 317^\circ$ according to data of the Yakutsk array from the sample "Total" at $E_0 = 10^{17.6-17.7}$ eV is shown in Fig. 7 by the dashed arrow *2*. Although these phases

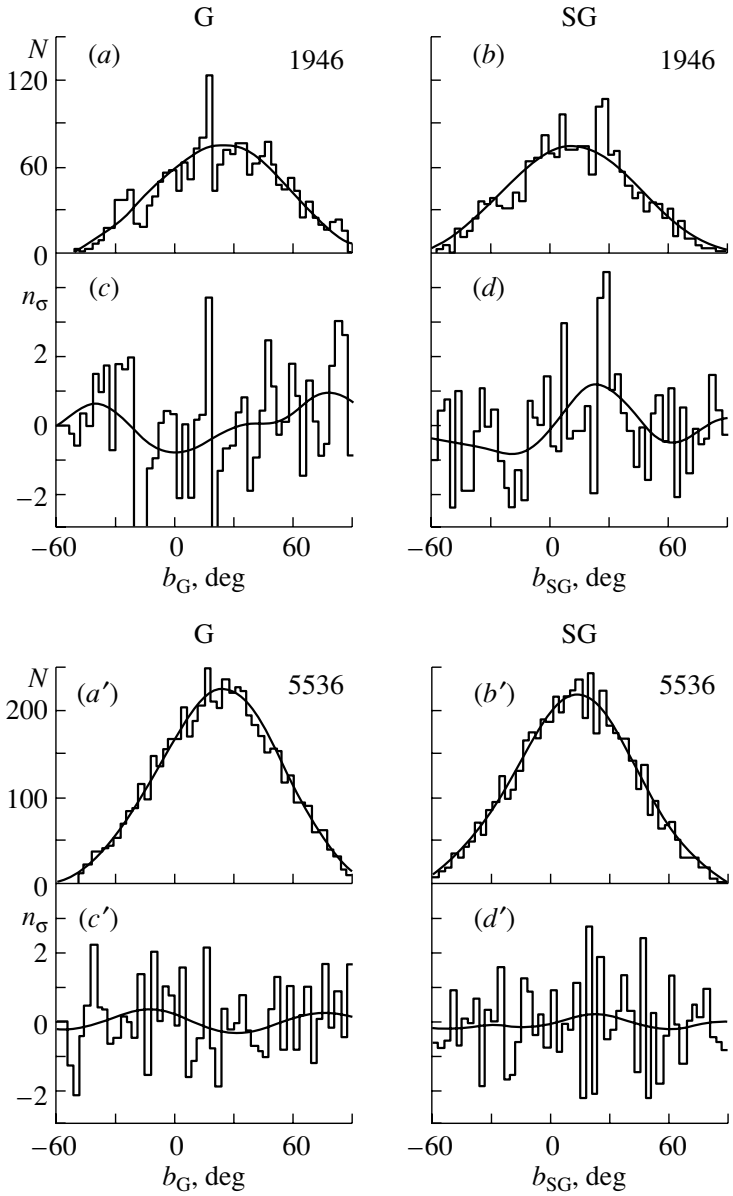

Fig. 3. Distributions for showers of energy in the range $E_0 = 10^{17.6-17.7}$ eV. The notation is identical to that in Fig. 2.

are somewhat different, agreement between the two results cannot be ruled out because of the errors in our experiment. At different energy values, the phases according to our data differ more strongly from those according to AGASA data.

In order to understand what occurs here, we consider the distribution of primary cosmic radiation for right ascension at the nodes and without them. For three energy intervals, they are shown in Fig. 8 by histograms *1* and *2*, respectively. The corresponding values of the phases and amplitudes are given in Table 2. In the distributions without nodes, there are insignificant distinctions between the fluxes in different hour angles; in view of this, the phases for them were found with large uncertainties. These data still indicate (see Figs. 2–4) that primary cosmic radiation is isotropic to a considerable extent.

As to the data on showers in the clusters in Fig. 8 (histograms *1*), they are in glaring contradiction, as might have been expected on the basis of the aforesaid, with the hypothesis of an isotropic distribution. For example, the scatter of data around the approximating curve (4) at $E_0 = 10^{17.7-17.8}$ eV leads to a value of $\chi^2 \approx 71.6$ for $k = 24$ degrees of freedom, this corresponding to a probability of $P < 10^{-5}$ for a random event. The distribution at $E_0 = 10^{17.8-17.9}$ eV leads to a still greater value of $\chi^2 \approx 118.2$. As to events generated by showers of energy in the range $E_0 = 10^{17.6-17.7}$ eV, we have $\chi^2 \approx 37.9$ for them, in

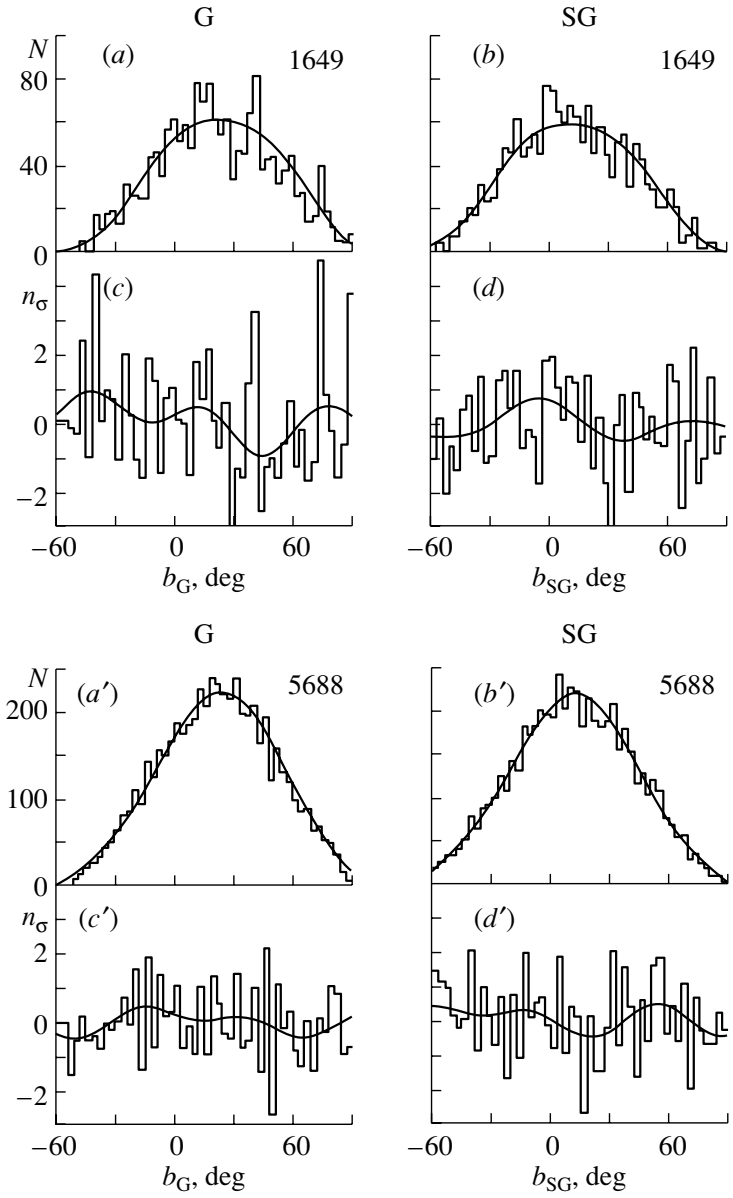

Fig. 4. Distributions for showers of energy in the range $E_0 = 10^{17.8-17.9}$ eV. The notation is identical to that in Fig. 2.

which case the probability of a random event is $P \approx 3.5 \times 10^{-2}$.

Let us highlight some important features of these distributions. The peak in Fig. 8*b* (histogram *1*) at $\alpha \approx 180°-195°$ is indicative of excessive radiation from the Supergalaxy disk in the vicinity of the center (C_{SG} in Fig. 7), while the peak at $\alpha \approx 15°-45°$ suggests the presence of an excessive flux along the line of intersection of the Galaxy and Supergalaxy planes ($\alpha \approx 40°$ in Fig. 7). They are in agreement with the peaks in these directions in Fig. 6*d*. The peaks in Fig. 8*c* (*1*) at $\alpha \approx 15°-180°$ may also be due to excessive radiation from various regions of the Supergalaxy disk; as to the peaks at $\alpha \approx 315°-345°$, they are likely to be associated with the Galaxy disk.

It can be assumed that clusters are formed near some local sources of primary cosmic radiation. From the data quoted above, it can be seen that, at $E_0 \approx 10^{17.7-17.8}$ eV, clusters indicate that there is some correlation with the Supergalaxy plane. In all probability, primary particles forming these clusters are electrically neutral; otherwise, they would lose, because of motion in the magnetic field of the Galaxy, any correlation in direction with their production sources. These can hardly be neutrons, because their Lorentz factor at the above energies is about 5×10^8, so that they can travel, prior to undergoing decay, a

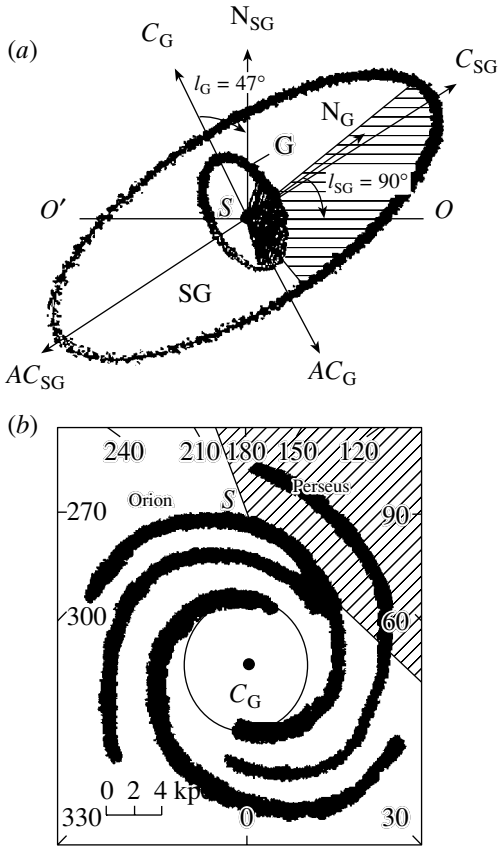

Fig. 5. (*a*) Diagram illustrating relative location of the Milky Way of the Galaxy (G) and the Milky Way of the Supergalaxy (SG): (C_G, C_{SG}) centers, (AC_G, AC_{SG}) anticenters, (N_G, N_{SG}) North Poles, (OO') line of the intersection of the planes, (S) observation point, and (shaded sectors) sectors visible to the Yakutsk array for studying extensive air showers; (*b*) schematic representation of the spiral structure of the Galaxy [7].

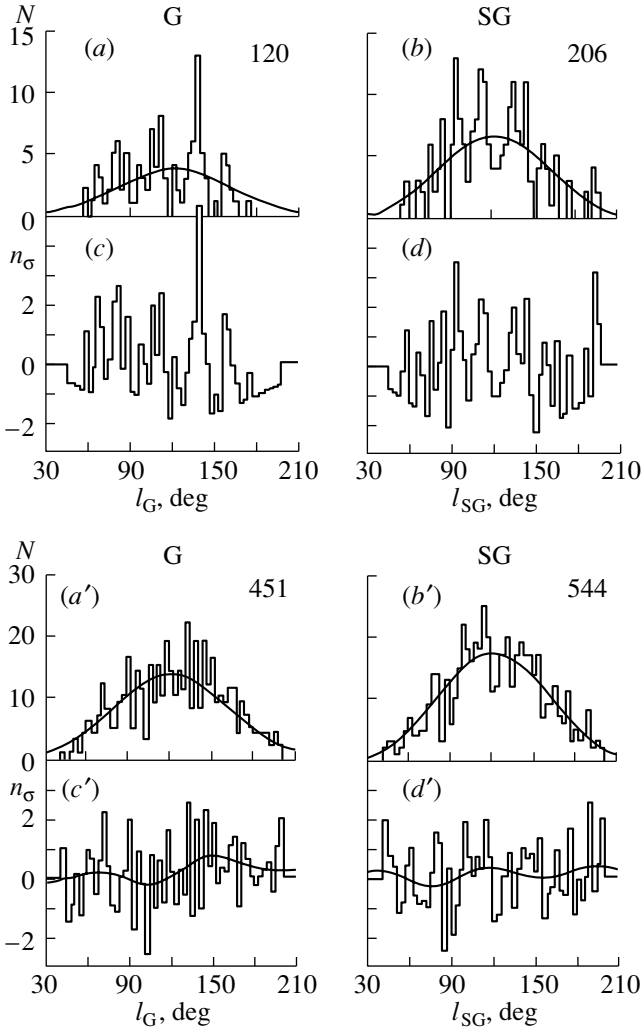

Fig. 6. Distributions of showers having energies in the range $E_0 = 10^{17.7-17.8}$ eV and arriving from the Galaxy (G) and Supergalaxy (SG) disks ($|b| \leq 2°$) versus the longitude of their arrival. The notation is identical to that in Fig. 2.

distance of about 5 kpc, which is much shorter than the Supergalaxy dimension (approximately 50 Mpc). Most likely, these are some other stable neutral particles.

In this connection, we will consider muons, whose threshold energy is $E_\mu \approx 1.0 \cdot \sec\theta$ GeV and whose content in showers is sensitive to the composition of primary cosmic radiation. The closed circles in Fig. 9 represent the lateral distribution of muons in showers having energies of $E_0 \approx 10^{17.7-17.8}$ eV, arriving at zenith angles satisfying the condition $\cos\theta \geqslant 0.9$, and belonging to the clusters. The solid curve is the approximation of the experimental data by the function

$$\rho_\mu(R) = N_\mu C_\mu (R/280)^{-0.75} \times (1 + R/280)^{0.75-b_\mu}(1 + R/2000)^{-6.5}, \quad (5)$$

where C_μ is a normalization constant, N_μ is the total number of muons at the observation level, and the fitted value of the parameter b_μ is $b_\mu = 2.67 \pm 0.04$. The open circles represent the average lateral distribution according to the data of our group from [9, 10] for showers without any selections with respect to arrival directions. The dashed curve corresponds to the approximation by the function in (5) with $b_\mu = 1.99 \pm 0.04$, and it is compatible with the results of the calculations in [9, 10] on the basis of the QGSJET model for the mixed composition of primary cosmic radiation from light nuclei, protons being dominant among them.

It can be seen that the lateral distribution of muons in showers forming clusters is very steep. For primary protons, the calculations in [9, 10] yielded a much more gently sloping distribution of the form in (5) with $b_\mu = 2.02$. Air showers initiated by protons and neu-

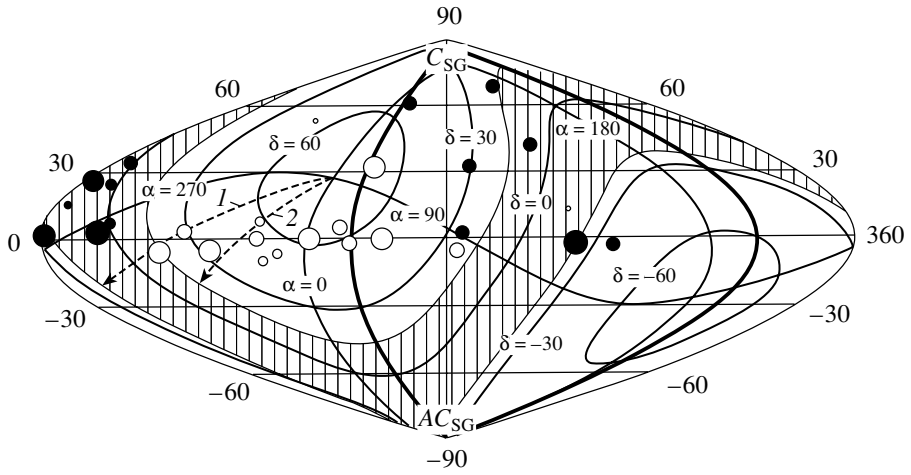

Fig. 7. Sky zones (in galactic coordinates) surveyed by the Yakutsk array (unshaded region), $\delta \approx 15^\circ - 90^\circ$, and by AGASA (shaded region), $\delta \approx -25^\circ - 90^\circ$. The closed and open circles show the disposition of the magnetic arms of the Galaxy [8] with directions, respectively, away from the observer and toward it, the dimensions of the circles being proportional to the field strength. The dashed arrows *1* and *2* correspond to the phases of the first harmonics of showers of energy in the range $E_0 = 10^{17.6-17.7}$ eV according to, respectively, the AGASA data from [1] and the data from the Yakutsk array.

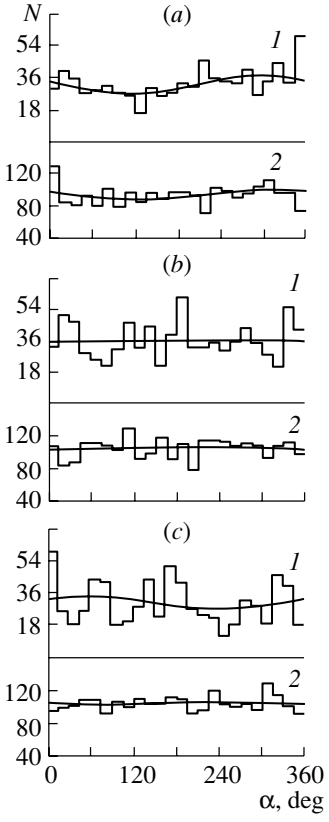

Fig. 8. Distribution of showers of energy in the ranges $E_0 =$ (*a*) $10^{17.6-17.7}$, (*b*) $10^{17.7-17.8}$, and (*c*) $10^{17.8-17.9}$ eV for right ascension (histograms *1*) at the nodes for $n \geq 3$ and $d \leq 3^\circ$ and (histograms *2*) in samples without nodes. The smooth curves represent the approximations by the function in (4).

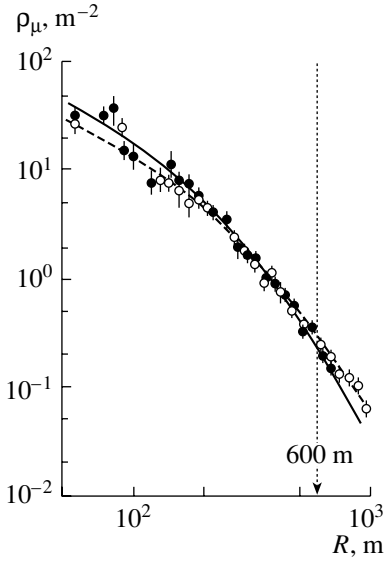

Fig. 9. Lateral distributions of muons (for a threshold energy of $E_\mu \approx 1.0 \cdot \sec\theta$ GeV) in showers having energies in the range $E_0 = 10^{17.7-17.8}$ eV and arriving at zenith angles satisfying the condition $\cos\theta \geq 0.9$: (closed circles) data for showers belonging to the clusters and (open circles) data for a sample without isolation of clusters. The solid and the dashed curve represent the approximations by the function in (5) with the parameter values of $b_\mu = 2.67 \pm 0.04$ and 1.99 ± 0.04, respectively.

trons develop identically. Therefore, neutrons cannot be hypothetical primary-cosmic-radiation particles either. Nor can these be photons, since, according to various estimates, they produce showers where the content of muons is 7 to 15 times less than that in

showers generated by protons. In all probability, these are some other stable neutral particles.

3. CONCLUSION

Summarizing the results quoted above, we arrive at the following pattern. Most likely, primary cosmic radiation of energy in the range $E_0 \approx 10^{17.6-17.9}$ eV consists of two components. One of these is approximately three times more intense than the other one and seems to include charged particles. They are vigorously stirred by the magnetic field of the Galaxy. A global anisotropy, with the first harmonic being $\varphi_1 \approx 280°-300°$ according to AGASA data [1, 6], is explained by the diffusion of protons from the Galaxy center. Possibly, the Galaxy arms are also operative here (see Fig. 7). Our experimental data and the results of the calculations of various features of extensive air showers on the basis of the QGSJET model [9–14] are also compatible with the hypothesis that, in this energy region, the composition of primary cosmic radiation is close to a purely protonic one.

The second component differs from the first one noticeably. In all probability, it consists of neutral particles forming, within $d \leq 3°$ solid angles, clusters near the sources of their generation. At the moment, it is difficult to deduce any specific information about these sources. Clusters at $E_0 \approx 10^{17.7-17.8}$ eV attract particular attention. They correlate with the Supergalaxy disk rather strongly (see Figs. 2*a*–2*d*, 6*a*–6*d*). Moreover, the lateral distribution of muons in these events proved to be anomalously steep (see Fig. 9).

ACKNOWLEDGMENTS

This work became possible owing to financial support extended by the Ministry for Science of the Russian Federation to the Yakutsk multipurpose array for studying extensive air showers (grant no. 01-30).

REFERENCES

1. N. Hayashida, M. Nagano, D. Nishikawa, *et al.*, Astropart. Phys. **10**, 303 (1999).
2. M. Teshima, M. Chikawa, M. Fukushima, *et al.*, in *Proceedings of the 27th ICRC, Hamburg, 2001,* p. 337.
3. J. A. Bellido, B. W. Clay, R. B. Dawson, and M. Johnston-Hollitt, astro-ph/0009039.
4. A. V. Glushkov, Pis'ma Zh. Éksp. Teor. Fiz. **48**, 513 (1988) [JETP Lett. **48**, 555 (1988)].
5. A. V. Glushkov and M. I. Pravdin, Zh. Éksp. Teor. Fiz. **119**, 1029 (2001) [JETP **92**, 887 (2001)].
6. A. V. Glushkov and M. I. Pravdin, Pis'ma Astron. Zh. **27**, 577 (2001) [Astron. Lett. **27**, 493 (2001)].
7. Y. M. Georgelin and Y. P. Georgelin, Map in *Cambridge Atlas of Astronomy*, Ed. by J. Audouze and G. Israel (Cambridge University Press, Cambridge, 1988), p. 308.
8. A. G. Lyne and F. Graham-Smith, *Pulsar Astronomy* (Cambridge University Press, Cambridge, 1990).
9. A. V. Glushkov, I. T. Makarov, M. I. Pravdin, *et al.*, Pis'ma Zh. Éksp. Teor. Fiz. **71**, 145 (2000) [JETP Lett. **71**, 97 (2000)].
10. A. V. Glushkov, M. I. Pravdin, I. E. Sleptsov, *et al.*, Yad. Fiz. **63**, 1557 (2000) [Phys. At. Nucl. **63**, 1477 (2000)].
11. A. V. Glushkov, I. T. Makarov, M. I. Pravdin, and I. E. Sleptsov, Izv. Akad. Nauk, Ser. Fiz. **63**, 538 (1999).
12. A. V. Glushkov, I. T. Makarov, E. S. Nikiforova, *et al.*, Astropart. Phys. **4**, 1274 (1995).
13. A. V. Glushkov, M. I. Pravdin, and I. E. Sleptsov, in *Proceedings of the 25th ICRC, Durban, 1997,* Vol. 6, p. 233.
14. A. V. Glushkov, V. B. Kosarev, I. T. Makarov, *et al.*, Pis'ma Zh. Éksp. Teor. Fiz. **67**, 361 (1998) [JETP Lett. **67**, 383 (1998)].

Translated by A. Isaakyan

Physics of Atomic Nuclei, Vol. 66, No. 5, 2003, pp. 864–877. From Yadernaya Fizika, Vol. 66, No. 5, 2003, pp. 896–909.

ELEMENTARY PARTICLES AND FIELDS
Theory

Magnetic Black Holes with String-Loop Corrections*

M. Z. Iofa**

Skobeltsyn Institute of Nuclear Physics, Moscow State University, Vorob'evy gory, Moscow, 119992 Russia

Received June 27, 2002

Abstract—String-loop corrections to magnetic black holes are studied. $4D$ effective action is obtained by compactification of the heterotic string theory on the manifold $K3 \times T^2$ or on a suitable orbifold yielding $N = 1$ supersymmetry in $6D$. In the resulting $4D$ theory with $N = 2$ local supersymmetry, the prepotential receives only one-string-loop perturbative correction. The loop-corrected black hole is obtained in two approaches: (i) by solving the system of the Einstein–Maxwell equations of motion derived from the loop-corrected effective action and (ii) by solving the system of spinor Killing equations (conditions for the supersymmetry variations of the fermions to vanish) and Maxwell equations. We consider a particular tree-level solution with the magnetic charges adjusted so that the moduli connected with the metric of the internal two-torus are constant. In this case, the loop correction to the prepotential is independent of coordinates, and it is possible to solve the system of the Einstein–Maxwell and spinor Killing equations in the first order in string coupling analytically. The set of supersymmetric solutions of the loop-corrected spinor Killing equations is contained in a larger set of solutions of the equations of motion derived from the string-loop-corrected effective action. Loop corrections to the metric and dilaton are large at small distances from the center of the black hole. © *2003 MAIK "Nauka/Interperiodica"*.

1. INTRODUCTION

At present, string theory is considered the best candidate for a fundamental theory that would provide a consistent quantum theory of gravity unified with the other interactions [1]. In particular, string theory provides a powerful approach to the physics of black holes (for a review, see [2, 3] and references therein). In this setting, we meet a fundamental problem of understanding how the intrinsically stringy effects modify the Einstein gravity.

In this paper, we discuss two of these effects: presence of scalar fields such as the dilaton and the moduli and higher genus contributions modifying the tree-level effective action. We focus on the higher genus corrections, because string theory, being a theory formulated on string world sheets, always contains string-loop corrections from higher world sheet topologies (these vanish only for higher supersymmetries $N \geq 4$), while α' corrections can vanish in certain constructions based on conformal field theories and for a large class of backgrounds [4, 5].

We consider solutions of the equations of motion derived from the $4D$ string effective action obtained by dimensional reduction of $6D$, $N = 1$ supersymmetric string effective action on the two-torus. For this class of compactifications, the effective $4D$ theory is $N = 2$ supergravity interacting with matter. As a concrete example of this construction, we have in view heterotic string theory compactified on the manifold $K3 \times T^2$ or its suitable orbifold limit, although we do not rely on any specific properties of this model.

We consider the perturbative one-string-loop (torus topology) corrections for a special class of backgrounds: $4D$ magnetic black holes provided by the "chiral null models" [4–6] embedded in heterotic string theory compactified on the manifold $K3 \times T^2$.

The universal sector of the theory contains supergravity and vector multiplets, the vector fields resulting from components $G_{m\nu}$ and $B_{m\nu}$ of the $6D$ metric and antisymmetric tensor with mixed $4D$ and internal indices, where the index $m = 1, 2$ refers to the two-torus T^2.

Due to $N = 2$ supersymmetry, the prepotential of the theory receives only one-string-loop corrections (from the string world sheets of torus topology) [7–9]. There are examples of explicitly calculated loop-corrected prepotential [7–10], although only its general structure is relevant for the present study. Using the prepotential, we calculate the loop-corrected Kähler potential and gauge couplings.

There are two ways to obtain classical solutions in supersymmetric theories: one can either solve the equations of motion derived from the loop-corrected effective action, which, for bosonic fields, are of the

*This article was submitted by the author in English.

**e-mail: iofa@theory.sinp.msu.ru

1063-7788/03/6605-0864$24.00

second order in derivatives, or solve "spinor Killing equations" resulting from the requirement that supersymmetry variations of the fermionic fields vanish. The latter are of the first order in derivatives. The first method, in general, provides a larger set of solutions that can include nonsupersymmetric ones. The second approach leads to supersymmetric solutions with partially broken supersymmetry.

In the case of a magnetic black hole with the charges P_1 and P_2, the string-tree-level dilaton $\phi = \ln[(r+P_1)(r+P_2)/r^2]$ increases, and the effective gauge couplings proportional to $e^{-\phi}$ decrease at small distances, so that effective gauge couplings are sensitive to string-loop corrections.

A technical simplification is achieved for a special choice of magnetic charges, in which case the tree-level metric of the two-torus G_{mn} is independent of coordinates, and the charges P_1 and P_2 are expressed via one charge P and the components of the metric G_{mn}. However, qualitatively, the results remain unchanged in a general case of unequal charges.

Solving the system of the equations of motion for the moduli and the Einstein–Maxwell equations, in the first order in the string-loop counting parameter $\epsilon = e^{\phi(r)}|_{r\to\infty}$, we obtain the loop-corrected metric and dilaton. A family of solutions of the equations of motion for the loop-corrected metric $ds^2 = -e^{2U(r)}dt^2 + e^{-2U(r)}(dr^2 + r^2 d\Omega^2)$ of a magnetic black hole is

$$2U = -\ln\left(1+\frac{P}{r}\right) + \epsilon\left(\frac{P}{r}A_1 - \frac{P}{r+P}A_2\right),$$

where A_1 and A_2 are arbitrary constants.

Next, in the first order in string coupling, we solve the loop-corrected system of Maxwell equations for the gauge fields and spinor Killing equations for the moduli. We obtain a family of solutions for the loop-corrected metric and dilaton of a magnetic black hole depending on one parameter C,

$$2U = -\ln\left(1+\frac{P}{r}\right) + \epsilon\left(\frac{P}{r}\left(\frac{V}{2}+C\right) - \frac{P}{r+P}\frac{V}{4}\right),$$

where V is the Green–Schwarz function that enters the Kähler potential for the moduli and which is strictly positive [9].

The family of supersymmetric solutions of spinor Killing equations is contained in the set of solutions of the equations of motion of the low-energy effective theory.

In Section 2, we review the structure of the action of the compactified heterotic string theory and implications on its structure of the $N = 2$ local supersymmetry.

In Section 3, we consider the tree-level dyonic and magnetic-black-hole solutions.

In Section 4, we construct the loop-corrected effective action in the first order in the string-loop counting parameter ϵ. Using the symplectic structure of the theory, we calculate the gauge couplings in a basis admitting the prepotential and, by symplectic transformation, obtain them in the heterotic basis (in which case the prepotential does not exist).

In Section 5, we solve the system of Maxwell equations and Bianchi identities.

In Section 6, we write the loop-corrected Einstein and dilaton equations of motion and, starting from the tree-level extremal magnetic-black-hole solution, in the first order in ϵ solve the system of the loop-corrected equations.

In Section 7, we review the structure of the spinor Killing equations for the gravitino and gaugino.

In Section 8, solving the system of Maxwell and spinor Killing equations, we obtain the tree-level magnetic-black-hole solution.

In Section 9, using this solution as an input, we obtain solution of the loop-corrected system of Maxwell and spinor Killing equations.

Concluding remarks are collected in Section 10.

2. HETEROTIC STRING COMPACTIFICATION AND $N = 2$ SUPERSYMMETRY

$4D$ effective string theories obtained by two-torus dimensional reductions of $6D$, $N = 1$ supersymmetric theories share a number of universal properties. The resulting $4D$ theory is $N = 2$ supersymmetric dilatonic supergravity interacting with matter. The bosonic part of the universal sector of this theory written in the standard form of $N = 2$ special geometry [11–17] is

$$I_4 = \int d^4x\sqrt{-g}\left[\frac{1}{2}R + (\bar{N}_{IJ}\mathcal{F}^{-I}\mathcal{F}^{-J} - N_{IJ}\mathcal{F}^{+I}\mathcal{F}^{+J}) + k_{i\bar{j}}\partial_\mu z^i\partial^\mu\bar{z}^j + \ldots\right]. \quad (1)$$

Here, $N_{IJ}(X)$ are the gauge couplings that are functions of the moduli X^I, the vector fields $\mathcal{A}^I_\mu$ are the superpartners of X^I, and the (anti)self-dual vector field strengths are

$$\mathcal{F}^{\pm I}_{\mu\nu} = \frac{1}{2}(\mathcal{F}^I_{\mu\nu} \pm i\sqrt{-g}\,{}^*\mathcal{F}^I_{\mu\nu}).$$

Here, ${}^*\mathcal{F}_{\mu\nu} = \frac{1}{2}e_{\mu\nu\rho\lambda}\mathcal{F}^{\rho l}$, where $e_{\mu\nu\rho\lambda}$ is the flat antisymmetric tensor.

The Kähler metric $k_{i\bar{j}}$ is

$$k_{i\bar{j}} = \frac{\partial^2 K}{\partial z^i \partial \bar{z}^j},$$

where K is the Kähler potential defined below. The moduli z^i are

$$\frac{X^1}{X^0} = z^1 = iy_1 = i\left(e^{-\phi} + ia_1\right), \qquad (2)$$
$$\frac{X^2}{X^0} = z^2 = iy_2 = i\left(e^{\gamma+\sigma} + ia_2\right),$$
$$\frac{X^3}{X^0} = z^3 = iy_3 = i\left(e^{\gamma-\sigma} + ia_3\right),$$

and dots in (1) stand for contributions from other moduli. Here and below, I, $J = 0, \ldots, 3$ and $i, j = 1, 2, 3$. The functions γ, σ, and a_3 are determined by comparing (2) with parametrization of the metric G_{mn} in (9); ϕ and a_1 are defined in (8) (see below). The moduli z^i and the vector fields are identified by comparing the action (1) with the action resulting from compactification (of the universal sector) of the action of the $6D$ theory,

$$I_6 = \int d^6x \sqrt{-G^{(6)}} e^{-\Phi} \qquad (3)$$
$$\times \left[R^{(6)} + (\partial\Phi)^2 - \frac{H^2}{12}\right] + \ldots,$$

on the two-torus. Dimensional reduction of the action (3) on the two-torus yields the $4D$ action [18]

$$I_4 = \int d^4x \sqrt{-G'} e^{-\phi} \Big[R + (\partial\phi)^2 - \frac{H^2}{12} \qquad (4)$$
$$- \frac{1}{4}\mathcal{F}(LML)\mathcal{F} + \frac{1}{8}\mathrm{Tr}(\partial ML \partial ML) + \ldots\Big].$$

Here,

$$G^{(6)}_{mn} = \begin{pmatrix} G'_{\mu\nu} & A^m_\mu G_{mn} \\ A^n_\nu G_{mn} & G_{mn} \end{pmatrix}, \qquad (5)$$

where $A^n_\mu = G^{nm} G_{m\mu}$ and $G'_{\mu\nu} = G_{\mu\nu} + A^m_\mu A^n_\nu G_{mn}$. Here, $\mu, \nu = 0, \ldots, 3$ and $m, n = 1, 2$. The second pair of vector fields are the components $B_{m\mu}$ of the antisymmetric field B. The matrices M and L are

$$M = \begin{pmatrix} G^{-1} & G^{-1}B \\ -BG^{-1} & G \end{pmatrix}, \quad L = \begin{pmatrix} 0 & I_2 \\ I_2 & 0 \end{pmatrix}. \qquad (6)$$

Here, $G \equiv (G_{mn})$, $B \equiv (B_{mn})$, and all contractions in (4) are performed with the metric G'_{mn}. Written in the Einstein frame, where $g_{\mu\nu} = e^{-\phi} G'_{\mu\nu}$, the action (4) is

$$I_4 = \int d^4x \sqrt{-g} \Big[R - \frac{1}{2}(\partial\phi)^2 - \frac{e^{-\phi}}{4}\mathcal{F}(LML)\mathcal{F} \qquad (7)$$
$$+ \frac{a_1}{4}(\mathcal{F}L\mathcal{F}L)^*\mathcal{F} + \frac{1}{8}\mathrm{Tr}(\partial ML \partial ML)\Big],$$

where

$$\phi = \Phi - \frac{1}{2}\ln\det(G_{mn}), \qquad (8)$$
$$\partial_\rho a_1 = -H'^{\mu\nu\lambda} e^{-2\phi}\sqrt{-g} e_{\mu\nu\lambda\rho},$$
$$H' \equiv H'_{\mu\nu\lambda} = H_{\mu\nu\lambda} - (A^{(1)n} H_{n\nu\lambda}$$
$$- A^{(1)m} A^{(1)n} H_{mn} + \text{cycl. perms.}),$$

and the metric of the two-torus is parametrized as [19]

$$G_{mn} = e^{2\sigma} \begin{pmatrix} e^{2\gamma-2\sigma} + a_3^2 - a_3 \\ -a_3 \qquad 1 \end{pmatrix}. \qquad (9)$$

The dilaton ϕ can be split into the sum of the constant part and a term vanishing at spatial infinity, $\phi = \phi_0 + \phi_1$. In string perturbation theory, higher order contributions enter with the factor $e^{\frac{1}{2}\chi\phi}$, where χ is the Euler characteristic of the string world sheet. The exponent $e^{\phi_0} \equiv \epsilon$ can be considered as a string-loop expansion parameter.

The moduli y_i (2) are conventional moduli S, T, U:

$$(y_1, y_2, y_3) = \Big(S = e^{-\phi} + ia_1, \quad T = \sqrt{G} + iB_{12},$$
$$U = \frac{(\sqrt{G} + iG_{12})}{G_{22}}\Big).$$

Here, a_1 is the axion dual to the field strength of the antisymmetric tensor, and $B_{mn} = a_2 \epsilon_{mn}$.

The gauge part of the action (4) with $G_{12} = 0$ and $B_{12} = 0$ is

$$-\frac{1}{4}G_{11}(\mathcal{F}^{(1)1})^2 - \frac{1}{4}G_{22}(\mathcal{F}^{(1)2})^2 \qquad (10)$$
$$- \frac{1}{4}G^{11}(\mathcal{F}^{(2)}_1)^2 - \frac{1}{4}G^{22}(\mathcal{F}^{(2)}_2)^2.$$

The vector fields labeled in correspondence with the moduli with which they form the superfields are

$$A^1_\mu = \sqrt{8}\hat{\mathcal{A}}^0_\mu, \quad B_{1\mu} = \sqrt{8}\hat{\mathcal{A}}^1_\mu, \qquad (11)$$
$$A^2_\mu = \sqrt{8}\hat{\mathcal{A}}^2_\mu, \quad B_{2\mu} = \sqrt{8}\hat{\mathcal{A}}^3_\mu.$$

The factor $\sqrt{8}$ is due to different normalizations of the gauge fields in the actions (1) and (7).

The dynamics of $N = 2$ supersymmetric theory is encoded in the holomorphic prepotential of the theory. In the case of the $N = 2$ supersymmetric compactification of heterotic string theory, the holomorphic prepotential receives only one-loop correction $h^{(1)}$ and is of the form [7, 8, 10]

$$F = -\frac{X^1X^2X^3}{X^0} - i\epsilon X^{0\,2}h^{(1)}\left(-i\frac{X^2}{X^0}, -i\frac{X^3}{X^0}\right) + \dots. \quad (12)$$

In holomorphic sections that admit the prepotential, the coupling constants in the action (1) are calculated using the formula

$$N_{IJ} = \bar{F}_{IJ} + 2i\frac{(\mathrm{Im}F_{IK}X^K)(\mathrm{Im}F_{JL}X^L)}{(X^M\mathrm{Im}F_{MN}X^N)}, \quad (13)$$

where $F_I = \partial_{X^I}F, F_{IJ} = \partial^2_{X^IX^J}F$, etc. Explicit calculation yields

$$N_{00} = iy^3\left(-1 + \epsilon\frac{n}{4y^3}\right), \quad (14)$$

$$N_{01} = -\epsilon\frac{n+2v}{4y_1} - i\epsilon a_1\frac{y_2y_3}{y_1},$$

$$N_{02} = -\epsilon\frac{n+2v-2y_2hy+4y_2h_2}{4y_2} - i\epsilon a_2\frac{y_1y_3}{y_2},$$

$$N_{03} = -\epsilon\frac{n+2v+2y_3hy+4y_3h_3}{4y_3} - i\epsilon a_3\frac{y_1y_2}{y_3},$$

$$N_{11} = -i\frac{y^3}{y_1^2}\left(1 + \epsilon\frac{n}{4y^3}\right),$$

$$N_{12} = \epsilon iy_3\frac{2y_2hy-n}{4y^3} + \epsilon a_3,$$

$$N_{13} = \epsilon iy_2\frac{2y_3hy-n}{4y^3} + \epsilon a_2,$$

$$N_{23} = \epsilon iy_1\frac{2yhy-4y_2h_{23}y_3-n}{4y^3} + \epsilon a_1,$$

$$N_{22} = -i\frac{y^3}{y_2^2}\left(1 - \epsilon\frac{y_2h_{23}y_3}{y_3} + \epsilon\frac{n}{4y^3}\right),$$

$$N_{33} = -i\frac{y^3}{y_3^2}\left(1 - \epsilon\frac{y_3h_{23}y_3}{y^3} + \epsilon\frac{n}{4y^3}\right).$$

Here, we introduced the following notation: $y^3 = y_1y_2y_3$, $hy = h_ay_a = h_2y_2 + h_3y_3$, $yhy = y_ah_{ab}y_b$, $h_a = \partial_{y_a}h$, $h_{ab} = \partial_{y_a}\partial_{y_b}h$, and

$$v = h - hy, \quad n = h - hy + yhy, \quad (15)$$
$$y_2hy = y_2h_{2a}y_b.$$

In the case of magnetic-black-hole solution, the tree-level moduli y_i are real. Because in (14) and below the one-loop corrections are calculated by substituting the tree-level moduli, in cases where there is no confusion, we use the same notation y_i for the real parts of the moduli y_i.

The Kähler potential is invariant under symplectic transformations and its part that depends on the moduli y_i is given by

$$K = -\ln[(y_1 + \bar{y}_1 + \epsilon V)(y_2 + \bar{y}_2)(y_3 + \bar{y}_3)], \quad (16)$$

where the Green–Schwarz function V is

$$V(y_2, \bar{y}_2, y_3, \bar{y}_3) = \frac{\mathrm{Re}h^{(1)} - \mathrm{Re}y_2\mathrm{Re}\partial_{y_2}h^{(1)} - \mathrm{Re}y_3\mathrm{Re}\partial_{y_3}h^{(1)}}{\mathrm{Re}y_2\mathrm{Re}y_3}. \quad (17)$$

In the first order in string coupling,

$$V = e^{-2\gamma}v.$$

The field equations and the Bianchi identities for the gauge field strengths are

$$\partial\mu\left(\sqrt{-g}\mathrm{Im}G_I^{-\mu\nu}\right) = 0, \quad (18)$$
$$\partial\mu\left(\sqrt{-g}\mathrm{Im}\mathcal{F}^{-J\mu\nu}\right) = 0,$$

where $G_I^{-\mu\nu} = \bar{N}_{IJ}\mathcal{F}^{-J\mu\nu}$. Equations (18) are invariant under symplectic transformations

$$O = \begin{pmatrix} A & B \\ C & D \end{pmatrix}, \quad (19)$$

where

$$A^TC - C^TA = 0, B^TD - D^TB = 0,$$
$$A^TD - C^TB = 1.$$

In sections that do not admit a prepotential (including that which naturally appears in compactification of the heterotic string action), the gauge couplings are obtained by making a symplectic transformation of the couplings calculated in the section with the prepotential

$$\hat{N} = (C + DN)(A + BN)^{-1}.$$

Here and below, the quantities with hats refer to the heterotic holomorphic section. At the tree level, transformation to the heterotic section is performed with the matrices [8]

$$A = \mathrm{diag}(1,0,1,1), \quad B = \mathrm{diag}(0,1,0,0),$$
$$C = \mathrm{diag}(0,1,0,0), \quad D = \mathrm{diag}(1,0,1,1).$$

We look for the transformation in the first order in string coupling in the form

$$A = \mathrm{diag}(1,0,1,1) + \epsilon(a_{ij}), \quad (20)$$
$$B = \mathrm{diag}(0,1,0,0) + \epsilon(b_{ij}),$$
$$C = \mathrm{diag}(0,1,0,0) + \epsilon(c_{ij}),$$
$$D = \mathrm{diag}(1,0,1,1) + \epsilon(d_{ij}),$$

where a, b, c, and d are constant matrices. The form of the matrices is constrained by the requirement that, in the heterotic section, the loop corrections to the couplings are proportional to ϵe^{ϕ}. This results in symplectic transformation with $a = b = 0$, c is an arbitrary symmetric matrix with $c_{1i} = 0$, and the only nonzero element of the matrix d is d_{11}.

Explicitly, the matrix of the loop-corrected couplings in the heterotic section is

$$\hat{N}_{IJ} = \begin{pmatrix} N_{00} + \epsilon c_{00} - \dfrac{N_{01}^2}{N_{11}} & \dfrac{N_{01}}{N_{11}} & N_{02} + \epsilon c_{02} - \dfrac{N_{01}N_{12}}{N_{11}} & N_{03} + \epsilon c_{03} - \dfrac{N_{01}N_{13}}{N_{11}} \\ \dfrac{N_{10}}{N_{11}} & -\dfrac{1}{N_{11}} + \epsilon d_{11} & \dfrac{N_{12}}{N_{11}} & \dfrac{N_{13}}{N_{11}} \\ N_{20} + \epsilon c_{20} - \dfrac{N_{21}N_{10}}{N_{11}} & \dfrac{N_{21}}{N_{11}} & N_{22} + \epsilon c_{22} - \dfrac{N_{21}^2}{N_{11}} & N_{23} + \epsilon c_{23} - \dfrac{N_{21}N_{13}}{N_{11}} \\ N_{30} + \epsilon c_{30} - \dfrac{N_{31}N_{10}}{N_{11}} & \dfrac{N_{31}}{N_{11}} & N_{32} + \epsilon c_{32} - \dfrac{N_{31}N_{12}}{N_{11}} & N_{33} + \epsilon c_{33} - \dfrac{N_{31}^2}{N_{11}} \end{pmatrix}. \quad (21)$$

From the symplectic transformation of the field strengths, we obtain the relations between the field strengths:

$$\hat{\mathcal{F}}^{-0} = \mathcal{F}^{-0}, \quad \hat{\mathcal{F}}^{-2} = \mathcal{F}^{-2}, \quad \hat{\mathcal{F}}^{-3} = \mathcal{F}^{-3}, \quad (22)$$

$$\hat{G}_0^- = G_0^- + c_{00}\mathcal{F}^{-0} + c_{02}\mathcal{F}^{-2} + c_{03}\mathcal{F}^{-3},$$
$$\hat{G}_1^- = -\mathcal{F}_1^- + d_{11}G^{-1},$$
$$\hat{G}_2^- = G_2^- + c_{20}\mathcal{F}^{-0} + c_{22}\mathcal{F}^{-2} + c_{23}\mathcal{F}^{-3},$$
$$\hat{G}_3^- = G_3^- + c_{30}\mathcal{F}^{-0} + c_{32}\mathcal{F}^{-2} + c_{33}\mathcal{F}^{-3},$$
$$\mathcal{F}^{-1} = -\frac{\bar{N}_{10}}{\bar{N}_{11}}\hat{\mathcal{F}}^{-0} + \frac{1}{\bar{N}_{11}}\hat{\mathcal{F}}^{-1} - \frac{\bar{N}_{12}}{\bar{N}_{11}}\hat{\mathcal{F}}^{-2} - \frac{\bar{N}_{13}}{\bar{N}_{11}}\hat{\mathcal{F}}^{-3}.$$

The expression for $\mathcal{F}^{-1}$ was obtained from the relation $\hat{G}_I^- = \bar{\hat{N}}_{IJ}\hat{F}^{-J}$ with any $I = 0, 1, 2, 3$ by substituting the gauge couplings (21) and field strengths into the heterotic holomorphic section. Below, it will be made clear that, for a restricted problem of solving equations for the metric and real parts of the moduli, the explicit expressions for the constants in (21) are not necessary.

3. MAGNETIC-BLACK-HOLE SOLUTION

A class of solutions of the equations of motion derived from (7) is [5, 6]

$$ds^2 = -\Lambda(r)dt^2 + \Lambda^{-1}(dr^2 + r^2 d\Omega_2^2), \quad (23)$$
$$\Lambda^2(r) = FK^{-1}kf^{-1},$$
$$\phi = \ln FK^{-1}fk^{-1},$$
$$G_{11} = FK, \quad G_{22} = fk,$$

where

$$K = A\left(1 + \frac{Q_1}{r}\right), \quad F^{-1} = B\left(1 + \frac{Q_2}{r}\right),$$
$$k^{-1} = a\left(1 + \frac{P^1}{r}\right), \quad f = b\left(1 + \frac{P^2}{r}\right)$$

are harmonic functions. Requiring that at spatial infinity the metric and dilaton be asymptotic to the Lorentzian metric and unity, we have $ABab = 1$ and $AB/ab = 1$, which is solved by $AB = 1$ and $ab = 1$. Here, $\mathcal{F}^{(1)1}$ and $\mathcal{F}_1^{(2)}$ are magnetic and $\mathcal{F}^{(1)2}$ and $\mathcal{F}_2^{(2)}$ are electric field strengths, and G_{11} and G_{22} are the nonzero components of the metric of the torus T^2. From the $4D$ point of view, the backgrounds are interpreted as charged black holes.

We shall concentrate on the case of tree-level solutions that are purely magnetic ($Q_1 = Q_2 = 0$) extremal black holes with the metric of the internal two-torus (9) independent of $4D$ coordinates and vanishing antisymmetric tensor B_{nm}. These solutions can be embedded in $4D$, $N = 2$ dilatonic supergravity and leave $1/2$ of the supersymmetry unbroken. In this case, the nonvanishing backgrounds of the chiral null model are expressed via a single function (we consider one-center solution) f_0:

$$ds^2 = -f_0^{-1}dt^2 + f_0 dx^{i2}, \quad (24)$$
$$\phi = \ln f_0, \quad a_\varphi = a^{-1}P(1 - \cos\vartheta),$$
$$b_\varphi = aP(1 - \cos\vartheta), \quad f_0(r) = 1 + P/r,$$

where a_φ and b_φ are nonzero components of potentials in spherical coordinates. The tree-level components of the internal metric G_{mn} are

$$G_{11} = a^2, \quad G_{22} = A^2. \quad (25)$$

The magnetic field strengths are

$$\hat{\mathcal{F}}^{(1)1}_{ij} = a^{-1}\hat{\mathcal{F}}_{ij}, \quad \hat{\mathcal{F}}^{(2)}_{1ij} = a\hat{\mathcal{F}}_{ij}, \quad \hat{\mathcal{F}}_{ij} = -\varepsilon_{ijk}\partial^k f_0 \tag{26}$$

and, in spherical coordinates, have a single nonzero component $\hat{\mathcal{F}}_{\vartheta\varphi} = P\sin\vartheta$.

4. LOOP-CORRECTED EFFECTIVE ACTION

4.1. Kinetic Terms of the Moduli

At the tree level, in the case of the magnetic-black-hole solution, the moduli a_i vanish and, if they appear at the one-loop level, are of order $O(\epsilon)$. The Green–Schwarz function, which is of the first order in string coupling, depends on the real parts of tree-level moduli. For a choice of magnetic charges discussed in the preceding section, the tree-level moduli $\mathrm{Re}T$ and $\mathrm{Re}U$ are constants, and $\partial\mathrm{Re}T$ and $\partial\mathrm{Re}U$ are of the first order in string coupling ϵ. Keeping only relevant terms up to the second order in ϵ, for the kinetic term of the moduli, we obtain

$$\begin{aligned} 4\frac{\partial^2 K}{\partial z_i \partial \bar{z}^{\bar{j}}}\partial_\mu z^i \partial^\mu \bar{z}^{\bar{j}} &= \frac{|\partial S|^2}{(\mathrm{Re}S)^2} \\ \times\left(1-\epsilon\frac{V}{\mathrm{Re}S}\right) &+ \frac{|\partial T|^2}{(\mathrm{Re}T)^2} + \frac{|\partial U|^2}{(\mathrm{Re}U)^2} \\ - \partial S\partial\bar{T}\epsilon\frac{V_{\bar{T}}}{(\mathrm{Re}S)^2} &- \partial\bar{S}\partial T\epsilon\frac{V_T}{(\mathrm{Re}S)^2} \\ - \partial S\partial\bar{U}\epsilon\frac{V_{\bar{U}}}{(\mathrm{Re}S)^2} &- \partial\bar{S}\partial U\epsilon\frac{V_U}{(\mathrm{Re}S)^2}. \end{aligned} \tag{27}$$

Here, $|\partial S|^2 = (\partial\mathrm{Re}S)^2 + (\partial a_1)^2$, etc., and $(\partial a_i)^2 = O(\epsilon^2)$.

From the above, it follows that, with accuracy of the terms of higher order in $O(\epsilon)$, the imaginary parts of the moduli S, T, and U do not enter the equations for the real parts. Since, in this paper, we are primarily interested in string-loop corrections to the metric and dilaton, in the following, we shall consider the real parts of the moduli.

Keeping the leading and the next-order terms in string coupling ϵ, we obtain the kinetic terms for the moduli as

$$\begin{aligned} 2\frac{\partial^2 K}{\partial z_i \partial \bar{z}^{\bar{j}}}\partial_\mu z^i \partial^\mu \bar{z}^{\bar{j}} &= \frac{(\partial\phi)^2}{2}(1-\epsilon e^\phi V) + (\partial\sigma)^2 \\ + (\partial\gamma)^2 - \partial\phi(\partial\gamma+\partial\sigma)\epsilon e^\phi \mathrm{Re}V_T \\ - \partial\phi(\partial\gamma-\partial\sigma)\epsilon e^\phi \mathrm{Re}V_U. \end{aligned} \tag{28}$$

4.2. Gauge Part of the Action

Let us consider the gauge part of the action. In the basis associated with the heterotic string compactification, the tree-level couplings calculated via (21) are

$$\hat{N}_{00} = -iy_1y_2y_3, \quad \hat{N}_{11} = -i\frac{y_1}{y_2y_3},$$
$$\hat{N}_{22} = -i\frac{y_1y_3}{y_2}, \quad \hat{N}_{33} = -i\frac{y_1y_2}{y_3}.$$

With accuracy to the terms of the first order in string coupling ϵ, general covariance fixes the form of the loop-corrected gauge part in the action (7) as

$$\begin{aligned} L_g = -\frac{1}{4}\Big[&(e^{-\phi}+\Delta_{11})G_{11}(\hat{\mathcal{F}}^{(1)1})^2 \\ &+ (e^{-\phi}+\Delta_{22})G^{11}(\hat{\mathcal{F}}^{(2)}_1)^2 + 2\Delta_{12}(\hat{\mathcal{F}}^{(1)1}\hat{\mathcal{F}}^{(2)}_1)\Big], \end{aligned} \tag{29}$$

where $\Delta_{IJ} = O(\epsilon)$. Using the expressions for the loop-corrected couplings $\hat{N}_{IJ}$, the corresponding terms in the action (1) written in the basis associated with the heterotic string compactification are

$$\begin{aligned} L_g = -2\Bigg[&\left(e^{-\phi+2\gamma} - \epsilon\frac{n}{4}\right)(\hat{\mathcal{F}}^0)^2 \\ &+ \left(e^{-\phi-2\gamma} - \epsilon\frac{n}{4}e^{-4\gamma}\right)(\hat{\mathcal{F}}^1)^2 + \epsilon\frac{n+2v}{2}(\hat{\mathcal{F}}^0\hat{\mathcal{F}}^1)\Bigg]. \end{aligned} \tag{30}$$

The gauge terms in the action (1) can also be written as

$$\mathrm{Im}\hat{N}_{IJ}\hat{\mathcal{F}}^I_{\mu\nu}\hat{\mathcal{F}}^{\mu\nu J} + \frac{1}{\sqrt{-g}}\mathrm{Re}\hat{N}_{IJ}\hat{\mathcal{F}}^{*I}_{\mu\nu}\hat{\mathcal{F}}^{\mu\nu J}. \tag{31}$$

Since at the tree level only magnetic fields are present, the second term in (31) is zero. At the one-loop level, this term can appear only if electric fields, with the charges of order $O(\epsilon)$, are generated. Because the couplings $\mathrm{Re}N_{0i}$ are of order $O(\epsilon)$, these (topological) terms are of order $O(\epsilon^2)$. To conclude, all the terms in the gauge part of the action that are absent at the tree level are of order $O(\epsilon^2)$ at the one-loop level.

Collecting the expressions for the loop-corrected gauge and moduli parts of the action and keeping only relevant terms needed for solving the Einstein equations and equations for moduli, we obtain the loop-corrected $4D$ action (in the Einstein frame) in the form

$$\begin{aligned} S = \int d^4x\sqrt{-g}\Bigg[&R - \frac{1}{2}(\partial\phi)^2(1-\epsilon e^\phi V) \\ &- (\partial\sigma)^2 - (\partial\gamma)^2 + \partial\phi(\partial\gamma+\partial\sigma)\epsilon e^\phi\mathrm{Re}V_T \\ &+ \partial\phi(\partial\gamma-\partial\sigma)\epsilon e^\phi\mathrm{Re}V_U \end{aligned} \tag{32}$$

$$-2\left(\left(e^{-\phi+2\gamma}-\epsilon\frac{n}{4}\right)(\mathcal{F}^{(1)1})^2 + \left(e^{-\phi-2\gamma}-\epsilon\frac{n}{4}e^{-4\gamma}\right)(\hat{\mathcal{F}}_1^{(2)})^2 + \epsilon\frac{n+2v}{4}(\hat{\mathcal{F}}^{(1)1}\hat{\mathcal{F}}_1^{(2)})\right)\Bigg].$$

Here and below,

$$(\mathcal{F}^2)\equiv\mathcal{F}_{\mu\nu}\mathcal{F}^{\mu\nu},\quad (\mathcal{F}^2)_{\mu\nu}\equiv\mathcal{F}_\mu^\lambda\mathcal{F}^{\nu\lambda}.$$

5. SOLUTION OF MAXWELL EQUATIONS

The system of Maxwell equations and Bianchi identities for the gauge field strengths obtained from the action (1) is

$$\partial_\mu\left(\sqrt{-g}\mathrm{Im}\hat{N}_{IJ}\hat{\mathcal{F}}^J+\mathrm{Re}\hat{N}_{IJ}\hat{\mathcal{F}}^{*J}\right)^{\mu\nu}=0 \quad (33)$$

and

$$\partial_\mu\hat{\mathcal{F}}^{*J\mu\nu}=0. \quad (34)$$

With the required accuracy, keeping only the terms of the leading and first order in ϵ, we obtain the Maxwell equations in the form

$$J=0:\quad \partial_n[\sqrt{-g}\mathrm{Im}\hat{N}_{00}\hat{\mathcal{F}}^0+\mathrm{Re}\hat{N}_{00}\,{}^*\hat{\mathcal{F}}^0+\mathrm{Re}\hat{N}_{01}\,{}^*\hat{\mathcal{F}}^1]^{nm}=0, \quad (35)$$

$$J=1:\quad \partial_n[\sqrt{-g}\mathrm{Im}\hat{N}_{11}\hat{\mathcal{F}}^1+\mathrm{Re}\hat{N}_{10}\,{}^*\hat{\mathcal{F}}^0+\mathrm{Re}\hat{N}_{11}\,{}^*\hat{\mathcal{F}}^1]^{nm}=0, \quad (36)$$

$$J=2:\quad \partial_n[\sqrt{-g}\mathrm{Im}\hat{N}_{22}\hat{\mathcal{F}}^2+\mathrm{Re}\hat{N}_{20}\,{}^*\hat{\mathcal{F}}^0+\mathrm{Re}\hat{N}_{21}\,{}^*\hat{\mathcal{F}}^1]^{nm}=0, \quad (37)$$

$$J=3:\quad \partial_n[\sqrt{-g}\mathrm{Im}\hat{N}_{33}\hat{\mathcal{F}}^3+\mathrm{Re}\hat{N}_{30}\,{}^*\hat{\mathcal{F}}^0+\mathrm{Re}\hat{N}_{31}\,{}^*\hat{\mathcal{F}}^1]^{nm}=0. \quad (38)$$

Only diagonal gauge couplings $\hat{N}_{II}$ contain terms of zero order in string coupling.

The $\nu=\vartheta$ component of Eq. (33) with $I=0$ (the $\nu=\varphi$ component yields the same result) with accuracy up to the terms of order $O(\epsilon)$ is

$$\partial_\varphi\left(\sqrt{-g}\mathrm{Im}\hat{N}_{00}\hat{\mathcal{F}}^0+\mathrm{Re}\hat{N}_{01}\hat{\mathcal{F}}^1\right)^{\vartheta\varphi}=0$$

and, for spherically symmetric fields, is satisfied identically. Here, ${}^*\mathcal{F}^{0r}=\mathcal{F}_{\vartheta\varphi}$ and ${}^*\mathcal{F}_{\vartheta\varphi}=-\mathcal{F}^{0r}$. A similar equation holds for $I=1$. Bianchi identities are

$$\partial_r\hat{\mathcal{F}}^{0,1}_{\vartheta\varphi}=0,$$

yielding the field strengths in the form

$$\hat{\mathcal{F}}^{0,1}_{\varphi\vartheta}=P^{0,1}\sin\vartheta. \quad (39)$$

Comparing (39) with the field strengths (26), we find that

$$P^0=\frac{e^{-\gamma_0}P}{\sqrt{8}},\quad P^1=\frac{e^{\gamma_0}P}{\sqrt{8}}, \quad (40)$$

where $a=e^{\gamma_0}$. Solving the Maxwell equations and Bianchi identities for electric field strengths, we obtain

$$\hat{\mathcal{F}}^{0\,0r}=\epsilon\frac{C_0-c_{00}P^0-a_1P^1}{\sqrt{-g'}\mathrm{Im}N_{00}}, \quad (41)$$

$$\hat{\mathcal{F}}^{1\,0r}=\epsilon\frac{C_1-d_{11}P^1-a_1P^0}{\sqrt{-g'}}\mathrm{Im}N_{11},$$

$$\hat{\mathcal{F}}^{2\,0r}=\frac{\epsilon C_2-(\mathrm{Re}N_{20}+\epsilon c_{20})P^0-\mathrm{Re}\frac{N_{21}}{N_{11}}P^1}{\sqrt{-g'}\mathrm{Im}N_{22}},$$

$$\hat{\mathcal{F}}^{3\,0r}=\frac{\epsilon C_3-(\mathrm{Re}N_{30}+\epsilon c_{30})P^0-\mathrm{Re}\frac{N_{31}}{N_{11}}P^1}{\sqrt{-g'}\mathrm{Im}N_{33}}. \quad (42)$$

In (41), we expressed all the couplings in the basis with the prepotential. All the electric field strengths are of the first order in the string coupling. Here, C_i are arbitrary constants, $\sqrt{-g'}=e^{-2U}r^2$. Depending on the boundary conditions imposed on the loop-corrected solution, one can require that either the loop-corrected solution, as the tree-level one, contain only magnetic charges, or any number of electric charges of the first order in string coupling can appear. By a suitable choice of arbitrary constants, any number of electric charges can be made equal to zero.

6. SOLUTION OF THE LOOP-CORRECTED EINSTEIN AND DILATON EQUATIONS

The general ansatz for the spherically symmetric metric is

$$ds_4^2=-e^\nu dt^2+e^\lambda dr^2+e^\mu d\Omega_2^2. \quad (43)$$

In the leading order, from (10), the metric components, dilaton, and moduli are

$$\nu_{(0)}=-\ln f_0,\quad \lambda_{(0)}=\ln f_0, \quad (44)$$
$$\mu_{(0)}=\ln f_0+2\ln r,\quad \phi_{(0)}=\ln f_0,$$

where the function f_0 was introduced in (24). The tree-level field strengths are those in (26), and

$$(\hat{\mathcal{F}}^2)^2_{(0)}=2q'^2,\quad q'\equiv f_0'/f_0.$$

In the first order in string coupling, we look for a solution in the form

$$\nu=-\ln f_0+\epsilon n,\quad \lambda=\ln f_0+\epsilon l, \quad (45)$$
$$\mu=\ln f_0+2\ln r+\epsilon m,\quad \phi=\ln f_0+\epsilon\phi_1,$$
$$\gamma=\gamma_0+\epsilon\gamma_1,\quad \sigma=\sigma_0+\epsilon\sigma_1.$$

Here $n, m, l, \phi_1, \gamma_1$, and σ_1 are unknown functions that are determined from the field equations. Keeping in the dilaton equation of motion the terms up to the order $O(\epsilon)$, we obtain

$$\frac{1}{\sqrt{-g}}\partial_\mu\left(g^{\mu\nu}\sqrt{-g}\partial_\nu\phi(1-\epsilon V e^{\phi})\right) + \frac{1}{2}(\partial\phi)^2\epsilon V e^{\phi} + \frac{1}{4}e^{-\phi}\left(e^{2\gamma}(\hat{\mathcal{F}}^{(1)1})^2 + e^{-2\gamma}(\hat{\mathcal{F}}_1^{(2)})^2\right) = 0. \quad (46)$$

With the required accuracy, the terms containing the gauge fields can be written as

$$\frac{1}{4}e^{-\phi}\left[e^{2\gamma_0}(1+2\epsilon\gamma_1)(\hat{\mathcal{F}}^{(1)1})^2 + e^{-2\gamma_0}(1-2\epsilon\gamma_1)(\hat{\mathcal{F}}_1^{(2)})^2\right].$$

In view of (40), the terms with γ_1 cancel, and we are left with

$$\frac{1}{\sqrt{-g}}\partial_\mu\left(g^{\mu\nu}\sqrt{-g}\partial_\nu\phi\right) - \frac{1}{2}\epsilon e^{\phi}(\partial\phi)^2 V + \frac{1}{2}e^{-\phi}(\hat{\mathcal{F}})^2(1+\epsilon e^{\phi}V) = 0, \quad (47)$$

where we inverted the bracket $(1-\epsilon V e^{\phi})$ in the first term in (46). The field $\hat{\mathcal{F}}$ is defined in (26). Here and below, all the expressions having the factor ϵ are calculated with the tree-level entries.

Up to the terms of the first order in string coupling, the Einstein equations are

$$R_{\mu\nu} - \frac{1}{2}g_{\mu\nu}R - \frac{1}{2}\left(\partial_\mu\phi\partial_\nu\phi - \frac{1}{2}g_{\mu\nu}(\partial\phi)^2\right)\times\left(1-\epsilon V e^{\phi}\right) + (L_g)_{\mu\nu} - \frac{1}{2}g_{\mu\nu}L_g = 0. \quad (48)$$

Here,

$$L_g = \frac{1}{4}\left[2e^{-\phi}+\epsilon V\right](\hat{\mathcal{F}}^2),$$
$$(L_g)_{\mu\nu} = \frac{1}{4}\left[2e^{-\phi}+\epsilon V\right](\hat{\mathcal{F}})^2_{\mu\nu}.$$

The field strengths squared have the following nonzero components:

$$(\hat{\mathcal{F}})^{2\,\varphi}_{\varphi} = (\hat{\mathcal{F}})^{2\,\vartheta}_{\vartheta} = \frac{(\hat{\mathcal{F}})^2}{2},$$

where

$$(\hat{\mathcal{F}})^2 = 2q'^2(1-2\epsilon m). \quad (49)$$

The functions σ_1 and γ_1 decouple from the above equations. Since in this paper we are interested in the form of the loop-corrected $4D$ metric and dilaton, we shall not determine these functions explicitly (the corresponding equations of motion are solved elsewhere). The Einstein Eqs. (48) (with one index lifted) take the form [20]

$$e^{-\lambda}\left(\mu'' + \frac{3}{4}\mu'^2 - \frac{\mu'\lambda'}{2}\right) - e^{-\mu} + \frac{1}{4}e^{-\lambda}\phi'^2 \times\left(1-\epsilon V e^{\phi}\right) + \frac{1}{4}\left(e^{-\phi}+\frac{\epsilon V}{2}\right)(\hat{\lambda})^2 = 0, \quad (50)$$

$$e^{-\lambda}\left(\frac{\mu'^2}{2} + \mu'\nu'\right) - 2e^{-\mu} - \frac{1}{2}e^{-\lambda}\phi'^2 \times\left(1-\epsilon V e^{\phi}\right) + \frac{1}{2}\left(e^{-\phi}+\frac{\epsilon V}{2}\right)(\hat{\mathcal{F}})^2 = 0, \quad (51)$$

$$e^{-\lambda}(2\mu'' + 2\nu'' + \mu'^2 + \nu'^2 - \mu'\lambda' - \nu'\lambda' + \mu'\nu') + e^{-\lambda}\phi'^2\left(1-\epsilon V e^{\phi}\right) - \left(e^{-\phi}+\frac{\epsilon V}{2}\right)(\hat{\mathcal{F}})^2 = 0. \quad (52)$$

In the first order in parameter ϵ, the Einstein equations (50)–(52) are[1)]

$$m'' + m'\left(q' + \frac{3}{r}\right) - l'\left(\frac{1}{2}q' + \frac{1}{r}\right) + \phi_1'\frac{q'}{2} - \frac{l-m}{r^2} + \frac{1}{2}q'^2 s = 0, \quad (53)$$

$$m'\frac{2}{r} + n'\left(q' + \frac{2}{r}\right) - \phi_1'q' - 2\frac{l-m}{r^2} + q'^2 s + V f_0 q'^2 = 0, \quad (54)$$

$$m'' + n'' + m'\frac{2}{r} - l'\frac{1}{r} + n'\left(-q' + \frac{1}{r}\right) + \phi_1'q' - q'^2 s - V f_0 q'^2 = 0. \quad (55)$$

Here,

$$s = l - \phi_1 - 2m. \quad (56)$$

We also need the equation for the dilaton (47) in the $O(\epsilon)$ order:

$$\phi_1'' + \frac{2}{r}\phi_1' + \frac{1}{2}(2m' + n' - l')q' + q'^2 s + a f_0 q'^2 = 0. \quad (57)$$

We look for a solution such that $l = -n$, because, in this case, as at the tree level, the components of the metric satisfy the relation $g_{tt} = g_{rr}^{-1}$. Substituting

[1)] Below, we work with dimensionless variable r. In the final expressions, P is reinstated by substitution $r \to r/P$.

this ansatz into the above equations and forming the combination of equations (53) − 1/2(54), we have

$$m'' + m'\left(q' + \frac{2}{r}\right) + \phi_1' q' - \frac{V}{2} f_0 q'^2 = 0. \quad (58)$$

Taking into account the explicit form of the functions f_0 and $q' = f_0'/f_0$, we integrate this equation and obtain the first integral as

$$m' + q'(C_1 + \phi_1) - \frac{Vq'}{2r} = 0, \quad (59)$$

where C_1 is an integration constant. Substituting (59) into the remaining equations, we find that the system is consistent.

Solving the resulting system of differential equations and requiring that, in the limit $r \to \infty$, our solutions should be asymptotic to the Lorentzian metric, we obtain

$$m = -\frac{P}{r}A_1 + A_2\frac{P}{r+P}, \quad (60)$$
$$n = \frac{P}{r}\left(A_1 - \frac{C_2}{2}\right) - A_2\frac{P}{r+P},$$

and

$$\phi_1 = \frac{P}{r}\left(A_1 + \frac{V}{2}\right) + A_2\frac{P}{r+P}. \quad (61)$$

Here, A_1, A_2, and C_2 are arbitrary constants.

By coordinate transformation the metric (43) can be reduced to the form

$$ds^2 = -e^{2U(R)}dt^2 + e^{-2U(R)}(dR^2 + R^2 d\Omega^2), \quad (62)$$

where the new variable R is determined from the relation

$$\ln\frac{R}{R_1} = \int_{r_1}^{r} dr' e^{\frac{1}{2}(\lambda-\mu)(r')}.$$

Here, r_1 is an arbitrary point and $R_1 = R(r_1)$. Substituting into (62) solution (60), we have $R = Ce^{\frac{\epsilon C_2}{2r}}$, where C is an arbitrary constant. In the new coordinates, the asymptotic form of the metric and dilaton are obtained by setting $C_2 = 0$ in (60).

7. $N = 2$ SUPERSYMMETRY TRANSFORMATIONS

To write the supersymmetry transformations, one introduces symplectic invariant expressions (for example, [13–15, 17])

$$S_{\mu\nu} = X^I \mathrm{Im}N_{IJ}\mathcal{F}^{-J}_{\mu\nu}, \quad (63)$$
$$T^-_{\mu\nu} = 2ie^{K/2}S_{\mu\nu},$$

and

$$G^{-i}_{\mu\nu} = -k^{i\bar{j}}\bar{f}^I_{\bar{j}}\mathrm{Im}N_{IJ}\mathcal{F}^{-J}_{\mu\nu}, \quad (64)$$

where $k^{i\bar{j}}$ is the inverse Kähler metric and

$$f^I_i = \left(\partial_i + \frac{1}{2}\partial_i K\right)e^{K/2}X^I.$$

Supersymmetry transformations of the chiral gravitino $\psi_{\alpha\mu}$ and gaugini $\lambda^{i\alpha}$ are

$$\delta\psi_{\alpha\mu} = D_\mu\epsilon_\alpha - T^-_{\mu\nu}\gamma^\nu\epsilon_{\alpha\beta}\epsilon^\beta, \quad (65)$$

$$\delta\lambda^i_\alpha = i\gamma^\mu\partial_\mu z^i\epsilon^\alpha + G^{-i}_{\mu\nu}\gamma^\mu\gamma^\nu\epsilon^{\alpha\beta}\epsilon_\beta, \quad (66)$$

where

$$D_\mu\epsilon_\alpha = \left(\partial_\mu - \frac{1}{4}w_\mu^{\hat{a}\hat{b}}\gamma_{\hat{a}}\gamma_{\hat{b}} + \frac{i}{2}Q_\mu\right)\epsilon_\alpha.$$

Here, $w_\mu^{\hat{a}\hat{b}}$ and Q_μ are the spin and Kähler connections. The tangent space indices are $\hat{a}$, $\hat{b}$, ..., and the curved space indices are without hats: a, b, ...

Requiring that supersymmetry variations of spinors vanish, we obtain a system of supersymmetric Killing equations for the moduli. We look for a solution of this system with the supersymmetry parameter satisfying the relation $\epsilon^\alpha = \gamma_{\hat{0}}\epsilon^{\alpha\beta}\epsilon_\beta$. The $\mu = 0$ component of the equation $\delta\psi_{\alpha\mu} = 0$ takes the form

$$\left(\frac{1}{2}w_0^{\hat{a}\hat{b}}\gamma_{\hat{a}}\gamma_{\hat{b}}\gamma_{\hat{0}} - T^-_{0n}e^{\hat{b}n}\gamma_{\hat{b}}\right)\epsilon_{\alpha\beta}\epsilon^\beta = 0. \quad (67)$$

Here, $e^{\mu\hat{b}}$ is the inverse Vielbein.

In the metric (62), the only nonvanishing components of the spin connection $w_0^{\hat{a}\hat{b}}$ are $w_0^{\hat{0}\hat{b}} = \frac{1}{2}\partial_b e^{2U}$. The Vielbein $e_\mu^{\hat{b}}$ is $e_\mu^{\hat{b}} = \delta_\mu^b e^U$. To have a nontrivial solution for the supersymmetry parameter, we must require that

$$\frac{1}{2}w_0^{\hat{0}\hat{n}} - e^U T^-_{0n} = 0. \quad (68)$$

Using the relations

$$G^-_{mn} = i\epsilon_{mnp0}G^{-p0}$$

and

$$G^-_{\mu\nu}\gamma^\mu\gamma^\nu\epsilon_\alpha = 4G^-_{0n}\gamma^0\gamma^n\epsilon_\alpha$$

valid for any self-dual tensor and chiral spinor, the condition that supersymmetry transformation of gaugini vanishes is written as

$$(i\gamma^n\partial_n z^i\gamma^{\hat{0}} + 4G^{-i}_{0n}\gamma^0\gamma^n)\epsilon^{\alpha\beta}\epsilon_\beta = 0. \quad (69)$$

There is a nontrivial solution provided

$$i\partial_n z^i + 4e^{-U}G^{-i}_{0n} = 0. \quad (70)$$

The factor e^{-U} is due to the relation $\gamma_{\hat{0}} = -\gamma^{\hat{0}} = -e_0^{\hat{0}}\gamma^0 = -e^U\gamma^0$. Convoluting Eq. (70) with the functions f_i^I and using the relation of special $N = 2$ geometry

$$k^{i\bar{j}} f_i^I \bar{f}_{\bar{j}}^J = -\frac{1}{2}(\mathrm{Im}N)^{IJ} - e^K \bar{X}^I X^J,$$

we finally obtain it in the form [22–24]

$$if_i^I \partial_n z^i + 4e^{-U}\left(\frac{1}{2}\mathcal{F}_{0n}^{-I} + e^K \bar{X}^I S_{0n}\right) = 0. \quad (71)$$

8. MAGNETIC-BLACK-HOLE SOLUTION OF SPINOR KILLING EQUATIONS

In this section, we solve the combined system of equations for the gauge field strengths and the moduli. We look for a string-tree-level solution with the metric in the form (62), two magnetic fields $\hat{\mathcal{F}}_{\mu\nu}^0$ and $\hat{\mathcal{F}}_{\mu\nu}^1$, and purely real moduli y_i (2). This means that we consider configurations with diagonal metrics G_{mn}, vanishing tensor B_{mn}, and vanishing functions a_1.

Using the field strengths (39) and the couplings (21), we obtain the tree-level expression for the function T_{0n}^- (63):

$$\begin{aligned} T_{0n}^- &= 2ie^{K/2}S_{0n} = 2ie^{K/2} \quad (72)\\ &\times (\mathrm{Im}N_{00}\hat{\mathcal{F}}_{0n}^{-0} + iy_1\mathrm{Im}N_{11}\hat{\mathcal{F}}_{0n}^{-1})\\ &= 2ie^{K/2}(-y_1y_2y_3\hat{\mathcal{F}}_{0n}^{-0} - y_1\hat{\mathcal{F}}_{0n}^{-1})\\ &= \left(\frac{y_1y_2y_3}{8}\right)^{1/2}\left(P^0 + \frac{P^1}{y_2y_3}\right)e^{2U}\frac{x^n}{r^3}. \end{aligned}$$

Here, K is the tree-level Kähler potential, $K = -\ln 8y_1y_2y_3$.

The gravitini Eq. (68) takes the form

$$\frac{1}{4}\partial_n e^{2U} - \left(\frac{y_1y_2y_3}{8}\right)^{1/2} e^{3U}\left(P^0 + \frac{P^1}{y_2y_3}\right)\frac{x^n}{r^3} = 0. \quad (73)$$

The tree-level gaugini Eqs. (71) written in the section associated with the prepotential are

$$\begin{aligned} I = 0: &\quad \frac{ie^{K/2}}{2}\partial_n \ln y_1y_2y_3 - 4e^{-U} \quad (74)\\ &\times\left(\frac{1}{2}\mathcal{F}_{0n}^{-0} + e^K S_{0n}\right) = 0,\\ I = 1: &\quad \frac{y_1e^{K/2}}{2}\partial_n \ln\frac{y_2y_3}{y_1} + 4e^{-U}\\ &\times\left(\frac{\hat{\mathcal{F}}_{0n}^{-1}}{2\bar{N}_{11}} - iy_1e^K S_{0n}\right) = 0,\\ I = 2: &\quad \frac{y_2e^{K/2}}{2}\partial_n \ln\frac{y_1y_3}{y_2} + 4e^{-U}\\ &\times\left(-iy_2e^K S_{0n}\right) = 0,\\ I = 3: &\quad \frac{y_3e^{K/2}}{2}\partial_n \ln\frac{y_1y_2}{y_3} + 4e^{-U}\\ &\times\left(-iy_3e^K S_{0n}\right) = 0. \end{aligned}$$

In Eq. (74) with $I = 1$, by using (22), we expressed the field strength in the basis with the prepotential via that in the heterotic section. The system of Eqs. (73) and (74) is solved by a general configuration of a magnetic black hole with two arbitrary magnetic charges [5, 6]. In the following, we shall consider a particular extremal solution

$$e^{-2U} = 1 + \frac{P}{r}, \quad y_1 = e^{-\phi} = \left(1 + \frac{P}{r}\right)^{-1}. \quad (75)$$

The charges P^0 and P^1 are expressed via the charge P (cf. (40)),

$$P^0 = \frac{P^1}{y_2y_3}, \quad P = \sqrt{8y_2y_3}P^0, \quad (76)$$

and the moduli y_2, y_3 are arbitrary real constants. The metric components G_{mn} of the torus are

$$G_{11} = y_2y_3 = e^{2\gamma}, \qquad G_{22} = y_2/y_3 = e^{2\sigma}.$$

As in (11), the factor $\sqrt{8}$ appears because of different normalizations of vector fields in (1) and (7).

9. SOLUTION OF THE LOOP-CORRECTED SPINOR KILLING EQUATIONS

Substituting solutions for the field strengths (41) and using the loop-corrected gauge couplings (14), we have

$$\begin{aligned} S_{0n} = \{[&P^0(\mathrm{Im}N_{00} + y_i\mathrm{Re}N_{i0} + \epsilon c_{0a}y_a) \quad (77)\\ &- P^1y_1 - \epsilon(C_2y_2 + C_3y_3)]\\ &- i\epsilon[P^0(a_1y_2y_3 + a_2y_1y_3 + a_3y_1y_2) + a_aQ_a\\ &+ a_1P^1 - (C_0 - c_{00}P^0)\\ &- (C_1 - d_{11}P^1)y_2y_3]\}\frac{i}{2}e^{2U}\frac{x^n}{r^3}. \end{aligned}$$

Only the couplings N_{00} and N_{i0}, $i = 1, 2, 3$, enter the final expression (77), yielding

$$\mathrm{Im}N_{00} + y_i\mathrm{Re}N_{i0} = -(y_1y_2y_3 + \epsilon(2v + h_ay_a)).$$

All the terms containing second derivatives of the prepotential have canceled. Note that $\mathrm{Re}S_{0n}$ depends only on the constants C_2 and C_3.

Since gaugini spinor Killing equations are linear in derivatives of the moduli, and the functions a_i are of the first order in string coupling, the equations for the real parts of the moduli, which are the real parts of spinor Killing equations, are independent of the imaginary parts of the moduli. The equations for the imaginary parts of the moduli decouple from those for the real parts. In the following, we shall discuss only the spinor Killing equations for the real parts of the moduli. The equations for the axions will be considered elsewhere.

Using the Kähler potential (16), we calculate the combinations $B_n^I = f_i^I \partial_n z^i$ that enter the spinor Killing equations (27) for the moduli z_i. We have

$$B_n^0 = -\frac{1}{2} e^{K/2} \left(1 - \epsilon \frac{V}{2y_1}\right) \partial_n \ln y^3, \qquad (78)$$

$$B_n^i = i y_i \left(B_n^0 + e^{K/2} \partial_n \ln y_i\right), \qquad i = 1,2,3.$$

All the expressions are calculated in the first order in the string coupling. In particular, all the factors multiplying the expression ϵV should be taken in the leading order in string coupling.

The function $2U$ in the metric will be written as $2U_0 + \epsilon u_1$. At the tree level [see (75)], we have

$$e^{-2U_0} = e^{\phi_0} = f_0 = 1 + P/r.$$

For the Kähler potential, we have

$$e^K = \frac{f_0 e^{-2\gamma_0}}{8} \left[1 + \epsilon \left(\phi_1 - 2\gamma_1 - \frac{V f_0}{2}\right)\right]. \qquad (79)$$

The function T_{0n}^- (63) which enters the gravitini Eq. (68) is transformed to the form

$$T_{0n}^- = e^{K/2} y_1 [P^0 e^{2\gamma} (1 + \epsilon(2V + h_a y_a e^{-2\gamma_0}) f_0) \qquad (80)$$
$$+ P^1 + \epsilon C_a y_a f_0] e^{2U} \frac{x^n}{r^3}.$$

The factors f_0 appear because the modulus y_1, when it multiplies an expression of the first order in string coupling, can be replaced by its tree-level value f_0^{-1}.

Using the expression for the Kähler potential (79) and expanding all the terms in (80) to the first order in string coupling, we obtain

$$T_{0n}^- = f_0^{-1/2} \frac{P}{4} \qquad (81)$$
$$\times \left[1 + \epsilon \left(-\frac{\phi_1}{2} + u_1 + \left(\frac{3V}{4} + C\right) f_0\right)\right] \frac{x^n}{r^3},$$

where the constant C is

$$C = \frac{1}{2} \left(h_a y_a + \frac{C_a y_a}{P^0}\right) e^{-2\gamma_0}. \qquad (82)$$

Substituting Eq. (81) into the gravitini spinor Killing equation, we obtain it in the form

$$\frac{1}{4} \partial_n [f_0^{-1}(1 + \epsilon u_1)] - \frac{P}{4} f_0^{-2} \qquad (83)$$
$$\times \left[1 + \epsilon \left(\frac{3u_1}{2} - \frac{\phi_1}{2} + \left(\frac{3V}{4} + C\right)\right)\right] \frac{x^n}{r^3} = 0.$$

In this equation, the combination of the tree-level terms vanishes; the remaining part of the first order in string coupling is

$$\frac{u_1'}{q'} + \frac{u_1 - \phi_1}{2} + \left(\frac{3V}{4} + C\right) f_0 = 0. \qquad (84)$$

Here, q' is defined after (44).

Let us consider the gaugini spinor Killing equations (71). Substituting the expression

$$e^K S_{0n} = -\frac{1}{4} \left(1 - \epsilon \left(\gamma_1 + \left(\frac{V}{2} + C\right) f_0\right)\right) \qquad (85)$$
$$\times \left(\frac{P e^{-\gamma_0}}{\sqrt{8}} \frac{i}{2} e^{2U} \frac{x^n}{r^3}\right),$$

we obtain the combination $(1/2)\mathcal{F}_{0n}^{-0} + e^K S_{0n}$ in the form

$$\frac{1}{2} \mathcal{F}_{0n}^{-0} + e^K S_{0n} \qquad (86)$$
$$= \frac{1}{4} \left(1 + \epsilon \left(\gamma_1 - \left(\frac{V}{2} + C\right) f_0\right)\right)$$
$$\times \left(\frac{P e^{-\gamma_0}}{\sqrt{8}} \frac{i}{2} e^{2U} \frac{x^n}{r^3}\right).$$

For the combination $1/2\mathcal{F}_{0n}^{-1} - i y_1 e^K S_{0n}$ that enters the gaugini Killing equation with $I = 1$, we obtain

$$\frac{1}{2} \mathcal{F}_{0n}^{-1} - i y_1 e^K S_{0n} \qquad (87)$$
$$= -\frac{i y_1}{4} \left(1 - \epsilon \left(3\gamma_1 + \left(\frac{V}{2} + C\right) f_0\right)\right)$$
$$\times \left(\frac{P e^{-\gamma_0}}{\sqrt{8}} \frac{i}{2} e^{2U} \frac{x^n}{r^3}\right).$$

Keeping the terms up to the first order in string coupling, we have the one-loop-corrected expressions for B_n^0 and B_n^1,

$$B_n^0 = \frac{q' {f_0}^{1/2} e^{-\gamma_0}}{2\sqrt{8}} \qquad (88)$$
$$\times \left[1 + \epsilon \left(\frac{{\phi_1}' - 2{\gamma_1}'}{q'} + \frac{\phi_1 - 2\gamma_1}{2} - \frac{3V f_0}{4}\right)\right] \frac{x^n}{r},$$

$$B_n^1 = -i \frac{q' {f_0}^{-1/2} e^{-\gamma_0}}{2\sqrt{8}}$$

$$\times \left[1+\epsilon\left(\frac{\phi_1{}'+2\gamma_1{}'}{q'}-\frac{\phi_1+2\gamma_1}{2}+\frac{Vf_0}{4}\right)\right]\frac{x^n}{r}.$$

Using the expressions (86)–(88), we verify that leading-order terms in Eqs. (71) with $I=0$ and $I=1$ cancel, and the remaining equations for the combinations of the terms of first-order in string coupling are

$$I=0: \quad \frac{\phi_1'-2\gamma_1'}{q'}+\frac{\phi_1-u_1}{2}-2\gamma_1 - \left(\frac{V}{4}-C\right)f_0=0, \tag{89}$$

$$I=1: \quad \frac{\phi_1'+2\gamma_1'}{q'}+\frac{\phi_1-u_1}{2}+2\gamma_1 - \left(\frac{V}{4}-C\right)f_0=0.$$

Equations (89) split into the following system:

$$\frac{\phi_1'}{q'}+\frac{\phi_1-u_1}{2}-\left(\frac{V}{4}-C\right)f_0=0, \tag{90}$$
$$\gamma_1'+q'\gamma_1=0.$$

Let us consider the remaining gaugini Killing equations (71) with $I=2$ and $I=3$. Substituting the expressions for the loop-corrected couplings (14) and the field strengths (41), we have

$$\hat{\mathcal{F}}^{-2}_{0n}=\frac{P^0}{y_1y_3}\left(\frac{v}{2}+h_2y_2+\frac{C_2y_2}{P^0}\right)\frac{1}{2}e^{2U}\frac{x^n}{r^3} \tag{91}$$
$$=y_2P^0f_0\left(\frac{V}{2}+L_2\right)\frac{1}{2}e^{2U}\frac{x^n}{r^3}$$

and a similar expression for $\mathcal{F}^{-3}_{0n}$ obtained by the substitution $2\to 3$. The field strengths $\mathcal{F}^{-2,3}$, absent at the string tree level, are of the first order in the string coupling. Here, we introduced

$$L_2=\left(h_2y_2+\frac{C_2y_2}{P^0}\right)e^{-2\gamma_0}, \tag{92}$$
$$L_3=\left(h_3y_3+\frac{C_3y_3}{P^0}\right)e^{-2\gamma_0}.$$

Subtracting Eq. (91) with $I=2$ from that with $I=0$ (the same for $I=3$) and using, for the combinations B^i_n, expressions (78), we have

$$ie^{K/2}\frac{\partial_n y_2}{y_2} \tag{93}$$
$$+4e^{-U}\left(\frac{\hat{\mathcal{F}}^{-2}_{0n}}{2iy_2}-\frac{1}{2}\hat{\mathcal{F}}^{-0}_{0n}-2e^KS_{0n}\right)=0.$$

Substituting the expressions for the field strengths $\hat{\mathcal{F}}^{-0}_{0n}$, $\hat{\mathcal{F}}^{-2}_{0n}$ and Eq. (85) for e^KS_{0n}, and keeping the terms of the first order in the string coupling, we obtain

$$\gamma_1{}'+\sigma_1{}'+(C-L_2-\gamma_1f_0^{-1})\frac{P}{r^2}=0, \tag{94}$$
$$\gamma_1{}'-\sigma_1{}'+(C-L_3-\gamma_1f_0^{-1})\frac{P}{r^2}=0.$$

The sum of Eqs. (94) is

$$\gamma'_1+\gamma_1q'+(2C-L_2-L_3)f_0'=0. \tag{95}$$

Using expressions (82) and (92) for C and L_a, we find that

$$2C-L_2-L_3=0, \tag{96}$$

so that Eq. (95) coincides with the second Eq. (90).

Let us solve the system of the gravitini Eq. (84) and the first Eq. (90). Adding and subtracting the equations, we obtain the solution

$$u_1+\phi_1=c_1-\left(\frac{V}{2}+2C\right)f_0, \tag{97}$$
$$u_1-\phi_1=\frac{c_2}{f_0}-\frac{Vf_0}{2},$$

where $c_{1,2}$ are arbitrary constants. Requiring that, at large distances from the center of the black hole, the metric and dilaton be asymptotic to the Lorentzian metric and the constant dilaton be equal to unity, we have

$$c_1=\frac{V}{2}+2C, \qquad c_2=\frac{V}{2}, \tag{98}$$

and we obtain

$$u_1=-\left(\frac{V}{2}+C\right)\frac{P}{r}-\frac{V}{4}\frac{P}{r+P}, \tag{99}$$
$$\phi_1=-C\frac{P}{r}+\frac{V}{4}\frac{P}{r+P}.$$

At the tree level, magnetic black hole is the extremal BPS saturated configuration [5, 6], where the function f_0 was introduced in (24). Provided supersymmetry is unbroken in perturbation theory, the loop-corrected solution must have the same properties. The ADM mass can be obtained from the $r\to\infty$ asymptotics of the metric. From (99), we have

$$M_{\rm ADM}=2P\left(1-\frac{3V}{4}-C\right).$$

The BPS mass is determined from the asymptotics of the function T^-, which can be written as

$$T^-_{\mu\nu}=(F_I\mathcal{F}^I_{\mu\nu}-X^IG_{I\mu\nu}). \tag{100}$$

Asymptotics of the fields $\mathcal{F}^I$ and G_I are proportional to electric and magnetic charges, respectively. Taking the limit $r\to\infty$ of the function T^-, we find the BPS mass that is equal to the ADM mass.

The loop-corrected metric can be considered as the leading and first-order terms in the expansion in ϵ of the metric

$$g_{ii} = -g^{00} = \frac{P + r + \epsilon PV/4}{r - \epsilon P(V/4 + C)} \qquad (101)$$

in the string-loop counting parameter ϵ. If the constant C can be taken such that $V/2 + C < 0$, the metric of the loop-corrected black hole, when extrapolated to the region of small r, has no singularity that is smeared by quantum corrections. This case is realized if the magnetic black hole is obtained from a dyonic black with the constant metric of the two-torus G_{mn} in the limit of vanishing electric charges [21]. In this case, $V/2 + C = \mathrm{Re}h$, which is known to be a negative function for all values of the moduli [10]. The Green–Schwarz function V is known to be positive [9], which ensures no extra singularities of the metric.

10. DISCUSSION

Solving the loop-corrected system of the Einstein–Maxwell equations, we obtained a two-parameter set of solutions for the loop corrections to the metric and dilaton:

$$u_1 = A_1\frac{P}{r} - A_2\frac{P}{r+P}, \qquad (102)$$
$$\phi_1 = \left(A_1 + \frac{V}{2}\right)\frac{P}{r} + A_2\frac{P}{r+P}.$$

The one-parameter family of solutions of the system of Maxwell and spinor Killing equations (99) is of the form (102) with $A_1 = -C - V/2$ and $A_2 = V/4$ and thus is contained in solution (102).

Near the locations of the enhanced symmetry points in the moduli space, the second derivatives of the prepotential have logarithmic singularities [7, 8]. In particular, for $y_2 \sim y_3$,

$$h^{(1)}(y_2, y_3) = (y_2 - y_3)^2 \log(y_2 - y_3)^2.$$

Although the loop-corrected gauge couplings (31) contain second derivatives of the prepotential, the final expressions for the metric and moduli contain only the first derivatives of the prepotential and thus are regular at the points of enhanced symmetry. Note that the Green–Schwarz function is positive [9], which also can be seen from the form of the Kähler potential for the moduli, which is a regular function at finite values of the moduli.

Our solution for the loop corrections is valid for all r for which the perturbation expansion in string coupling is valid. Since the dilaton increases at small distances, both the tree-level and the loop-corrected solutions are valid for $r/P > \epsilon V$.

Our treatment of spinor Killing equations is similar in spirit to [22–25]. However, in these papers, only the tree-level spinor Killing equations were discussed. Another distinction is that, in these papers, the emphasis was placed on the form of solution at the stabilization point [23, 26], whereas we were interested in the full coordinate dependence of the solution.

Our approach is different from that in [24, 27] based on the assumption that there is a "small" modulus which can be used as an expansion parameter for the loop-corrected action. In string-loop perturbative expansion, a natural expansion parameter is associated with the dilaton, and the loop correction to the tree-level prepotential is independent of the modulus $y_1 \equiv S$.

Finally, in the perturbative approach, we neglect the terms of the form $O(e^{2\pi S})$, and the duality properties of the full theory [28] cannot be checked in this setting.

ACKNOWLEDGMENTS

I thank Renata Kallosh for helpful correspondence.

This work was partially supported by the Russian Foundation for Basic Research, project no. 00-02-17679.

REFERENCES

1. M. Green, J. Schwarz, and E. Witten, *Superstring Theory* (Cambridge University Press, Cambrige, 1987).
2. D. Youm, Phys. Rep. **316**, 1 (1999).
3. A. W. Peet, Class. Quantum Grav. **15**, 3291 (1998).
4. G. T. Horowitz and A. A. Tseytlin, Phys. Rev. D **51**, 2896 (1995); A. A. Tseytlin, Mod. Phys. Lett. A **11**, 689 (1966).
5. M. Cvetič and A. A. Tseytlin, Phys. Lett. B **366**, 95 (1996).
6. M. Cvetič and D. Youm, Nucl. Phys. B **453**, 259 (1995).
7. I. Antoniadis *et. al.*, Nucl. Phys. B **447**, 35 (1995).
8. B. de Wit, V. Kaplunovsky, J. Louis, and D. Luest, Nucl. Phys. B **451**, 53 (1995).
9. E. Kiritsis, C. Kounnas, P. M. Petropoulos, and J. Rizos, Nucl. Phys. B **483**, 141 (1997).
10. J. A. Harvey and G. Moore, Nucl. Phys. B **463**, 315 (1996).
11. B. de Wit and A. Van Proeyen, Nucl. Phys. B **245**, 89 (1984); B. de Wit, P. Lauwers, and A. Van Proeyen, Nucl. Phys. B **255**, 569 (1985).
12. A. Strominger, Commun. Math. Phys. **133**, 163 (1990).
13. L. Castellani, R. D'Auria, and S. Ferrara, Phys. Lett. B **241**, 57 (1990).
14. A. Ceresole, R. D'Auria, and S. Ferrara, Nucl. Phys. B (Proc. Suppl.) **46**, 67 (1996).

15. R. D'Auria, S. Ferrara, and P. Fre, Nucl. Phys. B **359**, 705 (1991).
16. A. Ceresole, R. D'Auria, S. Ferrara, and A. Van Proeyen, Nucl. Phys. B **444**, 92 (1995).
17. L. Andrianopoli *et al.*, J. Geom. Phys. **23**, 111 (1997).
18. A. Sen, Int. J. Mod. Phys. A **9**, 3707 (1994).
19. M. J. Duff, J. T. Liu, and J. Rahmfeld, Nucl. Phys. B **459**, 125 (1996).
20. L. D. Landau and E. M. Lifshitz, *Field Theory* (Nauka, Moscow, 1985).
21. M. Z. Iofa, hep-th/0203046.
22. P. Fre, Nucl. Phys. B (Proc. Suppl.) **57**, 52 (1997).
23. S. Ferrara and R. Kallosh, Phys. Rev. D **54**, 1514 (1996).
24. K. Behrndt, D. Lűst, and W. A. Sabra, Nucl. Phys. B **510**, 264 (1998).
25. K. Behrndt *et al.*, Phys. Rev. D **54**, 6293 (1996).
26. S. Ferrara, R. Kallosh, and A. Strominger, Phys. Rev. D **52**, 5412 (1995); A. Strominger, Phys. Lett. B **383**, 39 (1996).
27. K. Behrndt and I. Gaida, Phys. Lett. B **401**, 263 (1997).
28. G. L. Cardoso *et al.*, Nucl. Phys. B **464**, 18 (1996); Phys. Lett. B **382**, 241 (1996).

Physics of Atomic Nuclei, Vol. 66, No. 5, 2003, pp. 878–892. Translated from Yadernaya Fizika, Vol. 66, No. 5, 2003, pp. 910–924.

ELEMENTARY PARTICLES AND FIELDS
Theory

Radiative Corrections to Observables of W-Boson Production in Collisions of Polarized Hadrons

V. A. Zykunov*

Gomel State Technical University, Gomel, Belarus

Received December 3, 2001; in final form, April 23, 2002

Abstract—A scheme is proposed for studying the nucleon spin with the aid of observables in the production of single W bosons in hadron–hadron collisions. Special attention is given to determining the distributions of polarized quarks in the low-x region. Lowest order electroweak radiative corrections to observables are calculated. For the conditions of future experiments at the RHIC facility, the relevant cross sections and single and double asymmetries are estimated numerically with allowance for radiative corrections.

1. INTRODUCTION

Despite considerable advances in solving the proton-spin problem [1] that were made in fixed-target experiments at CERN [2], SLAC [3], and HERMES [4], the distributions of polarized u, d, and s quarks and of a gluon in a nucleon have yet to be determined conclusively. Unfortunately, inclusive measurements that determine the spin structure functions $g_1(x, Q^2)$ for nucleons and deuterons make it possible to obtain information only about specific combinations of polarized-parton distributions. In order to perform a complete analysis and separate individual components, additional measurements are required. For example, investigation of semi-inclusive reactions at SMC [5] and HERMES [6] enables one to obtain parton-distribution combinations differing from the inclusive ones, but the accuracy of their determination is not very high since the results depend on fragmentation functions.

New combinations of polarized-quark distributions can also be deduced from experimental data on single (or double) spin asymmetries for the case where an unpolarized (or polarized) proton beam collides with polarized nucleons. Such an experiment is planned to be implemented in the near future at the RHIC facility [7]—in particular, the collider polarization experiments STAR and PHENIX at an energy of $\sqrt{s} \approx 500$ GeV will enable one to measure some single spin asymmetries. In addition, there are prospects for accelerating polarized protons at the Tevatron (Fermilab) collider [8] and, possibly, in the HERA-$\vec{N}$ experiments [9].

In the present study, we focus on the inclusive production of single W bosons in hadron–hadron interactions involving one or two longitudinally polarized beams,

$$\overset{(\rightarrow)}{h}_1 + \vec{h}_2 \to W^{\pm} + X \to l^{\pm} + X. \qquad (1)$$

As was mentioned above, the single and double spin asymmetries in W-boson production (for example, the single asymmetry A_L in [10]) are highly sensitive to the behavior of quark distributions in a polarized nucleon. In Section 2, we derive formulas for the single and double spin asymmetries in process (1) under the condition that only the charged lepton is detected in the experiment. We also show there how, by using the proposed asymmetries, one can study quark distributions in a polarized nucleon—in particular, in the region of low x.

Events that occur against the background of the main reaction and which originate from loop diagrams and (since we consider an inclusive reaction) from photon-bremsstrahlung diagrams cannot be isolated from it experimentally; therefore, they must be calculated theoretically, whereupon their contribution must be subtracted from observables. In the present study, we calculate the total electroweak radiative corrections of order α to the cross sections and polarization asymmetries for reaction (1) and present a detailed numerical calculation of their contributions to observables.

2. BORN CROSS SECTION AND ASYMMETRIES

Within the quark-parton model, the cross section for an inclusive hadron reaction is constructed by

*e-mail: zykunov@gstu.gomel.by

1063-7788/03/6605-0878$24.00

using the generally accepted formula

$$d\sigma_{\substack{(\rightarrow)\,\rightarrow \\ h_1\,h_2\rightarrow l^{\pm}X}} = \int\int dx_1 dx_2 \times \sum_{i,i';r_1,r_2} f_i^{(1),r_1}(x_1,Q^2) f_{i'}^{(2),r_2}(x_2,Q^2) d\hat{\sigma}_{ii'}^{\pm}, \quad (2)$$

where $f_i^{(a),r}(x,Q^2)$ is the density of the probability of finding, in hadron a, a parton of sort i having a helicity r and carrying a nucleon-momentum fraction x (at a momentum transfer squared Q^2), while $d\hat{\sigma}_{ii'}^{\pm}$ is the cross section for an elementary process that leads to the desired final state (Fig. 1). The sum is taken over all possible parton configurations and the helicities of the first and the second parton ($r_{1,2} = \pm 1$). The meaning of the "hat" operator will be explained below.

The production of a single W boson in a hadron–hadron collision is described within the quark-parton model by two pairs of elementary quark–antiquark subprocesses. For example, the elementary processes for W^- production are

$$q_i(p_1,\eta_1) + \bar{q}_{i'}(p_2,\eta_2) \rightarrow W^-(q) \rightarrow l^-(k_1) + \bar{\nu}(k_2), \quad (3)$$

$$\bar{q}_i(p_1,\eta_1) + q_{i'}(p_2,\eta_2) \rightarrow W^-(q) \rightarrow l^-(k_1) + \bar{\nu}(k_2), \quad (4)$$

while those for W^+ production are

$$q_i(p_1,\eta_1) + \bar{q}_{i'}(p_2,\eta_2) \rightarrow W^+(q) \rightarrow l^+(k_1) + \nu(k_2), \quad (5)$$

$$\bar{q}_i(p_1,\eta_1) + q_{i'}(p_2,\eta_2) \rightarrow W^+(q) \rightarrow l^+(k_1) + \nu(k_2). \quad (6)$$

Here, we have used the following notation (see Fig. 1): p_1 is the 4-momentum of the first (anti)quark of sort i having a mass m_1 and a polarization vector η_1, p_2 is the 4-momentum of the second (anti)quark of sort i' (the index i' everywhere labels the isospin partner of a quark of sort i) having a mass m_2 and a polarization vector η_2, k_1 is the 4-momentum of the charged lepton l^- or l^+ of mass m_l, k_2 is the (anti)neutrino 4-momentum, and $q = p_1 + p_2$ is the 4-momentum of a W boson of mass m_W. We employ the standard set of Mandelstam variables for elastic parton scattering; that is,

$$s_q = (p_1+p_2)^2, \qquad t = (p_1-k_1)^2, \qquad u = (k_1-p_2)^2. \quad (7)$$

Taking the squares of the matrix elements for parton subprocesses, we obtain the invariant cross section for elastic parton–parton scattering in the Breit–Wigner form (for the polarization vectors of initial particles, we use the covariant expressions presented, for example, in [11])

$$d\sigma_{ii'}^{\pm} = \frac{\alpha^2}{4N_c s_{\mathrm{W}}^4} \frac{|V_{ii'}|^2 B_{ii'}}{s_q((s_q-m_W^2)^2 + m_W^2\Gamma_W^2)} \times \delta(p_1+p_2-k_1-k_2)\frac{d^3k_1}{k_{10}}\frac{d^3k_2}{2k_{20}}, \quad (8)$$

where α is the fine-structure constant; $1/N_c = 1/3$ is a color factor; $s_{\mathrm{W}} = \sqrt{1-c_{\mathrm{W}}^2}$ is the sine of the Weinberg angle; $c_{\mathrm{W}} = m_W/m_Z$, m_Z being the Z-boson mass; Γ_W is the W-boson width; and $V_{ii'}$ is the Cabibbo–Kobayashi–Maskawa matrix. The quantities $B_{ii'}$ are formed by the products of terms depending only on invariants, $B_{ii'}^I$, and only on the helicities and polarization degrees, $B_{ii'}^P$; specifically, we have

$$B_{ii'} = B_{ii'}^I B_{ii'}^P = \begin{cases} u^2(1-r_1p_{h_1})(1-r_2p_{h_2}) & \text{for subprocess (3)}, \\ t^2(1-r_1p_{h_1})(1-r_2p_{h_2}) & \text{for subprocess (4)}, \\ t^2(1+r_1p_{h_1})(1+r_2p_{h_2}) & \text{for subprocess (5)}, \\ u^2(1+r_1p_{h_1})(1+r_2p_{h_2}) & \text{for subprocess (6)}, \end{cases}$$

where $p_{h_{1(2)}}$ is the degree of the longitudinal polarization of the first (second) hadron (it takes the values of ± 1).

The integration with respect to the 4-momentum of an unobserved neutrino leads to the relation

$$\int \frac{d^3k_2}{2k_{20}}\delta(p_1+p_2-k_1-k_2) = \delta(s_q+t+u-m_1^2-m_2^2-m_l^2). \quad (9)$$

Upon using this relation, we make, according to the rules of the quark-parton model, the substitutions $p_{1(2)} \rightarrow x_{1(2)}P_{1(2)}$, where $P_{1(2)}$ is the 4-momentum of the first (second) hadron of mass $m_{h_{1(2)}}$ and $x_{1(2)}$ is the first-hadron-momentum (second-hadron-momentum) fraction carried by the parton. The procedure consisting in this substitution is denoted by the operator "^". Further, we multiply the result by the parton distributions in the first and the second hadron, take the sum over quark helicities,

and perform integration with respect to x_1 and x_2 according to formula (2).

Let us introduce the Mandelstam invariants for the hadronic reaction. According to the quark-parton model (naturally, the transverse component of the quark momentum in a nucleon is disregarded), we neglect the parton and nucleon masses against the energies and the variables s_q, t, and u. For Eq. (1), these invariants are given by

$$s = 2P_1P_2, \quad T = -2P_1k_1, \quad U = -2P_2k_1, \quad (10)$$

so that, with allowance for all simplifications within the quark-parton model, we can write

$$\hat{s}_q = x_1x_2s, \quad \hat{t} = x_1T, \quad \hat{u} = x_2U. \quad (11)$$

Performing integration with respect to x_2 with the aid of the delta function and noticing that

$$\delta(\hat{s}_q + \hat{t} + \hat{u} - m_1^2 - m_2^2 - m_l^2) \approx \frac{1}{D}\delta\left(x_2 + \frac{x_1T}{D}\right), \quad (12)$$

where

$$D = x_1s + U, \quad (13)$$

we can prove that, in the case of Born kinematics considered here, we have

$$x_2 = x_2^0 \equiv -x_1T/D. \quad (14)$$

Below, we will label quantities for which this kinematics is applicable with the index "0."

Finally, we consider the general form of the cross section for the hadronic process (1). In order to write it, use is made of variables that are standard for the hadron–hadron reaction: the c.m. hadron energy ($\sqrt{s}$); the detected-lepton-momentum component orthogonal to the beam axes ($|k_{1\perp}| \equiv k_{1T}$); and the pseudorapidity (η), which, for the reaction being considered, is equal to the ordinary rapidity y since $m_l \ll k_{1T}$. As a result, we find that the invariant quantities T and U can be expressed as

$$T = -\sqrt{s}k_{1T}e^{-\eta}, \quad U = -\sqrt{s}k_{1T}e^{\eta}. \quad (15)$$

Upon integration with respect to the azimuthal angle Φ, we obtain the phase space $d^3k_1/k_{10} \to \pi d\eta k_{1T}^2$ and, finally, the Born cross section in the form

$$\sigma_0^{\pm} = \sum_{i,i'} \int dx_1 F_i^{(1)}(x_1, Q^2)\Sigma_0^{ii'}, \quad (16)$$

where $\sigma^{\pm}$ is the double differential cross section; that is,

$$\sigma^{\pm} \equiv \frac{d\sigma_{\substack{(\to)\to \\ h_1\,h_2\to l^{\pm}X}}}{d\eta dk_{1T}^2}. \quad (17)$$

This notation and the relation

$$\sigma^{\pm} = \bar{\sigma}^{\pm} + p_{h_2}\Delta\sigma^{\pm}, \quad (18)$$

where $\bar{\sigma}^{\pm}$ ($\Delta\sigma^{\pm}$) is the unpolarized (polarized) part of the cross section (we mean the polarization of the second nucleon), will be used below.

As can be seen, the Born cross section is proportional to the factor $\Sigma_0^{ii'} = \Sigma^{ii'}(x_2^0)$, where

$$\Sigma^{ii'}(x_2) = \frac{\pi\alpha^2}{4N_cs_W^4} \times \frac{|V_{ii'}|^2\hat{B}_{ii'}^I}{\hat{s}_q((\hat{s}_q - m_W^2)^2 + m_W^2\Gamma_W^2)D}F_{i'}^{(2)}(x_2, Q^2). \quad (19)$$

In expressions (16) and (19) for the cross sections, the combinations of the quark distributions in the hadrons ($a = 1, 2$) have the form

$$F_i^{(1)}(x_1, Q^2) = \bar{q}_i^{(1)}(x_1, Q^2) + c_ip_{h_1}\Delta q_i^{(1)}(x_1, Q^2), \quad (20)$$

$$F_{i'}^{(2)}(x_2, Q^2) = \bar{q}_{i'}^{(2)}(x_2, Q^2) - c_{i'}p_{h_2}\Delta q_{i'}^{(2)}(x_2, Q^2), \quad (21)$$

where

$$\bar{q}_i^{(a)}(x, Q^2) = f_i^{(a),+}(x, Q^2) + f_i^{(a),-}(x, Q^2), \quad (22)$$

$$\Delta q_i^{(a)}(x, Q^2) = f_i^{(a),+}(x, Q^2) - f_i^{(a),-}(x, Q^2) \quad (23)$$

are the distributions of, respectively, unpolarized and longitudinally polarized quarks and $c_{i(i')} = -1$ $(+1)$ for a quark (antiquark).

Let us denote the state where the degree of hadron polarization is $p_{h_a} = +1$ (-1) by the arrow $\uparrow$ $(\downarrow)$. Single asymmetries that are constructed for the interaction of the first unpolarized nucleon with the second one polarized longitudinally can then be represented in the form

$$A_L^{l^{\pm}}(\eta, k_{1T}) = \frac{\sigma^{\pm\uparrow} - \sigma^{\pm\downarrow}}{\sigma^{\pm\uparrow} + \sigma^{\pm\downarrow}} = \frac{\Delta\sigma^{\pm}}{\bar{\sigma}^{\pm}}. \quad (24)$$

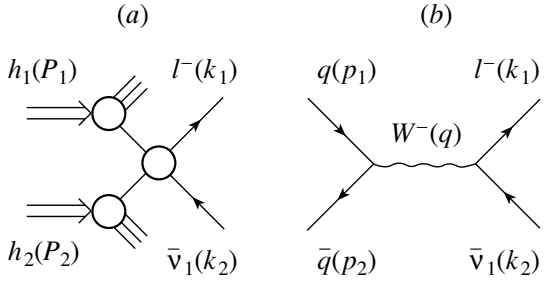

Fig. 1. (a) Illustration of the interaction of partons from the initial hadrons h_1 and h_2 that is followed by the production of a charged lepton and an antineutrino. The first (second) parton carries the hadron-momentum fraction x_1 (x_2). (b) Feynman diagram for the elementary process $q\bar{q} \to l^-\bar{\nu}$.

For the double asymmetries (both nucleons are longitudinally polarized, the first arrow corresponding to the first nucleon), we accordingly have

$$A_{LL}^{l^\pm}(\eta, k_{1T}) = \frac{\sigma^{\pm\uparrow\uparrow} - \sigma^{\pm\downarrow\uparrow} - \sigma^{\pm\uparrow\downarrow} + \sigma^{\pm\downarrow\downarrow}}{\sigma^{\pm\uparrow\uparrow} + \sigma^{\pm\downarrow\uparrow} + \sigma^{\pm\uparrow\downarrow} + \sigma^{\pm\downarrow\downarrow}}. \quad (25)$$

If the Cabibbo–Kobayashi–Maskawa matrix has a diagonal form, $V_{ii'} = \delta_{ii'}$, the flavors of the quarks and antiquarks participating in the reaction take the values

$$\begin{aligned} &i = d, s, b; \quad i' = \bar{u}, \bar{c}, \bar{t} \quad \text{for process (3)}; \quad (26)\\ &i = \bar{u}, \bar{c}, \bar{t}; \quad i' = d, s, b \quad \text{for process (4)};\\ &i = u, c, t; \quad i' = \bar{d}, \bar{s}, \bar{b} \quad \text{for process (5)};\\ &i = \bar{d}, \bar{s}, \bar{b}; \quad i' = u, c, t \quad \text{for process (6)}. \end{aligned}$$

Disregarding the contributions of the heavy quarks (c, b, t) and the contribution of the process $s\bar{u} \to W^-$ (because the matrix element $V_{s\bar{u}}$ is small), we can represent the Born asymmetries as

$$A_{L\ 0}^{l^+}(\eta, k_{1T}) \quad (27)$$
$$= \frac{\int dx_1 \left(-u'(x_1)\Delta\bar{d}(x_2^0) + \bar{d}'(x_1)\Delta u(x_2^0) \right)}{\int dx_1 \left(u'(x_1)\bar{d}(x_2^0) + \bar{d}'(x_1)u(x_2^0) \right)},$$

$$A_{L\ 0}^{l^-}(\eta, k_{1T}) = A_{L\ 0}^{l^+}(\eta, k_{1T})(u \leftrightarrow d), \quad (28)$$

$$A_{LL0}^{l^+}(\eta, k_{1T}) \quad (29)$$
$$= \frac{\int dx_1 \left(\Delta u'(x_1)\Delta\bar{d}(x_2^0) + \Delta\bar{d}'(x_1)\Delta u(x_2^0) \right)}{\int dx_1 \left(u'(x_1)\bar{d}(x_2^0) + \bar{d}'(x_1)u(x_2^0) \right)},$$

$$A_{LL0}^{l^-}(\eta, k_{1T}) = A_{LL0}^{l^+}(\eta, k_{1T})(u \leftrightarrow d). \quad (30)$$

Here, the polarized-quark distributions appear in the asymmetries in the form

$$\Delta u'(x_1) = K_t \Delta u(x_1), \quad \Delta\bar{u}'(x_1) = K_t \Delta\bar{u}(x_1), \quad (31)$$

$$\Delta d'(x_1) = K_u \Delta d(x_1), \quad \Delta\bar{d}'(x_1) = K_u \Delta\bar{d}(x_1) \quad (32)$$

[similar equations relate unpolarized distributions to the quantities $u'(x)$, $d'(x)$, $\bar{u}'(x)$, and $\bar{d}'(x)$, which appear in the asymmetries: for example, $u'(x_1) = K_t u(x_1)$]. We also note that, in all of the above formulas beginning from Eq. (27), we have omitted the argument Q^2 for the sake of simplicity. The factors K in the aforementioned formulas are combinations of invariant quantities:

$$K_{t(u)} = \left. \frac{\hat{t}^2(\hat{u}^2)}{\hat{s}_q((\hat{s}_q - m_W^2)^2 + m_W^2\Gamma_W^2)D} \right|_{x_2 = x_2^0}. \quad (33)$$

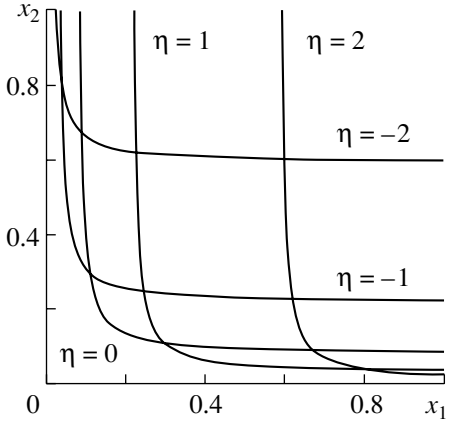

Fig. 2. Region of the variables x_1 and x_2. The curves represent the dependence of x_2^0 on x_1 at various values of η ($\sqrt{s} = 500$ GeV, $k_{1T} = 40$ GeV).

The physical region of variables x_1 and x_2 (Fig. 2) is determined by the inequalities

$$x_1^{\min} \le x_1 \le 1, \quad x_2^0 \le x_2 \le 1, \quad (34)$$

where

$$x_1^{\min} = -\frac{U}{s+T}. \quad (35)$$

In order to highlight the symmetry of this region, we express the dependence $x_2^0(x_1)$ in terms of k_{1T} and η explicitly; that is,

$$\frac{e^\eta}{x_1} + \frac{e^{-\eta}}{x_2^0} = \frac{\sqrt{s}}{k_{1T}}. \quad (36)$$

The symmetry in question is associated with the invariance of this equation under the substitutions $x_1 \leftrightarrow x_2^0$ and $\eta \to -\eta$. Noticing that, in the region of high x_1 and low $k_{1T}/\sqrt{s}$, the function x_2^0 is virtually independent of x_1 ($x_2^0 \approx -T/s = e^{-\eta}k_{1T}/\sqrt{s}$), we can somewhat simplify the equations relating the distributions to the observables. It should be borne in mind, however, that we propose only a version of simplification and that relations (27)–(30) must be used for a more precise analysis. Specifically, we break down the domain of integration in relations (27)–(30) by the parameter x_1^* (we can choose a value of x_1^* in such a way that, in the region $x_1 < x_1^*$, we will have the polarized quark distributions that are bounded and well defined since large x_2^0 correspond to low x_1); by factoring the functions depending on x_2^0 outside

the integral sign, we find that the asymmetry $A_L^{l^+}$ is related to the quark distributions by the equation

$$\Delta u(-T/s)\int\limits_{x_1^*}^{1} dx_1 \bar{d}'(x_1) \tag{37}$$

$$-\Delta\bar{d}(-T/s)\int\limits_{x_1^*}^{1} dx_1 u'(x_1) = A_{L\ 0}^{l^+}(\eta, k_{1T})$$

$$\times\int\limits_{x_1^{\min}}^{1} dx_1\Big(u'(x_1)\bar{d}(x_2^0)+\bar{d}'(x_1)u(x_2^0)\Big)$$

$$-\int\limits_{x_1^{\min}}^{x_1^*} dx_1\Big(\Delta u(x_2^0)\bar{d}'(x_1)-\Delta\bar{d}(x_2^0)u'(x_1)\Big)$$

and obtain a similar relation for $A_L^{l^-}$ by means of the substitutions $u \leftrightarrow d$. It is straightforward to derive a similar relation for the double asymmetry.

We note that the approach used here to calculate observables makes it possible to investigate quark distributions at rather low x. For example, the expression $-T/s$ at the kinematical point of the RHIC facility ($\sqrt{s} = 500$ GeV, $k_{1T} = 10$ GeV, $\eta = 2$) does not indeed exceed 0.0027.

Thus, equations of the type in (37) relate the polarized quark distributions to the observed single (and double) asymmetries and those combinations of the distributions that are rather well defined and studied. One can see that these equations are sufficient (there are four of them) for singling out unknown distributions of polarized quarks. If we invoke additional measurable quantities [for example, the expression obtained for $g_1(x)$ on the basis of the quark-parton model], we can restrict ourselves to the use of single asymmetries and, accordingly, to an experiment where unpolarized hadrons probe the spin structure of polarized ones. It is such experiments to which the spin program of the RHIC facility is devoted. If, in the future, there appears the possibility of polarizing both nucleon beams, measurement of double asymmetries will provide a basis for testing and further refining the result in question.

3. CONTRIBUTIONS OF ADDITIONAL VIRTUAL PARTICLES TO THE CROSS SECTIONS

In order to obtain precise and reliable information about observables, it is necessary to consider processes that cannot be isolated from that being investigated by experimental methods (we mean here radiative processes). For the first time, radiative corrections to W-boson production in collisions of unpolarized protons were calculated in [12]. Only the contribution induced by radiation from particles in the final state (final-state radiation) was estimated there. More precise calculation was performed in [13, 14], where radiation from particles in the initial state (initial-state radiation) was considered in addition to final-state radiation. For the final state, a collinear singularity, which consists in that the corrections in question are dominated by the contributions of photon emission from charged particles in the direction of their momentum, was isolated by a conventional method involving the introduction of a radiating-lepton mass. On the contrary, a collinear singularity of the initial state was singled out by introducing the collinear region and was absorbed in the parton distributions, in just the same was as this is done, for example, in QCD in taking into account gluon radiation. As a result, final formulas for corrections appear to be independent of parameters that are not physically well defined, such as the quark masses. Instead of them, there appears, in cross sections, a different parameter, δ_θ, that specifies the boundaries of the collinear region. Nevertheless, numerical calculations demonstrate but a weak dependence of the results on this parameter; therefore, the method is thought to be quite reliable.

The dependence of the results obtained in [13, 14] on another unphysical parameter (maximum energy of soft photons, E_{cut}) is an uncertainty that has a crucial effect on the validity of the interpretation of these results. This dependence arises in isolating the bremsstrahlung-cross-section component that involves an infrared divergence. The calculation performed in [15], where the corrections to the cross sections and single spin asymmetries for W-boson production in collisions of unpolarized hadrons and in collisions of a polarized and an unpolarized hadron were derived and estimated numerically, is completely free from this significant drawback. In [15], as well as in the calculation proposed in this article, the infrared divergence is singled out in a covariant way by using the method proposed in [16], so that the final expressions involve no dependence on E_{cut} or on some analog of it. However, the quark masses are used here within this method, as well as in the earlier studies reported in [17] and devoted to calculating corrections to the hadron current in deep-inelastic lepton–nucleon scattering (see also [18]), as parameters that regularize the collinear singularity of the initial state. The dependence of the results on the choice of quark-mass values is considered in [15] and in Section 5 below, where it is proven (and this is the most important fact) that spin asymmetries are virtually independent of this choice.

In this study, the one-loop contribution induced by the radiation of additional virtual particles (V contribution) was calculated in the 't Hooft–Feynman gauge and according to the on-shell renormalization scheme employing the constants α, m_W, and m_Z; the mass m_H of the Higgs boson; and the fermion masses as independent parameters. The corresponding Feynman diagrams are presented in Fig. 3.

The V-contribution cross section is proportional to the Born cross section and can be written in the form

$$\sigma_V^{\pm} = \sum_{i,i'} \int dx_1 F_i^{(1)}(x_1, Q^2) \hat{\delta}_V^{ii'}|_{x_2=x_2^0} \Sigma_0^{ii'}, \quad (38)$$

where the factor $\delta_V^{ii'}$ is independent of initial-hadron polarizations and is well known. It involves seven terms:

$$\delta_V^{ii'} = \delta_W + \delta_{Vl} + \delta_{Vq}^{ii'} + \delta_{Sl} + \delta_{Sq} + \delta_{\gamma W}^{ii'} + \delta_{ZW}^{ii'}. \quad (39)$$

We will not reproduce the exact expressions for these terms—they are presented in [18, 19]; instead, we will consider their origin and give necessary comments at the points where the results were rescaled and modified.

The correction δ_W is caused by the contribution to the cross section from the diagrams of the W-boson self-energy (Fig. 3, *1*); it has a form that differs from that in [18] (this is due to the s-channel resonance W-boson production); that is,

$$\delta_W = 2\mathrm{Re}\frac{s_q - m_W^2 - im_W\Gamma_W}{(s_q - m_W^2)^2 + m_W^2\Gamma_W^2}\hat{\Sigma}_T^W(s_q), \quad (40)$$

where $\hat{\Sigma}_T^W(s_q)$ is the renormalized transverse part of the W-boson self-energy (see [19]).

The term δ_{Vl} is the leptonic vertex function (Fig. 3, *2*) {see Eq. (2.10) in [18]}, while $\delta_{Vq}^{ii'}$ is the quark vertex function (Fig. 3, *3*) {see Eq. (2.11) in [18]}; in the present study, we retain the flavor index on this correction and on the contributions due to two-boson exchange. The term δ_{Sl} is the neutrino self-energy (Fig. 3, *4*) {see Eq. (2.12) in [18]}. The contribution of the u-quark self-energy (Fig. 3, *5*) can be written in the form

$$\delta_{Sq} = -\frac{\alpha}{4\pi}\left[Q_u^2\left(\ln\frac{m_Z^2}{m_u^2} - 2\ln\frac{m_u^2}{\lambda^2}\right)\right. \quad (41)$$
$$\left. - Q_d^2\left(\ln\frac{m_Z^2}{m_d^2} - 2\ln\frac{m_d^2}{\lambda^2}\right) + \frac{3}{2}\right].$$

This expression was obtained from formula (5.46) in [19] (see also the comment given below).

We have also rescaled the contributions of the box diagrams in terms of the quantities $I_{1,2}^{\gamma W,f}$ and $I_{1,2}^{ZW,f}$

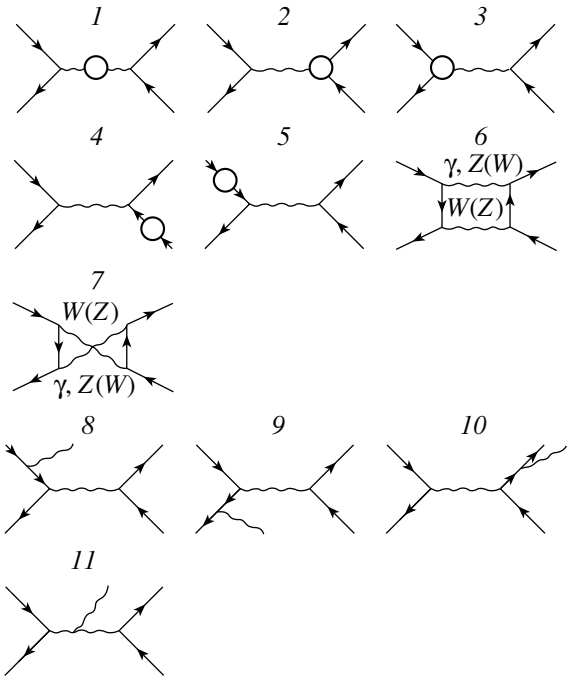

Fig. 3. (*1–7*) Set of Feynman diagrams for the process $q\bar{q} \to l^-\bar{\nu}$. Open blocks represent the contributions to self-energies and vertices; their exact content can be found in [18, 19]. (*8–11*) Feynman diagrams for the bremsstrahlung process $q\bar{q} \to l^-\bar{\nu}\gamma$.

from [18] and present them here in order to highlight the dependence of these functions on the type of particle involved in the reaction and on the reaction channel. The contribution of γW exchange to the cross section (Fig. 3, *6* and *7*) can be represented as

$$\delta_{\gamma W}^{u\bar{d}} = \delta_{\gamma W}^{\bar{u}d} = \delta_{\gamma W}, \quad (42)$$
$$\delta_{\gamma W}^{d\bar{u}} = \delta_{\gamma W}^{\bar{d}u} = \delta_{\gamma W}(t \leftrightarrow u, i \leftrightarrow i'),$$

where

$$\delta_{\gamma W} = \frac{2\alpha}{\pi}\mathrm{Re}Q_l[Q_i I_1^{\gamma W,i}(s_q, t) + Q_{i'} I_2^{\gamma W,i'}(s_q, u)]; \quad (43)$$

the contribution of ZW exchange (Fig. 3, *6* and *7*) can be expressed in terms of the corrections

$$\delta_{ZW}^{u\bar{d}} = \delta_{ZW}^{\bar{u}d} = \delta_{ZW}, \quad (44)$$
$$\delta_{ZW}^{d\bar{u}} = \delta_{ZW}^{\bar{d}u} = \delta_{ZW}(t \leftrightarrow u, i \leftrightarrow i'),$$

where

$$\delta_{ZW} = \frac{2\alpha}{\pi}\mathrm{Re}[((v_l + a_l)(v_i + a_i) \quad (45)$$
$$+ (v_\nu + a_\nu)(v_{i'} + a_{i'}))I_1^{ZW}(s_q, t) + ((v_l + a_l)$$
$$\times (v_{i'} + a_{i'}) + (v_\nu + a_\nu)(v_i + a_i))I_2^{ZW}(s_q, u)].$$

The vector and axial-vector coupling constants v_j and a_j (here, the index is spelled out as $j = l, \nu, i, i'$)

for the vertex corresponding to Z-boson emission from the j fermion are determined in terms of the fraction of the fermion charge Q_j in units of the proton charge (that is, $Q_u \equiv Q_{\bar{u}} = +2/3$; $Q_d \equiv Q_{\bar{d}} = -1/3$; $Q_l = -1$; and, naturally, $Q_\nu = 0$) and the 3-component of the weak isospin I_j^3:

$$v_j = \frac{I_j^3 - 2s_{\rm W}Q_j}{2s_{\rm W}c_{\rm W}}, \quad a_j = \frac{I_j^3}{2s_{\rm W}c_{\rm W}}. \tag{46}$$

Let us represent the V-contribution cross section as the sum of an infrared-divergent and a finite term; that is,

$$\sigma_V^{\pm} = \sigma_V^{\pm,{\rm IR}} + \sigma_V^{\pm,F} = \sum_{i,i'} \int dx_1 F_i^{(1)}(x_1, Q^2) \tag{47}$$
$$\times\, \Sigma_0^{ii'}(\hat{\delta}_V^{\rm IR} + \hat{\delta}_V^F)|_{x_2=x_2^0}.$$

The infrared divergence in the V contribution is regularized with the aid of the photon mass λ. For the correction $\delta_V^{\rm IR}$ involving an infrared divergence, we then arrive at the expression

$$\delta_V^{\rm IR} = \frac{\alpha}{2\pi} \ln \frac{s_q}{\lambda^2} J(0) \tag{48}$$

[a natural derivation for $J(0)$ will be given in the next section]; as to the finite part of the V contribution, it includes the correction

$$\delta_V^F = \delta_V^{ii'} - \delta_V^{\rm IR} = \delta_V^{ii'}(\lambda^2 \to s_q). \tag{49}$$

4. BREMSSTRAHLUNG CONTRIBUTION

In order to obtain, for an observable, a physically meaningful result—that is, that which is finite in the infrared limit—it is necessary to include, in the analysis, the contribution of that part of bremsstrahlung which cannot be experimentally separated from the process being studied. Reaction (1) is inclusive; therefore, we must calculate the contributions of both soft and hard bremsstrahlung photons to the cross section (Fig. 3, *8–11*).

We calculate the cross section for bremsstrahlung in the partonic process using conventional Feynman rules. The result is

$$d\sigma_{q_i\bar{q}_{i'}\to l\nu\gamma} = \frac{\alpha^3 |V_{ii'}|^2}{2^6\pi^2 s_{\rm W}^4 N_c s_q} \tag{50}$$
$$\times \sum_{\rm spin} |R|^2 \delta(p_1 + p_2 - k_1 - k_2 - k) \frac{d^3k_1}{2k_{10}} \frac{d^3k_2}{2k_{20}} \frac{d^3k}{2k_0},$$

where we perform summation over the spin states of final particles (leptons and photon) and averaging over the spin states of quarks. Further, we represent the square of the relevant matrix element as the sum of terms that correspond to radiation from the initial state (index i), radiation from the final state (index f), and their interference; that is,

$$\sum_{\rm spin} |R|^2 = (R_i R_i^+)^{nn'} + (R_f R_f^+)^{nn'} \tag{51}$$
$$+ (R_i R_f^+ + R_f R_i^+)^{nn'},$$

$$(R_i R_i^+)^{nn'} \tag{52}$$
$$= -\Pi_q \Pi_q^+ {\rm tr}[(G_i^{nn'})^{\mu\rho} U_{i,p}^n (G_i^{nn'T})_\rho^{\mu'} U_{i,a}^n]$$
$$\times\, {\rm tr}[\gamma_\mu U_{f,a}^{n'} \gamma_{\mu'} U_{f,p}^{n'}],$$
$$(R_f R_f^+)^{nn'} = -\Pi_l \Pi_l^+ {\rm tr}[\gamma_\mu U_{i,p}^n \gamma_{\mu'} U_{i,a}^n]$$
$$\times\, {\rm tr}[(G_f^{n'})^{\mu\rho} U_{f,a}^{n'} (G_f^{n'T})_\rho^{\mu'} U_{f,p}^{n'}],$$
$$(R_i R_f^+ + R_f R_i^+)^{nn'}$$
$$= -\Pi_l \Pi_q^+ ({\rm tr}[(G_i^{nn'})^{\mu\rho} U_{i,p}^n \gamma_{\mu'} U_{i,a}^n]$$
$$\times\, {\rm tr}[\gamma_\mu U_{f,a}^{n'} (G_f^{n'T})_\rho^{\mu'} U_{f,p}^{n'}]$$
$$+ {\rm tr}[\gamma_\mu U_{i,p}^n (G_i^{nn'T})_\rho^{\mu'} U_{i,a}^n]$$
$$\times\, {\rm tr}[(G_f^{n'})^{\mu\rho} U_{f,a}^{n'} \gamma_{\mu'} U_{f,p}^{n'}]).$$

The indices n and n' denote the process type: $n = -\,(+)$ for the $q\bar{q}$ ($\bar{q}q$) initial state and $n' = -\,(+)$ for the $l^-\bar{\nu}$ ($l^+\nu$) final state. The quantity Π_l (Π_q) is the W-boson propagator for the case of radiation from a lepton (quark) line. Specifically, we have

$$\Pi_l = 1/(s_q - m_W^2 + im_W\Gamma_W), \tag{53}$$
$$\Pi_q = -1/(s_q - 2kq - m_W^2 + im_W\Gamma_W)$$
$$= 1/(z + t_{W\Gamma}),$$

where

$$t_{W\Gamma} = t_W - im_W\Gamma_W, \quad t_W = v - s_q + m_W^2, \tag{54}$$
$$q = p_1 + p_2.$$

For kinematical variables that describe the radiative process, we use the invariant quantities

$$z = 2kk_1, \quad z_1 = 2kp_1, \quad t_1 = (p_2 - k_2)^2, \tag{55}$$
$$u_1 = 2kp_2 = v + z - z_1,$$
$$v = 2kk_2 = s_q + u + t - m_1^2 - m_2^2 - m_l^2,$$

where k is the 4-momentum of the radiated photon.

The matrices U originate from the products of the bispinor amplitudes and the matrices $(1 \pm \gamma_5)$, while G stands for a combination of the fermion propagators and the $WW\gamma$ vertex. Specifically, we have

$$U_{i,p}^- = (1 - \gamma_5)\hat{p}_1, \quad U_{i,a}^- = (1 + \gamma_5\hat{\eta}_2)(\hat{p}_2 - m_2), \tag{56}$$

$$U^+_{i,p} = (1-\gamma_5)\hat{p}_2, \quad U^+_{i,a} = \hat{p}_1 - m_1,$$
$$U^-_{f,a} = (1-\gamma_5)\hat{k}_2, \quad U^-_{f,p} = \hat{k}_1 + m,$$
$$U^+_{f,a} = (1-\gamma_5)\hat{k}_1, \quad U^+_{f,p} = \hat{k}_2 \ (\hat{p} = \gamma^\mu p_\mu),$$

$$(G_i^{-n'})^{\mu\rho} = Q_i\gamma^\mu\frac{2p_1^\rho - \hat{k}\gamma^\rho}{z_1} \tag{57}$$
$$- Q_{i'}\frac{2p_2^\rho - \gamma^\rho\hat{k}}{u_1}\gamma^\mu + (G_i^{W^{n'}})^{\mu\rho},$$
$$(G_i^{+n'})^{\mu\rho} = Q_i\frac{-2p_1^\rho + \gamma^\rho\hat{k}}{z_1}\gamma^\mu$$
$$- Q_{i'}\gamma^\mu\frac{-2p_2^\rho + \hat{k}\gamma^\rho}{u_1} + (G_i^{W^{n'}})^{\mu\rho},$$

$$(G_f^-)^{\mu\rho} = Q_l\frac{2k_1^\rho + \gamma^\rho\hat{k}}{z}\gamma^\mu + (G_f^{W^-})^{\mu\rho}, \tag{58}$$
$$(G_f^+)^{\mu\rho} = -Q_l\gamma^\mu\frac{2k_1^\rho + \hat{k}\gamma^\rho}{z} + (G_f^{W^+})^{\mu\rho},$$
$$(G_f^{W^+})_{\mu\rho} = \gamma^{\rho'}\frac{1}{2kq}C^3_{\rho\mu\rho'}(-k, q, k-q),$$
$$(G_f^{W^-})_{\mu\rho} = \gamma^{\nu'}\frac{1}{2kq}C^3_{\rho\nu'\mu}(-k, k-q, q),$$
$$(G_i^{W^+})_{\mu\rho} = \gamma^{\nu'}\frac{1}{2kq}C^3_{\rho\nu'\mu}(-k, q, k-q),$$
$$(G_i^{W^-})_{\mu\rho} = \gamma^{\rho'}\frac{1}{2kq}C^3_{\rho\mu\rho'}(-k, k-q, q),$$

where the matrix C^3 corresponds to the $WW\gamma$ vertex. In the case of the minimal standard model, it can be expressed in terms of the metric tensor $g_{\alpha\beta}$, its principal diagonal being $(1, -1, -1, -1)$, and 4-momenta entering this vertex:

$$C^3_{\mu\nu\rho}(p^0, p^+, p^-) = g_{\rho\nu}(p^- - p^+)_\mu \tag{59}$$
$$+ g_{\mu\nu}(p^+ - p^0)_\rho + g_{\mu\rho}(p^0 - p^-)_\nu.$$

Upon going over from the partonic cross section to the hadronic cross section in accordance with the prescriptions of the quark-parton model, we can represent the bremsstrahlung cross section (R contribution) as the sum of the soft term involving an infrared divergence and the hard contribution [16] [recall that we use the notation in (17) for the double differential cross section $\sigma^\pm$]:

$$\sigma_R^\pm = \sigma_R^{\pm,\mathrm{IR}} + \sigma_R^{\pm,F}. \tag{60}$$

Upon the substitution $dx_2 = d\hat{v}/D$ and some simple transformations, the infrared-divergent part (first term) of expression (60) takes the form

$$\sigma_R^{\pm,\mathrm{IR}} = \sum_{i,i'}\int dx_1 F_i^{(1)}(x_1, Q^2)\hat{\Sigma}_R^{\mathrm{IR},ii'}, \tag{61}$$

where

$$\hat{\Sigma}_R^{\mathrm{IR},ii'} = -\frac{\alpha}{\pi}\int\limits_{\hat{v}_{\min}}^{\hat{v}_{\max}} d\hat{v}\Sigma^{ii'}(x_2)I[\hat{F}^{\mathrm{IR}}]. \tag{62}$$

The procedure for integration over the phase space of the bremsstrahlung photon—the corresponding integral is defined as $I[A]$—is described in detail elsewhere (see formulas of Appendix A in [15]). By using the method for isolating infrared-divergent terms [16], we reduce the quantity F^{IR} to the form

$$F^{\mathrm{IR}} = Q_l^2\frac{m_l^2}{z^2} + c_lQ_lQ_i\frac{t}{zz_1} - c_lQ_lQ_{i'}\frac{u}{zu_1} \tag{63}$$
$$+ Q_i^2\frac{m_1^2}{z_1^2} - Q_iQ_{i'}\frac{s_q}{z_1u_1} + Q_{i'}^2\frac{m_2^2}{u_1^2},$$

where

$$c_l = \begin{cases} +1 & \text{for processes (3) and (6),} \\ -1 & \text{for processes (4) and (5).} \end{cases} \tag{64}$$

By introducing the function $J(\hat{v}) = \hat{v}\lim\limits_{\lambda\to 0} I[\hat{F}^{\mathrm{IR}}]$, we obtain two terms in the soft part of the bremsstrahlung contribution:

$$\hat{\Sigma}_R^{\mathrm{IR},ii'} = -\frac{\alpha}{\pi}\Sigma_0^{ii'}J(0)\int\limits_{\hat{v}_{\min}}^{\hat{v}_{\max}}\frac{d\hat{v}}{\hat{v}} \tag{65}$$
$$+ \frac{\alpha}{\pi}\int\limits_{\hat{v}_{\min}}^{\hat{v}_{\max}} d\hat{v}\left(\Sigma_0^{ii'}J(0)/\hat{v} - \Sigma^{ii'}(x_2)I[\hat{F}^{\mathrm{IR}}]\right).$$

The second term appears to be free from infrared divergences (in view of this, the lower limit of integration in it is set to zero), while the first term involves an infrared singularity in the lower limit of integration. By parametrizing the infrared divergence in terms of the photon mass, we write the first term in the c.m. frame of initial hadrons, which is of prime interest to us at the moment. Considering that, in this frame, the integration limits are given by

$$\hat{v}_{\min} = 2\lambda k_{20} = \lambda\tilde{v}, \quad \tilde{v} \approx \frac{D^2 + TU}{D\sqrt{s}}, \tag{66}$$
$$\hat{v}_{\max} = D(1 - x_2^0),$$

we can see that the first term in (65) assumes the simplest logarithmic dependence on the photon mass; that is,

$$-(\alpha/\pi)\Sigma_0^{ii'}J(0)\ln(\hat{v}_{\max}/\lambda\tilde{v}).$$

Upon summation of the divergent components in the V and R contributions [formulas (47) and (61)],

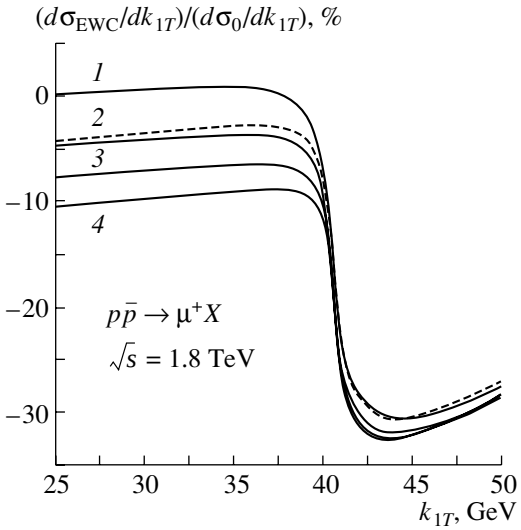

Fig. 4. Ratios of the cross section allowing for electroweak radiative corrections to the Born cross section versus k_{1T} at various values of the quark masses: (curve *1*) $m_u = 5$ MeV and $m_d = 8$ MeV, (curve *2*) $m_u = 30$ MeV and $m_d = 30$ MeV, (curve *3*) $m_u = 100$ MeV and $m_d = 100$ MeV, (curve *4*) $m_u = 0.33$ GeV and $m_d = 0.33$ GeV; the dashed curve corresponds to the choice in (74). The results are presented for the reaction $p\bar{p} \to \mu^+X$ (the proton and antiproton involved are unpolarized) at $\sqrt{s} = 1.8$ TeV, $-1.2 \le \eta \le 1.2$, and $\Delta\Phi = 2\pi$ (Tevatron collider kinematics). We have used the MRS LO 98 parametrization for parton distributions from [20].

we obtain the expression

$$\sigma_R^{\pm,\mathrm{IR}} + \sigma_V^{\pm,\mathrm{IR}} = \sum_{i,i'} \int dx_1 F_i^{(1)}(x_1, Q^2) \frac{\alpha}{2\pi} \quad (67)$$
$$\times \Sigma_0^{ii'} J(0) \ln \frac{\tilde{v}^2 \hat{s}_{q0}}{\hat{v}_{\max}^2} + \sum_{i,i'} \int dx_1 F_i^{(1)}(x_1, Q^2) \frac{\alpha}{\pi}$$
$$\times \int_0^{\hat{v}_{\max}} d\hat{v} \frac{\Sigma_0^{ii'} J(0) - \Sigma^{ii'}(x_2) J(\hat{v})}{\hat{v}},$$

where the infrared divergences cancel completely, leaving no unphysical parameters in the total cross section.

In performing integration over the photon phase space, $I[\hat{F}^{\mathrm{IR}}]$, we employed the expressions

$$I\left[\frac{1}{z^2}\right] = \frac{1}{m_l^2 v}, \quad I\left[\frac{1}{z_1^2}\right] = \frac{1}{m_1^2 v}, \quad (68)$$
$$I\left[\frac{1}{z z_1}\right] = -\frac{1}{vt} \ln \frac{t^2}{m_l^2 m_1^2},$$
$$I\left[\frac{1}{z u_1}\right] = -\frac{1}{vu} \ln \frac{u^2}{m_l^2 m_2^2},$$
$$I\left[\frac{1}{z_1 u_1}\right] = \frac{1}{v s_q} \ln \frac{s_q^2}{m_1^2 m_2^2}, \quad I\left[\frac{1}{u_1^2}\right] = \frac{1}{m_2^2 v}.$$

With the aid of these expressions, we can easily obtain the quantity $J(\hat{v})$ in the form [recall that $\hat{v} = D(x_2 - x_2^0)$ and that the case of $\hat{v} = 0$ corresponds to Born kinematics]

$$J(\hat{v}) = Q_l^2 - c_l Q_l Q_i \ln \frac{\hat{t}^2}{m_l^2 m_1^2} + c_l Q_l Q_{i'} \ln \frac{\hat{u}^2}{m_l^2 m_2^2} \quad (69)$$
$$+ Q_i^2 - Q_i Q_{i'} \ln \frac{\hat{s}_q^2}{m_1^2 m_2^2} + Q_{i'}^2.$$

Thus, the infrared-divergence-free cross section for the bremsstrahlung process $\overset{(\rightarrow)}{h_1}\overset{\rightarrow}{h_2} \to l^{\pm}\gamma X$ has the form

$$\sigma_R^{\pm,F} \quad (70)$$
$$= \sum_{i,i'} \int dx_1 dx_2 F_i^{(1)}(x_1, Q^2) F_{i'}^{(2)}(x_2, Q^2) \hat{\Sigma}_R^{F,ii'},$$

where

$$\Sigma_R^{F,ii'} = \frac{\alpha^3}{8 s_{\mathrm{W}}^4 s_q N_c} |V_{ii'}|^2 (Q_l^2 \Pi_l \Pi_l^+ V_l \quad (71)$$
$$+ Q_l \mathrm{Re}[\Pi_l V_{lq}] + V_q + Q_l \Pi_l \Pi_l^+ \mathrm{Re}[V_{lW}]$$
$$+ \mathrm{Re}[\Pi_l] V_{qW} + \Pi_l \Pi_l^+ V_W).$$

The indices on V mean the origin of the bremsstrahlung photon: l, q, and W refer to radiation from the lepton (Fig. 3, *10*), quark (Fig. 3, *8* and *9*), and W boson (Fig. 3, *11*), respectively. Double indices correspond to interference terms. The expressions for V are independent of particle polarizations and coincide with those given in Appendix C of [15].

Thus, we see that, in the $O(\alpha^3)$ cross section for process (1) (we label it with the subscript EWC, which means electroweak corrections), there are three terms—the finite components $\sigma_{V(R)}^{\pm,F}$ of the V (R) contributions and the term $(\sigma_V^{\pm,\mathrm{IR}} + \sigma_R^{\pm,\mathrm{IR}})$, where infrared divergences cancel in the sum. Specifically, we have

$$\sigma_{\mathrm{EWC}}^{\pm} = \sigma_V^{\pm,F} + \sigma_R^{\pm,F} + (\sigma_V^{\pm,\mathrm{IR}} + \sigma_R^{\pm,\mathrm{IR}}). \quad (72)$$

It is a remarkable feature of all of these terms that their dependence on initial-hadron polarization is factored out in the expressions for $F_i^{(1)}(x_1, Q^2)$ and $F_{i'}^{(2)}(x_2, Q^2)$. This factorization makes it possible to derive straightforwardly, from the formulas given

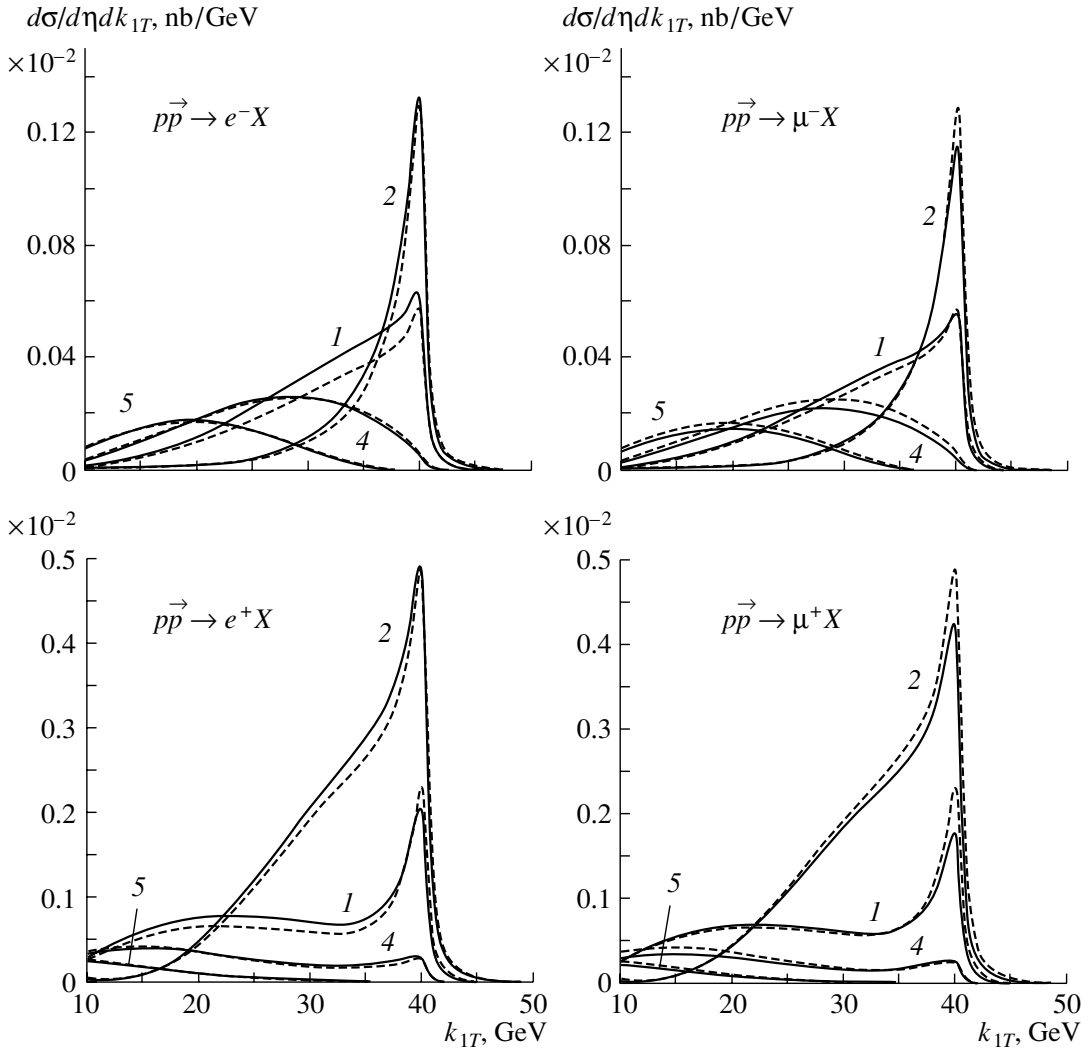

Fig. 5. Unpolarized part of the double differential cross section for the process $p\vec{p} \to l^{\pm} X$ at $\sqrt{s} = 500$ GeV and $\Delta\Phi = 2\pi$ (RHIC kinematics) versus k_{1T} for the pseudorapidity values of (curve *1*) $\eta = -1$, (curve *2*) $\eta = 0$, (curve *4*) $\eta = 1.5$, and (curve *5*) $\eta = 2$ for the cases of $e^{\pm}$ and $\mu^{\pm}$ production. The dashed and solid curves represent, respectively, the Born cross sections and the cross sections including electroweak radiative corrections. The distributions of unpolarized quarks were taken in the GRV94 form from [21].

above in this study, the cross section for any combination of initial-hadron polarizations via the simple substitutions

$$F_i^{(1)}(x_1, Q^2) \to \bar{q}_i^{(1)}(x_1, Q^2), \qquad (73)$$
$$F_{i'}^{(2)}(x_2, Q^2) \to \bar{q}_{i'}^{(2)}(x_2, Q^2),$$

which transform the hadron in question into an unpolarized one.

5. NUMERICAL RESULTS AND CONCLUSIONS

The objective of this section is to obtain numerical estimates for radiative and spin effects considered above.[1)] The question of comparing our results with those given previously in [13] and the problem of the quark-mass dependence of the corrections to the cross section that are calculated within the present approach are considered in detail elsewhere [15] (see also the comments in the recent study of Dittmaier and Kramer [14]). Here, we will briefly comment on the behavior of the radiative corrections to the cross section for W-boson production in collisions of an unpolarized proton and an unpolarized antiproton un-

[1)]The FORTRAN code for numerically calculating the total $O(\alpha)$ electroweak radiative correction to the cross sections and to the single and double spin asymmetries can be received from the present author by sending a request to his electronic address.

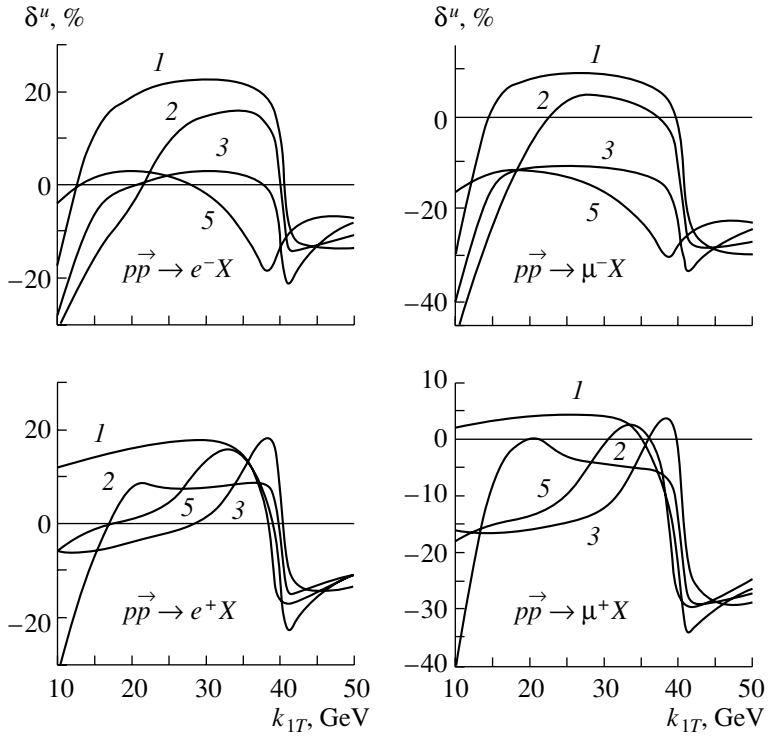

Fig. 6. Corrections δ^u for the process $p\vec{p} \to l^\pm X$ under the conditions of RHIC kinematics versus k_{1T} at the pseudorapidity values of (curve *1*) $\eta = -1$, (curve *2*) $\eta = 0$, (curve *3*) $\eta = 1$, and (curve *5*) $\eta = 2$ for the cases of $e^\pm$ and $\mu^\pm$ production.

der the kinematical conditions of the Tevatron collider. It can be seen that, in the resonance region, the cross section including the corrections is smaller by about 0.0025 nb/GeV {that is, by approximately 5% (see Fig. 4; see also Fig. 6 in [15])} than the Born cross section. As to the dependence of the corrections on the choice of quark masses, which parametrize here the collinear singularity of the initial state, we note that the corrections decrease by approximately 5% as the masses in question increase by one order of magnitude; of course, this would impose rather strong limitations on the region of applicability of our approach to estimating unpolarized observables. Considering that, within the quark-parton model, the masses of the initial-state quarks can be replaced by the expressions

$$m_1 = x_1 m_{h_1}, \quad m_2 = x_2 m_{h_2} \tag{74}$$

and that there are no other quarks in the reaction being studied, we can state, however, that our approach is free from an uncertainty in the choice of quark masses. The correction corresponding to the choice in (74) is shown by the dashed curve in Fig. 4. It can be seen that this correction virtually coincides with the correction calculated by using the current quark masses, this agreement being especially close in the resonance region and at high values of k_{1T}. Further, we will show that the problem of a strong quark-mass dependence is nonexistent in the case of polarization observables. Nevertheless, we will return to this problem once again at the end of this section.

Thus, we want to estimate numerically the electroweak radiative corrections for process (1). We are interested first in the effect of the electroweak radiative corrections on the cross section (Fig. 5) and then in the total correction $\delta^u_{l^\pm}$ to the unpolarized cross-section component (Fig. 6), which is given by

$$\sigma^\pm_{\mathrm{EWC}} = \bar{\sigma}^\pm_0(1 + \delta^u_{l^\pm}) + p_{h2}\Delta\sigma^\pm_0(1 + \delta^p_{l^\pm}); \tag{75}$$

further, we estimate the electroweak radiative corrections to the single and double spin asymmetries [$A^{l^\pm}_L$ (Figs. 7, 8) and $A^{l^\pm}_{LL}$ (Fig. 9), respectively] over a wide region of kinematical variables. By way of example, we take the region of the STAR experiment at the RHIC facility—that is, $\sqrt{s} = 500$ GeV, $-1 \le \eta \le 2$, and $\Delta\Phi = 2\pi$. We have used the standard set of electroweak parameters,

$$\alpha = 1/137.036, \quad m_W = 80.43 \text{ GeV},$$
$$m_Z = 91.19 \text{ GeV}, \quad m_H = 300.0 \text{ GeV},$$

and the fermion masses

$$m_u = 5 \text{ MeV}, \quad m_d = 8 \text{ MeV}, \quad m_s = 150 \text{ MeV},$$
$$m_c = 1.5 \text{ GeV}, \quad m_b = 4.5 \text{ GeV}, \quad m_t = 175 \text{ GeV}.$$

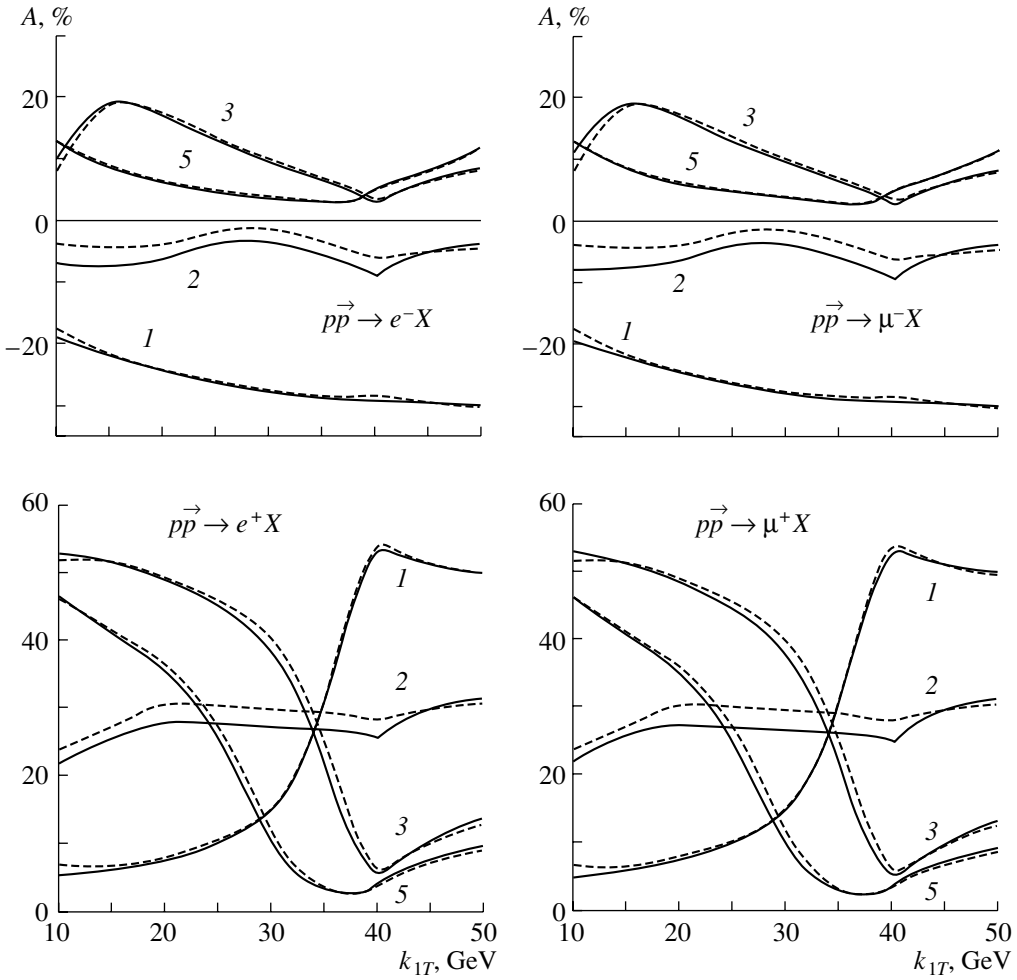

Fig. 7. Single polarization asymmetries for the process $p\vec{p} \to l^{\pm} X$ versus k_{1T} for various values of η in the Born approximation (dashed curves) and with allowance for electroweak radiative corrections (solid curves). The rest of the notation is identical to that in Fig. 6.

We have also employed the GRV94 parametrization [21] for the distributions of unpolarized quarks and the GRSV96 (LO) parametrization [22] for the distributions of polarized quarks. For the momentum transfer squared Q^2 in these Q^2-dependent distributions, we have chosen (as in [13]), the value of $Q^2 = m_W^2$. Using the exact value of Q^2 for the partonic reaction (for example, $Q^2 = \hat{s}_q$ for the Born cross section and for the final-state-radiation component), we have not found, however, any noticeable difference in the effects considered here. Finally, we note that, since the contributions to the observables of the processes in question from different origins are experimentally indistinguishable, we do not perform here their comparative analysis.

The numerical results obtained here for the cross-section component corresponding to the scattering of unpolarized hadrons are presented in Fig. 5 versus k_{1T} for various pseudorapidity values. One can see from this figure that, both for a positron and for an electron in the final state, the electroweak radiative corrections are significant and increase the Born cross section in the region $k_{1T} < m_W/2$ for $\eta = -1,\ 0$; further, the electroweak radiative corrections are insignificant at low k_{1T} for $\eta > 1$ and in the region $k_{1T} \geq m_W/2$ for all values of η. For a positively and a negatively charged muon in the final state, the electroweak radiative corrections are more significant in the resonance region at $\eta = -1,\ 0$ and for low values of k_{1T} at $\eta = 1.5,\ 2$ (here, the electroweak radiative corrections reduce the Born cross section).

Further, Fig. 6 displays the corrections δ^u to the unpolarized part of the Born cross section. It can be seen that the corrections are less in the muon-production than in the electron-production process (the difference is about 0.12). This fact conforms to the general character of the dependence of the electroweak radiative corrections on masses that regularize the collinear singularity since the mass m_μ is

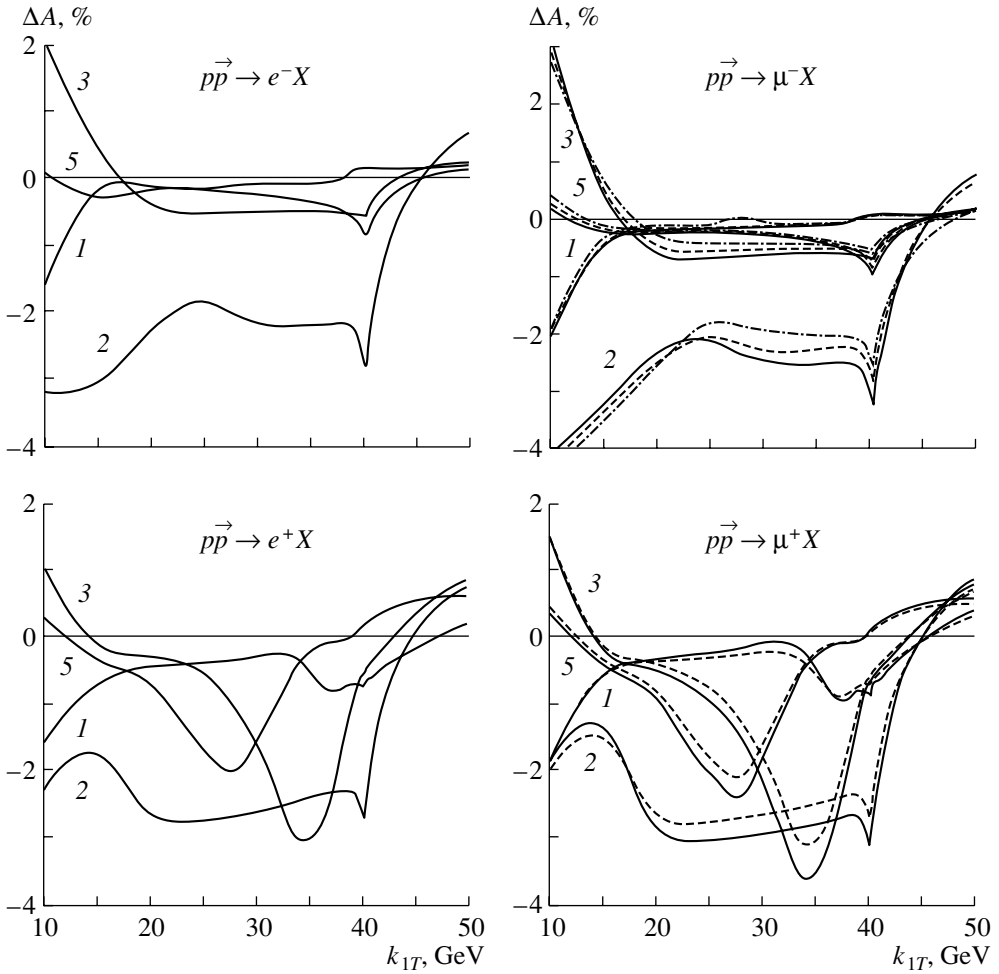

Fig. 8. Corrections to the single polarization asymmetries for the process $p\vec{p} \to l^{\pm} X$ versus k_{1T} for various values of η. The solid, dashed, and dash-dotted curves are plotted for, respectively, current quarks, the choice of $m_u = m_d = 30$ MeV, and the choice in (74). The rest of the notation is identical to that in Fig. 6.

greater than m_e by a factor of about 2×10^2. A feature that is common to the behavior of corrections for all cases ($e^{\pm}, \mu^{\pm}$) and at almost all values of η is that they increase in the region $k_{1T} < m_W/2$, decrease sharply in the vicinity of the resonance, and then grow smoothly in the region $k_{1T} > m_W/2$. We note that the corrections to the transverse-mass distribution that are displayed in Fig. 9 of [13] (see also [14]) exhibit a similar behavior.

Let us consider the effect of the electroweak radiative corrections on the observable single [Eqs. (27), (28)] and double [Eqs. (29), (30)] spin asymmetries. By way of example, Fig. 7 shows the Born asymmetries $A_{L0}^{l^{\pm}}$ and the asymmetries with allowance for the electroweak radiative corrections. One can see that the corrections to the single asymmetry are significant and that they reduce the Born asymmetries nearly over the entire region being investigated, with the exception of the low-k_{1T} and high-η regions. It should be noted that the corrections in question are virtually independent of the masses of final-state particles (m_e versus m_μ). In other words, the cross-section ratios (that is, asymmetries) are much less sensitive to variations in the mass values than the cross sections themselves. Because of this, the corrections to the asymmetries are weakly dependent on the quark masses as well. If, for example, we change the quark masses from the current values of $m_u = 5$ MeV and $m_d = 8$ MeV to the constituent values of $m_u = m_d = 0.33$ GeV, the asymmetries change by not more than 0.01% over the entire region investigated here; in the region specified by the values of $\eta = 2$ and $k_{1T} = 10$ GeV, which is of importance for analyzing the quark distributions at low x (see Section 2), this shift is as small as 0.0032% (0.0021%) for a negatively (positively) charged muon in the final state. A small distinction between the single asymmetries that arises in response to varying the quark masses is clearly seen in Fig. 8, which shows the quantities $\Delta A_L^{l^{\pm}} = A_{L\,\mathrm{EWC}}^{l^{\pm}} - A_{L\,0}^{l^{\pm}}$ versus k_{1T} at various values

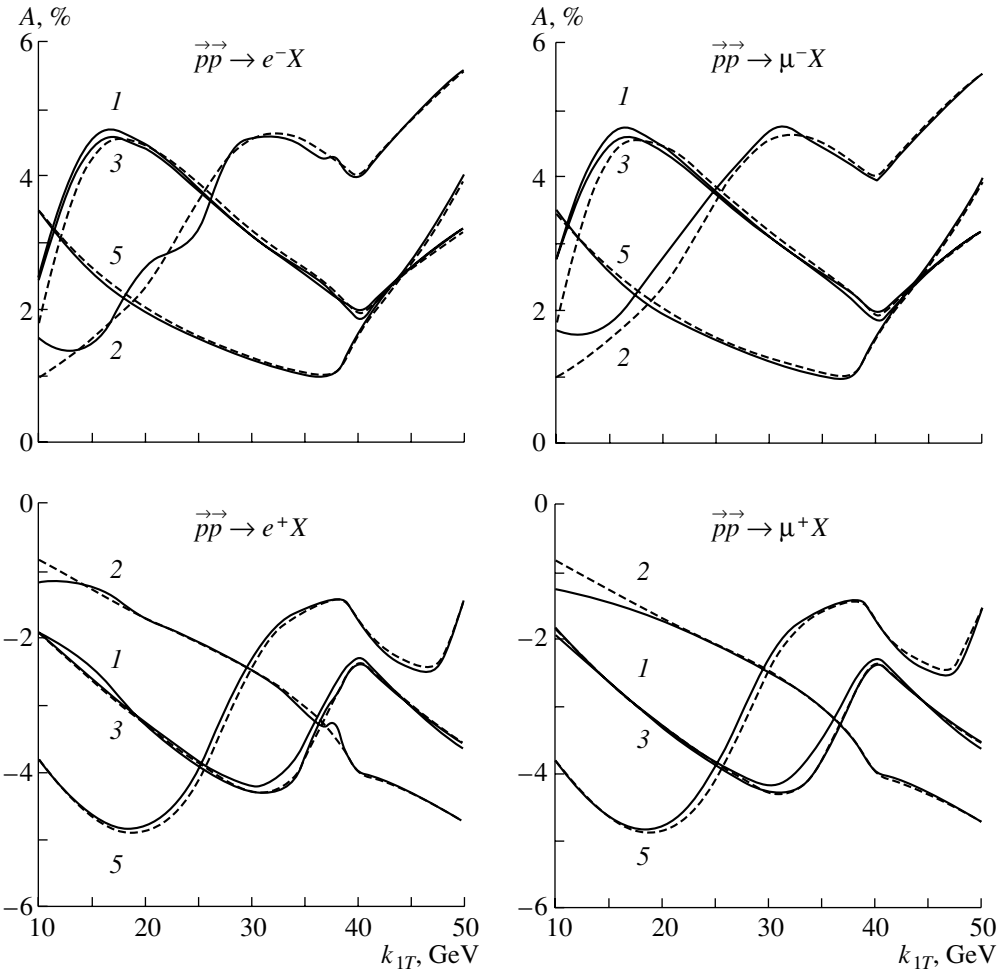

Fig. 9. Double polarization asymmetries for the process $\vec{p}\vec{p} \to l^{\pm} X$ versus k_{1T} for various values of η in the Born approximation (dashed curves) and with allowance for electroweak radiative corrections (solid curves). The notation is identical to that in Fig. 6.

of η. One can see that the variation of $\Delta A_L^{\mu^{\pm}}$ in response to the variation of the quark masses within a factor of about 5 does not exceed 0.2% over the entire kinematical region under consideration, including the region of our prime interest around the values of $\eta = 2$ and $k_{1T} = 10$ GeV, where $\Delta A_L^{\mu^{\pm}}$ is as low as about 0.015%. The curves corresponding to the choice of the quark masses in (74) (Fig. 8, μ^- in the final state) have a perfectly similar character, deviating nowhere from those for the current-quark-mass choice by more than 0.5%. Thus, we see that our approach to calculating the electroweak radiative corrections to the asymmetries is nearly free from the uncertainty in choosing the quark masses.

Finally, the double Born asymmetries and the double asymmetries with allowance for the total radiative correction are shown in Fig. 9. These asymmetries prove to be smaller than the single asymmetries, but they are quite sizable (about 5%) almost over the entire kinematical region being considered. We can see that the electroweak radiative corrections to these asymmetries are especially significant in the case of scattering at $\eta = 0$ and at low values of k_{1T}. There, the difference between the asymmetries is 0.5%; within the remaining region of variables, the correction is appreciably smaller. Figure 9 also demonstrates an interesting feature of the Born double asymmetries—the equality $A_{LL0}(\eta, k_{1T}) = A_{LL0}(-\eta, k_{1T})$. This relation follows from the structure of the double asymmetries and from the symmetry of the region of x_1 and x_2 [see Fig. 2 and formula (36)]. Naturally, it does not hold for the asymmetries calculated with allowance for the radiative corrections.

6. CONCLUSION

Thus, the results of the present study can be used in exploring the nucleon spin at hadron colliders—first of all, in interpreting data that will be obtained

in experiments at the RHIC facility. The analysis performed in this study makes it possible to estimate, for the first time, electroweak radiative corrections to a wide variety of observables in the production of single W bosons—that is, to the cross sections and to single and double polarization asymmetries. A numerical analysis of the results has revealed that the effects being considered are significant in experiments under the kinematical conditions of the RHIC facility.

ACKNOWLEDGMENTS

I am grateful to A.N. Ilyichev for assistance in calculating some of the integrals appearing in the hard contribution and to N.P. Merenkov for stimulating discussions and valuable comments.

REFERENCES

1. J. Ashman *et al.*, Phys. Lett. B **206**, 364 (1988); Nucl. Phys. B **328**, 1 (1989).
2. B. Adeva *et al.*, Phys. Rev. D **58**, 112001 (1998).
3. E154 Collab. (K. Abe *et al.*), Phys. Rev. Lett. **79**, 26 (1997); E155 Collab. (P. L. Anthony *et al.*), Phys. Lett. B **493**, 19 (2000).
4. A. Airapetian *et al.*, Phys. Rev. Lett. **84**, 2584 (2000).
5. SMC Collab. (B. Adeva *et al.*), Phys. Lett. B **420**, 180 (1998).
6. HERMES Collab. (K. Ackerstaff *et al.*), Phys. Lett. B **464**, 123 (1999).
7. G. Bunce *et al.*, Annu. Rev. Nucl. Part. Sci. **50**, 525 (2000).
8. Preprint HE 95-09, Hamburg, Univ. of Michigan (1995).
9. W.-D. Nowak, Preprint 96-095, DESY (Hamburg, 1996).
10. C. Bourrely *et al.*, Phys. Rep. **177**, 319 (1989).
11. I. V. Akushevich and N. M. Shumeiko, J. Phys. G **20**, 513 (1994).
12. F. Berends and R. Kleiss, Z. Phys. C **27**, 365 (1985).
13. U. Baur, S. Keller, and D. Wackeroth, Phys. Rev. D **59**, 013002 (1999).
14. S. Dittmaier and M. Kramer, Preprint No. BI-TP 2000/04 DESY 01-121 (Edinburgh, 2001).
15. V. A. Zykunov, hep-ph/0107059.
16. D. Yu. Bardin and N. M. Shumeiko, Nucl. Phys. B **127**, 242 (1977).
17. V. A. Zykunov, S. I. Timoshin, and N. M. Shumeiko, Yad. Fiz. **58**, 2021 (1995) [Phys. At. Nucl. **58**, 1911 (1995)]; **60**, 1415 (1997) [**60**, 1279 (1997)]; **62**, 723 (1999) [**62**, 674 (1999)]; N. M. Shumeiko, S. I. Timoshin, and V. A. Zykunov, J. Phys. G **23**, 1593 (1997).
18. M. Böhm and H. Spiesberger, Nucl. Phys. B **304**, 749 (1988).
19. M. Böhm *et al.*, Fortschr. Phys. **34**, 687 (1986).
20. A. D. Martin *et al.*, Preprint No. DTP/98/52 (Durham, 1998).
21. M. Glück *et al.*, Preprint No. 94-206, DESY (Hamburg, 1994).
22. M. Glück *et al.*, Phys. Rev. D **53**, 4775 (1996).

Translated by A. Isaakyan

Physics of Atomic Nuclei, Vol. 66, No. 5, 2003, pp. 893–901. Translated from Yadernaya Fizika, Vol. 66, No. 5, 2003, pp. 925–933.

ELEMENTARY PARTICLES AND FIELDS
Theory

Investigation of Logarithmic Contributions in the Electron-to-Muon Mass Ratio to the Shift of the *S* Energy Levels in the Muonium Atom

N. A. Boikova, S. V. Kleshchevskaya, Yu. N. Tyukhtyaev, and R. N. Faustov[1)]

Saratov State University, Astrakhanskaya ul. 83, Saratov, 490071 Russia

Received January 29, 2002; in final form, June 17, 2002

Abstract—New logarithmic corrections in the mass ratio to the shift of the $1S$ and $2S$ energy levels in the muonium atom are calculated analytically. Corrections of this type that have been obtained so far are discussed and systematized. © *2003 MAIK "Nauka/Interperiodica".*

The contribution to the fine shift of the S energy levels in a hydrogen-like atom from recoil effects was analyzed even at the early stage of investigations into the problem of bound states of two particles [1, 2]. The theoretical value found there for the shift and reproduced later on by other methods [3, 4] can be written in the form

$$\Delta E = \frac{(Z\alpha)^5\mu^3}{\pi m_1 m_2}\frac{1}{n^3}\left\{\frac{2}{3}\ln(Z\alpha)^{-1} - \frac{2}{3}\ln[k_0(n)] + \frac{2}{m_1^2 - m_2^2}\left[m_1^2\ln\eta_1' - m_2^2\ln\eta_2'\right] + C\right\}, \quad (1)$$

where Z is the charge of the nucleus being considered, n is the principal quantum number, $\ln[k_0(n)]$ is the Bethe logarithm, μ is the reduced mass, α is the fine-structure constant, $\eta_{1,2}' = m_{1,2}/(m_1+m_2)$, and C is the constant determining the contributions featuring no logarithms.

We emphasize that a rather high order logarithmic contribution in the mass ratio is present here; that is,

$$\Delta E^{\beta} = \frac{(Z\alpha)^5\mu^3}{\pi m_1 m_2}\frac{1}{n^3}\frac{2}{m_1^2 - m_2^2}\times\left[m_1^2\ln\eta_1' - m_2^2\ln\eta_2'\right] = \frac{2(Z\alpha)^5\mu^3}{\pi m_1 m_2}\frac{1}{n^3}\frac{1}{1-\beta^2}\left[\ln\frac{1}{1+\beta} - \beta^2\ln\frac{\beta}{1+\beta}\right] \sim \frac{2(Z\alpha)^5\mu^3}{\pi m_1 m_2}\frac{1}{n^3}\beta^2\ln\beta^{-1}, \quad (2)$$

where $\beta = m_1/m_2$ (m_1 and m_2 are the masses of the light and the heavy particle, respectively).

A feature peculiar to the procedure for deriving the quantity in (1) is that the Feynman diagram technique was modified in such a way as to take into account the effects of binding in virtual states of the system. In analyzing two-photon diagrams, it turns out that one must take into account the multiple exchange of Coulomb photons. However, the effects of binding manifest themselves only in the low-frequency region at virtual-momentum values of $|\mathbf{k}| < \varepsilon$, $\mu(Z\alpha)^2 \ll \varepsilon \ll \mu$, since the binding energy of a hydrogen-like atom is small. In view of this, it is reasonable to break down the interval of integration into the low- and the high-frequency regions:

$$\int d^3k dk_0 = \left[\int\limits_{|\mathbf{k}|<\varepsilon} d^3k\ldots + \int\limits_{|\mathbf{k}|>\varepsilon} d^3k\ldots\right]\int dk_0. \quad (3)$$

In taking the sums of the integrals involved, the boundary parameter ε is canceled, so that its exact value is immaterial.

In [4], use was made of the quasipotential approach to describing bound states. In the most general case [5, 6], the quasipotential can be expressed in terms of the amplitude τ_C as

$$V(\mathbf{p},\mathbf{q};E) = (\overline{G_C}^{+})^{-1}\overline{G_C\tilde{T}G_C}^{+}(\overline{G}^{+})^{-1} = \tau_C - \tau_C\overline{G_C}^{+}\tau_C + \ldots, \quad (4)$$

where $\tau_C = (\overline{G_C}^{+})^{-1}\overline{G_C\tilde{T}G_C}(\overline{G_C}^{+})^{-1}$,

$$\overline{G}^{+}(\mathbf{p},\mathbf{q};E) = u_1^*(\mathbf{p})u_2^*(-\mathbf{p})\bar{G}(\mathbf{p},\mathbf{q};E)\Gamma_0 u_1(\mathbf{q})u_2(-\mathbf{q}),$$

$$\bar{G}(\mathbf{p},\mathbf{q};E) = (2\pi)^{-2}\int dp_0 dq_0 G(p_0,q_0,\mathbf{p},\mathbf{q};E),$$

[1)] Scientific Council for the Interdisciplinary Problem Cybernetics, Russian Academy of Sciences, ul. Vavilova 40, Moscow, 117976 Russia.

1063-7788/03/6605-0893$24.00

$$u_i(\mathbf{p}) = N_{m_i p}\begin{pmatrix} w \\ \dfrac{\boldsymbol{\sigma}\cdot\mathbf{p}}{\varepsilon_{ip}+m_i}w \end{pmatrix},\quad N_{m_i p} = \sqrt{\frac{\varepsilon_{ip}+m_i}{2\varepsilon_{ip}}}. \tag{5}$$

Here, w is an arbitrary two-component quantity that satisfies only the normalization condition $w^*w = 1$; $\boldsymbol{\sigma}$ is the vector whose components are the Pauli matrices; E is the total energy of the system; $\varepsilon_{ip} = \sqrt{\mathbf{p}^2 + m_i^2}$; and $\Gamma_0 = \gamma_{10}\gamma_{20}$, γ_{i0} standing for the Dirac matrices ($i = 1, 2$).

The total Green's function of the system can be written as

$$G = G_{\mathrm{C}} + G_{\mathrm{C}}\tilde{T}G_{\mathrm{C}}, \tag{6}$$

where $\tilde{T}$ is the scattering amplitude,

$$\tilde{T} = \tilde{K} + \tilde{K}G\tilde{K}. \tag{7}$$

Here, $\tilde{K} = K_{\mathrm{BS}} - K_{\mathrm{C}}$, where K_{BS} is the kernel of the Bethe–Salpeter equation and $K_{\mathrm{C}} = v_{\mathrm{C}}\gamma_{10}\gamma_{20}$, v_{C} being the Coulomb potential.

The Coulomb Green's function has the form

$$G_{\mathrm{C}} = G_0 + G_0 K_{\mathrm{C}} G_{\mathrm{C}}, \tag{8}$$

where G_0 is the Green's function for noninteracting fermions.

An important feature peculiar to the quasipotential (4) is that, for each reducible diagram, there is an iteration term that improves its behavior in the infrared region [6]. In order to illustrate this statement, we will consider the simplest situation where the amplitude can be represented as

$$\tilde{T} = K_T \tag{9}$$
$$= -\frac{4\pi\alpha}{k_0^2 - \mathbf{k}^2 + i0}\left(\boldsymbol{\gamma}_1\cdot\boldsymbol{\gamma}_2 - \frac{(\boldsymbol{\gamma}_1\cdot\mathbf{k})(\boldsymbol{\gamma}_2\cdot\mathbf{k})}{\mathbf{k}^2}\right).$$

The index "T" symbolizes here the exchange of a transverse photon, while the effects of binding can be taken into account by means of the approximation

$$G_{\mathrm{C}} \cong G_0 + G_0 K_{\mathrm{C}} G_0. \tag{10}$$

By definition, we have

$$G_0(k, k'; E) = i(2\pi)^4\delta^4(k - k') \tag{11}$$
$$\times S_1(\eta_1 E + k_0, \mathbf{k}) S_2(\eta_2 E - k_0, -\mathbf{k}),$$
$$\eta_1 = \frac{E^2 + m_1^2 - m_2^2}{2E^2},\quad \eta_2 = \frac{E^2 + m_2^2 - m_1^2}{2E^2},$$

where

$$S_i(k_0, \mathbf{k}) = \Big(\Lambda_i^+(\mathbf{k})\,[k_0 - \varepsilon_{ik} + i0]^{-1} \tag{12}$$
$$+ \Lambda_i^-(-\mathbf{k})\,[k_0 + \varepsilon_{ik} - i0]^{-1}\Big)\gamma_{i0},$$
$$F(\mathbf{p}, \mathbf{q}) = (2\pi)^3\delta(\mathbf{p} - \mathbf{q})\,(E - \varepsilon_{1p} - \varepsilon_{2p})^{-1}.$$

Here, $\Lambda^+(\mathbf{p}) = \dfrac{\widehat{p} + m}{2\varepsilon_p}\gamma_0$ and $\Lambda^-(\mathbf{p}) = \gamma_0\dfrac{\widehat{p} - m}{2\varepsilon_p}$ are projection operators. From the above, we have

$$(\overline{G_{\mathrm{C}}}^{+})^{-1} \cong F^{-1} - K_{\mathrm{C}}^+,\quad \overline{G_0}^{+} = F. \tag{13}$$

For the amplitude τ_{C}, we then obtain the expression

$$\tau_{\mathrm{C}} = (K_T)_{0F}^+ + (K_{\mathrm{C}}G_0K_T)_{0F}^+ \tag{14}$$
$$- K_{\mathrm{C}}^+ F (K_T)_{0F} + (K_T G_0 K_{\mathrm{C}})_{0F}^+$$
$$- (K_T)_{0F}^+ F K_{\mathrm{C}}^+.$$

Here, we have used the notation

$$(\ldots)_{0F}^+ = F^{-1}\overline{G_0(\ldots)G_0}^{+}F^{-1}. \tag{15}$$

Upon performing integration in (14) with respect to the zeroth components of the initial- and the final-state momentum, we find, in the vicinity of the mass shell, that

$$\tilde{T}(\mathbf{p}, \mathbf{q}; E) = \tilde{T}(p_0 = 0, q_0 = 0, \mathbf{p}, \mathbf{q}; E), \tag{16}$$
$$F^{-1}\overline{G_0\tilde{T}G_0}^{+}F^{-1} = \tilde{T}_+(\mathbf{p}, \mathbf{q}; E)$$
$$= \bar{u}_1(\mathbf{p})\bar{u}_2(-\mathbf{p})\tilde{T}(\mathbf{p}, \mathbf{q}; E)u_1(\mathbf{q})u_2(-\mathbf{q}).$$

In our case, the quasipotential (4) takes the form

$$V = V^{(2)} + V^{(4)}, \tag{17}$$

where $V^{(2)} = (K_T)_+$,

$$V^{(4)} = (K_{\mathrm{C}}G_0K_T)_+ - (K_{\mathrm{C}})_+F(K_T)_+$$
$$+ (K_T G_0 K_{\mathrm{C}})_+ - (K_T)_+ F (K_{\mathrm{C}})_+.$$

Each of the leading contributions to the energy-level shift from the terms $(K_{\mathrm{C}}G_0K_T)_+$ and $(K_{\mathrm{C}})_+F(K_T)_+$ is individually proportional to α^4—that is, it is of the same order as the contribution of the quasipotential $V^{(2)}$. However, it should be noted that, because of the arising difference of the reducible-diagram contribution and the contribution of the corresponding iteration, the main corrections to the Coulomb energy level from the quasipotentials $V^{(2)}$ and $V^{(4)}$ appear to be, in one case, of lower order in α ($V^{(2)} \sim \alpha^4$) and, in the other case, of higher order in α ($V^{(4)} \sim \alpha^5$). As the number of events of Coulomb photon exchange increases in higher orders of perturbation theory, the conditions for the cancellation of the leading corrections in the differences of reducible diagrams and the corresponding iterations remain unchanged. Thus, summation of multiple exchanges of Coulomb photons as a means for removing infrared singularities retains value only for irreducible diagrams that can be associated with internal intermediate states of a nucleus.

The scattering amplitude $\tilde{T}_+$ describing the exchange of two transverse photons has no singularities

at the virtual-momentum value of $|\mathbf{k}| = 0$. Indeed, it follows from the results reported in [4] that, in the low-frequency region, the spin-independent part of the amplitude $\tilde{T}_+ = T_{TT}$ is given by

$$T_{TT}^{\mathrm{LF}} = -\frac{(Z\alpha)^2}{2\pi m_1 m_2} \times \int\limits_{|\mathbf{k}|\le\varepsilon} \frac{d^3k}{\sqrt{\mathbf{k}_p^2}\sqrt{\mathbf{k}_q^2}\left(\sqrt{\mathbf{k}_p^2}+\sqrt{\mathbf{k}_q^2}\right)}\left(1+\frac{(\mathbf{k}_p\cdot\mathbf{k}_q)^2}{\mathbf{k}_p^2\mathbf{k}_q^2}\right), \tag{18}$$

where $\mathbf{k}_r = |\mathbf{k}-\mathbf{r}|$, $\mathbf{r} = \mathbf{p}, \mathbf{q}$, and that the fine shift of the n, S energy levels due to the amplitude component in (18) has the form

$$\Delta E_{TT}^{\mathrm{LF}} = \langle nS|\, T_{TT}^{\mathrm{LF}}\, |nS\rangle\,. \tag{19}$$

The wave function $|nS\rangle = \Psi_{nS}(\mathbf{p})$ is a solution to the Schrödinger equation

$$\left(\mathbf{p}^2 + \frac{\alpha^2\mu^2}{n^2}\right)\Psi_{nS}(\mathbf{p}) = \frac{\alpha\mu}{\pi^2}\int\frac{d^3q}{(\mathbf{p}-\mathbf{q})^2}\Psi_{nS}(\mathbf{q}). \tag{20}$$

By breaking down the interval of integration into two parts ($0 \le |\mathbf{k}| \le \alpha\mu/n$ and $\alpha\mu/n \le |\mathbf{k}| \le \varepsilon$), we can easily find that, in the first part, $\Delta E_{TT}^{\mathrm{LF}} \sim \alpha^5$ does not involve the quantity $\ln\alpha^{-1}$ or $\ln\beta^{-1}$ and that, in the second part, we can use the δ approximation for wave functions; that is,

$$|nS\rangle = \Psi_{nS}(\mathbf{p}) \approx (2\pi)^3\Psi_{nS}(0)\delta(\mathbf{p}), \tag{21}$$
$$|\Psi_{nS}(0)|^2 = \frac{\alpha^3\mu^3}{\pi n^3}.$$

By using expressions (19), we can therefore obtain

$$\Delta E_{TT}^{\mathrm{LF}} = -\frac{(Z\alpha)^2}{2\pi m_1 m_2}\cdot 4\pi\,|\Psi_{nS}(0)|^2\int\limits_{\alpha\mu/n}^{\varepsilon}\frac{dk}{k} \tag{22}$$
$$= -\frac{2(Z\alpha)^2}{m_1 m_2}\,|\Psi_{nS}(0)|^2\ln\frac{\varepsilon n}{\alpha\mu}.$$

In the high-frequency region, the wave-function approximation (21) is also used for the initial and the final state of the system; therefore, radical expressions of the types ε_{ip} and ε_{iq} in the definition of the quasipotential (17) are replaced by the masses of the ith particle. At the same time, radical expressions of the type ε_{ik} are retained in the electron and muon propagators (14). Hence, we are to consider integrals of the type

$$m_2\int\frac{dk}{\sqrt{k^2+m_1^2}\sqrt{k^2+m_2^2}} \approx \ln\beta^{-1}, \tag{23}$$

which were previously discussed in [7].

At $n = 2$, it follows from the results presented in [4] that

$$T_{TT}^{\mathrm{HF}} = \frac{2(Z\alpha)^2}{m_1 m_2}\left[\ln\frac{2\varepsilon}{\mu} + \frac{m_1^2\ln\eta_1' - m_2^2\ln\eta_2'}{m_1^2-m_2^2}\right], \tag{24}$$

and the total correction to the fine shift from this diagram makes a logarithmic contribution in β over the entire interval of integration with respect to the virtual momentum:

$$\Delta E_{TT}^{\beta} = -\frac{(Z\alpha)^5\mu^3}{4\pi m_1 m_2}\frac{1}{m_2^2-m_1^2} \times\left[m_1^2\ln\frac{\mu}{m_2} - m_2^2\ln\frac{\mu}{m_1}\right] \sim \frac{(Z\alpha)^5\mu^3}{4\pi m_1 m_2}\beta^2\ln\beta^{-1}. \tag{25}$$

At $Z = 1$, the logarithmic contribution that we obtained perfectly coincides with that which appears in expression (2).

The calculations performed in [4] reveal that, in the δ approximation of wave functions, there exist no other contributions of order $[\alpha^5\mu^3/(m_1m_2)]\beta^2\ln\beta^{-1}$. It is obvious that, in this approximation, it is impossible to obtain corrections of order

$$\frac{\alpha^5\mu^3}{m_1m_2}\beta\ln\beta^{-1} \approx \frac{\alpha^6\mu^3}{m_1m_2}\ln\beta^{-1} > \frac{\alpha^5\mu^3}{m_1m_2}\beta^2\ln\beta^{-1}.$$

Let us now consider a different possibility. We assume that, in contrast to what occurs in expressions (25), the use of the δ approximation for wave functions leads to the vanishing of the integral.

By way of example, we choose the integral

$$I = \frac{\alpha^7\mu^3}{8\pi^6}\frac{\mu\beta}{1+\beta}\int\frac{d^3pN_p}{(p^2+\alpha^2\mu^2)^2} \times\int\frac{d^3qN_q}{(q^2+\alpha^2\mu^2)^2}\int\frac{d^3k}{\mathbf{k}_p^2(k^2+\alpha^2\mu^2)} \times\frac{M_{1k}}{\varepsilon_{1k}}\frac{M_{2k}}{\varepsilon_{2k}}\frac{M_{2k}}{M_{1k}+M_{2k}}\left(1-\frac{k^2}{\mathbf{k}_q^2}\right), \tag{26}$$

which is typical of practical calculations. Here,

$$M_{ik} = \varepsilon_{ik} + m_i$$

and

$$N_r = N_{m_1r}N_{m_2r} = \sqrt{\frac{\sqrt{\mathbf{r}^2+m_1^2}+m_1}{2\sqrt{\mathbf{r}^2+m_1^2}}} \times\sqrt{\frac{\sqrt{\mathbf{r}^2+m_2^2}+m_2}{2\sqrt{\mathbf{r}^2+m_2^2}}}$$

is the product of the normalization factors of the Dirac bispinors (5).

The use of the wave-function approximation (21) is equivalent to the substitution

$$\frac{1}{(r^2+\alpha^2\mu^2)^2} \cong \frac{\pi^2}{\alpha\mu}\delta(\mathbf{r}), \tag{27}$$

whereupon the quantity I vanishes, but this occurs only in the case where the integral must be calculated to terms of order α^5; by no means does this imply, however, that there are no higher order corrections, $\frac{\alpha^5\mu^3}{m_1m_2}\beta\ln\beta^{-1}$ or $\frac{\alpha^5\mu^3}{m_1m_2}\beta^2\ln\beta^{-1}$.

Suppose that we want to calculate the integral I to terms of order $[\alpha^5\mu^3/(m_1m_2)]\beta^2\ln\beta^{-1}$. In this case, we can make the following simplifications:

$$N_p \approx 1, \quad \frac{M_{1k}}{\varepsilon_{1k}} \approx \frac{M_{2k}}{\varepsilon_{2k}} \approx 2, \tag{28}$$
$$\frac{M_{2k}}{M_{1k}+M_{2k}} \approx \frac{m_2}{m_1+m_2} \text{ at } N_q \neq 1.$$

Furthermore, integration with respect to the 3-momentum $\mathbf{p}$ leads to the expression

$$I = \frac{\alpha^6\mu^3}{2\pi^4}\frac{\beta}{(1+\beta)^2}\int\frac{d^3qN_q}{(q^2+\alpha^2\mu^2)^2} \tag{29}$$
$$\times\int\frac{d^3k}{(k^2+\alpha^2\mu^2)^2}\left(1-\frac{k^2}{\mathbf{k}_q^2}\right)$$
$$= \frac{\alpha^6\mu^3}{2\pi^2}\frac{\beta}{(1+\beta)^2}\int\frac{d^3qN_q}{(q^2+\alpha^2\mu^2)^2}$$
$$\times\left(\frac{1}{\alpha\mu}-\frac{2}{q}\arctan\frac{q}{\alpha\mu}+\frac{\alpha\mu}{q^2+\alpha^2\mu^2}\right).$$

It is interesting to note that the quantity I vanishes as before if the δ approximation (27) is used at this stage.

Exact calculations show that the required logarithmic contribution in the particle-mass ratio comes from the integral

$$I \sim \frac{\alpha^6\mu^3}{2\pi^2}\frac{\beta}{(1+\beta)^2}\frac{1}{\alpha\mu}\int\frac{d^3qN_q}{(q^2+\alpha^2\mu^2)^2} \tag{30}$$
$$= \frac{\alpha^5\mu^3}{2\pi^2m_1m_2}\frac{\beta}{1+\beta}\int\frac{d^3qN_{1q}N_{\beta q}}{(q^2+\gamma^2)^2}.$$

Upon the change of variable $q = q'm_2$ in (30), it turns out that the integrand is characterized by the dimensionless variable of integration and the quantities

$$\gamma = \frac{\alpha\beta}{1+\beta}, \quad N_{1q} = \sqrt{\frac{\sqrt{q^2+1}+1}{2\sqrt{q^2+1}}},$$
$$N_{\beta q} = \sqrt{\frac{\sqrt{q^2+\beta^2}+\beta}{2\sqrt{q^2+\beta^2}}}.$$

The integral I involves two small parameters, γ and β. We note that, to the required degree of precision, we have $N_q = 1$ at $q = \gamma$ and $N_q = 1/\sqrt{2}$ at $\beta < q < 1$.

Taking this circumstance into account, we can obtain, to the required degree of precision, the relation

$$\int\frac{d^3qN_q}{(q^2+\alpha^2\mu^2)^2} = \frac{\pi^2}{\alpha\mu}+\frac{2\pi}{\mu}\left[\ln(1+\sqrt{2})-\sqrt{2}\right]$$
$$-\frac{\sqrt{2}\pi}{m_2(1+\sqrt{2})}\left[\ln(1+\sqrt{2})-\sqrt{2}\right] \tag{31}$$
$$-\frac{\pi\beta}{4\sqrt{2}m_2}\ln\beta^{-1}.$$

By comparing (31) with the result presented in (1), we deduce that the integral I involves a new logarithmic contribution in the parameter β,

$$I = -\frac{\sqrt{2}}{16\pi}\frac{\alpha^5\mu^3}{m_1m_2}\beta^2\ln\beta^{-1}. \tag{32}$$

Thus, diagrams that, in the δ approximation of wave functions, did not make a logarithmic contribution in β to the fine shift of energy levels are of greatest interest.

Let us write the fine shift due to the exchanges of a Coulomb photon and a transverse photon in the form

$$\Delta E_{nS} \tag{33}$$
$$= \left\langle\Psi'_{nS}\right|(K_{CT}+K_CG_0K_T+K_TG_0K_C)^+_{0F}\left|\Psi'_{nS}\right\rangle$$
$$-\left\langle\Psi'_{nS}\right|(K_T)^+_{0F}Fv_C\left|\Psi_{nS}\right\rangle$$
$$-\left\langle\Psi_{nS}\right|v_CF(K_T)^+_{0F}\left|\Psi'_{nS}\right\rangle.$$

Here, the subscript C symbolizes Coulomb photon exchange; K_{CT} is the kernel of the Bethe–Salpeter equation in the second order in α; and

$$\Psi'_{nS}(\mathbf{p}) = \Omega_p\Psi_{nS}(\mathbf{p}), \tag{34}$$

where $\Psi_{nS}(\mathbf{p})$ is determined by Eq. (20) and

$$\Omega_p = \frac{1}{2\mu}\frac{(\varepsilon_{1p}+E_1)(\varepsilon_{2p}+E_2)}{\varepsilon_{1p}+\varepsilon_{2p}+E_1+E_2}, \tag{35}$$
$$E_1 = m_1-\frac{\alpha^2\mu^2}{2m_1n^2}, \quad E_2 = m_2-\frac{\alpha^2\mu^2}{2m_2n^2}.$$

We also note that, from Eq. (20), it follows that

$$Fv_C\Psi_{nS} = \Omega_p\Psi_{nS} = \Psi'_{nS}. \tag{36}$$

Therefore, calculating the contribution from the iterative term reduces to calculating the appropriate contribution from the diagram involving the exchange of one transverse photon. Two-photon diagrams include two fermion lines; according to the definitions in (11) and (12), the contribution $\Delta E_{2\gamma}$ can then be represented in the form

$$\Delta E_{2\gamma} = \Delta E^{++}_{2\gamma}+\Delta E^{+-}_{2\gamma}+\Delta E^{-+}_{2\gamma}+\Delta E^{--}_{2\gamma}, \tag{37}$$

Table 1

Diagram	$\Delta E_{\rm par}$							
$\frac{\alpha^5\mu^3}{m_1m_2}\beta\ln\beta^{-1}$	$\frac{2}{\pi}^*$	$-\frac{2}{\pi}^* - \frac{2\sqrt{2}}{\pi}$	$\frac{2\sqrt{2}}{\pi}$	0	0	0	0	0
$\frac{\alpha^5\mu^3}{m_1m_2}\beta^2\ln\beta^{-1}$	$-\frac{1}{\pi}^*$	$\frac{1}{\pi}^* + \frac{7\sqrt{2}}{4\pi}$	$-\frac{7\sqrt{2}}{4\pi}$	$-\frac{\sqrt{2}}{8\pi}$	$-\frac{\sqrt{2}}{8\pi}$	0	0	0
$\frac{\alpha^6\mu^3}{m_1m_2}\beta\ln^2\beta^{-1}$	$\frac{2\sqrt{2}}{\pi^2}$	$-\frac{2\sqrt{2}}{\pi^2}$	$\frac{\sqrt{2}}{\pi^2}$	0	0	0	0	0
$\frac{\alpha^6\mu^3}{m_1m_2}\ln\beta^{-1}$	0	0	0	0	0	0	0	0

where the term $\Delta E_{2\gamma}^{++}$ involves the product $\Lambda_1^+\Lambda_2^+$ of the operators of projection onto positive-energy states and the term $\Delta E_{2\gamma}^{--}$ involves the product $\Lambda_1^-\Lambda_2^-$ of the analogous operators.

In order to represent expression (33) in a detailed form, we introduce the sum

$$\Delta E_{nS} = \Delta E_{\rm par} + \Delta E_{\rm cr}, \tag{38}$$

$$\Delta E_{\rm par} = \left\langle \Psi'_{nS}\right| \left(K_{\rm C}G_0K_T + K_TG_0K_{\rm C}\right)_{0F}^{+} \left|\Psi'_{nS}\right\rangle, \tag{39}$$

$$\Delta E_{\rm cr} = \left\langle \Psi'_{nS}\right| \left((K_{CT}) + (K_{T\rm C})\right)_{0F}^{+} \left|\Psi'_{nS}\right\rangle, \tag{40}$$

where the indices "par" and "cr" correspond to the contributions from diagrams featuring, respectively, parallel and crossed photon lines.

For the sake of definiteness, we consider here the case of $n = 1$. At $n \neq 1$, the corrections to the S energy levels decrease, in just the same way as in expression (1), in inverse proportion to the cube of the principal quantum number.

As the result of calculating the quantities in (39) and (40) to a high degree of precision, we have established the existence of new logarithmic contributions in the parameter β to the fine structure of S energy levels in the muonium atom, these contributions including those that are analogous to the contributions appearing in expression (1).

Let us now isolate the corrections $\Delta\varepsilon_{\rm par}$ and $\Delta\varepsilon_{\rm cr}$ in the expressions for $\Delta E_{\rm par}$ [Eq. (39)] and $\Delta E_{\rm cr}$ [Eq. (40)], respectively. The results are

$$\Delta\varepsilon_{\rm par} = -\frac{16}{\pi}\frac{\alpha^7\mu^5}{(2\pi)^5}\int\frac{d^3p\Omega_pN_p}{(p^2+\alpha^2\mu^2)^2} \tag{41}$$
$$\times\int\frac{d^3q\cdot q^2\Omega_qN_q}{(q^2+\alpha^2\mu^2)^2}\int\frac{d^3k}{(k^2+\alpha^2\mu^2)}\frac{1}{(\mathbf{p}-\mathbf{k})^2}$$
$$\times\frac{1}{(\mathbf{k}-\mathbf{q})^2}\frac{1}{\varepsilon_{2k}}\frac{M_{1k}}{\varepsilon_{1k}}\frac{M_{1k}}{M_{1q}}\frac{M_{2k}}{M_{1k}+M_{2k}}\frac{M_{2k}}{M_{2q}},$$

$$\Delta\varepsilon_{\rm cr} = \frac{8}{\pi}\frac{\alpha^7\mu^5}{(2\pi)^5}\int\frac{d^3p\Omega_pN_p}{(p^2+\alpha^2\mu^2)^2}\int\frac{d^3q\cdot q^2\Omega_qN_q}{(q^2+\alpha^2\mu^2)^2} \tag{42}$$
$$\times\int\frac{d^3k}{(k^2+\alpha^2\mu^2)}\frac{1}{(\mathbf{p}-\mathbf{k})^2}\frac{1}{(\mathbf{k}-\mathbf{q})^2}\frac{1}{\varepsilon_{2k}}\frac{M_{1k}}{\varepsilon_{1k}}$$
$$\times\left\{k^2 - \frac{M_{1k}(\varepsilon_{2kpq}+m_2)(\varepsilon_{1k}-\varepsilon_{1q})(\varepsilon_{2kpq}-\varepsilon_{2p})}{(\mathbf{k}-\mathbf{q})^2}\right\},$$

where $\varepsilon_{2kpq} = \sqrt{(\mathbf{k}-\mathbf{p}-\mathbf{q})^2+m_2^2}$.

First, it is obvious that, in the δ approximation for the Coulomb wave functions, both corrections vanish.

Second, if we want to calculate the quantities in (41) and (42) to terms of order $\frac{\alpha^5\mu^3}{m_1m_2}\beta\ln\beta^{-1}$, we can set

$$k^2 - \frac{M_{1k}\left(\varepsilon_{2kpq}+m_2\right)\left(\varepsilon_{1k}-\varepsilon_{1q}\right)\left(\varepsilon_{2kpq}-\varepsilon_{2p}\right)}{(\mathbf{k}-\mathbf{q})^2}$$
$$= k^2 - \frac{\left(\varepsilon_{1k}+m_1\right)\left(\varepsilon_{1k}-\varepsilon_{1q}\right)}{(\mathbf{k}-\mathbf{q})^2} \tag{43}$$
$$\times\left(1-\frac{p^2}{\left(\varepsilon_{2p}+m_2\right)\left(\varepsilon_{2kpq}+\varepsilon_{2p}\right)}\right)$$
$$\times\left((\mathbf{k}-\mathbf{q})^2 - 2\mathbf{p}\cdot(\mathbf{k}-\mathbf{q})\right) \approx \frac{q^2M_{1k}}{M_{1q}},$$

$$\Omega_p \approx 1, \quad N_p \approx 1, \quad \frac{M_{2k}}{M_{2q}} \approx 1, \tag{44}$$
$$\frac{M_{2k}}{M_{1k}+M_{2k}} \approx \frac{m_2}{m_1+m_2} \approx 1.$$

Upon integration with respect to the momentum $\mathbf{p}$, we obtain

$$\Delta\varepsilon_{\rm cr} = -\frac{1}{2}\Delta\varepsilon_{\rm par} = \frac{2\alpha^6\mu^3}{(2\pi)^4} \tag{45}$$
$$\times\int\frac{d^3q\cdot q^2N_q}{(q^2+\alpha^2\mu^2)^2}\frac{M_{2q}}{M_{1q}+M_{2q}}$$

Table 2

Diagram	$\Delta E_{\rm cr}$	ΔE_{TT}	ΔE_T	$\Delta E_{\rm it}$
$\frac{\alpha^5\mu^3}{m_1m_2}\beta\ln\beta^{-1}$	$-\frac{\sqrt{2}}{\pi}$	0	0	0
$\frac{\alpha^5\mu^3}{m_1m_2}\beta^2\ln\beta^{-1}$	$\frac{\sqrt{2}}{8\pi}$	$\frac{2}{\pi}$*	0	0
$\frac{\alpha^6\mu^3}{m_1m_2}\beta\ln^2\beta^{-1}$	$-\frac{\sqrt{2}}{2\pi^2}$	0	$-\frac{1}{\pi^2}$	$\frac{2}{\pi^2}$
$\frac{\alpha^6\mu^3}{m_1m_2}\ln\beta^{-1}$	0	0	$\frac{2\sqrt{2}}{\pi^2}\left[\ln(1+\sqrt{2})-\sqrt{2}\right]$	$-\frac{4\sqrt{2}}{\pi^2}\left[\ln(1+\sqrt{2})-\sqrt{2}\right]$

$$\times\int\frac{d^3k}{(k^2+\alpha^2\mu^2)^2}\frac{1}{(\mathbf{k}-\mathbf{q})^2}\frac{1}{\varepsilon_{2k}}\frac{M_{1k}^2}{\varepsilon_{1k}}.$$

After some simple algebra, the correction in question takes the form

$$\Delta\varepsilon_{\rm cr}^{\beta}=-\frac{1}{2}\Delta\varepsilon_{\rm par}^{\beta}=-\frac{\alpha^6\mu^3}{2\pi^4}\frac{\beta m_1}{1+\beta}\qquad(46)$$
$$\times\int\frac{d^3q\cdot N_q}{M_{1q}M_{2q}}\int\frac{d^3k}{(k^2+\alpha^2\mu^2)^2}\frac{1}{(\mathbf{k}-\mathbf{q})^2}\frac{1}{\varepsilon_{1k}}$$
$$=-\frac{\sqrt{2}}{2\pi}\frac{\alpha^5\mu^3}{m_1m_2}\beta\ln\beta^{-1}.$$

The logarithmic contribution in β that we obtained is the most significant contribution of the diagrams featuring crossed photon lines, but it is not the only one.

Contributions of orders $\frac{\alpha^5\mu^3}{m_1m_2}\beta\ln\beta^{-1}$ and $\frac{\alpha^6\mu^3}{m_1m_2}\beta\ln^2\beta^{-1}$ also appear in the expressions

$$\Delta E_{\rm par}^{+-}=\Delta E_{\rm par}^{-+}=\frac{\alpha^7\mu^5}{4\pi^6}\int\frac{d^3p\Omega_pN_p}{(p^2+\alpha^2\mu^2)^2}\int\frac{d^3q\Omega_qN_q}{(q^2+\alpha^2\mu^2)^2}\int\frac{d^3k}{\varepsilon_{1k}\varepsilon_{2k}}\frac{1}{(\mathbf{p}-\mathbf{k})^2}\qquad(47)$$
$$\times\frac{1}{(|\mathbf{k}-\mathbf{q}|+\varepsilon_{1k}+\varepsilon_{1q})\,(|\mathbf{k}-\mathbf{q}|+\varepsilon_{1q}-E_1+\varepsilon_{2k}-E_2)}\,[Q-S]=\Delta\varepsilon\,(Q)-\Delta\varepsilon\,(S)\,,$$

$$Q=k^2,\quad S=\frac{(\varepsilon_{2k}-\varepsilon_{2q})(\varepsilon_{1k}+\varepsilon_{1q})}{(\mathbf{k}-\mathbf{q})^2}M_{1k}^-M_{2k}^+,\quad M_{ik}^{\pm}=\varepsilon_{ik}\pm m_i;\qquad(48)$$

$$\Delta E_{\rm par}^{--}=-\frac{\alpha^7\mu^5}{4\pi^6}\int\frac{d^3p\Omega_pN_p}{(p^2+\alpha^2\mu^2)^2}\int\frac{d^3q\Omega_qN_q}{(q^2+\alpha^2\mu^2)^2}\int\frac{d^3k}{\varepsilon_{1k}\varepsilon_{2k}(M_{1k}^++M_{2k}^+)}\frac{1}{(\mathbf{p}-\mathbf{k})^2}\frac{1}{|\mathbf{k}-\mathbf{q}|}\qquad(49)$$
$$\times\left(\frac{1}{(|\mathbf{k}-\mathbf{q}|+\varepsilon_{1k}+\varepsilon_{1q})}+\frac{1}{(|\mathbf{k}-\mathbf{q}|+\varepsilon_{2k}+\varepsilon_{2q})}\right)[Q-R]=\Delta\varepsilon\,(Q)-\Delta\varepsilon\,(R)\,,$$

$$R=\frac{(\varepsilon_{2k}+\varepsilon_{2q})(\varepsilon_{1k}+\varepsilon_{1q})}{(\mathbf{k}-\mathbf{q})^2}\left\{M_{1k}^-M_{2k}^--(\mathbf{k}\cdot\mathbf{q})\left(\frac{M_{1k}^-}{M_{2q}^+}+\frac{M_{2k}^-}{M_{1q}^+}\right)+\frac{(\mathbf{k}\cdot\mathbf{q})^2}{M_{1q}^+M_{2q}^+}\right\}.\qquad(50)$$

In the differences $\Delta\varepsilon\,(Q)-\Delta\varepsilon\,(S)$ and $\Delta\varepsilon\,(Q)-\Delta\varepsilon\,(R)$, corrections of orders $\frac{\alpha^5\mu^3}{m_1m_2}\beta\ln\beta^{-1}$ and $\frac{\alpha^6\mu^3}{m_1m_2}\beta\ln^2\beta^{-1}$ cancel. The problem is that, in the quantity R, we must consider the total set of terms since only in this case is the singularity at $\mathbf{k}=\mathbf{q}$ canceled:

$$\left\{M_{1k}^-M_{2k}^--(\mathbf{k}\cdot\mathbf{q})\left(\frac{M_{1k}^-}{M_{2q}^+}+\frac{M_{2k}^-}{M_{1q}^+}\right)+\frac{(\mathbf{k}\cdot\mathbf{q})^2}{M_{1q}^+M_{2q}^+}\right\}_{\mathbf{q}=\mathbf{k}}\qquad(51)$$

$$= \left\{ \frac{k^4}{M_{1k}^+ M_{2k}^+} - k^2 \left(\frac{k^2}{M_{1k}^+ M_{2k}^+} + \frac{k^2}{M_{1k}^+ M_{2k}^+} \right) + \frac{k^4}{M_{1k}^+ M_{2k}^+} \right\} = 0.$$

The diagram involving parallel photon lines carries the most important information about the logarithmic contributions in the parameter β:

$$\Delta E_{\rm par} = -\frac{\alpha^7\mu^5}{\pi^6} \int \frac{d^3p\Omega_p N_p}{(p^2+\alpha^2\mu^2)^2} \int \frac{d^3q\Omega_q N_q}{(q^2+\alpha^2\mu^2)^2} \int \frac{d^3k}{(k^2+\alpha^2\mu^2)} \frac{1}{(\mathbf{p}-\mathbf{k})^2} \frac{1}{(\mathbf{k}-\mathbf{q})^2} \frac{1}{\varepsilon_{1k}\varepsilon_{2k}} \frac{M_{1k}M_{2k}}{M_{1k}+M_{2k}}$$
$$\times \left\{ k^2 - \frac{(k^2-q^2)^2}{(\mathbf{k}-\mathbf{q})^2} \frac{M_{1k}M_{2k}}{(\varepsilon_{1k}+\varepsilon_{1q})(\varepsilon_{2k}+\varepsilon_{2q})} + q^2 \frac{M_{1k}}{M_{1q}} \frac{M_{2k}}{M_{2q}} + (\mathbf{k}\cdot\mathbf{q}) \right. \quad (52)$$
$$\left. \times \left[\frac{M_{1k}}{M_{1q}} + \frac{M_{2k}}{M_{2q}} - \frac{(k^2-q^2)^2}{(\mathbf{k}-\mathbf{q})^2} \frac{M_{1k}}{M_{2q}} \frac{1}{(\varepsilon_{1k}+\varepsilon_{1q})(\varepsilon_{2k}+\varepsilon_{2q})} - \frac{(k^2-q^2)^2}{(\mathbf{k}-\mathbf{q})^2} \frac{M_{2k}}{M_{1q}} \frac{1}{(\varepsilon_{1k}+\varepsilon_{1q})(\varepsilon_{2k}+\varepsilon_{2q})} \right] + \Re \right\}.$$

Integration of the quantity

$$\Re = (\mathbf{p}\cdot\mathbf{k}) \left(\frac{k^2}{M_{1p}M_{1k}} + \frac{k^2}{M_{2p}M_{2k}} - \frac{\left(k^2-q^2\right)^2}{\left(\mathbf{k}-\mathbf{q}\right)^2} \right. \quad (53)$$
$$\left. \times \frac{1}{(\varepsilon_{1k}+\varepsilon_{1q})\,(\varepsilon_{2k}+\varepsilon_{2q})} \left(\frac{M_{1k}}{M_{2p}} + \frac{M_{2k}}{M_{1p}} \right) \right)$$
$$+ \frac{p^2k^4}{M_{1p}M_{2p}M_{1k}M_{2k}}$$

does not lead to the appearance of logarithmic contributions.

Table 1 summarizes the results of the calculations performed in this study, including the entire set of integrals in (52) that is required for analysis, irrespective of whether they include (or do not include) logarithmic contributions in β. The analytic expressions for the contributions to the fine shift of the S energy levels in hydrogen-like atoms from the exchange of one and two transverse photons were previously discussed in [4, 7].

As to the corrections from the diagrams involving crossed Coulomb and transverse-photon lines, expressions (40) and (42) give the idea of their analytic structure.

In Tables 1 and 2, the corrections from all of the aforementioned processes are given in a generalized form. The contributions that do not vanish in the δ approximation of wave functions are labeled with an asterisk in Tables 1 and 2.

Analyzing the entire set of various quantities in the parameter β, we can see that, in the δ approximation of wave functions, the only nonvanishing contribution is

$$\Delta E_{TT}(\ln\beta^{-1}) = \frac{2}{\pi}\frac{\alpha^5\mu^3}{m_1m_2}\beta^2\ln\beta^{-1}; \quad (54)$$

that is, in this approximation, there are no logarithmic contributions in the parameter β other than those discovered in [1]. All variety of the nonvanishing logarithmic corrections calculated in this study result from the use of the exact expressions for the wave functions and the quasipotential.

The contributions of each of these terms appearing in the expression for $\Delta E_{\rm par}$ are written in Table 1 in the same order as in expression (52).

The use of the Schrödinger equation with the Coulomb potential makes it possible to reduce the calculation of the contributions $\Delta E_{\rm it}$ from the iterated diagrams to the calculation of the corresponding corrections to the shifts of energy levels from one-photon exchanges.

We now go over to numerical estimates. In Tables 3 and 4, we present the corrections $\Delta E(1S)$ for, respectively, the muonium and the hydrogen atom. For $\Delta E(2S)$, we have $\Delta E(2S) = (1/8)\Delta E(1S)$.

The resulting total correction for fine shift is

$$\Delta E^{e\mu}(1S)^{\rm th} = -66.12\ {\rm kHz} \quad (55)$$

for the $1S$ energy level of the muonium atom and

$$\Delta E^{e\mu}(2S)^{\rm th} = -8.265\ {\rm kHz} \quad (56)$$

for the $2S$ energy level. The resulting value of $\delta\nu_{1S-2S}^{e\mu} = -57.855$ kHz is within the error corridor both for the currently known theoretical value [8] and for the last precision experimental result [9] on the $1S$–$2S$ shift of the energy levels in the muonium atom:

$$\delta\nu_{1S-2S}^{e\mu}({\rm theory}) = 2\,455\,528\,934.9(0.3)\ {\rm MHz}, \quad (57)$$

$$\delta\nu_{1S-2S}^{e\mu}({\rm expt.}) = 2\,455\,528\,941.0(9.8)\ {\rm MHz}. \quad (58)$$

As to the hydrogen atom, our calculations give here, as can be seen from Table 4, an appreciable value for the Lamb shift of the $2S$ level:

$$\Delta E^{ep}(2S)^{\rm th} \approx 1.1419\ {\rm kHz}. \quad (59)$$

Table 3. Correction values for the muonium atom (in kHz)

Diagram	$\Delta E_{\rm par}$	$\Delta E_{\rm cr}$	ΔE_{TT}	ΔE_T	$\Delta E_{\rm it}$	$\sum$
$\frac{\alpha^5\mu^3}{m_1m_2}\beta\ln\beta^{-1}$	0	−141.52	0	0	0	−141.52
$\frac{\alpha^5\mu^3}{m_1m_2}\beta^2\ln\beta^{-1}$	−0.17	0.09	0.97	0	0	0.89
$\frac{\alpha^6\mu^3}{m_1m_2}\beta\ln^2\beta^{-1}$	1.75	−0.88	0	−1.24	2.48	2.11
$\frac{\alpha^6\mu^3}{m_1m_2}\ln\beta^{-1}$	0	0	0	−72.4	144.8	72.4
$\sum$						−66.12

Table 4. Correction values for the hydrogen atom (in kHz)

Diagram	$\Delta E_{\rm par}$	$\Delta E_{\rm cr}$	ΔE_{TT}	ΔE_T	$\Delta E_{\rm it}$	$\sum$
$\frac{\alpha^5\mu^3}{m_1m_2}\beta\ln\beta^{-1}$	0	−2.56285	0	0	0	−2.56285
$\frac{\alpha^5\mu^3}{m_1m_2}\beta^2\ln\beta^{-1}$	−0.00035	0.00017	0.00197	0	0	0.00179
$\frac{\alpha^6\mu^3}{m_1m_2}\beta\ln^2\beta^{-1}$	0.04476	−0.02238	0	−0.03165	0.06330	0.05403
$\frac{\alpha^6\mu^3}{m_1m_2}\ln\beta^{-1}$	0	0	0	−11.64242	23.28484	11.64242
$\sum$						9.13539

The experimental values found with a high precision for the Lamb shift of the $2S_{1/2}$–$2P_{1/2}$ energy levels in the hydrogen atom and their high sensitivity to the values of the fine shift of the $2S_{1/2}$ energy level require a thorough comparison of the theory and experiment.

In [10], a comparison of the data on the Lamb shift of the $2S_{1/2}$–$2P_{1/2}$ levels was as follows:

$$\Delta E_{\rm L}^{\rm th} = 1\,057\,838(6)\ \text{kHz}, \quad (60)$$

$$\Delta E_{\rm L}^{\rm expt} = 1\,057\,845(9)\ \text{kHz (1981)}, \quad (61)$$

$$\Delta E_{\rm L}^{\rm expt} = 1\,057\,851(2)\ \text{kHz (1994)}, \quad (62)$$

$$\Delta E_{\rm L}^{\rm expt} = 1\,057\,839(12)\ \text{kHz (1994)}. \quad (63)$$

In the opinion of the authors, these results demonstrate that the theoretical and experimental data are in satisfactory agreement.

New data on the classical Lamb shift of the $2S_{1/2}$–$2P_{1/2}$ levels are quoted in the review article of Eides *et al.* [8]:

$$\Delta E_{\rm L}^{\rm th} = 1\,057\,833(4)\ \text{kHz}, \quad (64)$$

$$\Delta E_{\rm L}^{\rm expt} = 1\,057\,845(3)\ \text{kHz (1999)}. \quad (65)$$

From these data, it can be seen that the discrepancy between the theoretical and experimental values of the Lamb shift in the hydrogen atom is not less than 5 kHz.

In conclusion, we note that the numerical estimate obtained here for the Lamb shift of the $2S$ energy level in the hydrogen atom makes it possible to increase its theoretical value (64) by 1.1419 kHz, and this reduces the distinction between the theoretical [see (64)] and the experimental value of the Lamb shift of the $2S_{1/2}$–$2P_{1/2}$ energy levels in the hydrogen atom.

ACKNOWLEDGMENTS

We are grateful to S.N. Bagaev, V.I. Savrin, and O.A. Khrustalev for attention to this study.

REFERENCES

1. E. E. Salpeter and H. A. Bethe, Phys. Rev. **84**, 1232 (1951).
2. T. Fulton and P. C. Martin, Phys. Rev. **95**, 811 (1954).
3. H. Grotch and D. R. Yennie, Rev. Mod. Phys. **41**, 350 (1969).
4. N. E. Nyun'ko, Yu. N. Tyukhtyaev, and R. N. Faustov, Report R2-7493, JINR (Dubna, 1973).
5. R. N. Faustov, Preprint No. E2-6939, JINR (Dubna, 1973).
6. Yu. N. Tyukhtyaev, Teor. Mat. Fiz. **53**, 419 (1982).
7. N. A. Boikova, Yu. N. Tyukhtyaev, and R. N. Faustov, Yad. Fiz. **61**, 866 (1998) [Phys. At. Nucl. **61**, 781 (1998)].
8. M. I. Eides, H. Grotch, and V. A. Shelyuto, hep-ph/0002158.
9. V. Meyer, S. N. Bagaev, P. E. Baird, *et al.*, Phys. Rev. Lett. **84**, 1136 (2000).
10. K. Pachucki and H. Grotch, Phys. Rev. A **51**, 1854 (1995).

Translated by A. Isaakyan

Physics of Atomic Nuclei, Vol. 66, No. 5, 2003, pp. 902–913. From Yadernaya Fizika, Vol. 66, No. 5, 2003, pp. 934–945.

ELEMENTARY PARTICLES AND FIELDS
Theory

Muon Anomalous Magnetic Moment: A Consistency Check for the Next-to-Leading-Order Hadronic Contributions*

A. A. Pivovarov**

Institute for Nuclear Research, Russian Academy of Sciences,
pr. Shestidesyatiletiya Oktyabrya 7a, Moscow, 117312 Russia

Received January 29, 2002; in final form, June 11, 2002

Abstract—A duality-inspired model for verifying a consistency of the evaluation of the next-to-leading-order hadronic contributions to the muon anomalous magnetic moment with that of the leading-order ones is proposed. A part of the next-to-leading-order hadronic contributions related to the photon vacuum polarization function is rather accurately reproduced in the model. I find a new numerical value for the light-by-light hadronic contribution that leads to the agreement of the Standard Model theoretical prediction for the muon anomalous magnetic moment with the recent experimental result. © *2003 MAIK "Nauka/Interperiodica".*

1. INTRODUCTION

A numerical value of the muon anomalous magnetic moment measured experimentally with high precision can be used to test quantitatively the theories suggested for describing particle interactions. The experimental result for the muon anomalous magnetic moment presented in [1] reads

$$a_\mu^{\rm exp} = 116\,592\,023(151) \times 10^{-11} \qquad (1)$$

with the uncertainty equal to 151×10^{-11}. The main anomalous effect is due to the Schwinger term

$$a_\mu^{\rm Schw} = \frac{\alpha}{2\pi}, \qquad (2)$$

where α is a fine structure constant with the numerical value $\alpha^{-1} = 137.036\ldots$. The theoretical contributions presently computed in the Standard Model for the comparison with the experimental value given in Eq. (1) are divided into three parts: leptonic (QED), electroweak (EW), and hadronic (had). The pure leptonic part is computed in perturbative QED through α^5 order [2, 3]. The numerical value of the QED contribution to the muon anomalous magnetic moment reads (for a review and for further references, see [1])

$$a_\mu^{\rm QED} = 116\,584\,705.7(2.9) \times 10^{-11}. \qquad (3)$$

The electroweak corrections are well defined in the perturbation theory framework of the Standard Model and have been computed with the two-loop accuracy (for a review, see [1])

$$a_\mu^{\rm EW} = 152(4) \times 10^{-11}. \qquad (4)$$

Numerically this contribution matches the present uncertainty of the experimental result given in Eq. (1). The electroweak correction will be noticeable if a goal to reach the planned experimental accuracy of 40×10^{-11} is accomplished (as a review see [1]).

The hadronic contribution to the muon anomalous magnetic moment is sensitive to the infrared region of integration in Feynman diagrams and cannot be computed in perturbative QCD with light quarks. The current masses of light quarks are too small to provide a necessary infrared cutoff, and explicit models of hadronization are required for the quantitative analysis of the hadronic contributions to the muon anomalous magnetic moment. This constitutes the main difficulty of the theoretical evaluation of the muon anomalous magnetic moment in the Standard Model. Writing

$$a_\mu^{\rm SM} = a_\mu^{\rm QED} + a_\mu^{\rm EW} + a_\mu^{\rm had} \qquad (5)$$

and assuming

$$a_\mu^{\rm exp} = a_\mu^{\rm SM}, \qquad (6)$$

one finds a numerical value for the hadronic contribution to the muon anomalous magnetic moment

$$a_\mu^{\rm had}|_{\rm th} \qquad (7)$$
$$= (7165.3 \pm 151|_{\rm exp} \pm 2.9|_{\rm QED} \pm 4|_{\rm EW}) \times 10^{-11}$$

with the experimental error dominating the uncertainty.

Since the hadronic contribution is sensitive to the details of the strong coupling regime of QCD at low energies and cannot be unambiguously computed in the perturbation theory framework, the theoretical

*This article was submitted by the author in English.

**e-mail: aapiv@ms2.inr.ac.ru

prediction for the muon anomalous magnetic moment in the Standard Model depends crucially on how this contribution is estimated. In the absence of a reliable theoretical tool for the computation of the hadron spectrum in the infrared region, one turns to experimental data on low-energy hadron interactions for extracting the necessary numerical value for $a_\mu^{\rm had}$. In general terms, the hadronic contribution to the muon anomalous magnetic moment is determined by the correlation functions of hadronic electromagnetic currents. As the source for the electromagnetic current is readily available for a wide range of energies, one tries to extract these functions (or their characteristics necessary for the computation of the muon anomalous magnetic moment) from experiment. Without an explicit use of QCD, the correction $a_\mu^{\rm had}$ is generated through the electromagnetic interaction $ej_\mu^{\rm had}A^\mu$, with $j_\mu^{\rm had}$ being the hadronic part of the electromagnetic current in the Standard Model and A^μ being the photon field. At the leading order of electromagnetic interaction (α^2 in the formal power counting), only the two-point correlation function of the electromagnetic currents emerges in the analysis of the hadronic contributions to the muon anomalous magnetic moment:

$$\Pi_2 \sim \langle j_\mu^{\rm had}(x) j_\nu^{\rm had}(0)\rangle. \tag{8}$$

At the next-to-leading order in the electromagnetic interaction (α^3), the four-point correlation function appears:

$$\Pi_4 \sim \langle j_\mu^{\rm had}(x) j_\nu^{\rm had}(y) j_\alpha^{\rm had}(z) j_\beta^{\rm had}(0)\rangle. \tag{9}$$

These correlators are not calculable perturbatively in the region that is essential for the determination of the hadronic contributions to the muon anomalous magnetic moment. The leading-order hadronic contribution to the muon anomalous magnetic moment comes from the two-point correlator Eq. (8) referred to as the hadronic vacuum polarization contribution, while the four-point function Eq. (9) first emerges at the α^3 order, most explicitly as the light-by-light scattering. To avoid using QCD in the strong coupling mode, one has to extract the necessary contribution to the muon anomalous magnetic moment by studying these two correlation functions experimentally without an explicit realization of the hadronic electromagnetic current $j_\mu^{\rm had}$ in terms of elementary fields. Historically, this was a way of studying the electromagnetic properties of hadrons before QCD had emerged as a fundamental theory of strong interactions (see, e.g., [4]).

2. HADRONIC CONTRIBUTION AT THE LEADING ORDER

At the leading order in α, the hadronic contribution to the muon anomalous magnetic moment is described by the correlator

$$i\int \langle T j_\mu^{\rm had}(x) j_\nu^{\rm had}(0)\rangle e^{iqx}dx = (q_\mu q_\nu - g_{\mu\nu}q^2)\Pi^{\rm had}(q^2), \tag{10}$$

which reduces to a single function $\Pi^{\rm had}(q^2)$ of one variable q^2. The correlator is transverse due to the conservation of the hadronic electromagnetic current in the Standard Model. The function $\Pi^{\rm had}(q^2)$ gives a leading-order hadronic contribution to the muon anomalous magnetic moment (e.g., see [5])

$$a_\mu^{\rm had}({\rm LO}) = 4\pi\left(\frac{\alpha}{\pi}\right)^2 \int\limits_{4m_\pi^2}^{\infty} \frac{ds}{s} K(s) {\rm Im}\,\Pi^{\rm had}(s) \tag{11}$$

with the one-loop kernel of the form

$$K(s) = \int\limits_0^1 dx \frac{x^2(1-x)}{x^2 + (1-x)s/m_\mu^2}. \tag{12}$$

Here, ${\rm Im}\,\Pi^{\rm had}(s) = {\rm Im}\,\{\Pi^{\rm had}(q^2)|_{q^2=s+i0}\}$ and m_μ is the muon mass.

The leading-order hadronic contribution to the muon anomalous magnetic moment given in Eq. (11) is represented by an integral over the entire hadron spectrum. No specific information about the function ${\rm Im}\,\Pi^{\rm had}(s)$ is necessary pointwise except its threshold structure in the low-energy region. For applications at the leading order in electromagnetic interaction, the function ${\rm Im}\,\Pi^{\rm had}(s)$ can uniquely be identified with data extracted from the process of e^+e^- annihilation into hadrons. Introducing the experimental ratio $R^{\rm exp}(s)$,

$$R^{\rm exp}(s) = \frac{\sigma(e^+e^- \to {\rm hadrons})}{\sigma(e^+e^- \to \mu^+\mu^-)}, \qquad s = (p_{e^+} + p_{e^-})^2, \tag{13}$$

and identifying it with the theoretical quantity $R^{\rm th}(s)|_{\rm LO}$ for $s > 4m_\mu^2$ taken at the leading order in α as

$$R^{\rm th}(s)|_{LO} = 12\pi {\rm Im}\,\Pi^{\rm had}(s), \tag{14}$$

one finds

$$a_\mu^{\rm had}({\rm LO}) = \frac{1}{3}\left(\frac{\alpha}{\pi}\right)^2 \int\limits_{4m_\pi^2}^{\infty} \frac{R^{\rm exp}(s)K(s)}{s} ds. \tag{15}$$

Note that $m_\pi = 139.6$ MeV $> m_\mu = 106$ MeV. The hadronic contribution to the muon anomalous magnetic moment based on the representation given in Eq. (15) is well studied. Several determinations of the numerical value for the quantity $a_\mu^{\rm had}({\rm LO})$ based on different sets of experimental data are

$$a_\mu^{\rm had}({\rm LO}) = 7011(94) \times 10^{-11}\ [6]; \qquad (16)$$

$$a_\mu^{\rm had}({\rm LO}) = 6924(62) \times 10^{-11}\ [7]; \qquad (17)$$

$$a_\mu^{\rm had}({\rm LO}) = 6988(111) \times 10^{-11}\ [8]. \qquad (18)$$

In further analysis, I use a naive average of these three results (both central values and errors are averaged) for definiteness only, because they are consistent within error bars. The average reads

$$a_\mu^{\rm had}({\rm LO}) = 6974(89) \times 10^{-11}. \qquad (19)$$

Writing

$$a_\mu^{\rm had}|_{\rm th} = a_\mu^{\rm had}({\rm LO}) + a_\mu^{\rm had}({\rm NLO})$$

and comparing it with Eq. (7), one finds (in units 10^{-11})

$$a_\mu^{\rm had}({\rm NLO}) = [7165 \pm 151|_{\rm exp} \pm 2.9|_{\rm QED} \pm 4|_{\rm EW}] - [6974 \pm 89]|_{\rm LO} = 191 \pm 151|_{\rm exp} \pm 2.9|_{\rm QED} \pm 4|_{\rm EW} \pm 89|_{\rm had}. \qquad (20)$$

Assuming statistical independence of the uncertainties, one finds after adding them in quadratures

$$a_\mu^{\rm had}({\rm NLO}) = (191 \pm 175) \times 10^{-11}, \qquad (21)$$

which does not allow one to detect higher order hadronic effects clearly since the result in Eq. (21) is consistent with zero. The error given in Eq. (1) comes mainly from the error of the experimental value given in Eq. (19) and from the error of the leading-order hadronic data given in Eq. (20), the statistical correlation of which is supposed to be small as they come from different sources. Other errors in Eq. (20) are negligible. For the target experimental error of the muon anomalous magnetic moment at the level of 40×10^{-11} (instead of the present value of 151×10^{-11}), one finds that the uncertainty of the next-to-leading-order hadronic contribution becomes 98×10^{-11}. Assuming that the mean value of $a_\mu^{\rm exp}$ in the planned experiment will not change, one finds that the numerical value for the next-to-leading-order hadronic contribution becomes

$$a_\mu^{\rm had}({\rm NLO}) = (191 \pm 98) \times 10^{-11}, \qquad (22)$$

which makes the next-to-leading-order hadronic effects noticeable at the level of two standard deviations. If the mean value of $a_\mu^{\rm exp}$ changes in the range of the present experimental uncertainty of 151×10^{-11}, the next-to-leading order hadronic effects can be more or less pronounced. From the naive counting in α, a numerical value for the theoretical next-to-leading-order hadronic contribution about 50×10^{-11} can be expected. This number is comparable in magnitude with the uncertainty in Eq. (22) and should be taken into account.

3. HADRONIC CONTRIBUTION AT THE NEXT-TO-LEADING ORDER

In the next-to-leading order, there is no such transparency in determining hadronic contributions as in the leading order. Basically, two new features appear in the analysis. On the experimental side, the interpretation of data to be used in the next-to-leading-order theoretical calculations is more involved. The problem is to avoid double counting because part of the hadronic contributions have already been taken into account through the use of data at the leading order. On the theoretical side, a new correlation function Π_4 from Eq. (9), which is much more complicated than the two-point correlator, enters the game. At present, there is no accurate experimental determination of the four-point function in the kinematical range necessary for the muon anomalous magnetic moment computation and one has to rely on phenomenological models suggested for the evaluation of this function. It is difficult to control the accuracy of such models, which introduces an explicit model dependence in the calculation of the next-to-leading-order hadronic contribution and makes predictions less definite than in the leading order.

3.1. Interpretation of Data at the Next-to-Leading Order of Electromagnetic Interaction

For applications at the next-to-leading order in α, the extraction of data is more involved. For instance, one should explicitly take into account the next-to-leading-order corrections to theoretical factors that emerge in a description of the process from which a set of data is taken. These "theoretically corrected" data should be used in the next-to-leading-order applications for computing the muon anomalous magnetic moment. Since the sets of data are mainly extracted from the process of e^+e^- annihilation into hadrons, I discuss this particular process in some detail.

3.1.1. One-photon mediated e^+e^- annihilation. The main object studied experimentally in this sector is a full photon propagator $D(q^2)$:

$$D(q^2) = \frac{1}{-q^2}\frac{1}{1 + e^2\Pi(q^2)} \qquad (23)$$

with $\Pi(q^2) = \Pi^{\rm lept}(q^2) + \Pi^{\rm had}(q^2)$ being a one-particle irreducible block and $e^2 = 4\pi\alpha$. Note that, in higher orders in α, the one-particle irreducible block does not split into a sum of pure leptonic and pure hadronic contributions. It happens first at the next-next-to-leading order, which is far beyond practical interest though. I discuss only the next-to-leading-order contributions or α^3 terms in the formal α power counting. Since the data are collected at low energies, the electroweak sector can be excluded. With these restrictions, the cross section of e^+e^- annihilation into hadrons through the one-photon exchange at the next-to-leading order without the vertex corrections to initial states is proportional to

$$\begin{aligned} &{\rm Im}\{q^2 D(q^2)|_{q^2=s+i0}\} \qquad (24)\\ &= \frac{e^2 {\rm Im}\,\Pi(s)}{(1+e^2{\rm Re}\Pi(s))^2 + e^4({\rm Im}\,\Pi(s))^2}\\ &= \frac{e^2({\rm Im}\,\Pi^{\rm lept}(s) + {\rm Im}\,\Pi^{\rm had}(s))}{(1+e^2{\rm Re}\Pi(s))^2 + e^4({\rm Im}\,\Pi(s))^2}. \end{aligned}$$

The theoretical expression for the R ratio related to the photon propagator at the next-to-leading order reads

$$R^{\rm th}(s)|_{NLO} = \frac{{\rm Im}\,\Pi^{\rm had}(s)}{{\rm Im}\,\Pi^{\mu\mu}(s)}, \qquad (25)$$

where $\Pi^{\mu\mu}(s)$ is the vacuum polarization function due to virtual muon production. If $R^{\rm th}(s)|_{\rm NLO}$ is identified with $R^{\rm exp}(s)$ from Eq. (13), then ${\rm Im}\,\Pi^{\rm had}(s)$ can be restored by using a theoretically calculated ${\rm Im}\,\Pi^{\mu\mu}(s)$. For $s \gg m_\mu^2$, one finds with a next-to-leading-order accuracy

$$12\pi {\rm Im}\,\Pi^{\rm had}(s) = R^{\rm exp}(s)\left(1 + \frac{3}{4}\frac{\alpha}{\pi}\right). \qquad (26)$$

In some analyses, the cross section $\sigma(e^+e^- \to$ hadrons) divided by the normalization factor

$$\sigma_0 = \sigma(e^+e^- \to \mu^+\mu^-)|_{\rm LO} = \frac{4\pi\alpha^2}{3s} \qquad (27)$$

is used as a data set instead of the R ratio [1]. Then, the relation

$$12\pi {\rm Im}\,\Pi^{\rm had}(s) = \sigma(e^+e^- \to {\rm hadrons})/\sigma_0 + O(\alpha) \qquad (28)$$

is valid only at the leading order in α. One of the differences between the cross section and the R ratio at the next-to-leading order from Eq. (25) is the term ${\rm Re}\Pi^{\rm had}(s)$ from the denominator in Eq. (24). The quantity ${\rm Re}\Pi^{\rm had}(s)$ can be found by reiterating the leading-order term ${\rm Im}\,\Pi^{\rm had}(s)$ through the dispersion relation, which gives a relative error of α^2 order. The next-to-leading-order contribution in the denominator of the expression for the photon propagator is related to the running of the electromagnetic coupling constant and can partly be taken into account through the renormalization group technique for the energies far from the resonances [9]. Another difference is the corrections to the production vertex that should properly be taken into account as they enter the cross section. Extracting ${\rm Im}\,\Pi^{\rm had}(s)$ from the cross section requires subtraction of these corrections from the data in order to avoid double counting in the next-to-leading-order analysis of the muon anomalous magnetic moment if a theoretical next-to-leading-order kernel for averaging the two-point correlator is used.

The use of the R ratio is preferable from the theoretical point of view because it relates data to the imaginary part of the two-point hadronic correlator ${\rm Im}\,\Pi^{\rm had}(s)$ in a simple way. It is also preferable from the experimental point of view since the total normalization of the data is fixed, which helps to eliminate systematic errors. In this respect, a τ-data set that can be used to determine the part of the two-point function generated by the isovector part of the hadronic electromagnetic current in the limit of the exact isotopic invariance has a different normalization at the next-to-leading order compared to the data on e^+e^- annihilation and should be corrected by an explicit account of the contributions of the relative α order. Note that the next-to-leading-order correction emerging from the interpretation of data can be controlled theoretically within counting in α, while corrections due to the violation of isotopic invariance between the data sets obtained from the τ and e^+e^- channels can only be estimated in models. The problem of different normalization also persists for heavy hadrons if their contribution to the cross section is calculated from their leptonic branchings. The next-to-leading-order contribution of heavy flavors is not essential though, because it is small and also can reliably be evaluated in perturbation theory.

3.1.2. Two-photon-mediated e^+e^- annihilation. The next-to-leading-order cross section of the process of e^+e^- annihilation into hadrons contains a contribution of two-photon annihilation with one hadronic insertion into the photon propagator. This contribution requires a special treatment before the data set is related to the hadronic two-point function with the next-to-leading order accuracy. For instance, the next-to-leading-order kernel for the muon anomalous magnetic moment diagram with a vertex correction integrates the part of data emerging through the double-photon scattering channel in the process of e^+e^- annihilation. This can lead to double counting at the next-to-leading order for the evaluation of the muon anomalous magnetic moment.

Thus, one concludes that, at the next-to-leading-order in electromagnetic interaction, a strict correlation between sets of data and theoretical expressions for the next-to-leading-order kernels for the evaluation of the muon anomalous magnetic moment emerges. This leads to additional contributions of the relative α order, which numerically amount to about 1% of the leading-order contribution, which is the precision one is trying to reach for comparison with the experimental result for the muon anomalous magnetic moment.

3.2. Four-Point Correlator

At the next-to-leading order in electromagnetic interaction, a new correlation function of the hadronic electromagnetic currents enters the theoretical computation of the muon anomalous magnetic moment. This correlation function leads to a new effect that is known as light-by-light scattering. Besides this explicit effect a less pronounced mixed effect also emerges. The four-point function gives a contribution to the full photon propagator of the form

$$\int dxdyD_{\mu\nu}(x-y)\langle Tj_\mu^{\rm had}(x)j_\nu^{\rm had}(y)j_\alpha^{\rm had}(z)j_\beta^{\rm had}(0)\rangle, \tag{29}$$

where $D_{\mu\nu}(x)$ is a free-photon propagator with a scalar amplitude $D(x)\sim 1/x^2$. In other words, a projection of the four-point function of the form

$$\int \frac{dxdy}{(x-y)^2}\langle Tj_\mu^{\rm had}(x)j_\mu^{\rm had}(y)j_\alpha^{\rm had}(z)j_\beta^{\rm had}(0)\rangle \tag{30}$$

is present in the two-photon Green's function. In QCD and other models, where the electromagnetic current is explicitly expressed through the elementary fields, this contribution is interpreted as an electromagnetic correction to the one-particle irreducible block of the photon two-point function (the photon vacuum polarization).

Thus, an accurate account of the next-to-leading-order hadronic contributions to the muon anomalous magnetic moment from general principles is a rather challenging task, both experimentally and theoretically. As an approach to it, one can use an effective theory with a few free parameters providing a unique framework for the calculations at both leading and next-to-leading order. In such an approach, the leading-order information is used to obtain the numerical values for the model parameters. The next-to-leading-order results are then computed theoretically. This approach can also serve as a basis for verifying the consistency of the estimates for the next-to-leading-order hadronic contributions made in different phenomenological models.

4. A MODEL FOR EVALUATING THE HADRONIC CONTRIBUTIONS

In this section, I describe a duality-based model to check the consistency of the next-to-leading-order hadronic contributions with the results of the leading-order analysis for the muon anomalous magnetic moment. The simplest version of the model contains three light quarks with QCD quantum numbers and the mass m_q, which is the only model parameter. The numerical value of m_q is fixed from the leading-order hadronic contribution and then used to find the next-to-leading-order result. Heavy quarks enter the model with their Standard masses. In this model, the calculations are explicit and can be performed analytically, which is an advantage. Indeed, the model differs from the leptonic sector only by the QCD group factors and the numerical values of fermion masses.

4.1. Fixing the Numerical Value of the Model Parameter m_q from the Leading-Order Hadronic Contribution

A fermion with mass m_q without the QCD group factors (as a lepton) gives the leading-order contribution to the muon anomalous magnetic moment of the form

$$a_\mu^{\rm ferm}({\rm LO}) = I(m_q)\left(\frac{\alpha}{\pi}\right)^2, \tag{31}$$

with

$$I(m_q) = \int\limits_{4m_q^2}^{\infty}\frac{\rho_q(s)K(s)}{s}ds \tag{32}$$

and

$$\rho_q(s) = \frac{1}{3}\sqrt{1-\frac{4m_q^2}{s}}\left(1+\frac{2m_q^2}{s}\right). \tag{33}$$

Explicit integration over s with the kernel $K(s)$ from Eq. (12) gives

$$I(m_q) = \int\limits_0^1 dx(1-x)[-\pi(x,m_q)], \tag{34}$$

where

$$\pi(x,m_q) = \left(\frac{1}{3z}-1\right)\varphi(z)-\frac{1}{9} \tag{35}$$

and

$$\varphi(z) = \frac{1}{\sqrt{z}}{\rm arctanh}(\sqrt{z})-1, \tag{36}$$

$$z = \frac{m_\mu^2x^2}{4m_q^2(1-x)+m_\mu^2x^2}.$$

The analytical expression for the function $I(m_q)$ is known; however, the integral representation given in Eq. (34) is convenient and sufficient for practical applications.

The contributions of heavy c and b quarks can directly be computed in QCD perturbation theory independently of the model. In the present calculation, I use only the free-quark approximation for simplicity. For the c quark with the mass $m_c = 1.6$ GeV [10] and the electric charge $e_c = 2/3$, one finds from Eq. (31) multiplied by the group factor $3e_c^2 = 4/3$

$$a_\mu^{\rm mod}({\rm LO};\, c) = 69.3 \times 10^{-11}. \qquad (37)$$

The b-quark contribution for $m_b = 4.8$ GeV [11] and $e_b = -1/3$ is small and reads

$$a_\mu^{\rm mod}({\rm LO};\, b) = 1.9 \times 10^{-11}. \qquad (38)$$

Thus, the contribution of light hadronic modes that are represented in our model by light fermions with the mass m_q amounts to

$$a_\mu^{\rm mod}({\rm LO};\, uds) = (6974.3 - 69.3 - 1.9) \times 10^{-11} \qquad (39)$$
$$= 6903(89) \times 10^{-11}.$$

I assume that this result directly corresponds to the contribution of the photon two-point correlator at the leading order as given in Eq. (11). It means that a real data set is properly corrected to extract $\mathrm{Im}\,\Pi^{\rm had}(s)$. As was discussed earlier, the extraction of $\mathrm{Im}\,\Pi^{\rm had}(s)$ with the next-to-leading-order accuracy requires a careful interpretation of experimental data, which is assumed to have been done.

A numerical value for the single model parameter m_q is obtained from Eqs. (31)–(36) and (39) and reads

$$m_q = 179 \pm 1\ {\rm MeV}. \qquad (40)$$

This numerical value is rather close to the charged pion mass, $m_\pi = 139.6$ MeV, which is expected since the leading-order contribution is mainly sensitive to the first derivative at $q^2 = 0$ of the two-point function $\Pi^{\rm had}(q^2)$ given in Eq. (10). For definiteness, I give the leading-order contribution of the light hadronic modes within the model obtained literally with the numerical value from Eq. (40):

$$a_\mu^{\rm mod}({\rm LO};\, uds)(m_q = 179 \pm 1\ {\rm MeV}) \qquad (41)$$
$$= (6920 \pm 70) \times 10^{-11}.$$

Since in the framework of the model the next-to-leading-order hadronic contributions to the muon anomalous magnetic moment are determined by the single parameter m_q with the numerical value from Eq. (40), they can readily be found.

4.2. Hadronic Contributions at the Next-to-Leading Order in Electromagnetic Interaction

The first check is to use the model for computing the higher order hadronic contributions due to the photon vacuum polarization graphs. The data-based analysis gives for the next-to-leading-order effects of this type the following numerical result [12]:

$$a_\mu^{\rm had}({\rm vac};\, {\rm NLO}) = -101(6) \times 10^{-11}. \qquad (42)$$

This number is about 1.5% of the leading-order term, as expected from the naive estimate based on the numerical value of the fine structure constant. As was discussed above, at this level of precision, the numerical value for the next-to-leading-order contribution depends strongly on the data sets used in the analysis. For different data sets, the different expressions of the next-to-leading-order kernel should be used to avoid double counting. For example, if the R ratio is used in the one-loop computation, then the leading-order result should first be divided by the factor [cf. Eq. (26)]

$$12\pi\,\mathrm{Im}\,\Pi^{\mu\mu}(s)|_{s\gg m_\mu^2} = \left(1 + \frac{3}{4}\frac{\alpha}{\pi} + O\left(\frac{m_\mu^4}{s^2}\right)\right) \qquad (43)$$

before being used in the next-to-leading-order analysis, which changes the leading-order result by 12×10^{-11}, exceeding the uncertainty quoted in Eq. (42). In fact, even mass-suppressed terms can be important at this level of precision, and the entire function $\mathrm{Im}\,\Pi^{\mu\mu}(s)$ should be integrated since the mass terms from the leading order can partly cancel the next-to-leading-order corrections in α. For other types of data (τ data especially), the change can be larger. This uncertainty is a reflection of the mixture of contributions at the next-to-leading order.

In the proposed model, the analysis is unambiguous and straightforward. I present different contributions separately for a detailed comparison with the results of the data-based analysis from [12].

For the vertex-type contributions, I use the explicit analytical formulas in the leading order of the mass expansion as they are given in [13]. The exact expressions are presented in [14]. The analytical expression for the contribution of a fermion with mass m_q without any group factors reads

$$a_\mu^{\rm ferm}({\rm ver};\, m_q) = -\frac{2}{3}\left(\frac{m_\mu}{m_q}\right)^2 \qquad (44)$$
$$\times \left(-\frac{2689}{5400} + \frac{\pi^2}{15} + \frac{23}{90}\ln\frac{m_q}{m_\mu}\right)\left(\frac{\alpha}{\pi}\right)^3,$$

which leads to a numerical result for the light mode contribution in the model

$$a_\mu^{\rm mod}({\rm ver};\, {\rm NLO};\, uds) = -172 \times 10^{-11}. \qquad (45)$$

A more accurate evaluation (using numerical integration with the kernel given up to the third order in the mass expansion from [12]) gives for the contribution of light modes

$$a_\mu^{\rm mod}({\rm ver;\,NLO;}\ uds) = -188\times 10^{-11}. \qquad (46)$$

The difference from the result obtained by using only the first term of the mass expansion given in Eq. (45) is on the order of 10%. It is smaller than one could expect from the numerical value of the expansion parameter $(m_\mu/m_q)^2 = (0.106/0.179)^2 = 0.36$. For the c-quark contribution, one finds

$$a_\mu^{\rm mod}({\rm ver;\,NLO;}\ c) = -4\times 10^{-11}, \qquad (47)$$

while the b-quark contribution is small:

$$a_\mu^{\rm mod}({\rm ver;\,NLO;}\ b) = -0.2\times 10^{-11}. \qquad (48)$$

The total vertex contribution computed in the model,

$$a_\mu^{\rm mod}({\rm ver;\,NLO}) = -192\times 10^{-11}, \qquad (49)$$

should be compared with the result of the data-based analysis from [12],

$$a_\mu({\rm ver;\,NLO}) = -211(5)\times 10^{-11}. \qquad (50)$$

The next check of the model is done for a mixed contribution of the lepton–hadron type. This contribution contains the electron and τ-lepton loops and depends on three masses m_μ, m_q, and m_e or m_τ. For fermions without the QCD group factors, this double-bubble-type (db) contribution is given by the integral representation

$$a_\mu^{\rm ferm}({\rm db;}\ f_1\&f_2) = \left(\frac{\alpha}{\pi}\right)^3 \qquad (51)$$
$$\times \int_0^1 dx(1-x)\pi(x,m_{f_1})\pi(x,m_{f_2}).$$

For the combined contribution of light modes with the electron loop, one has

$$a_\mu^{\rm mod}({\rm db;\,NLO;}\ e\&uds) = 105\times 10^{-11} \qquad (52)$$

and, with the τ-lepton loop,

$$a_\mu^{\rm mod}({\rm db;\,NLO;}\ \tau\&uds) = 0.05\times 10^{-11}. \qquad (53)$$

The contribution of heavy modes is only visible for the combined insertion of the c-quark loop and the electron loop,

$$a_\mu^{\rm mod}({\rm db;\,NLO;}\ e\&c) = 1.1\times 10^{-11}. \qquad (54)$$

The results given in Eqs. (52)–(54) are in good agreement with the data-based estimate [12]

$$a_\mu({\rm lept\&had;\,NLO}) = 107(2)\times 10^{-11}. \qquad (55)$$

Next comes the contribution from the reiteration of hadronic insertions. The light modes give

$$a_\mu^{\rm mod}({\rm db;\,NLO;}\ uds\&uds) = 3\times 10^{-11}. \qquad (56)$$

The combination of the c-quark insertion with the light-mode loops gives

$$a_\mu^{\rm mod}({\rm db;\,NLO;}\ c\&uds) = 0.1\times 10^{-11}, \qquad (57)$$

while the contribution of the two c-quark insertions is negligible. The results of the model from Eqs. (56) and (57) are in agreement with the data-based estimates [12]

$$a_\mu({\rm had\&had;\,NLO}) = 2.7\times 10^{-11}. \qquad (58)$$

Thus, one sees good agreement of the model results with calculations based on data. However, in the model, there is a contribution that is missing in the explicit calculations based on data related to the internal structure of the hadronic block. In the data-based calculation, this contribution is hidden in the data, while in the model it can explicitly be resolved as a correction to the one-particle irreducible hadronic block. At the leading order of the mass ratio, the analytical expression for this contribution without group factors reads

$$a_\mu^{\rm ferm}(4;{\rm NLO;}\ m_q) = \frac{41}{486}\left(\frac{m_\mu}{m_q}\right)^2\left(\frac{\alpha}{\pi}\right)^3. \qquad (59)$$

The result for the light modes of the model is

$$a_\mu^{\rm mod}(4;{\rm NLO;}\ uds) = 25\times 10^{-11}, \qquad (60)$$

while the c-quark contribution is small:

$$a_\mu^{\rm mod}(4;{\rm NLO;}\ c) = 0.3\times 10^{-11}. \qquad (61)$$

One could argue that this contribution is already contained in the experimental data used for the evaluation of the leading-order contribution in Eqs. (11) and (15). As was discussed earlier, this ambiguity reflects the difficulty of the interpretation of the hadronic contributions with next-to-leading-order accuracy.

The result for the total next-to-leading-order hadronic contribution of the vacuum polarization type is

$$a_\mu^{\rm mod}({\rm vac;\,NLO}) = -58\times 10^{-11}. \qquad (62)$$

The difference from Eq. (42) representing the result obtained in the data-based analysis comes mainly from two sources: the vertex-type contributions and a new term related to the one-particle irreducible hadronic block. Both contributions are of the $(m_\mu/m_q)^2$ order, which explains the magnitude of the difference. All remarks about the double counting because of the data interpretation apply here. Note that only the first few terms of expansions in the mass

ratio $(m_\mu/m_q)^2$ are used for the numerical estimates, which provides a sufficient accuracy.

Thus, the duality-inspired model reproduces rather accurately the results for the next-to-leading-order hadronic contributions found in the data-based analysis for the graphs related to the photon vacuum polarization. This is expected since these results are obtained by the integration of the two-point correlation function with the next-to-leading-order kernel, which is rather similar to the leading-order one.

The next try for the model is the computation of the light-by-light contribution given by the four-point correlator. The analytical expression for a contribution of the fermion without group factors through the $(m_\mu/m_q)^4$ order reads [15]

$$a_\mu^{\rm ferm}({\rm lbl;\,NLO;}\ m_q) = \left(\frac{\alpha}{\pi}\right)^3 \times \left\{\left(\frac{m_\mu}{m_q}\right)^2\left(\frac{3}{2}\zeta(3)-\frac{19}{16}\right)+\left(\frac{m_\mu}{m_q}\right)^4 \times\left(-\frac{161}{810}\ln^2\left(\frac{m_q}{m_\mu}\right)-\frac{16\,189}{48\,600}\ln\left(\frac{m_q}{m_\mu}\right) +\frac{13}{18}\zeta(3)-\frac{161}{9720}\pi^2-\frac{831\,931}{972\,000}\right)\right\}. \quad (63)$$

With this formula, one finds the value for the light modes,

$$a_\mu^{\rm mod}({\rm lbl;\,NLO;}\ uds) = 140.5\times 10^{-11}, \quad (64)$$

and the value for the c quark,

$$a_\mu^{\rm mod}({\rm lbl;\,NLO;}\ c) = 2\times 10^{-11}. \quad (65)$$

The total light-by-light contribution predicted by the model,

$$a_\mu^{\rm mod}({\rm lbl;\,NLO}) = (140.5+2)\times 10^{-11} = 143\times 10^{-11}, \quad (66)$$

is different from the value used in the literature [1, 16, 17],

$$a_\mu^{\rm had}({\rm lbl;\,standard}) = -85(25)\times 10^{-11}. \quad (67)$$

Recently, the authors of [17] have corrected the sign of the neutral-pion contribution obtained in the explicit hadronization approach for the evaluation of the light-by-light contribution related to the four-point correlation function of electromagnetic currents [18]. The corrected results are closer to the values obtained within the duality model of the present paper. I postpone a more detailed discussion of this point until Section 5.

Thus, the next-to-leading-order hadronic contribution obtained in the model reads

$$a_\mu^{\rm mod}({\rm NLO}) = (-58+143)\times 10^{-11} = 85\times 10^{-11}. \quad (68)$$

It agrees with the present experimental result from Eq. (21), which we repeat here:

$$a_\mu^{\rm had} = (191\pm 175)\times 10^{-11}.$$

The agreement with the future experimental result for the muon anomalous magnetic moment depends on a possible change of the mean value of $a_\mu^{\rm exp}$, as one sees from Eq. (22).

The prediction of the next-to-leading-order hadronic contribution obtained in the model is fairly sensitive to the numerical value of the mass parameter for the light modes. This numerical value is, however, strictly determined by the leading-order result. To check how sensitive the obtained results are to the details of the model, I introduce a mass difference between s and u,d quarks [$SU(3)$ flavor violation in the mass sector in the approximation of exact isotopic invariance]. I write $m_s = m_q + 0.18$ GeV with 0.18 GeV being the value of the running mass for the strange quark. Then, one finds that the numerical value for the new model parameter m_q^1 becomes

$$m_q^1 = 166\pm 1\ {\rm GeV} \quad (69)$$

with

$$a_\mu^{\rm mod1}({\rm LO;}\ uds)(m_q^1 = 166\pm 1\ {\rm MeV}) = (6928\pm 71)\times 10^{-11}. \quad (70)$$

The prediction of the next-to-leading-order contribution in this case as compared to the $SU(3)$-symmetric one is

$$a_\mu^{\rm mod1}({\rm NLO}) - a_\mu^{\rm mod}({\rm NLO}) = (2+4+14)\times 10^{-11}, \quad (71)$$

where the first term comes from vertex corrections, the second term comes from insertions into the photon propagator, and the last term comes from the light-by-light graphs. The result is fairly stable. Finally, the model with $SU(3)$ flavor violation in the mass sector gives the next-to-leading order hadronic contribution to the muon anomalous magnetic moment

$$a_\mu^{\rm mod1}({\rm NLO}) = 105\times 10^{-11}, \quad (72)$$

which is rather close to the prediction of the model with $SU(3)$-symmetric mass arrangement from Eq. (68).

One could consider an even more sophisticated model including a violation of the isotopic invariance by using different masses for u and d quarks. An additional uncertainty emerges from the errors in the numerical value for the c-quark mass. By using the $\overline{MS}$ mass around 1.3 GeV for the c quark,

one could enhance its leading-order contribution by about 50% [a leading-order rescaling factor is $(m_c(\text{pole})/m_c(\overline{MS}))^2 = (1.6/1.3)^2 = 1.5$]. Within the proposed model, the use of the pole mass of the heavy quark looks more natural, while an account of the difference between the numerical values for the pole and $\overline{MS}$ masses is beyond the accuracy of the approximation used for the evaluation of the contributions of heavy quarks. It can readily be done though, since the contribution of heavy quarks is perturbative and corrections in the strong coupling constant can reliably be found.

5. DISCUSSION OF THE RESULTS

The underlying idea of the presented analysis is to introduce a framework for computing the next-to-leading-order hadronic contributions to the muon anomalous magnetic moment using the LO information. Presently, the results for the light-by-light contribution, which is the most interesting term at the next-to-leading order are available analytically for fermions, which dictates the choice of model from the technical point of view almost uniquely. Thus, a model of massive quarks with electromagnetic interaction emerges as a suitable candidate. It is not an approximation for QCD as a gauge model with constituent quarks. It is just a bridge from the leading-order results for hadronic contributions to a particular observable to the next-to-leading-order ones. Note that, for another important parameter of the Standard Model—the running electromagnetic coupling constant at the scale of the Z-boson mass—there is no possibility of using such kind of a model since there are no important next-to-leading-order terms to compute. Calculations for the infrared-sensitive observables using constituent quarks with masses around 300–500 MeV as the only infrared scales are unjustified in pQCD in general since the higher order corrections in the strong coupling constant cannot be found. Also, the introduction of finite masses for the light quarks explicitly violates chiral invariance, which is a well-established symmetry of the light hadronic sector. In this sense, the approximation for QCD with constituent quarks cannot be considered as a reasonable general framework. In the high-energy limit, the massless approximation for strong interactions is perturbative and quite precise. This means that the high-energy contributions to the muon anomalous magnetic moment can be represented by almost any model that satisfies the duality constraints. In this sense, the fermionic model fits the Standard Model approximation for large energies. However, the main contribution to the muon anomalous magnetic moment comes from the infrared region, where there is no sensible approximation for strong interactions deduced from QCD. Therefore, the necessary characteristics of the strong-interaction amplitudes relevant for the computation of the muon anomalous magnetic moment have to be extracted from data. The first amplitude, that emerges is the two-point correlator, which is given by a single function of one complex variable with simple analytic properties (see Eqs. (8), (10)). For computing the muon anomalous magnetic moment, one need not know the pointwise behavior of the spectrum but only the integral over all energies with some enhancement of the threshold region. A model of massive fermions is then well suitable to fit this integral over data. When hadrons are introduced into the threshold infrared region to fit the experiment, the effective masses of quarks increase. Therefore, an account of the low-energy hadronization for the two-point function entering the muon anomalous magnetic moment is achieved by introducing an explicit cut in energy in the spectral sum over the states. In practice, at the leading order, the hadron contributions are represented by the pion with an electromagnetic interaction of the form $ej_\mu^\pi A^\mu$, where, at the leading order, $j_\mu^\pi = i(\pi^+ \overset{\leftrightarrow}{\partial}_\mu \pi^-)$. The inclusion of pions leads to the scalar type of spectrum near the threshold,

$$\rho_\pi(s) = \frac{1}{12}\sqrt{1-\frac{4m_\pi^2}{s}}\left(1-\frac{4m_\pi^2}{s}\right), \qquad (73)$$

instead of the fermionic form given in Eq. (33). Furthermore, the fermionic contributions can be moved to higher energies by using the classical vector mesons ρ, ω, ϕ. In the vector-meson-dominance model, one identifies the electromagnetic current with the contribution of the canonically normalized elementary ρ-meson (or ω, ϕ) field ρ_μ through the relation $j_\mu^{\text{had}} = f_\rho \rho_\mu$. Here, f_ρ gives a form factor related to the leptonic width of the ρ meson. Because of the nature of the muon anomalous magnetic moment observable, this contribution can be well represented in the sense of duality by the contribution of light fermions since it resides at a rather large scale. This hadronization picture is transparent for the two-point function, which is sufficient for the leading-order analysis. At the next-to-leading order, a hadronization procedure for the four-point correlation function is necessary. Within a hadron picture of the low-energy spectrum, the most important contribution to the muon anomalous magnetic moment comes from pions. To handle contributions from the four-point function quantitatively, a quantum field model for pions given by the Lagrangian

$$L_{\text{low-energy}} = |D_\mu \pi|^2 - m_\pi^2 \pi^2, \quad D_\mu = \partial_\mu - ieA_\mu, \qquad (74)$$

is introduced. This model generates vertices that allow one to compute the pion contribution to the four-point hadronic electromagnetic current correlator that enters the light-by-light diagram explicitly. The high-energy contribution of this model should then be replaced by the Standard Model quark contributions. In the pure fermionic model with a small effective mass, this replacement is effectively made at rather low energies, which makes the separate contribution of pions small or even vanishing. Thus, the hadronization procedure of the model is effectively realized in the duality sense through the light massive quarks rather than the real hadrons. This is possible because of the inclusive nature of the observable—the muon anomalous magnetic moment—that depends on the contribution of many hadrons, i.e., on the integral over the entire hadronic spectrum. This is exactly the situation where the duality concept is applicable. Note that the hadronization picture need not be universal for all strong interaction processes but can specially be tailored for a given observable.

The results for the muon anomalous magnetic moment related to the photon two-point function, which have been obtained in the data-based analysis, are well reproduced by the model with the mass of the light fermion around the pion mass. Using the model prediction for the light-by-light graph, I find agreement of the next-to-leading-order hadron contribution to the muon anomalous magnetic moment with experiment. The results for the light-by-light graph in the pion model are available numerically. In the absence of analytical expressions for the light-by-light contributions in the pion model, I could not quantitatively check how fermionic contributions replace the pion ones when the effective fermion mass decreases. However, it seems probable that the explicit inclusion of the pion contributions in the framework of the present model will simply shift the effective mass of light quarks, making it larger.

The fermionic model gives a smooth spectrum at low energies, which can be considered as an average of the hadronic spectrum according to the duality concept. An important question is whether such a smooth spectrum is a reasonable approximation for computing the muon anomalous magnetic moment. In the two-point correlator of electromagnetic currents, there are no resonances in the relevant region. The contribution of the vector mesons (the ρ meson, for instance) is located at relatively large scales. In the axial channel, for instance, the situation is different because of the presence of the pion resonance and the use of the duality arguments requires special consideration [19]. Note, however, that, as soon as the pion is considered to be massive (not a pure Goldstone mode), the chiral invariance is explicitly broken, which makes quarks massive as well (or vice versa). Note also that a model can be suited for a description of a specific observable and need not give a universal approximation of any Green's function. For instance, in the case of the axial-vector two-point correlator, the projection related to spin-one particles contains only massive resonances and the spectrum of this invariant amplitude can be well approximated by a fermionic model without the pion pole. For the four-point functions, the situation is much more complicated, since it is a function of several complex variables. In the literature, there are models where the four-point correlation function at low energies is represented through the elementary fields of neutral pseudoscalar bosons in order to compute contributions of the light-by-light graphs to the muon anomalous magnetic moment. The representation employs the neutral-pion contribution to the four-point function through the iteration of an effective Lagrangian for the interaction of the neutral pion π^0 with photons due to the Abelian anomaly in the axial current (for a review, see [17]). The result for the light-by-light contribution obtained using the neutral-pion dominance, Eq. (67), is different from the one obtained in the present model Eq. (66). In [17], the sign of the neutral-pion contribution is negative, which produces a large difference with the prediction of the present paper based on the duality arguments. The sign of the neutral-pion contribution has recently been corrected in [18], making the neutral-pion contribution positive in accordance with the results of the present analysis based on the duality concept. Still, it is interesting to discuss the validity of the assumption about the neutral-pion dominance for the evaluation of the muon anomalous magnetic moment in more detail. In general, the reduction of the four-point amplitude of the hadronic electromagnetic currents to a two-point correlator of axial currents uses the operator product expansion at small distances

$$iTj_\mu^{\rm had}(x)j_\nu^{\rm had}(-x)|_{x\to 0} = \varepsilon_{\mu\nu\omega\lambda}x^\omega j_5^\lambda(0)C(x^2)+\ldots, \quad (75)$$

where $C(x^2)$ is a coefficient function of the local operator $j_5^\lambda(0)$, which has the quantum numbers of the axial current (see, e.g., [20]). In other words, the combination of two hadronic electromagnetic currents of the form

$$\varepsilon_{\mu\nu\omega\lambda}\xi^\lambda Tj_\mu^{\rm had}(x+\xi)j_\nu^{\rm had}(x-\xi)F(\xi^2) \quad (76)$$

taken at small ξ with some form factor $F(\xi^2)$ may act in some applications as a local axial current that can serve as an interpolation field for the neutral pion. Thus, this combination can be replaced by a fundamental pion field in a hadronization procedure. This kind of factorization for the four-point amplitude is quantitatively justified for the process of $\gamma\gamma\to\gamma\gamma$

scattering in a specific region of the phase space in kinematic variables where all three external momenta are essential. In other regions of the phase space, the saturation of the scattering amplitude with the pion-pole contribution can be invalid numerically in a sense that the pion contribution is not dominant for the integrals of the four-point amplitude relevant for the computation of the muon anomalous magnetic moment. The projection of the four-point function that emerges in the light-by-light graphs for the muon-anomalous-magnetic-moment calculation has the form

$$\int dx x^{\delta} \langle T j_{\mu}^{\mathrm{had}}(x) j_{\nu}^{\mathrm{had}}(y) j_{\alpha}^{\mathrm{had}}(z) j_{\beta}^{\mathrm{had}}(0)\rangle. \qquad (77)$$

In momentum space, this projection depends on two external momenta only as the third momentum is set to zero after the differentiation according to the definition of the muon anomalous magnetic moment. In the neutral pseudoscalar model, the projection of the four-point function given in Eq. (77) is saturated by the contribution of the neutral pion supplemented by the explicit cutoff of the high-energy contributions starting from the ρ-meson mass. The accuracy of this procedure is not under control because other hadronic contributions are important and the pion dominance cannot be justified quantitatively in the integral over the entire hadronic spectrum. In the absence of strong numerical dominance of the neutral-pion-pole contribution in the hadronization picture for the light-by-light graph, the fermionic model can be used for its computation on the same footing as was used for the vacuum polarization graphs. Note also that the corresponding contribution of the neutral pion to the projection of the four-point function emerging in the photon propagator and related to the process $\gamma^* \to \gamma\pi^0$ is usually not considered. In other words, the neutral-pion approximation for the four-point function should also be taken into account in Eq. (30). In this case, it leads to a cut starting from the pion mass square m_π^2 as in the physical decay process of an off-shell photon to a real photon and the pion $\gamma^* \to \gamma\pi^0$. This contribution was not used in the analysis of data in the process of e^+e^- annihilation into hadrons. This calls for a quantitative evaluation of the validity of the neutral-pion-dominance model for the calculation of the four-point correlation function in the kinematical region relevant for computing the next-to-leading-order hadronic contribution to the muon anomalous magnetic moment.

Despite the fact that the fermionic model with mass $m_q = 179$ MeV predicts a value for the next-to-leading-order hadronic contribution to the muon anomalous magnetic moment in good agreement with experiment, there remains a disturbing feeling that this prediction is obtained within an unrealistic approximation for strong interactions and, therefore, cannot be taken seriously. A historic reminiscence may be appropriate here. A century ago, thinking about light as existing in the form of discrete portions—photon quanta—was rather disturbing for classical physics. However, the quantum representation allowed for the quantitative explanation of experimental facts on photoeffect and blackbody radiation. It did not change the description of electromagnetic phenomena insensitive to the quantum nature of the light. It may happen that the muon anomalous magnetic moment is sensitive to the contribution of all hadrons in a way in which it would be sensitive to that of free fermions with an appropriate mass which is a standard realization of the duality concept. The direct application of this concept to a particular case of muon anomalous magnetic moment looks suspicious because the infrared region is explicitly involved in the analysis and the results depend strongly on the numerical value of the effective quark mass, which happens to be rather small. However, the model is only designed for computing the next-to-leading-order hadronic contribution to the muon anomalous magnetic moment using the leading-order result as input. This does not mean that this model approximation suited for computing the muon anomalous magnetic moment is in any sense a universal limit of QCD automatically applicable to other observables.

6. CONCLUSION

A duality-inspired model for describing the next-to-leading-order hadronic contributions to the muon anomalous magnetic moment is proposed. The model contains a single parameter, which is fixed from the experimental result for the leading-order hadronic contribution to the muon anomalous magnetic moment. The model describes the next-to-leading-order hadronic contributions of the vacuum polarization type in agreement with the existing estimates. It predicts a numerical value for the light-by-light contribution that has recently been confirmed after correcting the results based on the neutral-pion dominance with additional assumptions on the form of regularization of the ultraviolet behavior for the relevant amplitudes. The result of the present analysis has considerably changed the prediction of the total next-to-leading-order hadronic contribution to the muon anomalous magnetic moment used in the literature as a basis for the search for new physics . The prediction of the model agrees with the present experimental value for the muon anomalous magnetic moment, which confirms the validity of the Standard Model.

ACKNOWLEDGMENTS

I thank K.G. Chetyrkin, A.I. Davydychev, J.G. Körner, N.V. Krasnikov, and V.A. Rubakov for interesting discussions.

This work is partially supported by Russian Foundation for Basic Research under contracts nos. 99-01-00091 and 01-02-16171.

REFERENCES

1. A. Czarnecki and W. J. Marciano, Phys. Rev. D **64**, 013014 (2001).
2. T. Kinoshita, B. Nizic, and Y. Okamoto, Phys. Rev. D **41**, 593 (1990).
3. P. J. Mohr and B. N. Taylor, Rev. Mod. Phys. **72**, 351 (2000).
4. C. F. Cho and J. J. Sakurai, Phys. Lett. B **30B**, 119 (1969); J. J. Sakurai, Phys. Lett. B **46B**, 207 (1973).
5. S. Brodsky and E. de Rafael, Phys. Rev. **168**, 1620 (1968).
6. T. Kinoshita, B. Nizic, and Y. Okamoto, Phys. Rev. D **31**, 2108 (1985).
7. R. Alemany, M. Davier, and A. Höcker, Eur. Phys. J. C **2**, 123 (1998); M. Davier and A. Höcker, Phys. Lett. B **435**, 427 (1998).
8. S. Eidelman and F. Jegerlehner, Z. Phys. C **67**, 585 (1995).
9. J. G. Körner, A. A. Pivovarov, and K. Schilcher, Eur. Phys. J. C **9**, 551 (1999); A. A. Pivovarov, Yad. Fiz. **65**, 1352 (2002) [Phys. At. Nucl. **65**, 1319 (2002)]; hep-ph/0011135.
10. Particle Data Group (C. Caso *et al.*), Eur. Phys. J. C **3**, 1 (1998).
11. J. H. Kühn, A. A. Penin, and A. A. Pivovarov, Nucl. Phys. B **534**, 356 (1998); A. A. Penin and A. A. Pivovarov, Phys. Lett. B **435**, 413 (1998); Nucl. Phys. B **549**, 217 (1999).
12. B. Krause, Phys. Lett. B **390**, 392 (1997).
13. M. A. Samuel and G. Li, Phys. Rev. D **44**, 3935 (1991).
14. R. Barbieri and E. Remiddi, Nucl. Phys. B **90**, 233 (1975).
15. S. Laporta and E. Remiddi, Phys. Lett. B **301**, 440 (1993).
16. J. Bijnens, E. Pallante, and J. Prades, Phys. Rev. Lett. **75**, 1447, 3781 (Erratum) (1995); Nucl. Phys. B **474**, 379 (1996).
17. M. Hayakawa and T. Kinoshita, Phys. Rev. D **57**, 465 (1998).
18. M. Hayakawa and T. Kinoshita, hep-ph/0112102.
19. N. V. Krasnikov, A. A. Pivovarov, and A. N. Tavkhelidze, Z. Phys. C **19**, 301 (1983).
20. A. A. Pivovarov, Phys. Rev. D **47**, 5183 (1993); A. A. Penin and A. A. Pivovarov, Nucl. Phys. B **550**, 375 (1999); Yad. Fiz. **64**, 323 (2001) [Phys. At. Nucl. **64**, 275 (2001)].

Physics of Atomic Nuclei, Vol. 66, No. 5, 2003, pp. 914–927. From Yadernaya Fizika, Vol. 66, No. 5, 2003, pp. 946–959.

ELEMENTARY PARTICLES AND FIELDS
Theory

Two-Photon Partial Widths of Tensor Mesons*

A. V. Anisovich, V. V. Anisovich, **M. A. Matveev, and V. A. Nikonov**

Petersburg Nuclear Physics Institute, Gatchina, Russia

Received October 31, 2001; in final form, July 15, 2002

Abstract—Partial widths of the $\gamma\gamma$ decay of the tensor $q\bar{q}$ states $a_2(1320)$, $f_2(1270)$, and $f_2(1525)$ and their radial excitations $a_2(1660)$, $f_2(1640)$, and $f_2(1800)$, as well as ${}^3F_2 q\bar{q}$ states, are calculated. Calculations are performed in the framework of the same approach that was used before for the study of radiative decays $f_0(980) \to \gamma\gamma$, $a_0(980) \to \gamma\gamma$, and $\phi(1020) \to \gamma f_0(980)$: the assumption made is that of $q\bar{q}$ structure of $f_0(980)$ and $a_0(980)$ [A.V. Anisovich *et al.*, Phys. Lett. B **456**, 80 (1999); Yad. Fiz. **65**, 523 (2002)]. The description of the decay partial widths for $a_2(1320)$, $f_2(1270)$, $f_2(1525)$ and $f_0(980)$, $a_0(980)$ is reached with the approximately equal radial wave functions, thus giving a strong argument in favor of the fact that these scalar and tensor mesons are to be classified as members of the same P-wave $q\bar{q}$ multiplet.

1. INTRODUCTION

For the time being, the main problem of meson spectroscopy is the reliable determination of states belonging to the P-wave $q\bar{q}$ multiplet $1^3P_J q\bar{q}$. The solution of this problem is of fundamental importance for the quark systematics, as well as for the search for exotic mesons such as glueballs and hybrids (in connection with this problem, see [1–4]). The classification of mesons $f_0(980)$ and $a_0(980)$, which is of crucial meaning for the nonet of scalar mesons $1^3P_0 q\bar{q}$, gives rise to certain questions. In a set of papers [5–10], on the basis of the analysis of experimental data, it was argued that, for the states $f_0(980)$ and $a_0(980)$, the $1^3P_0 q\bar{q}$ component is dominant. However, another point of view on the structure of these mesons exists as well (see minireview [11] and references therein).

The investigation of radiative decays is a powerful tool for establishing the quark structure of hadrons. At an early stage of the quark model, radiative decays of vector mesons provided strong evidence for a constituent quark being a universal constructive element of mesons and baryons [12–15]. In our opinion, the radiative decays of the $1^3P_J q\bar{q}$ mesons are equally important for the determination of the P-wave multiplet.

Partial widths of the decays $f_0(980) \to \gamma\gamma$ and $a_0(980) \to \gamma\gamma$ were calculated in [9] assuming the mesons $f_0(980)$ and $a_0(980)$ to be dominantly $q\bar{q}$ states, that is, $1^3P_0 q\bar{q}$ mesons. The results of our calculation agree well with experimental data. In [10], on the basis of data [16] for the decay $\phi(1020) \to \gamma f_0(980)$ together with the value of partial width $f_0(980) \to \gamma\gamma$ obtained in the reanalysis [17], the flavor content of $f_0(980)$ was studied. Assuming the flavor wave function in the form $n\bar{n}\cos\varphi + s\bar{s}\sin\varphi$, where $n\bar{n} = (u\bar{u} - d\bar{d})/\sqrt{2}$, we described the experimental data with two allowed values of mixing angle: either $\varphi = -48^\circ \pm 6^\circ$ or $\varphi = 85^\circ \pm 4^\circ$ (the negative angle is preferable). Both values of mixing angle are in qualitative agreement with data on hadronic decays of $f_0(980)$ into $\pi\pi$ and $K\bar{K}$ [8, 18].

Although direct calculations of widths of radiative decays agree well with the hypothesis that the $q\bar{q}$ component dominates both $f_0(980)$ and $a_0(980)$, to be confident that these mesons are members of the $1^3P_0 q\bar{q}$ multiplet one more step is needed: it is necessary to check whether radiative decays of tensor mesons $a_2(1320)$, $f_2(1270)$, and $f_2(1525)$ can be calculated under the same assumption and within the same technique as was done for the reactions involving $f_0(980)$ and $a_0(980)$. The tensor mesons $a_2(1320)$, $f_2(1270)$, and $f_2(1525)$ are basic members of the P-wave $q\bar{q}$ multiplet, and just the existence of tensor mesons forms the basis of the nonet classification of mesons as $q\bar{q}$ states, with four P-wave nonets [19, 20].

In the framework of a spectral integration technique, we calculate the transition form factors for tensor meson transitions $a_2(1320) \to \gamma^*(Q^2)\gamma$, $f_2(1270) \to \gamma^*(Q^2)\gamma$, and $f_2(1525) \to \gamma^*(Q^2)\gamma$ in the region of small momentum transfer squared Q^2: these form factors, in the limit $Q^2 \to 0$, determine partial widths of reactions $a_2(1320) \to \gamma\gamma$, $f_2(1270) \to \gamma\gamma$, and $f_2(1525) \to \gamma\gamma$. The spectral

*This article was submitted by the authors in English.

** e-mail: anisovic@thd.pnpi.spb.ru

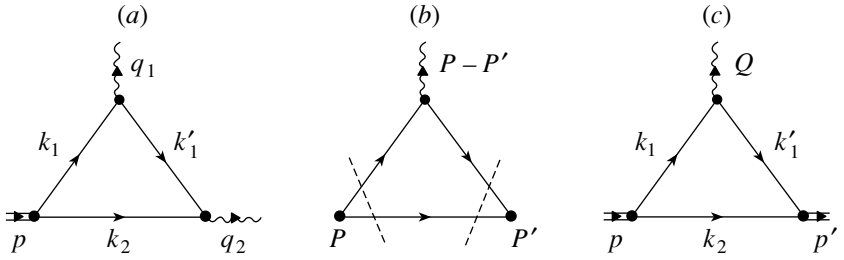

Fig. 1. (a) Triangle diagram for the transition form factor of the reaction $T \to \gamma(q_1^2)\gamma(q_2^2)$; ($b$) diagram for the double spectral representation over $P^2 = s$ and $P'^2 = s'$; the intermediate-state particles are on the mass shell, the cuts of the diagram are shown by dashed lines; (c) triangle diagram for the meson charge form factor.

representation technique was developed in [21] for the investigation of the transitions of pseudoscalar mesons such as $\pi^0 \to \gamma^*(Q^2)\gamma$, $\eta \to \gamma^*(Q^2)\gamma$, and $\eta' \to \gamma^*(Q^2)\gamma$. As is stated above, by using this technique, the calculation of the decay coupling constants of reactions $f_0(980) \to \gamma\gamma$, $a_0(980) \to \gamma\gamma$, and $\phi(1020) \to \gamma f_0(980)$ was performed in [9, 10].

In the region of moderately small Q^2, where strong QCD works, the form factor for transition $q\bar{q}$ meson $\to \gamma^*(Q^2)\gamma$ is determined by the quark loop diagram of Fig. 1a, which is a convolution of the $q\bar{q}$ meson and photon wave functions, $\psi_{q\bar{q}} \otimes \psi_\gamma$. The calculation of the process of Fig. 1a is performed in terms of the double spectral representation over $q\bar{q}$ invariant masses squared, $s = (m^2 + k_\perp^2)/(x(1-x))$ and $s' = (m^2 + k_\perp'^2)/(x(1-x))$, where $k_\perp^2$, $k_\perp'^2$, and x are the light-cone variables and m is the constituent-quark mass. Following [21], we represent the photon wave function as a sum of two components that describe the prompt production of the $q\bar{q}$ pair at large s' (with a pointlike vertex for the transition $\gamma \to q\bar{q}$, correspondingly) and the production in the low-s' region where the vertex $\gamma \to q\bar{q}$ has a nontrivial structure due to soft $q\bar{q}$ interactions. The necessity to include such a component can be argued, for example, by the vector-dominance model $\gamma \to \rho^0, \omega, \phi \to q\bar{q}$.

The process of Fig. 1a at moderately small Q^2 is mainly determined by the low-s' region, in other words, by the soft component of the photon wave function.

The soft component of the photon wave function was restored in [21], on the basis of the experimental data for the transition $\pi^0 \to \gamma^*(Q^2)\gamma$ at $Q^2 \leq 1$ GeV^2. Once the photon wave function is found, the form factors of reactions $a_2 \to \gamma^*(Q^2)\gamma$ and $f_2 \to \gamma^*(Q^2)\gamma$ at $Q^2 \leq 1$ GeV^2 provide us with the opportunity to investigate in detail the tensor-meson wave functions. However, when investigating a small-Q^2 region, we may restrict ourselves to a simplified, one-parameter wave function of the basic tensor mesons $1^3P_2q\bar{q}$, this parameter being the mean radius squared R_T^2.

Assuming the $q\bar{q}$ structure of tensor mesons, the flavor content of $a_2(1320)$ is fixed, thus allowing unambiguous calculation of the transition form factor of reaction $a_2(1320) \to \gamma\gamma$. Reasonable agreement with data has been obtained at $7 \leq R^2_{a_2(1320)} \leq 12$ GeV^{-2} (recall that, for a pion, $R_\pi^2 \simeq 10$ GeV$^{-2} \simeq 0.4$ fm^2). To describe the decay $a_0(980) \to \gamma\gamma$, the quark wave function of $a_0(980)$ should have nearly the same mean radius squared [9], $7 \leq R^2_{a_0(980)} \leq 12$ GeV^{-2}. Still, we do not exclude the possibility that the P-wave states may be rather compact. Hadronic reactions agree with this possibility: the estimation of the radius of $f_0(980)$ carried out by using GAMS data for $\pi^- p \to \pi^0\pi^0 n$ [22] proves that the $q\bar{q}$ component in $f_0(980)$ gives [7] $R^2_{f_0(980)} = 6 \pm 6$ GeV^{-2}.

Partial widths $\Gamma(f_2(1270) \to \gamma\gamma)$ and $\Gamma(f_2(1525) \to \gamma\gamma)$ depend on the relative weights of strange and nonstrange components in a tensor–isoscalar meson, $s\bar{s}$ and $n\bar{n}$. The study of hadronic decays tells us that $f_2(1270)$ is dominantly an $n\bar{n}$ state, while $f_2(1525)$ is, correspondingly, an $s\bar{s}$ one. It is in accordance with the calculated values of partial widths $\Gamma(f_2(1270) \to \gamma\gamma)$ and $\Gamma(f_2(1525) \to \gamma\gamma)$: at $R^2_{f_2(1270)} \simeq R^2_{f_2(1525)} \sim R^2_{f_0(980)}$, the agreement with data is reached with $n\bar{n}$- and $s\bar{s}$-dominated components in $f_2(1270)$ and $f_2(1525)$, respectively.

The two-photon decays of radial-excited states, $2^3P_2q\bar{q} \to \gamma\gamma$, are suppressed as compared to decays of basic states. The reason is that radial wave functions of the states $2^3P_2q\bar{q}$ change sign, so the convolution of wave functions $\psi_{2^3P_2q\bar{q}} \otimes \psi_\gamma$ is comparatively small. This fact is also the reason for a qualitative character of predictions for the decays $2^3P_2q\bar{q} \to \gamma\gamma$.

The paper is organized as follows. In Section 2, we present basic formulas for the calculation of the amplitudes for tensor mesons, members of the $1^3P_2q\bar{q}$

and $2^3P_2q\bar{q}$ nonets, decaying into $\gamma\gamma$. The results of the calculation are given in Section 3. In the Conclusion, we discuss the $q\bar{q}$-multiplet classification of tensor and scalar mesons resulting from radiative meson decays.

2. TENSOR-MESON DECAY AMPLITUDES $2^{++}(q\bar{q}) \to \gamma\gamma$

Below, the formulas are presented for the amplitudes of radiative decay of the $q\bar{q}$ tensor mesons belonging to the multiplets located at $\lesssim$2000 MeV: $1^3P_2q\bar{q}$, $2^3P_2q\bar{q}$, and $1^3F_2q\bar{q}$.

2.1. Spin–Momentum Structure of the Decay Amplitude

The decay amplitude for the process $T \to \gamma\gamma$, where T is the $2^{++}(q\bar{q})$ state, has the following structure:

$$A^{(T)}_{\mu\nu,\alpha\beta} = e^2\left[S^{(0)}_{\mu\nu,\alpha\beta}(p,q)F^{(0)}_{T\to\gamma\gamma}(0,0) + S^{(2)}_{\mu\nu,\alpha\beta}(p,q)F^{(2)}_{T\to\gamma\gamma}(0,0)\right], \quad (1)$$

where e is the electron charge ($e^2/4\pi = \alpha = 1/137$). Here, $S^{(0)}_{\mu\nu,\alpha\beta}$ and $S^{(2)}_{\mu\nu,\alpha\beta}$ are the moment operators, and indices α, β refer to photons and μ, ν to the tensor meson. The transition form factors for the decays into photons with transverse polarization $T \to \gamma_\perp(q_1^2)\gamma_\perp(q_2^2)$, namely, $F^{(0)}_{T\to\gamma\gamma}(q_1^2,q_2^2)$ and $F^{(2)}_{T\to\gamma\gamma}(q_1^2,q_2^2)$, depend on the photon momenta squared q_1^2 and q_2^2; the limit values $q_1^2 = 0$ and $q_2^2 = 0$ correspond to the two-photon decay. We also use the notation $p = q_1 + q_2$ and $q = (q_1 - q_2)/2$.

The moment operators read

$$S^{(0)}_{\mu\nu,\alpha\beta}(p,q) = g^{\perp\perp}_{\alpha\beta}\left(\frac{q_\mu q_\nu}{q^2} - \frac{1}{3}g^{\perp}_{\mu\nu}\right) \quad (2)$$

and

$$S^{(2)}_{\mu\nu,\alpha\beta}(p,q) = g^{\perp\perp}_{\mu\alpha}g^{\perp\perp}_{\nu\beta} + g^{\perp\perp}_{\mu\beta}g^{\perp\perp}_{\nu\alpha} - g^{\perp\perp}_{\mu\nu}g^{\perp\perp}_{\alpha\beta}, \quad (3)$$

where metric tensors $g^{\perp}_{\mu\nu}$ and $g^{\perp\perp}_{\alpha\beta}$ are determined as follows:

$$g^{\perp}_{\mu\nu} = g_{\mu\nu} - \frac{p_\mu p_\nu}{p^2}, \quad g^{\perp\perp}_{\alpha\beta} = g_{\alpha\beta} - \frac{q_\alpha q_\beta}{q^2} - \frac{p_\alpha p_\beta}{p^2}. \quad (4)$$

The moment operators are orthogonal in the space of photon polarizations: $S^{(0)}_{\mu\nu,\alpha\beta}S^{(2)}_{\mu'\nu',\alpha\beta} = 0$.

The spin structure of the amplitude $A^{(T)}_{\mu\nu,\alpha\beta}$ is discussed in more detail in Appendix A; also presented there is a connection between amplitudes written in terms of spin operators and standard helicity amplitudes.

2.2. Form Factor $F^{(H)}_{T\to\gamma\gamma}(q_1^2,q_2^2)$

Following the prescription of [21], we write the amplitude of the process of Fig. 1*a* in terms of the spectral representation in the channels related to tensor meson and photon $\gamma(q_2)$. The double spectral representation for the form factor $F^{(H)}_{T\to\gamma\gamma}(q_1^2,q_2^2)$ with $H = 0, 2$ reads

$$F^{(H)}_{T\to\gamma\gamma}(q_1^2,q_2^2) = Z_T\sqrt{N_c}\int\limits_{4m^2}^{\infty}\frac{dsds'}{\pi^2} \times \frac{G_{T\to q\bar{q}}(s)}{s - m_T^2}d\Phi(P,P';k_1,k_1',k_2) \times S^{(H)}(P^2,P'^2,\tilde{q}^2)\frac{G_{\gamma\to q\bar{q}}(s')}{s' - q_2^2}. \quad (5)$$

The right-hand side of Eq. (5), being a convolution of the $q\bar{q}$ vertices, $G_{T\to q\bar{q}}$ and $G_{\gamma\to q\bar{q}}$, is determined by the $q\bar{q}$ phase space $d\Phi$ and $q\bar{q}$ spin factor $S^{(H)}$. In the spectral integral (5), the momenta of the intermediate states differ from those of the initial/final states. The corresponding momenta for intermediate states are redenoted as is shown in Fig. 1*b*:

$$q_1 \to P - P', \quad q_2 \to P', \quad p \to P, \quad P^2 = s, \quad P'^2 = s', \quad (P'-P)^2 = \tilde{q}^2 = q_1^2. \quad (6)$$

It should be stressed that we fix $\tilde{q}^2 = q_1^2$, although $P' - P = \tilde{q} \neq q_1$. The triangle-diagram phase space $d\Phi(P,P';k_1,k_1',k_2)$ is equal to

$$d\Phi(P,P';k_1,k_1',k_2) = \frac{1}{4}\frac{d^3k_1}{(2\pi)^3\cdot 2k_{10}} \times \frac{d^3k_1'}{(2\pi)^3\cdot 2k_{10}'}\frac{d^3k_2}{(2\pi)^3\cdot 2k_{20}}(2\pi)^4\delta^{(4)}(P - k_1 - k_2) \times (2\pi)^4\delta^{(4)}\left(P' - k_1' - k_2\right). \quad (7)$$

The factor Z_T is determined by the quark content of the tensor meson. For the a_2 meson and $n\bar{n}$ or $s\bar{s}$ components in the f_2 meson, the charge factors are equal to

$$Z_{a_2} = 2\frac{e_u^2 - e_d^2}{\sqrt{2}}, \quad Z_{n\bar{n}} = 2\frac{e_u^2 + e_d^2}{\sqrt{2}}, \quad Z_{s\bar{s}} = 2e_s^2. \quad (8)$$

The factor $\sqrt{N_c}$, where $N_c = 3$ is the number of colors, is related to the normalization of the photon vertex made in [21]. We have two sorts of diagrams: with quark lines drawn clockwise and anticlockwise; the factor 2 in (8) stands for this doubling. The vertices $G_{\gamma\to n\bar{n}}(s')$ and $G_{\gamma\to s\bar{s}}(s')$ were found in [21]; the photon wave function $G_{\gamma\to n\bar{n}}(s)/s$ is shown in Fig. 2.

2.2.1. Wave functions for the $1^3P_2q\bar{q}$ and $2^3P_2q\bar{q}$ states. We parametrize the wave functions of mesons of the basic multiplet, $1^3P_2q\bar{q}$, in the exponential form

$$\psi_T(s) = \frac{G_{T\to q\bar{q}}(s)}{s - m_T^2} = Ce^{-bs}, \qquad (9)$$

where C is the normalization constant, $\psi_T \otimes \psi_T = 1$, and the parameter b can be related to the tensor-meson radius squared.

For mesons of the first radial excitation, $2^3P_2q\bar{q}$, the wave functions can be written using exponential approximation as

$$\psi_{T1}(s) = C_1e^{-b_1s}(D_1s - 1). \qquad (10)$$

The parameter b_1 can be related to the radius of the radial excitation state; then, the values C_1 and D_1 are fixed by the normalization and orthogonality requirements, $\psi_{T1} \otimes \psi_{T1} = 1$ and $\psi_T \otimes \psi_{T1} = 0$.

2.3. Spin Structure Factors $S^{(0)}(P^2, P'^2, \tilde{q}^2)$ and $S^{(2)}(P^2, P'^2, \tilde{q}^2)$

For the amplitude of Fig. 1*b* with transversely polarized photons, the spin structure factors are fixed by the vertex for transition $T \to q\bar{q}$, and we denote this vertex as $T_{\mu\nu}$. One has

$$\mathrm{tr}\left[\gamma_\beta^{\perp\perp}(\hat{k}_1' + m)\gamma_\alpha^{\perp\perp}(\hat{k}_1 + m)T_{\mu\nu}(\hat{k}_2 - m)\right] \qquad (11)$$
$$= S^{(0)}_{\mu\nu,\alpha\beta}(P, P'_\perp)S^{(0)}(P^2, P'^2, \tilde{q}^2)$$
$$+ S^{(2)}_{\mu\nu,\alpha\beta}(P, P'_\perp)S^{(2)}(P^2, P'^2, \tilde{q}^2).$$

Here, $\gamma_\alpha^{\perp\perp}$ and $\gamma_\beta^{\perp\perp}$ stand for photon vertices, $\gamma_\alpha^{\perp\perp} = g_{\alpha\alpha'}^{\perp\perp}\gamma_{\alpha'}$, while $g_{\alpha\alpha'}^{\perp\perp}$ is determined by (4) with the substitutions $q_1 \to P - P'$ and $q_2 \to P'$ [recall that, in (4), $p = q_1 + q_2$ and $q = (q_1 - q_2)/2$]. The moment operators $S^{(0)}_{\mu\nu,\alpha\beta}(P, P'_\perp)$ and $S^{(2)}_{\mu\nu,\alpha\beta}(P, P'_\perp)$ also work in the intermediate-state momentum space. Recall that the momenta k_1', k_1, and k_2 in (11) are on the mass shell.

The vertex $T_{\mu\nu}$ taken in a minimal form reads

$$T^{(k)}_{\mu\nu} = k_\mu\gamma_\nu + k_\nu\gamma_\mu - \frac{2}{3}g^\perp_{\mu\nu}\hat{k}, \qquad (12)$$

where $k = k_1 - k_2$ and $g^\perp_{\mu\nu}P_\nu = 0$. With $T_{\mu\nu}$ determined by (12), we present the spin structure factors $S^{(H)}(P^2, P'^2, \tilde{q}^2)$ at $q_2^2 = 0$ and small $q_1^2 = \tilde{q}^2 \equiv -Q^2$. Below, we denote $\Sigma = (s + s')/2$ and $\Delta = s - s'$ and consider that $\Delta \sim Q$. For the nonvanishing terms in the limit $Q^2 \to 0$, we have

$$S^{(0)}(P^2, P'^2, -Q^2) = \frac{64m^2\Sigma^2Q^4}{(\Delta^2 + 4\Sigma Q^2)^2} \qquad (13)$$

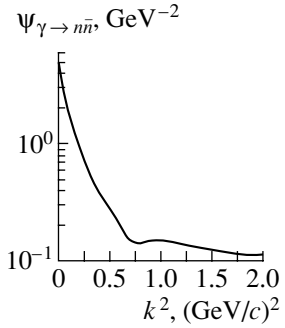

Fig. 2. Photon wave function for nonstrange quarks, $\psi_{\gamma\to n\bar{n}}(k^2) = G_{\gamma\to n\bar{n}}(s)/s = g_\gamma(k^2)/(k^2 + m^2)$, where $k^2 = s/4 - m^2$; the wave function for the $s\bar{s}$ component is equal to $\psi_{\gamma\to s\bar{s}}(k^2) = g_\gamma(k^2)/(k^2 + m_s^2)$, where m_s is the constituent s-quark mass.

$$\times\left(4m^2 - \Sigma\right) + \frac{4\Sigma Q^2\Delta^2}{(\Delta^2 + 4\Sigma Q^2)^2}\left(32m^4 + 8m^2\Sigma\right.$$
$$\left. - 3\Sigma^2\right) + \frac{4m^2\Delta^4}{(\Delta^2 + 4\Sigma Q^2)^2}\left(4m^2 + 3\Sigma\right)$$

and

$$S^{(2)}(P^2, P'^2, -Q^2) = \frac{8\Sigma^2Q^4}{(\Delta^2 + 4\Sigma Q^2)^2} \qquad (14)$$
$$\times\left(-16m^4 + \Sigma^2\right) + \frac{4\Sigma Q^2\Delta^2}{(\Delta^2 + 4\Sigma Q^2)^2}\left(-16m^4\right.$$
$$\left. - 4m^2\Sigma + \Sigma^2\right) + \frac{4m^2\Delta^4}{(\Delta^2 + 4\Sigma Q^2)^2}\left(-2m^2 - \Sigma\right).$$

2.3.1. Spin structure factors $S^{(H)}(P^2, P'^2, \tilde{q}^2)$ for pure $q\bar{q}(L = 1)$ and $q\bar{q}(L = 3)$ states. The $q\bar{q}(2^{++})$ state can be constructed in two ways, namely, with the $q\bar{q}$ orbital angular momenta of $L = 1$ and $L = 3$ (the $^3P_2q\bar{q}$ and $^3F_2q\bar{q}$ states). The vertex $T_{\mu\nu}$ of Eq. (12), corresponding to the dominant P-wave $q\bar{q}$ state, also includes a certain admixture of the F-wave $q\bar{q}$ state.

The vertex for the production of pure $q\bar{q}(L = 1)$ state reads

$$T^{(L=1),(k)}_{\mu\nu} = k_\mu\Gamma_\nu + k_\nu\Gamma_\mu - \frac{2}{3}g^\perp_{\mu\nu}(\Gamma k), \qquad (15)$$
$$\Gamma_\mu = \gamma_\mu^\perp - \frac{k_\mu}{2m + \sqrt{s}},$$

where the operator Γ_μ selects the spin-1 state for $q\bar{q}$, and $\gamma_\mu^\perp = g^\perp_{\mu\nu}\gamma_\nu$ (see [23, 24] for details). We present the corresponding spin factors, $S^{(0)}_{L=1}(P^2, P'^2, -Q^2)$ and $S^{(2)}_{L=1}(P^2, P'^2, -Q^2)$, in Appendix B.

The $(L = 3)$ operator for the $^3F_2q\bar{q}$ state is equal to

$$T^{(L=3),(k)}_{\mu\nu} = k_\mu k_\nu(\Gamma k) \qquad (16)$$

$$- \frac{k^2}{5}\left(g^{\perp}_{\mu\nu}(\Gamma k) + \Gamma_\mu k_\nu + \Gamma_\nu k_\mu\right).$$

The corresponding spin factors, $S^{(0)}_{L=3}(P^2, P'^2, -Q^2)$ and $S^{(2)}_{L=3}(P^2, P'^2, -Q^2)$, are also given in Appendix B.

2.4. Spectral Integral Representation

In formula (5), one can integrate over the phase space by using δ functions given by Eq. (7). Thus, we have

$$F^{(H)}_{T\to\gamma\gamma}(-Q^2, 0) = Z_T\sqrt{N_c}\int\limits_{4m^2}^{\infty}\frac{ds ds'}{\pi^2}\psi_T(s)\psi_\gamma(s') \tag{17}$$

$$\times\frac{\theta\left(ss'Q^2 - m^2\lambda(s, s', -Q^2)\right)}{16\sqrt{\lambda(s, s', -Q^2)}}S^{(H)}(s, s', -Q^2)$$

with

$$\lambda(s, s', -Q^2) = (s' - s)^2 + 2Q^2(s' + s) + Q^4. \tag{18}$$

The θ function restricts the integration region for different Q^2: $\theta(X) = 1$ at $X \geq 0$ and $\theta(X) = 0$ at $X < 0$.

In the limit $Q^2 \to 0$, one has

$$F^{(H)}_{T\to\gamma\gamma}(-Q^2 \to 0, 0) = Z_T\sqrt{N_c}$$

$$\times\int\limits_{4m^2}^{\infty}\frac{d\Sigma}{\pi}\psi_T(\Sigma)\psi_\gamma(\Sigma)\int\limits_{-b}^{+b}\frac{d\Delta}{\pi}\frac{S^{(H)}_{T\to\gamma\gamma}(s, s', -Q^2)}{16\sqrt{\Lambda(\Sigma, \Delta, Q^2)}},$$

$$b = Q\sqrt{\Sigma(\Sigma/m^2 - 4)}, \tag{19}$$

$$\Lambda(\Sigma, \Delta, Q^2) = \Delta^2 + 4\Sigma Q^2,$$

where the spin factors $S^{(H)}(s, s', -Q^2)$ are given in (13) and (14).

After integration with respect to Δ, the spectral representation for the form factor $F^{(H)}_{T\to\gamma\gamma}(0, 0)$ reads

$$F^{(H)}_{T\to\gamma\gamma}(0, 0) = \frac{Z_T\sqrt{N_c}}{16\pi}\int\limits_{4m^2}^{\infty}\frac{ds}{\pi}\psi_T(s)\psi_\gamma(s)I^{(H)}(s), \tag{20}$$

where

$$I^{(0)}(s) = -2\sqrt{s\,(s - 4m^2)}\left(12m^2 + s\right) \tag{21}$$

$$+ 4m^2\left(4m^2 + 3s\right)\ln\frac{s + \sqrt{s\,(s - 4m^2)}}{s - \sqrt{s\,(s - 4m^2)}}$$

and

$$I^{(2)}(s) = \frac{4\sqrt{s\,(s - 4m^2)}}{3}\left(5m^2 + s\right) \tag{22}$$

$$- 4m^2\left(2m^2 + s\right)\ln\frac{s + \sqrt{s\,(s - 4m^2)}}{s - \sqrt{s\,(s - 4m^2)}}.$$

The tensor-meson decay form factors of reaction $T \to \gamma\gamma$ with vertices for pure $q\bar{q}(L = 1)$ and $q\bar{q}(L = 3)$ states [see (15) and (16)] are given in Appendix C.

2.5. Light-Cone Variables

Formula (5) allows one to make the transformation to the light-cone variables easily using the boost along the z axis. Let us use the frame in which the initial tensor meson moves along the z axis with the momentum $p \to \infty$:

$$P = \left(p + \frac{s}{2p}, 0, p\right), \quad P' = \left(p + \frac{s' + Q^2}{2p}, \mathbf{Q}, p\right). \tag{23}$$

Then, the transition form factor of reaction $T \to \gamma^*(Q^2)\gamma$ reads

$$F^{(H)}_{T\to\gamma\gamma}(-Q^2, 0) = \frac{Z_T\sqrt{N_c}}{16\pi^3}\int\limits_0^1\frac{dx}{x(1 - x)^2} \tag{24}$$

$$\times\int d^2k_\perp\psi_T(s)\psi_\gamma(s')S^{(H)}(s, s', -Q^2),$$

where $x = k_{2z}/p$, $\mathbf{k}_\perp = \mathbf{k}_{2\perp}$, and the $q\bar{q}$ invariant mass squares are

$$s = \frac{m^2 + k^2_\perp}{x(1 - x)}, \quad s' = \frac{m^2 + (-x\mathbf{Q} + \mathbf{k}_\perp)^2}{x(1 - x)}. \tag{25}$$

2.6. Tensor-Meson Charge Form Factor

In order to relate the wave-function parameters C and b entering into (9) to the tensor-meson radius squared, we calculate the meson charge form factor averaged over polarizations; the corresponding process is shown diagrammatically in Fig. 1*c*. Thus, this form-factor amplitude has the structure

$$A_\mu = (p_\mu + p'_\mu)F_T(-Q^2), \tag{26}$$

where the meson charge form factor $F_T(Q^2)$ is the convolution of the tensor-meson wave functions, $\psi_T \otimes \psi_T$.

2.6.1. Charge form factor in the light-cone variables. Using light-cone variables, one can express the $q\bar{q}$-meson charge form factor as follows (see, for example, [10, 21]):

$$F_T(-Q^2) = \frac{1}{16\pi^3}\int\limits_0^1\frac{dx}{x(1 - x)^2} \tag{27}$$

$$\times\int d^2k_\perp\psi_T(s)\psi_T(s')S_T(s, s', -Q^2),$$

$S_T(s,s',-Q^2)$ being determined by the quark loop trace in the intermediate state:

$$\frac{1}{5}\mathrm{tr}[T^{(k)}_{\mu\nu}(\hat{k}_1+m)\gamma_\alpha(\hat{k}'_1+m)T^{(k')}_{\mu\nu}(\hat{k}_2-m)] \quad (28)$$
$$= [P'_\alpha + P_\alpha - \frac{s'-s}{Q^2}(P'_\alpha - P_\alpha)]S_T(s,s',-Q^2),$$

where $(P'-P)^2 = -Q^2$.

To relate the wave-function parameters to the tensor-meson radius squared, R_T^2 , we may restrict ourselves to the consideration of the low-Q^2 region. The low-Q^2 charge form factor can be expanded in a series in Q^2:

$$F_T(-Q^2) \simeq 1 - \frac{1}{6}R_T^2 Q^2. \quad (29)$$

At small Q^2, one has

$$S_T(s,s',-Q^2) = \frac{Q^2}{45(\Delta^2+4\Sigma Q^2)\Sigma^2} \quad (30)$$
$$\times\left[-48\Sigma^3\left(8m^2+3\Sigma\right)\left(4m^2-\Sigma\right)\right.$$
$$-16Q^2\Sigma^2\left(64m^4-22m^2\Sigma+9\Sigma^2\right)$$
$$\left.+8\Sigma\Delta^2\left(40m^4+29m^2\Sigma-9\Sigma^2\right)\right]$$
$$-\frac{Q^2\Sigma^3\left(8m^2+3\Sigma\right)\left(4m^2-\Sigma\right)}{45(\Delta^2+4\Sigma Q^2)^2}$$
$$\times\left[\frac{\Delta^4}{4\Sigma^4}+\frac{Q^2\Delta^2}{\Sigma^3}-\frac{Q^4}{\Sigma^2}\right].$$

Recall that $\Sigma = (s+s')/2$ and $\Delta = s-s'$.

2.6.2. Spectral integral representation for charge form factor. Expanded in a series in Q^2, the spectral integral for charge form factor, $F_T(-Q^2)$, reads

$$F_T(-Q^2) \simeq \frac{1}{16\pi}\int\limits_{4m^2}^{\infty}\frac{ds}{\pi}\psi_T^2(s) \quad (31)$$
$$\times\left(I(s)-\frac{Q^2}{6}I_R(s)\right),$$

where

$$I(s) = \frac{8\sqrt{s\,(s-4m^2)}}{15s}\left(8m^2+3s\right)\left(s-4m^2\right), \quad (32)$$

$$I_R(s) = \frac{4\sqrt{s\,(s-4m^2)}}{5s^3}\left(-64m^6-40m^4 s\right.$$
$$\left.+26m^2s^2+9s^3\right)+\frac{8}{15s}\left(16m^4-46m^2s+9s^2\right)$$
$$\times\ln\frac{s+\sqrt{s\,(s-4m^2)}}{s-\sqrt{s\,(s-4m^2)}}.$$

Comparison of this expression with formula (29) gives us the parameters of the tensor-meson wave function.

Formulas (31) and (32) can be used for the determination of the wave-function parameters for any $n^3P_2q\bar{q}$ meson.

3. RESULTS

Here, the results of the calculation of the $\gamma\gamma$ partial widths for mesons of the basic multiplet $1^3P_2q\bar{q}$, that is, $a_2(1320)$, $f_2(1270)$, and $f_2(1525)$, are presented. According to [25], mesons of the first radial excitation, $2^3P_2q\bar{q}$, are $a_2(1660)$, $f_2(1640)$, and $f_2(1800)$, and we calculate their $\gamma\gamma$ partial widths as well. We also estimate the $\gamma\gamma$ widths of the F-wave mesons, namely, the members of the $1^3F_2q\bar{q}$ nonet, these mesons being located in the vicinity of 2000 MeV [25].

3.1. Tensor-Meson $\gamma\gamma$ Decay Partial Width

Partial width $\Gamma_{T\to\gamma\gamma}$ is determined as follows:

$$m_T\Gamma_{T\to\gamma\gamma} = \frac{1}{2}\int d\Phi_2(p;q_1,q_2)\frac{1}{5}\sum_{\mu\nu,\alpha\beta}|A_{\mu\nu,\alpha\beta}|^2 \quad (33)$$
$$= \frac{4}{5}\pi\alpha^2\left[\frac{1}{6}\left(F^{(0)}_{T\to\gamma\gamma}(0,0)\right)^2+\left(F^{(2)}_{T\to\gamma\gamma}(0,0)\right)^2\right].$$

Here, m_T is the mass of the tensor meson; the summation is carried out over outgoing-photon polarizations (α,β), and the photon identity factor $1/2$ is written explicitly; averaging over the tensor-meson polarizations (μ,ν) results in the factor $1/5$. The two-particle invariant phase space is equal to

$$d\Phi_2(p;q_1,q_2) = \frac{1}{2}\frac{d^3q_1}{(2\pi)^3\cdot 2q_{10}} \quad (34)$$
$$\times\frac{d^3q_2}{(2\pi)^3\cdot 2q_{20}}(2\pi)^4\delta^{(4)}\left(p-q_1-q_2\right),$$

and for photons, $\int d\Phi_2(p;q_1,q_2) = 1/16\pi$.

3.2. Transition Form Factors $F^{(H)}_{n\bar{n}\to\gamma\gamma}$ and $F^{(H)}_{s\bar{s}\to\gamma\gamma}$ for Mesons of the $1^3P_2q\bar{q}$ Nonet

The transition form factors $F^{(H)}_{n\bar{n}\to\gamma\gamma}$ and $F^{(H)}_{s\bar{s}\to\gamma\gamma}$ are determined by Eq. (20). They depend on the quark mass and type of the vertex entering into the spin factor, as well as the tensor meson wave function. For nonstrange quarks, the ratios $F^{(H)}_{a_2\to\gamma\gamma}(0,0)/Z_{a_2}$ and $F^{(H)}_{n\bar{n}\to\gamma\gamma}(0,0)/Z_{n\bar{n}}$ are equal to each other, provided the a_2 and $(n\bar{n})_2$ states belong to the same $q\bar{q}$ multiplet. The magnitudes of $F^{(H)}_{n\bar{n}\to\gamma\gamma}(0,0)$ and

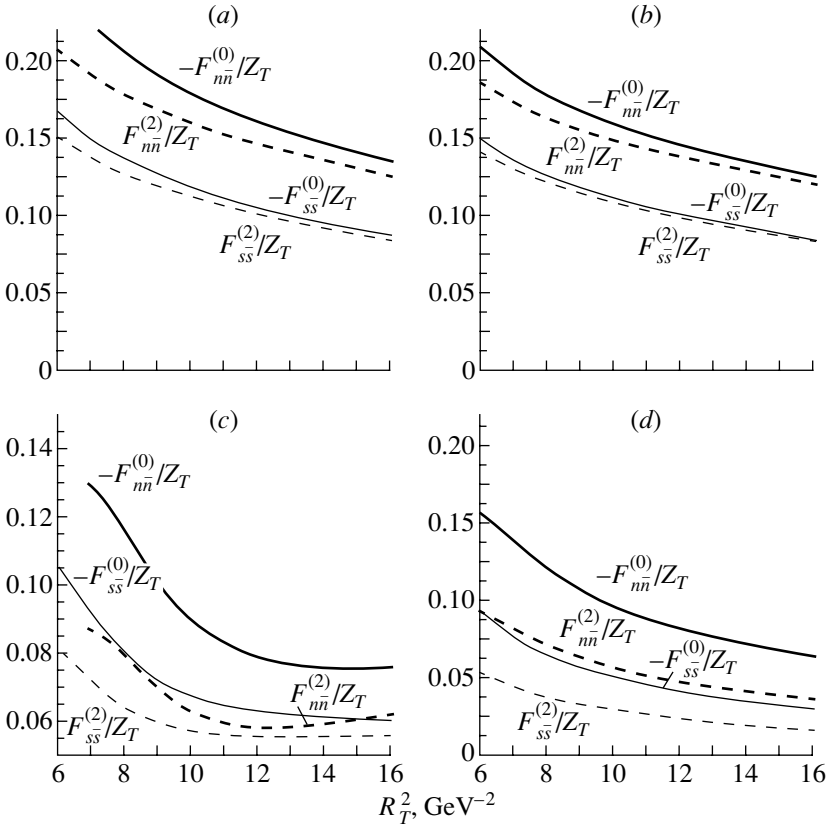

Fig. 3. Transition form factors of reaction $T \to \gamma\gamma$ [see (17) or (24)] for the nonstrange ($n\bar{n}$) and strange ($s\bar{s}$) quarks vs. mean tensor-meson radius squared R^2_T. (*a*) $F^{(H)}_{q\bar{q}}(0,0)$ for $1^3P_2q\bar{q}$ state with minimal vertex, Eqs. (9) and (12); (*b*) $F^{(H)}_{q\bar{q}}(0,0)$ for the vertex determined by (15); (*c*) $F^{(H)}_{q\bar{q}}(0,0)$ for $2^3P_2q\bar{q}$ state with the vertex given by (10) and (12); (*d*) $F^{(H)}_{q\bar{q}}(0,0)$ for $1^3F_2q\bar{q}$ state with vertex given by (9) and (16).

$F^{(H)}_{s\bar{s}\to\gamma\gamma}(0,0)$ are shown in Fig. 3 for different tensor mesons.

The transition form factors for mesons of the basic multiplet $1^3P_2q\bar{q}$ for the case where the transition vertex $T \to q\bar{q}$ is chosen in the minimal form (12) are shown in Fig. 3*a*. Form factors decrease noticeably with the increase in radius of the $q\bar{q}$ system in the interval $6 \le R^2_T \le 16$ GeV^{-2}. The calculated form factors reveal a strong dependence on the quark mass. In our calculations, we set $m = 350$ MeV for the nonstrange quark and $m = 500$ MeV for the strange quark. One can see that, with the increase in quark mass by 150 MeV, the transition form factors fall by a factor of 1.5.

In Fig. 3*b*, the form factors $F^{(H)}_{q\bar{q}\to\gamma\gamma}(0,0)/Z_{q\bar{q}}$ are shown for mesons $1^3P_2q\bar{q}$ in case where the vertex of reaction $T \to q\bar{q}$ is taken in the form (15), which corresponds to a pure P wave.

3.3. Decays $a_2 \to \gamma\gamma$

The form factor $F^{(H)}_{a_2\to\gamma\gamma}(0,0)$ is equal to that of the $n\bar{n}$ component, apart from the charge factor:

$$F^{(H)}_{a_2\to\gamma\gamma}(0,0) = \frac{Z_{a_2}}{Z_{n\bar{n}}} F^{(H)}_{n\bar{n}\to\gamma\gamma}(0,0). \qquad (35)$$

Since flavor structure of the a_2 meson is fixed, we can calculate partial $\gamma\gamma$ widths rather reliably.

In Fig. 4, the values of $\Gamma_{a_2(1320)\to\gamma\gamma}$ are shown vs. $R^2_{a_2(1320)}$ together with experimental data.

Recent measurements of the $\gamma\gamma$ partial width of the $a_2(1320)$ meson yielded $\Gamma_{a_2(1320)\to\gamma\gamma} = 0.98 \pm 0.05 \pm 0.09$ keV [26] and $\Gamma_{a_2(1320)\to\gamma\gamma} = 0.96 \pm 0.03 \pm 0.13$ keV [27] (corresponding areas are shown by close-hatched lines in Fig. 4). In addition, one should consider that the extraction of the signal $a_2(1320) \to \gamma\gamma$ faces the problem of correctly taking into account coherent background. In the analysis [28], it was shown that the measured value of $\Gamma_{a_2(1320)\to\gamma\gamma}$ can fall by a factor of $\sim$1.5 due to the "signal–background" interference. Therefore,

we estimate the allowed region for $\Gamma_{a_2(1320)\to\gamma\gamma}$ as $1.12 \le \Gamma_{a_2(1320)\to\gamma\gamma} \le 0.60$ keV (light-hatched lines in Fig. 4).

Figure 5*a* demonstrates a full set of the $a_2 \to \gamma\gamma$ widths. The thick solid curve is drawn for $\Gamma_{a_2(1320)\to\gamma\gamma}$ with the vertex given by (9) and (12), while the dashed curve presents $\Gamma_{a_2(1320)\to\gamma\gamma}$ for the vertex given by (9) and (15). The thin solid and dotted curves show, respectively, $\Gamma_{a_2(1660)\to\gamma\gamma}$ for the vertex given by (10) and (12) and $\Gamma_{a_2(2000)\to\gamma\gamma}$ for the vertex given by (9) and (16).

When comparing the calculated values with experimental data, one should keep in mind that quark masses are strictly fixed: as was mentioned above, $m = 350$ MeV for the nonstrange quark and $m = 500$ MeV for the strange quark. The same mass values were used in [10] for the calculation of the decays $a_0(980) \to \gamma\gamma$ and $f_0(980) \to \gamma\gamma$. Still, the two-photon decays of scalar mesons depend rather weakly on quark masses, while, for the tensor meson, the situation is quite the opposite: the decrease in constituent-quark mass by 10% results in the increase in the form factor $F^{(H)}_{n\bar{n}}(0,0)$ by approximately 10%, which means a 20% growth of the calculated value of $\Gamma_{a_2(1320)\to\gamma\gamma}$ at fixed $R^2_{a_2(1320)}$. The 10% uncertainty in the definition of the constituent-quark mass looks quite reasonable; therefore, the 20% accuracy of the model prediction for $\Gamma_{a_2(1320)\to\gamma\gamma}$ should be regarded as quite normal.

Coming back to the decay $a_2(1320) \to \gamma\gamma$, we conclude that the calculated values of $\Gamma_{a_2(1320)\to\gamma\gamma}$ demonstrate rather good agreement with data at $R^2_{a_2(1320)} \lesssim 12$ GeV^{-2}.

3.4. Decays $f_2(1270) \to \gamma\gamma$ and $f_2(1525) \to \gamma\gamma$

First, we consider the decays of mesons belonging to the basic $1^3P_2q\bar{q}$ nonet. We define flavor wave functions of $f_2(1270)$ and $f_2(1525)$ as follows:

$$\begin{aligned} f_2(1270): &\quad \cos\varphi_T n\bar{n} + \sin\varphi_T s\bar{s}, \\ f_2(1525): &\quad -\sin\varphi_T n\bar{n} + \cos\varphi_T s\bar{s}. \end{aligned} \tag{36}$$

Then, the form factors of the two-photon decays of f_2 mesons read

$$\begin{aligned} F^{(H)}_{f_2(1270)\to\gamma\gamma}(0,0) &= \cos\varphi_T F^{(H)}_{n\bar{n}\to\gamma\gamma}(0,0) \\ &\quad + \sin\varphi_T F^{(H)}_{s\bar{s}\to\gamma\gamma}(0,0), \\ F^{(H)}_{f_2(1525)\to\gamma\gamma}(0,0) &= -\sin\varphi_T F^{(H)}_{n\bar{n}\to\gamma\gamma}(0,0) \\ &\quad + \cos\varphi_T F^{(H)}_{s\bar{s}\to\gamma\gamma}(0,0). \end{aligned} \tag{37}$$

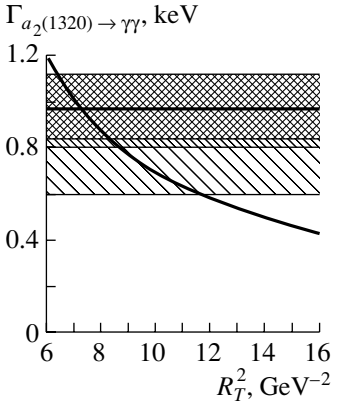

Fig. 4. Partial width $\Gamma_{a_2(1320)\to\gamma\gamma}$ (thick solid curve) along with the data (hatched areas—see Subsection 3.3) as a function of the mean meson radius squared R_T^2 for the vertex determined by Eqs. (9) and (12).

Hadronic decays tell us that $f_2(1270)$ is mainly the $n\bar{n}$ system, while $f_2(1525)$ is $s\bar{s}$, that is, the mixing angle φ_T is small.

Following [26–29], we accept partial widths as follows: $\Gamma_{f_2(1270)\to\gamma\gamma} = (2.60 \pm 0.25^{+0.00}_{-0.25})$ keV and $\Gamma_{f_2(1525)\to\gamma\gamma} = (0.097 \pm 0.015^{+0.00}_{-0.25})$ keV. The magnitude of the extracted signal depends on the type of model used for the description of the background. For the coherent background, the magnitude of the signal decreases, and the second error in $\Gamma_{f_2(1270)\to\gamma\gamma}$ and $\Gamma_{f_2(1525)\to\gamma\gamma}$ is related to the background uncertainties.

Figure 5*b* shows the values of $\Gamma_{f_2(1270)\to\gamma\gamma}$ and $\Gamma_{f_2(1525)\to\gamma\gamma}$ calculated under the assumption that $\varphi_T = 0$.

In Fig. 6, the results of the fit to data for $\Gamma_{f_2(1270)\to\gamma\gamma}$ and $\Gamma_{f_2(1525)\to\gamma\gamma}$ are shown without any fixation of φ_T. One can see that there exist two solutions: $\varphi_T \simeq 0^\circ$ and $\varphi_T \simeq 25^\circ$; in both cases, $R^2_T \lesssim 10$ GeV^{-2}. The rare-hatched areas correspond to the description of data near the low border: $2.10 \le \Gamma_{f_2(1270)\to\gamma\gamma} \le 2.35$ keV and $0.57 \le \Gamma_{f_2(1525)\to\gamma\gamma} \le 0.82$ keV.

3.5. Two-Photon Decays of the $2^3P_2q\bar{q}$ and $1^3F_2q\bar{q}$ States

As follows from [25], at 1600–1800 MeV, there are two tensor–isoscalar states—members of the $2^3P_2q\bar{q}$ multiplet: they are $f_2(1640)$ and $f_2(1800)$ (presumably $n\bar{n}$- and $s\bar{s}$-dominant states, correspondingly).

In Fig. 3*c*, the form factors of mesons from radial excitation nonet $2^3P_2q\bar{q}$ are shown: the transition vertex for reaction $T \to q\bar{q}$ is defined by the wave function (10) and spin matrix (12). A small magnitude

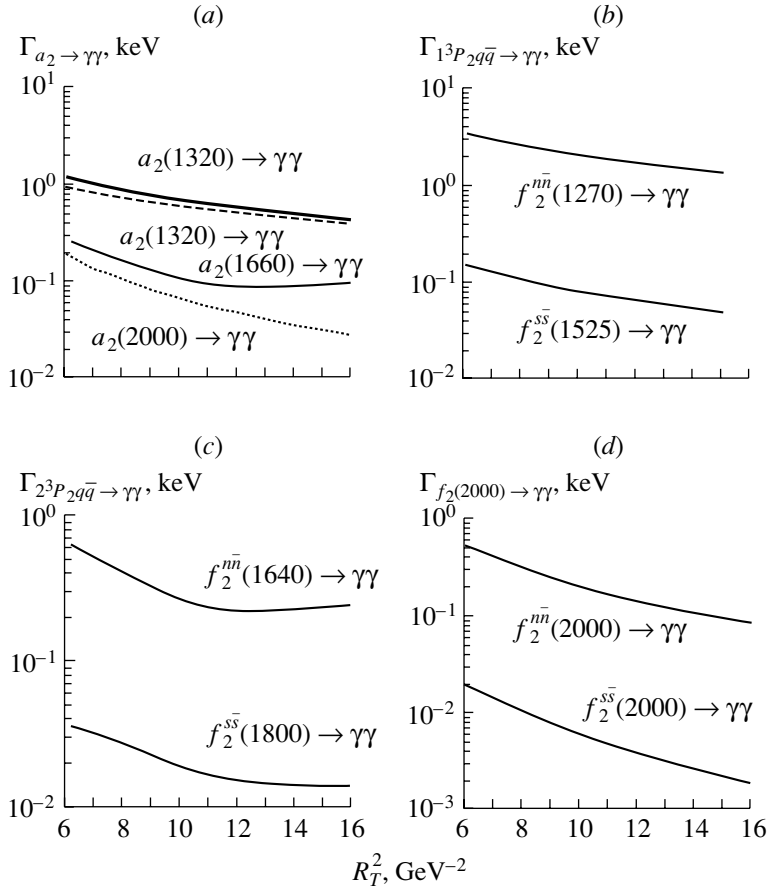

Fig. 5. Partial widths for a_2 and f_2 mesons vs. mean tensor-meson radius squared R_T^2. (*a*) Thick solid curve: $\Gamma_{a_2(1320)\to\gamma\gamma}$ for the vertex given by (9) and (12); dashed curve: $\Gamma_{a_2(1320)\to\gamma\gamma}$ for the vertex given by (9) and (15); dotted curve: $\Gamma_{a_2(2000)\to\gamma\gamma}$ for the vertex given by (9) and (16); thin solid curve: $\Gamma_{a_2(1660)\to\gamma\gamma}$ for the vertex given by (10) and (12). (*b*) Partial widths for isoscalar mesons of the basic $1^3P_2q\bar{q}$ nonet: for $f_2(1525)$ meson supposed to be a pure $s\bar{s}$ state and for $f_2(1270)$ assumed to be pure $n\bar{n}$. (*c*) Partial width for $f_2(1800)$ meson supposed to be a pure $2^3P_2s\bar{s}$ state and for $f_2(1640)$ considered as a pure $2^3P_2n\bar{n}$ state. (*d*) Partial widths for $1^3F_2s\bar{s}$ and $1^3F_2n\bar{n}$ states with mass $\sim$2000 MeV.

of transition form factors at $R_T^2 \gtrsim 10$ GeV^{-2} is due to a zero in the wave function (10). The form-factor values calculated for the transitions $2^3P_2q\bar{q}\to\gamma\gamma$ are in some way only approximate—they strongly depend on the details of the wave functions of $2^3P_2q\bar{q}$ states, and a comparatively weak variation, which, for example, does not change the mean radius squared, R^2, may affect the form-factor value by 100%.

A special feature of the two-photon decays of radial-excitation mesons is that their partial widths are considerably smaller than the corresponding widths of the basic mesons:

$$\Gamma_{1^3P_2n\bar{n}\to\gamma\gamma} \gg \Gamma_{2^3P_2n\bar{n}\to\gamma\gamma}, \qquad (38)$$
$$\Gamma_{1^3P_2s\bar{s}\to\gamma\gamma} \gg \Gamma_{2^3P_2s\bar{s}\to\gamma\gamma}.$$

The inequalities are due to the fact that the radial wave function of the $2^3P_2q\bar{q}$ state contains a zero; therefore, the convolution of wave functions, $\psi_{2^3P_2q\bar{q}}\otimes\psi_\gamma$, is significantly smaller than the convolution $\psi_{1^3P_2q\bar{q}}\otimes\psi_\gamma$ (wave function of basic state has no zeros).

In Fig. 5*c*, one can see partial widths for $f_2(1640)\to\gamma\gamma$ and $f_2(1800)\to\gamma\gamma$ calculated under the simple hypothesis that $f_2(1640)$ is a pure $n\bar{n}$ state, while $f_2(1800)$ is a pure $s\bar{s}$ state. One should emphasize that the probability for the transition $2^3P_2n\bar{n}\to\gamma\gamma$ is higher by an order of magnitude than $2^3P_2s\bar{s}\to\gamma\gamma$. This means that a comparatively small admixture of the $n\bar{n}$ component may considerably enhance the width of $\Gamma_{f_2(1800)\to\gamma\gamma}$, by a factor of 2 to 3 as compared to what follows from a pure $s\bar{s}$ state.

The verification of Eq. (38) has a fundamental meaning from the point of view of meson quark structure. Preliminary data of the L3 Collaboration [30] on the reaction $\gamma\gamma\to K_S^0K_S^0$ allow one to evaluate the transition $f_2(1800)\to\gamma\gamma$: Figure 7 shows the $K_S^0K_S^0$

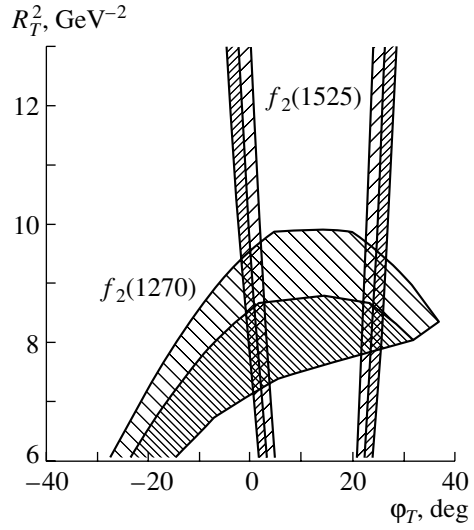

Fig. 6. The (R_T^2, φ) plot, where φ is the mixing angle for the flavor components $f_2(1270) = n\bar{n}\cos\varphi + s\bar{s}\sin\varphi$ and $f_2(1525) = -n\bar{n}\sin\varphi + s\bar{s}\cos\varphi$, with hatched areas that show the regions allowed by data for decays $f_2(1270) \to \gamma\gamma$ and $f_2(1525) \to \gamma\gamma$.

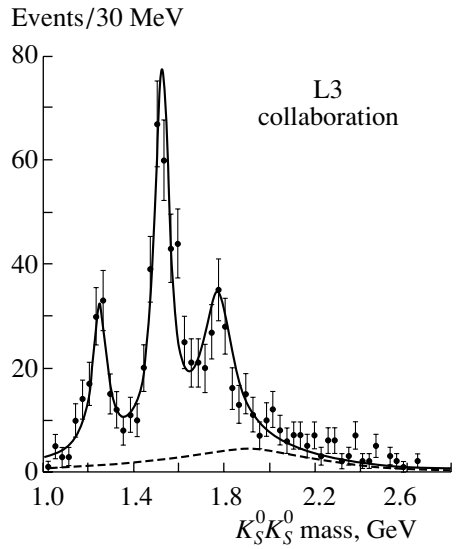

Fig. 7. The $K_S^0K_S^0$ mass spectrum in $\gamma\gamma \to K_S^0K_S^0$ [30] with production of $f_2(1525)$ and $f_2(1800)$. The dashed curve is the background, and the solid line is a full contribution.

spectrum, where the peaks corresponding to the production of $f_2(1525)$ and $f_2(1800)$ are distinctly seen. The description of these peaks in terms of Breit–Wigner resonances gives us the following relation:

$$\Gamma_{f_2(1800)\to\gamma\gamma} = \frac{\mathrm{BR}(f_2(1525) \to K\bar{K})}{\mathrm{BR}(f_2(1800) \to K\bar{K})} \times (0.10 \pm 0.05)\ \text{keV}. \quad (39)$$

Comparing (39) with partial width values shown in Fig. 5*c* proves that the L3 data agree qualitatively with (38), provided $\mathrm{Br}(f_2(1800) \to K\bar{K}) \sim \mathrm{Br}(f_2(1525) \to K\bar{K})$; that is, the decay channel $f_2(1800) \to K\bar{K}$ is not small. A rather large magnitude of the branching ratio for $f_2(1800) \to K\bar{K}$ looks natural because $f_2(1800)$ and $f_2(1525)$, according to the systematics in the (n, M^2) plane [25], should belong to the same trajectory, so they both have a rather large $s\bar{s}$ component. The fact that, according to (39), the partial width of the decay $f_2(1800) \to \gamma\gamma$ should be greater than $\Gamma_{2^3P_2s\bar{s}\to\gamma\gamma} \simeq 0.03$ keV may be explained by the 20–30% admixture of the $n\bar{n}$ component in $f_2(1800)$.

Figure 3*d* demonstrates form factors for mesons of the $1^3F_2q\bar{q}$ multiplet: the wave functions are defined by (9), while the vertex for reaction $T \to q\bar{q}$ has the form (16). In Fig. 5*d*, partial widths are shown for the transitions $1^3F_2n\bar{n} \to \gamma\gamma$ and $1^3F_2s\bar{s} \to \gamma\gamma$ calculated under the assumption that the masses of these states are on the order of 2000 MeV [25].

4. CONCLUSION

We have calculated the two-photon decays of tensor mesons, members of the $q\bar{q}$ multiplets $1^3P_2q\bar{q}$, $2^3P_2q\bar{q}$, and $1^3F_2q\bar{q}$.

The main goal was to calculate the decays of mesons of basic multiplet $1^3P_2q\bar{q}$: $a_2(1320)$, $f_2(1270)$, and $f_2(1525)$. All calculated partial widths of radiative decays of these mesons, $a_2(1320) \to \gamma\gamma$, $f_2(1270) \to \gamma\gamma$, and $f_2(1525) \to \gamma\gamma$, are in reasonable agreement with the hypothesis about the quark–antiquark structure of tensor mesons. In addition, radial wave functions of $a_2(1320)$, $f_2(1270)$, and $f_2(1525)$ are close to radial wave functions of $a_0(980)$ and $f_0(980)$ found in the study of radiative decays $a_0(980) \to \gamma\gamma$, $f_0(980) \to \gamma\gamma$, and $\phi(1020) \to \gamma\gamma$ [10]. The possibility of simultaneously describing scalar and tensor mesons using approximately equal wave functions may be considered as a strong argument in favor of the fact that all these mesons—tensor $a_2(1320)$, $f_2(1270)$, and $f_2(1525)$ and scalar $a_0(980)$ and $f_0(980)$—are members of the same P-wave $q\bar{q}$ multiplet.

The mesons of the first radial excitation, according to [25], are $a_2(1660)$, $f_2(1640)$, and $f_2(1800)$. We have calculated the partial $\gamma\gamma$ widths for all these mesons. The comparison with data of the L3 Collaboration on the reaction $f_2(1800) \to \gamma\gamma$ reveals qualitative agreement. However, it should be stressed that calculated values of partial $\gamma\gamma$ widths of mesons belonging to the $2^3P_2q\bar{q}$ multiplet are rather sensitive to the details of the wave function of the $q\bar{q}$ system.

We have also calculated the $\gamma\gamma$ width of mesons belonging to the $1^3F_2q\bar{q}$ multiplet. These mesons are located near 2000 MeV [25], and we may expect them to be a target for studying the reactions $\gamma\gamma \to$ hadrons.

ACKNOWLEDGMENTS

We are grateful to L.G. Dakhno and A.V. Sarantsev for useful discussions.

This study was supported by the Russian Foundation for Basic Research, project no. 01-02-17861.

APPENDIX A

Spin Structure of the Decay Amplitude $T \to \gamma\gamma$

The Completeness of Operators $S^{(H)}_{\mu\nu,\alpha\beta}$

Here we demonstrate that the convolution of the angular momentum operators for $L = 2$ and $L = 4$ with the helicity operator $S^{(2)}_{\alpha_1\alpha_2,\mu_1\mu_2}$ does not change the amplitude stucture given by (1).

The convolution of the helicity $H = 2$ operator with that of $L = 2$ reads

$$X^{(2)}_{\mu_2\beta}(q)S^{(2)}_{\alpha_1\alpha_2,\mu_1\beta}(p,q) \tag{A.1}$$
$$= \frac{3}{2}\left(q^{\perp}_{\mu_2}q^{\perp}_{\beta} - \frac{1}{3}q^2_{\perp}g^{\perp}_{\mu_2\beta}\right)$$
$$\times \left(g^{\perp\perp}_{\mu_1\alpha_1}g^{\perp\perp}_{\beta\alpha_2} + g^{\perp\perp}_{\mu_1\alpha_2}g^{\perp\perp}_{\beta\alpha_1} - g^{\perp\perp}_{\mu_1\beta}g^{\perp\perp}_{\alpha_1\alpha_2}\right)$$
$$= -\frac{q^2}{2}\left(g^{\perp\perp}_{\mu_1\alpha_1}g^{\perp\perp}_{\mu_2\alpha_2} + g^{\perp\perp}_{\mu_1\alpha_2}g^{\perp\perp}_{\mu_2\alpha_1} - g^{\perp\perp}_{\mu_1\mu_2}g^{\perp\perp}_{\alpha_1\alpha_2}\right)$$
$$= -\frac{q^2}{2}S^{(2)}_{\alpha_1\alpha_2,\mu_1\mu_2}(p,q).$$

The convolution of the helicity $H = 2$ operator with that of $L = 4$ also gives the term proportional to the $H = 2$ operator:

$$X^{(4)}_{\mu_1\mu_2\nu\lambda}(q)S^{(2)}_{\alpha_1\alpha_2,\nu\lambda}(p,q) = \frac{35}{8} \tag{A.2}$$
$$\times \left[q_{\mu_1}q_{\mu_2}q_{\nu}q_{\lambda} - \frac{q^2}{7}\left(g^{\perp}_{\mu_1\mu_2}q_{\nu}q_{\lambda} + g^{\perp}_{\mu_1\nu}q_{\mu_2}q_{\lambda}\right.\right.$$
$$\left.\left. + g^{\perp}_{\mu_2\nu}q_{\mu_1}q_{\lambda} + g^{\perp}_{\nu\lambda}q_{\mu_1}q_{\mu_2}\right)\right.$$
$$\left. - \frac{q^4}{35}\left(g^{\perp}_{\mu_1\mu_2}g^{\perp}_{\nu\lambda} + g^{\perp}_{\mu_1\nu}g^{\perp}_{\mu_2\lambda} + g^{\perp}_{\mu_1\lambda}g^{\perp}_{\mu_2\nu}\right)\right]$$
$$\times \left(g^{\perp\perp}_{\nu\alpha_1}g^{\perp\perp}_{\lambda\alpha_2} + g^{\perp\perp}_{\nu\alpha_2}g^{\perp\perp}_{\lambda\alpha_1} - g^{\perp\perp}_{\nu\lambda}g^{\perp\perp}_{\alpha_1\alpha_2}\right)$$
$$= \frac{q^4}{4}\left(g^{\perp\perp}_{\mu_1\alpha_1}g^{\perp\perp}_{\mu_2\alpha_2} + g^{\perp\perp}_{\mu_1\alpha_2}g^{\perp\perp}_{\mu_2\alpha_1} - g^{\perp\perp}_{\mu_1\mu_2}g^{\perp\perp}_{\alpha_1\alpha_2}\right)$$
$$= \frac{q^4}{4}S^{(2)}_{\alpha_1\alpha_2,\mu_1\mu_2}(p,q).$$

Thus, we see that both convolutions, the $H = 2$ operator with $L = 2$ and $L = 4$, give terms proportional to $S^{(2)}_{\alpha_1\alpha_2,\mu_1\mu_2}(p,q)$.

The Operators $S^{(H)}_{\mu\nu,\alpha\beta}$ and Standard Helicity Technique

To demonstrate the connection of the introduced operators with the standard helicity technique, we consider, as an example, the transition $\gamma\gamma \to 2^{++}$resonance $\to \pi^0\pi^0$. Using the momenta q_1 and q_2 for photons and k_1, k_2 for mesons, one has the following results for relative momenta and photon polarization vectors:

$$q = \frac{1}{2}(q_1 - q_2) = (0,0,0,q_z), \tag{A.3}$$
$$k = \frac{1}{2}(k_1 - k_2) = (0,k_x,k_y,k_z),$$
$$\epsilon = (0,\epsilon_x,\epsilon_y,0) = (0,\cos\phi,\sin\phi,0).$$

In the helicity basis,

$$\epsilon = (0,\epsilon_+,\epsilon_-,0), \tag{A.4}$$
$$\epsilon_+ = -\frac{1}{\sqrt{2}}(\epsilon_x + i\epsilon_y), \quad \epsilon_- = \frac{1}{\sqrt{2}}(\epsilon_x - i\epsilon_y).$$

The spin-dependent part of the amplitude with $H = 0$ reads

$$\epsilon^{(1)}_{\alpha}\epsilon^{(2)}_{\beta}g^{\perp\perp}_{\alpha\beta}X^{(2)}_{\mu\nu}(q)X^{(2)}_{\mu\nu}(k) \tag{A.5}$$
$$= \frac{9}{4}q^2k^2\left(\cos^2\theta - \frac{1}{3}\right)(\epsilon^{(1)}_{+}\epsilon^{(2)}_{+} + \epsilon^{(1)}_{-}\epsilon^{(2)}_{-}).$$

For $H = 2$, one has

$$\epsilon^{(1)}_{\alpha}\epsilon^{(2)}_{\beta}S^{(2)}_{\alpha\beta,\mu\nu}X^{(2)}_{\mu\nu}(k). \tag{A.6}$$

Different components are written as follows:

$$\epsilon^{(1)}_{+}\epsilon^{(2)}_{+}S^{(2)}_{++,\mu\nu}X^{(2)}_{\mu\nu}(k) = 0, \tag{A.7}$$
$$\epsilon^{(1)}_{+}\epsilon^{(2)}_{-}S^{(2)}_{+-,\mu\nu}X^{(2)}_{\mu\nu}(k) = \frac{3}{2}k^2\sin^2\theta$$
$$\times\left(1 + 2i\sin\phi e^{i\phi}\right),$$
$$\epsilon^{(1)}_{-}\epsilon^{(2)}_{+}S^{(2)}_{-+,\mu\nu}X^{(2)}_{\mu\nu}(k) = \frac{3}{2}k^2\sin^2\theta$$
$$\times\left(1 - 2i\sin\phi e^{-i\phi}\right),$$
$$\epsilon^{(1)}_{-}\epsilon^{(2)}_{-}S^{(2)}_{--,\mu\nu}X^{(2)}_{\mu\nu}(k) = 0.$$

Operators $S^{(H)}_{\mu\nu,\alpha\beta}$ and Analytic Properties of Vertex Function

The operators $S^{(H)}_{\mu\nu,\alpha\beta}$ are expressed in terms of the metric tensors $g^{\perp\perp}_{\alpha\beta}$ that work in the space perpendicular to the $T \to \gamma\gamma$ reaction plane. This metric tensor has the structure as follows:

$$g^{\perp\perp}_{\alpha\beta} = g_{\alpha\beta} - p_{\alpha}p_{\beta}/m^2_T + 4q_{\alpha}q_{\beta}/m^2_T. \tag{A.8}$$

The presence of factors $1/m^2_T$ may evoke the question about the behavior of the form-factor amplitude

at $m_T^2 = 0$. Of course, this is a far removed point for the reactions under consideration (the lowest tensor resonance is at $m_T \simeq 1600\ \mathrm{GeV}^2$). Still, this problem is important, so it should be considered it in detail.

When treating the reaction "composite system $\to \gamma\gamma$," one should distinguish it from the transition "constituents $\to \gamma\gamma$," in this case, $q\bar{q} \to \gamma\gamma$. These processes, though related to each other, are different: the amplitude for the process "composite system $\to \gamma\gamma$" (or $T \to \gamma\gamma$) is determined by the residue at the amplitude pole for reaction $q\bar{q} \to \gamma\gamma$ at $s = m_T^2$, where s is the invariant energy squared of the $q\bar{q}$ system. Both amplitudes should satisfy the requirement of gauge invariance (this requirement for the transition $T \to \gamma\gamma$ is imposed by the operators $S^{(H)}_{\mu\nu,\alpha\beta}$), but they have different analytic properties. In particular, the threshold theorems appropriate for $q\bar{q} \to \gamma\gamma$ do not work in the vertex function; i.e., for the residue at the pole $s = m_T^2$, the threshold theorems are realized by the interplay of pole and nonpole terms. Due to this fact, we must keep the mass of the tensor meson, m_T^2, in Eq. (A.8) at a fixed value.

The problem of interrelation of gauge invariance and analyticity in the spectral-integration technique was discussed in detail in [21, 23] for the transitions $q\bar{q} \to \gamma q\bar{q}$, $NN \to \gamma NN$, and $NN\gamma \to NN\gamma$ and the corresponding vertex functions describing composite systems (mesons and deuteron).

An opposite point of view according to which the threshold theorems should work for vertex functions was advocated in [31].

APPENDIX B

Spin Factors for Pure $q\bar{q}(L = 1)$ and $q\bar{q}(L = 3)$ States

At small Q^2, the spin factor $S^{(H=0)}_{L=1}(P^2 = s, P'^2 = s', -Q^2)$ for pure $(L = 1)$ state reads

$$S^{(0)}_{L=1}(s, s', -Q^2) = \frac{32\Sigma^2 Q^4}{(\Delta^2 + 4\Sigma Q^2)^2} \tag{A.9}$$
$$\times \left[2m^2\left(4m^2 - \Sigma\right) - \frac{m\left(4m^2 - \Sigma\right)^2}{2m + \sqrt{\Sigma}}\right]$$
$$+ \frac{4\Sigma Q^2\Delta^2}{(\Delta^2 + 4\Sigma Q^2)^2}\left[\left(32m^4 + 8m^2\Sigma - 3\Sigma^2\right)\right.$$
$$\left. - \frac{4m\left(16m^4 - \Sigma^2\right)}{2m + \sqrt{\Sigma}}\right] + \frac{4m^2\Delta^4}{(\Delta^2 + 4\Sigma Q^2)^2}$$
$$\times \left[\left(4m^2 + 3\Sigma\right) - \frac{4m\left(2m^2 + \Sigma\right)}{2m + \sqrt{\Sigma}}\right].$$

Recall that we use the notation $\Sigma = (s + s')/2$ and $\Delta = s - s'$.

For $H = 2$, one has

$$S^{(2)}_{L=1}(s, s', -Q^2) = \frac{8\Sigma^2 Q^4}{(\Delta^2 + 4\Sigma Q^2)^2} \tag{A.10}$$
$$\times \left[\left(-16m^4 + \Sigma^2\right) + \frac{2m\left(4m^2 - \Sigma\right)^2}{2m + \sqrt{\Sigma}}\right]$$
$$+ \frac{4\Sigma Q^2\Delta^2}{(\Delta^2 + 4\Sigma Q^2)^2}\left[\left(-16m^4 - 4m^2\Sigma + \Sigma^2\right)\right.$$
$$\left. + \frac{8m^3\left(4m^2 - \Sigma\right)}{2m + \sqrt{\Sigma}}\right] + \frac{4m^2\Delta^4}{(\Delta^2 + 4\Sigma Q^2)^2}$$
$$\times \left[\left(-2m^2 - \Sigma\right) + \frac{4m^3}{2m + \sqrt{\Sigma}}\right].$$

Correspondingly, the spin factors $S^{(H)}_{L=3}(s, s', -Q^2)$ for the pure $(L = 3)$ state are as follows:

$$S^{(0)}_{L=3}(s, s', -Q^2) = \frac{48\Sigma^2 Q^4}{5(\Delta^2 + 4\Sigma Q^2)^2} \tag{A.11}$$
$$\times \left[2m^2\left(4m^2 - \Sigma\right)^2 - \frac{m\left(4m^2 - \Sigma\right)^3}{2m + \sqrt{\Sigma}}\right]$$
$$+ \frac{12\Sigma Q^2\Delta^2}{5(\Delta^2 + 4\Sigma Q^2)^2}\left[\left(16m^4 + 4m^2\Sigma + \Sigma^2\right)\right.$$
$$\left. \times \left(4m^2 - \Sigma\right) - \frac{2m\left(4m^2 + \Sigma\right)\left(4m^2 - \Sigma\right)^2}{2m + \sqrt{\Sigma}}\right]$$
$$+ \frac{12m^2\Delta^4}{5(\Delta^2 + 4\Sigma Q^2)^2}\left[\left(8m^4 + 4m^2\Sigma + \Sigma^2\right)\right.$$
$$\left. - \frac{2m\left(4m^2 - \Sigma\right)\left(2m^2 + \Sigma\right)}{2m + \sqrt{\Sigma}}\right]$$

and

$$S^{(2)}_{L=3}(s, s', -Q^2) = \frac{4\Sigma^2 Q^4}{5(\Delta^2 + 4\Sigma Q^2)^2} \tag{A.12}$$
$$\times \left[\left(-6m^2 + \Sigma\right)\left(4m^2 - \Sigma\right)^2 + \frac{3m\left(4m^2 - \Sigma\right)^3}{2m + \sqrt{\Sigma}}\right]$$
$$+ \frac{2\Sigma Q^2\Delta^2}{5(\Delta^2 + 4\Sigma Q^2)^2}\left[\left(-24m^4 + 4m^2\Sigma - \Sigma^2\right)\right.$$
$$\left. \times \left(4m^2 - \Sigma\right) + \frac{12m^3\left(4m^2 - \Sigma\right)^2}{2m + \sqrt{\Sigma}}\right]$$
$$+ \frac{2m^2\Delta^4}{5(\Delta^2 + 4\Sigma Q^2)^2}\left[\left(-12m^4 + 2m^2\Sigma - \Sigma^2\right)\right.$$
$$\left. + \frac{6m^3\left(4m^2 - \Sigma\right)}{2m + \sqrt{\Sigma}}\right].$$

APPENDIX C

Transition Form Factors $F^{(H)}_{T(L)\to\gamma\gamma}(0,0)$

The spectral integral for the form factor $F^{(H)}_{T(L)\to\gamma\gamma}(0,0)$ with a pure $(L=1)$ or $(L=3)$ wave in the vertex $T\to q\bar q$ reads as follows:

$$F^{(H)}_{T(L)\to\gamma\gamma}(0,0)=\frac{Z_{q\bar q}\sqrt{N_c}}{16\pi} \times\int\limits_{4m^2}^{\infty}\frac{ds}{\pi}\psi_T(s)\psi_\gamma(s)I^{(H)}_L(s), \tag{A.13}$$

where, for $(L=1)$, one has

$$I^{(0)}_{L=1}(s)=-2\sqrt{s\,(s-4m^2)}\,\left(12m^2+3\right) + 4m^2\left(4m^2+3s\right)\ln\frac{s+\sqrt{s\,(s-4m^2)}}{s-\sqrt{s\,(s-4m^2)}} + \frac{16m^3}{2m+\sqrt{s}}\left[3\sqrt{s\,(s-4m^2)}-\left(2m^2+s\right) \times\ln\frac{s+\sqrt{s\,(s-4m^2)}}{s-\sqrt{s\,(s-4m^2)}}\right] \tag{A.14}$$

and

$$I^{(2)}_{L=1}(s)=\frac{4\sqrt{s\,(s-4m^2)}}{3}\left(5m^2+s\right) - 4m^2\left(2m^2+s\right)\ln\frac{s+\sqrt{s\,(s-4m^2)}}{s-\sqrt{s\,(s-4m^2)}} + \frac{4m}{2m+\sqrt{s}}\left[-\frac{\sqrt{s\,(s-4m^2)}}{3}\left(10m^2-s\right) + 4m^4\ln\frac{s+\sqrt{s\,(s-4m^2)}}{s-\sqrt{s\,(s-4m^2)}}\right]. \tag{A.15}$$

Analogously, for the $q\bar q(L=3)$ wave ($1^3F_2q\bar q$ multiplet), we have

$$I^{(0)}_{L=3}(s)=-\frac{2\sqrt{s\,(s-4m^2)}}{5}\left(72m^4 + 8m^2s+s^2\right)+\frac{12}{5}m^2\left(8m^4+4m^2s+s^2\right) \times\ln\frac{s+\sqrt{s\,(s-4m^2)}}{s-\sqrt{s\,(s-4m^2)}}+\frac{24m^3\left(s-4m^2\right)}{5(2m+\sqrt{s})} \times\left[-3\sqrt{s\,(s-4m^2)}+\left(2m^2+s\right) \times\ln\frac{s+\sqrt{s\,(s-4m^2)}}{s-\sqrt{s\,(s-4m^2)}}\right] \tag{A.16}$$

and

$$I^{(2)}_{L=3}(s)=\frac{2\sqrt{s\,(s-4m^2)}}{15}\left(30m^4 -4m^2s+s^2\right)-\frac{2}{5}m^2\left(12m^4-2m^2s+s^2\right) \times\ln\frac{s+\sqrt{s\,(s-4m^2)}}{s-\sqrt{s\,(s-4m^2)}}+\frac{m\left(s-4m^2\right)}{5(2m+\sqrt{s})} \times\left[\sqrt{s\,(s-4m^2)}\left(10m^2-s\right)-12m^4 \times\ln\frac{s+\sqrt{s\,(s-4m^2)}}{s-\sqrt{s\,(s-4m^2)}}\right]. \tag{A.17}$$

REFERENCES

1. E. Klempt, hep-ex/0101031.
2. L. Montanet, Nucl. Phys. B (Proc. Suppl.) **86**, 381 (2000).
3. R. Ricken, M. Koll, D. Merten, *et al.*, Eur. Phys. J. A **9**, 221 (2000).
4. V. V. Anisovich, Phys. Usp. **41**, 419 (1998).
5. V. V. Anisovich, Yu. D. Prokoshkin, and A. V. Sarantsev, Phys. Lett. B **389**, 388 (1996); V. V. Anisovich, A. A. Kondashov, Yu. D. Prokoshkin, *et al.*, Yad. Fiz. **63**, 1489 (2000) [Phys. At. Nucl. **63**, 1410 (2000)].
6. A. V. Anisovich and A. V. Sarantsev, Phys. Lett. B **413**, 137 (1997).
7. V. V. Anisovich, D. V. Bugg, and A. V. Sarantsev, Phys. Lett. B **437**, 209 (1998); Yad. Fiz. **62**, 1322 (1999) [Phys. At. Nucl. **62**, 1247 (1999)].
8. V. V. Anisovich, L. Montanet, and V. A. Nikonov, Phys. Lett. B **480**, 19 (2000).
9. A. V. Anisovich, V. V. Anisovich, D. V. Bugg, and V. A. Nikonov, Phys. Lett. B **456**, 80 (1999).
10. A. V. Anisovich, V. V. Anisovich, V. N. Markov, and V. A. Nikonov, Yad. Fiz. **65**, 523 (2002) [Phys. At. Nucl. **65**, 497 (2002)].
11. S. Spanier and N. A. Törnqvist, Eur. Phys. J. C **15**, 437 (2000).
12. V. V. Anisovich, A. A. Anselm, Ya. I. Azimov, *et al.*, Phys. Lett. **16**, 194 (1965).
13. W. E. Tirring, Phys. Lett. **16**, 335 (1965).
14. L. D. Solovjev, Phys. Lett. **16**, 345 (1965).
15. C. Becchi and G. Morpurgo, Phys. Rev. **140**, 687 (1965).
16. CMD-2 Collab. (R. R. Akhmetshin *et al.*), Phys. Lett. B **462**, 371, 380 (1999); SND Collab. (M. N. Achasov *et al.*), Phys. Lett. B **485**, 349 (2000).
17. M. Boglione and M. R. Pennington, Eur. Phys. J. C **9**, 11 (1999).
18. V. V. Anisovich, V. A. Nikonov, and A. V. Sarantsev, Yad. Fiz. **66**, 772 (2003) [Phys. At. Nucl. **66**, 741 (2003)]; hep-ph/0108188.
19. E. Borchi and R. Gatto, Phys. Lett. **14**, 352 (1965).

20. V. V. Anisovich, A. A. Anselm, Ya.I. Azimov, *et al.*, Pis'ma Zh. Éksp. Teor. Fiz. **2**, 109 (1965) [JETP Lett. **2**, 68 (1965)].
21. V. V. Anisovich, D. I. Melikhov, and V. A. Nikonov, Phys. Rev. D **55**, 2918 (1997); **52**, 5295 (1995).
22. Yu. D. Prokoshkin *et al.*, Phys. Dokl. **40**, 495 (1995); D. Alde *et al.*, Z. Phys. C **66**, 375 (1995).
23. V. V. Anisovich, M. N. Kobrinsky, D. I. Melikhov, and A. V. Sarantsev, Nucl. Phys. A **544**, 747 (1992); Yad. Fiz. **55**, 1773 (1992) [Sov. J. Nucl. Phys. **55**, 982 (1992)].
24. V. V. Anisovich, in *Hadron Spectroscopy and Confinement Problem*, Ed. by D. V. Bugg, NATO ASI Ser., Physics (Plenum Press, New York, 1996), Vol. 353, chap. V.
25. A. V. Anisovich, V. V. Anisovich, and A. V. Sarantsev, Phys. Rev. D **62**, 051502(R) (2000).
26. ARGUS Collab. (H. Albrecht *et al.*), Z. Phys. C **74**, 469 (1997).
27. L3 Collab. (M. Acciarri *et al.*), Phys. Lett. B **413**, 147 (1997).
28. ARGUS Collab. (H. Albrecht *et al.*), Z. Phys. C **48**, 183 (1990).
29. Particle Data Group (D. E. Groom *et al.*), Eur. Phys. J. C **15**, 1 (2000).
30. V. A. Schegelsky, in *Proceedings of the 9th International Conference on Hadron Spectroscopy, Protvino, Russia, 2001*.
31. N. N. Achasov, hep-ph/0110059.

Physics of Atomic Nuclei, Vol. 66, No. 5, 2003, pp. 928–940. From Yadernaya Fizika, Vol. 66, No. 5, 2003, pp. 960–972.

ELEMENTARY PARTICLES AND FIELDS
Theory

Process $\pi p \to \pi\pi N$ at High Energies and Moderate Momenta Transferred to the Nucleon and the Determination of Parameters of the $f_0(980)$ and $f_0(1300)$*

V. V. Anisovich** **and A. V. Sarantsev**

Petersburg Nuclear Physics Institute, Russian Academy of Sciences, Gatchina, 188350 Russia

Received April 11, 2002; in final form, July 15, 2002

Abstract—We present the results of simultaneous analysis of the S-wave $\pi\pi$ spectra in the reactions $\pi^- p \to (\pi\pi)_S n$ at $p_{\rm lab} = 38\,{\rm GeV}/c$ (GAMS) and $\pi^- p \to (\pi\pi)_S n$ at $p_{\rm lab} = 18\,{\rm GeV}/c$ (E852 Collaboration) at moderate momenta transferred to the nucleon, $|t| \lesssim 1.5\ ({\rm GeV}/c)^2$. The t distributions are described by the Reggeized π and a_1 exchanges provided by the leading and daughter trajectories, while the $M_{\pi\pi}$ spectra are determined by a set of scalar–isoscalar resonances. With $M_{\pi\pi}$ distributions averaged over different t intervals, we have found several solutions given by different t-channel-exchange mechanisms at $|t| \sim (0.5\text{–}1.5)\ ({\rm GeV}/c)^2$, with resonance parameters close to each other. We conclude that, despite a poor knowledge of the structure of the t exchange, the characteristics of resonances such as masses and widths can be reliably determined using the processes under discussion. As to pole positions, we have found $(1031 \pm 10) - i(35 \pm 6)$ MeV for $f_0(980)$ and $(1315 \pm 20) - i(150 \pm 30)$ MeV for $f_0(1300)$.

1. INTRODUCTION

The reactions of meson production in meson–nucleon collisions such as $\pi p \to \pi\pi N$, $K\bar{K}N$, $\eta\eta N$, and $KN \to \pi KN$ are traditionally a source of information about resonances in the two-meson spectra, namely, $\pi\pi$, $K\bar{K}$, $\eta\eta$, and πK (see, e.g., [1–3]). Therefore, it would be important to know what resonance characteristics could be reliably determined from these reactions and where one may encounter problems.

A set of the K-matrix analyses [4–10] are based on the three-meson production data in $p\bar{p}$ annihilation, together with data on the two-meson production in meson–nucleon high-energy collisions. The GAMS data for the reaction $\pi^- p \to \pi^0\pi^0 n$ at $p_{\rm lab} = 38\ {\rm GeV}/c$ [3], which represent the production of $\pi^0\pi^0$ at relatively large momentum transfers, are important for the investigation of the 1200–1400 MeV mass region: at the momentum transfer squared $|t| \sim 0.5\text{–}1.0\ ({\rm GeV}/c)^2$, a distinct peak was seen near 1300 MeV in $\pi^0\pi^0$ spectra.

The resonance $f_0(1300)$ (denoted as $f_0(1370)$ in the compilation [11]) was observed in the analysis of the $\pi\pi$ and $\eta\eta$ spectra obtained from the annihilation of $p\bar{p}$ (at rest, liquid H_2) $\to \pi^0\pi^0\pi^0$, $\pi^0\pi^0\eta$, $\pi^0\eta\eta$ [12–14]. In the most comprehensive analysis [13], where both resonance production (pole singularities of the amplitude) and meson rescattering in the final state (logarithmic singularities of the amplitude [15]) were taken into account, the magnitude for the complex-valued mass was found to be $M - i\Gamma/2 = (1335 \pm 40) - i(127^{+30}_{-20})$ MeV. In the analyses presented in [12, 14], a simplified fitting procedure was carried out, without accounting for logarithmic singularities: one obtained $(1340 \pm 40) - i(127^{+30}_{-20})$ MeV [14]. In the Crystal Barrel Collaboration paper [12], the claimed mass was 1365^{+20}_{-55} MeV, reflecting an attempt to make it closer to a scalar resonance, which was then defined at $1430 - i125$ MeV [16]. The existence of a scalar–isoscalar resonance was also claimed to be at $1430 - i73$ MeV [17] or $1420 - i110$ MeV [18].

But now it became obvious that the mass shift towards higher values is due to an insufficiently correct account of the interference resonance + background: the fact that, just due to a considerable interference in the $\pi\pi$ S wave, the resonance $f_0(1300)$ reveals itself not as a bump or minimum but as a shoulder in the spectrum was specially emphasized in [8, 13]. No visible structure was observed in the two-meson spectra from Crystal Barrel reactions $p\bar{p}$ (at rest, liquid H_2) $\to \pi^0\pi^0\pi^0$, $\pi^0\pi^0\eta$, $\pi^0\eta\eta$, although this state was strongly needed for the combined description of the three-meson Dalitz

*This article was submitted by the authors in English.

** e-mail: anisovic@thd.pnpi.spb.ru

plots and the two-pion production reactions [1, 3]: the combined fits [5, 6, 8] provide a strong restriction for the position of this state—it could be no higher than 1350 MeV. The notation $f_0(1370)$ used in the PDG compilation [11] is a tribute to these early (and exaggerated) values.[1)]

There is no common belief in the existence of $f_0(1300)$, and its parameters are supposed to be poorly defined: in the compilation [11], the mass and half-width are quoted as $M \simeq 1200$–1500 MeV and $\Gamma/2 \simeq 75$–125 MeV.

The data with direct evidence for this state were obtained by the GAMS group [3], where the peak associated with $f_0(1300)$ was clearly seen at large momenta transferred to the target nucleon. (Note that a hint to the smallness of the background at large momentum transfers was given by the $K\bar{K}$ production data [19], where events were collected in the interval $0.2 \le |t| \le 0.5$ GeV^2 and a strong bump was seen in the mass region ~ 1300 MeV.)

The GAMS data [3], where a strong enhancement in the spectra was observed in the 1300-MeV mass region, were included in recent K-matrix analyses of the $IJ^{PC} = 00^{++}$ amplitude [8–10]. In [10], the mass $(1300 \pm 20) - i(120 \pm 20)$ MeV was found for $f_0(1300)$. It became obvious that exchange by large momenta favors the production of this state, and new measurement of the $\pi^0\pi^0$ spectra at moderately large $|t|$ in the reaction $\pi^- p \to \pi^0\pi^0 n$ at $p_{\text{lab}} = 18$ GeV/c performed by the E852 Collaboration [20] provided an important contribution to verification of parameters of this resonance. The signal from $f_0(1300)$ is clearly seen in the $\pi^0\pi^0$ spectra at $|t| \sim 0.5$–1.5 (GeV/c)^2, for, as was stated above, the background at such momenta transferred is small.

However, the account of the pion-pair-production data in the K-matrix analysis meets with a poor knowledge of the details of the t-channel-exchange mechanism at such momenta. At small momenta, $|t| \lesssim 0.2$ (GeV/c)^2, the Reggeized pion exchange dominates. At $|t| \sim 0.2$–0.4 (GeV/c)^2, the behavior of the two-pion production cross section with the growth of $|t|$ changes: the decrease in $d\sigma/dtdM_{\pi\pi}$ becomes less steep. The change of the regime can be due to the onset of different t-channel-exchange mechanisms at moderate $|t|$ such as multi-Reggeon rescatterings, say, $\pi\mathbf{P}, \pi\mathbf{PP}$, and so on ($\mathbf{P}$ denotes the Pomeron), or to the contribution of the a_1 exchange and related branchings such as $a_1\mathbf{P}$ and $a_1\mathbf{PP}$.

[1)]Note that, in [11], in the discussion of the status of $f_0(1370)$, the papers [13] with the most detailed analysis of this resonance were not mentioned.

In [4], by performing the K-matrix analysis of the GAMS $\pi\pi$ spectra in the vicinity of $f_0(980)$, the t distributions were approximated by the effective pion exchange. It was supposed that, at small $|t|$, the Reggeized pion exchange dominates, while at increasing $|t|$ the change of regime is accompanied by a change of sign in the amplitude (recall that the $\pi\mathbf{P}$ branching changes the amplitude sign). In the analysis [9] of the $\pi\pi$ spectra in the region of $f_0(980)$ and $f_0(1300)$, a scenario with a large contribution of the Reggeized a_1 exchange at $|t| > 0.5$ (GeV/c)^2 was realized in the K-matrix fit. The hypothesis that the change of regime in the t distribution at $M_{\pi\pi} \sim 1000$ MeV is due to the a_1 exchange was also discussed in [21].

To decrease the uncertainties related to a poor knowledge of the t-channel-exchange mechanism, the $M_{\pi\pi}$ distributions averaged over a broad t interval $|t_1| \le |t| \le |t_2|$ were used in [4] to fit to data,

$$\frac{\langle d\sigma\rangle}{dM_{\pi\pi}} = \int_{t_1}^{t_2} dt \frac{d\sigma}{dtdM_{\pi\pi}}, \qquad (1)$$

for the t intervals as follows: $0 < |t| < 0.2$, $0.3 < |t| < 1.0$, $0.35 < |t| < 1.0$, $0.4 < |t| < 1.0$, $0.45 < |t| < 1.0$, and $0.5 < |t| < 1.0$ (GeV/c)^2. The averaged distributions, as one may believe, are not sensitive to the details of the t distribution, as the averaging over a broad momentum-transfer interval makes the particularities of t distributions smoother. Fitting to the spectra confirmed this statement [9, 10]. In the analysis of t distributions [9], where, together with pion exchange, the a_1 Reggeized exchange was included, the parameters of $f_0(980)$ and $f_0(1300)$ appeared to be weakly sensitive to different entries of the t-channel-exchange mechanism, thus giving us hope that a reliable determination of resonance pole singularities as well as pole residues (associated with partial widths) are possible in the framework of the averaging procedure (1).

Recent measurements of the $M_{\pi\pi}$ spectra in the reaction $\pi^- p \to \pi^0\pi^0 n$ at $|t| < 1.5$ (GeV/c)^2 [20] provide us with an opportunity to clarify the t-channel mechanism as well as to study to what extent the averaging of spectra (1) makes the extracted resonance parameters insensitive to the details of the t-exchange mechanism. The present paper is devoted to the consideration of these problems.

As in previous studies [4–10], we analyze the $\pi\pi$ spectra in terms of the K-matrix amplitude. Because of that, in Section 2, we recall the necessary K-matrix-technique formulas. Section 3 presents the results of the fit. In the Conclusion, we summarize our understanding on the t-channel-exchange mechanism and recall the properties of the $f_0(980)$ and

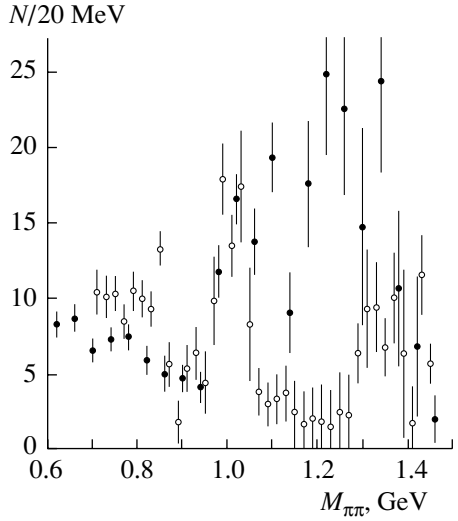

Fig. 1. Number of weighted events, $N/\Delta M_{\pi\pi}$, vs. $M_{\pi\pi}$ for the $|t|$ interval $0.3 \le |t| \le 0.4$ $(\mathrm{GeV}/c)^2$: comparison of GAMS (open circles) and E852 (closed circles) data. Open circles correspond to the subtraction of two sets of GAMS data, $|t| = 0.3$–1.0 $(\mathrm{GeV}/c)^2$ and $|t| = 0.4$–$1.0\,(\mathrm{GeV}/c)^2$.

$f_0(1300)$ resonances found in the K-matrix analysis based on the spectra measured by the GAMS group [3] and E852 Collaboration [20].

2. THE K-MATRIX AMPLITUDE

In this section, we present the formulas for the K-matrix analysis of the 00^{++} wave. The given analysis is a continuation of earlier work [8–10]. In the latter paper [10], the 00^{++} wave was reconstructed on the basis of the following data set:

(1) GAMS data on the S-wave two-meson production in the reactions $\pi p \to \pi^0\pi^0 n$, $\eta\eta n$, and $\eta\eta' n$ at small nucleon momenta transferred, $|t| < 0.2\,(\mathrm{GeV}/c)^2$ [3, 22, 23];

(2) GAMS data on the $\pi\pi$ S-wave production in the reaction $\pi p \to \pi^0\pi^0 n$ at large momenta transferred, $0.30 < |t| < 1.0\,(\mathrm{GeV}/c)^2$ [3, 22];

(3) BNL data on $\pi p^- \to K\bar{K}n$ [24];

(4) Crystal Barrel data on $p\bar{p}$ (at rest, liquid $\mathrm{H_2}$) $\to \pi^0\pi^0\pi^0$, $\pi^0\pi^0\eta$, $\pi^0\eta\eta$ [12, 25].

Now, the experimental basis has been much broadened, and additional samples of data are included in current analysis of the 00^{++} wave as follows:

(5) Crystal Barrel data on proton–antiproton annihilation in gas: $p\bar{p}$ (at rest, gaseous $\mathrm{H_2}$) $\to \pi^0\pi^0\pi^0$, $\pi^0\pi^0\eta$, $\pi^0\eta\eta$ [26];

(6) Crystal Barrel data on proton–antiproton annihilation in liquid $\mathrm{H_2}$: $p\bar{p}$ (at rest, liquid H_2) $\to \pi^+\pi^-\pi^0$, $K^+K^-\pi^0$, $K_SK_S\pi^0$ [26];

(7) Crystal Barrel data on neutron–antiproton annihilation in liquid deuterium $n\bar{p}$ (at rest, liquid $\mathrm{D_2}$) $\to \pi^0\pi^0\pi^-$, $\pi^-\pi^-\pi^+$, $K_SK^-\pi^0$, $K_SK_S\pi^-$ [26];

(8) E852 Collaboration data on the $\pi\pi$ S-wave production in the reaction $\pi^- p \to \pi^0\pi^0 n$ for nucleon momentum transfers squared $0 < |t| < 1.5\,(\mathrm{GeV}/c)^2$ [20].

Below, we set out the K-matrix formulas used for the data analysis of the S wave in the reaction $\pi^- p \to (\pi\pi)_S\, n$.

2.1. The K-Matrix Scattering Amplitude for the 00^{++} Partial Wave

The K-matrix technique is used for the description of the two-meson coupled channels:

$$\hat{A} = \hat{K}(\hat{I} - i\hat{\rho}\hat{K})^{-1}, \qquad (2)$$

where $\hat{K}$ is an $n \times n$ matrix (n is the number of channels under consideration) and $\hat{I}$ is the unity matrix. The phase-space matrix is diagonal: $\hat{\rho}_{ab} = \delta_{ab}\rho_a$. The phase space factor ρ_a is responsible for the threshold singularities of the amplitude: to keep the amplitude analytical in the physical region under consideration, we use analytical continuation for ρ_a below the threshold. For example, the $\eta\eta$ phase space factor $\rho_{\eta\eta} = (1 - 4m_\eta^2/s)^{1/2}$ is equal to $i(4m_\eta^2/s - 1)^{1/2}$ below the $\eta\eta$ threshold (s is the two-meson invariant energy squared). To avoid a false singularity in the physical region, we use for the $\eta\eta'$ channel the phase space factor $\rho_{\eta\eta'} = (1 - (m_\eta + m_{\eta'})^2/s)^{1/2}$.

For the multimeson phase volume in the isoscalar sector, we use the four-pion phase space defined as either the $\rho\rho$ or $\sigma\sigma$ phase space, where σ denotes the S-wave $\pi\pi$ amplitude below 1.2 GeV. The result hardly depends on whether we use the $\rho\rho$ or $\sigma\sigma$ state for the description of the multimeson channel: below, we provide formulas and the values of the obtained parameters for the $\rho\rho$ case, for which the fitted expressions are less cumbersome.

For the S-wave amplitude in the isoscalar sector, we use our standard parametrization [6, 8, 10]:

$$K^{00}_{ab}(s) = \left(\sum_\alpha \frac{g_a^{(\alpha)} g_b^{(\alpha)}}{M_\alpha^2 - s} + f_{ab}\frac{1\ \mathrm{GeV}^2 + s_0}{s + s_0}\right) \times \frac{s - s_A}{s + s_{A0}}, \qquad (3)$$

with the following notation for meson states: $1 = \pi\pi$, $2 = K\bar{K}$, $3 = \eta\eta$, $4 = \eta\eta'$, and $5 =$ multimeson

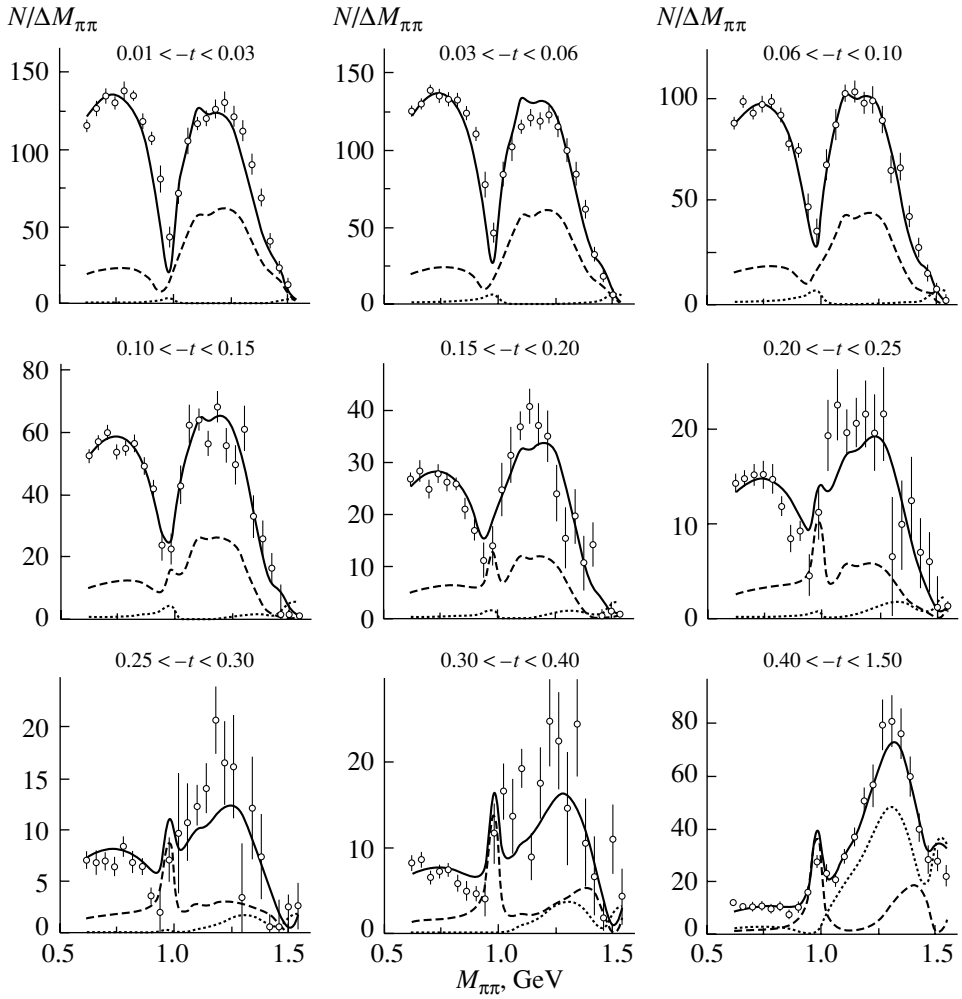

Fig. 2. Description of the E852 data: number of weighted events, $N/\Delta M_{\pi\pi}$, vs. $M_{\pi\pi}$ for different t intervals (in $(\mathrm{GeV}/c)^2$) for solution A. Dashed and dotted curves show the contribution of $a_{1(\mathrm{leading})}$ and $\pi_{(\mathrm{daughter})}$ trajectories, respectively; solid curves stand for the description of spectra, all contributions included.

states (four-pion state mainly at $\sqrt{s} < 1.6$ GeV). The term $g_a^{(\alpha)}$ is a coupling constant of the bare state α to the meson channel; the parameters f_{ab} and s_0 describe the smooth part of the K-matrix elements ($s_0 > 1.5$ GeV^2). We use the factor $(s - s_A)/(s + s_{A0})$ to suppress the effect of the false kinematical singularity at $s = 0$ in the amplitude near the $\pi\pi$ threshold. Parameters s_A and s_{A0} are kept to be of the order of $s_A \sim (0.1{-}0.5)m_\pi^2$ and $s_{A0} \sim 0.1{-}0.5)$ GeV^2 (note that the upper limit of s_{A0} coincides with the position of the ρ-meson left-hand singularity); for these intervals the results hardly depend on precise values of s_A and s_{A0}.

For the two-meson states, $\pi\pi$, $K\bar{K}$, $\eta\eta$, and $\eta\eta'$, the phase space matrix elements are equal to

$$\rho_a(s) = \sqrt{\frac{s - (m_{1a} + m_{2a})^2}{s}}, \quad a = 1, 2, 3, 4, \quad (4)$$

where m_{1a} and m_{2a} are masses of the pseudoscalars. The multimeson phase space factor is defined as

$$\rho_5(s) = \begin{cases} \rho_{51} & \text{at} \quad s < 1\ \mathrm{GeV}^2, \\ \rho_{52} & \text{at} \quad s \geq 1\ \mathrm{GeV}^2, \end{cases} \quad (5)$$

$$\rho_{51} = \rho_0 \int \frac{ds_1}{\pi} \int \frac{ds_2}{\pi} M^2 \Gamma(s_1)\Gamma(s_2)$$
$$\times \sqrt{(s + s_1 - s_2)^2 - 4ss_1}\, s^{-1}[(M^2 - s_1)^2$$
$$+ M^2\Gamma^2(s_1)]^{-1}[(M^2 - s_2)^2 + M^2\Gamma^2(s_2)]^{-1},$$

$$\rho_{52} = \left(\sqrt{\frac{s - 16m_\pi^2}{s}}\right)^n.$$

Here, s_1 and s_2 are the two-pion energies squared, M is the ρ-meson mass, and $\Gamma(s)$ is its energy-dependent width. The factor ρ_0 provides the continuity of $\rho_5(s)$ at $s = 1$ GeV^2. The power parameter n is

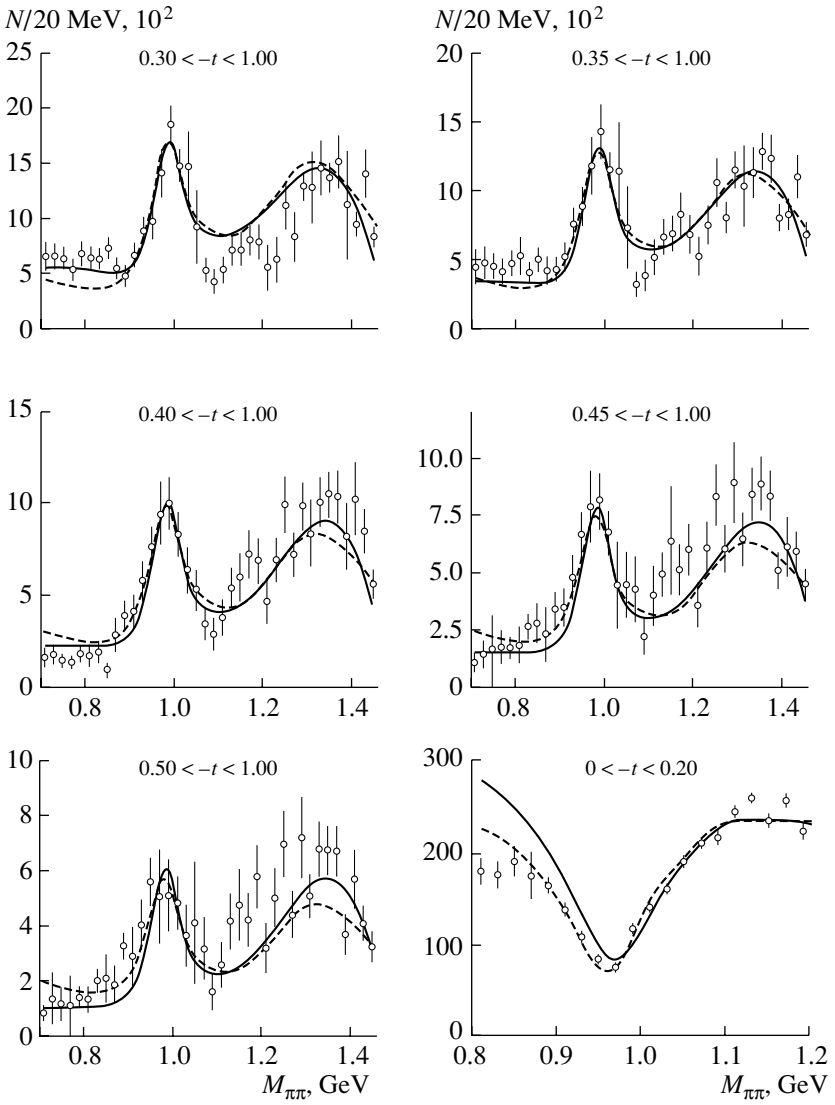

Fig. 3. Description of the GAMS data: number of weighted events, $N/\Delta M_{\pi\pi}$, vs. $M_{\pi\pi}$ for different t intervals [in $(\mathrm{GeV}/c)^2$] for solution A (solid curves). Dashed curves show the solution published previously [10] for the fit of GAMS data alone.

taken to be 1, 3, 5 for different variants of the fitting; the results are weakly dependent on these values (in our previous analysis [10], the value $n = 5$ was used).

2.2. The S-Wave $\pi\pi$, $K\bar{K}$, $\eta\eta$, and $\eta\eta'$ Production in High-Energy πp Collisions

Here, we present formulas for the high-energy S-wave production of $\pi\pi$, $K\bar{K}$, $\eta\eta$, and $\eta\eta'$ at small and moderate momenta transferred to the nucleon. In [3, 20, 22–24], the πp collisions were studied at $p_{\mathrm{beam}} \sim (15\text{–}40)$ GeV/c (or $s_{\pi N} \simeq 2m_N p_{\mathrm{beam}} \sim 30\text{–}80$ GeV^2). At such energies, two pseudoscalar mesons are produced due to the t-channel exchange by Reggeized mesons belonging to the π and a_1 trajectories, leading and daughter ones.

The π and a_1 Reggeons have different signatures, $\xi_\pi = +1$ and $\xi_{a1} = -1$. Accordingly, we write the π and a_1 Reggeon propagators as

$$e^{i\pi\alpha_\pi(t)/2}\frac{s_{\pi N}^{\alpha_\pi(t)}}{\sin(\pi\alpha_\pi(t)/2)}, \qquad (6)$$

$$ie^{-i\pi\alpha_{a1}(t)/2}\frac{s_{\pi N}^{\alpha_{a1}(t)}}{\cos(\pi\alpha_{a1}(t)/2)},$$

where α_π and α_{a1} are Reggeon intercepts. Following [27], we use for leading trajectories

$$\alpha_{\pi(\mathrm{leading})}(t) \simeq -0.015 + 0.72t, \qquad (7)$$

$$\alpha_{a1(\mathrm{leading})}(t) \simeq -0.10 + 0.72t$$

and for daughter ones

$$\alpha_{\pi(\mathrm{daughter})}(t) \simeq -1.10 + 0.72t, \qquad (8)$$

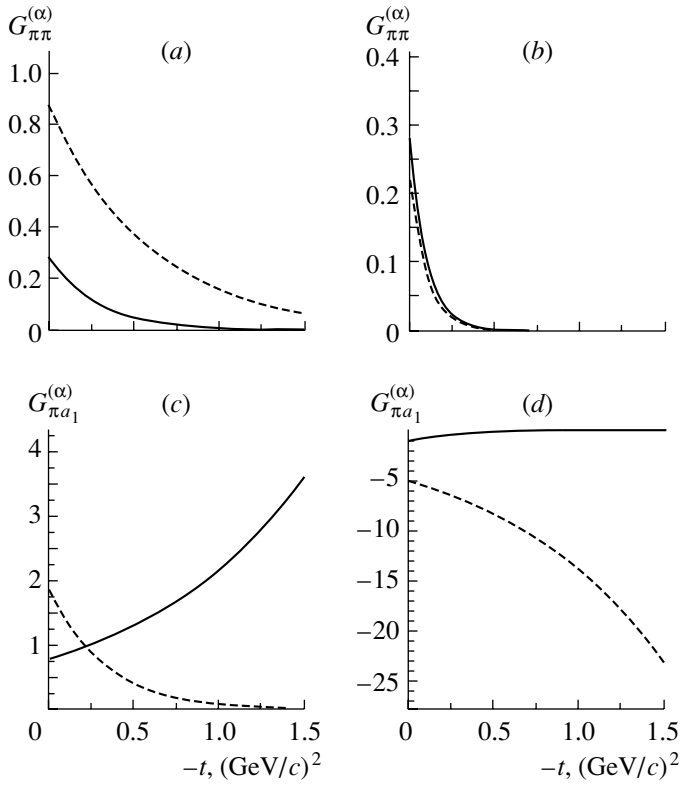

Fig. 4. The t dependence of the K-matrix couplings, $G^{(\alpha)}_{\pi\pi}$, for the $\pi_{\text{(leading)}}$ trajectory exchange in the solution A: *(a)* solid curve for $f_0^{\text{bare}}(720)$ and dashed curve for $f_0^{\text{bare}}(1250)$; *(b)* solid curve for $f_0^{\text{bare}}(1600)$ and dashed curve for $f_0^{\text{bare}}(1230)$; *(c, d)* t dependence of the same vertices for the $a_{1\text{(leading)}}$ trajectory exchange $G^{(\alpha)}_{\pi a_1}$ (notation is the same as in *a, b*).

$$\alpha_{a1\text{(daughter)}}(t) \simeq -1.10 + 0.72t.$$

Here, the slope parameters are in GeV units, $\alpha' = 0.72\ (\text{GeV}/c)^{-2}$. In the c. m. frame, which is the most convenient for the consideration of Reggeon exchanges, the incoming particles move along the z axis with momentum p. In the leading order of the $1/p$ expansion, the spin factors for π and a_1 trajectories read

$$\pi \text{ trajectory}: \qquad (\boldsymbol{\sigma}\cdot\mathbf{q}_\perp), \tag{9}$$

$$a_1 \text{ trajectory}: \qquad i(\boldsymbol{\sigma}\cdot\mathbf{n}_z),$$

where $\mathbf{n}_z = \mathbf{p}_{\text{beam}}/p_{\text{beam}}$ and $\mathbf{q}_\perp$ is the momentum transferred to the nucleon ($t \simeq -q_\perp^2$). The Pauli matrices $\boldsymbol{\sigma}$ work in the two-component spinor space for the incoming (φ_{in}) and outgoing (φ^*_{out}) nucleons: ($\varphi^*_{\text{out}}\boldsymbol{\sigma}\varphi_{\text{in}}$) (for more details, see, for example, [28, 29]). Consistent removal from the vertices (9) of the terms decreasing with $p \to \infty$ is necessary for a correct inclusion of the daughter trajectories, which should obey, similar to the leading ones, the constraints imposed by the t-channel unitarity condition.

In our calculations, we conventionally modify Reggeon propagators in (6). We replace

$$s_{\pi N} \to \frac{s_{\pi N}}{s_{\pi N0}}, \tag{10}$$

where the normalization parameter $s_{\pi N0}$ is of the order of 4–20 GeV^2. To eliminate the poles at $t < 0$, we introduce additional factors into the Reggeon propagators, the gamma functions, by replacing in (6)

$$\sin\left(\frac{\pi}{2}\alpha_\pi(t)\right) \to \sin\left(\frac{\pi}{2}\alpha_\pi(t)\right)\Gamma\left(\frac{\alpha_\pi(t)}{2}+1\right), \tag{11}$$

$$\cos\left(\frac{\pi}{2}\alpha_{a1}(t)\right) \to \cos\left(\frac{\pi}{2}\alpha_{a1}(t)\right)\Gamma\left(\frac{\alpha_{a1}(t)}{2}+\frac{1}{2}\right).$$

The K-matrix amplitude for the transitions $\pi R(t) \to \pi\pi$, $K\bar{K}$, $\eta\eta$, $\eta\eta'$, $\pi\pi\pi\pi$, where $R(t)$ refers to a Reggeon, reads

$$\hat{A}_{\pi R} = \hat{K}_{\pi R}(\hat{I} - i\hat{\rho}\hat{K})^{-1}, \tag{12}$$

where $\hat{K}_{\pi R}$ is the following vector:

$$K^{00}_{\pi R,b} = \left(\sum_\alpha \frac{G^{(\alpha)}_{\pi R}(t) g_b^{(\alpha)}}{M_\alpha^2 - s} + F_{\pi R,b}(t)\frac{1\ \text{GeV}^2 + s_{R0}}{s + s_{R0}}\right) \tag{13}$$

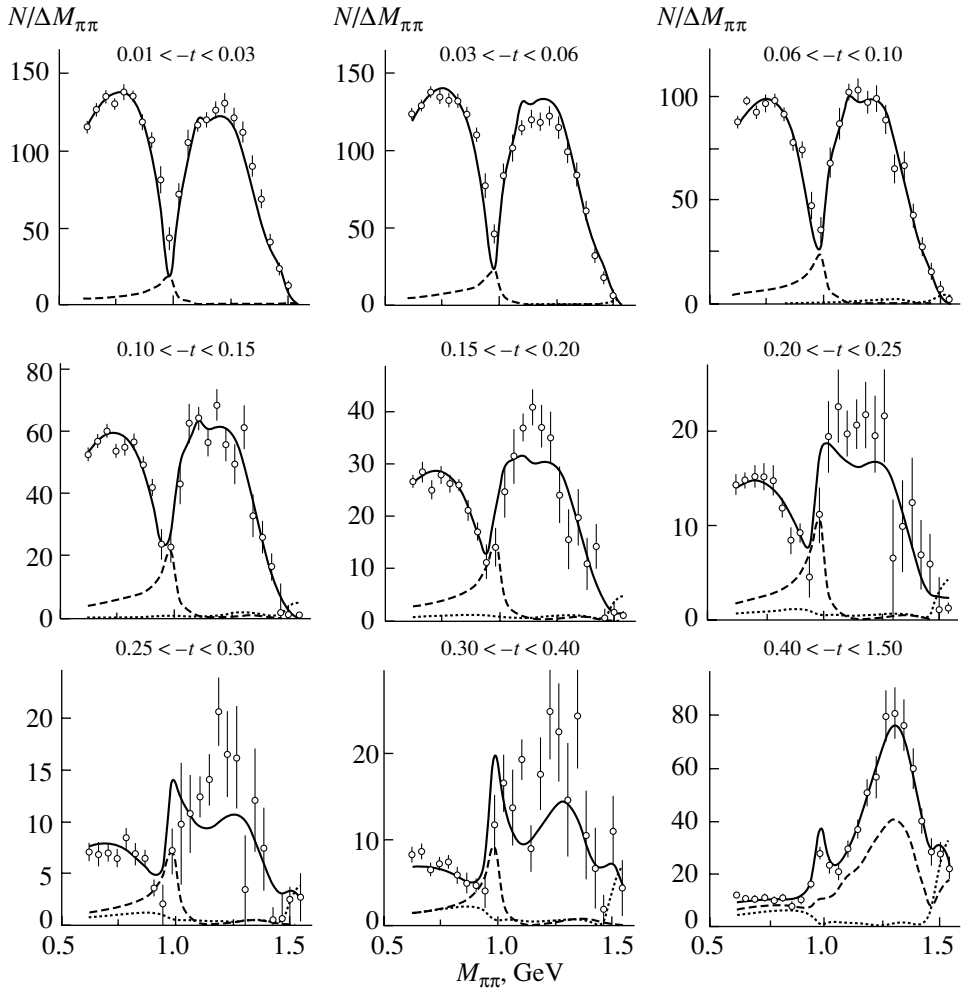

Fig. 5. The same as in Fig. 2, but for the solution $B1$.

$$\times \frac{s - s_A}{s + s_{A0}}.$$

Here, $G^{(\alpha)}_{\pi R}(t)$ and $F_{\pi R,b}(t)$ are the Reggeon t-dependent form factors; s_{R0}, s_A, and s_{A0} are parameters introduced into the K-matrix fit; they are of the order as follows:

$$s_{R0} \sim 1\text{–}5\ \text{GeV}^2,$$

$$s_A, s_{A0} \sim 0.1\text{–}0.5\ \text{GeV}^2.$$

For the t intervals under consideration, the results hardly depend on the precise values of s_{R0}, s_A, and s_{A0}. The following limits are imposed on the form factors:

$$G^{(\alpha)}_{\pi\pi}(t \to m_\pi^2) = g^{(\alpha)}_{\pi\pi}, \quad F_{\pi\pi,a}(t \to m_\pi^2) = f_{\pi\pi,a}, \tag{14}$$

where $g^{(\alpha)}_{\pi\pi}$ and $f_{\pi\pi,a}$ enter the matrix element (3).

Different parametrizations of the form-factor t dependence were investigated in our analysis. First, the t dependence of the form factors is introduced in exponential form (denoted as the A parametrization):

$$G^{(\alpha)}_{\pi R}(t) = g^{\alpha}_{\pi R} \exp\left(\beta^{(\alpha)}_R (t - m_\pi^2)\right), \tag{15}$$
$$F_{\pi\pi,a}(t) = f_{\pi\pi,a} \exp\left(\gamma_a (t - m_\pi^2)\right).$$

Here, for the sake of simplicity, we have used the same slopes, γ_α, for nonresonance K-matrix terms in the channels $\eta\eta$, $\eta\eta'$, and $\pi\pi\pi\pi$. Also, for the trajectories $a_{1(\text{leading})}$, $\pi_{(\text{daughter})}$, and $a_{1(\text{daughter})}$, the nonresonance couplings were set to zero.

In the second type of parametrization, denoted as B, a more complicated t dependence has been used for the π trajectory: it is assumed to be a two-term exponential form for the form factor, either

$$G^{(\alpha)}_{\pi\pi} = g^{(\alpha)}_{\pi\pi} \left[(1 - \Lambda) \exp\left(\beta^{(\alpha)}_1 (t - m_\pi^2)\right)\right. \tag{16}$$
$$\left. + \Lambda \exp\left(\beta^{(\alpha)}_2 (t - m_\pi^2)\right)\right],$$

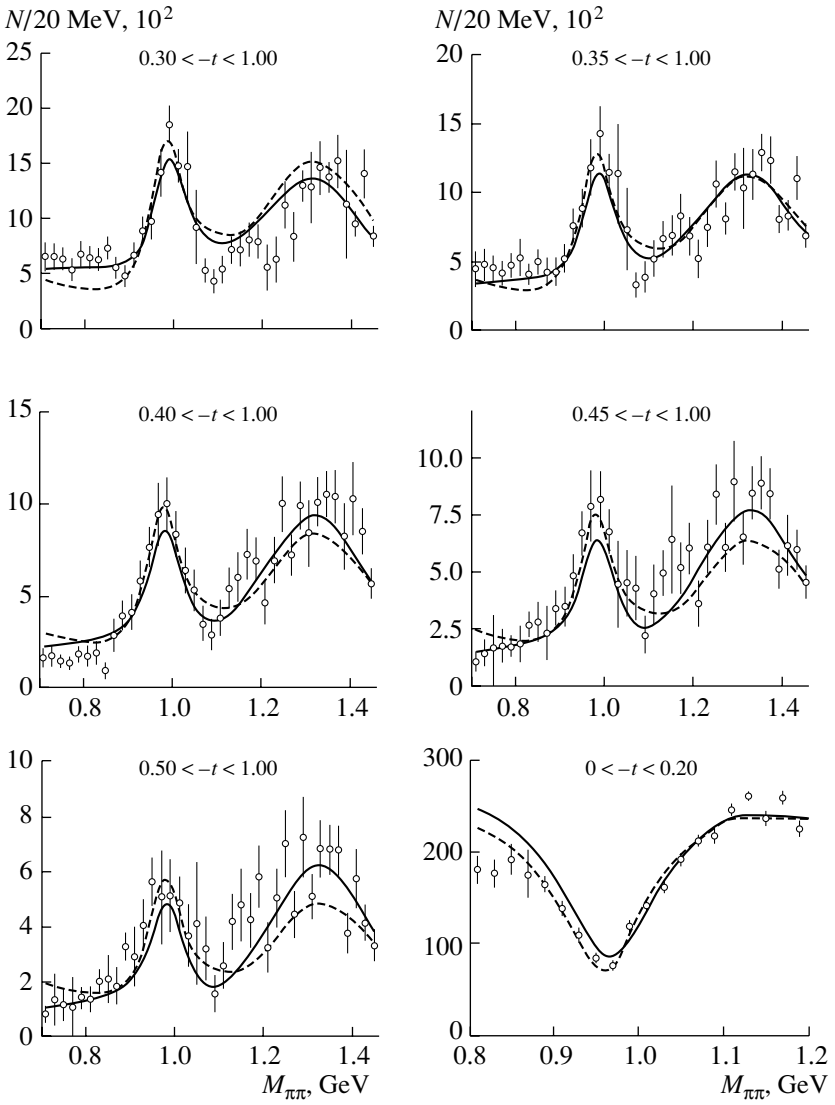

Fig. 6. The same as in Fig. 3, but for the solution $B1$.

or

$$G_{\pi\pi}^{(\alpha)} = g_{\pi\pi}^{(\alpha)} \left[\exp\left(\beta_1^{(\alpha)}(t-m_\pi^2)\right) + \Lambda(t-m_\pi^2)\exp\left(\beta_2^{(\alpha)}(t-m_\pi^2)\right)\right]. \quad (17)$$

The parametrization C assumes a weaker decrease with $|t|$ for the second term, which corresponds to the so-called Orear behavior [30]:

$$G_{\pi\pi}^{(\alpha)} = g_{\pi\pi}^{(\alpha)} \left[(1-\Lambda)\exp\left(\beta_1^{(\alpha)}(t-m_\pi^2)\right) + \Lambda\exp\left(-\beta_2^{(\alpha)}\sqrt{|t-m_\pi^2|}\right)\right], \quad (18)$$

$$G_{\pi\pi}^{(\alpha)} = g_{\pi\pi}^{(\alpha)} \left[\exp\left(\beta_1^{(\alpha)}(t-m_\pi^2)\right) + \Lambda(t-m_\pi^2)\exp\left(-\beta_2^{(\alpha)}\sqrt{|t-m_\pi^2|}\right)\right]. \quad (19)$$

The other form-factor terms are treated in the same way as in the parametrization A. As was stated above, the change of regime at $|t| > 0.5\,(\mathrm{GeV}/c)^2$ is possible due to multi-Pomeron exchanges, thus leading to the Orear behavior (see [31] and references therein).

3. RESULTS

In this section, we present the K-matrix analysis results related to the reactions $\pi^- p \to (\pi\pi)_S\, n$ at $p_{\mathrm{lab}} = 38$ GeV/c [3] and $\pi^- p \to (\pi\pi)_S\, n$ at $p_{\mathrm{lab}} = 18$ GeV/c [20].

In the partial-wave analysis performed by the E852 Collaboration [20], two solutions were found. We fit to the first one, which is called in [20] a physical solution because of its characteristics in the low-mass region. However, near 1100 MeV, both

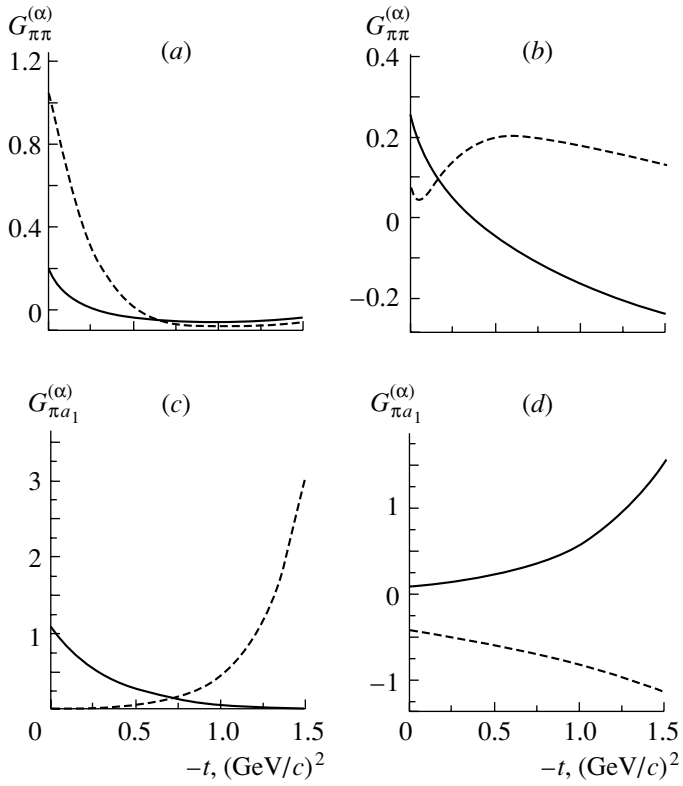

Fig. 7. The same as in Fig. 4, but for the solution $B1$.

solutions give close results, thus creating a problem of separating these solutions above 1100 MeV. Therefore, along with fitting to the first solution, we have performed an analysis where, in the mass region higher than 1100 MeV, the points of the second solution are used. It was found that fitting to this modified second solution does not lead to any qualitative change as compared to the first solution but a nonsignificant redefinition of parameters for the t dependence of Reggeon form factors. It is the reason for not presenting parameters for the modified second solution, and we restrict ourselves only to the discussion of the results obtained from fitting to the first E852 solution [20].

3.1. The Description of the $M_{\pi\pi}$ and t Distributions in the Reaction $\pi p \to (\pi\pi)_S n$ at $0 < |t| < 1.5$ (GeV/c)^2

A comparison of the spectra obtained at $p_{\rm lab} = 38$ GeV/c [3] and $p_{\rm lab} = 18$ GeV/c [20] points to a change in the t-dependence behavior with energy. This is clearly seen in Fig. 1, where the E852 data are plotted in the interval $|t| = 0.3$–0.4 (GeV/c)^2 vs. the difference of GAMS spectra for the intervals $|t| = 0.3$–1.0 (GeV/c)^2 and $|t| = 0.4$–1.0 (GeV/c)^2 (unfortunately, the E852 data are presented for other t intervals than those measured by GAMS). A strong difference of spectra is seen for $M_{\pi\pi} \sim 1100$–1350 MeV, which reveals a significant contribution of daughter trajectories to the formation of $M_{\pi\pi}$ and t distributions.

The description of data with form factors parametrized in the form A is shown in Figs. 2 and 3, and the corresponding t-dependence of the K-matrix coupling constants is presented in Fig. 4 (normalization constant being $s_{\pi N0} = 4$ GeV^2). In this solution, at large $|t|$ ($|t| > 0.4$ (GeV/c)^2), the a_1 exchange gives the peak in 1-GeV region, while the peak at 1300 MeV at large $|t|$ is due to the π daughter trajectory. At $|t|$ between 0.1 and 0.4 GeV^2, the $a_{1(\rm leading)}$ and $\pi_{(\rm daughter)}$ trajectories contribute to a small peak in 1000-MeV region. For this parametrization, the form factors do not cross the abscissas (see Fig. 4); that means the description of spectra is reached in terms of Regge poles, without Regge branchings. The description of GAMS data is quite satisfactory in this approach (see Fig. 3), although a certain deviation is observed at small $|t|$ in the mass region below 1000 MeV. The $f_0(1300)$ at large $|t|$ is mainly described by the $\pi_{(\rm daughter)}$-trajectory exchange. In this case, the $a_{1(\rm leading)}$ contribution is rather large at small $|t|$, providing a noticeable deviation from the one-term unitarized amplitude.

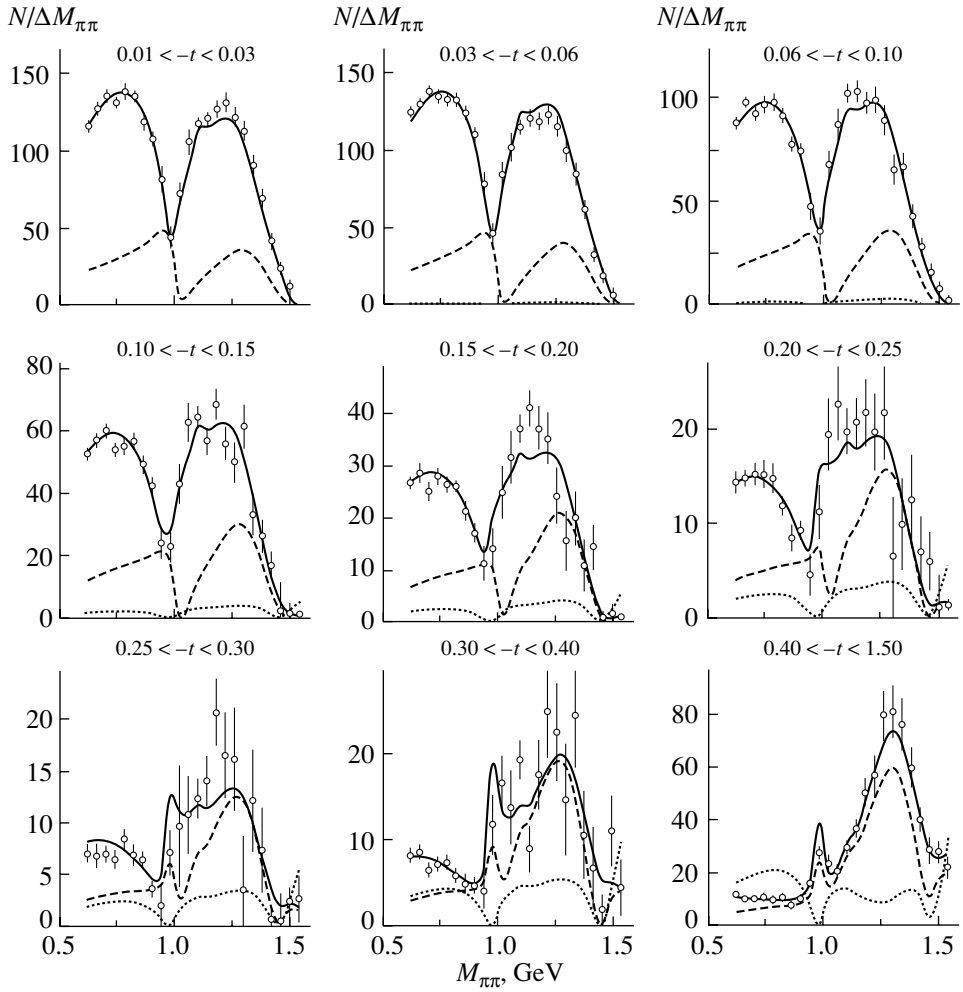

Fig. 8. The same as in Fig. 2, but for the solution $B2$.

Further improvement can be obtained with the form-factor parametrizations for the π trajectory in the form B: Figures 5–7 demonstrate the results for one of the variants of this parametrization. For the variant shown in Figs. 5–7, which we denote as $B1$, we omitted the $a_{1(\text{daughter})}$ trajectory. The $a_{1(\text{leading})}$ exchange is quite large at $|t| \leq 0.4$ $(\text{GeV}/c)^2$. At rather large $|t|$, the $\pi_{(\text{leading})}$ and $\pi_{(\text{daughter})}$ trajectories are responsible for the peak in the 1300-MeV mass region. The $\pi_{(\text{leading})}$ exchange is also responsible for the peak at 1000 MeV, while $\pi_{(\text{daughter})}$ exchange becomes very small here. For this solution, the pion-exchange form factors for the states $f_0^{\text{bare}}(720)$, $f_0^{\text{bare}}(1230)$, and $f_0^{\text{bare}}(1600)$ cross the abscissas, thus corresponding to the πP branching effective contribution. The coupling of the $f_0^{\text{bare}}(1230)$ state grows with $|t|$ at $|t| \leq 0.5$ $(\text{GeV}/c)^2$ due to the increase in relative weight of $f_0(1300)$ at large $|t|$. However, the description of the GAMS data within the parametrization $B1$ in the small-t region is not perfect (see Fig. 6). Adding the $a_{1(\text{daughter})}$ trajectory leads to a noticeable improvement of the description.

Adding the $a_{1(\text{daughter})}$ trajectory, we obtained the solution shown in Figs. 8–10 (parametrization $B2$); it has no visible problems with the description of either E852 or GAMS data. For the $\pi_{(\text{leading})}$ exchanges, this solution is similar to those found in our previous analyses [9, 10] by fitting to GAMS data only: two resonance couplings cross the abscissas at moderate $|t|$.

We have also fitted to data under the assumption that the change of the t-distribution structure at $|t| > 0.4\,(\text{GeV}/c)^2$ is due to the onset of the Orear regime, Eqs. (18) and (19). For this case (parametrization C), the results are close to those of the B parametrization, so we do not present here the $M_{\pi\pi}$ and t distributions.

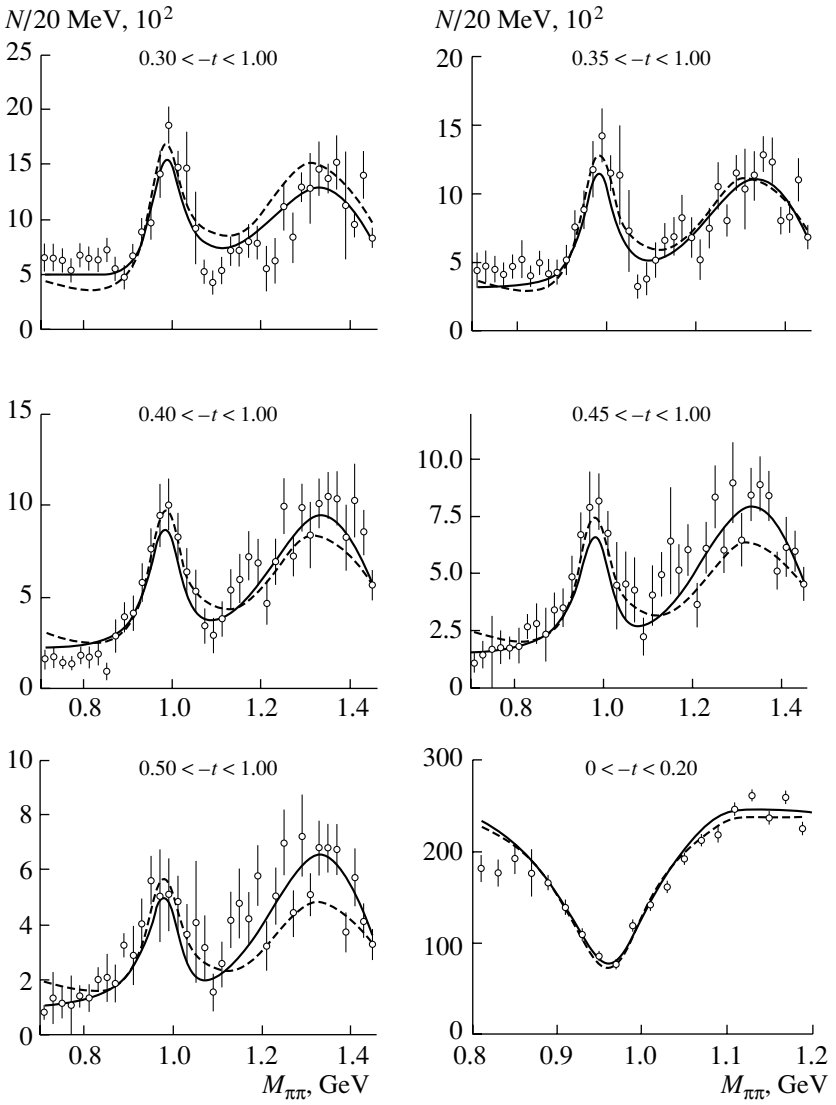

Fig. 9. The same as in Fig. 3, but for the solution $B2$.

3.2. Resonance Pole Positions for the $f_0(980)$ and $f_0(1300)$ States

Using the solutions found, we have determined the positions of poles corresponding to the resonances $f_0(980)$ and $f_0(1300)$:

$$(1031 \pm 10) - i(35 \pm 6)\ \text{MeV}, \qquad (20)$$
$$(1315 \pm 20) - i(150 \pm 30)\ \text{MeV}.$$

The pole for $f_0(980)$ is under the $\pi\pi$ and $\pi\pi\pi\pi$ cuts, the closest physical region to this pole being located below the $K\bar{K}$ threshold (for more detail, concerning the determination of sheets, see [10]).

Recall that, in the previous K-matrix analysis [10], we obtained for $f_0(1300)$ the mass value $(1300 \pm 20) - i(120 \pm 20)$ MeV, while for $f_0(980)$ it was $(1015 \pm 15) - i(43 \pm 8)$ MeV. One can see that the magnitudes quoted in [10] and (20) agree reasonably with each other.

By fitting to data on the two-meson spectra at $|t| \sim 0.5$–$1.0\ (\text{GeV}/c)^2$, we should definitely recognize that our a priori knowledge about the t-channel-exchange mechanism is poor. In the considered t region, together with the Regge pole terms (π and a_1 exchanges), the Regge branching contributions with additional Pomeron-induced interactions (πPP, πP P, or a_1P, a_1PP, etc., t-channel exchanges) should be significant. The contribution of Regge branchings is enhanced at moderately large $|t|$; this circumstance was known long ago (see, e.g., [31, 32]). The presence of a number of terms in the t-channel-exchange mechanism at $|t| \gtrsim 0.5\ (\text{GeV}/c)^2$ makes the model-independent reconstruction of the t-channel amplitude hardly plausible. Hence, a ne-

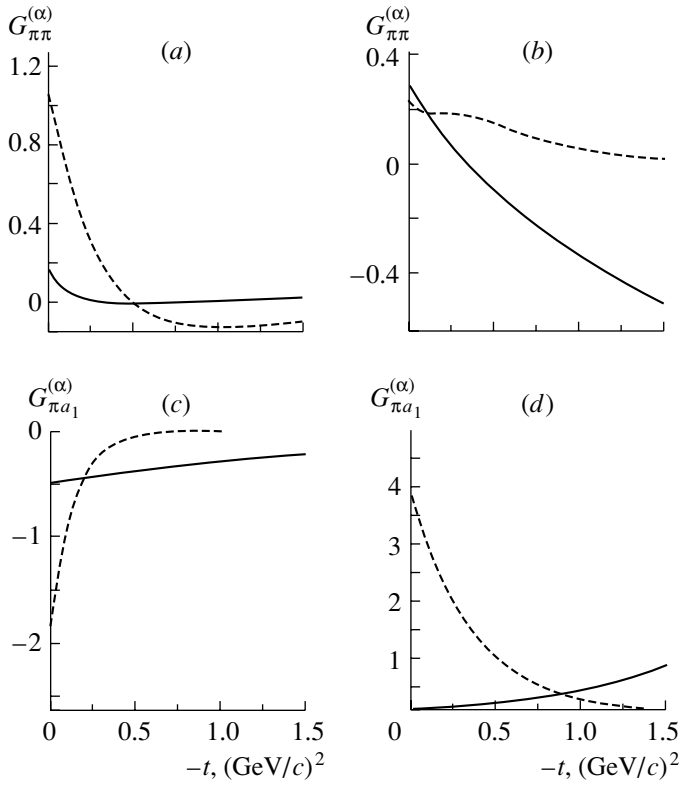

Fig. 10. The same as in Fig. 4, but for the solution $B2$.

cessity appears to use at moderately small momentum transfers the $M_{\pi\pi}$ distributions, which are not sensitive to the details of the t-channel mechanism. Let us stress once again that, in our opinion, the $M_{\pi\pi}$ distributions averaged over a broad interval of momentum transfers do respond to the problem of finding the masses and widths of the resonances.

4. CONCLUSION

We have performed the fitting to data to determine parameters of $f_0(980)$ and $f_0(1300)$ observed in the $(\pi\pi)_S$ spectra in the reaction $\pi^- p \to (\pi\pi)_S\, n$ [3, 20] by checking several hypotheses about the $|t|$ exchange mechanism.

Concerning the structure of the $|t|$-channel-exchange mechanism, one can see that the E852 data satisfy well the suggestion about Reggeized π exchange dominating small momentum transfers, $|t| < 0.2$ (GeV/c)^2; this very mechanism works at GAMS energies as well [4]. With the increase in $|t|$, the change of regime occurs, and the E852 data definitely confirm this. Yet, the details of the change of regime remain unclear: this may happen due to the inclusion of the a_1 exchange, or the branchings $\pi\mathbf{P}$, $a_1\mathbf{P}$ ($\mathbf{P}$ is the Pomeron), or even due to multiple rescatterings (the Orear regime). The E852 data reveal that, at $|t| > 0.2$ (GeV/c)^2, the daughter trajectories (pion or a_1 meson) contribute significantly, and the change of the structure of $|t|$ distributions with energy definitely proves it.

The fitting procedure uses the $M_{\pi\pi}$ spectra that are averaged over certain intervals of $|t|$. With different inputs for the t-channel-exchange mechanism at $|t| \simeq 0.4$ (GeV/c)^2, we have observed a stability of the resonance parameters found for $f_0(980)$ and $f_0(1300)$, and they are close to those obtained in previous analysis [10]. Thus, our analysis does not confirm the statement of [33] about a strong dependence of extracted parameters on the details of the t-channel-exchange mechanism at $|t| \geq 0.4$ (GeV/c)^2.

ACKNOWLEDGMENTS

We are grateful to A.V. Anisovich, D.V. Bugg, L.G. Dakhno, and V.A. Nikonov for useful and stimulating discussions. This study is supported by the Russian Federation for Basic Research, project no. 01-02-17861.

REFERENCES

1. G. Grayer *et al.*, Nucl. Phys. B **75**, 189 (1974).
2. D. Aston *et al.*, Nucl. Phys. B **296**, 493 (1988).
3. Yu. D. Prokoshkin *et al.*, Phys. Dokl. **40**, 495 (1995).

4. V. V. Anisovich, A. A. Kondashov, Yu. D. Prokoshkin, *et al.*, Phys. Lett. B **355**, 363 (1995).
5. V. V. Anisovich and A. V. Sarantsev, Phys. Lett. B **382**, 429 (1996).
6. V. V. Anisovich, Yu. D. Prokoshkin, and A. V. Sarantsev, Phys. Lett. B **389**, 388 (1996).
7. A. V. Anisovich and A. V. Sarantsev, Phys. Lett. B **413**, 137 (1997).
8. V. V. Anisovich, Usp. Fiz. Nauk **168**, 481 (1998) [Phys.-Usp. **41**, 419 (1998)].
9. V. V. Anisovich, D. V. Bugg, and A. V. Sarantsev, Yad. Fiz. **62**, 1322 (1999) [Phys. At. Nucl. **62**, 1247 (1999)].
10. V. V. Anisovich, A. A. Kondashov, Yu. D. Prokoshkin, *et al.*, Yad. Fiz. **63**, 1489 (2000) [Phys. At. Nucl. **63**, 1410 (2000)].
11. Particle Data Group (D. E. Groom *et al.*), Eur. Phys. J. C**15**, 1 (2000).
12. V. V. Anisovich, D. S. Armstrong, I. Augustin, *et al.* (Crystal Barrel Collab.), Phys. Lett. B **323**, 233 (1994).
13. V. V. Anisovich, D. V. Bugg, A. V. Sarantsev, and B. S. Zou, Phys. Rev. D **50**, 1972 (1994); Yad. Fiz. **57**, 1666 (1994) [Phys. At. Nucl. **57**, 1595 (1994)].
14. D. V. Bugg, V. V. Anisovich, A. V. Sarantsev, and B. S. Zou, Phys. Rev. D **50**, 4412 (1994).
15. I. J. R. Aitchison, Phys. Rev. **133**, 1257 (1964); B. N. Valuev, Zh. Éksp. Teor. Fiz. **47**, 649 (1964) [Sov. Phys. JETP **20**, 433 (1964)]; V. V. Anisovich and L. G. Dakhno, Phys. Lett. **10**, 221 (1964); Nucl. Phys. **76**, 665 (1966); A. V. Anisovich and V. V. Anisovich, Phys. Lett. B **345**, 321 (1995).
16. C. Amsler *et al.*, Phys. Lett. B **291**, 347 (1992).
17. R. Kamenski *et al.*, Phys. Rev. D **50**, 3145 (1994).
18. K. L. Au, D. Morgan, and M. R. Pennington, Phys. Rev. D **35**, 1633 (1987).
19. V. A. Polychronakos *et al.*, Phys. Rev. D **19**, 1317 (1979).
20. E852 Collab. (J. Gunter *et al.*), Phys. Rev. D **64**, 072003 (2001).
21. N. N. Achasov and G. N. Schestakov, Yad. Fiz. **62**, 548 (1999) [Phys. At. Nucl. **62**, 505 (1999)].
22. D. Alde *et al.*, Z. Phys. C **66**, 375 (1995); A. A. Kondashov *et al.*, in *Proceedings of the 27th International Conference on High Energy Physics, Glasgow, 1994*, p. 1407.
23. F. Binon *et al.*, Nuovo Cimento A **78**, 313 (1983); **80**, 363 (1984).
24. S. J. Lindenbaum and R. S. Longacre, Phys. Lett. B **274**, 492 (1992); A. Etkin *et al.*, Phys. Rev. D **25**, 1786 (1982).
25. Crystal Barrel Collab. (C. Amsler *et al.*), Phys. Lett. B **342**, 433 (1995); **355**, 425 (1995).
26. E. Klempt and A. V. Sarantsev, private communication.
27. A. V. Anisovich, V. V. Anisovich, and A. V. Sarantsev, Phys. Rev. D **62**, 051502 (2000).
28. A. B. Kaidalov and B. M. Karnakov, Yad. Fiz. **11**, 216 (1970) [Sov. J. Nucl. Phys. **11**, 121 (1970)].
29. G. D. Alkhazov, V. V. Anisovich, and P. E. Volkovitsky, *Diffractive Interaction of High Energy Hadrons with Nuclei* (Nauka, Leningrad, 1991), Chap. 1 (in Russian).
30. J. Orear, Phys. Lett. **13**, 190 (1964).
31. V. V. Anisovich and O. A. Khrustalev, Yad. Fiz. **9**, 1258 (1969) [Sov. J. Nucl. Phys. **9**, 734 (1969)]; **12**, 1262 (1970) [Sov. J. Nucl. Phys. **12**, 694 (1970)].
32. A. A. Anselm and I. T. Dyatlov, Yad. Fiz. **6**, 591 (1967) [Sov. J. Nucl. Phys. **6**, 430 (1967)].
33. N. N. Achasov and G. N. Shestakov, hep-ph/0107243.

Physics of Atomic Nuclei, Vol. 66, No. 5, 2003, pp. 941–949. From Yadernaya Fizika, Vol. 66, No. 5, 2003, pp. 973–982.

ELEMENTARY PARTICLES AND FIELDS
Theory

Transition Form Factors and Light-Cone Distribution Amplitudes of Pseudoscalar Mesons in the Chiral Quark Model*

A. E. Dorokhov, **M. K. Volkov**, and **V. L. Yudichev**

Joint Institute for Nuclear Research, Dubna, Moscow oblast, 141980 Russia

Received February 26, 2002

Abstract—It is shown that a chiral quark model of the Nambu–Jona-Lasinio type can be used to describe "soft"-momentum parts of the amplitudes with large momentum transfer. As a sample, the processes $\gamma^* \to \gamma(\pi, \eta, \eta')$, where one of the photons, γ^*, has large spacelike virtuality, are investigated. The $\gamma^* \to \gamma(\pi, \eta, \eta')$ transition form factors are calculated for a wide region of the momentum transfer. The results are consistent with the calculations performed in the instanton-induced chiral quark model and agree with experimental data. The distribution amplitudes of pseudoscalar mesons are derived. © *2003 MAIK "Nauka/Interperiodica".*

1. INTRODUCTION

Effective chiral quark models (ECQM) are very useful tools for the investigation of the nonperturbative sector of QCD. Of particular interest are the Nambu–Jona-Lasinio (NJL) model and its extensions [1–5], where the low-energy theorems are fulfilled and the mechanism of spontaneous breaking of chiral symmetry (SBCS) is realized in a simple and transparent way. The internal properties of the ground states of scalar, pseudoscalar, vector, and axial-vector mesons (such as masses, radii, and polarizabilities), as well as all the main decays and other low-energy strong and electroweak interactions of mesons, are satisfactorily described in NJL. Recently, noticeable progress has also been achieved in constructing a $U(3) \times U(3)$ NJL model for the description of first radial excitations of scalar, pseudoscalar, and vector mesons, including even the lightest scalar glueball [6–8].

As a rule, the NJL model is used in low-energy physics, in particular, for the description of processes with a low momentum transfer ($\leqslant 1$ GeV). And, in view of the above-mentioned success of the NJL model, it is quite interesting to extend the range of its application and to try, in particular, to describe some processes with a large momentum transfer. Indeed, for many of such processes, the factorization theorem [9–11] can be applied, which allows one to rewrite the amplitude of the process as a convolution of "hard" and "soft" parts. The hard part is described by perturbative QCD (pQCD), whereas the soft part requires a nonperturbative approach. Usually, in QCD, the nonperturbative dynamics of quarks inside a meson is parametrized by distribution amplitudes (DA) [9], the exact form of which cannot be derived from pQCD. However, an approximation for DA can be obtained in the QCD sum rules approach (see, e.g., [12–14]). On the other hand, one can calculate the soft part of the amplitude within a chiral quark model, where the dynamics of (constituent) quarks inside a meson is described by the corresponding quark–meson vertex instead of DA (however, one can restore the shape of DA on the basis of quark-model calculations). The validity of this approach is investigated in the present work.

In our paper, we calculate the form factors that describe the transition processes $\gamma^* \to P\gamma$ or $\gamma^*\gamma \to P$, where P is a pseudoscalar meson, for a wide range of transferred spacelike momenta. Of interest is the kinematic region, where one of the photons is not on mass-shell and has a large spacelike virtuality. It is also shown that our results do not contradict either the experimental data or other theoretical models. As to experiment, we refer to the data on the $\gamma^* \to \pi\gamma$, $\gamma^* \to \eta\gamma$, and $\gamma^* \to \eta'\gamma$ transition processes reported by the CLEO collaboration [15]. For comparison with other theoretical models, we choose the results recently obtained in the framework of the instanton-induced chiral quark model (IQM) [16].

The structure of our paper is as follows. In Section 2, we introduce the $\gamma^* \to P\gamma$ transition form factor. In Section 3, the part of the NJL Lagrangian describing the quark–meson interaction and the Lagrangian derived in the instanton vacuum model are introduced, and the asymptotic behavior of the

*This article was submitted by the authors in English.

** e-mail: dorokhov@thsun1.jinr.ru
*** e-mail: volkov@thsun1.jinr.ru

$\gamma^* \to P\gamma$ transition form factor for pseudoscalar mesons at high spacelike virtuality of one of the photons is investigated. In particular, the shapes of DA of π, η, and η' mesons are found. In the last section, we discuss the obtained results and compare them with experimental data. An outlook of further possible applications of our approach is also given.

2. THE $\gamma^* \to P\gamma$ TRANSITION FORM FACTOR

The transition process $\gamma^*(q_1) \to P(p)\gamma^*(q_2)$, where p is the final-state meson momentum, $P = \pi^0$, η, η', and q_1 and q_2 are photon momenta, is described by the amplitude

$$\begin{aligned} &\mathcal{T}\left(\gamma^*\left(q_1, e_1\right) \to P\left(p\right)\gamma^*\left(q_2, e_2\right)\right) \\ &= \mathcal{F}_P(q_1^2, q_2^2, p^2)\epsilon_{\mu\nu\rho\sigma} e_1^\mu e_2^\nu q_1^\rho q_2^\sigma, \end{aligned} \tag{1}$$

where e_i $(i = 1, 2)$ are the photon polarization vectors, $\mathcal{F}_P(q_1^2, q_2^2, p^2)$ is the transition form factor, and $\epsilon_{\mu\nu\rho\sigma}$ is the fully antisymmetric tensor.

Theoretically, at zero virtualities, the form factor

$$\mathcal{F}_P(0, 0, 0) = \frac{1}{4\pi^2 f_P} \tag{2}$$

is related to the axial anomaly [17, 18]. Here, f_P is a pseudoscalar-meson weak-decay constant defined by the well-known PCAC relation (for the pion, $f_\pi = 93$ MeV). At asymptotically large photon virtualities, its behavior is predicted by pQCD [19] and depends crucially on the internal meson dynamics parametrized by a nonperturbative DA, $\varphi_P^A(x)$, with x being the fraction of the meson momentum p carried by a quark.

Further, it is convenient to parametrize the photon virtualities as $q_1^2 = -(1+\omega)Q^2/2$ and $q_2^2 = -(1-\omega)Q^2/2$, where Q^2 and ω are, respectively, the total virtuality of the photons and the asymmetry in their distribution,

$$\begin{aligned} Q^2 &= -(q_1^2 + q_2^2) \geqslant 0, \\ \omega &= (q_1^2 - q_2^2)/(q_1^2 + q_2^2), \quad |\omega| \leqslant 1. \end{aligned} \tag{3}$$

Recent analysis of the experimental data on the form factors $\mathcal{F}_P$ for small virtuality of one of the photons, $q_2^2 \approx 0$, with the virtuality of the other photon being scanned up to 8 GeV^2 for the pion, 22 GeV^2 for the η, and 30 GeV^2 for the η' mesons has been published by the CLEO Collaboration [15]. According to this analysis, the process $\gamma^* \to P\gamma$ $(|\omega| = 1)$ can be fitted by a monopole form factor

$$\mathcal{F}_P(q_1^2 = -Q^2, q_2^2 \approx 0, p^2)\big|_{\text{fit}} = \frac{g_{P\gamma\gamma}}{1 + Q^2/\mu_P^2}, \tag{4}$$

$$\begin{gathered} g_{\pi\gamma\gamma} \simeq 0.27\ \text{GeV}^{-1}, \qquad g_{\eta\gamma\gamma} \simeq 0.26\ \text{GeV}^{-1}, \\ g_{\eta'\gamma\gamma} \simeq 0.34\ \text{GeV}^{-1}, \\ \mu_\pi \simeq 0.78\ \text{GeV}, \qquad \mu_\eta \simeq 0.77\ \text{GeV}, \\ \mu_{\eta'} \simeq 0.86\ \text{GeV}, \end{gathered}$$

where $g_{P\gamma\gamma}$ are the two-photon meson decay constants.

In the lowest order of pQCD, the light-cone operator product expansion (OPE) predicts the high-Q^2 behavior of the form factor as follows [19]:

$$\begin{aligned} &\mathcal{F}_P(q_1^2, q_2^2, p^2 = 0)\big|_{Q^2 \to \infty} \\ &= J_P\left(\omega\right)\frac{f_P}{Q^2} + O\left(\frac{\alpha_s}{\pi}\right) + O\left(\frac{1}{Q^4}\right), \end{aligned} \tag{5}$$

with the asymptotic coefficient given by

$$J_P\left(\omega\right) = \frac{4}{3}\int\limits_0^1 \frac{dx}{1 - \omega^2(2x-1)^2}\varphi_P^A(x), \tag{6}$$

where $\varphi_P^A(x)$ is the leading-twist meson light-cone DA normalized by $\int_0^1 dx\, \varphi_P^A(x) = 1$.

In (6), the asymptotic coefficient is expressed in terms of DA. Alternatively, as was mentioned in the Introduction, $J_P(\omega)$ can be calculated directly either from the NJL model or from IQM. In Section 3, one will see that, in both models, $J_P(\omega)$ can be rewritten in the form (6), and thus the shape of DA is extracted.

Since the meson DA reflects the internal nonperturbative meson dynamics, the prediction of the value of $J_P\left(\omega\right)$ is a rather nontrivial task, and its accurate measurement would provide quite valuable information. It is important to note that, for the considered transition process, the leading asymptotic term of pQCD expansion (5) is not suppressed by the strong coupling constant α_s. Hence, the pQCD prediction (5) can become reasonable at the highest of the presently accessible momenta $Q^2 \sim 10$ GeV^2. At asymptotically high Q^2, the DA evolves to $\varphi_P^{A,\text{as}}(x) = 6x(1-x)$ and $J_P^{\text{as}}\left(|\omega| = 1\right) = 2$. The fit of CLEO data for the pion corresponds to $J_\pi^{\text{CLEO}}(|\omega| \approx 1) = 1.6 \pm 0.3$, indicating that, even at moderately high momenta, this value is not too far from its asymptotic limit.

However, since the pQCD evolution of DA reaches the asymptotic regime very slowly, its exact form at moderately high Q^2 does not coincide with $\varphi_P^{A,\text{as}}(x)$. At lower Q^2, the power corrections to the form factor become important. Thus, the study of the behavior of the transition form factor at all experimentally accessible Q^2 is the subject of nonperturbative dynamics. Thus, the theoretical determination of the transition form factor is still challenging, and it is desirable to

perform direct calculations of $\mathcal{F}_P(q_1^2, q_2^2, p^2)$ without a priori assumptions about the shape of the meson DA.

The asymptotic coefficient of the light-cone transition form factor in the symmetric kinematics, $q_1^2 = q_2^2$ ($\omega = 0$), at high virtualities is given by the integral defining f_P. In the other extreme limit, where one photon is real ($|\omega| = 1$), the asymptotic coefficient is proportional to $\int_0^1 dx \varphi_P^A(x)/x$ and thus is very sensitive to a detailed form of the DA.

In [12], some progress was achieved by using a refined technique based on the OPE with nonlocal condensates [13], which is equivalent to the inclusion of the whole series of power corrections. By means of the QCD sum rules with nonlocal condensates, it was shown that this approach works in almost the whole kinematic region $|\omega| \lesssim 1$ and that, for high values of the asymmetry parameter $|\omega| \gtrsim 0.8$, the pion transition form factor is very sensitive to the nonlocal structure of the QCD vacuum.

3. THE $\gamma^* \to P\gamma$ TRANSITION FORM FACTOR IN ECQM MODELS

3.1. The NJL-Model Lagrangian

Let us consider the part of the effective quark–meson Lagrangian that is necessary in our calculations. It has the following form:

$$L = L_0 + L_{\rm int}, \tag{7}$$

$$L_0 = \bar{q}(i\,\partial\!\!\!/ - m)q, \tag{8}$$

$$L_{\rm int} = L_1 + L_2 + L_3 + \delta L, \tag{9}$$

$$L_1 = \bar{q} i\gamma_5 \left(g_\pi \sum_{a=1}^{3} \lambda^a \pi^a + g_{\eta_u} \lambda_u \eta_u + g_{\eta_s} \lambda_s \eta_s \right) q, \tag{10}$$

$$L_2 = \bar{q} i\,\partial\!\!\!/ \gamma_5 \left(f_\pi^{-1}(1 - Z_u^{-1}) \sum_{a=1}^{3} \lambda^a \pi^a \right. \tag{11}$$

$$\left. + f_u^{-1}(1 - Z_u^{-1})\lambda_u \eta_u + f_s^{-1}(1 - Z_s^{-1})\lambda_s \eta_s \right) q,$$

$$L_3 = \bar{q}\hat{\mathcal{Q}}\mathcal{A}\!\!\!/ q, \tag{12}$$

where m is the diagonal 3×3 flavor matrix of constituent quark masses, $m = \mathrm{diag}(m_u, m_d, m_s)$ (we consider the case of approximate isotopic symmetry $m_u = m_d$); λ_a are the Gell-Mann matrices; $\lambda_u = (\sqrt{2}\lambda_0 + \lambda_8)/\sqrt{3}$; $\lambda_s = (-\lambda_0 + \sqrt{2}\lambda_8)/\sqrt{3}$; q and π are, respectively, the quark and pion; and η_u and η_s are pure $\bar{u}u$ and $\bar{s}s$ pseudoscalar meson states.

The fields η_u and η_s in (10) and (11) are not physical, because they are subjected to singlet–octet mixing. Here, it is assumed that the terms responsible for the singlet–octet mixing are accumulated in the term[1)] δL [see (9)], the account of which results in the following relation between "nonphysical" η_u, η_s and "physical" η, η' meson fields:

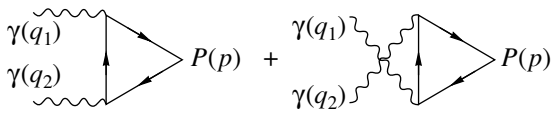

Fig. 1. The diagrams contributing to the process $\gamma^*\gamma^* \to P(\gamma^* \to P\gamma^*)$ amplitude.

$$\eta_u = \eta \sin(\theta_0 - \theta) + \eta' \cos(\theta_0 - \theta), \tag{13}$$

$$\eta_s = \eta \cos(\theta_0 - \theta) - \eta' \sin(\theta_0 - \theta), \tag{14}$$

where $\theta = -19^\circ$ is the singlet–octet mixing angle and $\theta_0 \approx 35.5^\circ$ is the ideal mixing angle [2, 20].

The quark–meson coupling constants (see [2]) are defined as follows:

$$g_\pi = g_u\sqrt{Z_\pi}, \quad g_{\eta_u} = g_u\sqrt{Z_{\eta_u}}, \quad g_{\eta_s} = g_s\sqrt{Z_{\eta_s}}, \tag{15}$$

where we introduced g_u and g_s:

$$g_a^{-2} = \frac{4N_{\rm c}}{(2\pi)^4} \int \frac{\theta(\Lambda_{\rm NJL}^2 - k^2)}{(k^2 + m_a^2)^2} d_e^4 k \tag{16}$$

$$(a = u, s).$$

The integration is performed in the Euclidean metric. The divergence is eliminated by a simple $O(4)$-symmetric cutoff on the scale $\Lambda_{\rm NJL}$ that characterizes the domain of SBCS.

The terms with derivatives of meson fields in L_2 [see (11)] appear because of π–a_1 transitions [2], which also result in additional renormalization factors Z_a in g_π, g_{η_u}, g_{η_s}. Further, we assume that Z_a for different mesons are approximately equal [see (15)]:

$$Z_{\eta_s} \approx Z_{\eta_u} \approx Z_\pi \equiv Z = \left(1 - \frac{6m_u^2}{M_{a_1}^2}\right)^{-1} \approx 1.45. \tag{17}$$

Here, $M_{a_1} = 1.23$ GeV is the mass of the a_1 meson [21].

The term L_3 in (12) describes the electromagnetic interaction of quarks. The photon fields are denoted by $\mathcal{A}$, and $\hat{\mathcal{Q}}$ stands for the charge matrix

$$\hat{\mathcal{Q}} = \frac{e}{2}\left(\lambda_3 + \frac{\lambda_8}{\sqrt{3}}\right), \tag{18}$$

where e is the elementary electric charge ($e^2 = 4\pi\alpha$, $\alpha^{-1} \approx 137$).

[1)] The singlet–octet mixing appears once the pseudoscalar gluon anomaly is taken into account [2]. One can also obtain the mixing after introducing the 't Hooft term into the quark Lagrangian [20].

The values of $\Lambda_{\rm NJL}$ and m_u are fixed by two equations [2, 20]: (i) the Goldberger–Treiman relation $m_u = g_\pi f_\pi$ and (ii) the ρ-meson decay constant [2, 22, 23]

$$g_\rho = \sqrt{6} g_u, \tag{19}$$

whose value of 6.1 is well known from the experimentally observed decay $\rho \to \pi\pi$. Taking into account these equations and the expression for Z [see (17)], one finds the constituent u-quark mass

$$m_u^2 = \frac{M_{a_1}^2}{12}\left(1 - \sqrt{1 - \frac{4 g_\rho^2 f_\pi^2}{M_{a_1}^2}}\right) \tag{20}$$

with the value $m_u = 280$ MeV. Equating the left-hand side of (19) to its experimental value and using the definition of g_u [see (15)] with $m_u = 280$ MeV, one obtains $\Lambda_{\rm NJL} = 1.25$ GeV [2]. The mass of the strange quark is fixed by the kaon mass,[2)] $m_s = 425$ MeV [20].

3.2. Meson Transition $\gamma^* \to P\gamma^*$ Form Factor

Let us consider the $\gamma^* \to P\gamma^*$ invariant amplitude corresponding to the triangle diagrams shown in Fig. 1,

$$\mathcal{T}\left(\gamma^*(q_1, e_1) \to P(p)\,\gamma^*(q_2, e_2)\right) \tag{21}$$
$$= t_{P\gamma\gamma}(q_1, e_1; q_2, e_2) + t_{P\gamma\gamma}(q_2, e_2; q_1, e_1),$$

$$t_{P\gamma\gamma}(q_1, e_1; q_2, e_2) = -N_c g_P \mathcal{Q}_P \tag{22}$$
$$\times \int \frac{d^4k}{(2\pi)^4} \mathrm{tr}\{i\gamma_5 S(k + p/2; m_a)\hat{e}_1$$
$$\times S(k - (q_1 - q_2)/2; m_a)\hat{e}_2 S(k - p/2; m_a)\},$$

where $\mathcal{Q}_P$ depends on the electric charges and flavors of quarks that constitute the meson, $\mathcal{Q}_{\pi^0} = 1/3$ for π^0, $\mathcal{Q}_{\eta_u} = 5/9$ for η_u, and $\mathcal{Q}_{\eta_s} = -\sqrt{2}/9$ for η_s; and S is the quark propagator,

$$S^{-1}(k; m_a) = \not{k} - m_a, \tag{23}$$

with the constituent quark mass, $m_a = m_u$ for $P = \pi$ or η_u and $m_a = m_s$ for $P = \eta_s$. Comparing (21) with (1), one obtains

$$\mathcal{F}_P(q_1^2, q_2^2, p^2) = \frac{g_P}{2\pi^2} m_a I_{P\gamma\gamma}(q_1^2, q_2^2, p^2). \tag{24}$$

The Feynman integral $I_{P\gamma\gamma}(q_1^2, q_2^2, p^2)$ is given (in Euclidean metric) by

$$I_{P\gamma\gamma}(q_1^2, q_2^2, p^2) = \int \frac{d_e^4 k}{\pi^2} \frac{\theta(\Lambda_{\rm NJL}^2 - k^2)}{[m_a^2 + (k + p/2)^2][m_a^2 + (k - p/2)^2][m_a^2 + (k - (q_1 - q_2)/2)^2]}. \tag{25}$$

In the chiral limit $p^2 = 0$, when both photons are on-mass-shell ($q_1^2 = q_2^2 = 0$), integral (25) becomes very simple. Formally, it is finite, and one can set the UV cutoff $\Lambda_{\rm NJL}$ to infinity and thus find that it is equal to $1/(2m_a^2)$. As a result, one reproduces the well-known result for the decay $\pi^0 \to \gamma\gamma$ [see (2)]. For the η and η' mesons, the result is similar, and the only difference is that the singlet–octet mixing should be taken into account:

$$\mathcal{F}_\eta(0,0,0) = \frac{1}{4\pi^2 \tilde{f}_\eta}, \quad \mathcal{F}_{\eta'}(0,0,0) = \frac{1}{4\pi^2 \tilde{f}_{\eta'}}, \tag{26}$$

$$\tilde{f}_\eta^{-1} = \frac{5}{3 f_u}\sin(\theta_0 - \theta) - \frac{\sqrt{2}}{3 f_s}\cos(\theta_0 - \theta), \tag{27}$$

$$\tilde{f}_{\eta'}^{-1} = \frac{5}{3 f_u}\cos(\theta_0 - \theta) + \frac{\sqrt{2}}{3 f_s}\sin(\theta_0 - \theta). \tag{28}$$

Here, the meson weak-decay constants are $f_u \equiv f_\pi$ and $f_s = m_s/g_s \approx 1.25 f_u$. Thus, we have $\tilde{f}_\eta = 83$ MeV and $\tilde{f}_{\eta'} = 73$ MeV. (For the discussion of singlet–octet mixing, see [25].)

[2)] The strange-quark mass can also be fixed from the ϕ-meson mass [24].

Let us now consider the high-virtuality region: $Q^2 \to \infty$ [see (3) for the definition]. We estimate the asymptotic form of the transition form factor. Let us rewrite the expression for integral (25) by using the Feynman α parametrization for the denominators and integrating over the angular variables. Then, the corresponding integral $I_{P\gamma\gamma}$ is given by

$$I_{P\gamma\gamma}(q_1^2, q_2^2, p^2) = \int_0^{\Lambda_{\rm NJL}^2/m_q^2} \frac{u\,du}{m_q^2 + u - \frac{p^2}{4}} \tag{29}$$
$$\times \int_0^1 d\alpha \left[\frac{1}{\sqrt{b^4 - a_+^4}\left(b^2 + \sqrt{b^4 - a_+^4}\right)}\right.$$
$$\left. + \frac{1}{\sqrt{b^4 - a_-^4}\left(b^2 + \sqrt{b^4 - a_-^4}\right)}\right],$$

where $u = k^2$ and

$$b^2 = m_a^2 + u + \frac{1}{2}\alpha Q^2 - \frac{1}{4}(1 - 2\alpha)\,p^2, \tag{30}$$
$$a_\pm^4 = 2u\alpha Q^2\left(\alpha \pm \omega(1 - \alpha)\right) - (1 - 2\alpha)\,up^2.$$

In this way, the expression (29) can be safely analyzed in the asymptotic limit of high total virtuality of the photons, $Q^2 \to \infty$. Moreover, the integral over α can be taken analytically, leading, in the chiral limit $p^2 = 0$, to the asymptotic expression given by (5), where (see [16])

$$J_P(\omega) \equiv J_{P,\mathrm{np}}(\omega) = \frac{g_P^2 \mathcal{Q}_P Z}{8\pi^2 \omega} \times \left\{ \int\limits_0^{\Lambda^2_{\mathrm{NJL}}/m_q^2} \frac{du}{1+u} \ln\left[\frac{1+u(1+\omega)}{1+u(1-\omega)}\right] \right\}, \quad (31)$$

$$a = u \text{ if } P = \pi, \eta_u; \quad a = s \text{ if } P = \eta_s. \quad (32)$$

The η and η' mesons appear as mixed η_u and η_s states [see (13) and (14)], and for them one has

$$J_\eta(\omega) = c_1 J_{\eta_u}(\omega) + c_2 J_{\eta_s}(\omega), \quad (33)$$

$$J_{\eta'}(\omega) = c_3 J_{\eta_u}(\omega) + c_4 J_{\eta_s}(\omega), \quad (34)$$

where the coefficients c_i are

$$c_1 = \frac{5f_u}{3f_\eta}\sin(\theta_0 - \theta), \quad c_2 = -\frac{\sqrt{2}f_s}{3f_\eta}\cos(\theta_0 - \theta), \quad (35)$$

$$c_3 = \frac{5f_u}{3f_{\eta'}}\cos(\theta_0 - \theta), \quad c_4 = \frac{\sqrt{2}f_s}{3f_{\eta'}}\sin(\theta_0 - \theta),$$

and the constants f_η and $f_{\eta'}$ are defined as[3)]

$$f_\eta = \frac{5}{3}f_u \sin(\theta_0 - \theta) - \frac{\sqrt{2}}{3}f_s\cos(\theta_0 - \theta) = 95\ \mathrm{MeV}, \quad (36)$$

$$f_{\eta'} = \frac{5}{3}f_u \cos(\theta_0 - \theta) + \frac{\sqrt{2}}{3}f_s\sin(\theta_0 - \theta) = 135\ \mathrm{MeV}. \quad (37)$$

One should also note an extra factor Z in the expression of $J_P(\omega)$ in (31). Analogously, the factor Z appears in the amplitude of the decay $\pi \to \mu\bar{\nu}_\mu$ that determines the pion weak coupling constant f_π. To obtain the correct result, one should take account of π–a_1 transitions by considering additional contributions going from the diagrams with axial-vector-type vertices [see the term L_2 in (11)]. When calculating both the $\pi \to \mu\bar{\nu}_\mu$ amplitude and the $\gamma^* \to P\gamma^*$ transition form factor, the account of π–a_1 transitions leads to cancellation of the factor Z.

[3)]Note that the definition of f_η and $f_{\eta'}$ differs from that of $\tilde{f}_\eta$ and $\tilde{f}_{\eta'}$ [see (27) and (28)].

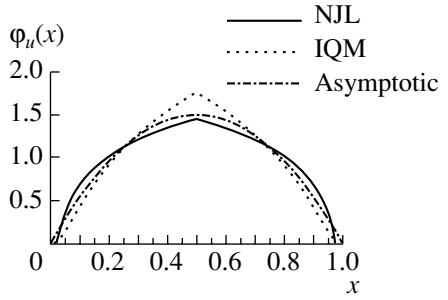

Fig. 2. The DA φ_u in the NJL and IQM models and the asymptotic DA.

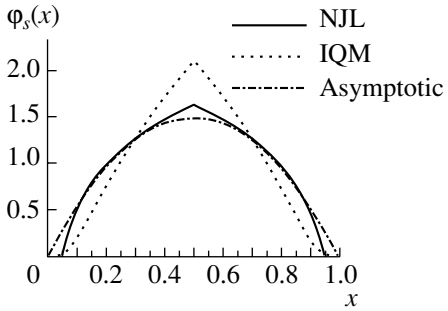

Fig. 3. The DA φ_s in the NJL and IQM models and the asymptotic DA.

3.3. Distribution Amplitudes of Pseudoscalar Mesons

The quark–meson interaction in the NJL model [2] is described by the vertices given in (7)–(12). One just has to calculate the integral (25). Formally, the integral (25) is convergent, and a UV cutoff is not necessary here; however, the extraction of its asymptotic behavior at large Q^2 would lead to a logarithmic dependence $\sim(\ln Q^2)^2/Q^2$, which is not expected, as is known from QCD. Therefore, the UV cutoff in the NJL model should be treated not only as a trick to make the integrals convergent, but also as a way to take into account the nontrivial nonlocal vacuum structure. The UV cutoff also forbids the large momenta flow through meson vertices.

From (31), it is clear that the prediction of the nonperturbative approach to the asymptotic coefficient $J_P(\omega)$ is rather sensitive to the ratio of the ultraviolet cutoff, Λ_{NJL}; to the value of the constituent mass m_a; and to the relative distribution of the total virtuality among photons, ω. In particular, for the off-shell process $\gamma^* \to \pi^0\gamma^*$ in the kinematic case of symmetric distribution of photon virtualities, $q_1^2 = q_2^2 \to -\infty$ ($\omega \to 0$), the result $J(|\omega| = 0) = 4/3$ obtained from (31) is in agreement with the OPE prediction.

Integral (25) is similar in its structure to the integral arising in the lowest order of pQCD treating the

quark–photon interaction perturbatively. In the latter case, its asymptotic behavior is due to the subprocess $\gamma^*(q_1)+\gamma^*(q_2)\to\bar q(\bar x p)+q(xp)$ with x ($\bar x=1-x$) being the fraction of the meson momentum p carried by the quark produced at the $q_1(q_2)$ photon vertex. The relevant diagram is similar to the handbag diagram for hard exclusive processes, with the main difference that one should use, as a nonperturbative input, a quark–meson vertex instead of the meson DA. As we see below, this similarity allows one to reconstruct the shape of the meson DA.

Both expressions for J_P, derived within the quark–meson model (31) and from the light-cone OPE (6), can be put into the common form

$$J_P(\omega)=\frac{2}{3\omega}\int\limits_0^1 d\xi R_P(\xi)\ln\left[\frac{1+\xi\omega}{1-\xi\omega}\right] \tag{38}$$

with

$$R_P^{\rm pQCD}(\xi)=-\frac{d}{d\xi}\varphi_P^A\left(\frac{1+\xi}{2}\right), \tag{39}$$

$$R_{P,\rm np}(\xi)=16\pi^2 g_a^2\theta\left(1-\frac{\xi}{1-\xi}\frac{m_a^2}{\Lambda_{\rm NJL}^2}\right)\frac{1}{1-\xi},$$

where $0\leqslant\xi\equiv(2x-1)\leqslant 1$, and similar expressions for $-1\leqslant\xi\leqslant 0$. Equating both contributions, we find the meson DA,

$$\varphi_P^A(x)=\frac{g_a^2}{4\pi^2}\int\limits_{|2x-1|}^1\theta\left(1-\frac{y}{1-y}\frac{m_a^2}{\Lambda_{\rm NJL}^2}\right)\frac{dy}{1-y}. \tag{40}$$

Thus, we show that (31) obtained within the NJL model is equivalent to the standard lowest order pQCD result (6), with the only difference that the nonperturbative information accumulated in the meson DA $\varphi_P^A(x)$ in pQCD is represented in NJL by the quark–meson vertex and is connected with the regularization procedure.

Within the NJL model, from (40), one can easily obtain analytic expressions for two special DA describing the distribution of $u(d)$ and s quarks, respectively,

$$\varphi_u^A(x)=\begin{cases}\ln\left|\dfrac{1-\xi_u}{1-|2x-1|}\right|/(\xi_u+\ln|1-\xi_u|), & |2x-1|\leqslant\xi_u,\\ 0, & |2x-1|>\xi_u,\end{cases} \tag{41}$$

where the constant ξ_u is defined as follows:

$$\xi_u=\frac{\Lambda_{\rm NJL}^2}{\Lambda_{\rm NJL}^2+m_u^2}; \tag{42}$$

$$\varphi_s^A(x)=\begin{cases}\ln\left|\dfrac{1-\xi_s}{1-|2x-1|}\right|/(\xi_s+\ln|1-\xi_s|), & |2x-1|\leqslant\xi_s,\\ 0, & |2x-1|>\xi_s,\end{cases} \tag{43}$$

$$\xi_s=\frac{\Lambda_{\rm NJL}^2}{\Lambda_{\rm NJL}^2+m_s^2}. \tag{44}$$

For the π, η, and η' mesons, one has

$$\varphi_\pi(x)=\varphi_u^A(x), \tag{45}$$

$$\varphi_\eta(x)=c_1\varphi_u^A(x)+c_2\varphi_s^A(x), \tag{46}$$

$$\varphi_{\eta'}(x)=c_3\varphi_u^A(x)+c_4\varphi_s^A(x), \tag{47}$$

where the coefficients c_i are defined in (35). The DA calculated in the NJL are shown in Figs. 2–5.

3.4. Instanton-Induced Effective Quark–Meson Lagrangian

Let us now consider the piece of the effective quark–meson Lagrangian that appears in IQM. The effective quark–meson dynamics can be summarized in the covariant nonlocal action given by

$$S_{\rm int}=-\int d^4x\,d^4y\,F\left[x+y/2,x-y/2;\Lambda_{\rm IQM}^{-2}\right] \tag{48}$$

$$\times\,\bar q(x+y/2)\,i\gamma_5\left[g_{\pi\bar qq}\sum_{a=1}^3\lambda^a\pi^a(x)+g_{\eta_u}\lambda_u\eta_u(x)+g_{\eta_s}\lambda_s\eta_s(x)\right]q(x-y/2).$$

The dynamic vertex $F\left[x+y/2,x-y/2;\Lambda_{\rm IQM}^{-2}\right]$ depends on the coordinates of the quark and antiquark and arises due to the quark–antiquark interaction

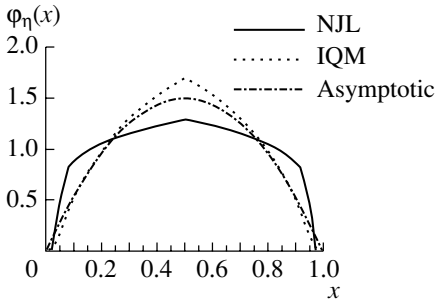

Fig. 4. The DA φ_η in the NJL and IQM models and the asymptotic DA.

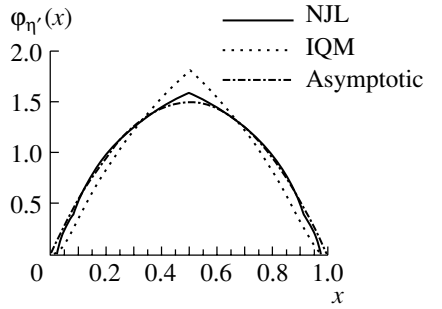

Fig. 5. The DA $\varphi_{\eta'}$ in the NJL and IQM models and the asymptotic DA.

induced by exchange of an instanton with size $\Lambda_{\rm IQM}^{-1} \simeq \rho_c$, $\Lambda_{\rm IQM} \approx 0.742$ GeV. The nonlocal vertex characterizes the coordinate dependence of the order parameter for SBCS and can be expressed in terms of nonlocal quark condensates.

We restrict ourselves to the approximation (see, e.g., [26])

$$F\left[x+y/2, x-y/2; \Lambda_{\rm IQM}^{-2}\right] \to F(y^2; \Lambda_{\rm IQM}^{-2}), \quad (49)$$

when the dynamic quark–meson vertex depends only on the relative coordinate of the quark and antiquark squared, y^2, if neglecting the dependence of the vertex on the angular variable (yx). The Fourier transform of the vertex function in the Minkowski space is defined as $\tilde{F}(k^2; \Lambda_{\rm IQM}^2) = \int d^4x F(x^2; \Lambda_{\rm IQM}^{-2}) \exp(-ikx)$ with normalization $\tilde{F}(0; \Lambda_{\rm IQM}^2) = 1$, and we assume that it rapidly decreases in the Euclidean region ($k^2 = -k_{\rm E}^2 \equiv -u$). As in the NJL model, we also approximate the momentum-dependent quark self-energy in the quark propagator $S^{-1}(k; m_a) = \not{k} - m_a$ by a constant quark mass [26] and neglect meson-mass effects. The quark masses are $m_u = 275$ MeV and $m_s = 430$ MeV, close to those obtained in the NJL model (see Subsection 3.1). We have to note that the approximations used here are not fully consistent. Further, as the reader will see below, the choice of the model for the quark–meson vertex (49), depending only on the relative coordinate, induces a certain artifact in the x behavior of DA. However, these deficiencies of the chosen approximation are not essential for the present purpose and do not lead to large numerical errors.

The quark–meson coupling is given by the condition [26]

$$g_q^{-2} = \frac{N_c}{8\pi^2} \int\limits_0^\infty du\, u\tilde{F}^2(-u; \Lambda_{\rm IQM}^2/m_q^2) \frac{3+2u}{(1+u)^3}, \quad (50)$$

and the meson weak decay constants $f_\pi \equiv f_u$ and f_s are expressed by

$$f_q = \frac{N_c g_q}{4\pi^2} M_q \int\limits_0^\infty du\, u\tilde{F}(-u; \Lambda_{\rm IQM}^2/m_q^2) \frac{1}{(1+u)^2}. \quad (51)$$

We have rescaled the integration variable by the quark mass squared. Within the instanton vacuum model, the size of nonlocality of the nonperturbative gluon field, $\rho_c \sim \Lambda_{\rm IQM}^{-1} \simeq 0.3$ fm, is much smaller than the quark Compton length m_q^{-1}.

To calculate the transition form factors, one can use the same formulas that have been obtained above in the NJL model. The only exception is that the θ function should be replaced by the nonlocal quark–meson vertex function $\tilde{F}(-u; \Lambda_{\rm IQM}^2/m_q^2)$. In the next section, we discuss numerical results obtained in IQM as compared with the NJL-model calculation and experimental data.

Let us note that we use an approximation to the model with constant constituent quark masses for all three quark lines in the diagrams of the process (see Fig. 1). However, the asymptotic result (31) is

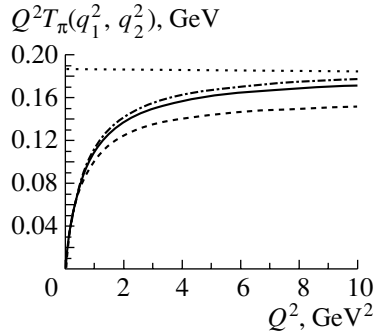

Fig. 6. The light-cone transition form factor for the pion. The solid curve corresponds to the NJL-model calculation, the dashed curve is a fit to the CLEO data, the dash-dotted curve corresponds to IQM, and the dotted line is $2f_\pi$.

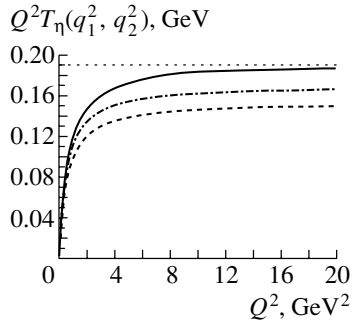

Fig. 7. The light-cone transition form factor for the η meson. The solid curve corresponds to the NJL-model calculation, the dashed curve is a fit to the CLEO data, the dash-dotted curve corresponds to IQM, and the dotted line is $2f_\eta$.

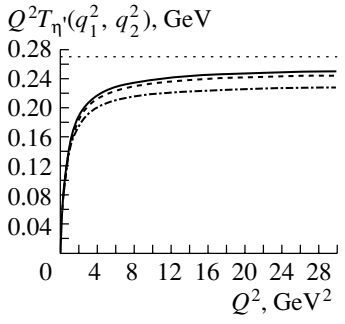

Fig. 8. The light-cone transition form factor for the η' meson. The solid curve corresponds to the NJL-model calculation, the dashed curve is a fit to the CLEO data, the dash-dotted curve corresponds to IQM, and the dotted line is $2f_{\eta'}$.

independent of the mass in the quark propagator with hard momentum flow, as it should be. The other two quark lines remain soft during the process; thus, the mass m_a can be considered as given on a certain characteristic soft scale in the momentum-dependent case m_a.

4. DISCUSSION AND CONCLUSION

Within the two ECQM under consideration that describe the quark–meson dynamics, we calculated the $\gamma^* \to P\gamma^*$ transition form factor at moderately high momentum transfers squared in a wide kinematic domain. From the model calculations, the normalization coefficient $J_P(\omega)$ of the leading Q^{-2} term is found [see (31)]. It depends on the ratio of the constituent quark mass to the UV cutoff Λ and also on the kinematics of the process. From the comparison of the kinematic dependence of the asymptotic coefficient of the transition form factors, given by pQCD and NJL, the meson distribution amplitudes (40) are derived. Analogously, a relation between DA and the dynamic quark–meson vertex function is obtained in IQM. In the specific case of symmetric kinematics ($q_1^2 = q_2^2$), our result agrees with the one obtained by OPE and also with the expression for the constant f_P that determines the decay $P \to \mu\bar{\nu}_\mu$ of meson P.

Let us discuss DA obtained in different approaches. In the NJL, we obtained explicit expressions for the DA of the pion, η meson, and η' meson. They are plotted in Figs. 2–5 (solid curve), from which one can see that the NJL model predicts a flatter distribution of quark momenta in a meson than IQM. To compare with other theoretical approaches, we also plotted, as a sample, the results obtained in IQM (dashed curve). Also given is the asymptotic pQCD expressions for DA: $\varphi^{\rm as}(x) = 6x(1-x)$ (dash-dotted curve). One can see that, for most x, the DA's shapes are similar in different approaches. A difference can be noticed near $x \approx 1/2$ and at the edges. The cusp at $x = 1/2$ and a very sharp decrease in DA near $x = 0$ and $x = 1$ are artifacts closely related to the UV regularization in the NJL model and to the shape of the nonlocal quark–meson vertex function in IQM. However, these deficiencies turned out not to be crucial in our calculations.

Now, we would like to make some notes regarding the definition of f_η and $f_{\eta'}$ used by the authors of [15]. In [15], f_P are obtained from the tabulated data on the decays $P \to \gamma\gamma$, using the low-energy limit of the process amplitude

$$\mathcal{F}_P(0,0,0) \simeq 1/(4\pi^2 \tilde{f}_P) \tag{52}$$

{see (6) in [15]}. This works well for the pion, but the case of the η and η' mesons is rather different because of the singlet–octet mixing. In the limit $Q^2 \to \infty$, one should expect

$$\lim_{Q^2\to\infty} Q^2\mathcal{F}_P(q_1^2 = -Q^2, q^2 = 0, p^2 = 0) = 2f_P, \tag{53}$$

where f_P are not the same as $\tilde{f}_P$ except for f_π, as one can see from comparing (36) and (37) with (27) and (28). That is why the CLEO fit noticeably disagrees with the limit $2f_{\eta'}$ {see Eq. (5) in [15] drawn in Fig. 23 [15]}. Therefore, it is not correct to use Eq. (7) in [15] to perform a fit. From our calculation, we see that, taking into account the singlet–octet mixing, one can avoid the discrepancy in the description of the $\gamma^* \to P\gamma$ interaction at both small and large Q^2.

Now, we compare our results for the case $\omega = 1$ ($\gamma^* \to P\gamma$) with those given by the CLEO Collaboration [15] for large Q^2. We calculate the product of Q^2 and transition form factor:

$$\mathcal{F}_P(\omega) = \lim_{Q^2\to\infty} Q^2\mathcal{F}_P(q_1^2, q_2^2, p^2). \tag{54}$$

Theoretically, we have

$$\mathcal{F}_P(\omega) = J_P(\omega) f_P, \tag{55}$$

according to (5). In the NJL model, $J_\pi(1) = 1.97$, $J_\eta(1) = 2.04$, and $J_{\eta'}(1) = 1.9$. Therefore, $\mathcal{F}_\pi(1) \approx 0.184$ GeV, $\mathcal{F}_\eta(1) \approx 0.193$ GeV, and $\mathcal{F}_{\eta'}(1) \approx 0.256$ GeV. The IQM predicts $J_\pi(1) = 1.78$, $J_\eta(1) = 1.83$, and $J_{\eta'}(1) = 1.73$ and $\mathcal{F}_\pi(1) \approx 0.16$ GeV, $\mathcal{F}_\eta(1) \approx 0.17$ GeV, and $\mathcal{F}_{\eta'}(1) \approx 0.23$ GeV.

An infinite value of Q^2 cannot be reached in experiment, so we determine $\mathcal{F}_P(\omega)$ at the value of the maximum accessible Q^2 in experiment. Thus, the CLEO collaboration gives $\mathcal{F}_\pi(1) = 0.17 \pm 0.3$ GeV at $Q^2 = 7.0$–9.0 GeV^2, $\mathcal{F}_\eta(1) \approx 0.16$ GeV at $Q^2 \sim 22$ GeV^2, and $\mathcal{F}_{\eta'}(1) \approx 0.25$ GeV at $Q^2 \sim 30$ GeV^2. The monopole interpolation for the transition form factors (5) obtained both theoretically and experimentally is shown in Figs. 6–8. One can see that the experiment gives values for the transition form factors lower than models. The biggest difference (about 20%) is seen for the η meson. The best agreement of models with the CLEO fit is obtained for π and η'.

The constants $g_{P\gamma\gamma}$ in the monopole ansatz (4) for the transition form factors are related to the $P \to \gamma\gamma$ decay width. It is interesting to compare their values predicted in different models with experimental data. According to (52), we obtain from NJL $g_{\pi\gamma\gamma} = 0.27$ GeV^{-1}, $g_{\eta\gamma\gamma} = 0.31$ GeV^{-1}, and $g_{\eta'\gamma\gamma} = 0.35$ GeV^{-1}. The same gives us IQM. From experiment, we have $g^{\exp}_{\pi\gamma\gamma} = 0.26$ GeV^{-1}, $g^{\exp}_{\eta\gamma\gamma} = 0.26$ GeV^{-1}, and $g^{\exp}_{\eta'\gamma\gamma} = 0.34$ GeV^{-1}. Again, the model prediction for π and η' is better suited to the experimental values, whereas for the η meson one has a noticeable discrepancy.

The results presented in our paper are in accordance with the conclusions made in [12, 14, 27] within the QCD sum rules, which is evidence that our approach is valid for the process under consideration and gives us hope that it can be applied to other processes with large momentum transfers as well.

We plan to use the ECQM approach approved here on the process $\gamma^* \to P\gamma$ for the description of the following processes: $\gamma^* \to P\rho$, $\gamma^* \to P\omega$, $\gamma^* \to P'\gamma$ (with P' being a radial excitation of a pseudoscalar meson), $\gamma^* \to S\gamma$ (with S being a scalar meson), $\gamma^* \to \gamma A$ (with A being an axial-vector meson), $\gamma^* \to \gamma\pi\sigma$, $\gamma^* \to \gamma\pi\rho$, $\gamma^*\gamma^* \to \pi\pi$, etc.

ACKNOWLEDGMENTS

This work is supported by the Heisenberg–Landau program and the Russian Foundation for Basic Research (project nos. 01-02-16231, 02-02-16194) and by INTAS (grant no. 2000-366).

REFERENCES

1. M. K. Volkov, Ann. Phys. (N. Y.) **157**, 282 (1984).
2. M. K. Volkov, Sov. J. Part. Nucl. **17**, 186 (1986).
3. D. Ebert, H. Reinhardt, and M. K. Volkov, Prog. Part. Nucl. Phys. **35**, 1 (1994).
4. H. Vogl and W. Weise, Prog. Part. Nucl. Phys. **27**, 195 (1991).
5. S. P. Klevansky, Rev. Mod. Phys. **64**, 649 (1992).
6. M. K. Volkov and V. L. Yudichev, Fiz. Élem. Chastits At. Yadra **31**, 576 (2000) [Phys. Part. Nucl. **31**, 282 (2000)].
7. M. K. Volkov and V. L. Yudichev, Eur. Phys. J. A **10**, 109 (2001).
8. M. K. Volkov and V. L. Yudichev, Eur. Phys. J. A **10**, 223 (2001).
9. V. L. Chernyak and A. R. Zhitnitsky, JETP Lett. **25**, 510 (1977).
10. A. V. Efremov and A. V. Radyushkin, Math. Phys. **42**, 97 (1980); Phys. Lett. B **94B**, 45 (1980).
11. S. J. Brodsky and G. P. Lepage, Phys. Lett. B **87B**, 359 (1979); Phys. Rev. D **22**, 2157 (1980).
12. S. V. Mikhailov and A. V. Radyushkin, Yad. Fiz. **52**, 1095 (1990) [Sov. J. Nucl. Phys. **52**, 697 (1990)].
13. S. V. Mikhailov and A. V. Radyushkin, JETP Lett. **43**, 712 (1986); Yad. Fiz. **49**, 794 (1989) [Sov. J. Nucl. Phys. **49**, 494 (1989)]; Phys. Rev. D **45**, 1754 (1992).
14. A. V. Radyushkin and R. T. Ruskov, Nucl. Phys. B **481**, 625 (1996); hep-ph/9706518.
15. CLEO Collab. (J. Gronberg *et al.*), Phys. Rev. D **57**, 33 (1998).
16. I. V. Anikin, A. E. Dorokhov, and L. Tomio, Phys. Lett. B **475**, 361 (2000); A. E. Dorokhov and L. Tomio, Phys. Rev. D **62**, 014016 (2000); I. V. Anikin, A. E. Dorokhov, and L. Tomio, Phys. Part. Nucl. **31**, 509 (2000).
17. S. Adler, Phys. Rev. **177**, 2426 (1969).
18. J. S. Bell and R. Jackiw, Nuovo Cimento A **60**, 47 (1969).
19. G. P. Lepage and S. J. Brodsky, Phys. Rev. D **22**, 2157 (1980).
20. M. K. Volkov and V. L. Yudichev, Nuovo Cimento A **112**, 225 (1999).
21. Particle Data Group (D. E. Groom *et al.*), Eur. Phys. J. C **15**, 1 (2000).
22. T. Eguchi, Phys. Rev. D **14**, 2755 (1976).
23. K. Kikkawa, Prog. Theor. Phys. **56**, 947 (1976).
24. M. K. Volkov and A. N. Ivanov, Theor. Math. Phys. **69**, 1066 (1986).
25. Th. Feldmann and P. Kroll, hep-ph/0201044.
26. H. Ito, W. W. Buck, and F. Gross, Phys. Rev. C **45**, 1918 (1992); Phys. Lett. B **287**, 23 (1992); I. Anikin, M. Ivanov, N. Kulimanova, and V. Lyubovitskii, Yad. Fiz. **57**, 1082 (1994) [Phys. At. Nucl. **57**, 1021 (1994)].
27. A. P. Bakulev and S. V. Mikhailov, Phys. Lett. B **436**, 351 (1998).

Physics of Atomic Nuclei, Vol. 66, No. 5, 2003, pp. 950–954. From Yadernaya Fizika, Vol. 66, No. 5, 2003, pp. 983–987.

ELEMENTARY PARTICLES AND FIELDS
Theory

Triangular and Y-Shaped Hadrons in QCD*

D. S. Kuzmenko and **Yu. A. Simonov*****

Institute of Theoretical and Experimental Physics,
Bol'shaya Cheremushkinskaya ul. 25, Moscow, 117259 Russia

Received October 11, 2002

Abstract—Gauge-invariant extended configurations are considered for the three fundamental (quarks) or adjoint (gluons) particles. For quarks, it is shown that the Y-shaped configuration is the only one possible. For adjoint sources, both Y-shaped and triangular configurations may exist. The corresponding static potentials are calculated by the method of field correlators and, in the case of baryons, shown to be consistent with the lattice simulations. For adjoint sources the potentials of Y-shaped and Δ-shaped configurations turn out to be close to each other, which leads to almost degenerate masses of $3^{--}3g$ glueballs and odderon trajectories. © *2003 MAIK "Nauka/Interperiodica".*

1. To make conclusions on the structure of gluonic fluxes confining color charges in physical states, one has to start from consideration of the space-extended gauge-invariant wave function of the hadron. It is easy then to show that, in the case of static charges, the Green's function of the hadron reduces to the Wilson loop, which in the case of the baryon has the Y-type shape and consists of the three contours formed by the quark trajectories and joined at the point of the string junction [1, 2]. The Wilson loop of the three adjoint sources is less well known than the $3q$ one. In the paper, we show that it can have both Y-type and Δ-type shape.

Using the formalism of the method of the field correlators (MFC), we compute the static potentials corresponding to the Wilson loops of the hadrons. In the case of the baryon, the static potential was used long ago in many dynamical calculations [3, 4]. Recently, it has been computed in lattice gauge theory in a number of papers [5–7]. We show that our potential is in good agreement with the latest lattice studies [6, 7].

In the case of adjoint sources, we find that the Y-type and Δ-type potentials remain near each other at the characteristic hadronic size. Using that, we estimate the masses of the lowest $3g$ glueballs, lying on the corresponding odderon trajectories, and show that they are close to each other, implying that there are two possible odderon trajectories with not much different Regge slopes. A short discussion of physical implications of these results concludes the paper.

To avoid confusion, we should stress that the term "Δ configuration" used in [5–8] in the context of the static baryon potential refers to the perimeter behavior of the potential, rather than to the gauge-invariant configurations or to the structures of fluxes discussed in the present paper.

2. Hadron building in $SU(3)$ starts with listing elementary building blocks: quarks q^α, $\alpha = 1, 2, 3$; gluons (or adjoint static sources) g^a, $a = 1, \ldots, 8$; parallel transporters (PTs) $\Phi^\beta_\alpha(x, y) = (P\exp(ig \times \int A_\mu(z)dz_\mu))^\beta_\alpha$ in a fundamental representation; adjoint parallel transporters $\Phi_{ab}(x, y)$; generators $t^{(a)\beta}_\alpha$; symmetric symbols δ^β_α, δ_{ab}, and d^{abc}; and antisymmetric symbols $e_{\alpha\beta\gamma}$ and f^{abc}. Note that we always use Greek indices for the fundamental representation and Latin ones for the adjoint. To construct a real extended (not pointlike) hadron, one uses all listed elements, PTs included, and forms a white (gauge-invariant) combination. It is convenient to form an extended quark (antiquark) operator

$$q^\alpha(x, Y) \equiv q^\beta(x)\Phi^\alpha_\beta(x, Y), \qquad (1)$$

$$\bar{q}_\alpha(x, Y) = \bar{q}_\beta(x)\Phi^\beta_\alpha(x, Y).$$

In this way, one has for the Y-shaped baryon

$$B_Y(x, y, z, Y) = e_{\alpha\beta\gamma}q^\alpha(x, Y)q^\beta(y, Y)q^\gamma(z, Y). \quad (2)$$

One can also define a quark operator with two lower indices: $e_{\alpha\beta\gamma}q^\alpha(x) \equiv q_{\beta\gamma}(x)$. However, an attempt to create a gauge-invariant combination from three operators $q_{\beta\gamma}(x)$ and three PTs to construct a Δ-type configuration fails: the structure

$$B_\Delta(x, y, z) = q_{\alpha\beta}(x)\Phi^\beta_\gamma(x, y)q_{\gamma\delta}(y) \qquad (3)$$

*This article was submitted by the authors in English.

** e-mail: kuzmenko@heron.itep.ru
*** e-mail: simonov@heron.itep.ru

$$\times \Phi^{\delta}_{\varepsilon}(y,z)q_{\varepsilon\rho}(z)\Phi^{\rho}_{\alpha}(z,x)$$

is not gauge-invariant, which can be checked directly, substituting in (3) $q^{\alpha}(x) \to U^{\alpha}_{\beta}(x)q^{\beta}(x)$. One can try all combinations, but it is impossible to form a continuous chain of indices to represent the Δ-type structure using as operators q_{α} as $q_{\alpha\beta}$. Thus, one can conclude that the Y-shaped configuration is the only possible gauge-invariant configuration of the wave function for baryons.

One may wonder, What is the relation between the spacial structures of the wave function of hadrons and their gluonic flux? The answer from the flux-tube models is that these structures coincide. In realistic lattice calculations, one has to use the Wilson loop, which describes the gauge-invariant state of a hadron generated at some initial and annihilated at some final moment of time. As is well known, for static charges, the Wilson loop consists of two wave functions [see, e.g., (2) or (3)] joined by PTs. Let us imagine now some evolution of the fluxes in a baryon that would lead to the emergence of the Δ-type configuration of fluxes at some intermediate time. First of all, we should note that the cross section of the Wilson loop by the timelike hypersurface will recover a gauge-invariant $3q$ state, i.e., the Y-type configuration. To have a Δ-shape for fluxes, one should admit that the fluxes have no relation to the wave function, which is improbable.

Consider now the adjoint source $g^{a}(x)t^{(a)\beta}_{\alpha} \equiv G^{\beta}_{\alpha}(x)$. We do not specify here the Lorentz structure of $g^{a}(x)$, but only impose the condition that it should gauge-transform homogeneously, $G^{\beta}_{\alpha} \to U^{+\beta}_{\beta'}G^{\beta'}_{\alpha'}U^{\alpha'}_{\alpha}$. Therefore, $g^{a}(x)$ can be either the field strength $F^{a}_{\mu\nu}(x)$ or the valence gluon field $a^{a}_{\mu}(x)$ in the background-field perturbation theory [9]. It is easy to construct a Δ-type configuration for three such sources:

$$G_{\Delta}(x,y,z) = G^{\beta}_{\alpha}(x)\Phi^{\gamma}_{\beta}(x,y)G^{\delta}_{\gamma}(y) \qquad (4)$$
$$\times \Phi^{\varepsilon}_{\delta}(y,z)G^{\rho}_{\varepsilon}(z)\Phi^{\alpha}_{\rho}(z,x).$$

It is clear that in (4) all repeated indices form gauge-invariant combinations and $G_{\Delta}(x,y,z)$ is a gauge-invariant Δ-type configuration, which was used previously for the $3g$ glueball in [10].

But one can persuade oneself that (4) is not the only $3g$ gauge-invariant configuration. Consider adjoint sources and adjoint PTs (here, distinguishing upper and lower indices is not necessary) and form as in (1) an extended gluon operator

$$g_{a}(x,Y) \equiv g^{b}(x)\Phi_{ab}(x,Y) \qquad (5)$$

and a Y-shaped configuration

$$G^{(f)}_{Y}(x,y,z,Y) = f^{abc}g_{a}(x,Y)g_{b}(y,Y)g_{c}(z,Y). \quad (6)$$

In the same way, one constructs $G^{(d)}_{Y}$ replacing f by d in (6). It is clear that G_{Y} is gauge-invariant and should be considered on the same grounds as G_{Δ}.

At this point it is necessary to clarify how (2) and (6) generate Green's functions and Wilson loops.

To this end, consider initial and final states made of (2), (4), and (6), and for simplicity of arguments, take all fundamental and adjoint sources to be static, i.e., propagating only in Euclidean time.

Then the Green's function for the object will be

$$\mathcal{G}_{i}(\bar{X},X) = \langle \Psi^{+}_{i}(\bar{X})\Psi_{i}(X)\rangle, \qquad (7)$$

where $\Psi_{i} = G_{\Delta}, G_{Y}, B_{Y}$; and $X = x,y,z$ for G_{Δ} and x, y, z, Y otherwise. Now, it is important that the vacuum average in (7) denoted by $\langle \dots \rangle$ produces a product of Green's functions for quarks or for valence gluons in the external vacuum gluonic field, which is proportional to the corresponding PTs, fundamental for quarks and adjoint for gluons. Namely,

$$\langle \bar{q}_{\beta}(\bar{x})q^{\alpha}(x)\rangle \sim \Phi^{\alpha}_{\beta}(\bar{x},x), \qquad (8)$$

$$\langle g_{a}(\bar{x})g_{b}(x)\rangle \sim \Phi_{ab}(\bar{x},x).$$

This statement is well known for static sources; for relativistic quarks and gluons, this follows directly from the exact Fock–Feynman–Schwinger representation (FFSR); see [11, 12] and for a review [13].

As a result, one obtains a gauge-invariant Wilson loop combination for each Green's function (7). In particular, for B_{Y} (2), one has a familiar three-lobe Wilson loop W_{Y}:

$$W_{Y}(\bar{X},X) = \mathrm{tr}_{Y}\prod_{i=1}^{3} W_{i}(C_{i}), \qquad (9)$$

where $\mathrm{tr}_{Y} = (1/6)e_{\alpha\beta\gamma}e_{\alpha'\beta'\gamma'}$, and the contour C_{i} in the open loop W_{i} passes from Y to $\bar{Y}$ through points $x,\bar{x}$ $(i=1)$, $y,\bar{y}$ $(i=2)$, or $z,\bar{z}$ $(i=3)$, as shown in Fig. 1.

This situation is well known and was exploited in numerous applications. Relatively less known are the Wilson loop configurations for G_{Y} and G_{Δ}. In the first case, the structure is the same with the replacement of fundamental lines and symbols by the adjoint ones: $e_{\alpha\beta\gamma} \to f^{abc}$ or $e_{\alpha\beta\gamma} \to d^{abc}$, $\Phi^{\beta}_{\alpha} \to \Phi_{ab}$, so that the whole structure in (9) is the same with this replacement. Contrary to the baryon case, we can contract adjoint indices in two ways, using antisymmetric symbol f^{abc} or symmetric symbol d^{abc}. The proper choice is related to the Bose statistics of the gluon system, which ensures symmetry of the full coordinate-spin function.

In the case of G_{Δ}, using (4) and (8), one can write the resulting structure symbolically as follows:

$$\mathcal{G}_{\Delta}(\bar{X},X) = \Delta_{a'b'c'}(\bar{x},\bar{y},\bar{z})\Phi_{a'a}(\bar{x},x) \qquad (10)$$

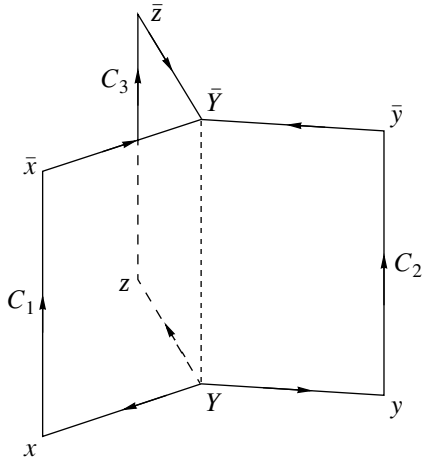

Fig. 1. Y-shaped Wilson loop.

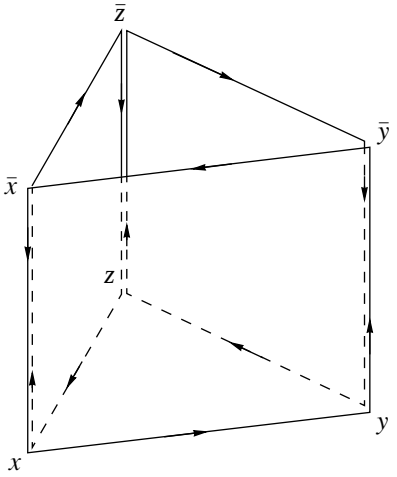

Fig. 2. Δ-shaped Wilson loop.

$$\times \Phi_{b'b}(\bar{y},y)\Phi_{c'c}(\bar{z},z)\Delta_{abc}(x,y,z),$$

where we have denoted

$$\Delta_{abc}(x,y,z) = t_\alpha^{(a)\beta}\Phi_\beta^\gamma(x,y)t_\gamma^{(b)\delta} \times \Phi_\delta^\varepsilon(y,z)t_\varepsilon^{(c)\rho}\Phi_\rho^\alpha(z,x). \quad (11)$$

To understand the structure of (10) better, one can use the large-N_c approximation, in which case one has

$$\Psi_{\alpha\alpha'}^{\beta\beta'} \equiv t_{\alpha'}^{(a')\beta'}\Phi_{a'a}(\bar{x},x)t_\alpha^{(a)\beta} \approx \frac{1}{2}\Phi_\alpha^{\beta'}(x,\bar{x})\Phi_{\alpha'}^\beta(\bar{x},x). \quad (12)$$

As a result, in this approximation, $\mathcal{G}_\Delta$ appears to be a product of three fundamental closed loops, properly oriented with respect to each other:

$$\mathcal{G}_\Delta(\bar{X},X) \sim W(\bar{x},\bar{y}|x,y)W(\bar{y},\bar{z}|y,z) \times W(\bar{z},\bar{x}|z,x) \equiv W_\Delta(\bar{X},X); \quad (13)$$

it is displayed in Fig. 2.

3. Static potentials for configurations (2), (4), and (6) can be computed using the MFC [14], through the equation

$$V = -\lim_{T\to\infty}\frac{1}{T}\ln\langle W\rangle, \quad (14)$$

where T is the time extension of the Wilson loop.

For the baryon in the case of three quarks forming the equilateral triangle, at distance R from the string junction Y, the static baryon potential is [15]

$$V^{(B)}(R) = 3V^{(M)}(R) + V^{(\mathrm{nd})}(R), \quad (15)$$

where

$$V^{(M)}(R) = \frac{2\sigma}{\pi}\left\{R\int_0^{R/T_g} dx x K_1(x) - T_g\left(2 - \frac{R^2}{T_g^2}K_2\left(\frac{R}{T_g}\right)\right)\right\} \quad (16)$$

is the mesonic confining potential with the asymptotic slope $\sigma \approx 0.18\ \mathrm{GeV}^2$ and the gluonic correlation length $T_g = 0.12$–0.20 fm [16], and the nondiagonal part of the potential,

$$V^{(\mathrm{nd})}(R) = \frac{2}{\sqrt{3}}\sigma T_g - \frac{3\sqrt{3}}{2\pi}\frac{\sigma R^2}{T_g} \times \int_{\pi/6}^{\pi/3}\frac{d\varphi}{\cos\varphi}K_2\left(\frac{\sqrt{3}R}{2T_g\cos\varphi}\right), \quad (17)$$

appears due to the interference of the gluonic fields on different lobes of the Wilson loop. Note the difference in the overall factor $-1/2$ with the previous calculations [17], where it was erroneously omitted. Let us denote by $L \equiv 3R$ the total length of the string. In Fig. 3 from [15], the dependence of the lattice nonperturbative baryon potential from [7] on L is shown along with the MFC potential (15)–(17) is shown. One can see that our potential is in complete agreement with the lattice results. In the asymptotic region $L \gtrsim 1.5$ fm, the potential has a linear form

$$V^{(B)}(R) \approx \sigma L + \left(\frac{2}{\sqrt{3}} - \frac{12}{\pi}\right)\sigma T_g. \quad (18)$$

The dotted tangent curve in Fig. 3 demonstrates that, in the range $0.3 \lesssim L \lesssim 1.5$ fm, the lattice data can be described by a linear potential with a slope some 10% less than σ.

The potential written so far contains only the nonperturbative confining part. To obtain the total potential, we should add to it the perturbative color

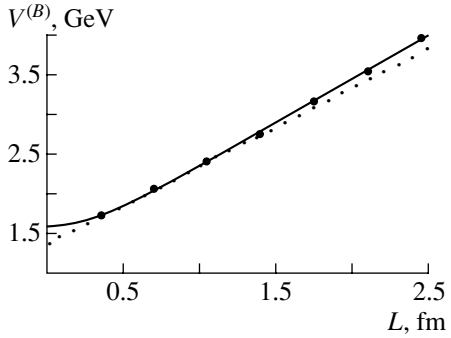

Fig. 3. The lattice nonperturbative baryon potential from [7] (points) for lattice parameter $\beta = 5.8$ and MFC potential $V^{(B)}$ (solid curve) with parameters $\sigma = 0.22$ GeV^2 and $T_g = 0.12$ fm vs. the length of the string L. The dotted curve is a tangent at $L = 0.7$ fm. This figure is taken from [15].

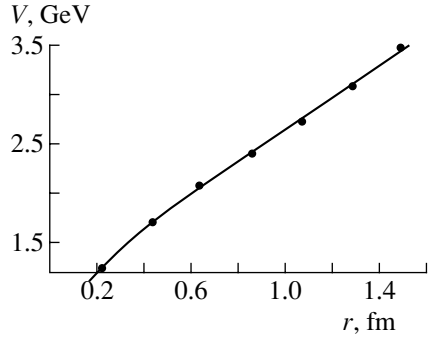

Fig. 4. The lattice baryon potential in the equilateral triangle with quark separations r from [6] (points) and the MFC potential $V^{(B)} + V^{\text{pert}}_{(\text{fund})}$ (solid curve) for lattice parameter $\beta = 5.8$ and MFC parameters $\alpha_s = 0.18$, $\sigma = 0.18$ GeV^2, and $T_g = 0.12$ fm.

Coulomb potential

$$V^{\text{pert}}_{(\text{fund})}(r) = -\frac{3}{2}\frac{C_2(\text{fund})\alpha_s}{r}, \qquad (19)$$

where $r = \sqrt{3}R$ is the interquark distance in the equilateral triangle and $C_2(\text{fund}) = 4/3$.

In Fig. 4, lattice data from [6] and the potential $V^{(B)}(r) + V^{\text{pert}}_{(\text{fund})}(r)$ are shown. One can see that our results are in complete agreement with this independent set of lattice data as well.

In a similar way, one can write the static potential for the adjoint sources, neglecting the nondiagonal term, which is different in symmetric and antisymmetric states:

$$V_Y^{(G)}(R) = \frac{C_2(\text{adj})}{C_2(\text{fund})}V_Y^{(B)}(R) = \frac{9}{4}V_Y^{(B)}(R). \quad (20)$$

Consider the Δ configuration in approximation (12). In this case, $V_\Delta^{(G)}(R)$ reduces to the sum of the mesonic potentials corresponding to area laws for all three loops minus the nondiagonal interference term, and one obtains

$$V_\Delta^{(G)}(r) = 3V^{(M)}(r) - 2V^{(\text{nd})}(r). \qquad (21)$$

Along with the adjoint perturbative potential

$$V^{\text{pert}}_{(\text{adj})}(r) = -\frac{3}{2}\frac{C_2(\text{adj})\alpha_s}{r}, \qquad (22)$$

where $C_2(\text{adj}) = 3$, we plot both $V_Y^{(G)}$ and $V_\Delta^{(G)}$ in Fig. 5 without the interference terms. We see from the figure that the curves intersect at $r \approx 0.5$ fm and are very close to each other.

4. To summarize our results, we have considered possible gauge-invariant configurations of three fundamental or adjoint sources and the corresponding Wilson loops, which have Y-type shape for fundamental charges and may have both Y-type and Δ-type shapes for the adjoint ones. We have shown that the static baryon potential obtained in the MFC is in complete agreement with the lattice data.

For adjoint sources, it was demonstrated that two possible configurations yield static potentials differing only a little. This in turn implies that $3g$ glueballs [10] may be of two distinct types, with no direct transitions between them (quark-containing hadrons must be involved as intermediate states). The mass of the Δ-shaped 3^{--} glueball was found in [10] to be $M_\Delta^{(3g)} = 3.51$ GeV for $\sigma = 0.18$ GeV^2 (or 4.03 GeV for $\sigma = 0.238$ GeV^2, to be compared with the lattice one calculated in [18] 4.13 ± 0.29 GeV). The mass of the Y-shaped glueball can easily be computed from the baryon mass calculated in [19], multiplying it by $\sqrt{9/4} = 3/2$. In this way, one obtains $M_Y^{(3g)} = 3.47$ GeV ($\sigma = 0.18$ GeV^2). The slope of the

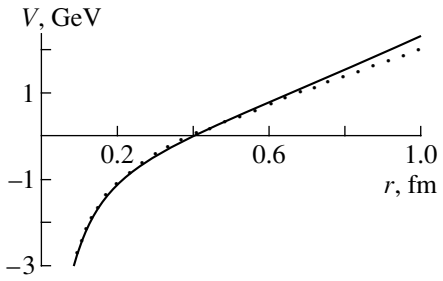

Fig. 5. Glueball potentials $V_Y^{(G)}(r) + V^{\text{pert}}_{(\text{adj})}(r)$ (solid curve) and $V_\Delta^{(G)}(r) + V^{\text{pert}}_{(\text{adj})}(r)$ (dotted curve) in the equilateral triangle with the quark separations r for $\alpha_s = 0.3$, $\sigma = 0.18$ GeV^2, and $T_g = 0.12$ fm. The nondiagonal terms are neglected.

corresponding odderon trajectory is almost the same and corresponds to the $g{-}gg$ configuration. Thus, one obtains the Δ odderon $(\text{slope})^{-1}$ to be twice the standard Regge slope, while for the Y odderon it is 9/4 of the standard slope. In both cases, the intercept turns out as in [10] to be rather low (-1.8 for the Y shape and -2.4 for the Δ shape), implying a very small odderon contribution to the reactions under investigation [20] in agreement with measurements. We plan to perform more accurate calculations of glueball potentials and spectra taking into account the string–string interference in subsequent publications.

ACKNOWLEDGMENTS

Yu.A. Simonov is grateful to D. Richards and R. Edwards for useful discussions; he was supported by DOE contract DE-AC05-84ER40150, under which SURA operates the Thomas Jefferson National Accelerator Facility. We acknowledge partial support from the Russian Foundation for Basic Research (project nos. 00-15-96786 and 00-02-17836) and INTAS (grant nos. 00-00110 and 00-00366).

REFERENCES

1. X. Artru, Nucl. Phys. B **85**, 442 (1975).
2. H. G. Dosch and V. Mueller, Nucl. Phys. B **116**, 470 (1976).
3. J. Carlson, J. Kogut, and V. R. Pandharipande, Phys. Rev. D **27**, 233 (1983); N. Isgur and J. Paton, Phys. Rev. D **31**, 2910 (1985).
4. Yu. A. Simonov, Phys. Lett. B **228**, 413 (1989); **515**, 137 (2001); M. Fabre de la Ripelle and Yu. A. Simonov, Ann. Phys. (N.Y.) **212**, 235 (1991).
5. G. S. Bali, Phys. Rep. **343**, 1 (2001).
6. C. Alexandrou, Ph. de Forcrand, and A. Tsaplis, Phys. Rev. D **65**, 054503 (2002); C. Alexandrou, Ph. de Forcrand, and O. Jahn, hep-lat/0209062.
7. T. T. Takahashi *et al.*, Phys. Rev. D **65**, 114509 (2002).
8. J. M. Cornwall, Phys. Rev. D **54**, 6527 (1996).
9. B. S. De Witt, Phys. Rev. **162**, 1195, 1239 (1967); L. F. Abbot, Nucl. Phys. B **185**, 189 (1981); Yu. A. Simonov, Yad. Fiz. **58**, 113 (1995) [Phys. At. Nucl. **58**, 107 (1995)]; hep-ph/9911237.
10. A. B. Kaidalov and Yu. A. Simonov, Yad. Fiz. **63**, 1507 (2000) [Phys. At. Nucl. **63**, 1428 (2000)]; Phys. Lett. B **477**, 163 (2000).
11. R. P. Feynman, Phys. Rev. **80**, 440 (1950); **84**, 108 (1951); V. A. Fock, Izv. Akad. Nauk SSSR, OMEN, 557 (1937); J. Schwinger, Phys. Rev. **82**, 664 (1951).
12. Yu. A. Simonov, Nucl. Phys. B **307**, 512 (1988); Yu. A. Simonov and J. A. Tjon, Ann. Phys. (N.Y.) **228**, 1 (1993).
13. Yu. A. Simonov and J. A. Tjon, in *The Michael Marinov Memorial Volume "Multiple Facets of Quantization and Supersymmetry",* Ed. by M. Olshanetsky and A. Vainshtein (World Sci., in press); hep-ph/0201005.
14. H. G. Dosch and Yu. A. Simonov, Phys. Lett. B **205**, 339 (1988).
15. D. S. Kuzmenko, hep-ph/0204250.
16. M. Campostrini, A. Di Giacomo, and G. Mussardo, Z. Phys. C **25**, 173 (1984); A. Di Giacomo and H. Panagopoulos, Phys. Lett. B **285**, 133 (1992); A. Di Giacomo, E. Meggiolaro, and H. Panagopoulos, Nucl. Phys. B **483,** 371 (1997); G. S. Bali, N. Brambilla, and A. Vairo, Phys. Lett. B **421**, 265 (1998); Yu. A. Simonov, Nucl. Phys. B **592**, 350 (2001).
17. D. S. Kuzmenko and Yu. A. Simonov, Phys. Lett. B **494**, 81 (2000); Yad. Fiz. **64**, 107 (2001).
18. C. Morningstar and M. Peardon, Nucl. Phys. B (Proc. Suppl.) **73**, 927 (1999); Phys. Rev. D **60**, 034509 (1999).
19. B. O. Kerbikov and Yu. A. Simonov, Phys. Rev. D **62**, 093016 (2000).
20. H1 Collab. (J. Olsson *et al.*), hep-ex/0112012.

Physics of Atomic Nuclei, Vol. 66, No. 5, 2003, pp. 955–967. From Yadernaya Fizika, Vol. 66, No. 5, 2003, pp. 988–999.

ELEMENTARY PARTICLES AND FIELDS
Theory

Hybrid Adiabatic Potentials in the QCD String Model*

Yu. S. Kalashnikova and D. S. Kuzmenko

Institute of Theoretical and Experimental Physics,
Bol'shaya Cheremushkinskaya ul. 25, Moscow, 117259 Russia

Received March 21, 2002; in final form, July 3, 2002

Abstract—The short- and intermediate-distance behavior of the hybrid adiabatic potentials is calculated in the framework of the QCD string model. The calculations are performed with the inclusion of the Coulomb force. The spin-dependent force and the so-called string correction term are treated as a perturbation at the leading-potential-type regime. Reasonably good agreement with lattice measurements takes place for adiabatic curves excited with magnetic components of field strength correlators. © *2003 MAIK "Nauka/Interperiodica".*

1. INTRODUCTION

Gluonic degrees of freedom in the nonperturbative region should manifest themselves as QCD bound states containing constituent glue, so one expects that purely gluonic hadrons (glueballs) should exist as well as hybrids, where the glue is excited in the presence of a $q\bar{q}$ pair. There is general agreement that the lightest hybrids occur in the mass range between 1.3 and 1.9 GeV, so the absolute mass scale remains somewhat imprecise in the absence of exact analytic methods of nonperturbative QCD. Existing experimental data seem to point towards gluonic excitations being present, and prima facie candidates are identified [1], but no conclusive evidence has ever been presented. There is no hope that, in the nearest future, data analyses could unambiguously pinpoint the signatures for gluonic mesons and settle the issue of constituent glue. The state of the art is that the predictions of different models on hadronic spectra and decays are involved in order to distinguish between gluonic mesons and conventional ones.

In such a situation, the lattice gauge calculations remain the only source of knowledge. Lattice calculations are now accurate enough to serve as a guide, so that the results of different QCD-motivated approaches can be compared and contrasted with lattice data. Of particular interest are the measurements of gluelump [2] and hybrid adiabatic potentials [3]. These simulations measure the spectrum of the glue in the presence of a static source in the adjoint color representation (gluelump) and in the presence of a static quark and antiquark separated by some distance R. These systems are the simplest ones and play the role of the hydrogen atom of soft glue studies, since, first, the gluonic effects are not obscured by light dynamical quarks and, second, the problem of center-of-mass motion separation is not relevant here.

The large-distance limit of hybrid adiabatic potentials is important, as one expects the formation of a confining string at large R. The short-range limit is relevant to the heavy hybrid mass estimations. One expects that, in the case of very heavy quarks, the hybrid resides in the bottom of the potential well given by the adiabatic curve, which, in accordance with lattice results [3], is somewhere around 0.25 fm for the lowest curves.

In the present paper, we study hybrid adiabatic potentials in the so-called QCD string model [4]. This model deals with quarks and pointlike gluons propagating in the confining QCD vacuum and is derived from the vacuum background correlator method. In the latter, the confining vacuum is parametrized by the set of gauge-invariant field strength correlators [5] responsible, among other phenomena, for the area law asymptotics. The basic assumption of the QCD string model is the minimal area law for the Wilson loop, so that the only nonperturbative input is the string tension σ.

The QCD string model describes the spectra of $q\bar{q}$ mesons with remarkable agreement [6, 7]. It is also quite successfull in describing glueballs [8], hybrids [9], and gluelump [10], as well as meson–hybrid–glueball mixing [11].

The first studies of hybrid adiabatic potentials in the QCD string model were performed in [12], with special attention paid to the large-distance limit. It was shown that, at large interquark distances, two kinds of QCD string vibrations take place, potential-type longitudinal and string-type transverse. Here, we consider the short-distance behavior of the excitation curves.

*This article was submitted by the authors in English.

1063-7788/03/6605-0955$24.00

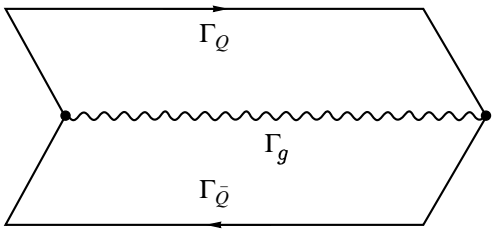

Fig. 1. Hybrid Wilson loop.

The paper is organized as follows. In Section 2, we briefly discuss the essentials of the QCD string approach for gluons. The effective Hamiltonian for a gluon bound by the static quark–antiquark pair is derived in Section 3. It is argued in Section 4 that, at short and intermediate interquark distances, the potential-type regime of string vibrations is adequate, and the lowest excitation curves are calculated. The spin-dependent forces and the so-called string corrections are considered in Section 5. Results and discussion are given in Section 6 together with conclusions and an outlook. Appendices contain the details of our variational calculations.

2. GLUONS IN THE CONFINING BACKGROUND

The QCD string model for gluons is derived in the framework of perturbation theory in the nonperturbative confining background [13]. The main idea is to split the gauge field as

$$A_\mu = B_\mu + a_\mu, \tag{1}$$

which allows one to distinguish clearly between confining field configurations B_μ and confined valence gluons a_μ. The valence gluons are treated as a perturbation in the confining background.

We start with the Green's function for the gluon propagating in the given external field B_μ [13]:

$$G_{\mu\nu}(x,y) = (D^2(B)\delta_{\mu\nu} + 2igF_{\mu\nu}(B))^{-1}, \tag{2}$$

where both covariant derivative D^{ca}_λ and field strength $F^a_{\mu\nu}$ depend only on the field B_μ:

$$D^{ca}_\lambda(B) = \delta^{ca}\partial_\lambda + gf^{cba}B^b_\lambda, \tag{3}$$

$$F^a_{\mu\nu}(B) = \partial_\mu B^a_\nu - \partial_\nu B^a_\mu + gf^{abc}B^b_\mu B^c_\nu \tag{4}$$

(a, b, and c are color indices). The term proportional to $F_{\mu\nu}(B)$ in (2) is responsible for the gluon spin interaction. We neglect it for the moment; it will be considered in Section 5.

Now we use the Feynman–Schwinger representation for the quark–antiquark–gluon Green's function [9], which, for a static quark and antiquark, is reduced to the form

$$G(x_g,y_g) = \int\limits_0^\infty ds \int Dz_g \exp(-K_g)\langle\mathcal{W}\rangle_B, \tag{5}$$

where angular brackets mean averaging over the background field. The quantity K_g is the kinetic energy of the gluon (to be specified below), and all the dependence on the vacuum background field is contained in the generalized Wilson loop $\mathcal{W}$, depicted in Fig. 1, where the contours Γ_Q and $\Gamma_{\bar{Q}}$ run over the classical trajectories of the static quark and antiquark, and the contour Γ_g runs over the gluon trajectory z_g in (5).

Expression (5) is the starting point of the QCD string model, as, under the minimal area law assumption, the Wilson loop configuration in the color $SU(N_c)$ case takes the form

$$\langle\mathcal{W}\rangle_B = \frac{N_c^2-1}{2}\exp(-\sigma(S_1+S_2)), \tag{6}$$

where S_1 and S_2 are the minimal areas inside the contours formed by quark and gluon and antiquark and gluon trajectories, respectively, and σ is the string tension.

3. EINBEIN FIELD FORM OF THE GLUONIC HAMILTONIAN

To proceed further, we must fix the gauge in the reparametrization transformations group. For the case of static quark and antiquark sources, the most natural way to do this is to identify the proper time τ of the Feynman–Schwinger representation with the laboratory time. Then, the classical quark and antiquark trajectories are given by

$$z_{Q\mu} = \left(\tau, \frac{\mathbf{R}}{2}\right), \quad z_{\bar{Q}\mu} = \left(\tau, -\frac{\mathbf{R}}{2}\right), \tag{7}$$

and the action of the system can be immediately obtained from representation (5):

$$A = \int\limits_0^T d\tau \tag{8}$$
$$\times\left\{-\frac{\mu}{2} + \frac{\mu\dot{r}^2}{2} - \sigma\int\limits_0^1 d\beta_1\sqrt{(\dot{w}_1w_1')^2 - \dot{w}_1^2w_1'^2}\right.$$
$$\left. - \sigma\int\limits_0^1 d\beta_2\sqrt{(\dot{w}_2w_2')^2 - \dot{w}_2^2w_2'^2}\right\}.$$

Here, $\mathbf{r}$ is the three-dimensional gluonic coordinate, and the minimal surfaces S_1 and S_2 are parametrized

by the coordinates $w_{i\mu}(\tau,\beta_i)$ $(i=1,2)$, $\dot{w}_{i\mu}=\partial w_{i\mu}/\partial\tau$, $w'_{i\mu}=\partial w_{i\mu}/\partial\beta_i$. Choosing the straight-line ansatz for the minimal surfaces, one has in the laboratory time gauge

$$w_{i0}=\tau, \quad \mathbf{w}_{1,2}=\pm(1-\beta)\frac{\mathbf{R}}{2}+\beta\mathbf{r}. \tag{9}$$

The kinetic energy in (8) is given in the so-called einbein field form [14]. The einbein field $\mu=\mu(\tau)$ is the auxiliary field introduced to deal with relativistic kinematics. Note that, in the case of a gluon, one is forced to introduce it from the very beginning, since it provides meaningful dynamics for the massless particle.

In order to pass to the Hamiltonian formulation, it is convenient to get rid of Nambu–Goto square roots in (8), introducing a continuous set of einbein fields $\nu_i=\nu_i(\tau,\beta_i)$, as was first suggested in [6]:

$$L=-\frac{\mu}{2}+\frac{\mu\dot{r}^2}{2}-\int\limits_0^1 d\beta_1\frac{\sigma^2r_1^2}{2\nu_1} \tag{10}$$
$$-\int\limits_0^1 d\beta_1\frac{\nu_1}{2}(1-\beta_1^2l_1^2)-\int\limits_0^1 d\beta_2\frac{\sigma^2r_2^2}{2\nu_2}$$
$$-\int\limits_0^1 d\beta_2\frac{\nu_2}{2}(1-\beta_2l_2^2),$$
$$l_{1,2}^2=\dot{r}^2-\frac{1}{r_{1,2}^2}(\mathbf{r}_{1,2}\cdot\dot{\mathbf{r}})^2, \quad \mathbf{r}_{1,2}=\mathbf{r}\pm\frac{\mathbf{R}}{2}.$$

Note that the Lagrangian (10) describes the constrained system. As no time derivatives of the einbeins enter it, the corresponding equations of motion play the role of second-class constraints [14].

The Hamiltonian $H=\mathbf{p}\cdot\dot{\mathbf{r}}-L$ is easily obtained from the Lagrangian (10):

$$H=H_0+\frac{\mu}{2}+\int\limits_0^1 d\beta_1\frac{\sigma^2r_1^2}{\nu_1}+\int\limits_0^1 d\beta_2\frac{\sigma^2r_2^2}{\nu_2} \tag{11}$$
$$+\int\limits_0^1 d\beta_1\frac{\nu_1}{2}+\int\limits_0^1 d\beta_2\frac{\nu_2}{2},$$

$$H_0=\frac{p^2}{2(\mu+J_1+J_2)}+\frac{1}{2\Delta(\mu+J_1+J_2)} \tag{12}$$
$$\times\left\{\frac{(\mathbf{p}\cdot\mathbf{r}_1)^2}{r_1^2}J_1(\mu+J_1)+\frac{(\mathbf{p}\cdot\mathbf{r}_2)^2}{r_2^2}J_2(\mu+J_2)\right.$$
$$\left.+\frac{2J_1J_2}{r_1^2r_2^2}(\mathbf{r}_1\cdot\mathbf{r}_2)(\mathbf{p}\cdot\mathbf{r}_1)(\mathbf{p}\cdot\mathbf{r}_2)\right\},$$
$$\Delta=(\mu+J_1)(\mu+J_2)-J_1J_2\frac{(\mathbf{r}_1\cdot\mathbf{r}_2)^2}{r_1^2r_2^2},$$
$$J_i=\int\limits_0^1 d\beta_i\beta_i^2\nu_i(\beta_i), \quad i=1,2.$$

The Hamiltonian (11) together with the constraints

$$\frac{\partial H}{\partial\mu}=0, \qquad \frac{\delta H}{\delta\nu_i(\beta_i)}=0 \tag{13}$$

completely defines the dynamics of the system at the classical level. To quantize, one should first find the extrema of einbeins from Eqs. (13) and substitute them back to the Hamiltonian (11). Then, the extremal values of einbeins would become the nonlinear operator functions of coordinate and momentum, and, in addition, the problem of operator ordering would arise. To avoid this complicated problem, the approximate einbein field method is usually applied in the QCD string model calculations. Namely, einbeins are treated as c-number variational parameters: the eigenvalues of the Hamiltonian (11) are found as functions of μ and ν_i and minimized with respect to einbeins to obtain the physical spectrum. Such a procedure, first suggested in [6], provides an accuracy of about 5–10% for the ground state (for details, see first entry in [7]).

4. POTENTIAL REGIME OF THE QCD STRING VIBRATIONS

The einbeins μ and $\nu_i(\beta_i)$ play the role of constituent gluon mass and energy densities along two strings. Note that, even with simplifying assumptions of the einbein field method, these quantities are not introduced as model parameters, but are calculated in the formalism. It is clear from the form (12) of the kinetic energy that two kinds of motion compete to form the spectrum: the potential-type longitudinal one with respect to $\mathbf{R}$ vibrations due to gluonic mass μ and the string-type transverse one due to the string inertia.

It was shown in [12] that, for large interquark distances, $R\gg1/\sqrt{\sigma}$, these two types of motion decouple, displaying the corrections to the leading σR behavior proportional to $(\sigma/R)^{1/3}$ in the case of longitudinal vibrations and proportional to $1/R$ for transverse ones.

On the contrary, for small R, one can neglect the terms J_i responsible for string inertia in the kinetic energy (12). Then, the Hamiltonian takes the form

$$H=\frac{p^2}{2\mu}+\frac{\mu}{2}+\int\limits_0^1 d\beta_1\frac{\sigma^2r_1^2}{2\nu_1}+\int\limits_0^1 d\beta_2\frac{\sigma^2r_2^2}{2\nu_2} \tag{14}$$

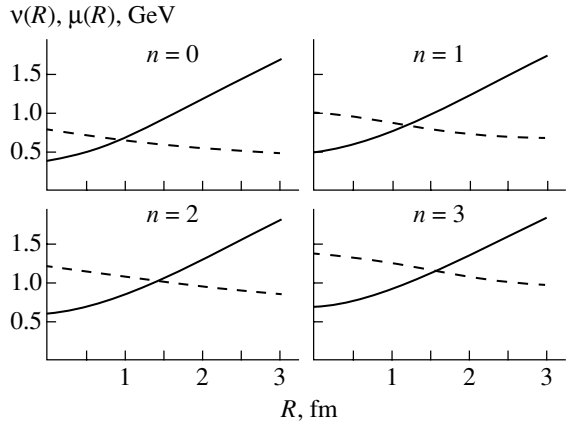

Fig. 2. Einbein fields $\nu_n(R)$ (solid curve) and $\mu_n(R)$ (dashed curve) for $n = 0, 1, 2, 3$ and $\sigma = 0.21$ GeV^2.

$$+\int_0^1 d\beta_1 \frac{\nu_1}{2} + \int_0^1 d\beta_2 \frac{\nu_2}{2}.$$

The spectrum of the Hamiltonian (14) was found in [12]. At small R, it reads

$$E_n(R) = 2^{3/2}\sigma^{1/2}\,(n+3/2)^{1/2} + \frac{\sigma^{3/2}R^2}{2^{3/2}(n+3/2)^{1/2}}. \quad (15)$$

The extremal values of einbeins are given by

$$\mu_n(R) = 2^{1/2}\sigma^{1/2}\left(n+\frac{3}{2}\right)^{1/2} - \frac{\sigma^{3/2}R^2}{2^{5/2}(n+3/2)^{1/2}}, \quad (16)$$

$$\nu_{1,2n}(R) = \frac{(n+3/2)^{1/2}\sigma^{1/2}}{2^{1/2}} + \frac{3\sigma^{3/2}R^2}{2^{7/2}(n+3/2)^{1/2}}, \quad (17)$$

where n is the number of oscillator quanta.

Expressions (16) and (17) immediately yield $J_{1,2}/\mu \approx 1/6$, so the neglect of string inertia is justified. The curves $\mu_n(R)$ and $\nu_n(R)$ for arbitrary R from [12] are shown in Fig. 2 for $n = 0$, 1, 2, 3 and $\sigma = 0.21$ GeV^2. It is clear that the potential-type Hamiltonian can be employed at $R \le 1$ fm for $n = 0$, 1 and at $R \le 1.5$ fm for $n = 2$, 3, and the corrections due to string inertia can be taken into account perturbatively.

The form (14) allows one to eliminate einbeins and arrive at the potential-type Hamiltonian

$$H = \sqrt{p^2} + \sigma r_1 + \sigma r_2. \quad (18)$$

Nevertheless, as we are going to calculate the spin-dependent forces and string correction, we prefer to eliminate only einbeins ν_i, treating the quantity μ in the framework of the einbein field method.

If only the confining force is taken into account, the QCD string model predicts the oscillator potential (15) with the minimum at $R = 0$. However, the minimum is shifted if the long-range confining force is augmented by the short-range Coulomb potential,

$$V_C = -\frac{3\alpha_s}{2r_1} - \frac{3\alpha_s}{2r_2} + \frac{\alpha_s}{6R}, \quad (19)$$

with the strong coupling $\alpha_s \approx 0.4$. The coefficients in (19) are in accordance with the color content of the $Q\bar{Q}g$ system [15]. The $Q\bar{Q}$ Coulomb force in (19) is repulsive, and it is compatible with the behavior of gluon energies [3] at small R. Note that such behavior comes out naturally in the QCD string model, since pointlike gluons do carry color quantum numbers.

The final form of our Hamiltonian reads

$$H = \frac{p^2}{2\mu} + \frac{\mu}{2} + \sigma r_1 + \sigma r_2 + V_C. \quad (20)$$

The angular momentum is not conserved in the Hamiltonian (20), but it is a good quantum number in the einbein-field Hamiltonian (14). For the case of a pure confining force, we have compared the spectra of exact and einbein-field Hamiltonians and have found that angular momentum is conserved within better than 5% accuracy. The same phenomenon is observed in the constituent gluon model [16] and seems to be a consequence of linear potential confinement embedded there.

The eigenvalue problem for the Hamiltonian (20) was solved variationally with wave functions

$$\mathbf{\Psi}_{jl\Lambda}(\mathbf{r}) = \phi_l(r)\sum_{\mu_1\mu_2} C^{j\Lambda}_{l\mu_1 1\mu_2} Y_{l\mu_1}\left(\frac{\mathbf{r}}{r}\right)\boldsymbol{\chi}_{1\mu_2}, \quad (21)$$

where $\boldsymbol{\chi}_{1\mu}$ is the spin-1 wave function, $\Lambda = |(\mathbf{j}\cdot\mathbf{R})/R|$ is the projection of total angular momentum $\mathbf{j}$ onto the z axis, and $\mathbf{z} \parallel \mathbf{R}$. The radial wave functions $\phi_l(r)$ were taken to be Gaussian, that is, of the form $\exp(-\beta^2 r^2/2)$ multiplied by the appropriate polynomials, with β treated as a variational parameter. The eigenvalues $E_{jl\Lambda}(\mu, R) \equiv \langle \mathbf{\Psi}_{jl\Lambda}|H(\mu,R)|\mathbf{\Psi}_{jl\Lambda}\rangle$ were found in such a way, and the resulting adiabatic potentials,

$$V^0_{jl\Lambda}(R) = E_{jl\Lambda}(\mu^*(R), R), \quad (22)$$

depend on the extremal value μ^* defined from the condition

$$\frac{\partial E_{jl\Lambda}(\mu, R)}{\partial \mu} = 0. \quad (23)$$

The details of this variational procedure are given in Appendix A.

In the QCD string model, the gluon is effectively massive and has three polarizations [8, 10]. Only two of them are excited with magnetic components of

field strength correlators used in lattice calculations. We list these states in the table in terms of j, l, Λ and standard notation borrowed from physics of diatomic molecules. For more details justifying such correspondence, see [10].

Quantum numbers of lowest levels

(a)	$j^{PC}=1^{+-}$	$j=1, l=1, \Lambda=0,1$	Σ_u^-, Π_u
(b)	$j^{PC}=1^{--}$	$j=1, l=2, \Lambda=0,1$	Σ_g^+, Π_g
(c)	$j^{PC}=2^{--}$	$j=2, l=2, \Lambda=0,1,2$	$\Sigma_g^-, \Pi_g, \Delta_g$
(d)	$j^{PC}=2^{+-}$	$j=2,\ l=3,\ \Lambda=0,1,2$	$\Sigma_u^+,\ \Pi_u,\ \Delta_u$

Fitting the ground lattice state with Coulomb + linear potential yields the values of parameters $\alpha_s = 0.4$ and $\sigma = 0.21$ GeV^2.

5. STRING CORRECTION AND SPIN-DEPENDENT INTERACTION

Now, we turn to the calculations of corrections to the leading potential regime (22).

Let us first consider the correction due to string inertia. It corresponds to the terms in (12) linear in J_i:

$$H^{\rm sc} = -\frac{J_1+J_2}{2\mu^2}p^2 + \frac{1}{2\mu^2}\left(\frac{(\mathbf{p}\cdot\mathbf{r}_1)^2}{r_1^2}J_1 + \frac{(\mathbf{p}\cdot\mathbf{r}_2)^2}{r_2^2}J_2\right). \quad (24)$$

In the potential regime, $\nu_i = \sigma r_i$ and $J_i = \sigma r_i/3$. So the string correction Hamiltonian takes the form

$$H^{\rm sc} = -\frac{\sigma}{6\mu^2}\left(\frac{1}{r_1^2}L_1^2 + \frac{1}{r_2^2}L_2^2\right), \quad (25)$$

where

$$\mathbf{L}_i = \mathbf{r}_i \times \mathbf{p}. \quad (26)$$

The choice (26) solves the ordering problem in (25), since it assures the hermiticity of the operator $H^{\rm sc}$.

In actual calculations, it is convenient to rewrite (25) as

$$H^{\rm sc} = -\frac{\sigma}{6\mu^2}\left\{\left(\frac{1}{r_1^2}+\frac{1}{r_2^2}\right)\left(L^2+\frac{R^2}{4}H_1\right) + \left(\frac{1}{r_1^2}-\frac{1}{r_2^2}\right)RH_2\right\}, \quad (27)$$

where

$$H_1 = -\left(\partial_\rho^2 + \frac{1}{\rho}\partial_\rho + \frac{1}{\rho^2}\partial_\phi^2\right), \quad (28)$$

$$H_2 = zH_1 + \rho\partial_\rho\partial_z + \partial_z. \quad (29)$$

The adiabatic potentials of the string correction are listed in Appendix B.

The spin-dependent force originates from the term proportional to $F_{\mu\nu}(B)$ in (2). This term generates the spin-dependent interaction as

$$-iF_{ik} = (\mathbf{S}\cdot\mathbf{B})_{ik}, \quad (30)$$

where spin operator $\mathbf{S}$ acts at the vector function $\mathbf{\Psi}$ as

$$(S_i\mathbf{\Psi})_j = -i\epsilon_{ijk}\Psi_k. \quad (31)$$

One averages this term over the background, as was done in [17], and, in our case, it gives

$$H^{\rm LS(np)} = -\frac{\sigma}{2\mu^2}\left(\frac{1}{r_1}(\mathbf{L}_1\cdot\mathbf{S}) + \frac{1}{r_2}(\mathbf{L}_2\cdot\mathbf{S})\right), \quad (32)$$

$$H^{\rm LS(p)} = \frac{3\alpha_s}{4\mu^2}\left(\frac{1}{r_1^3}(\mathbf{L}_1\cdot\mathbf{S}) + \frac{1}{r_2^3}(\mathbf{L}_2\cdot\mathbf{S})\right) \quad (33)$$

for nonperturbative and perturbative forces, respectively. One easily recognizes the contribution of Thomas precession in (32) and (33). The spin-dependent interaction is conveniently represented as

$$H^{\rm LS(np)} = -\frac{\sigma}{2\mu^2}\left\{\left(\frac{1}{r_1}+\frac{1}{r_2}\right)(\mathbf{L}\cdot\mathbf{S}) + \left(\frac{1}{r_1}-\frac{1}{r_2}\right)\frac{R}{2}H_R\right\}, \quad (34)$$

$$H^{\rm LS(p)} = \frac{3\alpha_s}{4\mu^2}\left\{\left(\frac{1}{r_1^3}+\frac{1}{r_2^3}\right)(\mathbf{L}\cdot\mathbf{S}) + \left(\frac{1}{r_1^3}-\frac{1}{r_2^3}\right)\frac{R}{2}H_R\right\}, \quad (35)$$

where

$$H_R = \frac{e^{-i\phi}}{2}\left(-\partial_\rho + \frac{i}{\rho}\partial_\phi\right)S_+ + \frac{e^{i\phi}}{2}\left(\partial_\rho + \frac{i}{\rho}\partial_\phi\right)S_-, \quad (36)$$

$$S_\pm = S_x \pm iS_y.$$

Spin-dependent potentials are given in Appendix C.

We would like to stress here that, in spite of the apparently nonrelativistic form of expressions (27) and (34), (35), these are not the nonrelativistic inverse mass expansions. The mass μ entering these expressions is replaced in matrix elements by the value μ^* obtained from stationary point Eq. (23). The latter plays the role of effective mass of the gluon and is not large. The R dependence of corrections is shown in Figs. 3 and 4.

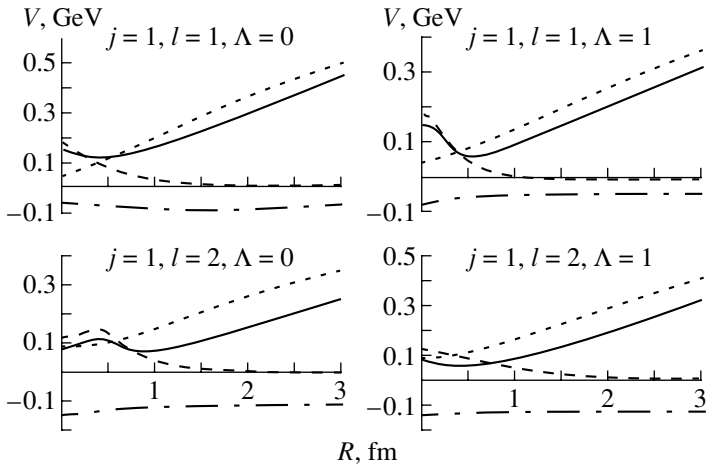

Fig. 3. Taken with opposite sign potentials of string $-V^{\rm sc}(R)$ (dotted curves), spin-dependent perturbative $-V^{\rm LS(p)}(R)$ (dashed curves), and nonperturbative $-V^{\rm LS(np)}(R)$ (dash-dotted curves) corrections along with their sum $-V^{\rm sc}(R) - V^{\rm LS(p)}(R) - V^{\rm LS(np)}(R)$ (solid curves) for levels (a) and (b) of the table.

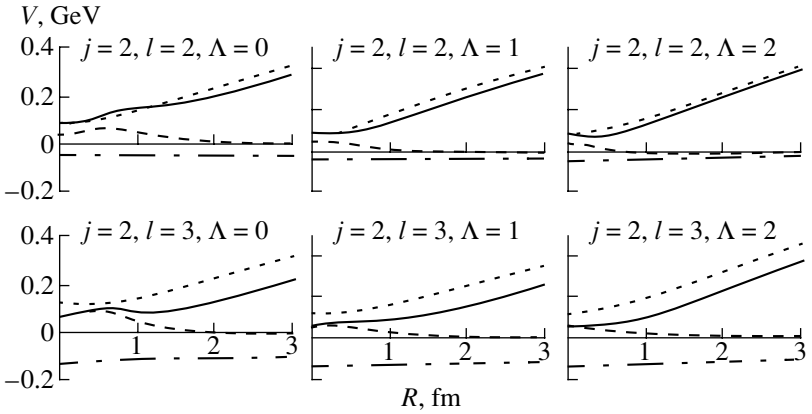

Fig. 4. The same as in Fig. 3, but for levels (c) and (d).

6. RESULTS AND DISCUSSION

The results of full QCD string calculations are given at Fig. 5 for the levels listed in the table, together with the lattice data [3]. As is seen from Fig. 5, at small distances, the calculated curves are in good agreement with lattice results, with an accuracy better than 100 MeV. The level ordering is reproduced too, with the exception of the Σ_g^-, Π_g, and Δ_g levels (Fig. 5c). Note that the lattice data claim only one Π_g level, and its R behavior is rather peculiar (see dashed thick gray curve in Fig. 5b). One expects that the curves should tend to form degenerate levels as the distance R decreases, fulfilling the angular-momentum-conservation demands at $R = 0$. This feature is made explicit in the QCD string model: our calculations reproduce the gluelump spectrum [10] for $R = 0$ after subtracting the $Q\bar{Q}$ Coulomb force [last term in (19)] and with the obvious replacement $2\sigma \to \sigma_{\rm adj} = (9/4)\sigma$, $2\alpha_s \to (9/4)\alpha_s$.

Lattice data indeed seem to follow such a tendency. Moreover, the curvatures of all potentials but Π_g are compatible with the dominance of the Coulomb force acting between static sources in the octet color representation. Thus, one suspects [18, 19] that something goes wrong with the lattice Π_g level, and its strange behavior could be due to the presence of several levels, severely mixed and poorly resolved by present simulations.

The most pronounced feature of the QCD string approach is the following. It was already mentioned that the gluon here is effectively massive and has three polarizations. As a consequence, the level ordering follows the increasing dimension of the valence gluon operator, or, in other words, the increasing orbital momentum l. This is in contrast to the standard viewpoint of constituent glue studies (see [20] and realization of this idea in the framework of potential NRQCD [18]). The level ordering there is supposed

to follow the increasing dimension of the operators E_i, B_i, D_iB_k, etc. The equations of motion, which relate different operators with the same quantum numbers, are involved to exclude spurious states in such a picture.

In our approach, we expect an extra family of levels to appear, namely, Σ_g^+ and Π_g, and the corresponding gluelump limit achieved with 1^{--} quantum numbers. The wave functions of these states contain mostly the $l = 0$ component, so these levels should be the lowest one-gluon ones. The search for this family, accessible only with electric field correlators, is of paramount importance in both gluelump and adiabatic potential settings. The presence or absence of such states would allow one to discriminate among models.

The flux-tube model [21], as well as its relativistic version [22], assumes that soft glue is stringlike, with phonon-type effective degrees of freedom. These string phonons are colorless, so that the $Q\bar{Q}$ pair is in a color-singlet state. Thus, the Coulomb $Q\bar{Q}$ interaction is to be attractive. Adiabatic potentials are calculated in [22], and, in order to improve the short-range behavior of adiabatic curves, the Coulomb interquark repulsion was added, which obviously contradicts the general philosophy of a flux tube. Without essential modifications of the dynamical picture at small interquark distances, the flux-tube-type models seem to be ruled out by lattice data [3]. A rather elaborate constituent gluon model [16], based on the field-theoretical Hamiltonian approach, agrees with lattice data on hybrid potentials at short and intermediate interquark distances only under the rather confusing assumption of gluon parity taken to be positive.

The gluelump spectrum, as well as the small-R limit of hybrid adiabatic potentials, is successfully calculated in the bag model [23]. The lowest bag-model gluelump state is 1^{+-}, and the Σ–Π splitting at small interquark distances is in accordance with lattice data. In this regard, we stress once more the importance of lattice measurements with electric field correlators. If the ground state Σ_g^+–Π_g family is not found, then, with above-mentioned drawbacks of the flux-tube and constituent-gluon pictures, it would mean that soft glue is baglike rather than stringlike or pointlike. To conclude, we have presented full QCD string calculations of hybrid adiabatic potentials. The results are in general agreement with lattice data. We outline the problems connected with a restricted set of gluonic operators used in lattice simulations and call for further studies of excitation curves with electric field operators.

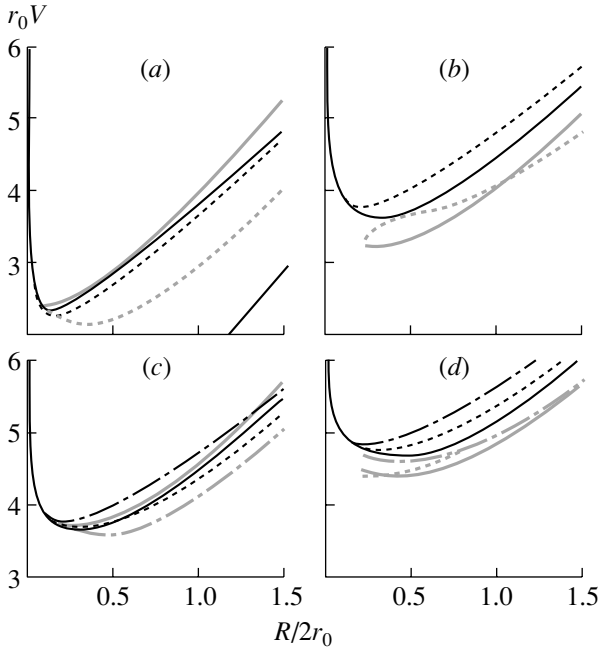

Fig. 5. Hybrid potentials with corrections included (black curves) compared to lattice ones (thick gray curves) in units $1/r_0 = 400$ MeV ($r_0 = 2.5$ GeV^{-1}); $Q\bar{Q}$ distance R is measured in $2r_0 \approx 1$ fm. States (a)–(d) are given in the table. Solid, dashed, and dash-dotted curves correspond to $\Lambda = 0, 1$, and 2. Solid line at right bottom corner of a represents the Coulomb + linear potential with $\alpha_s = 0.4$ and $\sigma = 0.21$ GeV^2.

ACKNOWLEDGMENTS

We are grateful to Yu.A. Simonov for numerous stimulating discussions.

The financial support of the Russian Foundation for Basic Research (project nos. 00-02-17836 and 00-15-96786) and INTAS OPEN (grant nos. 2000-110 and 2000-366) is acknowledged.

APPENDIX A

Variational Calculations of Adiabatic Potentials

In this appendix, we derive the explicit variational equations for adiabatic potentials (22).

The average momentum for an oscillatory wave function with orbital momentum l is given as

$$\langle p^2 \rangle_l = \frac{2l+3}{2}\beta^2, \qquad \text{(A.1)}$$

where β is a variational parameter with dimensions of mass. Thus, the calculation of the extremum over μ (23) leads to the expression

$$\mu^* = \beta\sqrt{\frac{2l+3}{2}}. \qquad \text{(A.2)}$$

Due to the symmetry of wave functions,

$$\langle r_1\rangle = \langle r_2\rangle\,, \qquad \left\langle \frac{1}{r_1}\right\rangle = \left\langle \frac{1}{r_2}\right\rangle. \tag{A.3}$$

Let us introduce the dimensionless variables

$$x = \beta\frac{R}{2}, \qquad \tilde r_1 = \beta r_1 \tag{A.4}$$

and define the dimensionless averages

$$\langle \tilde r_1\rangle \equiv f(x), \qquad \left\langle \frac{1}{\tilde r_1}\right\rangle \equiv g(x). \tag{A.5}$$

For the energy levels, we will get

$$E(\beta,x) = \frac{1}{\beta}2\sigma f(x) + \beta\left(\sqrt{\frac{2l+3}{2}} - 3\alpha_s g(x) + \frac{\alpha_s}{12x}\right).$$

Let us now calculate the extremum of the last equation over β, provided that x is a function of β and $\partial f(x(\beta))/\partial\beta = f'(x)x/\beta$. So we find that

$$\beta^2(x) = \frac{2\sigma(f(x) - xf'(x))}{\sqrt{\frac{2l+3}{2}} - 3\alpha_s(g(x) + xg'(x))}, \tag{A.6}$$

$$E(x) = \frac{2\sigma}{\beta(x)}f(x) + \beta(x)\left(\sqrt{\frac{2l+3}{2}} - 3\alpha_s g(x) + \frac{\alpha_s}{12x}\right), \tag{A.7}$$

$$R(x) = 2x/\beta(x). \tag{A.8}$$

Equations (A.7) and (A.8), along with calculated functions $f(x)$, $g(x)$, and $\beta(x)$, define adiabatic potentials (22) explicitly. Note that all expressions for the averages contain the error function

$$\mathrm{erf}(x) = \frac{2}{\sqrt{\pi}}\int\limits_0^x dte^{-t^2}. \tag{A.9}$$

We present them below for the levels of the table:

$$\langle \tilde r_1\rangle_{110} = x\left\{\mathrm{erf}(x)\left(1 + \frac{1}{x^2} - \frac{1}{4x^4}\right) + \frac{e^{-x^2}}{\sqrt{\pi}x}\left(1 + \frac{1}{2x^2}\right)\right\}, \tag{A.10}$$

$$\left\langle \frac{1}{\tilde r_1}\right\rangle_{110} = \frac{1}{x}\left\{\mathrm{erf}(x)\left(1 - \frac{1}{2x^2}\right) + \frac{e^{-x^2}}{\sqrt{\pi}x}\right\},$$

$$\beta^2_{110} = \frac{\frac{4\sigma}{x}\left\{\mathrm{erf}(x)\left(1 - \frac{1}{2x^2}\right) + \frac{e^{-x^2}}{\sqrt{\pi}x}\right\}}{\sqrt{\frac{5}{2}} - \frac{3\alpha_s}{x^3}\left(\mathrm{erf}(x) - \frac{2xe^{-x^2}}{\sqrt{\pi}}\right)};$$

$$\langle \tilde r_1\rangle_{111} = x\left\{\mathrm{erf}(x)\left(1 + \frac{3}{4x^2} + \frac{1}{8x^4}\right) + \frac{e^{-x^2}}{\sqrt{\pi}x}\left(1 - \frac{1}{4x^2}\right)\right\}, \tag{A.11}$$

$$\left\langle \frac{1}{\tilde r_1}\right\rangle_{111} = \frac{1}{x}\left\{\mathrm{erf}(x)\left(1 + \frac{1}{4x^2}\right) - \frac{e^{-x^2}}{\sqrt{\pi}}\left(x + \frac{1}{2x}\right)\right\},$$

$$\beta^2_{111} = \frac{\frac{2\sigma}{x}\left\{\frac{1}{2}\mathrm{erf}(x)\left(3 + \frac{1}{x^2}\right) - \frac{e^{-x^2}}{\sqrt{\pi}}\left(x + \frac{1}{x}\right)\right\}}{\sqrt{\frac{5}{2}} - \frac{3\alpha_s}{x^3}\left(-\frac{1}{2}\mathrm{erf}(x) + \frac{xe^{-x^2}}{\sqrt{\pi}}\left(1 + 2x^2 + 2x^4\right)\right)};$$

$$\langle \tilde r_1\rangle_{120} = x\left\{\mathrm{erf}(x)\left(1 + \frac{14}{15x^2} + \frac{9}{20x^4}\right) + \frac{e^{-x^2}}{\sqrt{\pi}x}\left(\frac{11}{15} - \frac{9}{10x^2}\right)\right\}, \tag{A.12}$$

$$\left\langle \frac{1}{\tilde r_1}\right\rangle_{120} = \frac{1}{x}\left\{\mathrm{erf}(x)\left(1 + \frac{7}{10x^2}\right) - \frac{xe^{-x^2}}{5\sqrt{\pi}}\left(\frac{8x^2}{3} + \frac{28}{3} + \frac{7}{x^2}\right)\right\},$$

$$\beta^2_{120} = \frac{\dfrac{2\sigma}{5x}\left\{\mathrm{erf}(x)\left(\dfrac{28}{3}+\dfrac{9}{x^2}\right)-\dfrac{2e^{-x^2}}{\sqrt{\pi}x}\left(9+\dfrac{22x^2}{3}+\dfrac{4x^4}{3}\right)\right\}}{\sqrt{\dfrac{7}{2}}-\dfrac{3\alpha_s}{5x^3}\left(-7\mathrm{erf}(x)+\dfrac{2xe^{-x^2}}{\sqrt{\pi}}\left(7+\dfrac{22x^2}{3}+\dfrac{16x^4}{3}+\dfrac{8x^6}{3}\right)\right)};$$

$$\langle\tilde{r}_1\rangle_{121} = x\left\{\mathrm{erf}(x)\left(1+\frac{77}{60x^2}-\frac{9}{40x^4}\right)+\frac{e^{-x^2}}{5\sqrt{\pi}x}\left(\frac{14}{3}+\frac{9}{4x^2}\right)\right\}, \tag{A.13}$$

$$\left\langle\frac{1}{\tilde{r}_1}\right\rangle_{121} = \frac{1}{x}\left\{\mathrm{erf}(x)\left(1-\frac{7}{20x^2}\right)+\frac{e^{-x^2}}{5\sqrt{\pi}}\left(\frac{7}{2x}-\frac{7x}{3}-\frac{2x^3}{3}\right)\right\},$$

$$\beta^2_{121} = \frac{\dfrac{2\sigma}{5x}\left\{\dfrac{1}{2}\mathrm{erf}(x)\left(\dfrac{77}{3}-\dfrac{9}{x^2}\right)+\dfrac{e^{-x^2}}{\sqrt{\pi}x}\left(9-\dfrac{11x^2}{3}-\dfrac{2x^4}{3}\right)\right\}}{\sqrt{\dfrac{7}{2}}-\dfrac{3\alpha_s}{5x^3}\left(\dfrac{7}{2}\mathrm{erf}(x)+\dfrac{xe^{-x^2}}{\sqrt{\pi}}\left(-7+\dfrac{2x^2}{3}+\dfrac{8x^4}{3}+\dfrac{4x^6}{3}\right)\right)};$$

$$\langle\tilde{r}_1\rangle_{220} = x\left\{\mathrm{erf}(x)\left(1+\frac{1}{x^2}+\frac{3}{4x^4}-\frac{3}{2x^6}\right)+\frac{e^{-x^2}}{\sqrt{\pi}x}\left(1+\frac{1}{2x^2}+\frac{3}{x^4}\right)\right\}, \tag{A.14}$$

$$\left\langle\frac{1}{\tilde{r}_1}\right\rangle_{220} = \frac{1}{x}\left(1+\frac{2}{x^2}\right)\left\{\mathrm{erf}(x)\left(1-\frac{3}{2x^2}\right)+\frac{3e^{-x^2}}{\sqrt{\pi}x}\right\},$$

$$\beta^2_{220} = \frac{\dfrac{2\sigma}{x}\left\{\mathrm{erf}(x)\left(2+\dfrac{3}{x^2}-\dfrac{9}{x^4}\right)+\dfrac{6e^{-x^2}}{\sqrt{\pi}x}\left(1+\dfrac{3}{x^2}\right)\right\}}{\sqrt{\dfrac{7}{2}}-\dfrac{3\alpha_s}{x^3}\left\{\mathrm{erf}(x)\left(-1+\dfrac{12}{x^2}\right)-\dfrac{2e^{-x^2}}{\sqrt{\pi}x}\left(12+7x^2+2x^4\right)\right\}};$$

$$\langle\tilde{r}_1\rangle_{221} = x\left\{\mathrm{erf}(x)\left(1+\frac{13}{12x^2}-\frac{1}{8x^4}+\frac{1}{x^6}\right)+\frac{e^{-x^2}}{\sqrt{\pi}x}\left(\frac{2}{3}-\frac{13}{12x^2}-\frac{2}{x^4}\right)\right\}, \tag{A.15}$$

$$\left\langle\frac{1}{\tilde{r}_1}\right\rangle_{221} = \frac{1}{x}\left\{\mathrm{erf}(x)\left(1+\frac{1}{4x^2}+\frac{2}{x^4}\right)-\frac{e^{-x^2}}{\sqrt{\pi}}\left(\frac{2x^3}{3}+\frac{7x}{3}+\frac{19}{6x}+\frac{4}{x^3}\right)\right\},$$

$$\beta^2_{221} = \frac{\dfrac{2\sigma}{x}\left\{\mathrm{erf}(x)\left(\dfrac{13}{6}-\dfrac{1}{2x^2}+\dfrac{6}{x^4}\right)-\dfrac{e^{-x^2}}{\sqrt{\pi}}\left(\dfrac{2x^3}{3}+\dfrac{11x}{3}+\dfrac{7}{x}+\dfrac{12}{x^3}\right)\right\}}{\sqrt{\dfrac{7}{2}}-\dfrac{3\alpha_s}{x^3}\left\{-\mathrm{erf}(x)\left(\dfrac{1}{2}+\dfrac{8}{x^2}\right)+\dfrac{e^{-x^2}}{\sqrt{\pi}x}\left(16+\dfrac{35x^2}{3}+6x^4+\dfrac{8x^6}{3}+\dfrac{4x^8}{3}\right)\right\}};$$

$$\langle\tilde{r}_1\rangle_{222} = x\left\{\mathrm{erf}(x)\left(1+\frac{4}{3x^2}-\frac{1}{4x^4}-\frac{1}{4x^6}\right)+\frac{e^{-x^2}}{\sqrt{\pi}x}\left(1+\frac{5}{6x^2}+\frac{1}{2x^4}\right)\right\}, \tag{A.16}$$

$$\left\langle\frac{1}{\tilde{r}_1}\right\rangle_{222} = \frac{1}{x}\left\{\mathrm{erf}(x)\left(1-\frac{1}{2x^2}-\frac{1}{2x^4}\right)+\frac{e^{-x^2}}{\sqrt{\pi}x}\left(\frac{5}{3}+\frac{1}{x^2}\right)\right\},$$

$$\beta^2_{222}=\frac{\dfrac{2\sigma}{x}\left\{\mathrm{erf}(x)\left(\dfrac{8}{3}-\dfrac{1}{x^2}-\dfrac{3}{2x^4}\right)+\dfrac{e^{-x^2}}{\sqrt{\pi}x}\left(4+\dfrac{3}{x^2}\right)\right\}}{\sqrt{\dfrac{7}{2}}-\dfrac{3\alpha_s}{x^3}\left\{\mathrm{erf}(x)\left(1+\dfrac{2}{x^2}\right)-\dfrac{2e^{-x^2}}{\sqrt{\pi}x}\left(2+\dfrac{7x^2}{3}+\frac{2x^4}{3}\right)\right\}};$$

$$\langle\tilde r_1\rangle_{230}=x\left\{\mathrm{erf}(x)\left(1+\frac{81}{70x^2}+\frac{33}{70x^4}+\frac{39}{28x^6}\right)-\frac{e^{-x^2}}{\sqrt{\pi}x}\left(\frac{4x^2}{35}+\frac{1}{35}+\frac{14}{5x^2}+\frac{39}{14x^4}\right)\right\},\qquad\text{(A.17)}$$

$$\left\langle\frac{1}{\tilde r_1}\right\rangle_{230}=\frac{1}{x}\left\{\mathrm{erf}(x)\left(1-\frac{36}{35x^2}+\frac{33}{14x^4}\right)-\frac{xe^{-x^2}}{\sqrt{\pi}}\left(\frac{33}{7x^4}+\frac{26}{5x^2}+\frac{26}{7}+\frac{44x^2}{35}+\frac{8x^4}{35}\right)\right\},$$

$$\beta^2_{230}=\frac{\dfrac{2\sigma}{7x}\left\{\mathrm{erf}(x)\left(\dfrac{81}{5}+\dfrac{66}{5x^2}+\dfrac{117}{2x^4}\right)-\dfrac{e^{-x^2}}{\sqrt{\pi}}\left(\dfrac{117}{x^3}+\dfrac{522}{5x}+\dfrac{278x}{5}+\dfrac{68x^3}{5}+\dfrac{8x^5}{5}\right)\right\}}{\dfrac{3}{\sqrt{2}}-\dfrac{3\alpha_s}{7x^3}\left\{-6\mathrm{erf}(x)\left(\dfrac{12}{5}+\dfrac{11}{x^2}\right)-\dfrac{4e^{-x^2}}{\sqrt{\pi}x}\left(33+\dfrac{146x^2}{5}+\dfrac{76x^4}{5}+\dfrac{32x^6}{5}+\dfrac{12x^8}{5}+\dfrac{4x^{10}}{5}\right)\right\}};$$

$$\langle\tilde r_1\rangle_{231}=x\left\{\mathrm{erf}(x)\left(1+\frac{93}{70x^2}+\frac{22}{35x^4}-\frac{13}{14x^6}\right)+\frac{e^{-x^2}}{7\sqrt{\pi}}\left(\frac{13}{x^5}-\frac{2}{15x^3}+\frac{23}{5x}-\frac{4x}{15}\right)\right\},\qquad\text{(A.18)}$$

$$\left\langle\frac{1}{\tilde r_1}\right\rangle_{231}=\frac{1}{x}\left\{\mathrm{erf}(x)\left(1+\frac{18}{35x^2}-\frac{11}{7x^4}\right)+\frac{e^{-x^2}}{7\sqrt{\pi}}\left(\frac{22}{x^3}+\frac{112}{15x}-\frac{98x}{15}-\frac{44x^3}{15}-\frac{8x^5}{15}\right)\right\},$$

$$\beta^2_{231}=\frac{\dfrac{2\sigma}{7x}\left\{\mathrm{erf}(x)\left(\dfrac{93}{5}+\dfrac{88}{5x^2}-\dfrac{39}{x^4}\right)-\dfrac{4e^{-x^2}}{\sqrt{\pi}}\left(\dfrac{39}{2x^3}+\dfrac{21}{5x}-\dfrac{107x}{30}-\dfrac{17x^3}{15}-\dfrac{2x^5}{15}\right)\right\}}{\dfrac{3}{\sqrt{2}}-\dfrac{12\alpha_s}{7x^3}\left\{\mathrm{erf}(x)\left(-\dfrac{9}{5}+\dfrac{11}{x^2}\right)+\dfrac{2e^{-x^2}}{\sqrt{\pi}x}\left(-11-\dfrac{83x^2}{15}-\dfrac{14x^4}{15}+\dfrac{8x^6}{15}+\dfrac{2x^8}{5}+\dfrac{2x^{10}}{15}\right)\right\}};$$

$$\langle\tilde r_1\rangle_{232}=x\left\{\mathrm{erf}(x)\left(1+\frac{129}{70x^2}-\frac{121}{140x^4}+\frac{13}{56x^6}\right)+\frac{e^{-x^2}}{\sqrt{\pi}x}\left(1+\frac{149}{105x^2}-\frac{13}{28x^4}\right)\right\},\qquad\text{(A.19)}$$

$$\left\langle\frac{1}{\tilde r_1}\right\rangle_{232}=\frac{1}{x}\left\{\mathrm{erf}(x)\left(1-\frac{36}{35x^2}+\frac{11}{28x^4}\right)+\frac{e^{-x^2}}{\sqrt{\pi}}\left(-\frac{11}{14x^3}+\frac{23}{15x}+\frac{8x}{105}\right)\right\},$$

$$\beta^2_{232}=\frac{\dfrac{2\sigma}{7x}\left\{\mathrm{erf}(x)\left(\dfrac{129}{5}-\dfrac{121}{5x^2}+\dfrac{39}{4x^4}\right)+\dfrac{e^{-x^2}}{\sqrt{\pi}}\left(-\dfrac{39}{2x^3}+\dfrac{177}{5x}+\dfrac{16x}{15}\right)\right\}}{\dfrac{3}{\sqrt{2}}-\dfrac{6\alpha_s}{7x^3}\left\{\mathrm{erf}(x)\left(\dfrac{36}{5}-\dfrac{11}{2x^2}\right)+\dfrac{e^{-x^2}}{\sqrt{\pi}x}\left(11-\dfrac{106x^2}{15}-\dfrac{52x^4}{15}-\dfrac{8x^6}{15}\right)\right\}}.$$

$$\underline{\qquad\qquad+\frac{e^{-x^2}}{\sqrt{\pi}x}\left(1+\frac{11}{2x^2}\right)\Big\},}$$

APPENDIX B

String Corrections

The string correction potentials, $V^{\mathrm{sc}}_{jl\Lambda}=\langle\mathbf{\Psi}_{jl\Lambda}|H^{\mathrm{sc}}|\mathbf{\Psi}_{jl\Lambda}\rangle$, have the following form:

$$V^{\mathrm{sc}}_{110}=-\frac{4\sigma x}{15\beta}\left\{\mathrm{erf}(x)\left(1+\frac{2}{x^2}-\frac{11}{4x^4}\right)\right.\qquad\text{(A.20)}$$

$$\left.+\frac{e^{-x^2}}{\sqrt{\pi}x}\left(5+\frac{13}{x^2}\right)\right\},$$

$$V^{\mathrm{sc}}_{111}=-\frac{\sigma x}{15\beta}\left\{3\mathrm{erf}(x)\left(1+\frac{3}{2x^2}-\frac{13}{6x^4}\right)\right.\qquad\text{(A.21)}$$

$$\left.+\frac{e^{-x^2}}{\sqrt{\pi}x}\left(5+\frac{13}{x^2}\right)\right\},$$

$$V_{120}^{\rm sc} = -\frac{2\sigma x}{105\beta}\left\{\mathrm{erf}(x)\left(\frac{28}{3}+\frac{67}{3x^2}-\frac{3}{2x^4}\right)\right. \quad (A.22)$$
$$\left. + \frac{e^{-x^2}}{\sqrt{\pi}}\left(\frac{3}{x^3}-\frac{32}{3x}-16x-\frac{16x^3}{3}\right)\right\},$$

$$V_{121}^{\rm sc} = -\frac{2\sigma x}{210\beta}\left\{\mathrm{erf}(x)\left(\frac{77}{3}+\frac{139}{6x^2}+\frac{3}{2x^4}\right)\right. \quad (A.23)$$
$$\left. + \frac{e^{-x^2}}{\sqrt{\pi}}\left(-\frac{3}{x^3}+\frac{47}{3x}-8x-\frac{8x^3}{3}\right)\right\},$$

$$V_{220}^{\rm sc} = -\frac{2\sigma x}{21\beta}\left\{\mathrm{erf}(x)\left(2+\frac{2}{x^2}-\frac{3}{2x^4}+\frac{9}{2x^6}\right)\right. \quad (A.24)$$
$$\left. + \frac{e^{-x^2}}{\sqrt{\pi}}\left(-\frac{9}{x^5}-\frac{3}{x^3}+\frac{2}{x}\right)\right\},$$

$$V_{221}^{\rm sc} = -\frac{2\sigma x}{21\beta}\left\{\mathrm{erf}(x)\left(\frac{13}{6}+\frac{59}{12x^2}+\frac{3}{4x^4}-\frac{3}{x^6}\right)\right. \quad (A.25)$$
$$\left. + \frac{e^{-x^2}}{\sqrt{\pi}}\left(\frac{6}{x^5}+\frac{5}{2x^3}-\frac{17}{6x}-4x-\frac{4x^3}{3}\right)\right\},$$

$$V_{222}^{\rm sc} = -\frac{2\sigma x}{21\beta}\left\{\mathrm{erf}(x)\left(\frac{8}{3}+\frac{5}{3x^2}+\frac{3}{4x^6}\right)\right. \quad (A.26)$$
$$\left. + \frac{e^{-x^2}}{\sqrt{\pi}}\left(-\frac{3}{2x^5}-\frac{1}{x^3}+\frac{8}{3x}\right)\right\},$$

$$V_{230}^{\rm sc} = -\frac{2\sigma x}{27\beta}\left\{\mathrm{erf}(x)\left(\frac{81}{35}+\frac{237}{70x^2}\right.\right. \quad (A.27)$$
$$\left.\left. +\frac{87}{70x^4}-\frac{9}{4x^6}\right)+\frac{e^{-x^2}}{\sqrt{\pi}x}\left(\frac{9}{2x^4}+\frac{18}{35x^2}+\frac{131}{35}\right.\right.$$
$$\left.\left. +\frac{8x^2}{7}+\frac{8x^4}{35}\right)\right\},$$

$$V_{231}^{\rm sc} = -\frac{2\sigma x}{27\beta}\left\{\mathrm{erf}(x)\left(\frac{93}{35}+\frac{277}{70x^2}\right.\right. \quad (A.28)$$
$$\left.\left. -\frac{1}{5x^4}+\frac{3}{2x^6}\right)+\frac{e^{-x^2}}{\sqrt{\pi}x}\left(-\frac{3}{x^4}-\frac{8}{5x^2}+\frac{53}{21}\right.\right.$$
$$\left.\left. +\frac{8x^2}{21}+\frac{8x^4}{105}\right)\right\},$$

$$V_{232}^{\rm sc} = -\frac{2\sigma x}{27\beta}\left\{\mathrm{erf}(x)\left(\frac{129}{35}+\frac{41}{10x^2}\right.\right. \quad (A.29)$$
$$\left.\left. -\frac{59}{140x^4}-\frac{3}{8x^6}\right)+\frac{e^{-x^2}}{\sqrt{\pi}x}\left(\frac{3}{4x^4}+\frac{47}{35x^2}+\frac{53}{15}\right)\right\}.$$

APPENDIX C

Spin–Orbit Corrections

The nonperturbative spin–orbit potentials, given as $V_{jl\Lambda}^{\rm LS(np)} = \langle \mathbf{\Psi}_{jl\Lambda}|H^{\rm LS(np)}|\mathbf{\Psi}_{jl\Lambda}\rangle$, are

$$V_{110}^{\rm LS(np)} = \frac{2\sigma}{5\beta x}\left\{\mathrm{erf}(x)\left(1-\frac{1}{2x^2}\right)+\frac{e^{-x^2}}{\sqrt{\pi}x}\right\}, \quad (A.30)$$

$$V_{111}^{\rm LS(np)} = \frac{\sigma}{5\beta x}\left\{\mathrm{erf}(x)\left(1+\frac{1}{2x^2}\right)-\frac{e^{-x^2}}{\sqrt{\pi}x}\right\}, \quad (A.31)$$

$$V_{120}^{\rm LS(np)} = \frac{18\sigma}{35\beta x}\left\{\mathrm{erf}(x)\left(1+\frac{1}{2x^2}\right)\right. \quad (A.32)$$
$$\left. - \frac{e^{-x^2}}{\sqrt{\pi}x}\left(1+\frac{8x^2}{9}\right)\right\},$$

$$V_{121}^{\rm LS(np)} = \frac{3\sigma}{35\beta x}\left\{\mathrm{erf}(x)\left(7-\frac{3}{2x^2}\right)\right. \quad (A.33)$$
$$\left. + \frac{e^{-x^2}}{\sqrt{\pi}x}\left(3-\frac{4x^2}{3}\right)\right\},$$

$$V_{220}^{\rm LS(np)} = \frac{2\sigma}{7\beta x}\left(1+\frac{2}{x^2}\right) \quad (A.34)$$
$$\times\left\{\mathrm{erf}(x)\left(1-\frac{3}{2x^2}\right)+\frac{3e^{-x^2}}{\sqrt{\pi}x}\right\},$$

$$V_{221}^{\rm LS(np)} = \frac{2\sigma}{7\beta x}\left\{\mathrm{erf}(x)\left(\frac{2}{3}-\frac{1}{2x^2}+\frac{2}{x^4}\right)\right. \quad (A.35)$$
$$\left. - \frac{xe^{-x^2}}{\sqrt{\pi}}\left(\frac{2}{3}+\frac{5}{3x^2}+\frac{4}{x^4}\right)\right\},$$

$$V_{222}^{\rm LS(np)} = \frac{2\sigma}{7\beta x}\left\{\mathrm{erf}(x)\left(\frac{1}{3}+\frac{1}{2x^2}-\frac{1}{2x^4}\right)\right. \quad (A.36)$$
$$\left. + \frac{e^{-x^2}}{\sqrt{\pi}x}\left(-\frac{1}{3}+\frac{1}{x^2}\right)\right\},$$

$$V_{230}^{\rm LS(np)} = \frac{2\sigma}{63\beta x}\left\{\mathrm{erf}(x)\left(16+\frac{54}{5x^2}+\frac{21}{x^4}\right)\right. \quad (A.37)$$
$$\left. - \frac{4e^{-x^2}}{\sqrt{\pi}}\left(\frac{21}{4x^3}+\frac{31}{5x}+4x+\frac{4x^3}{5}\right)\right\},$$

$$V_{231}^{\mathrm{LS(np)}} = \frac{4\sigma}{9\beta x}\left\{\mathrm{erf}(x)\left(\frac{26}{21}+\frac{3}{5x^2}-\frac{1}{x^4}\right)\right. \quad \text{(A.38)}$$
$$\left. + \frac{2e^{-x^2}}{\sqrt{\pi}}\left(\frac{1}{x^3}+\frac{1}{15x}-\frac{16x}{35}-\frac{8x^3}{105}\right)\right\},$$

$$V_{232}^{\mathrm{LS(np)}} = \frac{2\sigma}{9\beta x}\left\{\mathrm{erf}(x)\left(\frac{64}{21}-\frac{69}{35x^2}+\frac{1}{2x^4}\right)\right. \quad \text{(A.39)}$$
$$\left. + \frac{e^{-x^2}}{\sqrt{\pi}}\left(-\frac{1}{x^3}+\frac{344}{105x}-\frac{8x}{105}\right)\right\}.$$

The perturbative spin-dependent potentials, $V_{jl\Lambda}^{\mathrm{LS(p)}} = \langle \mathbf{\Psi}_{jl\Lambda}|H^{\mathrm{LS(p)}}|\mathbf{\Psi}_{jl\Lambda}\rangle$, are

$$V_{110}^{\mathrm{LS(p)}} = -\frac{3\alpha_s\beta}{5x^3}\left\{\mathrm{erf}(x)+\frac{2xe^{-x^2}}{\sqrt{\pi}}\right\}, \quad \text{(A.40)}$$

$$V_{111}^{\mathrm{LS(p)}} = \frac{3}{5}\alpha_s\beta\left\{\frac{\mathrm{erf}(x)}{2x^3}-\frac{e^{-x^2}}{\sqrt{\pi}}\left(2+\frac{1}{x^2}\right)\right\}, \quad \text{(A.41)}$$

$$V_{120}^{\mathrm{LS(p)}} = \frac{3}{7}\alpha_s\beta\left\{\frac{3\mathrm{erf}(x)}{5x^3}-\frac{2e^{-x^2}}{5\sqrt{\pi}}\right. \quad \text{(A.42)}$$
$$\left.\times\left(6+\frac{3}{x^2}+8x^2\right)\right\},$$

$$V_{121}^{\mathrm{LS(p)}} = -\frac{3}{7}\alpha_s\beta\left\{\frac{3\mathrm{erf}(x)}{10x^3}+\frac{e^{-x^2}}{5\sqrt{\pi}}\right. \quad \text{(A.43)}$$
$$\left.\times\left(6-\frac{3}{x^2}+4x^2\right)\right\},$$

$$V_{220}^{\mathrm{LS(p)}} = \frac{3}{7}\alpha_s\beta\left\{-\frac{\mathrm{erf}(x)}{x^3}\left(1+\frac{6}{x^2}\right)\right. \quad \text{(A.44)}$$
$$\left. + \frac{2e^{-x^2}}{\sqrt{\pi}}\left(2+\frac{5}{x^2}+\frac{6}{x^4}\right)\right\},$$

$$V_{221}^{\mathrm{LS(p)}} = \frac{3}{7}\alpha_s\beta\left\{\frac{4\mathrm{erf}(x)}{x^5}-\frac{4e^{-x^2}}{3\sqrt{\pi}}\right. \quad \text{(A.45)}$$
$$\left.\times\left(2+\frac{5}{x^4}+\frac{4}{x^2}+x^2\right)\right\},$$

$$V_{222}^{\mathrm{LS(p)}} = \frac{3}{7}\alpha_s\beta\left\{\frac{\mathrm{erf}(x)}{x^3}\left(1-\frac{1}{x^2}\right)\right. \quad \text{(A.46)}$$
$$\left. - \frac{e^{-x^2}}{\sqrt{\pi}}\left(\frac{4}{3}+\frac{2}{3x^2}-\frac{2}{x^4}\right)\right\},$$

$$V_{230}^{\mathrm{LS(p)}} = \frac{8}{21}\alpha_s\beta\left\{\frac{\mathrm{erf}(x)}{x^3}\left(1+\frac{9}{4x^2}\right)\right. \quad \text{(A.47)}$$
$$\left. - \frac{e^{-x^2}}{\sqrt{\pi}}\left(\frac{18}{5}+\frac{9}{2x^4}+\frac{5}{x^2}+\frac{12x^2}{5}+\frac{8x^4}{5}\right)\right\},$$

$$V_{231}^{\mathrm{LS(p)}} = \frac{4}{21}\alpha_s\beta\left\{\frac{\mathrm{erf}(x)}{x^3}\left(1-\frac{3}{x^2}\right)\right. \quad \text{(A.48)}$$
$$\left. + \frac{2e^{-x^2}}{\sqrt{\pi}}\left(-\frac{14}{15}+\frac{3}{x^4}+\frac{1}{x^2}-\frac{4x^2}{3}-\frac{8x^4}{15}\right)\right\},$$

$$V_{232}^{\mathrm{LS(p)}} = \frac{2}{21}\alpha_s\beta\left\{\frac{\mathrm{erf}(x)}{x^3}\left(-4+\frac{3}{2x^2}\right)\right. \quad \text{(A.49)}$$
$$\left. + \frac{e^{-x^2}}{\sqrt{\pi}}\left(\frac{4}{15}-\frac{3}{x^4}+\frac{6}{x^2}-\frac{8x^2}{15}\right)\right\}.$$

REFERENCES

1. A. Donnachie and Yu. S. Kalashnikova, Phys. Rev. D **60**, 114011 (1999).
2. M. Foster and C. Michael, Phys. Rev. D **59**, 094509 (1999).
3. K. J. Juge, J. Kuti, and C. J. Morningstar, Nucl. Phys. B (Proc. Suppl.) **73**, 590 (1999); Phys. Rev. Lett. **82**, 4400 (1999); hep-lat/0103008.
4. Yu. A. Simonov, in *Lectures at the XVII International School of Physics, Lisbon, 1999* (World Sci., Singapore, 2000); hep-ph/9911237.
5. A. Di Giacomo, H. G. Dosch, V. I. Shevchenko, and Yu. A. Simonov, hep-ph/0007223.
6. A. Yu. Dubin, A. B. Kaidalov, and Yu. A. Simonov, Phys. Lett. B **323**, 41 (1994).
7. V. L. Morgunov, A. V. Nefediev, and Yu. A. Simonov, Phys. Lett. B **459**, 653 (1999); Yu. S. Kalashnikova and A. V. Nefediev, Phys. Lett. B **492**, 91 (2002); Yu. S. Kalashnikova, A. V. Nefediev, and Yu. A. Simonov, Phys. Rev. D **64**, 014037 (2001); A. M. Badalian and B. L. G. Bakker, hep-ph/0202246.
8. A. B. Kaidalov and Yu. A. Simonov, Yad. Fiz. **63**, 1507 (2000) [Phys. At. Nucl. **63**, 1428 (2000)]; Phys. Lett. B **477**, 163 (2000).
9. Yu. A. Simonov, Nucl. Phys. B (Proc. Suppl.) **23**, 283 (1990); Yu. S. Kalashnikova and Yu. B. Yufryakov, Phys. Lett. B **359**, 175 (1995); Yad. Fiz. **60**, 374 (1997) [Phys. At. Nucl. **60**, 307 (1997)].
10. Yu. A. Simonov, Nucl. Phys. B **592**, 350 (2001).
11. Yu. A. Simonov, Yad. Fiz. **64**, 1959 (2001) [Phys. At. Nucl. **64**, 1876 (2001)].
12. Yu. S. Kalashnikova and D. S. Kuzmenko, Yad. Fiz. **64**, 1796 (2001) [Phys. At. Nucl. **64**, 1716 (2001)].
13. Yu. A. Simonov, Yad. Fiz. **58**, 113 (1995) [Phys. At. Nucl. **58**, 107 (1995)].
14. Yu.S. Kalashnikova and A. V. Nefediev, Yad. Fiz. **60**, 1529 (1997) [Phys. At. Nucl. **60**, 1389 (1997)]; Yad. Fiz. **61**, 871 (1998) [Phys. At. Nucl. **61**, 785 (1998)].

15. D. Horn and J. Mandula, Phys. Rev. D **17**, 898 (1978).
16. E. S. Swanson and A. P. Szczepaniak, Phys. Rev. D **59**, 014035 (1999).
17. Yu.A. Simonov, Nucl. Phys. B **324**, 67 (1989); A. M. Badalian and Yu. A. Simonov, Yad. Fiz. **59**, 2247 (1996) [Phys. At. Nucl. **59**, 2164 (1996)].
18. N. Brambilla, A. Pineda, J. Soto, and A. Vairo, Nucl. Phys. B **566**, 275 (2000).
19. G. S. Bali, Phys. Rep. **343**, 1 (2001).
20. R. L. Jaffe, K. Johnson, and Z. Ryzak, Ann. Phys. (N. Y.) **168**, 344 (1986).
21. N. Isgur and J. Paton, Phys. Rev. D **31**, 2910 (1985).
22. T. J. Allen, M. G. Olsson, and S. Veseli, Phys. Lett. B **434**, 110 (1998).
23. G. Karl and J. Paton, Phys. Rev. D **60**, 034015 (1999).

Physics of Atomic Nuclei, Vol. 66, No. 5, 2003, pp. 968–974. Translated from Yadernaya Fizika, Vol. 66, No. 5, 2003, pp. 1000–1006.

ELEMENTARY PARTICLES AND FIELDS
Theory

Instanton Liquid at a Finite Density of Quark Matter

G. M. Zinovjev[1)] and S. V. Molodtsov

Institute of Theoretical and Experimental Physics,
Bol'shaya Cheremushkinskaya ul. 25, Moscow, 117259 Russia

Received October 9, 2001; in final form, May 23, 2002

Abstract—For the case of finite quark and baryon densities, the interaction of light quarks with an instanton liquid is considered in a phase that involves a nonvanishing chiral condensate. The generating functional is considered in the tadpole approximation, and the behavior of the dynamical quark mass and the behavior of the chiral condensate, as well as the behavior of the instanton-liquid (gluon-condensate) density, which grows slightly with the quark chemical potential, are explored. Arguments are presented in favor of the statement that the quark-density threshold for the emergence of a diquark condensate grows sizably owing to interaction with the instanton liquid. © *2003 MAIK "Nauka/Interperiodica".*

Since the discovery of instantons, the formulation of quantum field theory in terms of a path integral has become very popular and, in some cases, nearly the only tool for studying the phenomenology of QCD. It enables one to identify nonperturbatively field configurations that dominate the action functional and to obtain deeper insight into the fundamental distinction between the physics of QCD and the physics of other complicated systems involving many degrees of freedom. In the overwhelming majority of cases, quanta that interacting fermions exchange in accordance with the original Lagrangian specify, for such systems, the form of the interaction potential. In the case of QCD, a dominant role of topological excitations of the gluon field (instantons and quantum oscillations about them) made it possible to reveal and to explain definitively a whole series of new physical effects concerning, first of all, chiral-symmetry breaking and put in doubt the the concept of potential (perturbative description).

Within a later period, a considerable amount of theoretical effort was expended in analytically going beyond the approximation of a dilute instanton gas [1]. As a result, it was shown that an effective instanton–anti-instanton interaction stabilizes the medium of these pseudoparticles [2] at a level of reasonable phenomenological parameters (mean size of pseudoparticles and mean spacing between them), more likely forming an instanton liquid [3]. The approach developed in [2] even makes it possible to obtain quite justified quantitative predictions, although only lattice QCD was able to provide a serious theoretical basis for the problem of studying the role of instantons [4]. Yet, this concerns primarily lattice QCD at zero and finite temperatures—lattice QCD at finite quark densities has received much less adequate study, largely because of technical difficulties involved in realizing the lattice approximation. Nowadays, investigation of QCD at high densities of quark matter provides a new possibility for a direct experimental examination of instantons (along with searches for small-size instantons in deep-inelastic collisions [5]) since a flavor superconducting phase can be realized in collisions of ultrarelativistic nuclei [6].

The present study is devoted to exploring the interaction of light quarks with an instanton liquid in a phase featuring a nonzero chiral condensate at finite quark and baryon densities and is a continuation of investigations initiated in [7], where a method was proposed that makes it possible to take into account the reaction of the instanton liquid to the presence of quarks. We recall that, in the instanton-liquid model [2], the generating functional is represented as the product of a gluon and a quark component; that is,

$$\mathcal{Z} = \mathcal{Z}_g \cdot \mathcal{Z}_\psi.$$

The first factor furnishes information about the gluon condensate, while the fermion component serves for describing quarks in an instanton medium—in particular, a quark and a diquark condensate and their excitations [2]. The component $\mathcal{Z}_g$ is calculated in the semiclassical approximation under the assumption that a superposition of pseudoparticle fields $A_{\bar{I}I}(x;\gamma)$ defined as Euclidean solutions to the Yang–Mills equations—they are referred to as (anti)instantons ($\bar{I}I$) and are characterized by the parameters $\gamma = \rho, z, U$, where ρ is the size of a pseudoparticle, z is

[1)] Bogolyubov Institute for Theoretical Physics, National Academy of Sciences of Ukraine, Metrologicheskaya ul. 14b, Kiev, 03143 Ukraine.

the coordinate of its center, and U is the orientation in the color space of the $SU(N_c)$ group—is a dominant saturating configuration. For the sake of definiteness, we assume that there are N pseudoparticles in the 4-volume V and, additionally, that $N_+ = N_- = N/2$ (a plus and a minus sign correspond to $\bar{I}$ and I, respectively). On the basis of the variational maximum principle, we can obtain the following estimate for the gluon component:

$$\mathcal{Z}_g \simeq e^{-\langle S\rangle}.$$

Here, the averaged instanton-liquid action $\langle S\rangle$ is given by the additive functional

$$\langle S\rangle = \int dz \int d\rho n(\rho) s(\rho), \tag{1}$$

the action per instanton,

$$s(\rho) = \beta(\rho) + 5\ln(\Lambda\rho) - \ln\tilde{\beta}^{2N_c} + \beta\xi^2\rho^2 \int d\rho_1 n(\rho_1)\rho_1^2, \tag{2}$$

being averaged by using the equilibrium size distribution of instantons, which has the form

$$n(\rho) = C_1 e^{-s(\rho)} = C\rho^{-5}\tilde{\beta}^{2N_c} e^{-\beta(\rho)-\nu\rho^2/\overline{\rho^2}}, \tag{3}$$

where $\overline{\rho^2} = \int d\rho\rho^2 n(\rho)/n = \left(\dfrac{\nu}{\beta\xi^2 n}\right)^{1/2}$, $n = \int d\rho n(\rho) = \dfrac{N}{V}$, $\nu = \dfrac{b-4}{2}$, $b = \dfrac{11N_c - 2N_f}{3}$, and N_f is the number of flavors. The constant C is determined self-consistently from the variational maximum principle, while $\beta(\rho) = \dfrac{8\pi^2}{g^2} = -\ln C_{N_c} - b\ln(\Lambda\rho)$ ($\Lambda = \Lambda_{\overline{MS}} = 0.92\Lambda_{\text{P.V.}}$, and g is the strong coupling constant), with C_{N_c} being renormalization-scheme dependent: $C_{N_c} \approx \dfrac{4.66\exp(-1.68N_c)}{\pi^2(N_c-1)!(N_c-2)!}$. The parameters $\beta = \beta(\bar{\rho})$ and $\widetilde{\beta} = \beta + \ln C_{N_c}$ are fixed at the scale of the mean pseudoparticle size $\bar{\rho}$. The constant $\xi^2 = \dfrac{27}{4}\dfrac{N_c}{N_c^2-1}\pi^2$ characterizes the interaction in a stochastic ensemble of pseudoparticles. The resulting parameters of the instanton liquid—for example, the mean pseudoparticle size $\bar{\rho}$ and the instanton-liquid density n—are in reasonably good agreement with analogous estimates obtained within the phenomenology of the QCD vacuum.

In the quark determinant $\mathcal{Z}_\psi$, the quark fields are considered to be affected by a preset stochastic ensemble of pseudoparticles, while the inverse effect of quarks on the instantons is disregarded; that is,

$$\mathcal{Z}_\psi \simeq \int D\psi^\dagger D\psi \langle\langle e^{S(\psi,\psi^\dagger,A)}\rangle\rangle_A.$$

Since the instanton liquid is dilute (the characteristic packing-fraction parameter $n\bar{\rho}^4$ is small), we also disregard correlations between pseudoparticles; in addition, we will consider the approximation of $N_c \to \infty$. The leading contribution to the action functional for fermion fields is mainly determined by zero modes $\Phi(x-z;\mu)$, which are solutions to the Dirac equation with the chemical potential μ,

$$[i\hat{D}(A_{\bar{I}I}) - i\mu\gamma_4]\Phi_{\bar{I}I} = 0,$$

in the (anti)instanton field $A_{\bar{I}I}$. The Weyl components of the solution,

$$\Phi(x;\mu) = \begin{vmatrix}\Phi_{\bar{I}}(x;\mu)\\ \Phi_I(x;\mu)\end{vmatrix},$$

have the explicit form [8]

$$[\Phi_{R,L}(x)]^{\alpha i} = \frac{\rho}{2\sqrt{2}\pi} e^{\mu x_4}\sqrt{\Pi(x)}\partial_\mu \times \left(\frac{e^{-\mu x_4}F(x;\mu)}{\Pi(x)}\right)(\sigma^\pm)^i_j \varepsilon^{jk} U^\alpha_k,$$

where

$$\Pi(x) = 1 + \frac{\rho^2}{x_4^2 + r^2};$$

$$F(x;\mu) = \frac{1}{x_4^2+r^2}\left[\cos(\mu r) + \frac{x_4}{r}\sin(\mu r)\right];$$

$\Phi_{R,L} = P_\pm\Phi$; $P_\pm = \dfrac{1\pm\gamma_5}{2}$; $\sigma_\mu^\pm = (\pm i\boldsymbol{\sigma}, 1)$, $\boldsymbol{\sigma}$ being the 3-vector of the Pauli matrices; $x = (\mathbf{x}, x_4)$; $r = |\mathbf{x}|$; and ε is an antisymmetric tensor. For the particular case of $N_f = 1$, the quark determinant can be represented as

$$\mathcal{Z}_\psi \simeq \int D\psi^\dagger D\psi \left(\frac{Y^+}{VR}\right)^{N_+}\left(\frac{Y^-}{VR}\right)^{N_-} \times \exp\left\{\int dx\psi^\dagger(x)(i\hat{\partial} - i\mu\gamma_4)\psi(x)\right\}, \tag{4}$$

where R is a factor that reduces the result to a dimensionless form. The preexponential factors describe the instanton-induced quark interaction [9],

$$Y^\pm = i\int dz dU d\rho n(\rho)/n \times \int dx dy \psi^\dagger_{L,R}(x)(i\partial - i\mu)^\mp \times \Phi_{\bar{I}I}(x-z)\widetilde{\Phi}_{\bar{I}I}(y-z)(i\partial - i\mu)^\pm\psi_{L,R}(y),$$

averaging over color orientations being given by integration with respect to U. The notation $\widetilde{\Phi}$ was introduced for the conjugate zero mode, $\widetilde{\Phi}_I(x;\mu) = \Phi^\dagger_I(x;-\mu)$; $\mu^\pm$ and similar conventions are used for

the 4-vectors associated with the matrices $\sigma_\nu^\pm$: $\mu^\pm = \mu^\nu \sigma_\nu^\pm$, $\mu_\nu = (\mathbf{0}, \mu)$.

With the aid of integration with respect to the auxiliary parameter λ, the quark determinant $\mathcal{Z}_\psi$ can be reduced to an exponential form, which is convenient for calculations by the saddle-point method. The result is

$$\mathcal{Z}_\psi \simeq \int \frac{d\lambda}{2\pi} \exp\left\{N \ln\left(\frac{N}{i\lambda VR}\right) - N\right\} \times \int D\psi^\dagger D\psi \exp\left\{\int \frac{dk}{(2\pi)^4} \times \psi^\dagger(k)\left(-\hat{k} - i\hat{\mu} + \frac{i\lambda}{N_c}\gamma_0(k;\mu)\right)\psi(k)\right\}.$$

The complex-valued function $\gamma_0(k;\mu)$ appearing in the above expression is determined by Fourier components of zero modes; that is,

$$\gamma_0(k;\mu) = (k+i\mu)_\alpha (k+i\mu)_\alpha h_\beta(k;\mu) h_\beta(k;\mu),$$
$$\Phi(k;\mu)^{i\alpha} = h_\mu(k;\mu)(\sigma_\mu^\pm)_j^i \varepsilon^{jk} U_k^\alpha,$$

$$h_4(k_4,k;\mu) = \frac{\pi\rho^3}{4k}\{(k-\mu-ik_4)[(2k_4+i\mu)f_1^- + i(k-\mu-ik_4)f_2^-] + (k+\mu+ik_4) \times [(2k_4+i\mu)f_1^+ - i(k+\mu+ik_4)f_2^+]\},$$

$$h_i(k_4,k;\mu) = \frac{\pi\rho^3 k_i}{4k^2}\Big\{(2k-\mu)(k-\mu-ik_4)f_1^- + (2k+\mu)(k+\mu+ik_4)f_1^+ + \Big[2(k-\mu) \times (k-\mu-ik_4) - \frac{1}{k}(\mu+ik_4)[k_4^2+(p-\mu)^2]\Big]f_2^- + \Big[2(k+\mu)(k+\mu+ik_4) + \frac{1}{k}(\mu+ik_4) \times [k_4^2+(p+\mu)^2]\Big]f_2^+\Big\},$$

where $k = |\mathbf{k}|$ for the spatial components of the 4-vector,

$$f_1^\pm = \frac{I_1(z^\pm)K_0(z^\pm) - I_0(z^\pm)K_1(z^\pm)}{z^\pm},$$

$$f_2^\pm = \frac{I_1(z^\pm)K_1(z^\pm)}{z_\pm^2}, \quad z^\pm = \frac{\rho}{2}\sqrt{k_4^2 + (k\pm\mu)^2},$$

and I_i and $K_i (i = 0, 1)$ are modified Bessel functions.

In order to avoid encumbering the formulas with extra factors, it is convenient to introduce dimensionless variables via the substitutions

$$\frac{k_4\bar{\rho}}{2} \to k_4, \quad \frac{k\bar{\rho}}{2} \to k, \quad \frac{\lambda\bar{\rho}^3}{2N_c} \to \lambda,$$

$$\psi(k) \to \bar{\rho}^{5/2}\psi(k).$$

It can be shown that, in terms of these variables, the saddle-point equation has the form

$$\frac{n\bar{\rho}^4}{\lambda} - 2N_c \int \frac{dk}{\pi^4} \frac{[\lambda^2\gamma_0^2(k;\mu)]'_\lambda}{(k+i\mu)^2 + \lambda^2\gamma_0^2(k;\mu)} = 0, \quad (5)$$

where a prime denotes differentiation with respect to λ.

It was shown in [7, 10] that the reaction of quarks to the instanton liquid can be described within perturbation theory by considering small variations of the instanton-liquid parameters, δn and $\delta\rho$, in the vicinity of their equilibrium values n and $\bar{\rho}$, the variations being included in the theory if use is made of deformable field configurations (crumpled instantons) of dimension ρ as a function of x and z—that is, $\rho \to \rho(x,z)$. In the case of perturbations whose wavelength is much longer than the characteristic instanton size $\bar{\rho}$ (this is so for the example of π mesons), the averaged action per instanton is supplemented with the kinetic-energy-type term generated by deformable (anti)instantons; that is,

$$\langle S\rangle \simeq \int dz \int d\rho n(\rho)\left\{\frac{\kappa}{2}\left(\frac{\partial\rho}{\partial z}\right)^2 + s(\rho)\right\}, \quad (6)$$

where κ is the kinetic coefficient that is calculated within the semiclassical approach. To the precision adopted in this study, the kinetic coefficient is fixed at some characteristic scale—for example, as $\kappa \sim \kappa(\bar{\rho})$. For this coefficient, our estimations yield $\kappa \sim c\beta$—that is, the instanton action multiplied by a factor of $c \sim 1.5$–6, its specific value being dependent on the ansatz adopted for the saturating configuration. Retaining second-order terms in the deviation from the point $\left.\frac{ds(\rho)}{d\rho}\right|_{\rho_c} = 0$, at which the action functional attains a minimum, and approximately setting

$$s(\rho) \simeq s(\bar{\rho}) + \frac{s^{(2)}(\bar{\rho})}{2}\varphi^2, \quad (7)$$

where $s^{(2)}(\bar{\rho}) \simeq \left.\frac{d^2 s(\rho)}{d\rho^2}\right|_{\rho_c} = \frac{4\nu}{\bar{\rho}^2}$ and where the scalar field $\varphi = \delta\rho = \rho - \rho_c \simeq \rho - \bar{\rho}$ is the field of deviations from the equilibrium value $\rho_c = \bar{\rho}\left(1 - \frac{1}{2\nu}\right)^{1/2} \simeq \bar{\rho}$, one can easily see that the deformation field is

described in terms of the Lagrangian density[1)]

$$\mathcal{L} = \frac{n\kappa}{2}\left\{\left(\frac{\partial\varphi}{\partial z}\right)^2 + M^2\varphi^2\right\},$$

where $M^2 = \dfrac{s^{(2)}(\bar\rho)}{\kappa} = \dfrac{4\nu}{\kappa\overline{\rho^2}}$ is the mass gap; $M \approx 1.21\Lambda$ for an instanton liquid in the quenched approximation with parameters $N_c = 3$, $c = 4$, $\bar\rho\Lambda \approx 0.37$, $\beta \approx 17.5$, and $n\Lambda^{-4} \approx 0.44$ [10].

The inclusion of a variation of zero modes in the quark determinant reduces to replacing these modes by $\Phi_{\bar I I}(x-z,\rho) \simeq \Phi_{\bar I I}(x-z,\rho_c) + \Phi^{(1)}_{\bar I I}(x-z,\rho_c)\times\delta\rho(x,z)$, where $\Phi^{(1)}_{\bar I I}(u,\rho_c) = \partial\Phi_{\bar I I}(u,\rho)/\partial\rho|_{\rho=\rho_c}$; in accordance with the adiabaticity condition, we must set here $\delta\rho(x,z) \simeq \delta\rho(z,z) = \varphi(z)$. The additional contributions from scalar fields generate corrections in the kernels of the factors $Y^{\pm}$; these corrections are considered in the linear approximation in φ, and the approximate relation $\rho_c \simeq \bar\rho$ is used everywhere. As a result, we arrive at a generating functional that involves an effective Lagrangian of the Yukawa type and which has the form

$$\begin{aligned}\mathcal{Z} &\simeq \int d\lambda\mathcal{Z}'_g\int D\psi^\dagger D\psi D\varphi \qquad (8)\\ &\times\exp\left\{nV\left(\ln\frac{n\bar\rho^4}{\lambda}-1\right)\right.\\ &\left.-\int\frac{dk}{\pi^4}\frac{1}{2}\varphi(-k)\cdot 4[k^2+M^2]\varphi(k)\right\}\\ &\times\exp\left\{\int\frac{dkdl}{\pi^8}\psi^\dagger(k)\cdot 2\left[\pi^4\delta(k-l)(-\hat k - i\hat\mu\right.\right.\\ &\left.\left.+ i\lambda\gamma_0(k;\mu)) + i\lambda\gamma_1(k,l;\mu)\varphi(k-l)\right]\psi(l)\right\},\end{aligned}$$

where φ is a colorless scalar field interacting with quarks and $\mathcal{Z}'_g$ denotes that part of the gluon component of the generating functional which survives upon expanding the action per instanton in terms of a small deviation from the equilibrium instanton size; it should be recalled that we use here dimensionless variables: $\varphi(k) \to (n\kappa)^{-1/2}\bar\rho^3\varphi(k)$ for the scalar field and $M\bar\rho/2 \to M$ for its mass. In this study, we will not need a general form of the kernel $\gamma_1(k,l;\mu)$ since, in view of the presence of a quark condensate, we can make a significant simplification, retaining only higher order contributions from the functional in (8), which are given by tadpole-type diagrams. In this particular case, the following scheme of perturbation theory in the deviation from the condensate value is applicable:

$$\psi^\dagger\psi\varphi = \langle\psi^\dagger\psi\rangle\varphi + \{\psi^\dagger\psi - \langle\psi^\dagger\psi\rangle\}\varphi. \qquad (9)$$

Here, the first term generates the leading contribution, the expansion being performed in the second, small, term. As a result, the vertex is obtained in the form

$$\begin{aligned}\gamma_1(k;\mu) = \frac{2}{(n\bar\rho^4\kappa)^{1/2}}\{&[kh + (k_4+i\mu)h_4]\\ &\times[k\delta h + (k_4+i\mu)\delta h_4] + [(k_4+i\mu)h - kh_4]\\ &\times[(k_4+i\mu)\delta h - k\delta h_4]\}.\end{aligned}$$

Here, we have introduced the component h aligned with the unit vector k_i/k, $h_i = (k_i/k)h$, while δh and δh_4 can be derived from h and h_4 by means of the substitutions $f_i^{\pm} \to g_i^{\pm}$, where

$$g_1^{\pm} = f_1^{\pm} + 2(I_0^{\pm}K_0^{\pm} - I_1^{\pm}K_1^{\pm}), \quad g_2^{\pm} = -f_1^{\pm} - f_2^{\pm}.$$

In the present study, we will take into account two corrections. One is associated with the change in the dynamical quark mass and the chiral condensate due to interaction with the scalar field, while the other is associated with the change in the instanton-liquid density due to the shift of the equilibrium pseudoparticle size. The first correction is described by the contribution

$$\begin{aligned}&2(i\lambda)^2\int\frac{dkdldk'dl'}{\pi^{16}}\gamma_1(k,l;\mu)\gamma_1(k',l';\mu) \qquad (10)\\ &\times\psi^\dagger(k)\psi(l)\psi^\dagger(k')\psi(l')\underline{\varphi(k-l)\varphi(k'-l')}\\ &\simeq 4\lambda^2\int\frac{dk}{\pi^4}\gamma_1(k;\mu)\psi^\dagger(k)\psi(k)\\ &\times\int\frac{dl}{\pi^4}\gamma_1(l;\mu)\mathrm{tr}S(l)D(0),\end{aligned}$$

where $\gamma_1(k;\mu) = \gamma_1(k,k;\mu)$; in expression (10), use is made of natural definitions for the convolution of the scalar field,

$$\underline{\varphi(k)\varphi(l)} = \pi^4\delta(k+l)D(k),$$
$$D(k) = \frac{1}{4(k^2+M^2)},$$

and for the quark Green's function $S(k)$,

$$\langle\psi^\dagger(k)\psi(l)\rangle = -\pi^4\delta(k-l)\mathrm{tr}S(k).$$

The expression in front of the combination $\psi^\dagger(k)\psi(k)$ in (10) describes an additional contribution to the dynamical quark mass, $\lambda\gamma_0(k;\mu) \to \lambda\Gamma(k;\mu) = \lambda\gamma_0(k;\mu) + \lambda\delta\gamma_0(k;\mu)$, where

$$\delta\gamma_0(k;\mu) = \gamma_1(k;\mu)(-2i\lambda) \qquad (11)$$

[1)] In our opinion, the physical meaning of the deformation fields is analogous to the meaning of phonons in solid-state physics; therefore, we refer to them as phonon-like excitations of an instanton liquid [10].

$$\times \int \frac{dl}{\pi^4}\gamma_1(l;\mu)\,\mathrm{tr}S(l)D(0).$$

Let us introduce an auxiliary function $c(\lambda)$ such that it would enable us to isolate the explicit dependence on the parameters in $\delta\gamma$ in a convenient form; that is,

$$\delta\gamma_0(k;\mu) = \frac{N_c}{(n\bar\rho^4\kappa)^{1/2}}\frac{\kappa}{\nu}\lambda^2 c(\lambda)\gamma_1(k;\mu).$$

Using the quark Green's function, we can derive the closed integral equation for determining the function $c(\lambda)$,

$$c(\lambda) = (n\bar\rho^4\kappa)^{1/2}\int\frac{dk}{\pi^4}\gamma_1(k;\mu) \qquad (12)$$
$$\times \frac{\Gamma(k;\mu)}{(k+i\mu)^2+\lambda^2\Gamma^2(k;\mu)},$$

whence we can find $S(k)$.

It was found in [7] that the change in the instanton-liquid density is due to the shift of the equilibrium pseudoparticle size and is given by the tadpole contribution $\varphi(0)\Delta$, $\Delta = \dfrac{4N_c}{n\bar\rho^4}\lambda^2 c(\lambda)$, which leads to an additional term in the averaged action per instanton:

$$\langle S\rangle = \int dzn\left\{\langle s\rangle - \left\langle \Delta\frac{\rho-\rho_c}{\bar\rho}\right\rangle\right\}.$$

With the aid of the variational maximum principle, we can find explicitly the mean pseudoparticle size, $\bar\rho\Lambda = \exp\left\{-\dfrac{2N_c}{2\nu-1}\right\}$, and derive the following quadratic equation for determining the instanton-liquid density [7]:

$$(n\bar\rho^4)^2 - \frac{\nu}{\beta\xi^2}n\bar\rho^4 = \frac{\Delta}{\beta\xi^2}\frac{\Gamma(\nu+1/2)}{2\sqrt{\nu}\Gamma(\nu)}. \qquad (13)$$

Finally, we can show that the saddle point of the generating functional (8) is determined by the equation

$$\frac{n\bar\rho^4}{\lambda} - 2N_c\int\frac{dk}{\pi^4}\frac{2\lambda\Gamma^2(k;\mu)+\lambda^2\Gamma(k;\mu)\Gamma'(k;\mu)}{(k+i\mu)^2+\lambda^2\Gamma^2(k;\mu)} \qquad (14)$$
$$-(n\bar\rho^4)'\ln\frac{n\bar\rho^4}{\lambda} = 0,$$

which enables one to take into account the change in the instanton-liquid density. Here, a prime denotes differentiation with respect to λ. In order to close the equation, it is also necessary to find the derivative c'. With the aid of (12), we can obtain

$$(1-\lambda^2 A(\lambda))c'(\lambda) = 2\lambda A(\lambda)c(\lambda) + B(\lambda).$$

The functions $A(\lambda)$ and $B(\lambda)$ appearing in this expression are given by

$$A(\lambda) = \alpha(\lambda)\frac{N_c\kappa}{\nu}\int\frac{dk}{\pi^4}$$
$$\times\frac{\gamma_1^2(k;\mu)[(k+i\mu)^2-\lambda^2\Gamma^2(k;\mu)]^2}{[(k+i\mu)^2+\lambda^2\Gamma^2(k;\mu)]^4},$$

$$B(\lambda) = -2\lambda(n\bar\rho^4\kappa)^{1/2}\int\frac{dk}{\pi^4}$$
$$\times\frac{\gamma_1(k)\Gamma^3(k)}{[(k+i\mu)^2+\lambda^2\Gamma^2(k;\mu)]^2},$$

where the factor $\alpha(\lambda)$ has the form

$$\alpha(\lambda) = 1-\lambda^2\frac{N_c}{\beta\xi^2}\frac{\Gamma(\nu+1/2)}{\nu^{1/2}\Gamma(\nu)}\frac{c(\lambda)}{n\bar\rho^4\left(n\bar\rho^4-\dfrac{\nu}{2\beta\xi^2}\right)}.$$

A transition to the case of many flavors, $N_f > 1$, is implemented as follows [7, 11]: the additional contribution to the dynamical mass in expression (10) and the factor Δ in the tadpole contribution are increased by the factor N_f, and the logarithmic term $\ln\dfrac{n\bar\rho^4}{\lambda}$ on the right-hand side of Eq. (14) for the saddle point is replaced by $\ln\left(\left(\dfrac{n\bar\rho^4}{2}\right)^{1/N_f}\dfrac{1}{\lambda}\right)$. It should be emphasized that, for the sake of definiteness, we everywhere set the renormalization factor R [see, for example, (4)] to unity. As a result, the dimensional parameters of the theory are expressed only in terms of the corresponding powers of Λ_{QCD}—for example, $\rho\Lambda$—and are obtained in a self-consistent way upon determining the saddle point. In general, however, the renormalization factor could be considered as a free parameter.

The results obtained by calculating the positive root of Eq. (13),

$$n\bar\rho^4 = \frac{\nu}{2\beta\xi^2} + \left[\left(\frac{\nu}{2\beta\xi^2}\right)^2 + \frac{\Delta}{\beta\xi^2}\frac{\Gamma(\nu+1/2)}{2\sqrt{\nu}\Gamma(\nu)}\right]^{1/2},$$

for the dynamical quark mass $\lambda\Gamma(0,\mu)$ and for the quark condensate $-i\langle\psi^\dagger\psi\rangle$ are displayed in Fig. 1 (solid and dashed curves, respectively) versus the chemical potential μ at $\Lambda = 280$ for the case of $N_c = 3$ and $N_f = 2$. The lower curves were obtained with allowance for the contribution appearing in the tadpole approximation. With allowance for the resulting values, the dynamical quark mass and the chiral condensate do not go beyond the boundaries prescibed by the phenomenology of the QCD vacuum; in principle, better agreement can be reached by fitting the model parameters—for example, Λ_{QCD}.

We can see from Fig. 2 that, in the case where the quarks are in the phase of a nonvanishing chiral condensate, the change in the instanton-liquid density is insignificant; by and large, we can say that,

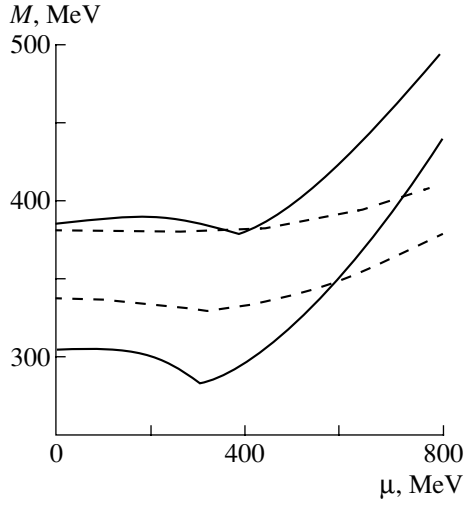

Fig. 1. Dynamical masses (solid curves) and chiral condensates (dashed curves) versus the chemical potential μ at $\Lambda = 280$ for the case of $N_c = 3$ and $N_f = 2$. The lower curves were obtained with allowance for instanton-liquid perturbations.

in this phase, allowance for the quark effect on the instanton liquid leads to a small enhancement of the gluon condensate—that is, an additional attraction appears in the system formed by quarks and an instanton liquid. The results obtained in this study are in agreement with those reported in [12], where the behavior of an instanton liquid is considered within the model of instanton liquid featuring an admixture of (anti)instanton molecules (cocktail model) and where, in the phase of broken chiral symmetry, the instanton-liquid density remains nearly constant, as in the case being considered, up to the phase-transition point.

Figure 3 shows the values of the saddle-point parameter λ at $N_c = 3$ and $N_f = 2$. We recall that, to the one-loop approximation, this parameter is proportional to the free energy of the system. The upper curve was obtained without taking into account the quark effect on the instanton liquid. The results presented in this figure make it possible to predict qualitatively the possible behavior of the critical chemical-potential value μ_c at which there occurs a transition to the color-superconductivity phase. In view of the results reported in [12, 13], one can conjecture that the point μ_c can be noticeably shifted toward greater values since, at subcritical values of μ, the parameter λ for the diquark phase always lies above the corresponding curves for the phase of broken chiral symmetry. This means that the point at which the curve corresponding to the diquark phase intersects the lower curve always lies farther than the point of intersection with the upper curve. As a result, it may turn out that, in the vicinity of the phase transition, the quark-matter density becomes commensurate with (or higher than) a normal nuclear density. However, it is worth noting that, at very large values of the chemical potential, the instanton-liquid model is inapplicable (the region of the transition to the perturbative phase of quark–gluon matter). As the quark-matter density increases, the mean interquark spacing appears to be so small that gluon (Coulomb) fields become commensurate with (or greater than) instanton fields. In this region, it is already illegitimate to consider an (anti)instanton ensemble as a saturating configuration, so that the instanton-liquid model

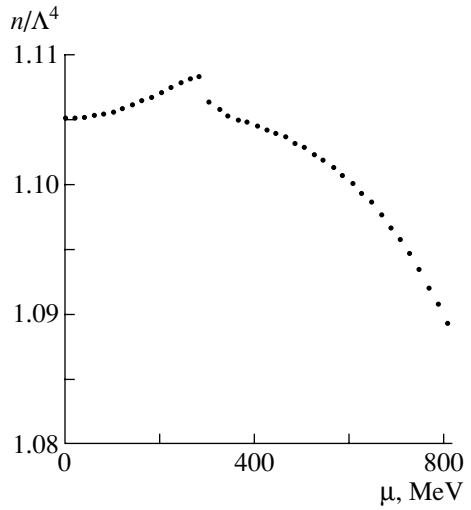

Fig. 2. Instanton-liquid density in the chiral-condensate phase at $N_c = 3$ and $N_f = 2$ as a function of the chemical potential μ.

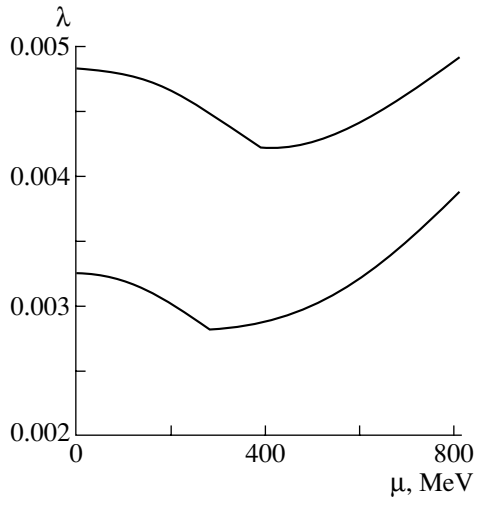

Fig. 3. Saddle-point parameter λ in the phase of broken chiral symmetry at $N_c = 3$ and $N_f = 2$ as a function of μ. The upper curve was obtained without taking into account quark effects on the instanton liquid.

and the treatment of color superconductivity on its basis become invalid. In other words, it may occur that the region of the diquark-condensate phase is very narrow.

ACKNOWLEDGMENTS

This work was supported in part by CERN-INTAS (grant no. 2000-349) and NATO (grant no. 2000-PST.CLG 977482). We thank the Fabergé Foundation for providing excellent conditions for work. S.V. Molodtsov is grateful to Prof. M. Namiki and the HUUJUKAI Fund for financial support.

REFERENCES

1. C. G. Callan, R. Dashen, and D. J. Gross, Phys. Rev. D **17**, 2717 (1978); Phys. Lett. B **66B**, 375 (1977).
2. D. I. Diakonov and V. Yu. Petrov, Nucl. Phys. B **245**, 259 (1984); in *Hadronic Matter under Extreme Conditions*, Ed. by V. Shelest and G. Zinovjev (Naukova Dumka, Kiev, 1986), p. 192; D. I. Diakonov, V. Yu. Petrov, and P. V. Pobylitsa, Phys. Lett. B **226**, 471 (1989).
3. E. V. Shuryak, Nucl. Phys. B **203**, 93, 116, 140 (1982); **328**, 85, 102 (1989); E.-M. Ilgenfritz and M. Müller-Preussker, Nucl. Phys. B **184**, 443 (1981); T. Schäfer and E. V. Shuryak, Rev. Mod. Phys. **70**, 323 (1998).
4. J. W. Negele, hep-lat/9810053.
5. F. Schrempp, hep-ph/0109032.
6. M. Alford, K. Rajagopal, and F. Wilczek, Phys. Lett. B **422**, 247 (1998); R. Rapp, T. Schäfer, E. V. Shuryak, and M. Velkovsky, Phys. Rev. Lett. **81**, 53 (1998).
7. G. M. Zinovjev, S. V. Molodtsov, and A. M. Snigirev, Yad. Fiz. **65**, 961 (2002) [Phys. At. Nucl. **65**, 929 (2002)].
8. A. A. Abrikosov, Jr., Nucl. Phys. B **182**, 441 (1981); A. A. Abrikosov, Jr., Yad. Fiz. **37**, 772 (1983) [Sov. J. Nucl. Phys. **37**, 459 (1983)]; C. A. Carvalho, Nucl. Phys. B **183**, 182 (1981).
9. G. 't Hooft, Phys. Rev. D **14**, 3432 (1976).
10. S. V. Molodtsov, A. M. Snigirev, and G. M. Zinovjev, Phys. Rev. D **60**, 056006 (1999); in *Lattice Fermions and Structure of the Vacuum*, Ed. by V. Mitrjushkin and G. Schierholz (Kluwer Acad. Publ., Dordrecht, 2000), p 307; G. M. Zinovjev, S. V. Molodtsov, and A. M. Snigirev, Yad. Fiz. **63**, 975 (2000) [Phys. At. Nucl. **63**, 903 (2000)].
11. D. I. Diakonov, M. V. Polyakov, and C. Weiss, Nucl. Phys. B **461**, 539 (1996); D. I. Diakonov, hep-ph/9802298.
12. R. Rapp, T. Schäfer, E. V. Shuryak, and M. Velkovsky, Ann. Phys. (N.Y.) **280**, 35 (2000).
13. G. W. Carter and D. I. Diakonov, Phys. Rev. D **60**, 016004 (1999).

Translated by A. Isaakyan

Physics of Atomic Nuclei, Vol. 66, No. 5, 2003, pp. 975–981. Translated from Yadernaya Fizika, Vol. 66, No. 5, 2003, pp. 1007–1014.

ELEMENTARY PARTICLES AND FIELDS
Theory

Angular Correlations in the Decays of Two Unstable Identical Particles with Close Momenta

R. Lednicky, V. V. Lyuboshitz, and V. L. Lyuboshitz

Joint Institute for Nuclear Research, Dubna, Moscow oblast, 141980 Russia

Received January 24, 2002; in final form, July 12, 2002

Abstract—For the decay of two identical particles with close momenta, the angular correlations between the directions of emission of decay products are considered on the basis of the model of independent single-particle sources emitting unstable unpolarized particles of nonzero spin. These correlations reflect spin correlations that are caused by quantum-statistics and final-state-interaction effects. A general theory of angular correlations in the decays of two arbitrarily polarized particles (resonances) is constructed. © *2003 MAIK "Nauka/Interperiodica".*

1. Previously, a theoretical analysis of spin correlations in the system of two spin-1/2 particles was performed in [1–7]. The angular correlations in the parity-nonconserving decays of Λ-hyperon pairs [5–7] (see also [8]), unstable leptons, and t quarks [7] were studied in this connection. It was shown in [7] that investigation of angular correlations in the asymmetric decays of two unstable particles provides a unique possibility for experimentally testing the implications of quantum-mechanical coherence for two-particle systems—in particular, those that are associated with violation of the classic Bell inequalities [9, 10].

The present article is devoted to studying, for the decay of two unpolarized identical particles having close momenta and an arbitrary spin, the angular correlations between the directions of emission of decay products. These angular correlations are due to quantum-statistics effects (symmetrization or antisymmetrization of two-particle wave functions), as well as effects induced by the final-state interaction of unstable particles [11].[1)] In the Appendix, we derive general formulas for angular correlations in the decays of two arbitrary, identical or nonidentical, particles that have arbitrary polarizations (see also [5]).

2. The normalized (to unity) angular distribution of the direction $\mathbf{n}$ of emission of one of the particles originating from the two-particle decay of an unstable spin-j particle, or of the direction of the normal to the plane of three-body particle decay, or of the direction of any vector that characterizes a multiparticle decay has a common structure [13]; that is,

$$dW(\mathbf{n}) = \frac{1}{4\pi}\sum_m\sum_{m'}\sum_{\Lambda}(2j+1)D^{(j)}_{\Lambda m}(\mathbf{n}) \times D^{*(j)}_{\Lambda m'}(\mathbf{n})R_\Lambda\rho_{mm'}d\Omega_{\mathbf{n}}, \quad (1)$$

where $\mathbf{n}$ is a unit vector that is specified in the rest frame of the decaying particle; $d\Omega_{\mathbf{n}}$ is the solid-angle element in the direction of $\mathbf{n}$;

$$D^{(j)}_{\Lambda m}(\mathbf{n}) \equiv D^{(j)}_{\Lambda m}(\phi,\theta,0) = d^{(j)}_{\Lambda m}(\theta)e^{im\phi}$$

are elements of the finite-rotation matrix (generalized spherical Wigner functions [13–15]),[2)] θ and ϕ being, respectively, the polar and the azimuthal angle of the vector $\mathbf{n}$ in a coordinate frame where the z axis is aligned with the spin-quantization axis; $\rho_{mm'}$ are elements of the spin density matrix for an unstable particle (m and m' are the spin projections onto the z axis); and R_Λ are nonnegative parameters (the probabilities that the projections of the decaying-particle spin onto the vector $\mathbf{n}$ take the values Λ), these probabilities being normalized by the condition

$$\sum_{\Lambda=-j}^{j} R_\Lambda = 1. \quad (2)$$

We note that, if $\mathbf{n}$ is a polar vector and if parity is conserved, the equality $R_\Lambda = R_{-\Lambda}$ holds. In this case, the angular distribution for the decays of an unstable spin-1/2 particle will be isotropic for any polarization; an anisotropy (asymmetry) arises only

[1)] In general, one considers the interaction of stable particles. Instability reduces somewhat final-state interaction [12]. A discussion of this issue is beyond the scope of this study.

[2)] In [5, 13, 16], the elements of the matrix that is the inverse of the final-rotation matrix $D^{(j)}$ used in [14, 15] and in the present study were considered as generalized spherical functions.

1063-7788/03/6605-0975$24.00

in weak decays of the type $\Lambda \to p + \pi^-$, which are accompanied by P violation ($R_{1/2} \neq R_{-1/2}$), parity-nonconserving decay playing here the role of an analyzer of the decaying-particle spin [5–7]. But if $\mathbf{n}$ is an axial vector aligned, for example, with the normal to the plane of three-particle decay, an anisotropy may also arise in the parity-conserving decays of spin-1/2 particles. At $j \geq 1$, two-particle and multiparticle decays are, in general, anisotropic, irrespective of the presence of symmetry with respect to space inversion.

3. Let us now consider the system of two unstable particles whose spins are denoted by j_1 and j_2. For the decays of this system, the two-dimensional distribution of the directions of decay-product emission can be represented in the form

$$d^2W(\mathbf{n}_1,\mathbf{n}_2) = \frac{(2j_1+1)(2j_2+1)}{16\pi^2} \tag{3}$$
$$\times \sum_{m_1}\sum_{m_1'}\sum_{m_2}\sum_{m_2'}\sum_{\Lambda_1}\sum_{\Lambda_2} D^{(j_1)}_{\Lambda_1 m_1}(\mathbf{n}_1) D^{*(j_1)}_{\Lambda_1 m_1'}(\mathbf{n}_1)$$
$$\times D^{(j_2)}_{\Lambda_2 m_2}(\mathbf{n}_2) D^{*(j_2)}_{\Lambda_2 m_2'}(\mathbf{n}_2) R_{\Lambda_1}\widetilde{R}_{\Lambda_2}\rho^{(1,2)}_{m_1 m_1';m_2 m_2'}$$
$$\times d\Omega_{\mathbf{n}_1} d\Omega_{\mathbf{n}_2},$$

where $d\Omega_{\mathbf{n}_1}$ and $d\Omega_{\mathbf{n}_2}$ are the solid-angle elements corresponding to the directions $\mathbf{n}_1$ and $\mathbf{n}_2$ that are specified in the rest frames of, respectively, the first and the second decaying particle; $\rho^{(1,2)}_{m_1 m_1';m_2 m_2'}$ are elements of the spin density matrix for the system of two unstable particles; and R_{Λ_1} and $\tilde{R}_{\Lambda_2}$ are parameters that characterize the decay of the first and the second particle, respectively.

The properties of the spin density matrix for two identical particles with close momenta were discussed in [1, 2]. Within the model of independent single-particle sources, which is generally applied to describing narrow pair momentum correlations [17], it can be shown that, in the case where the sources emit particles of spin j that have the spin density matrix $\hat{\rho}$ and where there is no Coulomb interaction, the elements $\hat{\rho}^{(1,2)}$ of the spin density matrix for two identical particles, which satisfies the condition $\mathrm{tr}(\hat{\rho}^{(1,2)}) = 1$, have the form [1]

$$\rho^{(1,2)}_{m_1 m_1';m_2 m_2'} \tag{4}$$
$$= \frac{1}{P(p,q)}\left\{\rho_{m_1 m_1'}\rho_{m_2 m_2'}[1 + B_{\mathrm{int}}(p,q)]\right.$$
$$\left. + (-1)^{2j}\rho_{m_1 m_2'}\rho_{m_2 m_1'}[|F(p,q)|^2 + B_{\mathrm{int}}(p,q)]\right\},$$

where p and q are, respectively, the half-sum and the difference of the 4-momenta of the identical particles in question, while

$$P(p,q) = 1 + B_{\mathrm{int}}(p,q) \tag{5}$$
$$+ (-1)^{2j}\mathrm{tr}(\hat{\rho}^2)[|F(p,q)|^2 + B_{\mathrm{int}}(p,q)]$$

is the momentum correlation function [1, 2]. In expression (5), the quantity $|F(p,q)|^2$ describes the effect of Bose statistics (at integral values of j) or Fermi statistics (at half-integer values of j) and $B_{\mathrm{int}}(p,q)$ is the contribution of the s-wave strong final-state interaction [11, 18].[3)] Each of the functions F and B_{int} depends on the spatial and time parameters of the region of multiparticle generation and tends to zero at high values of the relative momentum q; the function $F(p,q)$ is the Fourier component of the distribution of the 4-coordinates of the sources [17, 18]:

$$F(p,q) = \int W(p,x)e^{iqx}d^4x;$$
$$F(p,0) = 1.$$

For the emission of unpolarized particles, in which case we have

$$\rho_{mm'} = \frac{\delta_{mm'}}{2j+1},$$

formulas (4) and (5) yield

$$\rho^{(1,2)}_{m_1 m_1';m_2 m_2'} = \frac{1}{(2j+1)^2}\frac{1}{P_0(p,q)} \tag{6}$$
$$\times \left\{\delta_{m_1 m_1'}\delta_{m_2 m_2'}[1 + B_{\mathrm{int}}(p,q)]\right.$$
$$\left. + (-1)^{2j}\delta_{m_1 m_2'}\delta_{m_2 m_1'}[|F(p,q)|^2 + B_{\mathrm{int}}(p,q)]\right\},$$

$$P_0(p,q) = 1 + B_{\mathrm{int}}(p,q) \tag{7}$$
$$+ \frac{(-1)^{2j}}{2j+1}[|F(p,q)|^2 + B_{\mathrm{int}}(p,q)],$$

where $\delta_{mm'}$ is a Kronecker delta symbol. It should be emphasized that formulas (4)–(7) involve exchange terms (with a plus sign for identical bosons and with a minus sign for identical fermions) violating statistical independence.

4. Upon substituting expression (6) into formula (3) at $j_1 = j_2 = j$ and considering that, in view of the unitarity of the finite-rotation matrix, the equalities

$$\sum_{m_1} D^{(j)}_{\Lambda_1 m_1}(\mathbf{n}_1) D^{*(j)}_{\Lambda_1 m_1}(\mathbf{n}_1) = 1,$$

[3)] The total spin S and the total orbital angular momentum L of the system of two identical particles in their c.m. frame are related by the equation $(-1)^{L+S} = 1$ (see, for example, [14]). In view of this, the s-wave interaction of two identical particles (both bosons and fermions) manifests itself only in states having even values of the spin S. Formula (4) was written under the assumption that the interaction potential is independent of the spin quantum numbers, so that, for $j \geq 1$, the function $B_{\mathrm{int}}(p,q)$ is the same for all states having even values of the spin S (at $j = 1/2$, the total spin takes only one even value: $S = 0$).

$$\sum_{m_2} D^{(j)}_{\Lambda_2 m_2}(\mathbf{n}_2) D^{*(j)}_{\Lambda_2 m_2}(\mathbf{n}_2) = 1$$

hold [14, 15], we find that, for the decay of two unpolarized identical unstable particles with correlated spins, the two-dimensional distribution of the directions of decay-product emission (axes of the spin analyzer) can be represented as

$$\frac{d^2W(\mathbf{n}_1,\mathbf{n}_2)}{d\Omega_{\mathbf{n}_1} d\Omega_{\mathbf{n}_2}} = \frac{1}{16\pi^2 P_0(p,q)} \times [1 + B_{\text{int}}(p,q) + (-1)^{2j} A(|F(p,q)|^2 + B_{\text{int}}(p,q))], \quad (8)$$

where $P_0(p,q)$ is defined according to (7) and

$$A = \sum_{\Lambda_1}\sum_{\Lambda_2} R_{\Lambda_1}\widetilde{R}_{\Lambda_2} \left| \sum_m D^{(j)}_{\Lambda_2 m}(\mathbf{n}_2) D^{*(j)}_{\Lambda_1 m}(\mathbf{n}_1) \right|^2. \quad (9)$$

Further, we can represent the operator $\hat{D}^{(j)}(\mathbf{n}_2)$ as the product of the successive-rotation operators that first transform the z axis into the vector $\mathbf{n}_1$ and then transform $\mathbf{n}_1$ into the vector $\mathbf{n}_2$ [14, 15]; that is,

$$D^{(j)}_{\Lambda_2 m}(\mathbf{n}_2) = \sum_\mu d^{(j)}_{\Lambda_2\mu}(\beta) e^{i\mu\psi} D^{(j)}_{\mu m}(\mathbf{n}_1), \quad (10)$$

where β is the angle between the vectors $\mathbf{n}_1$ and $\mathbf{n}_2$[4)] and ψ is the azimuthal angle of the rotation of the vector $\mathbf{n}_2$ about the vector $\mathbf{n}_1$. With allowance for the unitarity condition for the operators of finite rotations,

$$\sum_m D^{(j)}_{\mu m}(\mathbf{n}) D^{*(j)}_{\Lambda_1 m}(\mathbf{n}) = \delta_{\mu\Lambda_1},$$

we obtain

$$\sum_m D^{(j)}_{\Lambda_2 m}(\mathbf{n}_2) D^{*(j)}_{\Lambda_1 m}(\mathbf{n}_1) = d^{(j)}_{\Lambda_2\Lambda_1}(\beta) e^{i\Lambda_1\psi}.$$

As a result, we arrive at

$$A \equiv A(\beta) = \sum_{\Lambda_1}\sum_{\Lambda_2} R_{\Lambda_1}\widetilde{R}_{\Lambda_2} \left(d^{(j)}_{\Lambda_1\Lambda_2}(\beta) \right)^2. \quad (11)$$

We note that, without loss of generality, we can consider the solid-angle element $d\Omega_{\mathbf{n}_1}$ in the coordinate frame where the spin density matrix in question is defined and the solid-angle element $d\Omega_{\mathbf{n}_2}$ in the coordinate frame where the z axis is parallel to the vector $\mathbf{n}_1$. We then have

$$d\Omega_{\mathbf{n}_2} = \sin\beta d\beta d\psi. \quad (12)$$

Upon integration of the two-dimensional distribution (8) over the solid angle $\Omega_{\mathbf{n}_1}$ and with respect to the azimuthal angle ψ, we obtain the following expression for the angular correlation between the directions $\mathbf{n}_1$ and $\mathbf{n}_2$:

$$dN(\beta) = \frac{1}{2} \frac{1 + B_{\text{int}}(p,q) + (-1)^{2j} A(\beta)[|F(p,q)|^2 + B_{\text{int}}(p,q)]}{1 + B_{\text{int}}(p,q) + ((-1)^{2j}/(2j+1))\,[|F(p,q)|^2 + B_{\text{int}}(p,q)]} d\cos\beta. \quad (13)$$

Formula (13) can be recast into the form

$$dN(\beta) = \frac{1}{2}\left[1 + 2K\left(A(\beta) - \frac{1}{2j+1}\right)\right]\sin\beta d\beta, \quad (14)$$

where

$$K = (-1)^{2j} \frac{|F(p,q)|^2 + B_{\text{int}}(p,q)}{2P_0(p,q)}. \quad (15)$$

Within the model of independent single-particle sources emitting unpolarized particles, it can be shown that, because of the effects of symmetrization or antisymmetrization of the two-particle wave functions and of the s-wave final-state interaction, the total relative weights (fractions) of states in which two identical particles have even total spins (even orbital angular momenta) and odd total spins (odd orbital angular momenta) become

$$\rho_{\text{even}} = \frac{1}{2}\left(1 + (-1)^{2j}\frac{1}{2j+1}\right) \times \frac{1 + |F(p,q)|^2 + 2B_{\text{int}}(p,q)}{P_0(p,q)}, \quad (16)$$

$$\rho_{\text{odd}} = \frac{1}{2}\left(1 - (-1)^{2j}\frac{1}{2j+1}\right)\frac{1 - |F(p,q)|^2}{P_0(p,q)}. \quad (17)$$

In accordance with relation (7) for $P_0(p,q)$, we additionally have $\rho_{\text{even}} + \rho_{\text{odd}} = 1$. As a result, we find that, for integral values of j,

$$K = \frac{2j+1}{4}\left(\frac{\rho_{\text{even}}}{j+1} - \frac{\rho_{\text{odd}}}{j}\right) \quad (18)$$

[4)] Formally, the angle β is determined by the formula $\cos\beta = \mathbf{n}_1 \cdot \mathbf{n}_2$. Here, it is implied that the systems of spatial coordinate axes where the vectors $\mathbf{n}_1$ and $\mathbf{n}_2$ are specified are made to be coincident with each other. This is achieved in the following way. In the c.m. frame of the pair of unstable particles, one chooses the directions of the coordinate axes. Further, it is necessary go over to the rest frame of the first and second particles by using the corresponding Lorentz transformations along the direction of the relative momentum of the particles under consideration. Thus, the unit vectors $\mathbf{n}_1$ and $\mathbf{n}_2$ and the elements of the spin density matrix for two-particle decay are determined with respect to a unified system of spatial coordinate axes. In this system, we can construct the scalar product of the three-dimensional vectors $\mathbf{n}_1$ and $\mathbf{n}_2$, which specifies the angle between these vectors.

and that, for half-integer values of j,

$$K = -\frac{2j+1}{4}\left(\frac{\rho_{\text{even}}}{j} - \frac{\rho_{\text{odd}}}{j+1}\right). \qquad (19)$$

As the difference q of the momenta tends to zero, the states in which two identical particles have nonvanishing total orbital angular momenta L in the c.m. frame of the pair die out, so that only states where $L = 0$ and where the total spin S is even survive [14] (see also Footnote 3). In this limiting case, we have $K = (2j+1)/4(j+1)$ at integral values of the spin j and $K = -(2j+1)/4j$ at half-integer values of the spin j.

Considering that d functions satisfy the normalization condition [14]

$$\int_0^\pi \left(d^{(j)}_{\Lambda_1\Lambda_2}(\beta)\right)^2 \sin\beta d\beta = \frac{2}{2j+1}$$

and that the parameters R_{Λ_1} and $\tilde{R}_{\Lambda_2}$ are normalized to unity [see Eq. (2)], we can easily see that the function $A(\beta)$ satisfies the relation

$$\int_0^\pi A(\beta)\sin\beta d\beta = \frac{2}{2j+1}. \qquad (20)$$

By virtue of (20), the angular correlation specified by Eqs. (13) and (14) is normalized to unity.

5. It should be emphasized that the present consideration applies both to the same and to different modes of decay of identical unstable particles. By $\mathbf{n}_1$ and $\mathbf{n}_2$, we generally mean the directions of the axes of analyzers that select the projections of unstable-particle (resonance) spins according to decay modes. Below, we consider some pairs of decays.

(a) In the decays $\omega \to \pi^0\gamma$ and $\omega \to \pi^+\pi^-\pi^0$, the direction of the photon (or π^0-meson) momentum in the rest frame of the ω meson plays the role of the vector $\mathbf{n}_1$, while the direction of the normal to the plane of ω-meson decay into three π mesons plays the role of the vector $\mathbf{n}_2$. In this case, we have $j = 1$ and the nonvanishing parameters R_{Λ_1} and $\widetilde{R}_{\Lambda_2}$ take the values [13]

$$R_{+1} = R_{-1} = \frac{1}{2}; \quad \widetilde{R}_0 = 1.$$

According to (11), we then obtain

$$A(\beta) = \frac{1}{2}\left[\left(d^{(1)}_{10}(\beta)\right)^2 + \left(d^{(1)}_{-10}(\beta)\right)^2\right] = \frac{\sin^2\beta}{2}. \qquad (21)$$

(b) For the pair of the decays $\omega \to \pi^0\gamma$ and $\omega \to \pi^0\gamma$, as well as for $V \to e^+e^-$ and $V \to \mu^+\mu^-$ (where $V = \rho^0, \omega, \phi,\ J/\psi,\ \Upsilon$; it is assumed that $m^2_{e,\mu} \ll m^2_V$), we have $j = 1$,

$$R_{+1} = R_{-1} = \widetilde{R}_{+1} = \widetilde{R}_{-1} = \frac{1}{2}; \qquad (22)$$

$$A(\beta) = \frac{1}{4}\left[\left(d^{(1)}_{11}(\beta)\right)^2 + \left(d^{(1)}_{1-1}(\beta)\right)^2 + \left(d^{(1)}_{-11}(\beta)\right)^2 + \left(d^{(1)}_{-1-1}(\beta)\right)^2\right] = \frac{1}{4}(1+\cos^2\beta).$$

(c) For $\phi \to K^+K^-$ and $\phi \to K^0_SK^0_L$, as well as for $\omega \to \pi^+\pi^-\pi^0$ and $\omega \to \pi^+\pi^-\pi^0$, the corresponding values are the following: $j = 1$,

$$R_0 = \widetilde{R}_0 = 1; \qquad (23)$$

$$A(\beta) = \left(d^{(1)}_{00}(\beta)\right)^2 = \cos^2\beta.$$

(d) Finally, we consider the decay processes $f_2(1270) \to \pi^+\pi^-$ and $f_2(1270) \to K^+K^-$, in which case $j = 2$; here, the results are

$$R_0 = \widetilde{R}_0 = 1; \qquad (24)$$

$$A(\beta) = \left(d^{(2)}_{00}(\beta)\right)^2 = \frac{1}{4}(3\cos^2\beta - 1)^2.$$

Let us now examine the angular correlation in the parity-nonconserving decays of two unpolarized Λ particles with close momenta through the channel $\Lambda \to p + \pi^-$ [5–8]. In this case, we have $j = 1/2$,

$$R_{1/2} = \widetilde{R}_{1/2} = \frac{1+\alpha}{2},$$
$$R_{-1/2} = \widetilde{R}_{-1/2} = \frac{1-\alpha}{2},$$

where $\alpha = 0.642$ is the coefficient of P-odd asymmetry in the angular distribution of protons originating from the decay of the polarized Λ particle.[5)] We then have

$$A(\beta) = \frac{(1+\alpha)^2}{4}\left(d^{(1/2)}_{1/2\,1/2}(\beta)\right)^2 + \frac{(1-\alpha)^2}{4}\left(d^{(1/2)}_{-1/2\,-1/2}(\beta)\right)^2 + \frac{1-\alpha^2}{4} \times \left[\left(d^{(1/2)}_{1/2\,-1/2}(\beta)\right)^2 + \left(d^{(1/2)}_{-1/2\,1/2}(\beta)\right)^2\right] = \frac{1+\alpha^2}{2}\cos^2\frac{\beta}{2} + \frac{1-\alpha^2}{2}\sin^2\frac{\beta}{2} \qquad (25)$$

[5)] This angular distribution has the form $dW(\mathbf{n}) = (1 + \alpha\mathbf{P}\cdot\mathbf{n})d\Omega_{\mathbf{n}}/4\pi$, where $\mathbf{P}$ is the polarization vector and $\mathbf{n}$ is the unit vector directed along the proton momentum in the rest frame of the Λ particle.

$$= \frac{1}{2}(1 + \alpha^2 \cos\beta).$$

Upon substituting expression (25) into formula (14) at $j = 1/2$, we obtain (compare with the result quoted in [6])

$$dN(\beta) = \frac{1}{2}(1 + K\alpha^2 \cos\beta)\sin\beta d\beta, \qquad (26)$$

where

$$K = -\frac{|F(p,q)|^2 + B_{\rm int}(p,q)}{2 - |F(p,q)|^2 + B_{\rm int}(p,q)}. \qquad (27)$$

It should be noted that, if the channels of decays of two identical particles or resonances are identical (or if they are different, but there are identical particles among the final-state particles), additional exchange corrections to the relations for the angular correlations arise owing to symmetrization or antisymmetrization with respect to the momenta of identical final-state particles originating from the two decays. These corrections may be significant in the case of rather broad resonances. It should be emphasized that, if there are no identical particles among the decay products in the two channels, such corrections vanish at any resonance width.

An analysis reveals that the relative contribution of the exchange corrections to formulas (11) and (13)–(15) is maximal for identical two-particle decay channels and that, at $\beta = 0$ and $q = 0$, it is 100%, irrespective of the resonance width. With increasing β and q, this contribution decreases. But if each of the parameters $\tilde{p}^2/m\Gamma$ and $\tilde{q}\tilde{p}/m\Gamma$ is less than or on the order of unity ($\tilde{p}$ is the decay momentum; $\tilde{q}$ is the absolute value of the difference of the momenta of the two decaying resonances in the rest frame of one of them; and m and Γ are the resonance mass and the resonance width, respectively), formulas (11) and (13)–(15) are inapplicable at any values of the angle β. In particular, this directly applies to the decay pair $\rho^0 \to \pi^+\pi^-$ and $\rho^0 \to \pi^+\pi$ ($\tilde{p}^2/m\Gamma \approx 1.1$) or $f_2 \to \pi^+\pi^-$ and $f_2 \to \pi^+\pi^-$ ($\tilde{p}^2/m\Gamma \approx 1.6$).

In the case of narrow resonances ($\tilde{p}^2/m\Gamma \gg 1$), the additional exchange corrections are small at the angles $\beta \gg \sqrt{m\Gamma}/\tilde{p}$; specifically, they are on the order of

$$\epsilon = \min\left[\left(\frac{\tilde{p}^2\beta^2}{m\Gamma}\right)^{-1}, \left(\frac{\tilde{q}\tilde{p}}{m\Gamma}\right)^{-1}\right].$$

For the above case of the decays of two ω mesons through the channel $\omega \to \pi^0\gamma$, the parameter $\tilde{p}^2/m\Gamma$ is approximately equal to 21.8; therefore, the disregard of the additional exchange corrections can be considered to be justified in the angular region $\beta > 0.2$ rad. In the case of the decays of two J/ψ resonances through the channel $J/\psi \to e^+e^-$ (or $J/\psi \to \mu^+\mu^-$), the parameter $\tilde{p}^2/m\Gamma$ is approximately equal to 0.9×10^4, whence it follows that, beyond the narrow angular region $\beta \leq 10^{-2}$ rad, the angular correlation has the same character as that for the decays of two J/ψ resonances through different leptonic channels [see formula (22) for the function $A(\beta)$].

As to the decays of two Λ particles through the channel $\Lambda \to p\pi^-$ ($\tilde{p}^2/m\Gamma \approx 3.9 \times 10^{12}$), the question of additional symmetrization with respect to the momenta of two π^- mesons (or antisymmetrization with respect to the momenta of two protons) does not arise in principle, since the experimentally detected vertices of the decay of long-lived particles are separated by a macroscopic distance.

We have considered the simplest angular correlations induced by the identity of decaying unpolarized particles. These correlations are described by formulas (13)–(15), where the function $A(\beta)$ is defined according to relation (11). A general theory of angular correlations in the decays of two arbitrary resonances having the spins j_1 and j_2 and arbitrary polarizations can be constructed in a similar way (see Appendix).

ACKNOWLEDGMENTS

This work was supported in part by the Russian Foundation for Basic Research (V.L. Lyuboshitz and V.V. Lyuboshitz), project no. 01-02-16230, and by GA CR (R. Lednicky), grant no. 202/01/0779.

APPENDIX

From the expansion of the product of general spherical functions {see formula (110.1) in [14]}, the relation

$$D^{*(j)}_{\Lambda m'}(\mathbf{n}) = (-1)^{\Lambda - m'} D^{(j)}_{-\Lambda - m'}(\mathbf{n}),$$

and the properties of Clebsch–Gordan coefficients, it follows that

$$D^{(j)}_{\Lambda m}(\mathbf{n}) D^{*(j)}_{\Lambda m'}(\mathbf{n}) \qquad (A.1)$$
$$= (-1)^{\Lambda - m'} \sum_L C^{L0}_{j\Lambda j-\Lambda} C^{LM}_{jmj-m'} D^{(L)}_{0M}(\mathbf{n})$$
$$= \sum_L \frac{2L+1}{2j+1} C^{j\Lambda}_{j\Lambda L0} C^{jm}_{jm'LM} D^{(L)}_{0M}(\mathbf{n}),$$

where

$$M = m - m'.$$

With allowance for (A.1), the general formula (3), which describes, for the decay of two unstable particles, the two-dimensional distribution of the directions of decay-product emission, can be recast into the form [5, 16]

$$d^2W(\mathbf{n_1}, \mathbf{n_2}) = \frac{1}{16\pi^2} \qquad (A.2)$$

$$\times \sum_{L_1}\sum_{L_2}\sum_{M_1}\sum_{M_2}(2L_1+1)(2L_2+1)t_{L_1M_1;L_2M_2}$$
$$\times T^{(1)}_{L_10}T^{(2)}_{L_20}D^{(L_1)}_{0M_1}(\mathbf{n}_1)D^{(L_2)}_{0M_2}(\mathbf{n}_2)d\Omega_{\mathbf{n}_1}d\Omega_{\mathbf{n}_2},$$

where $t_{L_1M_1;L_2M_2}$ are the multipole parameters for the production of two unstable particles,

$$t_{L_1M_1;L_2M_2} = (-1)^{M_1+M_2}t_{L_1-M_1;L_2-M_2} \qquad (A.3)$$
$$= \sum_{m_1}\sum_{m_1'}\sum_{m_2}\sum_{m_2'}C^{j_1m_1}_{j_1m_1'L_1M_1}C^{j_2m_2}_{j_2m_2'L_2M_2}\rho^{(1,2)}_{m_1m_1';m_2m_2'},$$

while $T^{(1)}_{L_10}$ and $T^{(2)}_{L_20}$ are the multipole parameters for their decay [16],

$$T^{(1)}_{L_10} = \sum_{\Lambda_1}R_{\Lambda_1}C^{j_1\Lambda_1}_{j_1\Lambda_1L_10}, \qquad (A.4)$$
$$T^{(2)}_{L_20} = \sum_{\Lambda_2}\widetilde{R}_{\Lambda_2}C^{j_2\Lambda_2}_{j_2\Lambda_2L_20}.$$

We now integrate the distribution in (A.2) with respect to the angles, fixing only the angle β between the vectors $\mathbf{n}_1$ and $\mathbf{n}_2$. According to (12), we can write

$$d\Omega_{\mathbf{n}_1}d\Omega_{\mathbf{n}_2} = d\Omega_{\mathbf{n}_1}\sin\beta d\beta d\psi.$$

In accordance with (10), we have

$$D^{(L_2)}_{0M_2}(\mathbf{n}_2) = \sum_{\mu}d^{(L_2)}_{0\mu}(\beta)e^{i\mu\psi}D^{(L_2)}_{\mu M_2}(\mathbf{n}_1) \qquad (A.5)$$
$$= \sum_{\mu}d^{(L_2)}_{0\mu}(\beta)e^{i\mu\psi}(-1)^{\mu-M_2}D^{*(L_2)}_{-\mu-M_2}(\mathbf{n}_1).$$

The orthogonality relation for D functions yields

$$\int D^{(L_1)}_{0M_1}(\mathbf{n}_1)D^{*(L_2)}_{-\mu-M_2}(\mathbf{n}_1)d\Omega_{\mathbf{n}_1}$$
$$= \frac{4\pi}{2L_2+1}\delta_{L_1L_2}\delta_{\mu0}\delta_{M_1-M_2}.$$

Thus, we have

$$\int D^{(L_1)}_{0M_1}(\mathbf{n}_1)D^{(L_2)}_{0M_2}(\mathbf{n}_2)d\Omega_{\mathbf{n}_1}d\psi \qquad (A.6)$$
$$= \frac{8\pi^2}{2L_2+1}\delta_{L_1L_2}\delta_{M_1-M_2}(-1)^{-M_2}d^{(L_2)}_{00}(\beta).$$

By taking into account relation (A.6), we find that the angular correlations between the spin-analyzer directions characterizing the decays of two unstable particles (resonances) can be represented as

$$dN(\beta) = \frac{1}{2}\sum_{L}(2L+1)T^{(1)}_{L0} \qquad (A.7)$$
$$\times T^{(2)}_{L0}K_LP_{\mathrm{L}}(\cos\beta)\sin\beta d\beta,$$

where

$$K_L = \sum_{M}(-1)^Mt_{LM;L-M} \qquad (A.8)$$

and $P_{\mathrm{L}}(\cos\beta) = d^{(L)}_{00}(\beta)$ is a conventional Legendre polynomial.

It should be emphasized that the coefficients K_L are scalar quantities (that is, they are invariant under rotations of the coordinate frame in three-dimensional space). In view of the unitarity of the finite-rotation matrix, we do indeed have

$$K'_L = \sum_{M'}(-1)^{M'}t_{LM';L-M'}$$
$$= \sum_{M'}\sum_{M_1}\sum_{M_2}(-1)^{M'}D^{(L)}_{M'M_1}D^{(L)}_{-M'M_2}t_{LM_1;LM_2}$$
$$= \sum_{M_1}\sum_{M_2}\sum_{M'}(-1)^{M_2}D^{(L)}_{M'M_1}D^{*(L)}_{M'-M_2}t_{LM_1;LM_2}$$
$$= \sum_{M_1}\sum_{M_2}(-1)^{M_2}\delta_{M_1-M_2}t_{LM_1;LM_2} = K_L.$$

We can see that the coefficients K_L are linear combinations that are formed by the elements of the two-particle spin density matrix and which are invariant under the transformations of the rotation group. The same applies to the weights ρ_S of two-particle states that are pure in the total spin S. By definition, we do indeed have

$$\rho_S = \sum_m\rho_{SS;mm}, \quad \sum_S\rho_S = 1, \qquad (A.9)$$

where

$$\rho_{SS';mm'} = \sum_{m_1}\sum_{m_1'}\sum_{m_2}\sum_{m_2'}C^{Sm}_{j_1m_1j_2m_2} \qquad (A.10)$$
$$\times C^{S'm'}_{j_1m_1'j_2m_2'}\rho^{(1,2)}_{m_1m_1';m_2m_2'}$$

are elements of the two-particle density matrix in the representation of pure states in the total spin S and its projection m. It is obvious that the trace of the submatrix $\hat{\rho}^{(S)}$ corresponding to the value $S' = S$ is invariant under unitary transformations of the group of rotations; therefore, the weights ρ_S are scalar quantities. The scalar quantities K_L and ρ_S must obviously be related by a linear equation. By using the algebra of $3j$ and $6j$ coefficients [14], one can show that

$$K_L = \sum_S a_{SL}\rho_S,$$

where the coefficients a_{SL} are proportional to $6j$ coefficients (Racah coefficients):

$$a_{SL} = \sqrt{(2j_1+1)(2j_2+1)}(-1)^{S-j_1-j_2} \qquad (A.11)$$
$$\times W(j_1j_2j_1j_2;SL).$$

In particular, we have $K_0 = 1$ and

$$K_1 = \sum_S\frac{S(S+1)-j_1(j_1+1)-j_2(j_2+1)}{2\sqrt{j_1(j_1+1)j_2(j_2+1)}}\rho_S. \qquad (A.12)$$

For two spin-1/2 particles, the corresponding result is

$$K_1 = -\rho_0 + \frac{\rho_1}{3},$$

while, for $L \geq 2$, the coefficients K_L are equal to zero.

For the parity-nonconserving decays of two Λ hyperons through the channel $\Lambda \to p + \pi^-$, we have

$$T_{10}^{(1)} = T_{10}^{(2)} = \frac{\alpha}{\sqrt{3}},$$

where $\alpha = R_{+1/2} - R_{-1/2}$ is the coefficient of P-odd asymmetry in the angular distribution of protons. In the case being considered, formula (A.7) leads to the result [compare with formulas (14) and (26)]

$$dN(\beta) = \frac{1}{2}\left[1 + \frac{\alpha^2}{3}(\rho_t - 3\rho_s)\cos\beta\right]\sin\beta d\beta, \tag{A.13}$$

which was previously obtained in [5–8]. Here, $\rho_t \equiv \rho_1$ is the relative weight of the triplet states, while $\rho_s \equiv \rho_0$ is the relative weight of the singlet state.

One can test that, at $j_1 = j_2 = j$, formulas (8) and (13) for unpolarized identical particles follow from the general formulas (A.2) and (A.7) upon the substitution of the density matrix (6) into expression (A.3) for the multipole parameters of the production process. Here, it is necessary to consider that the function $A(\beta)$ defined according to (11) is related to the multipole parameters for the decay processes by the equation

$$A(\beta) = \sum_L \frac{2L+1}{2j+1} T_{L0}^{(1)} T_{L0}^{(2)} P_{\mathrm{L}}(\cos\beta).$$

For the vector-meson and f_2-meson decays considered above, the following multipole parameters (apart from $T_{00} = 1$) take nonzero values:

$$T_{20}(\omega \to \pi^0\gamma, V \to e^+e^-, V \to \mu^+\mu^-) = \sqrt{1/10},$$

$$T_{20}(\omega \to 3\pi, \phi \to K\bar{K}) = -\sqrt{2/5},$$

$$T_{20}(f_2 \to 2\pi, f_2 \to K\bar{K}) = -\sqrt{2/7},$$

$$T_{40}(f_2 \to 2\pi, f_2 \to K\bar{K}) = \sqrt{2/7}.$$

REFERENCES

1. V. L. Lyuboshitz and M. I. Podgoretsky, Yad. Fiz. **59**, 476 (1996) [Phys. At. Nucl. **59**, 449 (1996)].
2. V. L. Lyuboshitz and M. I. Podgoretsky, Yad. Fiz. **60**, 45 (1997) [Phys. At. Nucl. **60**, 39 (1997)].
3. V. L. Lyuboshitz, Preprint No. E2-98-274, JINR (Dubna, 1998); in *Proceedings of XIV Int. Seminar on High Energy Physics Problems "Relativistic Nuclear Physics and Quantum Chromodynamics,"* Ed. by A. M. Baldin and V. V. Burov (Dubna, 2000), p. 143.
4. V. V. Lyuboshitz and V. L. Lyuboshitz, Yad. Fiz. **63**, 837 (2000) [Phys. At. Nucl. **63**, 767 (2000)].
5. R. Lednicky, Preprint No. 99-10, MPI-PhE (Munich, 1999).
6. V. L. Lyuboshits, *Proceedings of XXXIV Winter School at St.-Petersburg Nucl. Phys. Inst. "Physics of Atomic Nuclei and Elementary Particles", St.-Petersburg, 2000*, p. 402.
7. R. Lednicky and V. L. Lyuboshitz, Phys. Lett. B **508**, 146 (2001).
8. G. Alexander and H. J. Lipkin, Phys. Lett. B **352**, 162 (1995).
9. J. S. Bell, Physics **1**, 195 (1964).
10. J. S. Bell, in *Proceedings of Fermi International School, Course II "Foundations of Quantum Mechanics"* (Academic, New York, 1971), p. 171.
11. R. Lednicky and V. L. Lyuboshits, Yad. Fiz. **35**, 1316 (1982) [Sov. J. Nucl. Phys. **35**, 770 (1982)].
12. V. S. Fadin and V. A. Khoze, Yad. Fiz. **48**, 487 (1988) [Sov. J. Nucl. Phys. **48**, 309 (1988)].
13. S. M. Berman and M. Jacob, Phys. Rev. **139**, 1023 (1965).
14. L. D. Landau and E. M. Lifshitz, *Course of Theoretical Physics*, Vol. 3: *Quantum Mechanics: Non-Relativistic Theory* (Nauka, Moscow, 1989, 4th ed.; Pergamon, New York, 1977, 3rd ed.).
15. V. B. Berestetskiĭ, E. M. Lifshits, and L. P. Pitaevskiĭ, *Quantum Electrodynamics* (Nauka, Moscow, 1989; translation of 2nd ed. Pergamon Press, Oxford, 1982).
16. R. Lednicky, Yad. Fiz. **43**, 1275 (1986) [Sov. J. Nucl. Phys. **43**, 817 (1986)].
17. M. I. Podgoretskiĭ, Fiz. Élem. Chastits At. Yadra **20**, 628 (1989) [Sov. J. Part. Nucl. **20**, 266 (1989)].
18. V. L. Lyuboshits, Yad. Fiz. **48**, 1501 (1988) [Sov. J. Nucl. Phys. **48**, 956 (1988)].

Translated by A. Isaakyan

Physics of Atomic Nuclei, Vol. 66, No. 5, 2003, pp. 982–996. From Yadernaya Fizika, Vol. 66, No. 5, 2003, pp. 1015–1029.

ELEMENTARY PARTICLES AND FIELDS
Theory

Toward Thermodynamic Consistency of Quasiparticle Picture*

T. S. Biró , A. A. Shanenko[1)], and V. D. Toneev

Research Institute for Particle and Nuclear Physics, Hungarian Academy of Sciences, Budapest, Hungary

Received May 15, 2002

Abstract—The purpose of the present article is to call attention to some realistic quasiparticle-based description of quark/gluon matter and its consistent implementation in thermodynamics. A simple and transparent representation of the thermodynamic consistency conditions is given. This representation allows one to review critically and systemize available phenomenological approaches to the deconfinement problem with respect to their thermodynamic consistency. Particular attention is paid to the development of a method for treating the string screening in the dense matter of unbound color charges. The proposed method yields an integrable effective pair potential that can be incorporated into the mean-field picture. The results of its application are in reasonable agreement with lattice data on the QCD thermodynamics.

1. INTRODUCTION

With the advent of the RHIC and LHC, there is a growing need for a deeper understanding of various properties of QCD matter at high temperature and finite density. At the moment, we are still far from a satisfactory level in this respect, even for equilibrium properties of quark–gluon plasma. Indeed, although such a system can in principle be approximated as a gas of quarks and gluons, a fully perturbative calculation with these degrees of freedom does in practice not work well at any reasonable temperature since the perturbative series are badly converged due to infrared-sensitive contributions. On the other hand, the QCD lattice calculation, the only systematic fully nonperturbative method available, is restricted in the presence of light dynamical quarks and even more so in the presence of a finite baryon density (see [1] where the current state of the art is summarized). Therefore, various phenomenological, QCD-motivated models are considered for describing the thermodynamics of highly excited nuclear matter and its equation of state (EoS).

General arguments from QCD and lattice data tell us that a kind of string is developed between quarks and antiquarks at large distance and it is natural to identify such $q\bar{q}$ system with conventional mesons. Treating quark and gluon propagation in the confining QCD vacuum within non-Abelian $SU(3)$ gauge theory, the string dynamics was successfully applied to conventional mesons, hybrids, glueballs, and gluelumps. However, if such a string is surrounded by unbound quarks and gluons, the $q\bar{q}$ system can be excited not only in color-singlet states, but also in color-octet states, even dissociate into constituent elements. The latter will signal, in general, the deconfinement phase transition. These phase transformations are intimately related to the change in string properties (in particular, color charges of quarks are screened in a quark–gluon environment): string behavior becomes medium-dependent.

At present, there are number of simplified models for describing static hadron properties as well as a highly excited, deconfined state of quark matter, the quark–gluon plasma (QGP). A common feature of these models is that they all are based on a quasiparticle picture, considering isolated particle-like degrees of freedom and assuming that these quasiparticles are moving in a background mean field. Two- and many-particle correlations are included in the mean-field contributions and in the modification of the one-particle spectra. Well-known examples are the original bag model and its later versions [2–4], phenomenological approaches with a temperature-dependent bag constant [5, 6], string-motivated density-dependent corrections to an ideal (massive or massless) quark matter equation of state, the very consideration of hadrons as composite objects in QCD, excluded volume corrections [7, 8], and finally mixed phase [9] and chemical mixture [10, 11] models dealing with the transition between quark matter and hadron matter in a phenomenological way.

The present paper concerns the quasiparticle description of the QCD thermodynamics with the particular emphasis on the mean-field treatment of in-medium strings. The paper is organized as follows.

*This article was submitted by the authors in English.

[1)]Permanent address: Joint Institute for Nuclear Research, Dubna, Moscow oblast, 141980 Russia.

1063-7788/03/6605-0982$24.00

In Section 2, we consider the thermodynamic consistency of the quasiparticle description in general. Any phenomenological approach involving quasiparticle interaction usually operates with a Hamiltonian that may depend on the thermodynamic characteristics of the surrounding matter, like the temperature T and density n. As has been known for a long time (for details, see [12, 13]), there exist certain restrictions on the dependence of such a Hamiltonian on the thermodynamic variables. In this section, a transparent and useful representation of these restrictions is derived [see Eqs. (21) and (22)] that directly involves the quasiparticle spectra. The obtained representation of thermodynamic consistency allows us to get an instructive relation between a number of modern approaches dealing with the deconfinement problem at the framework of a quasiparticle picture, as exemplified at the end of Section 2. The QCD-motivated interactions, in particular, stringlike interactions [14], are investigated in Section 3. A comprehensive model of string formation in the dense matter of unbound color charges is developed, which supports the choice of the mean field proportional to an inverse power of the color-charge density, as proposed in the papers [9, 12, 15–17]. This quasiparticle scheme is applied in Section 4 for thermodynamics of the deconfined QCD phase. The case when the system is in thermal but not chemical equilibrium is also considered. The results are summarized in the concluding Section 5.

2. QUASIPARTICLE HAMILTONIAN

In order to obtain an effective quasiparticle description of a medium made of unbound color charges, one should operate with screened long-range potentials. A natural way to introduce the screening in quark matter is based on using the probability density $P(r)$ to form a string of the length r. It is worth noting that this investigation scheme has much in common with another one which deals with the probability density that the nearest neighbor occurs at a distance r [16]. Both approaches involve thermodynamic variables, which lead to a screened pair potential depending on thermodynamic quantities. Due to such effects, the quasiparticle Hamiltonian becomes density- and temperature-dependent, which in turn leads to a modification of a thermodynamic potential (e.g., the Gibbs free energy). Eventually, a nonideal EoS emerges.

2.1. General Structure of Hamiltonian

We start with the general quasiparticle Hamiltonian

$$\hat{H} = \sum_i \sum_{\mathbf{k}} \epsilon_{ki}(T,n) a^\dagger_{\mathbf{k}i} a_{\mathbf{k}i} + V\Phi(T,n). \qquad (1)$$

Here, $a^\dagger_{\mathbf{k}i}$ and $a_{\mathbf{k}i}$ are the usual creation and annihilation operators for quasiparticles of the ith sort with momentum $\mathbf{k}$. They also may depend on other internal degrees of freedom like spin, color, and isospin. The volume V is constant and rather large (infinite in the thermodynamic limit). Thus, in this limit, the summation over quantum states labeled by $\mathbf{k}$ can be replaced by a phase space integral (including the internal degeneracy factor d_i):

$$\sum_{\mathbf{k}} \to V d_i \int \frac{d^3k}{(2\pi)^3}. \qquad (2)$$

In general, the one-particle energy $\epsilon_{\mathbf{k}i}(T,n) \equiv \epsilon_{ki}(T,n)$ and the background field contribution $\Phi(T,n)$ to the energy density both depend on the temperature T and the set of particle densities $n \equiv \{n_1, n_2, \ldots\}$. Note that the quantity $V\Phi(T,n)$ is nothing else but the energy of the quasiparticle vacuum. Generally speaking, it differs from the vacuum of primordial particles, which leads to the c-number term $V\Phi(T,n)$ appearing in Eq. (1). In the present paper, we consider the situation when, similarly to the case of the Hartree–Fock quasiparticles, the expectation value of the quasiparticle number operator $\hat{N}_i = \sum_{\mathbf{k}} a^\dagger_{\mathbf{k}i} a_{\mathbf{k}i}$ is equal to the number of primordial particles $N_i = n_i V$. This implies that we deal with the picture of quasiparticles interacting and, thus, correlating with each other. In turn, the expectation value of the Hamiltonian has to be equal to the mean energy of the system under consideration. This leads to the following relations:

$$\langle \hat{H} \rangle = E = V \sum_i d_i \int \frac{d^3k}{(3\pi)^3} \epsilon_{ki} \nu_{ki} + V\Phi, \qquad (3)$$

$$\langle \hat{N}_i \rangle = N_i = V d_i \int \frac{d^3k}{(2\pi)^3} \nu_{ki}, \qquad (4)$$

with the occupation numbers $\nu_{ki} = \langle a^\dagger_{\mathbf{k}i} a_{\mathbf{k}i} \rangle$. There is another way of calculating the mean energy $E = V\varepsilon(T,n)$ and mean multiplicity $N_i = V n_i$ that proceeds from a thermodynamic potential rather than from Eqs. (3) and (4). For density- and temperature-dependent Hamiltonians, these different ways may lead to different results (see, for example, [9, 12]). Hence, in what concerns the dependence on n and T, the quasiparticle Hamiltonian will have a correct structure only if the thermodynamic consistency requirements (3) and (4) are satisfied when starting with either the Hamiltonian or the thermodynamic potential.

2.2. Chemical Potentials

Using temperature T and number densities $n_i = N_i/V$ as basic descriptive variables, the thermodynamic behavior and the appropriate EoS can be derived from the corresponding thermodynamic potential, the free energy $F(V, N, T)$:

$$F \equiv Vf = T\sum_i \xi_i d_i \int \frac{d^3k}{(2\pi)^3} \ln\left(1 - \xi_i e^{-z_{ki}}\right) + V\sum_i \mu_i n_i + V\Phi. \quad (5)$$

Here, $\xi_i = \pm 1$ is determined by the quasiparticle statistics, μ_i stands for the chemical potential of the quasiparticles of the ith sort, and z_{ki} is defined by

$$z_{ki} = \frac{\epsilon_{ki} - \mu_i}{T}. \quad (6)$$

The simplest way of calculating the free energy implies the use of the grand-canonical ensemble when particle numbers are known only on average and chemical potentials μ_i are introduced instead of N_i as descriptive thermodynamic variables. To calculate the partition function in this case, the quasiparticle Hamiltonian (1) should be modified to

$$\hat{H}' = \hat{H} - \sum_i \mu_i \hat{N}_i, \quad (7)$$

where $\hat{H}$ is defined by Eq. (1). We recall that the physical meaning of μ_i is the energy loss due to removing a quasiparticle of the ith species while the total entropy and volume of the system are kept constant. This chemical potential a priori has nothing to do with the fact whether this particle really carries a conserved charge or not. However, there are Lagrange multipliers associated with the conservation laws of such charges like the baryon number, strangeness, or electric charge. In order to elucidate the difference between chemical potentials in general and those associated to the conserved charges, let us consider a particle mixture of many sorts whose abundance is known only on average. The mixture components (not necessarily all of them) carry some conserved charges. The conservation of these charges is controlled by the appropriate chemical potential. We denote such a charge of type b carried by a particle belonging to the ith component of the mixture as q_{bi}. Then, for conserved quantities, we have

$$Q_b = \sum_i q_{bi} N_i. \quad (8)$$

Usually there are more components than the number of conserved charges. In particular, it is the case for quark–gluon matter, to which we pay special interest in the present paper. Besides the case of a single-component system, Eq. (8) is insufficient for calculating all mean numbers for the mixture components. Therefore, we need some additional requirements that would allow us to determine the particle numbers N_i by making use of Eq. (8). Chemical equilibrium is usually assumed, and then these additional requirements are given by

$$\mu_i^{\rm eq} = \sum_b q_{bi}\mu_b, \quad (9)$$

where μ_b stands for the chemical potential associated to the charge sort b. In the general case, when the system is out of chemical equilibrium and the component concentrations become time-dependent, the chemical potential can be split into two parts,

$$\mu_i = \sum_b q_{ib}\mu_b + \tilde{\mu}_i, \quad (10)$$

and Eq. (7) is reduced to

$$\hat{H}' = \hat{H} - \sum_b \mu_b \hat{Q}_b - \sum_i \tilde{\mu}_i \hat{N}_i. \quad (11)$$

The quantities $\tilde{\mu}_i$ describe the deviation from chemical equilibrium in the thermally equilibrated system. They are exactly zero in the chemical equilibrium limit, resulting in the familiar relation

$$\hat{H}'_{\rm eq} = \hat{H} - \sum_b \mu_b \hat{Q}_b. \quad (12)$$

Below, we shall investigate consistency of the quasiparticle picture in a thermodynamic treatment including the possibility of deviations from chemical equilibrium in a mixture.

2.3. Thermodynamic Consistency

As mentioned above, any approach starting with a thermodynamic potential appears to be thermodynamically consistent. In other words, if all the quantities of interest can be calculated only through the derivatives of this thermodynamic potential, one is prevented from encountering thermodynamic inconsistency. Problems arise, however, when the calculation can proceed not only from the constructed thermodynamic potential but also from a more fundamental level, some quasiparticle Hamiltonian at a given temperature and/or density. In the last case, the result may depend on the calculation method unless the quantities $\epsilon_{ki}(T, n)$ and $\Phi(T, n)$ obey relations derived in accordance with the consistency requirements (3) and (4). Below, these relations are called the conditions of thermodynamic consistency.

To elaborate on these conditions, let us consider a system with the Hamiltonian defined by Eqs. (1)

and (7). If the abundance of all mixture components is known only on average, the proper thermodynamic potential has the form

$$\Omega = E - TS - \sum_i \mu_i N_i, \tag{13}$$

with S being the total entropy. The grand-canonical partition function corresponding to H' can readily be calculated:

$$Z = \mathrm{tr}(e^{-\hat{H}'/T}) \tag{14}$$
$$= \left(\prod_{\mathbf{k},i}\sum_{n_{ki}} e^{-z_{ki}n_{ki}}\right) e^{-\Phi V/T} = e^{-\Omega/T}.$$

Recall that, in the Fermi gas case, the integer quantity n_{ki} equals either 0 or 1, while in the Bose one it runs from 0 to ∞. Hence, from Eq. (14), it follows that

$$\frac{\Omega}{V} = T\sum_i d_i\xi_i \int \frac{d^3k}{(2\pi)^3}\ln\left(1-\xi_i e^{-z_{ki}}\right) + \Phi. \tag{15}$$

Note that Eq. (15) covers Eq. (5) with the definition $F = E - TS$. It is well known that, for the Hamiltonian H', the average quasiparticle occupation number ν_{ki} is

$$\nu_{ki} = \langle n_{ki}\rangle = \frac{1}{e^{z_{ki}} - \xi_i}, \tag{16}$$

which together with Eq. (15) leads to

$$\frac{\Omega}{V} = \Phi - T\sum_i d_i\xi_i \int \frac{d^3k}{(2\pi)^3}\ln\left(1+\xi_i\,\nu_{ki}\right). \tag{17}$$

The total differential of the thermodynamic potential Ω is given by

$$d\Omega = dV\left(\Phi - T\sum_i d_i\xi_i\int\frac{d^3k}{(2\pi)^3}\ln\left(1+\xi_i\nu_{ki}\right)\right) \tag{18}$$
$$- VT\sum_i d_i\xi_i\int\frac{d^3k}{(2\pi)^3}$$
$$\times\left(\frac{dT}{T}\ln\left(1+\xi_i\nu_{ki}\right) + \frac{\xi_i d\nu_{ki}}{1+\xi_i\nu_{ki}}\right) + Vd\Phi.$$

Since in the grand-canonical ensemble the quasiparticle densities n_i and average occupation numbers ν_{ki} are functions of the temperature T and chemical potentials μ_i, all the differentials can be expanded in terms of dT, dV, and $d\mu_i$. In particular, we have

$$d\nu_{ki} = -\nu_{ki}(1+\xi_i\,\nu_{ki})d\left(\frac{\epsilon_{ki}-\mu_i}{T}\right),$$

$$d\epsilon_{ki} = \frac{\partial\epsilon_{ki}}{\partial\mu_j}d\mu_j + \frac{\partial\epsilon_{ki}}{\partial T}dT,$$

$$d\Phi = \frac{\partial\Phi}{\partial\mu_j}d\mu_j + \frac{\partial\Phi}{\partial T}dT.$$

Inserting these relations into Eq. (18) and then comparing the derived result with the general formula

$$d\Omega = -pdV - SdT - \sum_i N_i d\mu_i,$$

one can arrive at

$$\varepsilon = \sum_i d_i\int\frac{d^3k}{(2\pi)^3}\epsilon_{ki}\nu_{ki} + \Phi \tag{19}$$
$$- \sum_i \mu_i C_i - TC_T,$$

$$n_i = d_i\int\frac{d^3k}{(2\pi)^3}\nu_{ki} - C_i, \tag{20}$$

where

$$C_T = \frac{\partial\Phi}{\partial T} + \sum_j d_j\int\frac{d^3k}{(2\pi)^3}\frac{\partial\epsilon_{kj}}{\partial T}\nu_{kj},$$

$$C_i = \frac{\partial\Phi}{\partial\mu_i} + \sum_j d_j\int\frac{d^3k}{(2\pi)^3}\frac{\partial\epsilon_{kj}}{\partial\mu_i}\nu_{kj}.$$

Equations (19) and (20) should be compared to the consistency requirements given by Eqs. (3) and (4). It leads to the conditions $C_T = 0$ and $C_i = 0$. This result can be rewritten in a more manageable form that allows for relating our specific case based on Eq. (1) to a more general one. To elucidate this connection, let us consider the derivative matrix

$$M_{ij} = \partial n_i/\partial\mu_j.$$

Its elements can, in principle, have arbitrary values, and we expect that the determinant of M_{ij} is not zero. This is indeed the case since the derivative matrix is given by the implicit relation

$$\frac{\partial n_i}{\partial\mu_j} = \frac{1}{T}\,d_i\int\frac{d^3k}{(2\pi)^3}\nu_{kj}(1+\nu_{kj})\left(\delta_{ij} - \frac{\partial\epsilon_{ki}}{\partial\mu_j}\right),$$

leading to the matrix equation

$$M_{jk} = A_{jk} - \sum_i M_{ik}B_{ij}$$

with

$$A_{jk} = \delta_{jk}\frac{1}{T}d_j\int\frac{d^3k}{(2\pi)^3}\nu_{kj}(1+\nu_{kj}),$$

$$B_{ij} = \frac{1}{T}d_j\int\frac{d^3k}{(2\pi)^3}\nu_{kj}(1+\nu_{kj})\frac{\partial\epsilon_{kj}}{\partial n_{ki}}.$$

This matrix equation has a formal solution $M = (1 + B)^{-1}A$. While B may have zero eigenvalues, A does

not, so the determinant $\det M = \det A/\det(1+B)$ cannot vanish. Using this information, the equalities $C_T = 0$ and $C_i = 0$ can be rewritten as follows:

$$\frac{\partial\Phi}{\partial T} + \sum_j d_j \int \frac{d^3k}{(2\pi)^3}\frac{\partial\epsilon_{kj}}{\partial T}\nu_{kj} = 0, \qquad (21)$$

$$\frac{\partial\Phi}{\partial n_i} + \sum_j d_j \int \frac{d^3k}{(2\pi)^3}\frac{\partial\epsilon_{kj}}{\partial n_i}\nu_{kj} = 0. \qquad (22)$$

Equations (21) and (22) represent a particular case of the more general relations [9, 12]

$$\left\langle \frac{\partial H_{\text{eff}}}{\partial T} \right\rangle = 0, \qquad \left\langle \frac{\partial H_{\text{eff}}}{\partial n_i} \right\rangle = 0. \qquad (23)$$

These conditions of the quasiparticle consistency are reduced to Eqs. (21) and (22) when the (temperature- and density-dependent) effective Hamiltonian H_{eff} has the quasiparticle form (1). Equations (23) were first derived in [12] (see also [9]) under the requirement that all the statistical ensembles of the system governed by the density- and temperature-dependent Hamiltonian H_{eff} yield the same thermodynamics in the infinite volume limit. Thus, to avoid thermodynamic inconsistency, the constraints (23) should be satisfied in construction of the effective quasiparticle Hamiltonians.

Let us emphasize that thermodynamic consistency is not sufficient by itself when the thermodynamics is constructed starting from the level of a thermodynamic potential but the Hamiltonian structure is ignored. In this case, nonphysical expressions can be involved even if there is no problem with thermodynamic consistency and all the thermodynamic quantities are derived by differentiating a thermodynamic potential. We suggest that relations (21) and (22) should also be employed in a situation like that to avoid unreasonable expressions for quasiparticle spectra which can be met in the literature. For instance, see the papers on the compressible bag model [18]. It is thermodynamically consistent, but the quasiparticle spectra used there have nothing to do with (21) and (22). Another example concerns the approach of [19] that has no problem with thermodynamics either. However, the shift of the chemical potential proposed in that article is equivalent to the introduction of a temperature-dependent vector-type mean field. It is shown below from Eqs. (21) and (22) (see the next subsection, Example 1) that a mean field like this cannot depend on the temperature explicitly. By the way, it is quite possible that the nonphysical feature of the quasiparticle spectra used in [19] is an actual reason for causality violation when the sound velocity becomes larger than the velocity of light (for more details, see [20]).

Note that, when temperature and density dependence of the effective Hamiltonian is mediated only by some thermodynamic quantity Λ, the consistency conditions (23) are equivalent to $\langle \partial H_{\text{eff}}/\partial\Lambda\rangle = 0$. This relation comes from the well-known expression $\delta F = \langle \delta H_{\text{eff}}\rangle$ [21], where δF and δH_{eff} stand for infinitesimal changes of the free energy and Hamiltonian, respectively. This expression can easily be derived by analogy with the familiar Hellmann–Feynman theorem and, taken in conjunction with the extremum condition for the free energy with respect to the parameter Λ, leads to $\langle \partial H_{\text{eff}}/\partial\Lambda\rangle = 0$.

2.4. Quasiparticle Spectra

Conditions of thermodynamic consistency (21) and (22) result in certain physical restrictions to the mean-field potential depending on the structure of quasiparticle spectra without going into any detail of interaction between constituents. We shall demonstrate that in a few cases used in phenomenological treatments.

Example 1. Let the energy of a quasiparticle of the ith sort moving with the 3-momentum $\mathbf{k}$ be approximated as (for instance, see [9, 12, 15–17, 22–24])

$$\epsilon_{ki}(T,n) = \omega_i(k) + U_i(T,n), \qquad (24)$$

where $\omega_i(k)$ stands for the energy of the free particles of the ith sort and, as above, n denotes the set of particle number densities $\{n_1, n_2, \ldots\}$. Generally, the mean-field potential $U_i(T,n)$ is a function of temperature and particle densities. The free-particle energy can be given in either the relativistic form, $\omega_i(k) = \sqrt{k^2 + m_{0i}^2}$, or in the nonrelativistic one, $\omega_i(k) = k^2/2m_{0i}$. It depends only on the momentum k and bare particle mass m_{0i}. Then, the conditions of quasiparticle consistency (21) and (22) are reduced to the following equations:

$$\frac{\partial\Phi}{\partial T} + \sum_j n_j \frac{\partial U_j}{\partial T} = 0, \quad \frac{\partial\Phi}{\partial n_i} + \sum_j n_j \frac{\partial U_j}{\partial n_i} = 0. \qquad (25)$$

As is seen, ignoring the background field contribution $\Phi(T,n)$, as, for example, in [17, 22], results in a loss of thermodynamic consistency. It is important to note that Eqs. (25) are compatible only if the mean field U_i does not depend on the temperature explicitly. Indeed, the first equation in (25) has an integral of the form

$$\sum_j n_j U_j + \Phi = \varphi,$$

where $\varphi = \varphi(n)$ is an arbitrary function of the quasiparticle densities. By differentiating this expression

with respect to n_i, we get

$$\frac{\partial\varphi}{\partial n_i} = U_i + \sum_j n_j \frac{\partial U_j}{\partial n_i} + \frac{\partial\Phi}{\partial n_i}.$$

Taken in conjunction with the second equation in (25), the obtained relation is reduced to $\partial\varphi/\partial n_i = U_i$. It follows then that U_i and Φ are temperature-independent functions. In other words, when quasiparticle spectra are defined by Eq. (24), the thermodynamically consistent mean-field potential may depend only on particle densities: $U_i = U_i(n), \Phi = \Phi(n)$. Note that this important point is missed in some papers [25], where the excluded volume effects are treated by means of the mean-field approximation.

Equations (25) lead to one more interesting result,

$$\frac{\partial U_i}{\partial n_j} = \frac{\partial U_j}{\partial n_i}. \tag{26}$$

This crossing relation, first presented in [24], follows from the second equality in Eqs. (25). To derive Eq. (26), one should differentiate the second equation in (25) with respect to n_l. Then, by interchanging the indices l and i and comparing the obtained expression with the previous one, we arrive at Eq. (26). By doing so, one should keep in mind that

$$\frac{\partial^2 U_j}{\partial n_l \partial n_i} = \frac{\partial^2 U_j}{\partial n_i \partial n_l}, \qquad \frac{\partial^2\Phi}{\partial n_l \partial n_i} = \frac{\partial^2\Phi}{\partial n_i \partial n_l}.$$

This is valid provided that the second derivatives of U_j and Φ are continuous functions of T and n, which is usually the case. Note that Eq. (26) is very useful when dealing with the mean fields U_i for many-component systems. For example, see the investigation of quark–hadron interactions in [9]. The crossing relation (26) should be fulfilled when constructing the mean fields acting on quasiparticles of different species in a many-component system. Otherwise, the thermodynamic consistency can be lost. As an example, one can point out the paper [23], where mean fields were chosen as $U_i = n_{\rm tot}(\tilde{m}/m_{0i})^\delta$ with $\delta = 1$ or 2. Here, $\tilde{m}$ denotes the nucleon mass and $n_{\rm tot} = \sum n_j$.

Example 2. Another popular form of quasiparticle spectra $\epsilon_{ki}(T,n)$ is given as

$$\epsilon_{ki}(T,n) = \sqrt{k^2 + m_i^2(T,n)}; \tag{27}$$

i.e., an effective quasiparticle mass $m_i \equiv m_i(T,n)$ is introduced in a way similar to scalar mass in the relativistic mean-field theory [26]. In this case, Eqs. (21) and (22) can be rewritten as follows:

$$\frac{\partial\Phi}{\partial T} + \sum_j n_j^{(s)} \frac{\partial m_j}{\partial T} = 0, \tag{28}$$

$$\frac{\partial\Phi}{\partial n_i} + \sum_j n_j^{(s)} \frac{\partial m_j}{\partial n_i} = 0,$$

where the Lorentz scalar quasiparticle density $n_i^{(s)}$ is defined by

$$n_j^{(s)} = d_j \int \frac{d^3k}{(2\pi)^3} \nu_{kj} \frac{m_j}{\sqrt{k^2 + m_j^2}}. \tag{29}$$

For the sake of simplicity, let us limit ourselves to the case of one sort of quasiparticles. Differentiating the first equation in (28) with respect to n and the second one with respect to T, we arrive at

$$\frac{\partial n^{(s)}}{\partial T}\frac{\partial m}{\partial n} - \frac{\partial n^{(s)}}{\partial n}\frac{\partial m}{\partial T} = 0, \tag{30}$$

provided the mixed second derivatives of Φ and m are equal to each other. As follows from Eq. (30), the gradients of functions $n^{(s)}(T,n)$ and $m(T,n)$ are parallel vectors in the Tn plane. Hence, m is left constant along any line where $n^{(s)}$ is constant. Since $n^{(s)}(T,n)$ and $m(T,n)$ are differentiable functions of T and n, the Tn plane is densely covered by lines of constant $n^{(s)}$. Therefore, in a thermodynamically consistent model with one sort of quasiparticles, whose energy is defined by (27), the effective quasiparticle mass depends on temperature and quasiparticle density only through the scalar density. The Walecka model [26] without vector field (for zero baryon density) is a particular case of the considered variant. Another example can be found in the paper of Boal, Schachter, and Woloshin in [15], where interactions in the quark–gluon plasma are described by introducing the effective masses of quarks and gluons depending on the sum of the color-charge densities. As has been proven above, this version is inconsistent. One can expect that the case of many quasiparticle species is described by equations similar to Eq. (28), i.e., m_i is a function of the set of $n_i^{(s)}$. As a consequence, Φ depends on T and n through the scalar densities too and satisfies

$$\Phi = -\int \sum_j n_j^{(s)} dm_j. \tag{31}$$

Deconfinement models dealing with the temperature- and density-dependent masses of quarks and gluons [5, 27, 28] are also related to Example 2. Here, it is often assumed $n^{(s)} \propto m^3$ and $\Phi \propto m^4$. A purely temperature-dependent bag constant, $\Phi(T)$, without mass modifications, on the other hand, is inconsistent. The same is related to the situation when temperature-dependent masses without the background term are used [29]. To go into more detail, see also [13].

Example 3. If the mean field in Eq. (24) is scaled with some coupling constant, $U_i = g_i U$ (see, for example, [9, 12, 24]), then conditions of thermodynamic consistency take the form

$$\frac{\partial\Phi}{\partial T} + \rho\frac{\partial U}{\partial T} = 0, \qquad \frac{\partial\Phi}{\partial n_i} + \rho\frac{\partial U}{\partial n_i} = 0 \qquad (32)$$

with

$$\rho = \sum_j g_j n_j.$$

Using a procedure similar to that described in the previous example, one can be convinced that the density dependence of the mean field U is mediated by $\rho(n)$ only. If g_i is proportional to the baryon number b_i of the quasiparticle i, $g_i = g b_i$, then we get $\rho = g\sum_i b_i n_i \equiv g n_b$, where n_b is the total baryon density. A similar situation is realized when the quasiparticle interaction is mediated by a vector field.

Now let us return to [23], mentioned at the end of Example 1. Equations (32) suggest how one can correct the mean field $U_i = n_{\rm tot}(\tilde{m}/m_{0i})^\delta$ used in that paper in such a way as to keep the relation $U_i \propto (\tilde{m}/m_{0i})^\delta$. It turned out that the unique solution is given by $U_i = \varphi(\rho)(\tilde{m}/m_{0i})^\delta$, where instead of $n_{\rm tot}$ we use $\rho = \sum_j (\tilde{m}/m_{0j})^\delta n_j$ and an arbitrary function $\varphi(\rho)$ which can be chosen as $\varphi(\rho) = \rho$.

Sometimes, it is convenient to subdivide the full set of coupling constants into two groups: $g_i^{(a)} < 0$ (corresponding to attractive interaction) and $g_i^{(r)} > 0$ (related to repulsive interaction—see, for example, [24]). In this case, $U_i = g_i^{(r)} U_r - |g_i^{(a)}| U_a$, and we can expect that the repulsive-interaction component U_r is a function of $\rho_r = \sum_i g_i^{(r)} n_i$, while the attractive one U_a depends on quasiparticle densities through $\rho_a = \sum_i g_i^{(a)} n_i$.

Example 4. By analogy with the approximation $U_i = g_i U$ considered in Example 3, the effective quasiparticle mass of Example 2 can also be scaled as $m_i = g_i M(T, n)$. In particular, $M(T, n)$ can be the constituent quark mass, whereas g_i is the number of quarks in the baryon cluster of the ith sort. Generally, a cluster of g_i constituents may consist of quarks, antiquarks, and gluons (i.e., forming baryons, mesons, hybrids, and glueballs) as well. By doing so, we get

$$\frac{\partial\Phi}{\partial T} + \rho^{(s)}\frac{\partial M}{\partial T} = 0, \qquad \frac{\partial\Phi}{\partial n_i} + \rho^{(s)}\frac{\partial M}{\partial n_i} = 0, \quad (33)$$

with

$$\rho^{(s)} = \sum_j g_j n_j^{(s)}.$$

The thermodynamics of such a system depends on the descriptive variables T and n through the quantity $\rho^{(s)}(T, n)$.

3. MEAN-FIELD TREATMENT OF STRING INTERACTIONS

Until now, we have discussed general restrictions to the phenomenological Hamiltonian due to the thermodynamic consistency. It can be further elaborated by specifying the interaction between generic constituents. The quasiparticle properties ought to be derived from this underlying interaction. In our phenomenological treatment, we consider a particular case of strong pair interaction mediated by strings stretched between color charges. The main difficulty here is that such a system is plagued with long-range interaction, and only in-medium screening renders the problem treatable, even in the weak-correlation approximation.

Strings are particular QCD field constructions involved in the interaction between two color charges in vacuum. We consider here how this interaction will behave in a medium consisting of pointlike color charges. Let some reference color charge creating a string be placed at the origin of coordinates and other color charges be distributed around with the density $n(\ell)$, where ℓ is the distance from the reference charge. Physically, we can expect that the string formation is characterized by a probability depending on its length, but not on its formation history. Let $P(\ell)d\ell$ be the probability for a string to have a length between ℓ and $\ell + d\ell$. The quantity $P(\ell)$ can be represented as a product of two factors:

$$P(\ell) = \left(1 - \int_0^\ell dx P(x)\right) w(\ell). \qquad (34)$$

The first factor in Eq. (34) is the probability for the string to have a length not less than ℓ. The second factor $w(\ell)$ is related to the conditional probability, $w(\ell)d\ell$, meaning that a string is formed between ℓ and $\ell + d\ell$ (provided it has already reached the length ℓ).

For gradually growing strings, the quantity $w(\ell)$ can be obtained by invoking arguments similar to those used in calculation of the mean-free path of a particle moving through a medium in a given direction. In this scenario, we assume that a string is caught by any color charge within a cylinder of the radius a and with an axis along the considered string direction. This leads to

$$w(\ell) = \pi a^2 n(\ell). \qquad (35)$$

The factor πa^2 is interpreted as a string cross section accounting also for a lack of string dynamics. The effective radius a may depend on the medium.

In another scenario, the strings are assumed to wildly fluctuate in direction. The gross factor $w(\ell)$ is rather well approximated in this case by the relation

$$w(\ell) = 4\pi\ell^2 n(\ell). \tag{36}$$

Equation (36), having an additional ℓ^2 factor, can be derived by analogy to Eq. (35) if the whole area of the spherical shell, $4\pi\ell^2 d\ell$, at the distance ℓ is taken into account. Here, all possible partner charges, located at the distance ℓ, potentially participate in the screening. Note that, in both cases, $n(\ell)$ stands for the number density of potential partners on which a string of length ℓ can be closed.

Usually, it turns out to be more convenient to deal with the integro-differential equations rather than with the integral ones. After differentiating Eq. (34), we arrive at

$$\frac{dP}{d\ell} = -w(\ell)\,P(\ell) + \frac{dw}{d\ell}\left(1 - \int\limits_0^\ell P(x)dx\right). \tag{37}$$

After substituting here the integral definition (34), we get

$$\frac{dP}{d\ell} = -w(\ell)P(\ell) + \frac{dw}{d\ell}\,\frac{P}{w}. \tag{38}$$

This ordinary differential equation is separable and has the following explicit solution:

$$P(\ell) = bw(\ell)e^{-\int_0^\ell w(x)\,dx}. \tag{39}$$

The integration constant b is determined by normalization of the probability density:

$$\int\limits_0^{+\infty} P(x)dx = 1. \tag{40}$$

Let us consider now Eqs. (35), (36), and (39) in more detail. Neglecting the spatial charge correlations (i.e., taking $n(\ell) = n = \text{const}$), Eqs. (35) and (39) (belonging to the first, straight string, scenario) result in an exponential screening

$$P(\ell) = \pi a^2 n e^{-\pi a^2 n\,\ell}. \tag{41}$$

From here, the probability for a string to be shorter than or equal to η is given by

$$Q(\eta) = \int\limits_0^\eta P(x)\,dx = 1 - e^{-\pi a^2 n\,\eta} \tag{42}$$

and the average string length is

$$\langle\ell\rangle = \int\limits_0^\infty xP(x)dx = \frac{1}{\pi a^2 n}. \tag{43}$$

Noting that the probability distribution (41) can be represented in the form

$$P(\ell) \propto e^{-E(\ell)/E(\langle\ell\rangle)} = e^{-\ell/\langle\ell\rangle} \tag{44}$$

with $E(\ell) = \sigma\ell$, one sees that short strings are energetically favored. This looks like a natural conclusion, but, nevertheless, it is not trivial, because "energy" arguments have not been involved explicitly in the reasoning.

Within the second scenario of the string screening [i.e., strings wildly fluctuating—see Eq. (36)], the corresponding probability density becomes

$$P(\ell) = 4\pi n\ell^2 e^{-4\pi n\ell^3/3}. \tag{45}$$

This expression covers the result of [16], where the probability of string formation has been calculated in the nearest neighbor approximation. The probability of the string length to be less than or equal to η now has the form

$$Q(\eta) = \int\limits_0^\eta P(x)dx = 1 - e^{-\frac{4}{3}\pi n\eta^3}, \tag{46}$$

and the average string length is given by

$$\langle\ell\rangle = \Gamma\left(\frac{1}{3}\right)\left(\frac{3}{4\pi n}\right)^{1/3}, \tag{47}$$

with $\Gamma(\ldots)$ being Euler's gamma function. By analogy with the representation (44), Eq. (45) can be rewritten as

$$P(\ell) \propto (\ell)^2 \exp\left(-\left(\Gamma\left(\frac{1}{3}\right)\frac{\ell}{\langle\ell\rangle}\right)^3\right), \tag{48}$$

which also agrees with the argument that short strings are favorable.

As noted above the straight-string scenario based on Eq. (35) involves the effective string radius, a, which may depend on thermodynamic variables. Indeed, the string survives only in the case when the characteristic length a does not exceed the mean distance between neighboring color charges, $r_0 = (4\pi n/3)^{-1/3}$. Therefore, operating with Eq. (35) and Eqs. (41)–(44), we should employ $a \le r_0$. Now, estimating $a \approx cr_0$ ($c < 1$ is some constant), we obtain from Eq. (43)

$$\langle\ell\rangle = \left(\frac{4}{3c^3}\right)^{2/3}\frac{1}{(\pi n)^{1/3}} \tag{49}$$

in accordance with Eq. (47) under the choice $c = 2/\sqrt{3\Gamma(1/3)} \approx 0.7 < 1$. In summary, the thermodynamics of string interactions is ruled by the average length of in-medium strings. Thus, in spite of differences in $P(\ell)$, both considered scenarios of the string

screening lead to qualitatively similar thermodynamic pictures. It is interesting that the density-dependent interpretation of a in Eq. (41) leads to a density-dependent screening:

$$e^{-\pi a^2 n r} = e^{-M_{\rm scr} r},$$

with the screening mass $M_{\rm scr} = (3c^3/4)^{2/3}(\pi n)^{1/3}$. At sufficiently high temperatures, the QCD thermodynamics approaches the Stefan–Boltzmann regime where $n \sim T^3$. This yields $M_{\rm scr} \propto T$, which is nicely consistent with perturbative QCD.

The modification of the energy density due to presence of in-medium strings can be constructed as

$$\Delta\varepsilon = n\sigma\langle\ell\rangle, \tag{50}$$

with the string tension σ. In this case, the color constituents of the system are affected by the following mean field:

$$U = \sigma\langle\ell\rangle = An^{-\gamma}, \tag{51}$$

where the constants A and γ carry information about the sort of color charges and character of the in-medium string screening. Note that the results of lattice simulations for $SU(3)$ symmetry can be approximated by $\gamma \approx 2/3$ [9, 12]. This is in qualitative agreement with our rough estimate $\gamma \sim 1/3$ neglecting the spatial correlations of color charges. Indeed, in respect to the thermodynamic character of the EoS, only the fact that γ lies between 0 and 1 is decisive.

Concluding this section, we sketch how one should, in principle, deal with the case when spatial correlations of color charges are taken into account. Let us consider a reference color charge placed at the origin. The important point is that the ratio

$$g(\ell) = \frac{n(\ell)}{n} \tag{52}$$

is nothing else but the radial distribution function [30] which determines the pair particle correlations in the uniform system of color charges with the density n given by

$$n = \lim_{\ell\to\infty} n(\ell).$$

As follows from Eq. (52), Eqs. (41) and (45) operate with $g(\ell) = 1$, which corresponds to neglecting the spatial correlations of color charges. To go beyond this simplification, one should replace $n(\ell)$ by $ng(\ell)$ in Eq. (36). In particular, using Eq. (35), one can derive the following equation:

$$P(\ell) = b\pi a^2 n g(\ell)\, e^{-\pi a^2 n \int_0^\ell g(x)dx}, \tag{53}$$

the average length of the in-medium strings being dependent on the charge–charge spatial correlations. Note that, for $\ell \to \infty$ the quantity $g(\ell)$ tends to 1, and we arrive at the same exponential decay of $P(\ell)$ as in Eq. (41), but with a different prefactor. In principle, this difference can lead to another estimate of γ being closer to the lattice result mentioned above. Thus, the probability density $P(\ell)$ should not be identified with the radial distribution function as was done in [16].

4. APPLICATION TO QCD THERMODYNAMICS

The developed technique allows one to construct a thermodynamic potential in a self-consistent way starting from the microscopic level. The Hamiltonian structure of a particular phenomenological model is defined by the physical assumptions used. Some simple models for QCD thermodynamics are considered below in order to illustrate the convenience and power of the conditions of thermodynamic consistency (21), (22) and to show the rationality of our treatment of in-medium strings.

4.1. Ideal Gas in a Baglike Model

Let us consider an ideal gas of particles whose one-particle spectrum is independent of medium parameters,

$$\epsilon_{ki}(n, T) = \omega_i(k). \tag{54}$$

Then Eqs. (21) and (22) have the form

$$\frac{\partial\Phi}{\partial T} = 0, \qquad \frac{\partial\Phi}{\partial n_i} = 0, \tag{55}$$

leading to a constant background energy $\Phi = B$. It is frequently associated with the bag constant. In this relatively simple case, the chemical potentials are nevertheless determined by the set of the implicit equations

$$n_i = d_i \int \frac{d^3k}{(2\pi)^3}\, \frac{1}{e^{(\omega_i(k)-\mu_i)/T} - \xi_i}. \tag{56}$$

However, in the classical approximation, we have $\nu_{ki} \ll 1$ [see the definition (16)] and Eq. (56) is reduced to the expression

$$n_i = d_i \int \frac{d^3k}{(2\pi)^3} e^{-(\omega_i(k)-\mu_i)/T} = \chi_i(T) e^{\mu_i/T}.$$

Here, the second equality defines $\chi_i(T)$, which relates to the chemical potential as

$$\mu_i = T \ln\left(\frac{n_i}{\chi_i(T)}\right). \tag{57}$$

Thus, for the internal energy density, we obtain

$$\varepsilon = 3T\sum_i n_i + B, \tag{58}$$

whereas the pressure is given by

$$p = T\sum_i n_i - B. \tag{59}$$

These equations constitute the classical approximation to the familiar MIT bag model [2, 31], being a popular approach of investigating the thermodynamics of the quark–gluon plasma.

4.2. Temperature-Dependent Scalar Mean Field

The temperature-dependent scalar mean field accounts for a temperature-dependent mass. In this situation, for the one-component system, the quasiparticle spectrum is given by [cf. (27)]

$$\epsilon_k(T,n) = \sqrt{k^2 + m^2(T)}, \tag{60}$$

the corresponding scalar density [cf. Eq. (29)] depending only on temperature. The gluon and quark plasma (at zero baryon density) is of particular interest, where approximately

$$m^2(T) = m_0^2 + g^2T^2. \tag{61}$$

Neglecting the derivative of the slowly changing temperature function $g(T)$, from Eq. (60), we obtain

$$\frac{\partial\epsilon_k}{\partial T} = \frac{m(T)}{\epsilon_k}\frac{dm(T)}{dtT} = \frac{g^2T}{\epsilon_k}. \tag{62}$$

Hence, the $C_T = 0$ constraint leads to

$$\frac{\partial\Phi}{\partial T} + g^2Td\int\frac{d^3k}{(2\pi)^3}\frac{\nu_k}{\epsilon_k} = 0. \tag{63}$$

In the high-temperature regime, the influence of m_0 can be ignored, and for chemical equilibrium ($\mu = 0$), one obtains

$$\varepsilon = \mathcal{K}T^4 + B, \quad p = \frac{1}{3}\mathcal{K}T^4 - B, \tag{64}$$

where $\mathcal{K}$ is given by the integral

$$\mathcal{K} = d\int\frac{d^3x}{(2\pi)^3}\frac{1}{e^{\sqrt{x^2+g^2}} - \xi}\frac{x^2 + \frac{3}{4}g^2}{\sqrt{x^2+g^2}}. \tag{65}$$

The $g = 0$ case provides the original MIT-bag EoS.

4.3. Density-Dependent Mean Field

Our next example deals with a system of quasiparticles of a single sort with the density-dependent spectrum justified in Section 3:

$$\epsilon_k(T,n) = \omega(k) + An^{-\gamma}, \tag{66}$$

where A and γ have been discussed above. In this case, Eqs. (21) and (22) give rise to the following form of the background energy density:

$$\Phi(n) = \frac{\gamma}{1-\gamma}An^{1-\gamma}. \tag{67}$$

Hence, in the Boltzmann approximation, we find

$$\mu = T\ln\frac{n}{\chi(T)} + An^{-\gamma}, \tag{68}$$

whereas for the internal energy and pressure one can derive

$$\varepsilon = \frac{nd}{\chi(T)}\int\frac{d^3k}{(2\pi)^3}\omega(k)e^{-\omega(k)/T} + \frac{1}{1-\gamma}An^{1-\gamma}, \tag{69}$$

$$p = nT - \frac{\gamma}{1-\gamma}An^{1-\gamma}. \tag{70}$$

As follows from our consideration in Section 3, $0 < \gamma < 1$. In this case, the chemical potential grows with decreasing density (e.g., due to string pulling), and therefore such systems reveal a strong tendency to form clusters. Free sources of strings, or long strings, respectively, will eventually be purged out of the system.

4.4. Massless Gluons with String Interaction

Let us consider in more detail the case given by Eq. (66) for massless $SU(3)$ gluons. The choice $\gamma = 1/3$ and $A = (2/3)\sigma$ satisfies Eqs. (49) and (51) at $a \approx r_0 = (3/4\pi n)^{1/3}$. The relation between density and nonequilibrium chemical potential [see Eq. (10)] is now given by

$$n = d\int\frac{d^3k}{(2\pi)^3}\frac{1}{e^{(k+\frac{2}{3}\sigma n^{-1/3}-\mu)/T} - 1}. \tag{71}$$

In the Boltzmann approximation, which is quite appropriate to the system of interest, this equation yields

$$\mu = \frac{2}{3}\sigma n^{-1/3} + T\ln\frac{n}{\chi(T)}, \tag{72}$$

where $\chi(T)$ is proportional to T^3:

$$\chi(T) = (\lambda T)^3, \quad \lambda = \left(\frac{d}{\pi^2}\right)^{1/3}. \tag{73}$$

We seek the solution of the chemically equilibrium state defined by $\mu = 0$,

$$n_{\rm eq} = \chi(T)e^{-\frac{2}{3}\sigma n_{\rm eq}^{-1/3}/T}. \tag{74}$$

This can be transformed into a simple transcendental equation by denoting

$$z = Tn_{\rm eq}^{-1/3}, \qquad \tilde\sigma = \frac{2}{9}\frac{\sigma}{T^2}. \tag{75}$$

We get

$$\lambda z = e^{\tilde\sigma z}. \tag{76}$$

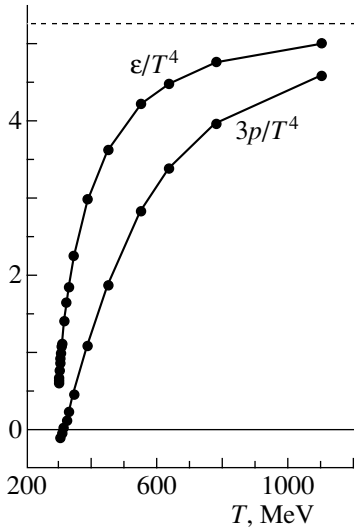

Fig. 1. Normalized energy density and pressure of a massless gluon gas with string-like interaction. Dashed line demonstrates the Stephan–Boltzmann regime corresponding to the case of a gas of noninteracting gluons.

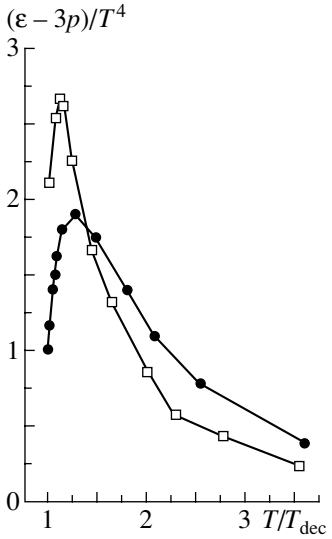

Fig. 2. The interaction measure $(\varepsilon - 3p)/T^4$ of the $SU(3)$ gluon system: circles are our data for the massless gluons interacting via screened strings; squares show the lattice results from [32]. Our data are plotted for the case $T_{\rm dec} = 303$ MeV.

This equation has no real solution above the value of $\tilde{\sigma}$ corresponding to a temperature, $T_{\rm chem}$. At this chemical critical temperature, the left-hand side and right-hand side of Eq. (76) and their derivatives should be equal to each other. Thus, the last condition gives

$$\lambda = \tilde{\sigma} e^{\tilde{\sigma} z_{\rm cr}}. \tag{77}$$

Comparing with Eq. (76), we obtain

$$z_{\rm cr} = 1/\tilde{\sigma}, \qquad \lambda = \tilde{\sigma} e, \tag{78}$$

where $e = e^1$. Finally reexpressing the temperature, we arrive at the result that, below the value

$$T_{\rm chem} = \sqrt{\frac{2e}{9\lambda}}\sqrt{\sigma}, \tag{79}$$

there is no equilibrium solution for the stringlike EoS. Assuming $SU(3)$ symmetry for massless gluons with $d = 16$ degrees of freedom, we have $\lambda \approx 1.175$ and arrive at the estimate

$$T_{\rm chem} \approx 0.718\sqrt{\sigma}, \tag{80}$$

which for $\sigma = 0.22$ GeV^2 gives $T_{\rm chem} \approx 337$ MeV. It is noteworthy that a similar relation between the color deconfinement temperature and string tension, $T_c = (0.60–0.65)\sqrt{\sigma} = 280–305$ MeV, has been obtained in the Monte Carlo simulation of the lattice $SU(3)$ quenched QCD [1, 32].

In Fig. 1 the quantities ε/T^4 and $3p/T^4$ are plotted as functions of the temperature for the system of gluons with the spectrum Eq. (66) beyond the Boltzmann approximation. As is seen, Eq. (80) indeed provides a good estimate for the limiting temperature $T_{\rm chem}$, which is now 303 MeV. The deviation of the pressure and energy curves from the ideal-gas value reflects essential attraction even at $\approx 2T_c$. It is now interesting to clarify to what extent our treatment of the in-medium string interactions agrees with the nonperturbative lattice QCD. This can be understood with the help of the special quantity $(\varepsilon - 3p)/T^4$ that is often called the interaction measure. This quantity is directly related to remnant interactions that survive in the high-temperature QCD phase because, for ideal massless quarks and gluons, $\varepsilon = 3p$. In Fig. 2, the interaction measure for the $SU(3)$ gluon plasma is shown. As is seen, our treatment of the in-medium strings provides quite reasonable results. The quantity $(\varepsilon - 3p)/T^4$ turns out to be very sensitive to the QCD interactions. Indeed, it is still equal to zero even in the one-gluon-exchange approximation, provided the temperature dependence of the running coupling constant is neglected. The agreement with the lattice calculations could be even better if we chose $\gamma \approx 2/3$, as in [33]. Thus, an interesting question arises as to what additional arguments, being able to change γ from 1/3 to 2/3, should be taken into account for our picture of the in-medium string screening. In this respect, the spatial correlations of color charges may be of importance (see Section 3).

In the transchemistry [11], the reduced effective value $\sigma = 0.5$ GeV/fm $= 0.1$ GeV^2 is used, which results in $T_{\rm chem} = 185$ MeV. It seems that the transchemistry model starts at slightly lower temperature where the chemical equilibrium for the quarks would not be possible at all. On the other hand, this simulation begins with a huge oversaturation of the quark

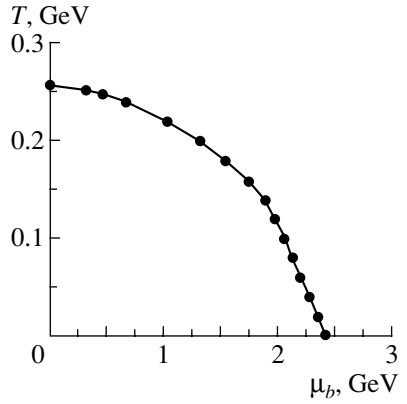

Fig. 3. The critical curve (line with closed circles) on the temperature–chemical potential plane, below which chemical equilibrium ceases for a massless quark gas with stringlike interaction.

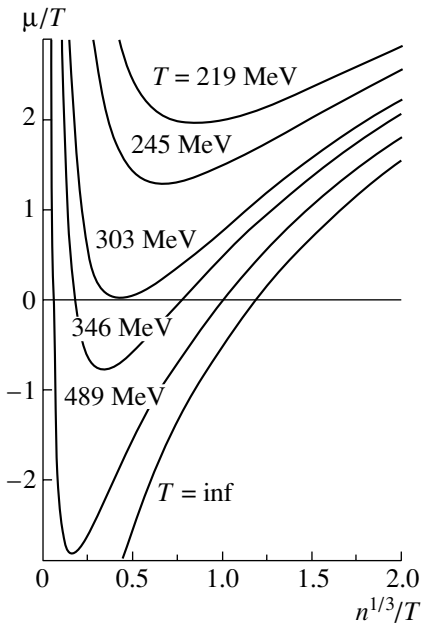

Fig. 4. The scaled chemical potential μ/T as a function of $n^{1/3}/T$ for massless Boltzmann gas with stringlike interaction. The chemical equilibrium condition is $\mu = 0$.

number, so a later reheating of the system brings the massive quark matter in an overcritical state. Eventually, expansion and cooling leads to dynamical hadronization at low temperatures ($T < T_{\rm chem}$), where the quark component cannot be in chemical equilibrium anymore.

Now, returning to the Boltzmann statistics, for the critical number density we have

$$n_{\rm chem} = \left(\frac{2\lambda}{9e}\,\sigma\right)^{3/2}. \qquad (81)$$

Substituting this quantity into Eq. (70) and taking $\gamma = 1/3$ and $A = (2/3)\sigma$, we get a negative pressure,

$$p_{\rm chem} = -\frac{2\lambda}{81e}\sigma^2, \qquad (82)$$

at the critical point. It means that the mechanical equilibrium ceases at a somewhat higher temperature than the chemical one.

Equations similar to Eq. (76) were considered by Boal, Schachter, and Woloshin [15] and by Moskalenko and Kharzeev [17] as well. However, investigation of the quark plasma at zero baryon density, presented in the latter paper, did not take into account the important background term Φ. As to the former one, only the boundary for the high-temperature QCD phase, rather than the full thermodynamics, was studied without any reference to the problem of thermodynamic consistency. This is why one of the considered spectrum of unbound partons in that paper is not consistent with Eqs. (21) and (22). In addition, none of these papers uses the relevant classical approximation providing analytical results like Eqs. (79), (81), and (82), which would have significantly simplified the understanding. Finally, an advantage of our treatment is that it is based on the elaborated model of the in-medium string formation that enables us to derive the mean-field term (51) rather than postulate it by invoking the nearest neighbor approximation inspired by the analogy with the Ising model (see the third paper in [15]).

4.5. Fermions with String Interaction

Another interesting case is massless quarks at zero temperature. The number density integral is given by

$$n = \frac{d}{2\pi^2}\int \Theta(\mu - \frac{2}{3}\sigma n^{-1/3} - k)k^2 dk. \qquad (83)$$

Here, d is the color, light flavor, and spin degeneracy factor, and $\Theta(x)$ denotes the Heaviside step function. Expression (83) can be readily rewritten as

$$n = \zeta^3\left(\mu - \frac{2}{3}\sigma n^{-1/3}\right)^3 \qquad (84)$$

with $\zeta = (d/6\pi^2)^{1/3}$. In the situation considered, we have one conserved charge: the baryon number with the density $n_b = n/3$. Then, the chemical equilibrium is specified by the relation $\mu = \mu_b/3$, where μ_b is the baryon chemical potential (see Section 2). The magnitude of μ_b is determined by the equation

$$n_b = \frac{\zeta^3}{81}\left(\mu_b - \frac{2}{3^{1/3}}\sigma n_b^{-1/3}\right)^3.$$

Using $z = \zeta n_b^{-1/3}/3^{4/3}$, we get

$$\frac{1}{z} = \mu_b - \tilde{\sigma}_1 z \tag{85}$$

with $\tilde{\sigma}_1 = 6\sigma/\zeta$. Equation (85) has a solution provided

$$\mu_b \geq \mu_{\rm chem} = 2\sqrt{\tilde{\sigma}_1}, \tag{86}$$

i.e., the chemical potential (Fermi energy) is larger than the minimum value of $(\tilde{\sigma}_1 z + 1/z)$. It means that the Fermi energy of quarks should be larger than $2\sqrt{\tilde{\sigma}_1}/3$. A typical numerical value, $\mu_{\rm chem} \approx 2.442$ GeV, can be found using $d = 12$ and $\sigma = 0.18\ {\rm GeV}^2$.

At finite temperature, we obtain a T- and μ_b-dependent consistency equation, which can be solved only numerically. Figure 3 shows the resulting boundary in the $T\mu_b$ plane.

4.6. Chemical Off-Equilibrium in the Classical Approximation

If an isolated system is out of chemical equilibrium and expands as a perfect fluid, the relation

$$dE + pdV = TdS + \sum_i \mu_i dN_i = 0 \tag{87}$$

is fulfilled and the entropy production rate

$$\dot{S} = -\sum_i \frac{\mu_i}{T}\dot{N}_i \tag{88}$$

is either positive or zero. This means that, in the one-component case for quasiparticles with positive μ, the corresponding particle number $N = Vn$ decreases, while it increases for negative values of μ.

Figure 4 shows the off-equilibrium chemical potential scaled with the temperature, μ/T as a function of the scaled density $n^{1/3}/T$ for a one-component, massless Boltzmann gas made of particles with the $SU(3)$-gluon degrees of freedom and interacting via strings. Chemical equilibrium corresponds to $\mu = 0$, which is not reachable below a certain temperature. Here, the strings pull the charges together, never reaching a screened equilibrium state: the chemical potential remains positive, driving the density of this component towards zero.

The situation is more complicated in a many-component mixture due to possible constituent exchange between different species of quasiparticles. In both cases, the chemical equilibrium, corresponding to $\mu_i = 0$, is stable. In some special cases for nonideal EoS, it may happen that the $\mu(n,T)$ curve for a constant T (isoterm) does not cross the $\mu = 0$ line at all; i.e., no chemical equilibrium is possible and the system is driven towards a state with either zero or infinite particle numbers. In a many-component system, it means that this particular component will dominate or vanish in the mixture.

Another remark concerns with the chemical potential assigned to the conserved charges (e.g., baryon number). This is a physically different situation when the term $-\mu_b Q_b$ (see Section 2) is added to the Hamiltonian, which is not compensated by its expectation value in the background field. As a consequence, the chemical equilibrium point (if any) is placed not at $\mu = 0$ but at $\mu = \mu_{\rm B}$. This situation is quite customary in nuclear physics.

5. CONCLUSION

A useful representation of the conditions of thermodynamic consistency of quasiparticle description, Eqs. (21) and (22), has been found. The advantage of this representation is that it directly involves the effective quasiparticle spectra, which results in important restrictions on the form of these spectra. In particular, two essential findings can be mentioned. If the interaction with surrounding matter is taken into account by introducing a mean field, the latter should be either temperature-independent (Example 1, Section 2) or, when in-medium effects are included in the Hamiltonian by means of the effective mass (Example 2, Section 2), this mass should depend on the temperature or/and the quasiparticle density exclusively through the scalar density of quasiparticles. In the large market of available phenomenological models, these general restrictions in the majority of cases were used intuitively, but sometimes were erroneously missed.

The structure of the thermodynamic potential, derived from the medium-dependent Hamiltonian in a thermodynamically consistent way, has been further detailed by implementing the string picture for the interaction between generic constituents. With this aim, the elaborated mean-field model of the in-medium string interactions has been developed. This model supports the use of the inverse power of the color charge density in the color mean field [see Eq. (51)] that was introduced earlier by various authors assuming validity of the nearest neighbor approximation [15–17]. Results of our treatment of the in-medium strings are found to be in reasonable agreement with the lattice data on QCD thermodynamics. Further probing of these interactions can be an application of the developed equation of state to (hydro)dynamical calculations allowing direct comparison with observables. Some steps towards this direction have been done recently by analyzing the excitation function for nucleon directed flow [34] and the relation of the "softest point" of EoS with chemical freeze-out [35] in heavy-ion collisions.

Along with other results, we would like to comment on the excluded volume modification of the single-particle energy. In our treatment, the conditions $C_T = 0, C_1 = 0$ have no solution in this case without some additional assumptions. A resolution of this issue was done in [8] and in the first paper of [12].

ACKNOWLEDGMENTS

A.A.S. and V.D.T. are grateful to KFKI Research Institute and the heavy-ion group of Prof. Zimányi for the kind hospitality during their visits to Hungary supported by the Fund for Scientific Collaborations MTA–Dubna. Discussions with B. Müller, D. Blaschke, D. Rischke, J. Zimányi, and P. Lévai are gratefully acknowledged.

This work has been supported by the Hungarian National Fund for Scientific Research OTKA (project no. T034269). V.D.T. was also partially supported by DFG (project no. 436 Rus 113/558/0-2) and the Russian Foundation For Basic Research (project no. 03-02-04008-NNIO).

REFERENCES

1. F. Karsch, E. Laermann, A. Peikert, *et al.*, Nucl. Phys. B (Proc. Suppl.) **94**, 411 (2001); F. Karsch, E. Laermann, and A. Peikert, Phys. Lett. B **487**, 447 (2000); Nucl. Phys. B **605**, 579 (2001).
2. A. Chodos, R. L. Jaffe, K. Johnson, and C. B. Thorn, Phys. Rev. D **10**, 2599 (1974); K. Johnson and C. B. Thorn, Phys. Rev. D **13**, 1934 (1976); K. Johnson, Phys. Lett. B **78B**, 259 (1978); J. F. Donoghue and K. Johnson, Phys. Rev. D **21**, 1975 (1980); P. Hasenfratz and J. Kuti, Phys. Rep. **40**, 75 (1978); B. K. Patra and C. P. Singh, Z. Phys. C **74**, 699 (1997); R. Hofmann, T. Gutsche, M. Schumann, and R. D. Viollier, Eur. Phys. J. C **16**, 677 (2000).
3. R. Giles, Phys. Rev. D **13**, 1670 (1976).
4. G. A. Miller, A. W. Thomas, and S. Theberge, Phys. Lett. B **91B**, 192 (1980); S. Theberge, A. W. Thomas, and G. A. Miller, Phys. Rev. D **22**, 2838 (1980); **23**, 2106 (1981); A. W. Thomas, S. Theberge, and G. A. Miller, Phys. Rev. D **24**, 216 (1981); S. Lee and K. J. Kong, Phys. Lett. B **202**, 21 (1988); G. G. Bunatian, Yad. Fiz. **49**, 1071, 1363 (1989) [Sov. J. Nucl. Phys. **49**, 664, 847 (1989)]; Y. Futami and S. Akiyama, Prog. Theor. Phys. **84**, 377 (1990); G. A. Miller and A. W. Thomas, Phys. Rev. C **56**, 2329 (1997).
5. P. Lévai and U. Heinz, Phys. Rev. C **57**, 1879 (1998).
6. A. Peshier, B. Kämpfer, and G. Soff, Phys. Rev. C **61**, 045203 (2000); B. Kämpfer, A. Peshier, and G. Soff, J. Phys. G **27**, 535 (2001).
7. J. Rafelski and R. Hagedorn, in *Proceedings of Symposium on Statistical Mechanics of Quarks and Hadrons, Bielefeld, Germany, 1980*; Phys. Lett. B **97B**, 136 (1980); *Workshop on Hadronic Matter at Extreme Energy Density, Erice, Italy, 1978*.
8. J. Cleymans, M. I. Gorenstein, J. Stalnacke, and E. Suhonen, Phys. Scr. **48**, 277 (1993); V. K. Tiwari, N. Prasad, and C. P. Singh, Phys. Rev. C **58**, 439 (1998); V. K. Tiwari, K. K. Singh, N. Prasad, and C. P. Singh, Nucl. Phys. A **637**, 159 (1998); M. I. Gorenstein, A. P. Kostyuk, and Y. D. Krivenko, J. Phys. G **25**, L75 (1999); A. Kostyuk, M. I. Gorenstein, S. Stoecker, and W. Greiner, Phys. Rev. C **63**, 044901 (2001).
9. E. G. Nikonov, V. D. Toneev, and A. A. Shanenko, Yad. Fiz. **62**, 1301 (1999) [Phys. At. Nucl. **62**, 1226 (1999)]; E. Nikonov, A. Shanenko, and V. Toneev, Heavy Ion Phys. **8**, 89 (1998).
10. H. W. Barz, B. L. Friman, J. Knoll, and H. Schulz, Nucl. Phys. A **484**, 661 (1988); **519**, 831 (1990); Phys. Rev. D **40**, 157 (1989); Phys. Lett. B **242**, 328 (1990).
11. T. S. Biró, P. Lévai, and J. Zimányi, J. Phys. G **25**, 1311 (1999); Phys. Rev. C **59**, 1574 (1999).
12. A. A. Shanenko, E. P. Yukalova, and V. I. Yukalov, Physica A **197**, 629 (1993); Yad. Fiz. **56**, 151 (1993) [Phys. At. Nucl. **56**, 372 (1993)].
13. M. I. Gorenstein and S. N. Yang, Phys. Rev. D **52**, 5206 (1995); J. Phys. G **21**, 1053 (1995).
14. T. Celik, F. Karsch, and H. Satz, Phys. Lett. B **97B**, 128 (1980); H. Satz, Nucl. Phys. A **642**, 130 (1998); S. Fortunato and H. Satz, Phys. Lett. B **475**, 311 (2000); S. Fortunato, F. Karsch, P. Petreczky, and H. Satz, Nucl. Phys. B (Proc. Suppl.) **94**, 204 (2001).
15. K. A. Olive, Nucl. Phys. B **190**, 483 (1981); **198**, 461 (1982); D. H. Boal, J. Schachter, and R. M. Woloshin, Phys. Rev. D **26**, 3245 (1982).
16. D. Blaschke, F. Reinholz, G. Röpke, and D. Kremp, Phys. Lett. B **151B**, 439 (1985).
17. M. Plumer, S. Raha, and R. M. Weiner, Nucl. Phys. A **418**, 549 (1984); V. V. Balashov, I. V. Moskalenko, and D. E. Kharzeev, Yad. Fiz. **47**, 1740 (1988) [Sov. J. Nucl. Phys. **47**, 1103 (1988)]; I. V. Moskalenko and D. E. Kharzeev, Yad. Fiz. **48**, 1122 (1988) [Sov. J. Nucl. Phys. **48**, 713 (1988)].
18. S. Kagiyama, A. Minaka, and A. Nakamura, Prog. Theor. Phys. **89**, 1227 (1993); **95**, 793 (1996); hep-ph/0101036; hep-ph/0202108.
19. D. H. Rischke, M. I. Gorenstein, H. Stöcker, and W. Greiner, Z. Phys. C **51**, 485 (1991); Q. R. Zhang, Z. Phys. A **351**, 89 (1995).
20. N. Prasad, K. K. Singh, and C. P. Singh, Phys. Rev. C **62**, 037903 (2000).
21. N. N. Bogoliubov and N. N. Bogoliubov, Jr., *Introduction to Quantum Statistical Mechanics* (World Sci., Singapore, 1982), Sections 3.4.1 and 3.4.2.
22. U. Heinz, W. Greiner, and W. Scheid, J. Phys. G **5**, 1383 (1979); U. Heinz, P. R. Subramanian, H. Stöcker, and W. Greiner, J. Phys. G **12**, 1237 (1986).
23. J. I. Kapusta and K. A. Olive, Nucl. Phys. A **408**, 478 (1983).
24. J. Zimányi, B. Lukács, P. Lévai, *et al.*, Nucl. Phys. A **484**, 647 (1988).

25. D. V. Anchishkin, Sov. Phys. JETP **75**, 195 (1992); D. Anchishkin and E. Suhonen, Nucl. Phys. A **586**, 734 (1995); V. K. Tiwary, N. Prasad, and C. P. Singh, Phys. Rev. C **58**, 439 (1998).
26. J. D. Walecka, Ann. Phys. (N. Y.) **83**, 491 (1974); Phys. Lett. B **59B**, 109 (1975).
27. V. Goloviznin and H. Satz, Z. Phys. C **57**, 671 (1993).
28. D. H. Rischke, Nucl. Phys. A **583**, 663 (1995).
29. Pin-zhenBi and Yao-mingShi, Z. Phys. C **75**, 735 (1997).
30. A. A. Shanenko, Phys. Rev. E **54**, 4420 (1996).
31. E. Suhonen, J. Cleymans, and J. Stalnacke, Nucl. Phys. B (Proc. Suppl.) **24**, 260 (1991); J. Cleymans, M. Marais, and E. Suhonen, Phys. Rev. C **56**, 2747 (1997); A. Keranen, J. Cleymans, and E. Suhonen, J. Phys. G **25**, 275 (1999).
32. G. Boyd *et al.*, Nucl. Phys. B **469**, 419 (1996).
33. V. D. Toneev, E. G. Nikonov, and A. A. Shanenko, in *Nuclear Matter in Different Phases and Transitions*, Ed. by J.-P. Blaizot, X. Campi, and M. Ploszajczak (Kluwer A. P., 1999), p. 309; Preprint GSI-98-30 (Darmstadt, 1998).
34. Yu. Ivanov, N. Nikonov, W. Norenberg, *et al.*, Heavy Ion Phys. **15**, 117 (2002).
35. V. Toneev, J. Cleymans, E. Nikonov, *et al.*, J. Phys. G **27**, 827 (2001).

Physics of Atomic Nuclei, Vol. 66, No. 5, 2003, pp. 997–1004. From Yadernaya Fizika, Vol. 66, No. 5, 2003, pp. 1030–1037.

ELEMENTARY PARTICLES AND FIELDS
Theory

σ Meson in Hot and Dense Matter*

M. K. Volkov, **A. E. Radzhabov, and N. L. Russakovich**

Joint Institute for Nuclear Research, Dubna, Moscow oblast, 141980 Russia

Received April 1, 2002; in final form, July 15, 2002

Abstract—An important role of the scalar isoscalar σ meson in low-energy physics is discussed. The behavior of the σ meson in a hot and dense medium is studied. It is shown that, in the vicinity of the critical values of the temperature (T) and the chemical potential (μ), the σ meson can become a sharp resonance. This effect can lead to a strong enhancement of the processes $\pi\pi \to \gamma\gamma$ and $\pi\pi \to \pi\pi$ near the two-pion threshold. Experimental observation of this phenomenon can be interpreted as a signal of approaching the domain where the chiral symmetry restoration and the phase transition of hadron matter into quark–gluon plasma take place. © *2003 MAIK "Nauka/Interperiodica"*.

1. INTRODUCTION

In recent years, the problem of studying the scalar isoscalar σ-meson properties has attracted the attention of many authors [1, 2]. The subjects of investigations are internal properties of the σ-meson and its role as an intermediate particle in various processes, both in vacuum and in hot and dense matter. The latter problem is especially important, because many experiments on heavy-ion collision are performed and planned (CERN, Brookhaven, DESY, Darmstadt). One of the aims of those experiments is to study the problem of phase transition of hadron matter into quark–gluon plasma. Special workshops were dedicated to the study of the σ-meson properties in Japan (June 2000) [1] and in France (September 2001) [2]. Very interesting talks on this topic were given by Kunihiro [3–5]. In this article, we will follow these reports. However, here we will use the results obtained only in our previous works.

Let us start with the experimental status of the σ meson. The experimental value of the σ-meson mass is not accurately determined and lies in a wide interval [6]:

$$M_\sigma = 400\text{–}1200 \text{ MeV}. \quad (1)$$

This can be explained by large values of the decay width of this meson into two pions [6]:[1)]

$$\Gamma_\sigma = 600\text{–}1000 \text{ MeV}. \quad (2)$$

However, at high temperature and density, M_σ can become lower than the mass of two pions. Therefore, the decay $\sigma \to \pi\pi$ is closed, and the σ meson becomes a stable particle. As a result, the σ meson can give sharp resonance when it participates in processes as an intermediate state.

Now let us describe the theoretical status of the σ meson. The σ meson is a chiral partner of the π meson in different linear $SU(2) \times SU(2)$ σ models [7]. On the other hand, it is a scalar isoscalar singlet in a $U(3) \times U(3)$-symmetric quark model of the Nambu–Jona-Lasinio (NJL) type [8].

In the NJL model, the σ meson mass can be expressed via the pion mass M_π and the constituent quark mass m:[2)]

$$M_\sigma^2 = M_\pi^2 + 4m^2. \quad (3)$$

Here, we assume that the constituent masses of up and down quarks are equal to each other: $m_u \approx m_d = m$.

Formula (3) plays a very important role in the description of different processes in hot and dense matter, where the σ meson participates as an intermediate particle. Indeed, from (3), it follows that, in vacuum, M_σ is larger than M_π because $m \approx 280$ MeV, $M_\pi \approx 140$ MeV, and $M_\sigma \approx 580$ MeV [8]. A different situation occurs in hot and dense matter in the vicinity of the critical values of the temperature and chemical potential, where $m \to m_0 \approx 0$ and $M_\sigma \to M_\pi$. This corresponds to the restoration of the chiral symmetry. As will be shown below, this behavior of M_σ can lead to the resonant enhancement of some processes, where the σ meson participates as an intermediate

*This article was submitted by the authors in English.

**e-mail: volkov@thsun1.jinr.ru

[1)]Note that for a long time information about the σ meson was absent in PDG and appeared only in 1998 as $f_0(400\text{–}1200)$.

[2)]We would like to note that, for a more accurate description of the mass spectra of scalar mesons, it is necessary to take into account the singlet–octet mixing of scalar isoscalar mesons with each other and with the scalar glueball [9, 10].

1063-7788/03/6605-0997$24.00

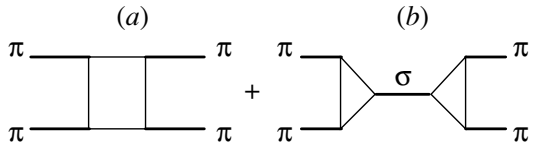

Fig. 1. The quark diagrams describing the $\pi\pi$ scattering. All loops in Figs. 1–4 consist of constituent quarks.

particle (for example, $\pi\pi \to \gamma\gamma$, $\pi\pi \to \pi\pi$). Observation of such effects, for instance, in heavy-ion collisions, could indicate approaching the domain of T, μ values where the phase transition from hadron matter into quark–gluon plasma appears. The possibility of such a phase transition and the chiral-symmetry restoration is a subject of intensive investigation at present.

The paper is organized as follows. In Section 2, we demonstrate the important role of the σ meson for the correct description of different processes in vacuum. In Section 3, we compare the behavior of the σ-meson propagator in vacuum and hot dense matter. We show that, in hot and dense matter, the σ-meson propagator can be a sharp resonance. Processes $\pi^+\pi^- \to \gamma\gamma$ and $\pi^0\pi^0 \to \gamma\gamma$ in vacuum and hot dense matter are investigated in Section 4. Noticeable enhancement of these reaction cross sections near the two-pion threshold in the vicinity of the critical T, μ values is found. In the last section, a short discussion of the results is given. Theoretical and experimental results concerning the $\pi\pi$-scattering process in hot and dense matter are discussed.

2. σ MESON IN VACUUM

Before describing the σ-meson properties in hot and dense matter, we show a very important role of the σ meson in a set of processes taking place in vacuum. Let us consider some of them here: $\pi\pi$ scattering, $\pi\pi \to \gamma\gamma$, the rule $\Delta I = 1/2$ (where I is the isospin of the meson system) in kaon decays and the calculation of the pion–nucleon Σ term in π–nucleon scattering. We give only a qualitative picture of these processes. Details can be found in the original works [11–16].

Let us start with $\pi\pi$ scattering. In the $SU(2) \times SU(2)$ chiral NJL model, this process can be described by the Lagrangian[3)]

$$L(q, \bar{q}, \sigma, \pi) \tag{4}$$
$$= \bar{q}(x)\left(i\hat{\partial} - M + g\left(\sigma(x) + i\gamma^5 \boldsymbol{\tau}\boldsymbol{\pi}(x)\right)\right) q(x),$$

where $\bar{q}(x) = (\bar{u}(x), \bar{d}(x))$ is the quark field; $\sigma(x)$ and $\boldsymbol{\pi}(x)$ are σ- and π-meson fields, respectively; M is the diagonal mass matrix of the constituent quarks; $\boldsymbol{\tau}$ are the Pauli matrices; and g is the quark–meson strong coupling constant

$$g = (4I_2)^{-1/2}, \tag{5}$$

where I_2 is a logarithmical divergent integral that appears in the quark loop. I_n $(n = 1, 2)$ is equal to

$$I_n = \frac{N_c}{(2\pi)^4}\int d^4_{\rm E}k \frac{\Theta(\Lambda^2 - k^2)}{(m^2 + k^2)^n}, \tag{6}$$

where Λ is a cut off parameter ($\Lambda = 1.25$ GeV) [8], the symbol $d^4_{\rm E}k$ stands for the integration in the Euclidean metric, and N_c is the number of quark colors.

Diagrams describing $\pi\pi$ scattering are given in Fig. 1. Then, using Lagrangian (4), we obtain the following expression for the amplitude $A_{\pi\pi}$ [8, 11]:

$$A_{\pi\pi} = -4g^2 + \frac{(4mg)^2}{M_\sigma^2 - s} = \frac{s - M_\pi^2}{F_\pi^2}, \tag{7}$$

where $F_\pi = 93$ MeV is the pion weak decay constant and $s = (p_1 + p_2)^2$, p_1 and p_2 being the momenta of the incoming pions.

The final expression for $A_{\pi\pi}$ is the famous formula that describes the $\pi\pi$-scattering amplitude at low energies. This formula was first obtained by Weinberg in the 1960s. It was one of the basic formulas demonstrating the chiral symmetry of strong interaction [7]. The following relations were used to derive this formula:

(i) The Goldberger–Treiman identity $g = m/F_\pi$;

(ii) The formula for the σ-meson mass (3);

(iii) The amplitude for the $\sigma \to \pi^+\pi^-$ decay $A_{\sigma\to\pi^+\pi^-} = 4mg$.

We can see from Eq. (7) that the constant part of the σ-pole diagram cancels the contribution of the box diagram. The remaining part of the σ-pole diagram determines the s dependence of the $\pi\pi$-scattering amplitude in agreement with the chiral symmetry requirements [7].

The σ-pole diagram plays an important role for describing the polarizability of the pion, which is a significant characteristic of its electromagnetic structure [8, 17, 18]. The σ meson is also necessary for description of the processes $\pi\pi \to \gamma\gamma$ and $\gamma\pi \to \gamma\pi$ in hot and dense matter [12, 13]. Below, we will discuss the process $\pi\pi \to \gamma\gamma$ in detail.

The famous rule $\Delta I = 1/2$ is connected with an experimentally observable enhancement of the decay $K_S \to \pi\pi$ as compared with kaon decays with $\Delta I = 3/2$. This effect can be explained by the presence of the channel with the intermediate σ meson (see Fig. 2) in this process. Indeed, the σ-pole diagram

[3)] For simplicity, we do not take into account π–a_1 transitions (a_1 is the axial-vector meson).

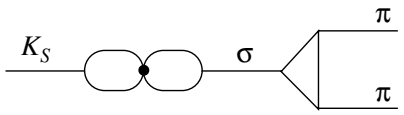

Fig. 2. The diagram describing the $K_S \to \pi\pi$ decay with $\Delta I = 1/2$. The dot is a weak vertex.

in the process $K_S \to \pi\pi$ leads to the appearance of a resonance factor in the decay amplitude. This factor takes the form

$$\frac{1}{M_\sigma^2 - M_{K_S}^2 - iM_\sigma\Gamma_\sigma}, \tag{8}$$

where Γ_σ is the decay width of the σ meson. The kaon mass M_{K_S} is close to the σ-meson mass. That gives a noticeable enhancement of this channel as compared with the channels with $\Delta I = 3/2$, where the σ-pole diagram cannot exist and pions are emitted directly from quark loops containing a weak vertex [14].

We would also like to emphasize an important role of the σ-pole diagram in the calculation of the pion–nucleon Σ term [15, 16]. The value of the Σ term is determined by diagrams in Fig. 3. These diagrams lead to the following expression (see [16]):

$$\langle\pi^+(0)|\bar{u}u + \bar{d}d|\pi^+(0)\rangle \tag{9}$$
$$= 4m\left[1 + (I_1 - 2m^2 I_2)\frac{8g^2}{M_\sigma^2}\right].$$

In this formula, the first term corresponds to the triangle quark diagram (Fig. 3a) and the second term corresponds to the σ-pole diagram (Fig. 3b).

Taking into account the relations $g = (4I_2)^{-1/2} = m/F_\pi$ and $M_\sigma \approx 2m$, we see that the first term is canceled by the part of the second term containing I_2. The remaining part of Eq. (9) takes the form[4)]

$$\langle\pi^+(0)|\bar{u}u + \bar{d}d|\pi^+(0)\rangle \tag{10}$$
$$\approx 4m\left[2I_1\frac{g^2}{m^2} = 2\frac{I_1}{F_\pi^2} \approx 5.8\right].$$

It is easy to see that the contribution from the sum of diagrams a and b in Fig. 3 is 5.8 times as large as the contribution from diagram a. As a result, in our work [15], the Σ term for πN, was found to be $\Sigma_{\pi N} = 50 \pm 10$ MeV. Note that, in [19–21], where the πN Σ term was calculated in the framework of nonlinear chiral models, the authors obtained a small value for the Σ term because they did not take into account the contribution from the scalar σ meson.

[4)]Here, we neglect the momentum and mass of the pion and use the formula $I_1 = 3\left(\Lambda^2 - m^2\ln(\Lambda^2/m^2 + 1)\right)/(4\pi)^2 = 0.025\ \mathrm{GeV}^2$.

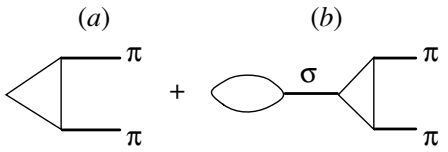

Fig. 3. The quark diagrams describing the matrix element $\langle\pi^+(0)|\bar{u}u + \bar{d}d|\pi^+(0)\rangle$. The left vertices are scalar quark vertices interacting with a nucleon.

3. σ-MESON PROPAGATOR IN VACUUM AND HOT DENSE MATTER

Up to now, we have considered the above-mentioned processes only in vacuum. Now let us study the σ-meson properties in hot and dense matter. It is especially interesting to investigate the behavior of the σ-meson propagator for the process $\pi\pi \to \pi\pi$, $\pi\pi \to \gamma\gamma$

$$\Delta_\sigma(s) = \frac{1}{M_\sigma^2 - s - iM_\sigma\Gamma_\sigma(s)}, \tag{11}$$

where $s = (p_1 + p_2)^2$, p_1 and p_2 being the momenta of the incoming pions. The decay width Γ_σ in the NJL model has the form

$$\Gamma_\sigma(s) = \frac{3m^4}{2\pi M_\sigma F_\pi^2}\sqrt{1 - \frac{4M_\pi^2}{s}}. \tag{12}$$

In vacuum, when $T = 0$ and $\mu = 0$ and the constituent quark mass is $m = 280$ MeV, we can consider two extreme cases:

(i) $s \approx M_\sigma^2$. In this case, the real part of the denominator of $\Delta_\sigma(s)$ (11) is equal to zero but the imaginary part is large: $M_\sigma\Gamma_\sigma \approx 0.3\ \mathrm{GeV}^2$.

(ii) $s \approx 4M_\pi^2$. In this case, the imaginary part of the denominator is close to zero; however, its real part is large: $M_\sigma^2 - 4M_\pi^2 \approx 0.25\ \mathrm{GeV}^2$.

Therefore, in vacuum, the real and imaginary parts of the denominator cannot be close to zero simultaneously, and the σ-pole diagram cannot give a sharp resonance in the whole energy domain.

A more interesting situation can arise in a hot and dense medium. The constituent quark mass decreases and the pion mass slightly increases with increasing T and μ. Therefore, the case where $4m^2 \approx 3M_\pi^2$ is possible. Then, if we consider the above-mentioned processes near the two-pion threshold at $s = 4M_\pi^2(1 + \epsilon)$ ($\epsilon \ll 1$), we can see that the real and imaginary parts of the $\Delta_\sigma(s)$ denominator become very small simultaneously:

$$\mathrm{Re}\left(\Delta_\sigma(s)^{-1}\right) \tag{13}$$
$$= M_\sigma^2 - s = 4m^2 - 3M_\pi^2 - 4M_\pi^2\epsilon \approx -4M_\pi^2\epsilon,$$
$$\mathrm{Im}\left(\Delta_\sigma(s)^{-1}\right) = -M_\sigma\Gamma_\sigma \tag{14}$$

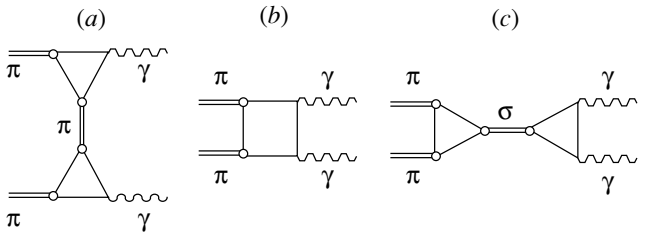

Fig. 4. The quark diagrams describing the matrix element $\pi\pi \to \gamma\gamma$.

$$= -\frac{3m^4}{2\pi F_\pi^2}\sqrt{\frac{\epsilon}{1+\epsilon}} \approx -\frac{3m^4}{2\pi F_\pi^2}\sqrt{\epsilon}.$$

As a result, the propagator takes the form

$$\Delta_\sigma \approx 1/\left(-4M_\pi^2\epsilon - i\frac{3m^4}{2\pi F_\pi^2}\sqrt{\epsilon}\right). \qquad (15)$$

The formula shows that, in hot and dense matter in the vicinity of the critical T and μ values, the σ-meson propagator can become a sharp resonance. This leads to a noticeable enhancement of processes where the σ meson participates as an intermediate particle.

In the next section, we demonstrate this effect on the basis of the process $\pi\pi \to \gamma\gamma$ following [12, 13].

4. PROCESS $\pi\pi \to \gamma\gamma$ IN VACUUM AND HOT DENSE MATTER

To describe the processes $\pi^+\pi^- \to \gamma\gamma$ and $\pi^0\pi^0 \to \gamma\gamma$ it is necessary to consider quark loop diagrams of three types (see Fig. 4).

In Fig. 4, diagram *a* exists only for charged pions; diagrams *a* and *b* define the Born terms in a local approximation (see Fig. 5). In this approximation, only divergent parts of quark diagrams are considered and the Lagrangian for the photon–meson vertices takes the form

$$L^{\rm Born} = ieA_\mu\left[\pi^-\partial_\mu\pi^+ - \pi^+\partial_\mu\pi^-\right] + (A_\mu)^2\pi^+\pi^-. \qquad (16)$$

Here, π^+ and π^- are the charged pion fields and A_μ is the photon field. In the next order of the k^2 expansion, only diagrams *b* and *c* in Fig. 4 give nontrivial contributions. The Lagrangians corresponding to the vertices $\pi\pi \to \gamma\gamma$ and $\sigma \to \gamma\gamma$ take the form

$$L^{\rm box} = \frac{\alpha}{18\pi F_\pi^2}\left[\pi^+\pi^- + 5\pi^0\pi^0\right]F_{\mu\nu}^2, \qquad (17)$$

$$L^{\sigma\to\gamma\gamma} = \frac{5\alpha}{9\pi F_\pi}\sigma F_{\mu\nu}^2; \qquad (18)$$

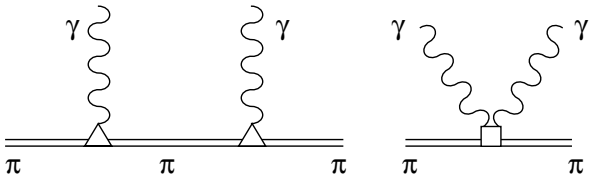

Fig. 5. The quark diagrams in the Born approximation describing the matrix element $\pi\pi \to \gamma\gamma$.

here, we use the notation $\alpha = e^2/(4\pi) \approx \frac{1}{137}$ (e is the electron charge); $F_{\mu\nu} = \partial_\mu A_\nu - \partial_\nu A_\mu$. The Lagrangian describing the vertex $\sigma \to \pi\pi$ has the form

$$L^{\sigma\pi\pi} = 2mg\sigma\boldsymbol{\pi}^2. \qquad (19)$$

These Lagrangians allow us to define the total amplitude describing processes $\pi\pi \to \gamma\gamma$:[5)]

$$T^{\mu\nu}(s) = T^{\mu\nu}_{\rm Born}(s) + T^{\mu\nu}_{k^2}(s), \qquad (20)$$

$$T^{\mu\nu}_{\rm Born}(s) = 2e^2\left[g^{\mu\nu} - \frac{p_1^\mu p_2^\nu}{p_1k_1} - \frac{p_2^\mu p_1^\nu}{p_2k_1}\right], \qquad (21)$$

$$T^{\mu\nu}_{k^2}(s) = e^2A(s)[g^{\mu\nu}k_1k_2 - k_1^\mu k_2^\nu], \qquad (22)$$

$$A(s) = \frac{1}{(6\pi F_\pi)^2}\left[\frac{40m^2}{M_\sigma^2 - s - iM_\sigma\Gamma_\sigma} - 1\right], \qquad (23)$$

where $s = (p_1+p_2)^2$; p_i and k_i are the momenta of the pions and photons, respectively; $g^{\mu\nu}$ is the metric tensor; and Γ_σ is the decay width of the σ meson [see (12)].

For the process $\pi^0\pi^0 \to \gamma\gamma$, the Born term is absent. The contribution of the box diagram increases by a factor of 10 [8].

The cross section of the process $\pi^+\pi^- \to \gamma\gamma$ consists of three parts:

$$\sigma_{\pi^+\pi^-\to\gamma\gamma} = \frac{\pi\alpha^2}{4s\kappa}\left[\tilde\sigma_1 + \tilde\sigma_2 + \tilde\sigma_3\right], \qquad (24)$$

where

$$\kappa = \sqrt{1 - \frac{4M_\pi^2}{s}}. \qquad (25)$$

Here, $\tilde\sigma_1$ corresponds to the Born term, $\tilde\sigma_3$ corresponds to contributions from the σ-pole and box diagrams, and $\tilde\sigma_2$ is the interference term of the Born and k^2-order contributions. For the neutral pion, we have only the $\tilde\sigma_3$ term and the box contribution is 10 times larger than in the case with charged pions. Further, we will consider these processes near the

[5)] Let us note that, in the Born approximation, only diagrams *a* and *b* (see Fig. 4) together give a gauge-invariant expression for amplitudes. In the k^2 order, diagrams *b* and *c* give a gauge-invariant expression separately.

two-pion threshold. Variables s and κ in this domain take the form

$$s = 4M_\pi^2(1+\epsilon), \quad \kappa = \sqrt{\frac{\epsilon}{1+\epsilon}}, \tag{26}$$

where $\epsilon \ll 1$. Then, for $\tilde{\sigma}_1$, $\tilde{\sigma}_2$, and $\tilde{\sigma}_3$, we have

$$\tilde{\sigma}_1 = 16\left[2 - \kappa^2 - \frac{1-\kappa^4}{2\kappa}\ln\frac{1+\kappa}{1-\kappa}\right], \tag{27}$$

$$\tilde{\sigma}_2 = 4s\mathrm{Re}A(s)\frac{1-\kappa^2}{\kappa}\ln\frac{1+\kappa}{1-\kappa},$$

$$\tilde{\sigma}_3 = s^2|A(s)|^2.$$

The $\tilde{\sigma}_3$ term has the form

$$\tilde{\sigma}_3 = \left((1+\epsilon)\left(\frac{M_\pi}{3\pi F_\pi}\right)^2\right)^2 \tag{28}$$

$$\times\left\{\left[\frac{40m^2a(s)}{a(s)^2 + M_\sigma^2\Gamma_\sigma^2} - 1\right]^2 + \frac{(40m^2M_\sigma\Gamma_\sigma)^2}{[a(s)^2 + M_\sigma^2\Gamma_\sigma^2]^2}\right\},$$

where $a(s) = M_\sigma^2 - s = M_\sigma^2 - 4M_\pi^2(1+\epsilon)$. This expression consists of two parts. The first part contains the contributions from the box diagram and from the real part of the σ-pole diagram (the expression in the square brackets). The second part corresponds to the contribution from the imaginary part of the σ-pole diagram. Both parts have the common small factor δ:

$$\delta = \left(\frac{M_\pi}{3\pi F_\pi}\right)^4. \tag{29}$$

Now, let us compare the behavior of $\tilde{\sigma}_1$ and $\tilde{\sigma}_3$ near the two-pion threshold $s = 0.1$ GeV^2 in vacuum and in a dense medium at $T = 100$ MeV and $\mu = 290$ MeV, where $m = 138$ MeV, $M_\pi = 156$ MeV, and $F_\pi = 57$ MeV [22]. The value of $\tilde{\sigma}_1$ changes very little from 12 in vacuum, where $\epsilon = 0.28$, to 15.5 in matter, where $\epsilon = 0.02$.

The opposite situation takes place for $\tilde{\sigma}_3$. Indeed, in vacuum, we have $\delta = 6.5 \times 10^{-4}$ and the main part of $\tilde{\sigma}_3$ is defined by the contribution connected with the real part of the σ-pole diagram:

$$\left(\frac{40m^2a}{a^2 + M_\sigma^2\Gamma_\sigma^2}\right)^2 \approx 84. \tag{30}$$

We can see that the contribution from $\tilde{\sigma}_3$ is very small compared to the contribution of the Born term in this case.

In hot and dense matter, the imaginary part of the σ-pole diagram gives a dominant contribution to $\tilde{\sigma}_3$. The parameter δ in this case equals 7×10^{-3}, and the main contribution from the imaginary part has the form

$$\left(\frac{40m^2}{M_\sigma\Gamma_\sigma}\right)^2 \approx 10^4 \qquad (a \ll M_\sigma\Gamma_\sigma). \tag{31}$$

As a result, the contribution from the σ-pole diagram becomes comparable with the contribution from the Born term.

This effect plays an especially important role for the neutral pion. In vacuum, the cross section of the process $\pi^0\pi^0 \to \gamma\gamma$ is very small. However, in hot and dense matter, the cross sections of the reactions $\pi^+\pi^- \to \gamma\gamma$ and $\pi^0\pi^0 \to \gamma\gamma$ can be comparable.

After qualitative estimations, let us give a more exact numerical calculation for the above-considered cases.

The value $s = 0.1$ GeV^2 corresponds to the energy of outgoing photons, $\omega_\gamma = 160$ MeV. In vacuum ($T = 0$, $\mu = 0$), we have the following values for masses m and M_σ and parameters ϵ and κ: $m = 280$ MeV, $M_\sigma = 580$ MeV, $\epsilon = 0.28$, $\kappa = 0.46$. Using these values, we obtain for the charged pions $\tilde{\sigma}_1 \approx 12$, $\tilde{\sigma}_2 \approx 1.8$, and $\tilde{\sigma}_3 \approx 0.1$. For the neutral pion, we have $\tilde{\sigma}_3 \approx 0.04$.

The cross sections $\sigma_{\pi^+\pi^-\to\gamma\gamma}$ and $\sigma_{\pi^0\pi^0\to\gamma\gamma}$ are approximately

$$\sigma_{\pi^+\pi^-\to\gamma\gamma} \approx 4.8\ \mu\mathrm{b}, \quad \sigma_{\pi^0\pi^0\to\gamma\gamma} \approx 0.015\ \mu\mathrm{b}. \tag{32}$$

Now, let us consider these processes in hot and dense matter when $T = 100$ MeV and $\mu = 290$ MeV. Here, the parameters ϵ and κ are equal to 0.02 and 0.14, respectively. The masses m, M_π, and M_σ and value of F_π are given above. After substituting the parameters and masses into (27), we obtain

$$\tilde{\sigma}_1 \approx 15.5, \quad \tilde{\sigma}_2 \approx 2.83, \quad \tilde{\sigma}_3 \approx 57.4 \tag{33}$$

for charged pions and

$$\tilde{\sigma}_3 \approx 57.5 \tag{34}$$

for neutral pions. For the cross sections $\sigma_{\pi^+\pi^-\to\gamma\gamma}$ and $\sigma_{\pi^0\pi^0\to\gamma\gamma}$, we have

$$\sigma_{\pi^+\pi^-\to\gamma\gamma} \approx 75.6\ \mu\mathrm{b}, \quad \sigma_{\pi^0\pi^0\to\gamma\gamma} \approx 57.5\ \mu\mathrm{b}. \tag{35}$$

So, we see that, in this domain of T and μ near the two-pion threshold, $\tilde{\sigma}_3$ increases dramatically. As a result, the cross section of the charged mode increases approximately by one and a half orders of magnitude. The cross section of the neutral mode increases by more than three orders of magnitude and becomes comparable with those of the charged mode.

The cross sections σ and σ_1, σ_2, and σ_3 ($\sigma_i = \pi\alpha^2\tilde{\sigma}_i/(4s\kappa)$, $i = 1,\ 2,\ 3$) of the process $\pi^+\pi^- \to \gamma\gamma$ are plotted in Figs. 6 and 7 as a function of s. Figure 6 shows the numerical results for vacuum, where the main contribution comes from the Born terms. The situation changes at a finite temperature and chemical potential. As is shown in Fig. 7, the σ-pole diagram gives the dominant contribution and the cross section strongly increases at the threshold. The behavior of the $\pi^0\pi^0 \to \gamma\gamma$ cross section is shown in

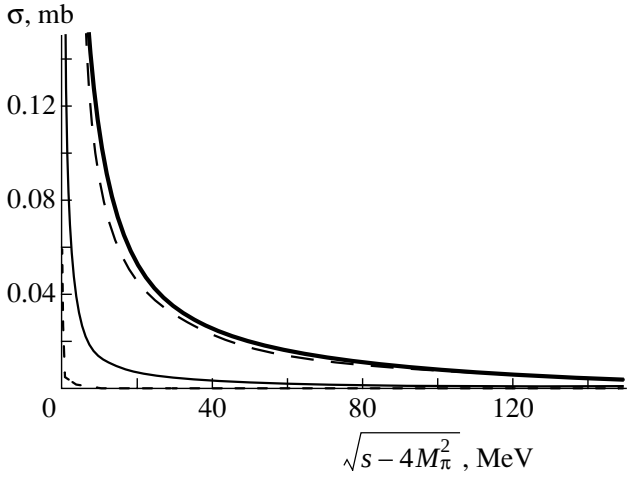

Fig. 6. The total cross section σ (thick solid curve) for the process $\pi^+\pi^- \to \gamma\gamma$ and partial cross sections σ_1 (long-dashed curve), σ_2 (thin solid curve), and σ_3 (short-dashed curve) in vacuum.

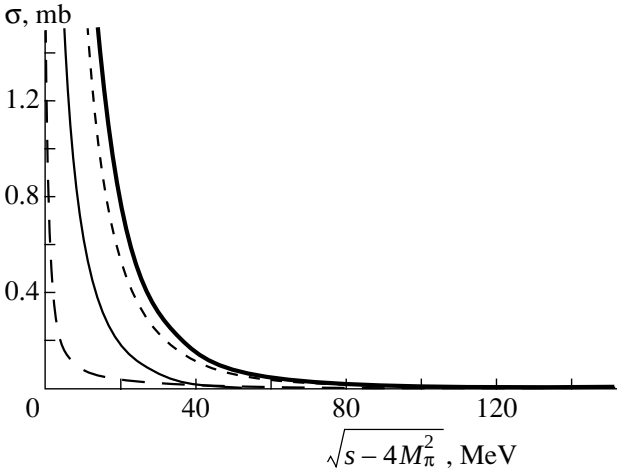

Fig. 7. The total cross section σ (thick solid curve) for the process $\pi^+\pi^- \to \gamma\gamma$ and partial cross sections σ_1 (long-dashed curve), σ_2 (thin solid curve), and σ_3 (short-dashed curve) in hot and dense matter at $T = 100$ MeV and $\mu = 290$ MeV.

Fig. 8 in vacuum and in hot and dense matter. It is easy to see from Fig. 8 that the contribution from the σ-pole diagram dramatically increases near the two-pion threshold.

Here, we used the approximate expression for the amplitudes where the dependence of quark loops on T and μ was neglected. A more careful calculation was made in [12, 13].

5. DISCUSSION AND CONCLUSION

We have shown that the scalar σ meson plays an important role in low-energy meson physics. The σ-pole diagram gives the main contribution to the $\pi\pi$-scattering amplitude and ensures its chiral invariance [8, 11, 23]. The intermediate σ meson gives a dominant contribution to charged pion polarizability in the process $\gamma\pi \to \gamma\pi$ [8, 17]. Using the σ-pole diagram, we can explain the rule $\Delta I = 1/2$ in kaon decays [14, 24]. The diagram with the σ meson determines the value of the pion–nucleon Σ term [15, 16, 25]. It is not a complete list of significant physical results where taking the σ meson into account allows us to describe hadron properties in vacuum correctly.[6)]

However, the behavior of the σ meson is especially interesting in a hot and dense medium. Here the σ meson can become a sharp resonance in the vicinity of the critical values of T and μ. This situation leads to a strong increase in the processes where the σ meson participates as an intermediate particle. In this work, we have demonstrated this effect on the basis of the process $\pi\pi \to \gamma\gamma$ (see [12, 13]). Similar results were obtained in [26, 27]. An analogous situation can also occur in the $\pi\pi$-scattering process.

The spectral function of a $\pi\pi$ system in the σ channel has been studied for finite densities in [3–5]. Characteristic enhancement of the spectral function near the two-pion threshold is found. This effect is close to our results obtained for the process $\pi\pi \to \gamma\gamma$ (see Section 4).

In [5], Kunihiro pointed out the first experimental support of his theoretical results. The CHAOS collaboration [28, 29] studied the differential cross sections $M^A_{\pi\pi} = d\sigma^A/dM_{\pi\pi}$ for the $\pi A \to \pi^+\pi^\pm A'$ reaction on nuclei $A = 2,\ 12,\ 40,\ 208$. The observable composite ratio

$$C^A_{\pi\pi} = \frac{M^A_{\pi\pi}\sigma^N_{\rm tot}}{M^N_{\pi\pi}\sigma^A_{\rm tot}} \tag{36}$$

was chosen to disentangle the acceptance issue because it is slightly dependent on the reaction mechanism and nuclear distortion (here, $\sigma^N_{\rm tot}$ and $\sigma^A_{\rm tot}$ are the total cross sections on the nucleon and nucleus, respectively). It was found that the $C^A_{\pi^+\pi^-}$ distributions for different nuclei peak at the $2m_\pi$ threshold and their yield increases as A increases. At the same time, the $C^A_{\pi^+\pi^+}$ distribution depends weakly on A. This means that nuclear matter weakly affects the $(\pi\pi)_{I,J=2,0}$ interactions, whereas the $(\pi\pi)_{I=J=0}$ state forms a

[6)]It is worth noting that, to describe the decay $\eta \to \pi^0\gamma\gamma$ in agreement with experiment, it is also necessary to take into account the channel with the intermediate scalar–isovector meson $a_0(980)$.

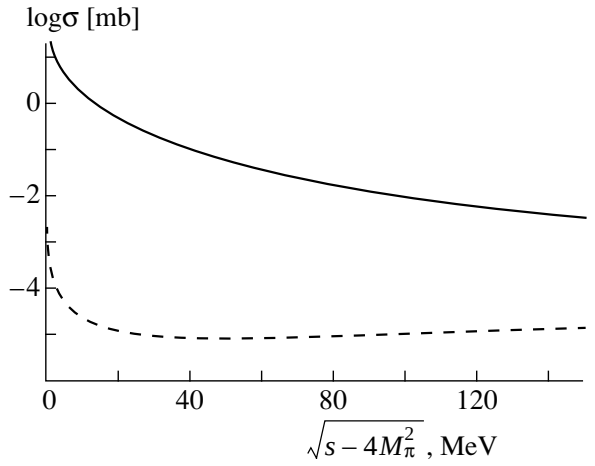

Fig. 8. The cross section for the process $\pi^0\pi^0 \to \gamma\gamma$ in vacuum (dashed curve) and in hot and dense matter at $T = 100$ MeV and $\mu = 290$ MeV (solid curve).

strongly interacting system (the intermediate σ meson). The experimental results were compared with some theoretical models, and the best agreement was found with the models that take into account the medium modifications of the scalar isoscalar σ meson and the partial restoration of chiral symmetry in nuclear matter.

The Crystal Ball (CB) Collaboration [30] studied the reaction $\pi^- A \to \pi^0\pi^0 A'$ on H, D, C, Al, and Cu. They reported that there was no peak near the $2m_\pi$ threshold, observed by the CHAOS Collaboration, but the increase in strength as a function of A was also observed in the $\pi^0\pi^0$ system. Later, the CB results were reanalyzed [31] in terms of the composite ratio (36) and accounting for different acceptances of the two experiments. It was shown that, as far as the $(\pi\pi)_{I=J=0}$ interacting system is concerned, the results agree with each other very well. This agreement may be interpreted as an independent confirmation by the CB experiment of the modification of the σ-meson properties in nuclear matter first reported by CHAOS.

The above-described experimental data for $\pi\pi$ scattering allow us to hope that similar results can be experimentally obtained for the processes $\pi\pi \to \gamma\gamma$ in hot and dense matter. It is especially interesting to study $\pi^0\pi^0 \to \gamma\gamma$, because the cross section of this process can increase by several orders of magnitude near the two-pion threshold. Experimental observation of all these effects will be evidence for approaching the boundary of the domain where the partial restoration of chiral symmetry and the phase transition of hadron matter into quark–gluon plasma take place.

ACKNOWLEDGMENTS

We thank D. Blaschke, T. Kunihiro, and E.A. Kuraev for fruitful discussions. M.K. Volkov acknowledges support by the Russian Foundation for Basic Research (project no. 02-02-16194) and the Heisenberg–Landau program. A.E. Radzhabov acknowledges support by UNESCO.

REFERENCES

1. *Proceedings of the International Workshop"Possible Existence of the σ Meson and Its Implications to the Hadron Physics", Kyoto, 2000,* Ed. by S. Ishida *et al.*, KEK Proc. 2001-4 (2001).
2. *Proceedings of the International Workshop on Chiral Fluctuations in Hadronic Matter, IPN Orsay, France, 2001* (in press).
3. T. Kunihiro, in *Proceedings of the International Workshop"Possible Existence of the σ meson and Its Implications to the Hadron Physics", Kyoto, 2000,* Ed. by S. Ishida *et al.*, KEK Proc. 2001-4 (2001), p. 6.
4. T. Hatsuda and T. Kunihiro, in *Proceedings of the International Workshop on Chiral Fluctuations in Hadronic Matter, IPN Orsay, France, 2001* (in press); nucl-th/0112027.
5. T. Kunihiro, hep-ph/0111121.
6. Review of Particle Physics, Eur. Phys. J. C **15**, 1 (2000).
7. V. De Alfaro, S. Fubini, G. Furlan, and C. Rossetti, *Currents in Hadron Physics* (Elsevier, New York, 1973).
8. M. K. Volkov, Sov. J. Part. Nucl. **17**, 186 (1986).
9. M. K. Volkov and V. L. Yudichev, Eur. Phys. J. A **10**, 109 (2001).
10. M. K. Volkov, M. Nagy, and V. L. Yudichev, Nuovo Cimento A **112**, 225 (1999).
11. M. K. Volkov and A. A. Osipov, Yad. Fiz. **39**, 694 (1984) [Sov. J. Nucl. Phys. **39**, 440 (1984)].
12. M. K. Volkov *et al.*, Phys. Lett. B **424**, 235 (1998).
13. E. A. Kuraev and M. K. Volkov, Yad. Fiz. **62**, 133 (1999) [Phys. At. Nucl. **62**, 128 (1999)].
14. A. N. Ivanov, N. I. Troitskaya, and M. K. Volkov, Yad. Fiz. **47**, 1157 (1988) [Sov. J. Nucl. Phys. **47**, 736 (1988)].
15. A. N. Ivanov, N. I. Troitskaya, M. Nagy, and M. K. Volkov, Phys. Lett. B **235**, 331 (1990).
16. M. Nagy, N. L. Russakovich, and M. K. Volkov, Acta Phys. Slov. **51**, 299 (2001).
17. M. K. Volkov and A. A. Osipov, Yad. Fiz. **41**, 1027 (1985) [Sov. J. Nucl. Phys. **41**, 659 (1985)].
18. M. K. Volkov *et al.*, Z. Phys. C **75**, 127 (1997).
19. J. Gasser and M. E. Sainio, hep-ph/0002283.
20. J. Gasser, H. Leutwyler, M. P. Locher, and M. E. Sainio, Phys. Lett. B **213**, 85 (1988).
21. P. Büttiker and Ulf-G. Meissner, Nucl. Phys. A **668**, 97 (2000); hep-ph/9908247.
22. D. Ebert, Yu. L. Kalinovskii, L. Munchow, and M. K. Volkov, Int. J. Mod. Phys. A **8**, 1295 (1993).

23. E. Quack *et al.*, Phys. Lett. B **348**, 1 (1995).
24. T. Morozumi, C. S. Lim, and A. I. Sanda, Phys. Rev. Lett. **65**, 404 (1990).
25. T. Kunihiro and T. Hatsuda, Phys. Lett. B **240**, 209 (1990); Nucl. Phys. B **387**, 715 (1992).
26. T. Kunihiro, Prog. Theor. Phys. Suppl. **120**, 75 (1995).
27. S. Chiku and T. Hatsuda, Phys. Rev. D **58**, 076001 (1998).
28. F. Bonutti *et al.*, Phys. Rev. Lett. **77**, 603 (1996).
29. F. Bonutti *et al.*, Nucl. Phys. A **677**, 213 (2000).
30. A. Starostin *et al.*, Phys. Rev. Lett. **85**, 5539 (2000).
31. P. Camerini *et al.*, nucl-ex/0109007.